RESERVOIR MODELING OF OLIGOCENE OSMANCIK FORMATION IN KARACALI-YULAFLI FIELD, THRACE BASIN BY USING SEDIMENTOLOGY, STATISTICS AND PETROPHYSICS

A THESIS SUBMITTED TO
THE GRADUATE SCHOOL OF NATURAL AND APPLIED SCIENCES
OF
MIDDLE EAST TECHNICAL UNIVERSITY

BY

TANER ARPACI

IN PARTIAL FULFILLMENT OF THE REQUIREMENTS
FOR
THE DEGREE OF DOCTOR OF PHILOSOPHY
IN
GEOLOGICAL ENGINEERING

AUGUST 2023

Approval of the thesis:

RESERVOIR MODELING OF OLIGOCENE OSMANCIK FORMATION IN KARACALI-YULAFLI FIELD, THRACE BASIN BY USING SEDIMENTOLOGY, STATISTICS AND PETROPHYSICS

submitted by **TANER ARPACI** in partial fulfillment of the requirements for the degree of **Doctor of Philosophy** i**n Geological Engineering, Middle East Technical University** by,

Prof. Dr. Halil Kalıpçılar
Dean, Graduate School of **Natural and Applied Sciences** _____

Prof. Dr. Erdin Bozkurt
Head of the Department, **Geological Engineering** _____

Prof. Dr. İsmail Ömer Yılmaz
Supervisor, **Geological Engineering, METU** _____

Prof. Dr. Serhat Akın
Co-Supervisor, **Petroleum and Natural Gas Eng., METU** _____

Examining Committee Members:

Prof. Dr. Sevinç Altıner
Geological Engineering, METU _____

Prof. Dr. İsmail Ömer Yılmaz
Geological Engineering, METU _____

Prof. Dr. Günay Çifçi
Geophysical Engineering, DEÜ _____

Prof. Dr. Emin Uğur Ulugergerli
Geophysical Engineering, ÇOMÜ _____

Assoc. Prof. Dr. Çağlar Sınayuç
Petroleum and Natural Gas Engineering, METU _____

Date: 23.08.2023

I hereby declare that all information in this document has been obtained and presented in accordance with academic rules and ethical conduct. I also declare that, as required by these rules and conduct, I have fully cited and referenced all material and results that are not original to this work.

Name Last name: Taner Arpacı

Signature:

ABSTRACT

RESERVOIR MODELING OF OLIGOCENE OSMANCIK FORMATION IN KARACALI-YULAFLI FIELD, THRACE BASIN BY USING SEDIMENTOLOGY, STATISTICS AND PETROPHYSICS

Arpacı, Taner
Doctor of Philosophy, Geological Engineering
Supervisor: Prof. Dr. İsmail Ömer Yılmaz
Co-Supervisor: Prof. Dr. Serhat Akın

August 2023, 371 pages

Several gas fields in Thrace basin, Turkey, have been developed and almost depleted in the last decade. Yulaflı-Karacalı field is located in the east of the basin and producing mainly from gas reservoirs of the Osmancık Formation. This is a very special field in terms of unexpected reservoir properties. An extension of Terzili Fault Zone is divided the field into two halves. In the field, deeper sections of the Osmancık Formation produces from the lower block of the fault zone, while its part in the upper block controversially does not or less produce.

The aim of this study is to characterize porosity and permeability variations and facies properties of deeper Osmancık Formation. The first objective is to interpret newly processed data and build a structural model to specify geometry. The second objective is to investigate the difference in facies and petrophysical behaviour of shallower and deeper parts of the Osmancık Formation in terms of geology and geophysics, using sedimentology and quantitative seismic interpretation. The final objective indicates a geological reservoir modeling study, including property and

facies modelling, to find answers to the questions mentioned above using geostatistical techniques such as Sequential Indicator Simulation and Sequential Gaussian Simulation. This study indicates that porosity and permeability values decrease and properties of the facies worsen as a consequence of diagenesis process at higher depths of the Osmancık Formation. Mapping of the results from the applied methods in this field will improve our understanding of reservoir properties in the study field.

Keywords: Reservoir Characterization, Sedimentology, Geostatistical Facies and Property Modeling, Osmancık Formation, Thrace Basin.

ÖZ

SEDİMANTOLOJİ, İSTATİSTİK VE PETROFİZİKSEL YÖNTEMLERİ KULLANARAK OLIGOSEN YAŞLI OSMANCIK FORMASYONUNUN REZERVUAR MODELLEMESİ, KARAÇALI-YULAFLI SAHASI, TRAKYA BASENİ

Arpacı, Taner
Doktora, Jeoloji Mühendisliği
Tez Yöneticisi: Prof. Dr. İsmail Ömer Yılmaz
Ortak Tez Yöneticisi: Prof. Dr. Serhat Akın

Ağustos 2023, 371 sayfa

Trakya baseninde bulunan gaz sahaları son yıllarda geliştirilmiş ve neredeyse tüketilmiştir. Yulaflı-Karaçalı sahası bu basenin doğusunda yer almaktadır. Sahada Osmancık formasyonundan gaz üretimi yapılmaktadır. Beklenmeyen rezervuar özellikleri göz önüne alındığında, Trakya Baseni'nde bulunan çok özel bir sahadır. Sahadan Terzili fayının uzantısı geçmekte olup sahayı iki kısma bölmüştür. Osmancık formasyonu fayın düşük bloğunda kalan kısımdan üretirken, yüksek bloğunda kalan kısımda üretim yapılmamaktadır veya üretim miktarı çok azdır.

Bu çalışmanın amacı derin Osmancık Formasyonu'nda gözeneklilik ve geçirgenlik değişiminin ve fasiyes özelliklerinin karakterize edilmesidir. Çalışmanın ilk hedefi yeni işlenmiş sismik verinin yorumlanması ve geometrinin ortaya çıkarılması için yapısal bir model oluşturulmasıdır. Çalışmanın ikinci hedefi Osmancık Formasyonu sığ ve derin seviyelerdeki fasiyes ve petrofiziksel davranışın, sedimantoloji ve kantitatif sismik yorumlar kullanılarak, jeoloji ve jeofizik açısından araştırılması ve değerlendirilmesidir. Çalışmadaki son aşama ise Sequential Indicator Simulation (SIS) ve Sequential Gaussian Simulation (SGS) gibi jeoistatistiksel yöntemlerden

yararlanılarak fasiyes ve rezervuar parametrelerinin modellenmesi ve bilinmeyen konulara açıklık getirilmesidir. Çalışmanın sonucunda Osmancık Formasyonu'nun derinlerine gidildikçe, diyajenez etkisi ile gözeneklilik ve geçirgenlik değerlerinin düştüğü ve fasiyes özeliklerinin kötüleştiği gözlenmiştir. Sismik yorumların, rezervuar jeofiziği çıktılarının ve fasiyes, gözeneklilik ve geçirgenlik modelleme çalışmalarının haritalanması, rezervuar özelliklerini anlamamıza önemli katkılar sağlayacaktır.

Anahtar Kelimeler: Rezervuar Karakterizasyonu, Sedimantoloji, Jeoistatistiksel Fasiyes ve Petrofiziksel Modelleme, Osmancık Formasyonu, Trakya Baseni.

To my wife Seval, my daughter Derin and my son Ozan

ACKNOWLEDGMENTS

I would like to thank to my advisor Prof. Dr. İsmail Ömer Yılmaz for giving me the opportunity to study and to complete this research. My greatest appreciation goes to him for sharing his valuable experiences and for providing me with continuous guidance. Secondly, I would like to thank my co-advisor Prof. Dr. Serhat Akın. He has played an important role in shaping my thesis. He has provided insightful and positive feedback during the incremental stages of my research. My appreciation goes to my committee members, Prof. Dr. Sevinç Altıner, Prof. Dr. Emin Ulugergerli, Prof. Dr. Günay Çiftçi and Assoc. Dr. Çağlar Sınayuç for their support and comments.

I am very grateful Turkish Petroleum Corporation (TP) that generously provided my thesis data.

I would also like to thank my friends Damla Altıntaş and Ergin Karaca for their suggestions, comments and supports.

I would like to express my grateful thanks to my colleagues; Aytekin Murathan, Fatma Şanal, Eren Deniz Berberoğlu, Musa Çetin, Sezer Sevinç, Burak Salantur and Barış Dadak for their invaluable contributions. Special thanks to Arzu Aktosun and Sevim Yavuz Bayram for their support and assistance.

Finally, I would like to thank to my wife, Seval Arpacı, for her endless support and patience. I am greateful to her for encouraging me in each step of my research. My daughter Derin Arpacı and my son Ozan Arpacı deserve special thanks for letting me complete this thesis instead of spending enjoyable time together.

TABLE OF CONTENTS

ABSTRACT v
ÖZ vii
ACKNOWLEDGMENTS x
TABLE OF CONTENTS xi
LIST OF TABLES xvi
LIST OF FIGURES xviii
LIST OF SYMBOLS AND ABBREVIATIONS xliii
1 PURPOSE AND SCOPE 1
2 INTRODUCTION 3
3 PREVIOUS STUDIES 7
3.1 Regional Based 7
3.2 Reservoir Modeling Based 12
3.3 Method Based 16
4 GEOLOGICAL SETTINGS 19
4.1 Introduction 19
4.2 Evolution of the Thrace Basin 19
4.3 Tectonic Settings 23
4.4 Lithostratigraphic Settings 26
4.4.1 Eocene Age Formations 26
4.4.2 Oligocene Age Formations 29
4.4.3 Miocene Age Formations 30
5 LITHOSTRATIGRAPHY OF THE OSMANCIK FORMATION 33

5.1 Introduction 33
5.2 Lithostratigraphy 33
5.3 Contact Formations 42
6 METHODOLOGY AND DATA SETS 45
6.1 Introduction 45
6.2 Methodology 45
6.2.1 Sedimentology 47
6.2.2 Petrophysics 48
6.2.3 Conventional (Qualitative) Seismic Interpretation 50
6.2.4 Quantitative Seismic Interpretation 52
6.2.5 Geostatistics 54
6.3 Data Sets 54
6.3.1 Location of the Study Area 55
6.3.2 Available Data Sets 55
7 SEDIMENTOLOGY 67
7.1 Introduction 67
7.2 Evaluation of the Core Samples 71
7.2.1 Well-12 71
7.2.2 Well-13 71
7.2.3 Well-15 78
7.2.4 Well-16 79
7.2.5 Well-21 85
7.2.6 Well-32 88
7.3 Examination of Thin Sections 90

7.3.1 Thin sections from Well-12 90
7.3.2 Thin sections from Well-13 104
7.3.3 Thin sections from Well-15 115
7.3.4 Thin sections from Well-16 133
7.3.5 Thin sections from Well-32 140
7.3.6 Summary: The evaluation of the Thin Section 148
7.4 Diagenesis in Deeper Osmancık Formation 151
8 PETROPHYSICS 157
8.1 Introduction 157
8.2 Core Measurements: Porosity and Permeability 157
8.2.1 Core Measurements for Well-12 157
8.2.2 Core Measurements for Well-13 161
8.2.3 Core Measurements for Well-15 165
8.2.4 Core Measurements for Well-16 169
8.2.5 Core Measurements for Well-21 172
8.2.6 Core Measurements for Well-32 176
8.2.7 Compilation of Core Measurements 179
8.3 Estimation of Permeability Curve 181
8.3.1 Statistical Permeability Estimation 181
8.3.2 Theoretical Permeability Estimation 186
8.3.3 Results 199
9 GEOPHYSICS 205
9.1 Introduction 205
9.2 Conventional (Qualitative) Seismic Interpretation 205

9.2.1 Seismic Wavelet Extraction and Well-to-Seismic Tie 206
9.2.2 Fault and Horizon Interpretation 214
9.2.3 Velocity Model Building and Time to Depth Conversion 221
9.2.4 Structural Model Building 221
9.3 Quantitative Seismic Interpretation 226
9.3.1 Seismic Data Preconditioning 226
9.3.2 Well Log Data Editing and Shar Wave Estimation 227
9.3.3 Amplitude Versus Offset/Angle Analysis 236
9.3.4 Seismic Inversion 246
9.3.5 Neural Network Applications 262
10 GEOSTATISTICAL RESERVOIR MODELING 279
10.1 Introduction 279
10.2 Conceptual Model 279
10.3 Gridding 280
10.4 Experimental and Model Variograms 282
10.4.1 Experimental Variogram 283
10.4.2 Variogram Modeling 284
10.5 Geostatistical Methods for Modelling 286
10.6 Seismic Data Resampling 287
10.7 Modeling Workflow 289
10.8 Validation of the Modelling Results 290
10.9 Facies Modeling 290
10.9.1 Well Log Upscaling 290
10.9.2 Data Analysis 297

10.9.3 Facies Distribution 304
10.10 Property Modeling 310
10.10.1 Well Log Upscaling 310
10.10.2 Data Analysis 310
10.10.3 Secondary Volumes for Porosity and Permeability 320
10.10.4 Property Distribution 323
10.10.5 Comparison of Facies and Property Models 333
11 DISCUSSION 343
12 CONCLUSION 349
REFERENCES 353
CURRICULUM VITAE 371

LIST OF TABLES

TABLES

Table 6.1 Seismic Acquisition Parameters. 57
Table 6.2 Available logs in each well used as input for the study. 61
Table 6.3 Available core plugs and depth intervals. 65
Table 7.1 Facies Properties of Thin Sections. 150
Table 7.2 X-Ray diffraction analysis (XRD) for Core-1 of Well-13 and Well-15 (in percentage). 156
Table 8.1 Core Analysis of plugs in Well-12. 158
Table 8.2 Core Analysis of plugs in Well-13. 162
Table 8.3 Core Analysis of plugs in Well-15. 166
Table 8.4 Core Analysis of plugs in Well-16. 169
Table 8.5 Core Analysis of plugs in Well-21. 173
Table 8.6 Core Analysis of plugs in Well 32. 176
Table 8.7 Sorting index. 187
Table 8.8 RMSE and NRMSE for RESERVOIR I and RESERVOIR II (m=1.65). 188
Table 8.9 Observed and estimated permeabilities of the first ten samples for RESERVOIR I. 189
Table 8.10 Observed and estimated permeabilities of the first ten samples for RESERVOIR II. 189
Table 8.11 Observed and estimated permeabilities for the shallower reservoir. 192
Table 8.12 Observed and estimated permeabilities for the deeper reservoir. 192
Table 8.13 RMSE and NRMSE for both reservoir intervals of Well-21. 193
Table 8.14 Observed and estimated permeabilities for the shallower reservoir (Well-15). 194
Table 8.15 Observed and estimated permeabilities for the deeper reservoir (Well-15). 194

Table 8.16 RMSE and NRMSE for both reservoir intervals of Well-15. 199
Table 9.1 Input list for seismic facies classification. 271
Table 10.1 Modelled variogram parameters. 304
Table 10.2 Orientation and lag distance of the modelled variogram. 304
Table 10.3 Modelled variogram parameters. 320
Table 10.4 Orientation and lag distance of the modelled variogram. 320

LIST OF FIGURES

FIGURES

Figure 2.1. (A) An illustration of the parts of a deltaic system consisting of Oligocene formations is given. In this system, delta-front sandstones of the Osmancık Formation are the most productive facies. (B) Going deeper in the Osmancık Formation, petrophysical and facies properties are worsened because of decreasing energy in the environment. Deeper parts are closer to prodeltaic facies of the Mezardere Formation resulting in small grain sizes (Modified from Nichols, 2009) (Only for illustrative purpose). 4
Figure 4.1. Location map of the Thrace Basin (modified from Bürkan, 2010, TPAO report) 21
Figure 4.2. Orogenic belt of Turkey including west to east trending pondites: (1) Western Pondities, (2) Central Pondities and (3)Eastern Pondites (modified from Yılmaz et al., 1997) 22
Figure 4.3. Geological cross-section from south to north showing Intra-pondite subduction zone and tectonic activities of the Thrace Basin (modified from Görür and Okay, 1996) 24
Figure 4.4. Geological map of the basin is shown in this figure. Oligocene sediments are exposed on the south and south-east part of the basin and basement rocks (shown as Tyd, Tyo and Tym). Miocene and Pliocene formations, Kırçasalih and Eregene, are observed to cover most of the area in the Thrace Basin (modified from Siyako and Huvaz, 2007). 25
Figure 4.5. Geologic sections indicating formations in (A) NW-SE and (B) S-N directions. Study covers Yulaflı and Karaçalı wells shown in NW-SE directions (modified from Gürgey, 2005). 27
Figure 5.1. Generalized stratigraphy of the Thrace Basin showing reservoir and source rock properties including petrophysical properties, depositional environment, geological events and total organic carbon content (modified from Huvaz et al., 2005). 34

Figure 5.2. A location map indicating the spread area of the outcrops from the Osmancık Formation (illustrated with yellow color).....36
Figure 5.3. Sandstone facies and channels around Marmara Ereğlisi. Channels are marked with dashed yellow line. 37
Figure 5.4. A clear lense shaped sand channel is pointed out, which is drawn with a yellow dashed line around Marmara Ereğlisi.....38
Figure 5.5. Distributary channel facies is observed and pointed out around Paşayiğit location.....39
Figure 5.6. Location of another outcrop representing the Osmancık Formation (Gökçeada), which is located SW of the main outcrops.....40
Figure 5.7. (A) Delta-front sandstones of the Osmancık Formation and (B) leaf fossils which are transported by paleo-delta and deposited into delta-front sandstones around Gökçeada. 41
Figure 5.8. General stratigraphic correlation of the Yenimuhacır Group formations (modified from Siyako, 2006).....43
Figure 6.1. Modeling Workflow for deeper Osmancık Formation in Thrace Basin. 46
Figure 6.2. ZEISS Axio imager A2m microscope 48
Figure 6.3. Porosimeter and permeameter systems. 50
Figure 6.4. Location map of the study area. Red rectangle indicates the location of study area. 56
Figure 6.5. Chart of the process sequence of seimic data. 60
Figure 6.6. Geometry and location map of 3D seismic survey and wells. 62
Figure 6.7. Well groups and locations in base map. 63
Figure 6.8. Zoomed display of well group-1 (top), group-2 (middle) and group-3 (bottom) wells.....64
Figure 7.1. The Udden-Wentworth (Udden 1914; Wentworth 1922) scale according to grain sizes of clastic sediments.....69
Figure 7.2. The Pettijohn classification (1975). 70

Figure 7.3. Location of the wells with core samples. Well 12, 13, 15 and 16 are group-1 wells, Well-21 is group-2 well and well 32 belongs to group-3. 74
Figure 7.4. Core-1 from Well-12 (1347-1351.5 meters). Horizontal shale lamina and convolute lamination are observed in core plugs. 75
Figure 7.5. Core-1 from Well-13 (1305-1314.60 meters). Sandstone-siltstone alternations are illustrated. 76
Figure 7.6. Core-2 from Well-13 (1489-1497.50 meters). Laminated shale-sandstone alternations with varying thickness are indicated. 77
Figure 7.7. Shallower part of Core-1 between 1361-1364 meters from Well-15. Parallel lamination, rip-up shale clast and deformation structures observed. 81
Figure 7.8. Deeper part of Core-1 between 1365-1369 meters from Well-15. Rip-up shale clast, parallel and cross laminations are observed in this section. 82
Figure 7.9. Core-2 between 1404.5-1413.5 meters from Well-15. Parallel and wavy laminations, load structures-frame structures and thick sandstones are observed in this core. 83
Figure 7.10. Core sample between 1527-1531m. from Well-16. Core plug is not well preserved. Alternating sandstone and shale is observed. Shale with abundant varves is also shown in the figure. 84
Figure 7.11. Core sample between 1706-1714 m. from Well-21. Sandstone and shale alternation with deformation structure, parallel and wavy laminated sandstone. ...87
Figure 7.12. On the left, core-1 between 1463-1470 m. is shown. Totally, shale with high amount of organic matter is observed. On the right, core-2 between 1798-1805.7 m. is shown. Core-2 consists of sandstone-shale alternation and parallel and wavy lamination can be observed. 89
Figure 7.13. PPL display of thin section from 1351.25 m. 92
Figure 7.14. XPL display of thin section from 1351.25 m. 93
Figure 7.15. Evaluation of thin section from 1351.25 m. Numbers indicate length of grains, which are shown with dashed red lines. The scale of the thin section is 200 μm. 94

Figure 7.16. Evaluation of thin section using XPL view from 1351.25 m. Blue rectangle indicates feldspar while red circles demonstrate polycrystalline quartz. 95
Figure 7.17. Histograms and regarding thresholds of each component are pointed out on the top of the figure. After the application of thresholds (middle) and coloration of each display (below) for grain, matrix, lithic fragment and pores are displayed in the figure. 96
Figure 7.18. Merged colors of each component and calculated statistical values. Note that matrix percentage is less than 15 % and grain percentage is around 30 %. 97
Figure 7.19. PPL display of thin section from 1348.25 m. 98
Figure 7.20. XPL display of thin section from 1348.25 m. 98
Figure 7.21. Evaluation of thin section from 1348.25 m. Numbers indicate length of grains, which are shown with dashed red lines. The scale of the thin section is 200 μm. A clear shale lamina is observed and drawn with green dashed line. 99
Figure 7.22. Merged colors of each component and calculated statistical values in depth of 1348.25. Note that matrix percentage is more than 15 % and grain percentage is around 55 %. 100
Figure 7.23. PPL display of thin section from 1349 m. 101
Figure 7.24. XPL display of thin section from 1349 m. 101
Figure 7.25. Merged colors of each component and calculated statistical values in depth of 1349 m. Note that matrix percentage is more than 15 % and grain percentage is around 55 %. Percentage of components in depth of 1349 m. is similar to 1348.25 m. 102
Figure 7.26. From left to right: GR, DT, PHIE, SW, VCL, upscaled facies and completions. The most productive interval, between 1341-1365 m., among group 1 wells are displayed within p1_G and p1_C tops. Blue arrow indicates non-producing depths (1348.25 m. and 1349 m.), which is evaluated as lithic wacke. Red arrow points out producing depth, which is shown with yellow rectangle and evaluated as lithic arenite facies (1351.25 m.). 103
Figure 7.27. PPL display of thin sections regarding each sample of depth between 1305 m. and 1314 m. 106

Figure 7.28. Evaluated PPL displays of thin sections regarding each sample. Quartz, lithic fragments, matrix and length of grains are illustrated on the figures A, B, C, D and E. Common property of each section is observed as small grain sizes and high amount of matrix. 107
Figure 7.29. Merged colors of each component and calculated statistical values. Note that matrix percentage is higher than 50% for each sample and grain percentage varies from 10% to 30%..... 108
Figure 7.30. (A) PPL and (B) XPL displays of the thin section and (C) evaluated section. Calculated length of three different grains are illustrated with red dashed lines. The scale of the thin section is 200 μm. Quartz minerals covers a high range of grains..... 110
Figure 7.31. Merged colors of each component and calculated statistical values. Note that matrix percentage is higher than 50% and grain percentage is almost 29.34%. 111
Figure 7.32. (A) PPL and (B) XPL displays of the thin section and (C) evaluated section. Calculated length of three different grains are illustrated with red dashed lines. Grain sizes are variable. The scale of the thin section is 200 μm. Quartz minerals covers a high range of grains similar to the thin section at depth of 1489.45 m. 112
Figure 7.33. Merged colors of each component and calculated statistical values. Note that matrix percentage is higher than 50% and grain percentage is almost 19.7%. 113
Figure 7.34. From left to right: Gamma-ray (GR), p-slowness (DT), effective porosity (PHIE), water saturation (SW), volume of clay (VCL), facies log and completions for well-13. Number 1 shows low producing, then, abandoned zone in which core-1 is drilled out. Grain sizes vary between very fine to fine sand particles. Number 2 indicates productive zone where core-2 is taken out. Although matrix content is similar to each other, grain size of core-2 interval changes from fine to medium sand size particles, resulting higher porosity and better reservoir condition. 114

Figure 7.35. (A) PPL display, (B) XPL display and (C) interpretation of thin section at a sample depth of 1360.85 m. Mainly quartz mineral is observed in the section. An unstable feldspar mineral covering 0.4% is observed and illustrated with an orange ellipse. (B) XPL section assits to evaluate the feldspar grain. Red dashed lines display the length of different quartz grains. Blue dyed stain in the sections indicates porous areas. 118
Figure 7.36. (A) PPL display, (B) XPL display and (C) interpretation of thin section at a sample depth of 1365.54 m. Mainly quartz mineral is observed in the section, which some of them are pointed out with red arrows. Purple ellipses indicate accessory minerals, which have a direction and distinctive color in (B) XPL section. Red ellipse points out feldspar mineral in (B) XPL display clearly. Red dashed lines display the length of different grains. Blue dyed stain in the sections indicates porous areas. 119
Figure 7.37. (A) PPL display, (B) XPL display and (C) interpretation of thin section at a sample depth of 1366.35 m. Mainly quartz mineral is observed in the section, which some of them are pointed out with red arrows. Purple ellipses indicate accessory minerals. Red dashed lines display the length of different quartz grains. Blue dyed stain in the sections indicates porous areas. 120
Figure 7.38. (A) PPL display, (B) XPL display and (C) interpretation of thin section at a sample depth of 1367.35 m. High percent of matrix is detected in this sample. Shale lamina is shown and drawn with dashed green line. This lamina is evaluated as possible flow barrier, which worsens reservoir condition. Purple ellipses indicate accessory minerals. Red dashed lines display the length of different quartz grains. Blue dyed stain is absent in this section. 121
Figure 7.39. (A) PPL display, (B) XPL display and (C) interpretation of thin section at a sample depth of 1368.5 m. Higher percent of pores comparing other sections is seen and calculated values are given in Figure 7.40. Red dashed lines display the length of different quartz grains. 122
Figure 7.40. Estimation of the percentage for different depth of samples; (A) 1360.85 m., (B) 1365.50 m., (C) 1366.35 m., (D) 1367.35 m. and (E) 1368.50 m.

Approximate porosity values are calculated, except for 1367.35 m. due to lack of blue dyed stain. The highest matrix content is seen in the fourth sample (D) with 1367.35 depth. Sample 1 and 2 (A and B) have the highest percent of grain values. The fifth sample (E) indicates the highest porosity among thin sections of core-1. Percentage of lithic fragments for each sample are closer, except the sample 4 which includes high amount of matrix. 123
Figure 7.41. (A) PPL display, (B) XPL display and (C) interpretation of thin section at a sample depth of 1405.4 m. Mainly quartz mineral is observed in the section. Cement development is illustrated with a green dashed line, which causes preventing porosity development. Red dashed lines display the length of different quartz grains. Blue dyed stain in the sections indicates porous areas. 126
Figure 7.42. (A) PPL display, (B) XPL display and (C) interpretation of thin section at a sample depth of 1406.55 m. Mainly quartz mineral is observed in the section. Red dashed lines illustrate the length of different quartz grains. Blue dyed stain in the sections indicates porous areas. 127
Figure 7.43. (A) PPL display, (B) XPL display and (C) interpretation of thin section at a sample depth of 1407.55 m. Mainly quartz minerals with different sizes are observed in the section. Red dashed lines demonstrate the length of different quartz grains. Blue dyed stain in the sections indicates porous areas. 128
Figure 7.44. (A) PPL display, (B) XPL display and (C) interpretation of thin section at a sample depth of 1408.55 m. Addition to quartz minerals, feldspar and chert grains (with the aid of XPL (B)) are also illustrated in the section. Red dashed lines indicate the length of different grains. Blue dyed stain in the sections indicates porous areas. 129
Figure 7.45. (A) PPL display, (B) XPL display and (C) interpretation of thin section at a sample depth of 1410.25 m. Mainly quartz grains with high rate of lithic fragments and matrix are observed. Red dashed lines indicate the length of different grains. Blue dyed stain is missing in this section, which is expected to be used for the evaluation of pores. 130

Figure 7.46. Estimation of the percentage of different components for five samples; (A) 1405.40 m., (B) 1406.55 m., (C) 1407.55 m., (D) 1408.55m. and (E) 1410.25 m. Approximate porosity values are calculated, except for 1410.25 m. (E) due to lack of blue dyed stain. The highest matrix content is seen in the fifth sample (E) with 1410.25 depth. Although this sample has the highest percent of grain values, quality of the thin section is weak, which is not very reliable. The fourth sample (E) indicates the highest porosity among thin sections of core-2..... 131
Figure 7.47. From left to right: Gamma-ray (GR), p-slowness (DT), effective porosity (PHIE), water saturation (SW), volume of clay (VCL), facies logs and completions for well-15. Number 1 is non-productive interval from core-1 although this zone has high effective porosity and low amount of clay volume. Number 2 indicates productive zone where core-2 is drilled out. Water saturation is 100% for number-1 interval, which means that the zone is lack of hydrocarbon presence. However, number-2 interval includes lower water saturation dropping around 50%, resulting the presence of hydrocarbon. 132
Figure 7.48. (A) PPL display, (B) XPL display and (C) interpretation of thin section at a sample depth of 1527.35 m. Mainly quartz mineral is observed in the section. Red dashed lines display the length of different quartz grains. Blue dyed stain in the sections indicates porous areas. Mostly, pores are not connected resulting low effective porosity. 135
Figure 7.49. (A) PPL display, (B) XPL display and (C) interpretation of thin section at a sample depth of 1527.85 m. Mainly quartz mineral is encountered in the section. Red dashed lines display the length of different grains. Blue dyed stain in the sections indicates porous ones, which covers a small area. 136
Figure 7.50. (A) PPL display, (B) XPL display and (C) interpretation of thin section at a sample depth of 1528.85 m. Similar to other thin sections in this well, quartz mineral is dominant. Red dashed lines display the length of different grains. Blue dyed stain in the sections shows porous area. 137
Figure 7.51. Merged colors of each component and calculated statistical values in thin sections of Well-16. Matrix percentage is similar varying between 27-37% for

each sample and grain percentage changes from 20% to 30%. Porosity is low in all sections, which the largest value is around 9.4% and the smallest one is about 4.5%. 138
Figure 7.52. From left to right: Gamma-ray (GR), p-slowness (DT), effective porosity (PHIE), water saturation (SW), volume of clay (VCL), facies log and completions for well-16. Although, the presence of a thick sandstone column and relatively higher effective porosity, hydrocarbon is only available in an interval less than 1 m, which is observable in water saturation log values. Rest of the values for SW is 100%. Core interval is shown with red rectangle and is pointed out with red arrows.....139
Figure 7.53. PPL displays (left panel) and XPL images (right panel) of each sample. A1, B1, C1 and D1 indicate PPL sections while A2, B2, C2 and D2 includes XPL sections of the sample depth with 1798.75, 1800.9, 1803.2 and 1804.35 m. are illustrated respectively. 142
Figure 7.54. Evaluated thin section for the sample with a depth of 1798.75 m. Calculated length of three diffrent grains are illustarted with red dashed lines. The scale of the thin section is 200 μm. Quartz minerals covers a high range of grains. Matix is the dominant component of the section covering high amount of the area. 143
Figure 7.55. Evaluated thin section for the sample with a depth of 1800.9 m. Quartz mineral is dominant within grains. Additionally, opaque minerals are observed. Calculated length of three diffrent grains are illustarted with red dashed lines. The scale of the thin section is 200 μm.....144
Figure 7.56. Evaluated thin section for the sample with a depth of 1803.2 m. Additionally, opaque minerals are observed. Mostly, quartz minerals are available. Calculated length of three diffrent grains are illustrated with red dashed lines. A coarse quartz mineral is observed, which is rare in thin sections of deeper Osmancık Formation. The scale of the thin section is 200 μm.....145
Figure 7.57. Evaluated thin section for the sample with a depth of 1804.35 m. Additionally, opaque minerals and chert are observed. Quartz minerals are dominant

within grains. High content of matrix is available. Calculated length of three diffrent grains are illustrated with red dashed lines. The scale of the thin section is 200 μm. 146
Figure 7.58. Merged colors of each component for the samples ((A): 1798.75 m., (B): 1800.9 m., (C): 1803.2 m. and (D): 1804.35 m.) and calculated statistical values in Well-32. Quatz content is similar for each sample while matrix show a big difference within these samples, varying from 32.6% to 54.7%. 147
Figure 7.59. Well-12, Core-1, SEM photomicrographs between 1347 and 1351.5 m. On the left, chlorite development reducing porosity is illustrated. On the right side, another result of diagenesis process, quartz overgrowth, is detected. 153
Figure 7.60. Well-13 SEM photomicrographs: (A) Clean section with high and dense interparticle porosity in 1307.8 m. of core 1 is illustrated. (B) Smectite mineral covering grains is detected in 1489.45 m. of core-2. 154
Figure 7.61. Well-15 SEM photomicrographs: (A) Interparticle porosities are observed in 1307.8 m. of core-1, (B) Interparticle porosities and quartz overgrowth resulting in reduction of pore throat sizes and chlorite development are displayed in 1489.45 m. of core-2. 155
Figure 8.1. Porosity versus permeability cross-plot of the core sample of Well-12. 159
Figure 8.2. Measured-processed logs and core measurements of Well-12. From Left to right: Tack 1: Gamma-Ray Track 2: P-sonic; Track 3: Effective porosity; Track 4: Water saturation; Track 5: Core porosity; Track 6: Core permeability; Track 7: Well completion. 160
Figure 8.3. Porosity versus Permeability cross-plot of the core sample of Well-13. Green data points represent measured data for core-1 (1305-1314 m.) and red points are the data for core-2 (1489-1497.5 m.). 163
Figure 8.4. Measured-processed logs and core measurements of Well-13. From Left to right: Tack 1: Gamma-Ray; Track 2: P-sonic; Track 3: Effective porosity; Track 4: Water saturation; Track 5: Core porosity; Track 6: Core permeability; Track 7: Well completion. 164

Figure 8.5. Porosity versus Permeability cross-plot of the core sample of Well-15. Green data points represent measured data for core-1 (1360.7-1369 m.) and red points are the data for core-2 (1404.5-1413.5 m.). 167
Figure 8.6. Measured-processed logs and core measurements of Well-15. From Left to right: Tack 1: Gamma-Ray; Track 2: P-sonic; Track 3: Effective porosity; Track 4: Water saturation; Track 5: Core porosity; Track 6: Core permeability; Track 7: Well completion. 168
Figure 8.7. Porosity versus Permeability cross-plot of the core sample of Well-16. 170
Figure 8.8. Measured-processed logs and core measurements of Well-16. From Left to right: Tack 1: Gamma-Ray; Track 2: P-sonic; Track 3: Effective porosity; Track 4: Water saturation; Track 5: Core porosity; Track 6: Core permeability; Track 7: Well completion. Note that there is no production in this well. 171
Figure 8.9. Porosity versus Permeability cross-plot of the core sample of Well-21. Green data points represent measured data for core-1 (1651-1654 m.) and red points are the data for core-2 (1706-1714 m). 174
Figure 8.10. Measured-processed logs and core measurements of Well-21. From Left to right: Tack 1: Gamma-Ray; Track 2: P-sonic; Track 3: Effective porosity; Track 4: Water saturation; Track 5: Core porosity; Track 6: Core permeability; Track 7: Well completion. Note that both intervals in which cores cutting out are highly productive in this well. 175
Figure 8.11. Porosity versus Permeability cross-plot of the core sample of Well-32. 177
Figure 8.12. Measured-processed logs and core measurements of Well-32. From Left to right: Tack 1: Gamma-Ray; Track 2: P-sonic; Track 3: Effective porosity; Track 4: Water saturation; Track 5: Core porosity; Track 6: Core permeability; Track 7: Well completion. Note that log curves except GR and DT are not available within the range of the core data. 178

Figure 8.13. All available core measurements for porosity and permeability are shown. In the crossplot, all data points for Well-12, 13, 15, 16, 21 and 32 are shown in order with green, pink, dark blue, orange, red and black color. 180
Figure 8.14. Porosity versus permeability cross-plot of core measurements including all wells. 182
Figure 8.15. Discrimination of porosity versus permeability trend of Well-21 from the trend of all wells. 183
Figure 8.16. Porosity versus permeability cross-plot of core measurements, revealing a distictive trend for Well-21. 184
Figure 8.17. Porosity versus permeability cross-plot of core measurements. A different trend of measurement from Well-21 is observed. 185
Figure 8.18. From left to right: Effective porosity log, theoretical permeability curves and completions are given for Well-21. Core porosity and permeability measurements are displayed with red circles. Four models; Van Baaren's (black line), Berg's (dashed green line), RGPZ (dashed blue line) and Timur's (dashed pink) equations are shown on the permeability curve track. 195
Figure 8.19. From left to right: Effective porosity, theoretical permeability curve and completions are given for Well-12. Van Baaren's model was used to estimate permeability from porosity. Core permeability and theoretical permeability curve show a good match. 196
Figure 8.20. From left to right: Effective porosity log, theoretical permeability curves and completions are given for Well-13. The results of Van Baaren's model (dashed red curve) and edited Van Baaren's model (black line) are compared. These results are similar. However, edited model is closer core permeability. 197
Figure 8.21. From left to right: Effective porosity log, theoretical permeability curves and completions are given for Well-15. The results of Van Baaren's model (dashed red curve) and edited Van Baaren's model (black line) are compared. At shallower zone, results are similar. However, edited model curve shows a clear match with core permeability at deeper zone and predicts these values more accurately. 198

Figure 8.22. From left to right: Effective porosity log, calculated permeability curves and completions are given for Well-21. Comparison of statistical and theoretical estimations shows that statistical method results are more compatible for this well. 201
Figure 8.23. From left to right: Effective porosity log, calculated permeability curves and completions are given for Well-25 and 28. Comparison of statistical and theoretical estimations shows that permeability curves generated by using statistical approach fails in deeper sections in the case porosity values are very low. 202
Figure 8.24. From left to right: Effective porosity log, calculated permeability curves and completions are given for Well-15 and 18. Comparison of statistical and theoretical estimations shows that permeability curves estimate very low values in shallower producing zones although both porosity and permeability should be much higher. 203
Figure 9.1. Reflected/refracted P and S waves when a P wave is partitioned. P1 and P2 are the reflected and refracted P waves. S1 and S2 are the reflected and refracted S waves. θ_1 is the angle of reflected P wave, θ_2 is the angle of refracted P wave, λ_1 is the angle of reflected S wave, and λ_2 is the angle of refracted S wave. 206
Figure 9.2. An illustration of convolution of seismic reflection and wavelet. s(t) is wavelet, r(t) is reflection coefficient and r(t)*s(t) is the convolved signal reaching a receiver. 207
Figure 9.3. A statistical seismic wavelet extracted by autocorrelation of seismic traces. 207
Figure 9.4. Well correlation window for Well-21. From left to right: P-sonic log, density log, computed impedances, computed reflectivities, synthetic traces (blue colored), extracted composite traces from seismic data and seismic section are displayed. Synthetic and real data show a clear match after well-to-seismic tie process.....209
Figure 9.5. Composite line views of (A) well group 1, (B) well group 2 and (C) well group 3. 210

Figure 9.6. Correlation between synthetic traces obtained from logs and real seismic data for well group 1 composite section (see Figure 9.5 A) are given. Traces along the wellbores represent synthetic traces and rest of the data are real one. There is a high correlation between real and synthetic traces. 211
Figure 9.7. Correlation between synthetic traces obtained from logs and real seismic data for well group 2 composite section (see Figure 9.5 B) are given. Traces along the wellbores represent synthetic traces and rest of the data are real one. There is a high correlation between real and synthetic traces. 212
Figure 9.8. Correlation between synthetic traces obtained from logs and real seismic data for well group 3 composite section (see Figure 9.5 C) are given. Traces along the wellbores represent synthetic traces and rest of the data are real one. There is a high correlation between real and synthetic traces. 213
Figure 9.9. Location map of the field indicating inline 7360 (red line), (B) seismic section without interpretation, (C) seismic section after fault and horizon interpretation, (D) chaos structural attribute and (E) chaos attribute with fault interpretation are shown. Green and red faults are north branches of Terzili Fault Zone. Purple horizon indicates the top of the Danişmen Formation, red one is the Osmancık Formation and green one is the Mezardere Formation. Blue horizon is a level inside deeper Osmancık Formation. 215
Figure 9.10. Location map of the field indicating inline 7210 (red line), (B) seismic section without interpretation, (C) seismic section after fault and horizon interpretation, (D) chaos structural attribute and (E) chaos attribute with fault interpretation are shown. Green and red faults are north branches of Terzili Fault Zone. Purple horizon indicates the top of the Danişmen Formation, red one is the Osmancık Formation and green one is the Mezardere Formation. Blue horizon is a level inside deeper Osmancık Formation. 216
Figure 9.11. Location map of the field indicating inline 6950 (red line), (B) seismic section without interpretation, (C) seismic section after fault and horizon interpretation, (D) chaos structural attribute and (E) chaos attribute with fault interpretation are shown. Green and red faults are north branches of Terzili Fault

Zone. Purple horizon indicates the top of the Danişmen Formation, red one is the Osmancık Formation and green one is the Mezardere Formation. Blue horizon is a level inside deeper Osmancık Formation. 217
Figure 9.12. Location map of the field indicating inline 6950 (red line), (B) seismic section without interpretation, (C) seismic section after fault and horizon interpretation, (D) chaos structural attribute and (E) chaos attribute with fault interpretation are shown. Green and red faults are north branches of Terzili Fault Zone. Purple horizon indicates the top of the Danişmen Formation, red one is the Osmancık Formation and green one is the Mezardere Formation. Blue horizon is a level inside deeper Osmancık Formation. 218
Figure 9.13. (A) Main fault plains on a base map and (B) all picked faults together are seen in this figure. Main faults are the north branches of Terzili Fault Zone. 219
Figure 9.14. Horizon picks of (a) Danişmen, (b) Osmancık, (b) Mezardere and grids of (d) Danişmen, (e) Osmancık, (f) Mezardere Formations are illustrated. Note that the intensity of picked horizon for the Osmancık Formation is greater. Red colors show the shallowest time ranges while purple one indicates deeper areas in time. 220
Figure 9.15. Average velocities for each formation surface. From left to right; average velocities of the Danişmen, Osmancık and Mezardere Formation tops are given. Red color indicates lower velocities and purple color is higher ones. The surfaces were contoured in every 50 m/s. 222
Figure 9.16. Danişmen (left), Osmancık (middle) and Mezardere (right) top surfaces in depth. The unit is meter. White lines show faults. 223
Figure 9.17. This figure demonstrates converted faults in depth domain. From left to right; Danişmen, Osmancık and Mezardere formation surfaces (in depth) were embedded. 224
Figure 9.18. Zones of created structural model (from left to right; the Danişmen (a), Osmancık (b) and Mezardere (c) Formations) and the whole display (d) of this model are given. Faulting structures are clearly identified. 225

Figure 9.19. Raw offset gathers (on the left) are flatten (on the right) using trim statics..... 228
Figure 9.20. To increase signal to noise ratio, bad signals at far offsets were eliminated using parabolic radon transform. Offset gathers before parabolic radon transform (left), after the application of the process (middle) and eliminated random noises (right) are displayed on the right side of this figure..... 229
Figure 9.21. Using iterative ray tracing, offset dependent gathers were converted to angle dependent gathers. These angle gathers are used as AVO and pre-stack seismic input for seismic inversion..... 230
Figure 9.22. V_P/V_S ratio of the wells with measured S-velocity. Well A, B and C represent the wells from other fields. Surrounding wells confirm that the optimum ratio in the area changes from 1.5 to 2.5..... 231
Figure 9.23. Mathematical relationships of P-wave versus S-wave velocities for each well are shown..... 232
Figure 9.24. P-velocity versus S-velocity cross-plot of the wells used for comparison. Well-36 (black color) and Well-11 (green color) have lower S-velocities than the rest of the wells resulting higher V_P/V_S ratio..... 233
Figure 9.25. After normalization of s-velocities for Well-36 (on the left) and Well-111 (on the right). From left to right for each well: Normalized s-velocities (red color), original logs (black color) and comparison of both curves are given. 234
Figure 9.26. Comparison of the cross-plots of P-velocity versus S-velocity before (left) and after (right) normalization of S-velocity values for Well-111 and Well-36. Note that after the normalizations, P-S relationship for all wells fit on almost at the same trend. 235
Figure 9.27. Reflection coefficients indicating different class types of gas-sands with increasing angle of incidence (Castagna et al., 1998)..... 240
Figure 9.28. From left to right panels: Angle gathers (2-42 degrees), individual angle gather with picked top (red) and base (green) of the reservoir and amplitude versus angle of incidence for the picked events are shown. Red rounded rectangle on the left panel illustrates the producing reservoir zone for Well-18. For the top of reservoir

(red curve), amplitudes start with high negative values and increase in amplitude with changing incidence angle, which represents A class III type of AVO anomaly (right panel). 242
Figure 9.29. Stack seismic section at the location of Well-18 is given. Producing interval is pointed out with rounded rectangle. A clear bright spot as a result of class-3 AVO type is observed. 243
Figure 9.30. From left to right panels: Angle gathers (2-42 degrees), individual angle gather with picked top (red) and base (green) of the reservoir and amplitude versus angle of incidence for the picked events are shown. Red rounded rectangle on the left panel illustrates the producing reservoir zone for Well-12. For the top of the reservoir (red curve), amplitudes start with low positive values and drop until reaching a certain angle of incidence. Then, the polarity changes and start to increase in magnitude at negative side, which represents A class III type of AVO anomaly (right panel). 244
Figure 9.31. Stack seismic section at the location of Well-12 is given. Producing interval shown rounded rectangle. Seismic reflection is too weak to be detected, as a result of polarity changing AVO anomaly. 245
Figure 9.32. On the left side, the convolution of an earth model with an extracted wavelet to calculate synthetics is shown. On the right side, the inversion process by deconvolution of an extracted wavelet from recorded seismic traces to calculate earth model is displayed (Barclay et al., 2008). 246
Figure 9.33. Workflow of pre-stack seismic inversion 247
Figure 9.34. Amplitude Spectrum of the seismic data. Maximum low frequency is 15 Hz. 249
Figure 9.35. P-impedance model calculated from the product of p-sonic and density logs using kriging method (on the left) and the filtered model (on the right) are given. 251
Figure 9.36. S-impedance model calculated from the product of estimated s-sonic and density logs using kriging method (on the left) and the filtered model (on the right) are given. 252

Figure 9.37. Density model using measured density logs using kriging method (on the left) and the filtered model (on the right) are given. 253
Figure 9.38. Seismic composite section (see Figure 9.5 A) from well group-1. Dashed rounded rectangles represent hydrocarbon producing intervals. Producing zones right below the entrance of the Osmancık Formation are clearly identified as bright spots showing strong reflections. Going deeper, the reflections of the producing zones become weaker due to low impedance contrast between layers resulting of increasing compaction of the lithology. 254
Figure 9.39. Seismic composite section (see Figure 9.5 B) from well group-2. Dashed rounded rectangles and ellipse represent hydrocarbon producing intervals. Producing two shallow zones between 950 and 1200 ms at well-25 are easily detected due to lower impedances of sand reservoirs while highly productive intervals below 1200 ms are not differentiated from other. Going deeper, the reflections of the producing zones become weaker due to low impedance contrast between layers resulting of increasing compaction of the lithology. 255
Figure 9.40. A composite section (see Figure 9.5 A) showing acoustic impedance variations for well group 1. The shallowest gas bearing zones of Well-10, 12, 15, 18, and 19 have distinctive lower impedance values as a result of class-III AVO responses. The lithology consists of mainly uncompacted sandstone and shale alternation. At deeper productive zones, impedances become higher as a result of class-II responses because of compacted reservoirs. The impedance contrast is too low to differentiate sand and shale lithology at deeper zones. 256
Figure 9.41. A composite section (see Figure 9.5 B) showing acoustic impedance variations for well group 2. Acoustic impedances of two shallow gas bearing zones at Well-25 can be distinguished as a result of class-III AVO responses. The lithology consists of mainly uncompacted sandstone and shale alternation similar to well group 1. At deeper productive zones, impedances become higher and harder to be detected as a result of class-II responses due to compacted lithologies. 257
Figure 9.42. A composite section (see Figure 9.5 A) indicating V_P/V_S ratio for well group 1. Low values (green and yellow color) indicate producing zones. Due to

similar behavior of P- (acoustic) and S-impedances, this ratio is not affected by compaction or impedance contrast. 258
Figure 9.43. A composite section (see Figure 9.5 B) indicating V_P/V_S ratio for well group 2. Low values (green and yellow color) indicate producing zones. Similar to well group-1, V_P/V_S ratio is not affected from compaction or impedance contrast. Mostly, the lowest values which are color-coded as green are productive sandstones and low values color-coded as yellow and red are non-productive sandstones. Shale lithology have higher V_P/V_S ratio (blue-purple colors). 259
Figure 9.44. A composite section (see Figure 9.5 A) indicating (A) λρ and (B) μρ for well group 1. Lower values for λρ are hydrocarbon indicators while μρ are used as lithology indicator. The intervals showing decrease in λρ values and remaining still or increasing in μρ are evaluated as producing or potential hydrocarbon bearing zones. Due to the impedance contrast, optimum color scale was selected. Reservoir zones have higher μρ values compared to encasing lithology. 260
Figure 9.45. A composite section (see Figure 9.5 B) indicating (A) λρ and (B) μρ for well group 2. Lower values for λρ are hydrocarbon indicators while μρ are used as lithology indicator. The intervals showing decrease in λρ values and remaining still or increasing in μρ are evaluated as producing or potential hydrocarbon bearing zones. Due to the impedance contrast, optimum color scale was selected. Reservoir zones have higher μρ values compared to encasing lithology. 261
Figure 9.46. Input data sets used for probabilistic neural network is given in this figure. 263
Figure 9.47. Workflow of probabilistic neural network (PNN) using inputs illustrated in Figure 9.46..... 264
Figure 9.48. Training and validation errors for each well determined to be used. 265
Figure 9.49. The comparison of actual GR (black curve) and estimated GR (red curve) logs for well group 2 (lower panel) and well group-3 (upper panel) are given. 266
Figure 9.50. The cross-plot of actual versus predicted gamma ray logs is given in this Figure. Correlation coefficient was calculated as 82%..... 267

Figure 9.51. Training error (black curve) and validation error (red cure) are given. Until the 6th attribute is reached, both errors decrease. Then, validation remains still. 268
Figure 9.52. The selected 10 attributes after step wise regression. The first six attributes displayed with yellow color were used. After the 6th attribute, contribution of the attributes is neglectable. 268
Figure 9.53. Gamma-Ray distribution representing the deeper section of the Osmancık Formation is given. GR values are higher in the north-east of the field. Well group-3 sands (on the west of the area) seem to be clearer than the sediments of other two groups. Well group 2 and 3 wells are very productive while well group 1 wells are not as it was discussed in previous chapters. 269
Figure 9.54. Cross-plot of components versus Eigen Values. 20 attributes were calculated. After 6th component, any significant improvement was not observed. 272
Figure 9.55. After the 6th attribute, contribution of additional ones is minimal. After the 12th attribute, additional ones are even neglectable. Optimum number of components was specified as 6. 272
Figure 9.56. (A) Classification of waveforms, (B) histogram showing frequency of colors representing each class. (A) Five classes were selected. Purple and blue colors represent sandy intervals while brown and orange ones are mostly shaly or silty lithology. Green is mostly mix facies. (B) Histogram view showing frequency of color used for classification. This figure shows that colors have similar counts which means sand and shale alternation is very intensive. 273
Figure 9.57. Location map of the composite section related to Well Group 1 is shown on the top and seismic facies classification section is on the bottom in this figure. Gamma-ray log curves are inserted. Purple and blue ones are mostly sandy while orange and brown colors mostly small grain sized sand/shale/silt lithologies. Green color represents mixed facies of sand and shale. 275
Figure 9.58. Location map of the composite section related to well group 2 is shown on the top and seismic facies classification section is on the bottom in this figure.

Gamma-ray logs inserted. Purple and blue ones are mostly sandy while orange and brown colors mostly small grain sized sand/shale/silt lithologies. Green color represents mixed facies of sand and shale. 276
Figure 9.59. Location map of the composite section related to well group 3 is shown on the top and seismic facies classification section is on the bottom in this figure. Gamma-ray logs inserted. Purple and blue ones are mostly sandy while orange and brown colors mostly small grain sized sand/shale/silt lithologies. Green color represents mixed facies of sand and shale. 277
Figure 10.1. A 3D display of structural framework including the Danişmen Formation (purple color), Osmancık Formation (red color) and Mezardere Formation (green color) horizons with the combination of fault framework. 280
Figure 10.2. Thickness map of the Osmancık Formation. The maximum thickness (purple color) is 1200 m. and minimum thickness is 200 m (red color). 281
Figure 10.3. Gridded structure volume (120x120x300) of the Osmancık Formation zone. 282
Figure 10.4. Chart of a semi-variogram showing terms. 284
Figure 10.5. Illustration of fitting techniques for variogram modeling (Tolosana-Delgado and Mueller, 2021). 285
Figure 10.6. Resampled (A) acoustic impedance, (B) shear impedance, (C) V_P/V_S ratio, (D) density, (E) $\lambda\rho$ and (F) $\mu\rho$ cubes. 288
Figure 10.7. Gridded GR volume (left) and gridded seismic facies volume (right) are shown. GR volume was generated by supervised PNN and seismic facies volume was created from only seismic trace differences using unsupervised neural network. 289
Figure 10.8. Base map indicating the input and validation wells. The wells used as a blind are shown with red ellipse. 292
Figure 10.9. Well section display of the blind well, well-12T. From left to right: Gamma-Ray (GR), p-sonic (DT), effective porosity (PHIE), water saturation (SW), volume of clay (VCL) and completions are illustrated. 293

Figure 10.10. Well section display of the blind well, Well-210. From left to right: Gamma-Ray, p-sonic (DT), effective porosity (PHIE), water saturation (SW), volume of clay (VCL) and perforation tops are given. 294
Figure 10.11. Facies log of Well-21 on the left column represents original facies. On the right column, upscaled facies are shown created by “most of the facies” method. As an example, approximately, between 1730 and 1745 m., shale-siltststone alternation is observed. Because siltstone thickness is very low in this interval, dominant shale facies is assigned into the structural grid. 295
Figure 10.12. Upscaled facies logs in a 3D window. 296
Figure 10.13. Estimated facies proportion (left) and proportion curves (right). Sandstone (yellow): 25.2%; siltstone (orange): 38.22%; clay (green): 3.8% and shale: (grey) 32.27%. 297
Figure 10.14. Relations between mu*rho values and (A) sand probability with yellow color, (B) silt probability with orange color, (C) clay probability with green color, (D) shale probability with grey color are illustrated. 299
Figure 10.15. Experimental and modelled variograms of sand facies. Vertical (top), major (middle) and minor (bottom) variograms are shown. 300
Figure 10.16. Experimental and modelled variograms of silt facies. Vertical (top), major (middle) and minor (bottom) variograms are given. 301
Figure 10.17. Experimental and modelled variograms of clay facies. Vertical (top), major (middle) and minor (bottom) variograms are illustrated. 302
Figure 10.18. Experimental and modelled variograms of shale facies. Vertical (top), major (middle) and minor (bottom) variograms are indicated. 303
Figure 10.19. Well section of Well-12T is given. From left to right: GR, DT, RHOB, PHIT, PHIE, SW and VCL logs, completions and modelled facies at the well location are demonstrated. The facies column shown with number 10 represents the best fitted facies model generated by the combination of variogram and μσ attribute. Black lines restricted with red brackets indicate the clearly identified facies types by the interpretation of given logs. 306

Figure 10.20. Composite facies representing well group 1 wells. Dashed red ellipse indicates the facies from the best producing interval among well group 1.....307
Figure 10.21. Well section of Well-210 is shown. From left to right: GR, DT, PHIE, SW and VCL logs and modelled facies are replaced. p1, p2 and p3 tops represent perforated intervals. Note that p3 interval does not produce while p1 and p2 are active producers.....308
Figure 10.22. Composite facies section of well group 2 is shown. From right to left (SE-NW) sand facies become thinner and decrease in grain sizes except the most westernmost part of shallower Osmancık Formation. 309
Figure 10.23. Property logs and upscaled versions at Well-21 are illustrated. First three tracks include processed total porosity, effective porosity and estimated permeability curves. Last three tracks represent upscaled log versions, in orderly. 312
Figure 10.24. Data trends of (A) total porosity, (B) effective porosity and (C) permeability.....313
Figure 10.25. Histograms (left column) and normal distribution (right column) of PHIT, PHIE and permeability from top to bottom are displayed, respectively. ...314
Figure 10.26. Vertical variograms calculated by using upscaled effective porosity logs are given. The compared methods are (A) Gaussian, (B) Exponential and (C) Spherical models.....315
Figure 10.27. Experimental and modelled variograms for vertical (top), major (middle) and minor directions of total porosity.....316
Figure 10.28. Experimental and modelled variograms for vertical (top), major (middle) and minor directions of effective porosity. 317
Figure 10.29. Experimental and modelled variograms for vertical (top), major (middle) and minor directions of permeability.....318
Figure 10.30. A comparison between (A) vertical, (B) major and (C) minor directions of exponential modelled variograms and (D) vertical, (E) major and (F) minor directions of Gaussian modelled variograms of upscaled permeability logs is given. 319

Figure 10.31. P-impedance (Acoustic) and effective porosity logs (on the left) and cross-plot of these parameters (on the right) are demonstrated. 321
Figure 10.32. V_P/V_S ratio and effective porosity logs (on the left) and cross-plot of these parameters (on the right) are demonstrated. 322
Figure 10.33. For deeper Osmancık Formation, acoustic impedance changes little with increasing porosity (on the left) while V_P/V_S ratio is more sensitive to changes in porosity variations (on the right). 323
Figure 10.34. Well section of Well-12T is given. From left to right: GR, DT, RHOB, PHIT, PHIE, SW and VCL logs, total porosity, effective porosity and permeability models and completions at the well location are given. Except the interval between 1350 and 1400 m. modelled properties are reasonable. 325
Figure 10.35. Well section of Well-210 is shown. From left to right: GR, DT, RHOB, PHIT, PHIE, SW and VCL logs, total porosity, effective porosity and permeability models and tops of perforated intervals at the well location are given. P1 and p2 intervals are producers while p3 interval does not produce. 326
Figure 10.36. Composite total porosity model representing well group 1 wells. Total porosity values for shallower depths are higher due to unconsolidated facies while a clear decrease in total porosity is observed in deeper levels. 327
Figure 10.37. Composite effective porosity model representing well group 1 wells. Effective porosity values are high enough especially in hydrocarbon bearing zones. Effective porosity properties on the east direction are better in terms of reservoir potential. 328
Figure 10.38. Composite permeability model representing well group 1 wells. Permeability values on the east direction are higher in similar to effective porosity variations. 329
Figure 10.39. Composite total porosity model representing well group 2 wells. Similar to well group 1, total porosities are higher in shallower depths. 330
Figure 10.40. Composite effective porosity model representing well group 2 wells. Effective porosity values are in balanced at entire intersection. The westernmost part

includes some intervals in shallower Osmancık Formation, which indicate potential reservoir zones. 331
Figure 10.41. Composite permeability model representing well group 2 wells. Similar to effective porosity variations, permeability values are in balanced at entire intersection. Increase in permeability in the westernmost part is clearly observed, which can be considered as potential reservoir intervals. 332
Figure 10.42. (A) Facies, (B) total porosity, (C) effective porosity and (D) permeability models representing a producing zone in shallower Osmancık Formation. Sand facies with good reservoir quality is observed in the zone shown with an ellipse. 335
Figure 10.43. (A) Facies, (B) total porosity, (C) effective porosity and (D) permeability models in figure 10.42 include available wells in group-1. 336
Figure 10.44. Total porosity (top), effective porosity (middle) and permeability (bottom) models for the best productive interval in deeper Osmancık Formation among group 1 wells. 337
Figure 10.45. (A) Facies, (B) total porosity, (C) effective porosity and (D) permeability models of a productive reservoir interval (shown with a black ellipse), in which wells in group 2 are the producers. 338
Figure 10.46. (A) Facies, (B) total porosity, (C) effective porosity and (D) permeability models in figure 10.45 with available wells in group-2. 339
Figure 10.47. (A) Facies, (B) total porosity, (C) effective porosity and (D) permeability models of a deeper productive reservoir interval (shown with a black ellipse), in which wells in group 2 are the producers. Note that increasing depth causes a decrease in porosity and permeability values. 340
Figure 10.48. (A) Facies, (B) total porosity, (C) effective porosity and (D) permeability models in figure 10.47 contain available wells in group-2. 341

LIST OF SYMBOLS AND ABBREVIATIONS

Symbols / Abbreviations	Definition
AI	Acoustic Impedance
AVA	Amplitude versus angle
AVO	Amplitude versus offset
CALI	Caliper
CDP	Common depth point
DT	Compressional sonic log (slowness)
DTS	Shear sonic log (slowness)
g/cc	Gram/cubic centimeters
GR	Gamma ray log
GRFS	Gaussian random function simulation
HCA	Hierarchical cluster analysis
HRS	Hampson-Russell Software
IK	Indicator Kriging
k	Permeability
LLD	Lateral log deep
LLS	Lateral log shallow
Log_max	Maximum log value
Log_min	Minimum log value
m	Meter
md	Millidarcy
MPS	Multiple Point Statics
MRGC	Multi resolution graph-based clustering
ms	Millisecond
MSFL	Micro-Spherical Focused Log
Norm_Log	Normalized log curves
NPHI	Neutron Porosity
OBM	Object Based Modeling
P1	Reflected P-wave
P2	Refracted P-wave
PCA	Principle component analysis
PHIE	Effective porosity
PI	P-Impedance
RC	Reflection coefficient
RHOB	Bulk density
RMS	Root mean square

Rp	P-wave reflectivity
Rs	S-wave reflectivity
S1	Reflected S-wave
S2	Refracted S-wave
SGS	Sequential Gaussian simulation
SI	S-wave impedance
SIS	Sequential indicator simulation
SOM	Self-organizing maps
SP	Self Potential
Sw	Water saturation
TGS	Truncated Gaussian simulation
TWT	Two-way travel time
VCl	Volume of Clay
Vp	P-wave velocity
Vs	S-wave velocity
Z	Impedance
α	P-wave velocity
β	S-wave velocity
γh	Semivariance
ΔVs	Difference in P-wave velocity
ΔVs	Difference in S-wave velocity
$\Delta \rho$	Difference in density
θ	Angle of incidence
λ	Incompressibility
μ	Rigidity
ρ	Density
%	Percent

CHAPTER 1

PURPOSE AND SCOPE

Main productive reservoirs in the Thrace Basin are located in Oligocene Osmancık Formation. Conventional seismic studies have been used to reveal these gas sand reservoirs due to main characteristics of seismic amplitude. Bright spots are clearly identified to spot sand pockets filled with hydrocarbon fluid. Baytok et. al. (2017) and Arpacı and Özdemir (2020) indicated how these sweet spots are used to locate hydrocarbon reservoirs. These bright spots become undetectable with increasing depth of the Osmancık Formation due to diminishing porosity and permeability values. In this respect, the probability of drilling successful wells decreases in contrast to shallower parts of the formation.

The main purpose of this study is to characterize deeper parts of the Osmancık Formation in terms of facies and petrophysical properties. Depositional environment is a deltaic system in the Thrace Basin and the Osmancık Formation is composed of delta front depositional facies. Therefore, going deeper, energy of the environment decreases resulting in lower grain sizes causing low porosity and permeability values.

To conduct this study successfully, Karaçalı-Yulaflı Field was selected due to its distinct petrophysical characteristics. Production has been made from both shallower and deeper parts of the Osmancık Formation. However, the lower block of the Terzili Fault Zone (TFZ) is more productive in deeper Osmancık Formation. Several qualitative and quantitative methods were utilized to implement this study.

The major steps of this study include:

(1) Sedimentology to analyze facies types, mineral contents and properties, porosity variations, sedimentary structures and to integrate with multidisciplinary studies to understand properties of deeper Osmancık Formation,

(2) Petrophysical evaluation of measured and calculated data from well logs and cores to understand porosity and permeability relation between producing and non-producing levels,

(3) Conventional seismic interpretation to delineate structural behavior of the field,

(4) Velocity modeling using seismic and well log data to convert seismic and generated volumes from time to depth domain and to generate structural model,

(5) Amplitude-versus-offset/angle analysis to explain the main difference between shallower and deeper parts of the Osmancık Formation,

(6) Pre-stack seismic inversion to create elastic outputs for quantitative evaluation of the field and producing zones,

(7) Geostatistical modeling of facies, total-effective porosity and permeability variations in the field.

Outputs obtained from applied methods mentioned above will be examined and evaluated to characterize and reveal reservoir properties in the field. As a result, this study will enlighten to similar fields in the Thrace Basin.

CHAPTER 2

INTRODUCTION

The Thrace Basin is situated in NW part of Turkey. The basin includes several hydrocarbon-producing fields, and these fields have almost been depleted in recent years (Arpacı and Özdemir, 2020). The main production is made from porous and permeable sand patches located in shallower parts, approximately first 1000 m., of Oligocene Osmancık Formation.

Oligocene formations in the basin are deposited in a fluvial and wave dominated deltaic system. This system consists of progradational deltaic lobs. Figure 2.1(A) illustrates the behavior of the deltaic system containing the Danişmen, Osmancık and Mezardere Formations. Delta front sandstone facies are potential reservoirs in this deltaic system. Producing gas pockets have been detected as bright spot reflectivities in seismic data. However, increasing depth causes lessen of porosity and permeability due to decreasing grain sizes resulting narrower throat sizes. In this respect, bright spots replace with dim spots, which makes harder to locate hydrocarbon-bearing reservoirs. Even if the presence of hydrocarbon has been detected, due to insufficient petrophysical properties such as too low porosity and permeability, production is possible to fail. A geological illustration of shallower and deeper parts of the Osmancık Formation is given in Figure 2.1(B).

This study will help to locate porous and permeable zones as much as facies distribution to reduce risk to drill dry wells in deeper Osmancık Formation using sedimentology, petrophysics and statistics methods. The focus of the study is the characterization of facies and petrophysical properties in deeper Osmancık Formation.

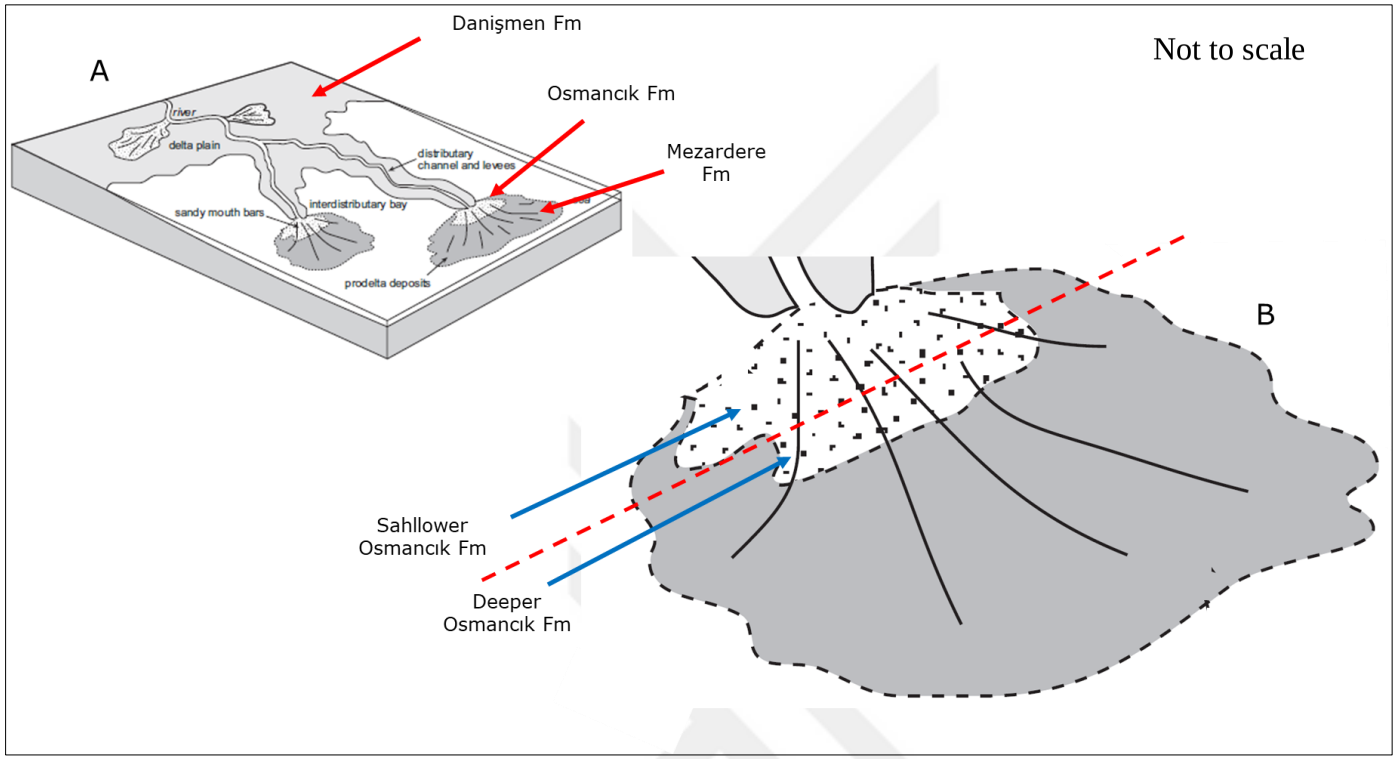

Figure 2.1. (A) An illustration of the parts of a deltaic system consisting of Oligocene formations is given. In this system, delta-front sandstones of the Osmancık Formation are the most productive facies. (B) Going deeper in the Osmancık Formation, petrophysical and facies properties are worsened because of decreasing energy in the environment. Deeper parts are closer to prodeltaic facies of the Mezardere Formation resulting in small grain sizes (Modified from Nichols, 2009) (Only for illustrative purpose).

Karaçalı-Yulaflı field has been producing from both shallower and deeper Osmancık Formation. It is the main reason why this field was selected for the study. The first step is to interpret faults and seismic reflections in stack seismic data to generate a structural model of the field. Then, an average velocity model was created and utilized to convert seismic data from time to depth domain. This method was used to reveal structural behavior of the field.

Pre-stack seismic data was used to interpret amplitude-versus-offset (AVO) anomalies. The main difference between shallower and deeper parts of the Osmancık Formation could be explained by this method. AVO classification is used to identify how these parts differentiate from each other.

Quantitative seismic inversion is one of the most significant methods used in this study. Elastic properties could be distributed and behavior of these properties for producing and non-producing zone could be evaluated via this method. Moreover, shallower and deeper parts of the formation will be explained by using some of the elastic properties. In addition, the outputs of quantitative seismic inversion will be utilized as a secondary volume to distribute facies and petrophysical properties, which indicate main targets for the study.

Sedimentology is also one of the main aspects in this research. Using cores and thin sections; facies types, mineral contents, porosity changes and sedimentary structures are defined and evaluated. This method will be utilized to assess how facies types and properties are effective in producing and non-producing zones in deeper Osmancık Formation.

Petrophysical studies using measured core porosity and permeability data as much as calculated petrophysical logs from measured log data will be the core of the research. Evaluation of measured and calculated petrophysical data provide a direction to this research. This subject will be evaluated in detail.

Data analysis will construct the base of facies and petrophysical modeling. Therefore, statistics is one of the main subjects to distribute modeling parameters in

a reliable way. Variogram modeling and statistical analysis of the data will be discussed in statistics part. The theory of used statistical methods and their applications in Karaçalı-Yulaflı field will be given in this section.

The last but not least part of this research is reservoir modeling. Using modeling methods such as sequential indicator simulation (SIS) and sequential Gaussian simulation (SGS), facies, total-effective porosities and, finally, permeability values are distributed all over the field. The resulted volumes will be shown and discussed.

This research will enlighten facies distribution and petrophysical properties in deeper parts of the Osmancık Formation. In this way, similar studies could be conducted to reveal such properties in different fields. This study leads to create a workflow which can be followed for other fields in the Thrace Basin. In addition, this research indicates that multidisciplinary studies are the only way to understand behavior of deeper Osmancık Formation. Therefore, missing one among the methods mentioned above remains this study to be unsolved.

CHAPTER 3

PREVIOUS STUDIES

3.1 Regional Based

Foley (1938) is the first geoscientist mapping the Osmancık Formation. However, he did not give name to the formation and he evaluated all strata as in Miocene age. "Lignitic sandstone" term was used firstly by Parejas (1939) and followed by Ternek (1949). Holmes (1961) is the first one working on stratigraphic units of the Thrace Basin in detail. He used the term of Osmancık-Ceylan sandstone as a member of Yenimuhacır Group. Ünal (1967) updated the status of the Osmancık Member to the Osmancık Formation.

Beer (1960) reported a study on the geology of the North East of Uzun Köprü. The study area was seperated into two different groups called as Malkara and Ergene Clastic Groups. The Malkara Clastic Group is composed of the Danişmen Formation and firstly mentioned in this report.

Homes (1961) performed the first detailed study including hydrocarbon potential of the Thrace Basin. In the report, a fast subsiding basin and stable platform were mentioned as two representative environments of the basin.

Keskin (1966, 1971) studied carbonates in detail around Çayırdere-Evrencik location. In this study, microfacies of reefal carbonate complex (Eocene Soğucak Formation) of Pınarhisar were investigated. Four depositional environments; (1) reef core, (2) reef front, (3) reef back and (4) reef complex were specified in these researches.

Gökçen (1967, 1971) worked on sedimentology of Keşan Formation. In this study, sandstones in the formation were categorized in three groups: (1) proximal, (2) medial and (3) distal turbidites.

Lebküchner (1974) also mentioned Oligocene sediments as lignitic sandstones in the south-central location of the basin and studied mostly on coal exploration. Four tuff layers and ten coal beds were recognized and mapped in this study.

Kaşar et al. (1983) mapped the south part of the Thrace Basin and subdivided subsiding units with Eocene transgression into five different groups: (1) Istranca Massif and Istanbul Paleozoic, (2) Marmara complex, (3) Cretaceous-Mid Eocene deposits, (4) Mid Eocene-Oligocene deposits and (5) Neogene deposits.

Siyako et al. (1989) studied tertiary rocks in the Biga and Gelibolu Peninsulas and their hydrocarbon potential and Okay et al. (1990) published another paper presenting more detail in tectonic evolution of Biga Peninsula.

Turgut et al. (1991) published a paper on the evolution of the Thrace Basin in terms of sedimentary deposition and hydrocarbon prospectivity. In this paper, sedimentology and stratigraphy, basin tectonics, maturation of source rock and hydrocarbon fields in the basin were discussed.

Atalık (1992) carried out a reseach leading to PhD on depositional environment of the Osmancık Formation in the Basin. A comprehensive sedimentology study was conducted including detailed facies analysis to reveal facies association of the formation. Additionally, four parasequences which are evaluated as the results of fourth and fifth order cycles were examined. To sum up, facies, cyclicity and depositional systems of the formation were studied in this thesis.

Görür and Okay (1996) conducted a study proposing the Thrace Basin developed as a for-arc basin during mid Eocene to Oligocene. Metamorphic rocks of the Strandja massif, and the accretionary sediments of the subducting Intra-Pontide Ocean are suggested as the boundary of the basin.

Okay et al. (1996) studied Paleo- and Neo-Tethyan events in the Thrace Basin. In this paper, original evoluation of the basin was discussed. Rock association and tectonic framework were investigated.

Coşkun (1997) evaluated the relationship between hydrocarbon fields and tectonic activity in the Trace Basin. It was also stated in this paper that different formations were formed in deltaic, fluival and turbiditic depositional environments. Additionally, it was mentioned that the orientation of the structures chance according to relevant ages.

Yılmaz et al. (1997) explained Eastern, Central and Western Pontides in terms of the geology and tectonic evolution in the Thrace Basin.

Yılmaz and Polat (1998) published a paper about geology of volcanism of the Thrace Basin and its evolution using geochemistry.

Sarkınç et al. (1999) studied different facies associations during Neogone. A detail explanation was given in stratigraphy of the formation in Pliocene and Miocene ages. Structural settings and palaeogeographical evolution of the Thrace Basin related to Neogene period were illustrated in this paper.

Turgut and Eseller (2000) explained sequence stratigraphy of eastern Thrace Basin by integrating seismic, well and core data. Tectonic setting and depositional process of the eastern Thrace Basin were investigated.

Gürgey et al. (2005) studied on maturity of hydrocarbon in the Thrace Basin by geochemical and isotopic analysis using collected 16 natural gas and 10 associated condensate samples from 11 different producing fields. It was also showed in the paper that the source rock of gas/condensate is from Eocene Hamitabat Formation and Oligocene Mezardere Formation. Hoşgörmez and Yalçın (2005) evaluated petroleum systems in the basin using molecular and isotopic analysis and basin modelling. The results indicate that the source rock for thermogenic gases in the basin can be either Hamitabat or Mezardere Formation, and these results are compatible with the research of Gürgey et al. (2005).

Huvaz et al. (2005) studied dogleg pattern in maturity profiles in the basin by 1-D basin modeling using chronostratigraphy and lithological data. Additionally, petrophysical modeling was performed to understand how porosity and permeability parameters are effective on compaction profile, which is important for thermal modeling parameters.

Siyako (2006) studied lignitic sandstones which are also called as Danişmen and Osmancık sandstones in the Thrace Basin. In this paper, depositional environment and facies association of the formations were discussed.

Siyako et al. (2006) published a detailed paper on lithostratigraphic units of the Thrace Basin to eliminate confusion about formation naming.

Siyako and Huvaz (2007) worked on the stratigraphic evolution of the Thrace Basin during early-mid Eocene ages using stratigraphic and tectonic models created by seismic, well and core data.

Sünnetçioğlu (2008) conducted a PhD research on sequence stratigraphy of Upper Eocene Hamitabat turbidite system which was analyzed in three depocenters; Western, Northwestern and Northeastern depocenters. According to this study, Hamitabat turbidite system was mainly controlled by regional tectonics, geographical properties and eustatic fluctuations.

Gürgey (2009) performed a geochemical study to reveal all aspects of Hamitabat petroleum system including source rock, migration, hydrocarbon potential, trap machanism, seal.

Varol et al. (2009) studied outcropping reefal limestones of the Soğucak Formation and the evolution of this formation in terms of sedimentology and stratigraphy in the Thrace Basin.

Okay et al. (2010) published a paper focusing on the Eocene events, basement types and evolution of the Southern Thrace Basin.

Bürkan (2010) reported a comprehensive study on tectonic evolution and hydrocarbon potential of the basin. In this report, formations from upper Miocene to the basement were studied, and their properties were explained.

Elmas (2012) conducted a research indicating evolution of the Palaeogene formations of the Thrace Basin. In this paper, the Thrace Palaeogene Basin was subdivided in the sequences of northeastern, northern, central and southern parts, and related stratigraphic, structural and tectonic evolution were explained.

Perinçek et al. (2015) worked on potential of lignitic sandstones in the Danişmen Formation and their economic evaluations, using a great number of wells and several seismic lines.

Şen and Yıllar (2016) studied the Eocene Gaziköy and Keşan Formations. In the paper, depositional environment of these formation was explained. Facies were analyzed and related facies associations were revealed in this research.

Yılmaz et al. (2016) published a paper in the subject of unconventional tight gas development and potential in the Mezardere Formation, Thrace Basin. It is stated in the paper that more than 600 m thickness of marine sediments in the basin have unconventional hydrocarbon potential.

Erarslan and Örgün (2017) worked on coal minerology and geochemical characterization of Saray and Pınarhisar coals in the Northwest Thrace Basin. The content of pyritic and organic sulfure were used to understand depositional environment.

Güldürek (2019) conducted a research on the topic of micropaleontology of southwest Cenesoic deposits of the Thrace Basin. Şafak et al. (2022) published a paper related to this thesis on micropaleontological studies and mineral properties of the Neogene Ergene Formation.

Büyüktutku and Göçer (2020) studied the Hamitabat Formation submarine fan deposits and their hydrocarbon potentials in the Thrace Basin, using petrographic

and petrophysical data taken from samples of 16 drilling wells. In this paper, lithofacies of submarine fan environment were examined.

Karayiğit et al. (2021) conducted a study on minerology and petrography of the Oligocene coal seems in a coal field, Malkara, in the Thrace Basin. It was mentioned in the paper that samples taken from different locations show distinct characteristics and indicate varying TOC, Tmax and HI values and high H.

3.2 Reservoir Modeling Based

Scientists define Geostatisitcs term in different ways. Deutsch (2002) explains this term as the examination of phenomena changing in space/time. Olea (1991) expresses geostatistics as the acquisition of different samples indicating characterization of attributes spatially. Isaaks and Srivastava (1989) defines geotatistics as a way of distributing the data spatially and adapting regression methods using spatial continuity.

Krige (1951, 1966) initiated statistical methods to estimate ore grades using samples in the gold mines, South Africa. Mathematical expressions were developed using this approach by Matheron (1963, 1965) and kriging term was introduced.

Sequential Indicator Simulation (SIS) is considered as variogram-based method which was developed by Alabert (1987). In the case geological bodies or facies are not identified clearly, SIS method can be utilized with the aid of variograms (Pyrcz and Deutsch, 2014). SIS technique was modified by several geoscientists (Gómez-Hernández and Srivastava, 1990; Deutsch, et al., 1992; Goovaerts, 1994; Goovaerts, 1997) enabling the use of secondary parameters. This algorithm is frequently used for the spatially distribution of discrete/categorical variables such as facies estimation. The most important input parameters are considered as upscaled facies and variograms (Deutsch and Journel, 1998).

Among types of Kriging methods, Ordinary Kriging is found to be the most successful linear unbiased technique (Isaaks and Srivastava, 1989). However, due to the nature of smoothing effect of this technique, very small values are over-estimated while large ones are underestimated causing a decrease of variance estimation and lack of reproducing given variogram and histogram (Yamamoto, 2005). To overcome this issue, Deutsch and Journel (1998) developed a new technique called as Sequential Gaussian Simulation (SGS) (Bai and Tahmasebi, 2022).

Numerous case studies using geostatistical reservoir modeling algorithms were published. Several publications are given below:

Al-Khalifah and Makkawi (2002) created and compared porosity models using sequential Gaussian Simulation (SGS) methods in offshore Berri Field, Saudi Arabia.

Strebelle et al. (2003) modeled a deep water turbidite reservoir from ChevronTexoco using principle component cluster analysis to connect sand bodies and Multiple Point Statics (MPS) to integrate conceptional geological model, well logs and seismic derived properties.

Pranter et al. (2007) modeled intermediate-scale reservoir heterogeneity from outcrop of exposed fluvial deposits in Williams Fork Formation in Coal Canyon, Piceance Basin, Colorado using stochastic and deterministic methods for petrophysical properties and grain size distribution.

Pranter et al. (2008) characterized point bar deposits with Object Based Modeling (OBM). Sandstone facies of fluvial sandstones were distributed using sequential indicator simulation (SIS) in the Williams Fork Formation, Rulison Field, Piceance Basin, Colorado.

Labourdette et al. (2008) modeled a unit in Sincor Field, Venezuela using object-based modeling (OBM) to reveal distributary channel sand bodies.

dell'Arciprete et al. (2012) compared the results of sequential indicator simulation (SIS), transition probability geostatistical simulation and multiple point statistics (MPS) methods to model alluvial aquifer analogue.

Nazarpour et al. (2014) modeled spatial distribution of porosity benefiting from Kriging and Gaussian conditional simulation.

Zhao et al. (2014) carried out geostatistical modeling to distribute thickness, porosity and permeability in an oil field using simple kriging, ordinary kriging, co-kriging and sequential Gaussian simulation (SGS) methods. Similarly, Liu et al. (2015) benefited from SGS to model porosity distribution and object-based modeling (OBM) to populate different facies and geometries.

Soleimani and Shokri (2015) reveals petrophysical properties of a producing field using seismic-constrained geostatistical modeling methods.

Edigbue et al. (2015) integrated sequence stratigraphy and geostatistical methods to identify and delineate reservoir sands and petrophysical properties in Otumara field, Niger Delta.

Kiaeia et al. (2015) identified reservoir electrofacies using three clustering methods; hierarchical cluster analysis (HCA), multi resolution graph-based clustering (MRGC) and self-organizing maps (SOM) Sequential indicator simulation (SIS) was utilized to distribute electrofacies on the field.

Li et al. (2016) modeled and characterized the behavior of fractured reservoirs using truncated Gaussian simulation (TGS) in strong water condition which causes to decrease in oil-production in Jiangsu Basin, China.

Sacchi et al. (2016) benefited from object based facies modeling (OBFM) and multiple point statistics (MPS) methods for 3D probability distribution of depositional lithofacies proportions.

Soleimani et al. (2017) carried out a petrophysical modeling study for a fractured and heterogeneous reservoir environment in the Savak Formation, SW Iran.

Carvalho et al. (2017) modeled and compared results of facies using object based modeling (OBM), multiple point statistics (MPS) and Sequential Indicator Simulation (SIS) methods.

Hosseini et al. (2019) applied kriging and SGS methods to distribute porosity and permeability variations, indicating direction of anisotrophy for each variable in the Shurijeh B reservoir in Khangiran gas field. All aspects related to data analysis and application of property modeling were given in detail.

Ali et al. (2019) generated facies and petrophysical models for the C Member of the Six Hills Formation in Egypt. Sand, shale and siltstone facies were distinguished using SIS algorithm. SGS method was used for the purpose of petrophysical properties including porosity, permeability, water saturation and hydrocarbon saturation variations in the reservoir interval.

Abdelmaksoud et al. (2020) is one of the geoscientists working on facies and pertophysical modeling in Abu Gharadig oil and gas field, Egypt. The aim of the study was to figure out whether petrophysical variations such as porosity and water saturation are related to facies properties or structures in Upper Bahariya Member. The results indicate that reservoir is good quality and petrophysical variations are directly related to lateral and vertical facies properties.

Islam et al. (2021) performed structural and petrophysical modeling to characterize the Mangahewa Formation, Pohokura Gas-Condensate Field, located in the Taranaki Basin, New Zealand. After interpretation of the data set in the field, a structural model was generated and gridded to conduct property modeling for spatial distribution of effective porosity, net-to-gross ratio, water saturation and porosity variations.

Iltaf et al. (2021) studied unconventional tight sandstones in Heshui Oil Field, Ordos Basin, China. In this research, facies and petrophysical models were created using different algorithms. For facies modeling, three different facies modeling methods were discussed: (1) Sequential Indicator Simulation, (2) Multi Point Statistics and

(3) Indicator Kriging (IK). For petrophysical modeling: (1) Sequential Gaussian simulation and Gaussian random function simulation were run. MPS for facies modeling and GRFS for petrophysical models were found more successful.

Ali et al. (2022) presented a case study on structural and property modeling aspects for complex clastic reservoirs from the Matulla Formation of July Oilfield in Egypt. Using well logs, seismic and petrophysical analysis, facies distribution and porosity and permeability continuity were aimed to be solved.

3.3 Method Based

Uygur et al. (2000) published a comprehensive sedimentology report covering eastern and central fields and wells in the Thrace Basin. In this report, deltaic facies of the Oligocene Formations were characterized for Karaçalı and Yulaflı Fields. Core measurements and sedimentological descriptions were given in this report and most facies were described as lithic arenite. Using sequence stratigraphy, sand/shale ratios were estimated and local facies distributions were mapped. A limited number of wells were utilized in the report.

Renoux and Bouteldja (2010) prepared a report in the subject of reservoir modeling in the Yulaflı Field. In this report, porosity, net-to-gross ratio and permeability models were given and volumetric calculations for producing zones were calculated.

Ceyda Çetinkaya et al. (2011) published a conference paper about reservoir geology study to characterize petrophysical variations covering Yulaflı region. In this study, producing shallower Osmancık sands were evaluated locally.

Arpacı and Özdemir (2016 and 2020) published a conference and a journal papers indicating the comprehensive reservoir geophysics research illustrating case studies to step out new locations.

Arpacı (2018) published a report in Karaçalı-Yulaflı Field including quantitative reservoir characterization studies. Arpacı (2021) developed the workflow and used a reprocessed data set covering merged 7 different producing fields and demonstrated results of two productive wells.

CHAPTER 4

GEOLOGICAL SETTINGS

4.1 Introduction

The Thrace Basin is located in NW of Turkey and composed of Tertiary sedimentary depositions resulted of extensional movement of late Middle Eocene to late Oligocene ages. As a consequence of rapid subsidence due to basement dependent normal faulting, thick marine clastics were deposited in the basin. The Thrace Basin is the biggest basin containing Tertiary sediments in Turkey. The basin is wrapped with the Aegean Sea and Greece on the west, Bulgaria on the north-west, the Black sea on the north, Bosphorus on the east and the Maramara Sea on the south (Figure 4.1). The northwest and southeast of the basin are thinner compared with rest of the directions due to paleo-highs. Marine clastics were mostly deposited in the center of the basin during deposition and they cover the biggest part of the basin (Turgut et al., 1991). Additionally, the basin is the most significant gas provinces in the country.

4.2 Evolution of the Thrace Basin

The primary evolution of the Thrace Basin began during Early-Middle Eocene times. A compressional regime is the result of the collision of the Sakarya Continent with the Rhodope–Pontide Fragment in Late Cretaceous–Paleocene. This movement enables accommodation space for deposition of the sediments in the basin. Paleo-highs in E-W direction resulted the basin to deepen eastwards and sediment deposition in Early Eocene. The reason of the occurrence of various facies association is the simultaneous erosional and depositional events in diverse locations

of the basin. (Siyako and Huvaz, 2007). The basin began to from during early Middle Eocene with the subsidence over metamorphic and crystalline basement (Turgut et al., 1991). Morphology of the basement represents platform and deep basin depositions. In the ages of Middle to Late Eocene, facies distributions were formed locally. In early times, normal faults controlled on tectonics evolution while reverse faults had more control on later stages. Sediment accumulation and subsidence are result of normal faulting in Late Eocene to Early Oligocene. Later stages tectonic movements cause severe deformation in the Early to Middle Miocene resulting uplifting/folding or erosion of south-east and north parts of the basin (Turgut and Eseller, 2000).

The Pontides in the Thrace Basin are orogenic belt having a trend from west to east and consisting of three parts, which are the Western, the Central and the East Pondites (Figure 4.2):

(1) The Western Pondites contain the Istranca Massif, the İstanbul-Zonguldak Zone, the Armutlu-Almacık Zone and the Sakarya Continent. (2) The Eastern Pondites indicate magmatic belt, for-arc basin fill, a belt of metamorphic massif, an ophiolitic suture zone and remnant basin fill. (3) The Central Pondites illustrate a tectonic area where Eastern and Western parts of the Pondites have been juxtaposed (Yılmaz et al., 1997).

Görür and Okay (1996) suggest that the Thrace Basin is formed as a for-arc basin related to the stratigraphy, structure and the regional context from the mid Eocene to the Oligocene, above subducting Intra-Pontide Ocean. Three main evidences are illustrated for this suggestion (see Dickinson 1995): (1) The basin is situated between Pondite magmatic arc and Intra-Pontide suture zone. (2) The basin fill is shoaling upward sequence from turbidity system showing marine to terrestrial sequence. (3) Petrographic and sedimentological characteristics of basin fill for arc massif and subduction complex (Turgut and Eseller, 2000).

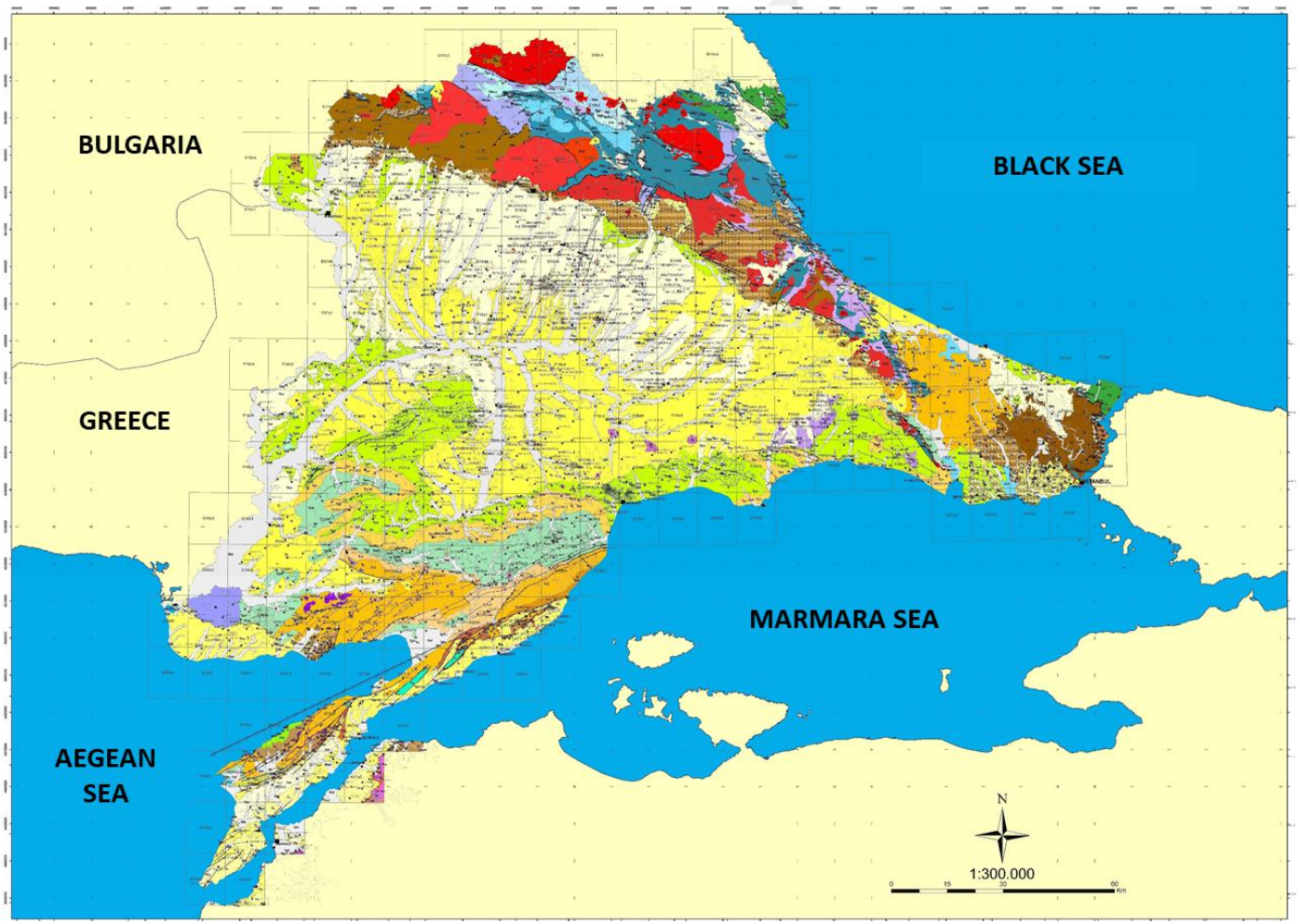

Figure 4.1. Location map of the Thrace Basin (modified from Bürkan, 2010, TPAO report)

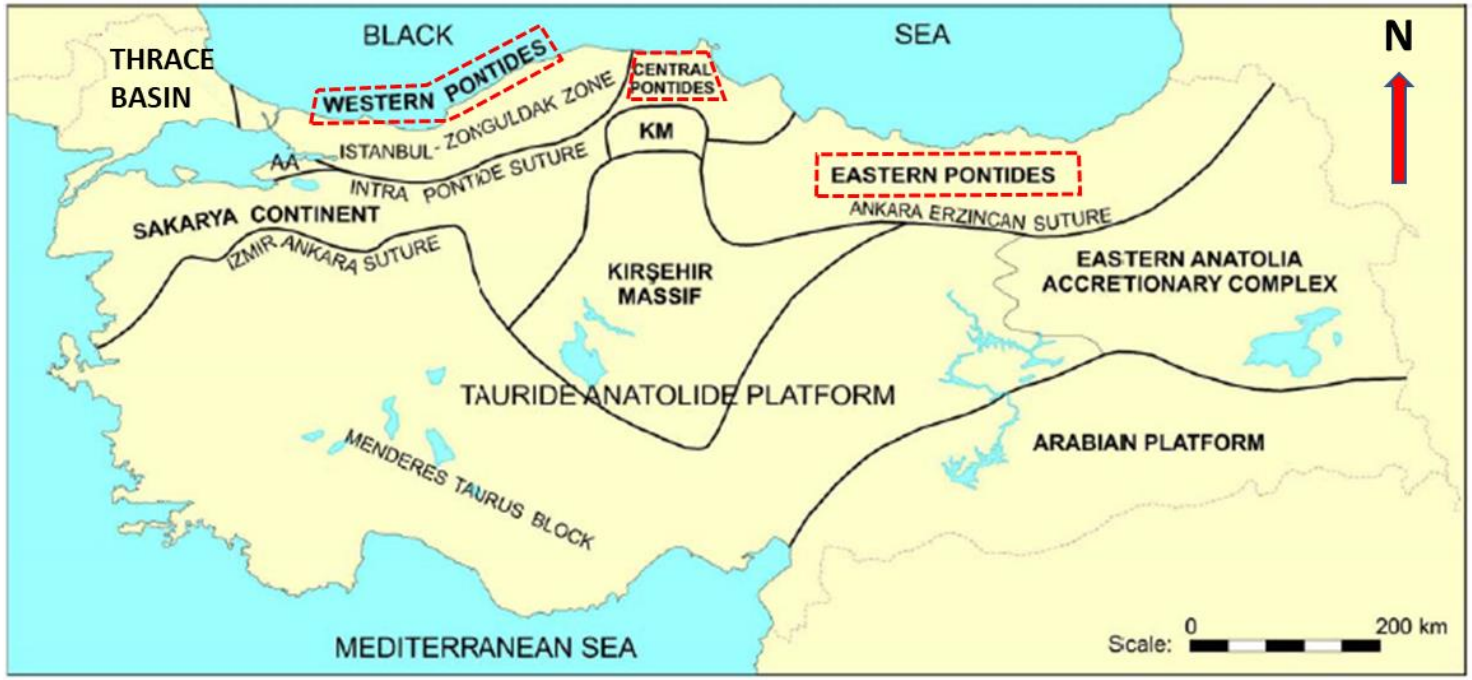

Figure 4.2. Orogenic belt of Turkey including west to east trending pondites: (1) Western Pondities, (2) Central Pondities and (3)Eastern Pondites (modified from Yılmaz et al., 1997).

4.3 Tectonic Settings

The Thrace Basin was developed by the tectonic activities of Terzili Fault zone (TFZ) and Ganos Fault Zone (GFZ) (Perinçek, 1991; Yaltırak, 1995; Tapırdamaz and Yaltırak, 1997; Sarkınç et al., 1999) (Figure 4.3). These fault zones result in establishing the Neogene palaeogeography of the area. TFZ is located in the north, and this fault zone began to be formed around Kırklareli region. Therefore, it was called as Kırklareli Fault Zone by Perinçek (1987). Perinçek (1991) evaluates the Kırıkkale Fault zone as a branch of North Anatolian Fault Zone (NAFZ). This zone is the third major zone around the region. It was formed after Late Miocene (Ketin, 1948, 1969; ¸Sengör, 1979; Barka and Hancock, 1985; ¸Sengör et al., 1985; Barka and Gülen, 1988; Gorür et. al., 1997).

The main deformation for Eocene and Oligocene sediments in south and north-northeast of the region is the result of the activities of different fault splays. These movements led to form of west part of NAFZ. This fault zone covers a very wide area reaching the Aegean Sea and Sea of Marmara after movement of more than 1 km path in east-west direction of northern Turkey (Şengör, 1979; Perinçek, 1991). The east-west trending NAFZ is considered as a young event and the age of this zone is evaluated as beginning Plio-Pleistocene. This fault zone is still active. However, TFZ, in northwest-southeast direction (Turgut et al., 1991), caused deformation in all sedimentary sections older than Plio-Quaternary age and lost its activity. As a result of lateral and reverse faulting of both fault zones, Oligocene sediments are exposed on the south and south-east part of the basin and basement rocks while Eocene sediments are exposed at north and northeast (Turgut and Eseller, 2000) (Figure 4.4).

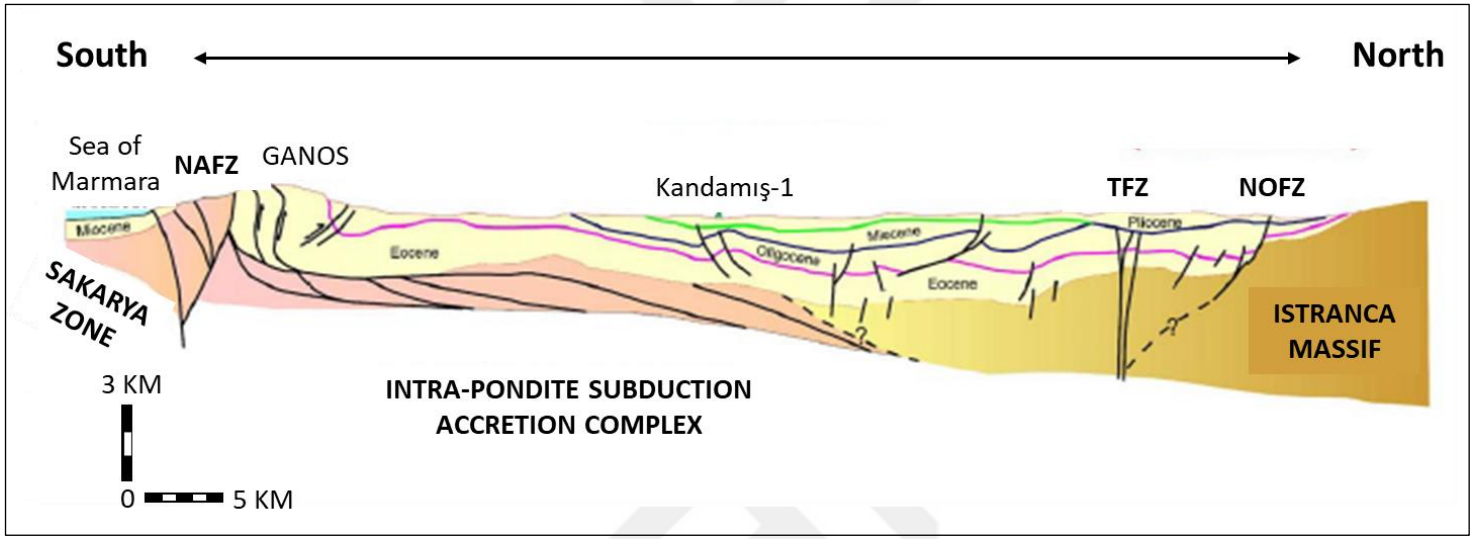

Figure 4.3. Geological cross-section from south to north showing Intra-pondite subduction zone and tectonic activities of the Thrace Basin (modified from Görür and Okay, 1996)

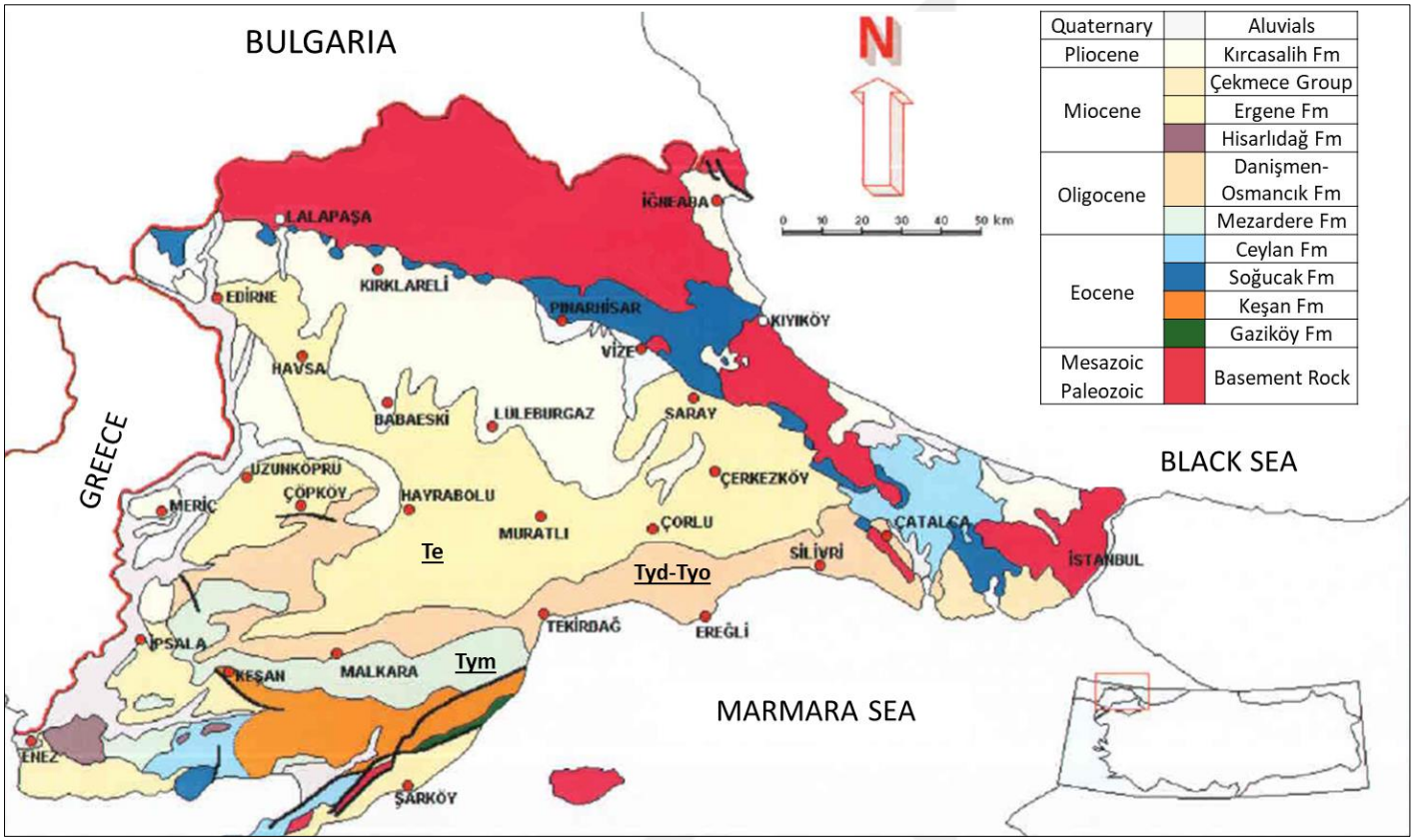

Figure 4.4. Geological map of the basin is shown in this figure. Oligocene sediments are exposed on the south and south-east part of the basin and basement rocks (shown as Tyd, Tyo and Tym). Miocene and Pliocene formations, Kırçasalih and Eregene, are observed to cover most of the area in the Thrace Basin (modified from Siyako and Huvaz, 2007).

4.4 Lithostratigraphic Settings

The Tertiary sedimentary successions are composed of interbedded fine and coarse grained clastics, limestones, lava flows and tuffaceous interbeds. Also, thin and thick coal beds interbedded with clastic sediments are observed (Turgut and Eseller, 2000). In the basin, Gazikoy, Keşan, Hamitabat, Koyunbaba, Sogucak and Ceylan formations were deposited in Eocene times; Mezardere, Osmancık and Danişmen formations were deposited in Oligocene; and Hisarlıdağ, Ergene and Kırcasalih formations in Miocene time sedimentary units. Geological cross-sections of the Thrace Basin are given in Figure 4.5.

4.4.1 Eocene Age Formations

Gaziköy Formation: The Gaziköy Formation was firstly described by NV Turkse Shell (1972). This formation is the oldest one and consists of interbedded thin sandstone, siltstone and dominantly shale size clastic sediments. Tuffs are also observed in the formation (Yaltırak 1995; Turgut and Eseller, 2000). Distal turbiditic facies indicates a marine depositional environment of this formation (Yaltırak 1995).

Keşan Formation: Keşan Formation was described by Gökçen (1967). Thickness of the Keşan Formation reaches around 2.5 km. in the basin. Lower part of the formation, approximately 1 km., is in the Middle Eocene and the rest of the formation is in the Upper Eocene (Siyako and Huvaz, 2007). Sümegen and Terlemez (1991) described the main lithology of the formation as thinly bedded, fine-grained and alternating sandstone, siltstone and mudstone. According to Yaltırak (1995), characteristic features of turbiditic sequence is observed.

Hamitabat Formation: The Hamitabat Formation was firstly described by Keskin (1974).

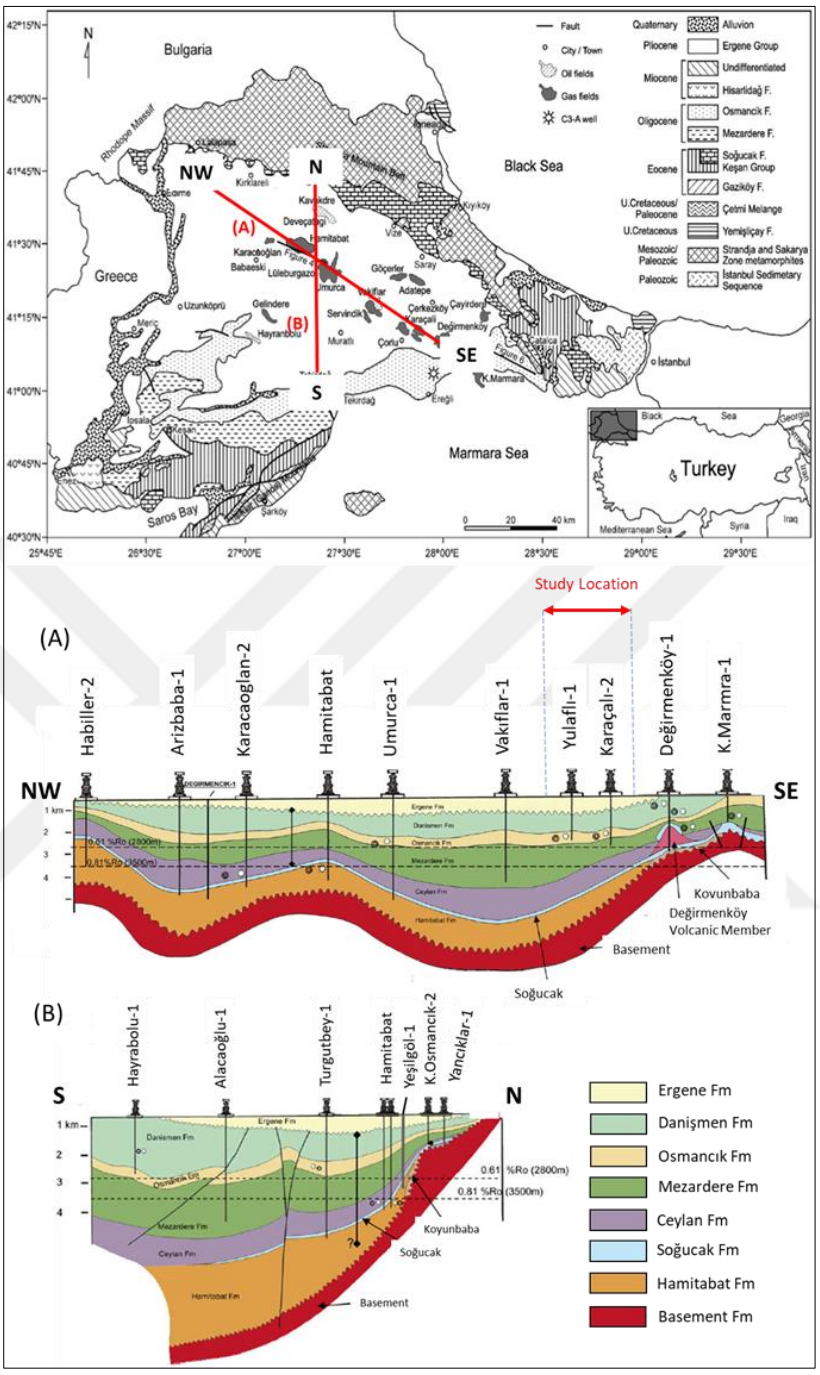

Figure 4.5. Geologic sections indicating formations in (A) NW-SE and (B) S-N directions. Study covers Yulaflı and Karaçalı wells shown in NW-SE directions (modified from Gürgey, 2005).

The formation consists of grey conglomerate, sandy conglomerate, sandstone and sandstone-dark shale alternation lithology. Depositional environment of the formation changes from shallow to deep marine. Sandstone lithologies are developed as proximal, distal and inter-channel turbidities in deep marine deposition system (Sünnetçioğlu, 2008) and these lithologies are a part of a wide submarine fan environment. Büyüktutku and Geçer (2020) categorizes the facies of the formation into three lithofacies according to petrographic properties. (1) Lithofacies A; coarse grain size, subrounded-subangular and moderate-bad sorting grains consisting of upper part of the fan, (2) lithofacies B; medium grain size, subrounded-rounded grains and moderate-good sorting indicating middle part of the fan, (3) lithofacies C; very fine grain sizes and lower part of the submarine fan. Middle part of the fan shows better reservoir quality comparing to upper and lower parts (Büyüktutku and Geçer, 2020).

Koyunbaba Formation: The Koyunbaba Formation was firstly identified by Krausert and Malal (1957). The formation overlies the Hamitabat Formation (Turgut and Eseller, 2000). Pebbly sandstones are observed at lowermost of the formation. Conglomerate-sandstone-siltstone-marn alternations are found at upper sections (Sarı et al., 2015). Middle-Late Eocene transgression is the source of shallow marine facies resulting these lithologies (Turgut and Eseller, 1999). Seismic and log correlations show that the thickness of the formation decreases at paleo-highs (Sünnteçioğlu, 2008).

Soğucak Formation: Holmes (1961) is the first one using the name of the Soğucak Formation. The formation is composed of reefal carbonates and thin clastics as a result of transgression during Early-Middle Eocene and Early Oligocene. Soğucak Formation is a reservoir rock and potential hydrocarbon producer in the basin (Varol et al., 2009).

Ceylan Formation: The Ceylan formation was firstly studied and identified by Ünal (1967). The formation covers upper part of Eocene and consists of turbiditic

sediments (Hoşgörmez and Yalçın, 2005). Ceylan formation underlies Mezardere Formation and overlies Soğucak Formation. The formation includes dark gray to greenish gray shales, carbonates (argillaceous limestone) containing volcanic and tuffaceous strata (Turgut and Eseler, 2000). Ceylan Formation is considered as a potential source rock due to fulfilling requirements in terms of maturity and the presence of organic matter (Hoşgörmez and Yalçın, 2005).

4.4.2 Oligocene Age Formations

Mezardere Formation: The Mezardere Formation was described by Ünal (1967). The formation is a prodeltaic facies of a deltaic environmet and transitional zone with underlying the Keşan and Ceylan Formations and overlying the Osmancık formation. The formation is considered as source rock for hydrocarbon bearing Osmancık and Danişmen Formations. The Mezardere Formation is composed of interbedded greenish to gray shales, siltstones, fine-grained sandstones, marlstones and tuffites. (Siyako, 2005; Moslow et al., 2014) Lithology content shows that tectonical activities are rare and depositional environment varies from shallow to moderate deep marine. (Yılmaz et al., 2016).

Due to lower energy of prodeltaic environment, lithology consists of mostly shales, especially, at the top of the formation. However, when petrographic characteristics and pressure gradient do not change significantly, the lithology becomes sandier at lower parts of the formation (Yılmaz et al., 2016).

Osmancık Formation: The Osmancık Formation was firstly defined by Holmes (1961) and named by Ünal (1967). The formation overlies Mezardere Formation and underlies Danişmen Formation. This formation is characterized with delta-front facies. The lithology of the formation consists of mainly alternation of sandstone and shales. Sandstones are greenish or yellowish grey, fine to medium size, moderately-well sorted, laminated and shale interbedded. Shales are greenish grey colored (Kesgin and Varol, 2003). Deposited sandstone reservoirs of the Osmacık Formation

are the most productive zones among Oligocene Formations; Danişmen, Osmancık and Mezardere Formations (Arpacı and Özdemir, 2016; 2020).

Danişmen Formation: The Osmancık Formation was firstly defined by Boer (1954). The Danişmen Formation is the shallowest unit of regressive deltaic system. The litology of the formation consists of shale, claystone, sandstone, pebble and coal seam (Perinçek et al., 2015). The observed thickness reaches about 1000 m. (Kasar et. al.., 1983; Siyako, 2005). However, due to erosion of the formation, it is suggested that the real thickness should be more than observed thickness (Siyako, 2005; Perinçek, 2015).

Although sand deposits in the Osmancık Formation are the most potential hydrocarbone zones in Oligocene age, sands in the Danişmen Formation are also potential reservoirs and hydrocarbon producer (Arpacı and Özdemir, 2016; 2020).

4.4.3 Miocene Age Formations

Hisarlıdağ Formation: The Hisarlıdağ Formation was firstly defined by Siyako (2006a) as a product of a volcanism varying bazaltic to andesit lithology containing silica (Güçtekin, 2017).

Ergene Formation: The first definition for the Ergene Formation was introduced by Boer (1954) (Siyako, 2006b). Because of the unconsolidated lithology, it mostly does not observe on the surface. The formation covers a wide area in the basin and has the lithology consisting of cross-bedded conglomerate, sandstone, mudstone, and claystone (Umut et al., 1983a, b; Duman et al., 2004; Siyako, 2006b). The thickness of the formation increases from edge to centre of the basin Yurtsever (1998).

Kırcasalih Formation: The Kırcasalih Formation was named by Boer (1954) and firstly used by Unal (1967). The formation was deposited discordantly to most of the older sediments (İmik, 1988; Siyako, 2006b). The lithology is composed of

unconsolidated pebbles, coarse grained pebbles and sandstone and sparse claystone. The formation was deposited in a fluvial sedimentary environment (Siyako, 2006b).

CHAPTER 5

LITHOSTRATIGRAPHY OF THE OSMANCIK FORMATION

5.1 Introduction

The Osmancık Formation was deposited during Oligocene age. The formation is underlain by Oligocene Mezardere Formation and overlain by Oligocene Danişmen Formation. The Osmancık Formation consists of upward coarsening deltaic facies (Siyako, 2006). Approximate maximum thickness of the Osmancık Formation was defined as 9000 meters (Koop et al. 1969, Turgut et al. 1991, Siyako 2005, 2006). A deltaic deposition system formed from beginning of Early Oligocene to end of Late Oligocene (Kaşar et al. 1983, Atalık 1992, Siyako 2006), which formations are called as Mezardere Formation (Kaşar et al. 1983, Siyako 2006)), Osmancık Formation (Ünal 1967, Kaşar et al., 1983, Siyako 2006) and Danişmen Formation (Boer 1954, Ünal 1967, Kaşar et al., 1983, Siyako 2006). A vertical generalized stratigraphic section is given in Figure 5.1.

5.2 Lithostratigraphy

Yenimuhacır group is composed of deltaic facies. The Osmancık formation consists of progressive delta-front deposits, which deltaic directions are specified by paleogeographic locations in the basin (Bürkan, 2010).

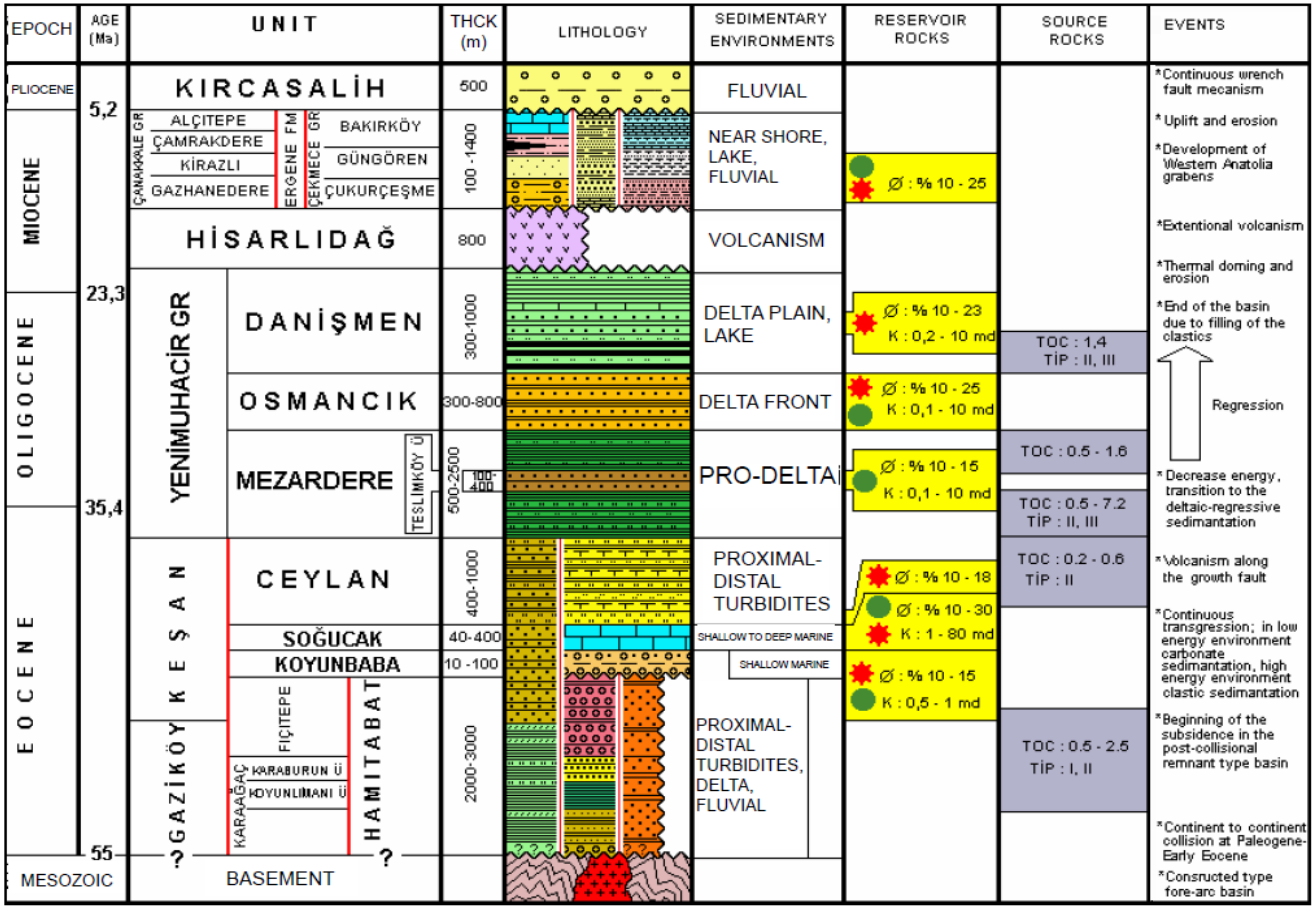

Figure 5.1. Generalized stratigraphy of the Thrace Basin showing reservoir and source rock properties including petrophysical properties, depositional environment, geological events and total organic carbon content (modified from Huvaz et al., 2005).

The age of the formation was defined from paleontological studies. Lamella branch, gastropod and ostracod fossils in the Osmancık Formation identify the age of the formation as Oligecene (Lebküchner, 1974). Studies according to terrestrial and marine palynomorphs, the age of the formation varies between early-late Oligocene (Ediger and Alişan, 1989, Batı et al., 1993, 2002, Akyol and Akgün, 1995).

The main lithology of the Osmancık Formation is sandstone facies with interbedded shales. Also, thin limestone and tuffs are observed. Facies in the formation are composed of cream-grayish colored, mostly thin-medium layered, fine-medium grained, fossil shell sandstones and blackish dark grey, plant clastic shales (Bürkan, 2010).

The main outcrops of the Osmancık Formation are located in the S-SW part of the Basin, covering İpsala, Keşan, Malkara, Tekirdağ and Marmara Ereğlisi from west to east (Figure 5.2).

Delta-front channel facies of the Osmancık Formation is clearly observed in Marmara-Ereğlisi and given in Figure 5.3 and 5.4. Also, around Paşayiğit, distributary channels are seen and discriminated from the deltaic facies by higher grain sizes consisting of conglomerates and sand sized particles (Figure 5.5). However, delta-front channel facies around Marmara Ereğlisi is composed of sand and silt sized particles. These outcrop photographs were used with the permission of the Thrace Basin Department, TPAO.

Another location for outcrops of the Osmancık Formation is Gokçeada (Figure 5.6). Sandstones interbedded with marn and shales are observed in this section (Fig. 5.7 A). Leaf fossil are also available in the section (Figure 5.7 B) (Gürcan et al., 2016).

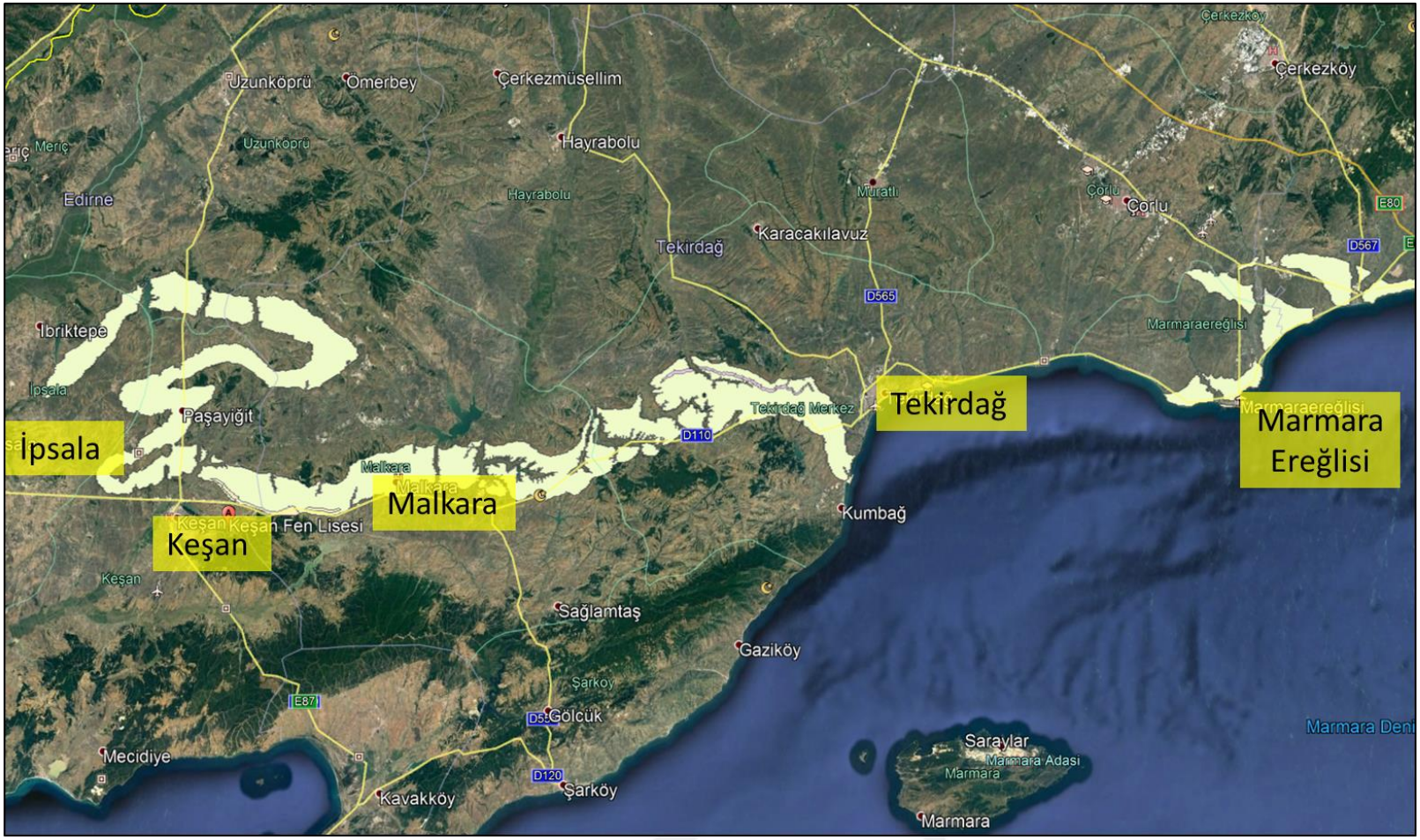

Figure 5.2. A location map indicating the spread area of the outcrops from the Osmancık Formation (illustrated with yellow color).

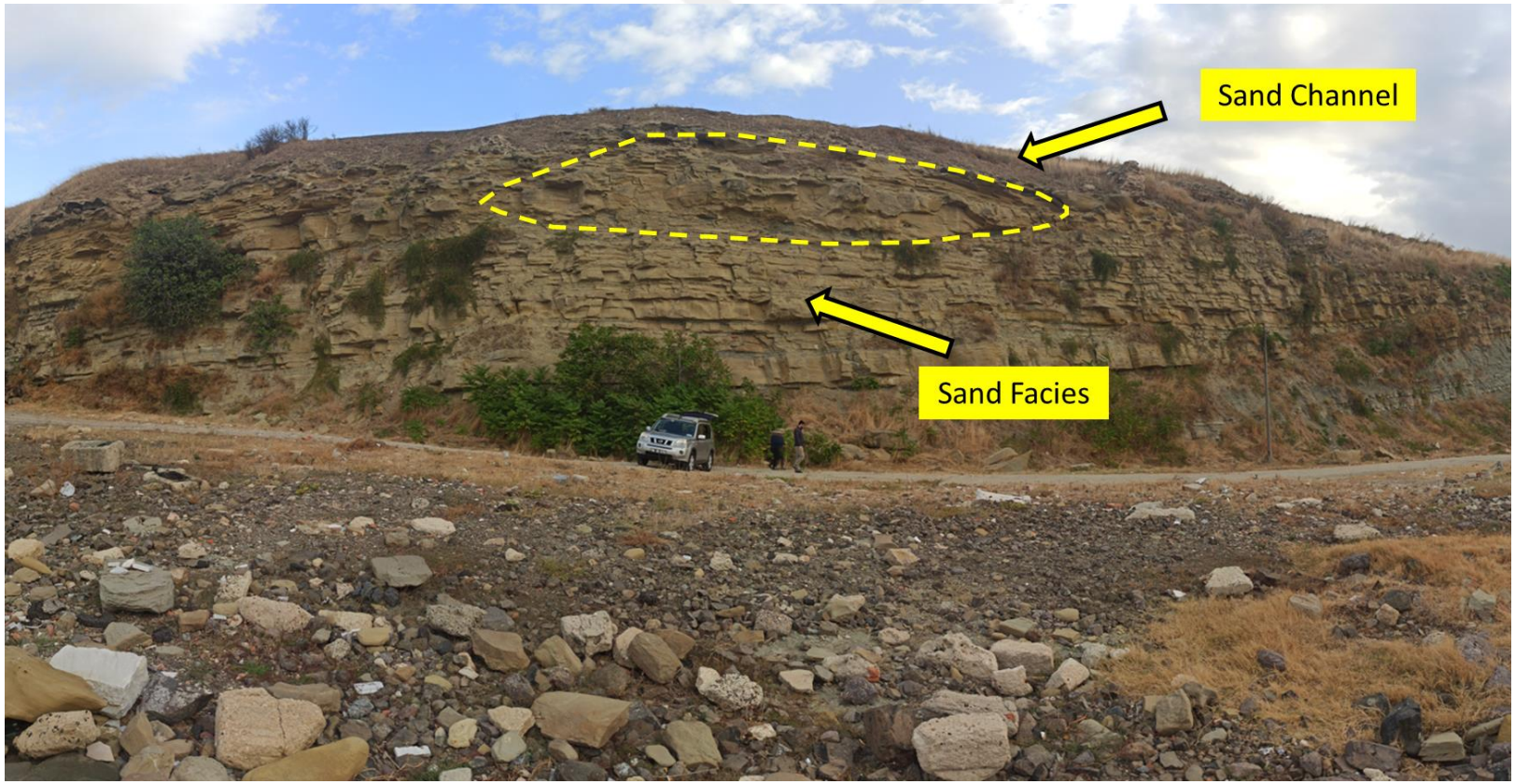

Figure 5.3. Sandstone facies and channels around Marmara Ereğlisi. Channels are marked with dashed yellow line.

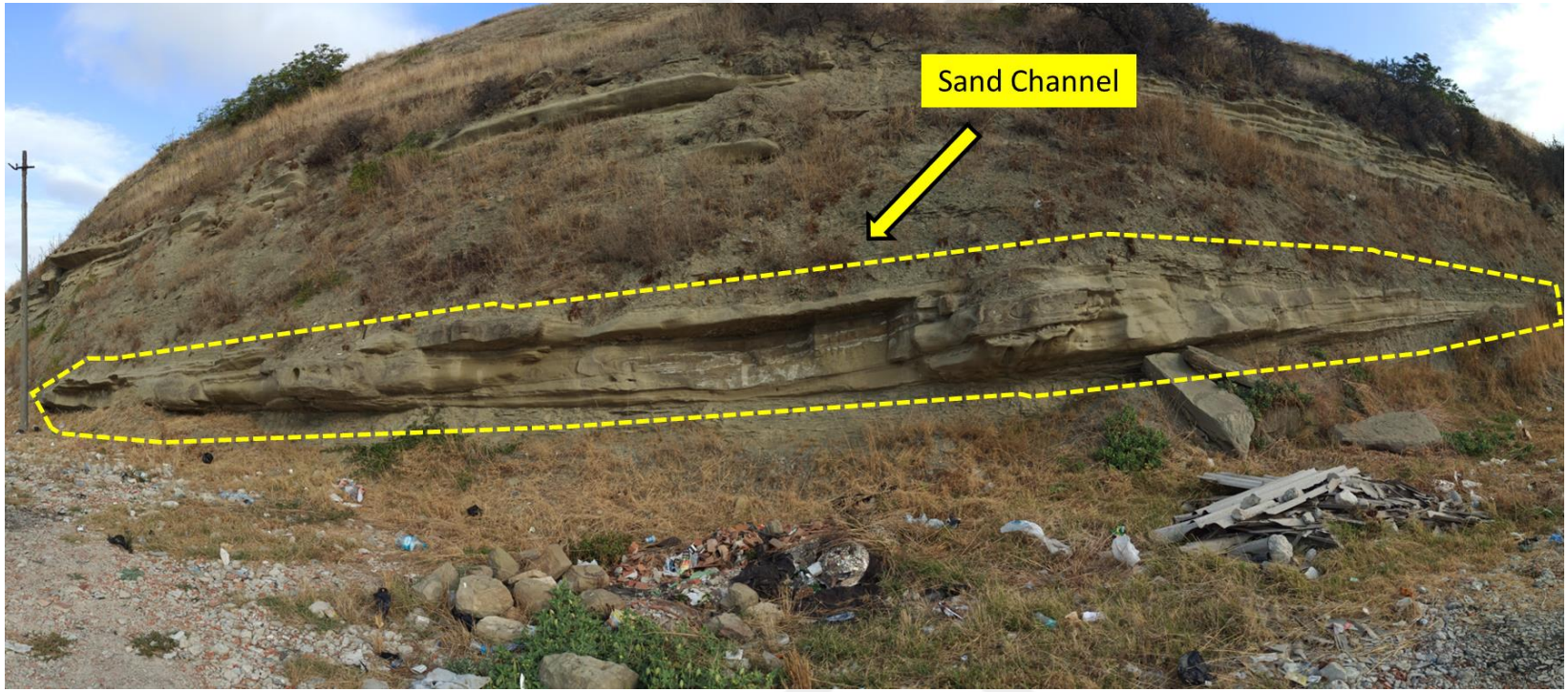

Figure 5.4. A clear lense shaped sand channel is pointed out, which is drawn with a yellow dashed line around Marmara Ereğlisi.

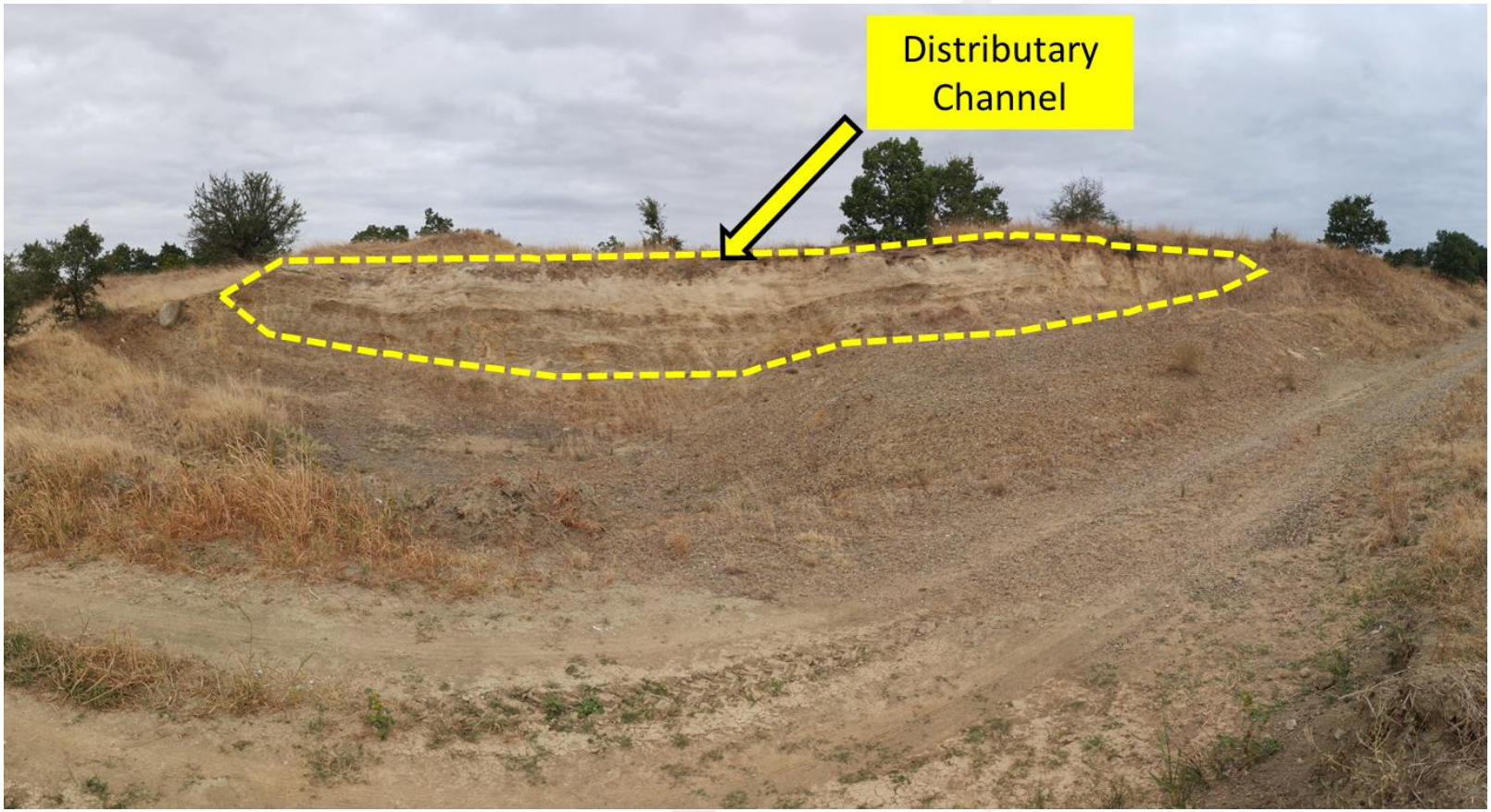

Figure 5.5. Distributary channel facies is observed and pointed out around Paşayiğit location.

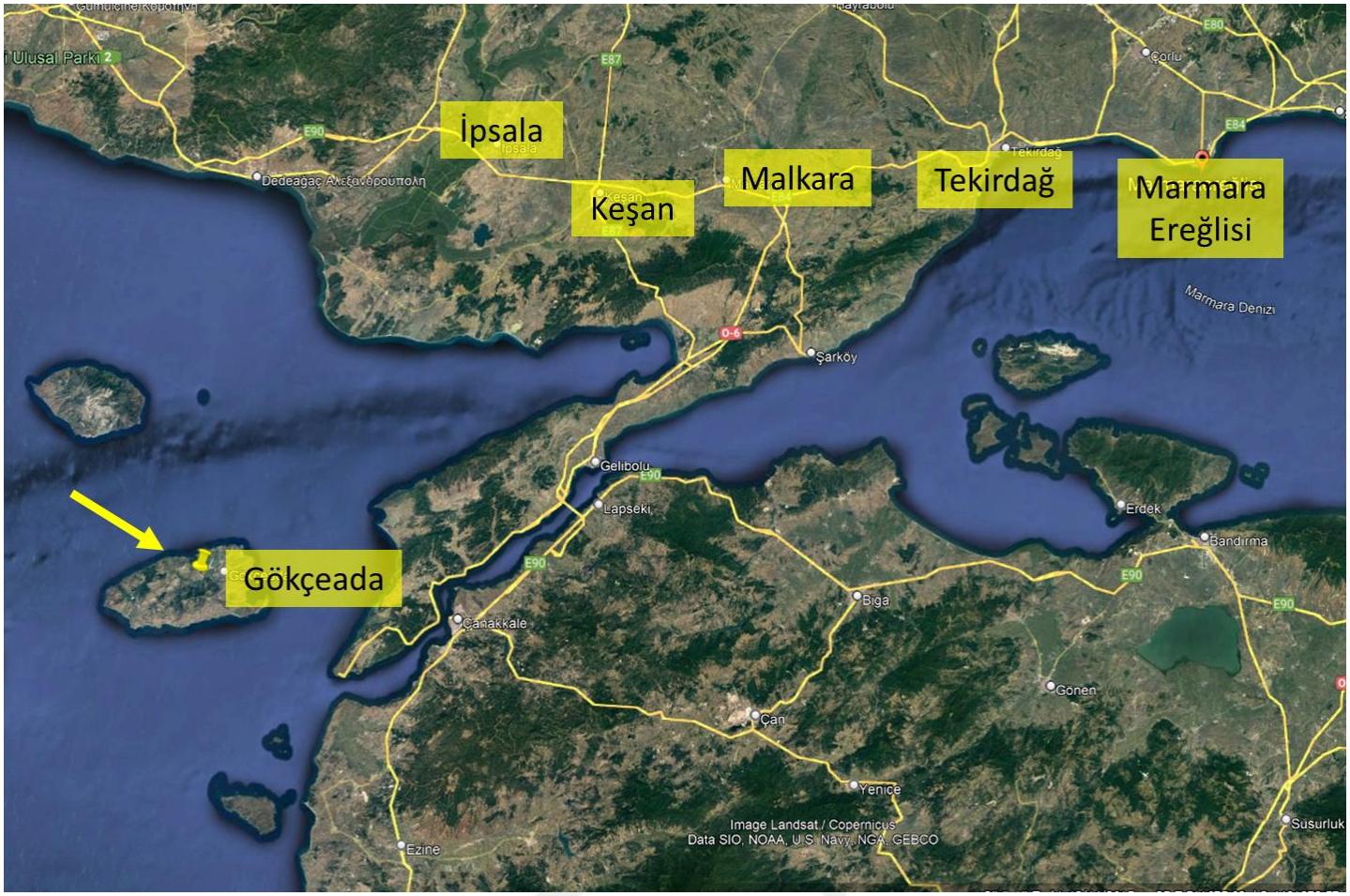

Figure 5.6. Location of another outcrop representing the Osmancık Formation (Gökçeada), which is located SW of the main outcrops.

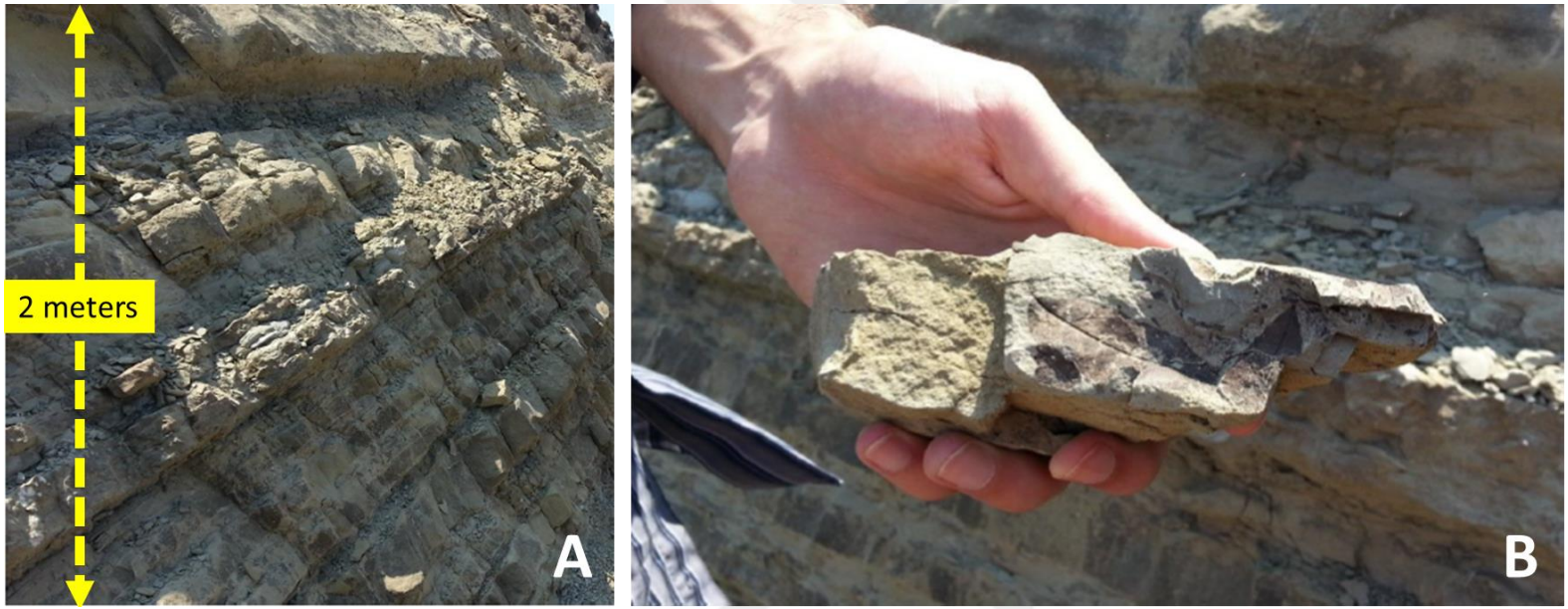

Figure 5.7. (A) Delta-front sandstones of the Osmancık Formation and (B) leaf fossils which are transported by paleo-delta and deposited into delta-front sandstones around Gökçeada.

5.3 Contact Formations

A transitional zone between Osmancık-Danişmen contact is observed and the quality of outcrops are insufficient to specify real contact between these formations. As a result of a multidisciplinary study, including field work, well-lithology studies and seismic interpretation and evaluation, coal seam layer was identified as Osmancık-Danişmen contact, which previously called as intra-Danismen (Siyako, 2005, 2006). Although the Osmancık Formation is overlain with the Danişmen Formation conformably, in the locations where the Danişmen Formation is eroded, the Osmancık Formation is overlain with the Ergene Formation and Miocene-Pliocene deposits unconformably (Atalık, 1992) (Figure 5.8).

The Mezardere Formation underlying the Osmancık Formation consists of pro-deltaic facies of the Yenimuhacır deltaic system. The Mezardere Formation includes mostly silt-sized sands and shale lithologies. Facies in this formation are gradually transited to the Osmancık Formation. (Siyako, 2006). The contact between Osmancık and Mezardere Formation is not very specified and mostly defined from the use of log and seismic data together.

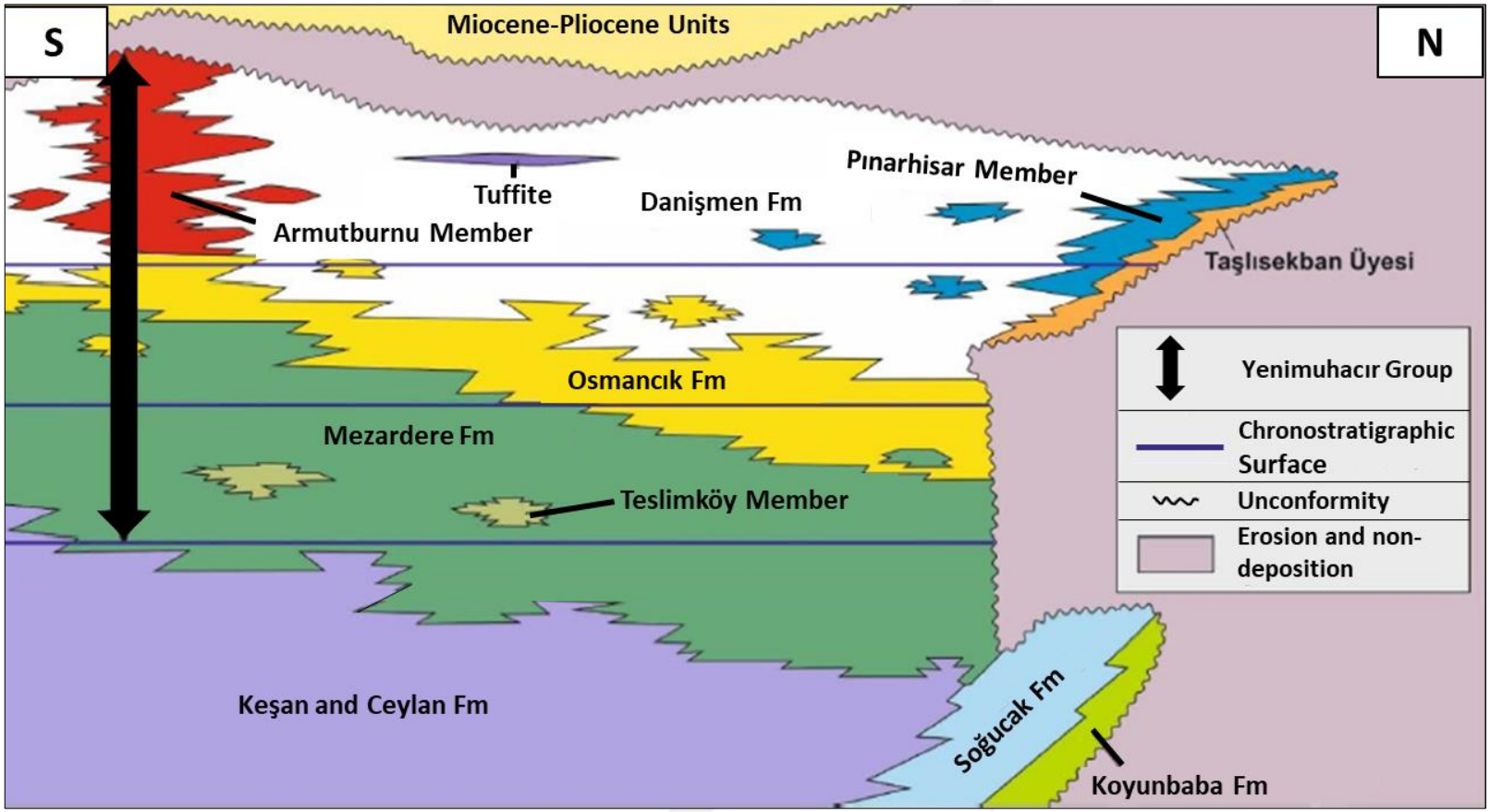

Figure 5.8. General stratigraphic correlation of the Yenimuhacır Group formations (modified from Siyako, 2006)

CHAPTER 6

METHODOLOGY AND DATA SETS

6.1 Introduction

Several methods have been applied to characterize reservoir properties of Oligocene Osmancık Formation in Karaçalı-Yulaflı Field. In this chapter, firstly, methodology of the study including qualitative and quantitative seismic interpretation, sedimentology, petrophysics and statistics will be discussed. Utilized softwares and tools will be explained.

The second part of this chapter includes location of the study area, utilized seismic data sets including acquisition and processing parameters, available well logs and their distribution all over the field and core data with measured parameter. All these aspects will be clarified in the following headings.

6.2 Methodology

A detailed workflow has been followed during this research from data editing to reservoir modeling. A summary of workflow is illustrated in Figure 6.1. All data used in the research was integrated to generate facies and petrophysical models.

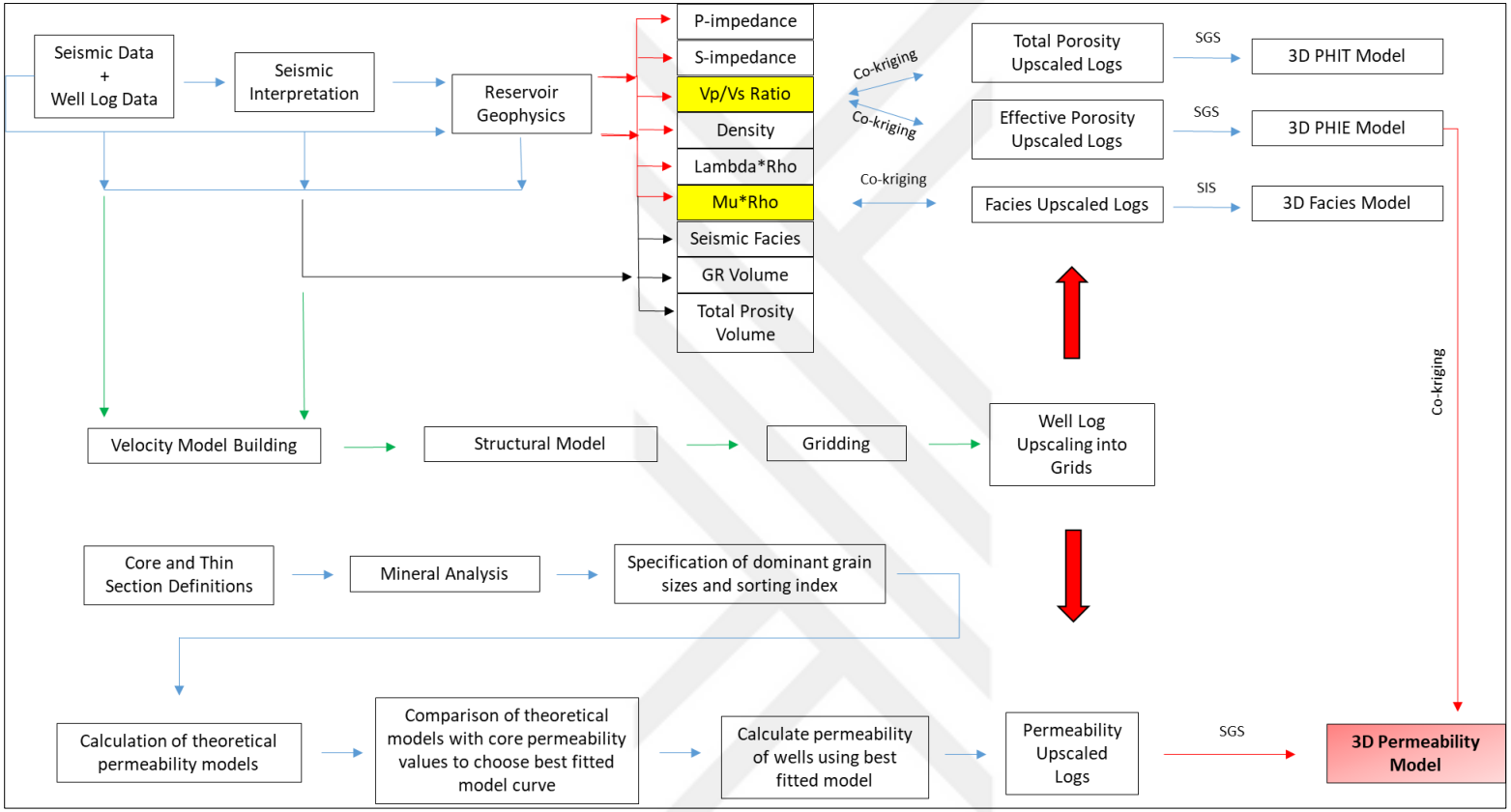

Figure 6.1. Modeling Workflow for deeper Osmancık Formation in Thrace Basin.

6.2.1 Sedimentology

Core data and thin sections were used to evaluate sedimentary structures and petrographic features of the sediments in deeper Osmancık Formation.

6.2.1.1 Preparation of Thin Sections

To prepare thin sections, firstly, a slab was cut out directly from a drilled core using a diamond saw. Then, one side of the slab was labelled while the other side is lapped and smoothed on a cast iron lap. For this purpose, 400 grit carborundum was used. Then, it is put on a glass plate and completed with 600 grit carborundum. A hot plate was used to dry it. After drying process, a glass slide was added and glued on the lapped side. Next, a thin section saw was used to cut off the section. A thin section grinder was utilized to make the section thinner. Last, a glass plate was used to create a thickness of 30 microns section by lapping on hand. Finally, the section was embedded on a holder and polished on a polishing machine until it was polished suitable enough.

6.2.1.2 Evaluation of Thin Sections

To understand the variability in lithology, thin sections from core data in several wells were examined. For this purpose, ZEISS Axio imager A2m microscope was used (Figure 6.2). To get the image of thin sections, a software called ZEN was benefited. Because point counter was not available during this study, to understand and evaluate thin sections and identify type of facies and related components, an image tool, called as FIJI-Imagej, was utilized. The results will be given and evaluated in detailed in the Chapter 7.

Figure 6.2. ZEISS Axio imager A2m microscope

6.2.2 Petrophysics

All wells drilled in the field includes processed petrophysical and volumetric logs such as total-effective porosity, water saturation and volume of clay. Petrophysical evaluation of producing zones in each well, having core measurement, was conducted.

The crossplot of measured core porosity and permeability data was utilized to understand petrophysical behavior of deeper Osmancık Formation, in which cores are available (Chapter 8).

6.2.2.1 Core Measurement Process

To achieve core measurement, firstly, hydrocarbon fluid was extracted from plug samples using Soxhlet toluene extraction system. Then, the samples were cleaned under alcohol bath and put in a vacuumed-oven system to eliminate salt content

remaining in the pores because of drilling fluid and formation water. Afterward, these samples were dried in an oven. After drying, weights and dimensions of the samples were measured.

A helium gas expansion porosimeter was utilized to measure porosity values of the samples taken out from the cores, and porosity values were measured by using "Boyle's Law". The samples were put in the matrix cap which is connected to porosimeter. Helium was diffused into the matrix cap and into the pores at a specific pressure and volume. During this process, pores were expanded. The volume of this expansion was recorded to measure volume of the grains. Bulk volumes were calculated by the dimensions of the samples using mathematical equations.

The core plug samples, which are cleaned by under alcohol bath and dried in an oven, were placed in a core holder of an air permeameter. The flow rate of the dry air going through the sample was monitored and differential pressure was calculated to obtain air permeability using "Darcy's Law". "Klinkenberg Correction" was utilized for the correction of air permeability to get liquid permeability.

HEP-P Helium gas expansion porosimeter and GASPERM steady state gas permeameter systems of Vinci Technologies were used to measure core porosity and permeability values (Figure 6.3).

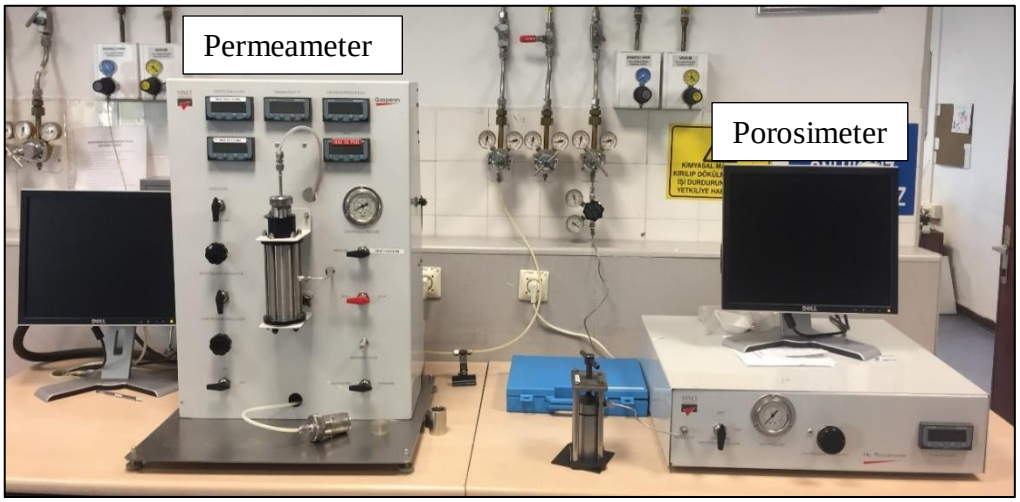

Figure 6.3. Porosimeter and permeameter systems.

6.2.2.2 Evaluation of Petrophysical Logs and Estimation of Permeability Curves

All wells having measured core data were evaluated and compared with processed petrophysical logs. Core measurements and their relationships with calculated log curves were explained in producing zones. Additionally, missing permeability curves were estimated using statistical and theoretically derived methods. For these purposes, Petrel software (version 2019) were used.

6.2.3 Conventional (Qualitative) Seismic Interpretation

Seismic reflections are the results of acoustic impedance contrast between two layers, which impedances are product of velocity and density. When the difference between impedances within encasing media is higher, reflections become stronger. These reflections are evaluated in terms of stratigraphic and structural behaviors of changing lithology and formation boundaries.

Qualitative interpretation is the fundamental step of this study. Using horizon and fault interpretations, a structural model was generated, which was a crucial part of

this study. This structural model was used for the following facies and property modeling sections as well.

Qualitative interpretation of the field in this research includes:

- well-to-seismic tie,
- seismic horizon and fault interpretation,
- velocity modeling and time to depth conversion,
- structural model generation aspects.

6.2.3.1 Well-to-Seismic Tie

While well log data is measured in depth domain, seismic data is acquired in time domain. To evaluate both data sets, scales should be correlated. For this purpose, well data is upscaled into seismic scale using extracted seismic wavelet. Paradigm Software (version 18) was utilized to implement the correlation between well and seismic data sets.

6.2.3.2 Seismic Horizon and Fault Interpretation

Interpretation of the faults and seismic reflections gives an insight about tectonic behavior, stratigraphy and structure of the field. Picking events of seismic reflections which are also called as horizon interpretation and selecting faults provide a general evaluation of the field, which is also significant to spot hydrocarbon-bearing zones. To implement seismic interpretation, Petrel Software (version 16) was utilized.

6.2.3.3 Velocity Modeling and Time to Depth Conversion

Seismic signals, sent subsurface by a seismic source, reflected from seismic interface and received by geophones are highly dependent on the acoustic impedances of seismic reflectors. When velocity and density values of a layer are high, seismic

signals move faster or vice a verse. In this respect, thicker formations with higher acoustic impedances may appear as thinner than what is in the reality. Therefore, the seismic data in time scale is necessary to be converted into depth scale. For this purpose, velocity of the field is required to be modeled. To create velocity model of the area, sonic logs and tops of each well and seismic horizons were used. Kriging method was performed to reveal velocity model. Petrel Software (version 16) was used as a for well-to-seismic correlation.

6.2.3.4 Generation of Structural Model

Integration of horizon and fault interpretation which are converted into depth domain leads to generate structural model of the study field. This structural model is not only important for the evaluation of the field geometry but also preparation of the framework for geostatistical reservoir modeling. To create this model, Petrel (version 16) was utilized.

6.2.4 Quantitative Seismic Interpretation

Conventional seismic methods are inadequate to understand the presence of hydrocarbon reservoirs. Quantitative seismic interpretation methods, also called as reservoir geophysics, are widely-used techniques such as amplitude-versus-offset (AVO) analysis, seismic inversion and seismic petrophysics.

6.2.4.1 Seismic Data Preconditioning

Pre-stack seismic gathers are the main inputs for quantitative interpretation techniques. Although data processing steps turn shot gathers into interpretable CDP gathers, some steps are necessary to apply to improve these gathers that are used as inputs for AVO and inversion studies such as angle mute, trim statics and parabolic

radon transform. For seismic data conditioning, Hampson Russell Software (HRS) (version 10.6) was used.

6.2.4.2 Log Data Editing and Shear Wave Estimation

The used log data set in this research is high quality. However, some distorted signals should be removed or edited and some missing log parameters are needed to be calculated and replaced. Especially, s-sonic log, which is one of the main inputs in quantitative seismic interpretation methods, is rarely measured. Therefore, this missing log parameter is necessary to be estimated for each well. Well log editing and shear wave estimation were completed using HRS (version 10.6).

6.2.4.3 AVO Analysis

Amplitude-versus-offset or amplitude-versus-angle is an important technique for those siliciclastic environments. Gas bearing and water bearing sandstone reservoirs with encasing shale lithology show different behavior of amplitudes with increasing offset or angle of incidence. AVO anomalies and classification help us to identify clastic reservoirs. This topic will be discussed in detail (Chapter 9). AVO/AVA analysis was implemented using HRS (version 10.6).

6.2.4.4 Prestack Seismic Inversion

Prestack seismic inversion is a well-known technique to estimate compressional and shear impedance information within formations. Using pre-stack seismic gathers, root-mean-square (RMS) velocity and well-log data sets, elastic parameters such as P-impedance, S-impedance, VP/VS ratio, density, lambda*rho and mu*rho can be obtained. This method is not only used for understanding lithology and fluid behavior on the field but also provide significant input for reservoir modeling. HRS

(version 10.6) and Paradigm (version 18) were utilized to implement pre-stack seismic inversion in Karaçalı-Yulaflı field.

6.2.4.5 Artificial intelligence

Supervised neural network: Well logs, stacked seismic data, elastic volumes generated from seismic inversion and calculated any attribute from seismic data are used to distribute petrophysical or lithological parameters (measured/calculated from well logs) with the aid of probabilistic neural network. Using this method, Gamma-Ray volume was created. HRS (version 10.6) was used for this purpose.

Un-supervised neural network: Using only seismic based data sets and principle component analysis (PCA), seismic traces were classified. These classes were evaluated in terms of lithology variations in this study. Paradigm (version 18) was benefitted to obtain classified seismic volume.

6.2.5 Geostatistics

Facies and property modeling methods were conducted to distribute facies, porosity and permeability parameters all over the area. For the purpose of modeling, geostatistical techniques, such as “Sequential Indicator Simulation” (SIS) and “Sequential Gaussian Simulation” (SGS), were implemented using Petrel Software (version 2019). Resulted volumes were mapped and displayed in the Petrel Software (version 2021).

6.3 Data Sets

In this section, location of the study area and available and used data sets will be given.

6.3.1 Location of the Study Area

The Thrace Basin is located in North-West part of the Turkey. Karaçalı field is located in south-east of the basin and in the block of 19C. The field is wrapped with Degirmenkoy and Corlu fields in the east and Cerkezkoy, Vakiflar and Cayirdere fields in the north direction (Figure 6.4).

6.3.2 Available Data Sets

The data set in this study consists of a 3D vibroseis seismic data covering an area of 104 km^2. Two seismic data sets were acquired and merged to create 3D seismic survey used in this study. East part of the field was acquired in 1996 and the west of the part is in 1997. Acquisition parameters are the same for both parts. SERCEL-SN-388 recording system was used and 540 channels were utilized. Recording length is 5 second and sampling rate is 2 milliseconds. Group and source intervals are 40 m. A 27 folded seismic data was collected for both east and west parts of the area. Distance between geophone lines is 240 m and source lines is 200 m. Near offset is 28 m. and far offset is 2031 m. Four vibro trucks were used for both seismic surveys. Sweep length is 8 s. and sweep number is 6. 5232 shots for east part and 8743 shots for west part were triggered (Table 6.1).

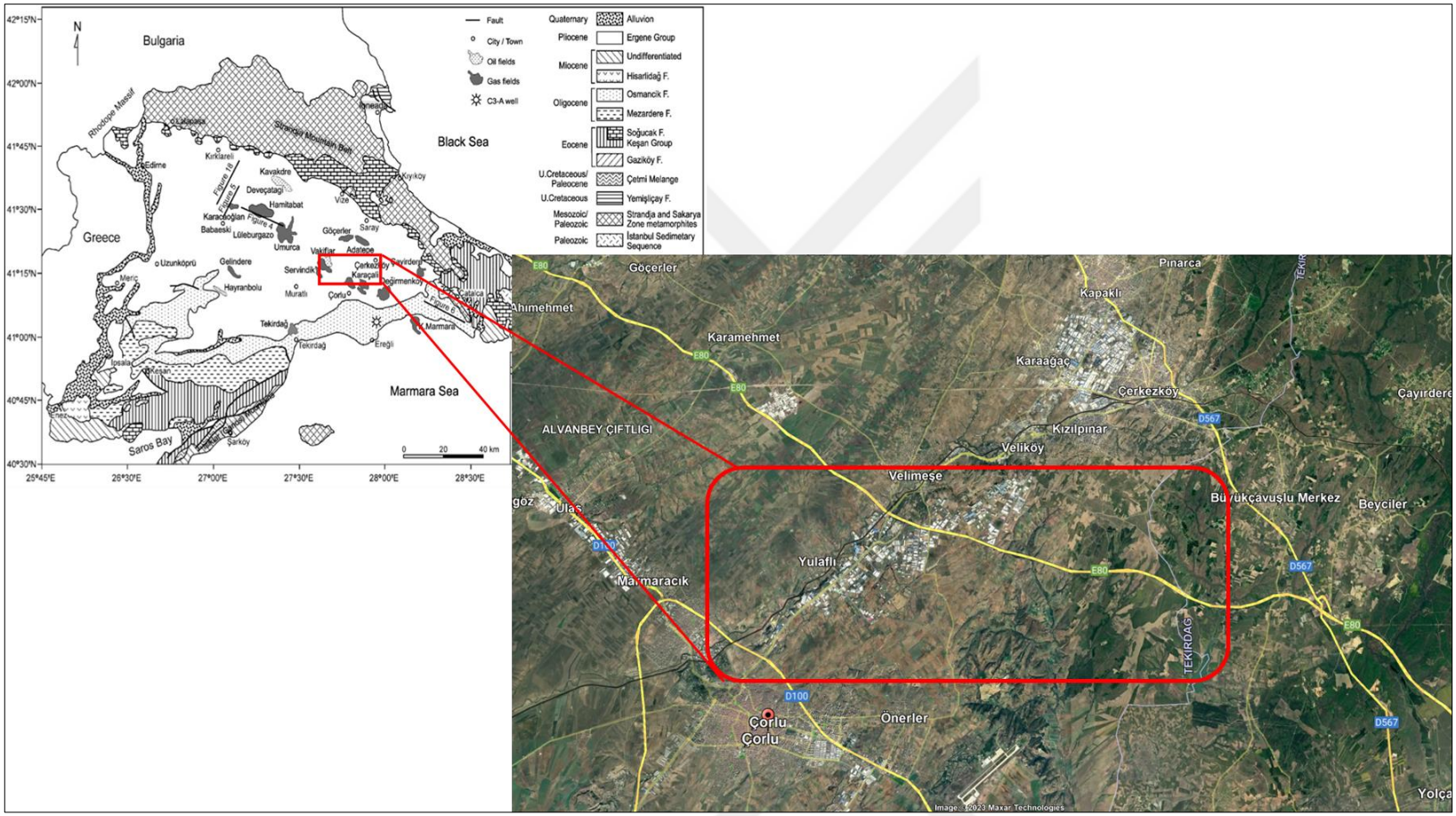

Figure 6.4. Location map of the study area. Red rectangle indicates the location of study area.

Table 6.1 Seismic Acquisition Parameters.

	Survey	KARAÇALI-3D	YULAFLI-3D
	Year	1996	1997
	Start Date	10/20/1996	10/13/1997
	Finish Date	11/10/1996	12/6/1997
RECORDING PARAMETERS	Channel Number (Per Lines)	90	90
	Number of Geophones in each Swath	6	6
	Recording System	SERCEL-SN-388	SERCEL-SN-388
	Channel Number	540	540
	Record Length	5 sn	5 sn
	Sampling Interval	2 msn	2 msn
	Min. Filter	OUT	OUT
	Max. Filter	125 Hz.	125 Hz.
	Group Interval	40 m	40 m
	Shot Interval	40 m	40 m
	Bin size	20x20 m	20x20 m
	Fold	27	27
	Geophone Line-up	1*24 INLINE	1*24 INLINE
	Geophone Line Distance	240 m	240 m
	Shot Line Distance	200 m	200 m

Table 6.1 (cont'd)

	Near Offset	28 m	28 m
	Far Offset	2031 m	2031 m
SHOT PARAMETERS	Seismic Source	Vibrator (VVCA/E)	Vibrator (TR-4-TI)
	Vibro Number	4	4
	Sweep Starting Frequency	12 Hz.	10 Hz.
	Sweep Finishing Frequency	74 Hz.	80 Hz.
	Sweep Length	8 sn	8 sn
	Sweep Number	6	6
	Sweep Type	Non-linear+3dB/Oct	Non-linear+3dB/Oct
	Taper	0,3 sn	0,3 sn
TOPGRAPHY	Total Shot Number	5232	8743
	Total Station Number	5167	8164
	Total Station Line Number	34	35
	Total Geophone Line Number	36	54
	Total Swath Number	11	17
	Toplam Field	46,894 Km^2	76,637 Km^2

After the acquisition of seismic data had been completed, raw gathers were obtained. These raw shot gathers were processed to prepare data for interpretation. A workflow has been summarized in Figure 6.5. From the creation of geometry to generation of seismic gathers and stacked seismic data, several steps were followed as it is outlined in the workflow chart. The resulted volumes were used for the purpose of interpretation and reservoir geophysics studies.

In the study field, three well groups are available. Ten wells in group-1, nine wells in group-2, seven wells in group-3 and two wells out of these well groups; totally, 28 wells with full-set logs are available (Table 6.2). TPAO is the owner of these wells. The company has done all the measurements for each well log data. Two drilled wells during the application of this study were used for blind test. One belongs to well group-1 (well-12T) and another is in well group-2 (well-210). These wells will be discussed in Chapter 10. Location of input wells and group displays are illustrated in Figure 6.6 and 6.7. Zoomed display of the wells belonging each group is given in Figure 6.8. Additionally, core data from Well-12, 13, 15, 16, 21 and 32 are available. These cores were drilled in deeper part of the Osmancık Formation. Porosity and permeability values were also measured. Table 6.3 shows core depth intervals in each well. Thin sections were also prepared in each core except well-21. Several SEM photographs are also present in the study.

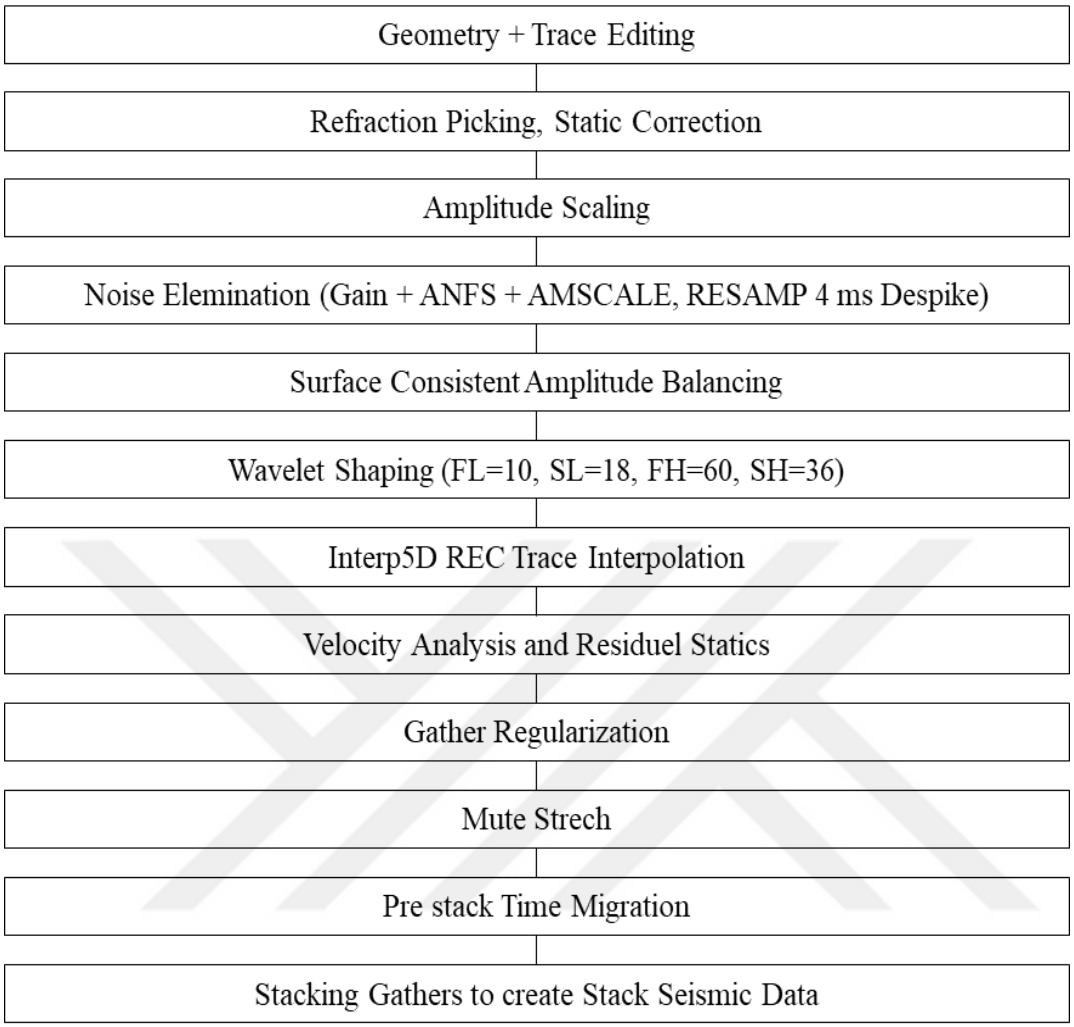

Figure 6.5. Chart of the process sequence of seimic data.

Table 6.2 Available logs in each well used as input for the study.

Well	GR	SP	CALI	DT	DTS	NPHI	RHOB	MSFL/ LLS/ LLD	Processed Logs
12	√	√	√	√	X	√	√	√	√
13	√	√	√	√	X	√	√	√	√
15	√	√	√	√	X	√	√	√	√
16	√	√	X	√	X	√	√	√	√
17	√	√	√	√	X	√	√	√	√
18	√	√	√	√	X	√	√	√	√
19	√	√	√	√	X	√	√	√	√
110	√	√	√	√	X	√	√	√	√
111	√	√	√	√	√	√	√	√	√
112	√	√	√	√	√	√	√	√	√
21	√	√	√	√	X	√	√	√	√
22	√	√	√	√	X	√	√	√	√
23	√	√	X	√	X	√	√	√	√
24	√	√	√	√	X	√	√	√	√
25	√	√	√	√	X	√	√	√	√
26	√	√	√	√	X	√	√	√	√
27	√	√	√	√	X	√	√	√	√
28	√	√	√	√	X	√	√	√	√
29	√	√	√	√	X	√	√	√	√
31	√	√	√	√	X	√	√	√	√
32	√	√	√	√	X	√	√	√	√
33	√	√	√	√	X	√	√	√	√
35	√	√	√	√	X	√	√	√	√
36	√	√	√	√	√	√	√	√	√
37	√	√	√	√	X	√	√	√	√
38	√	√	√	√	X	√	√	√	√
41	√	√	√	√	X	√	√	√	√
51	√	√	√	√	X	√	√	√	√

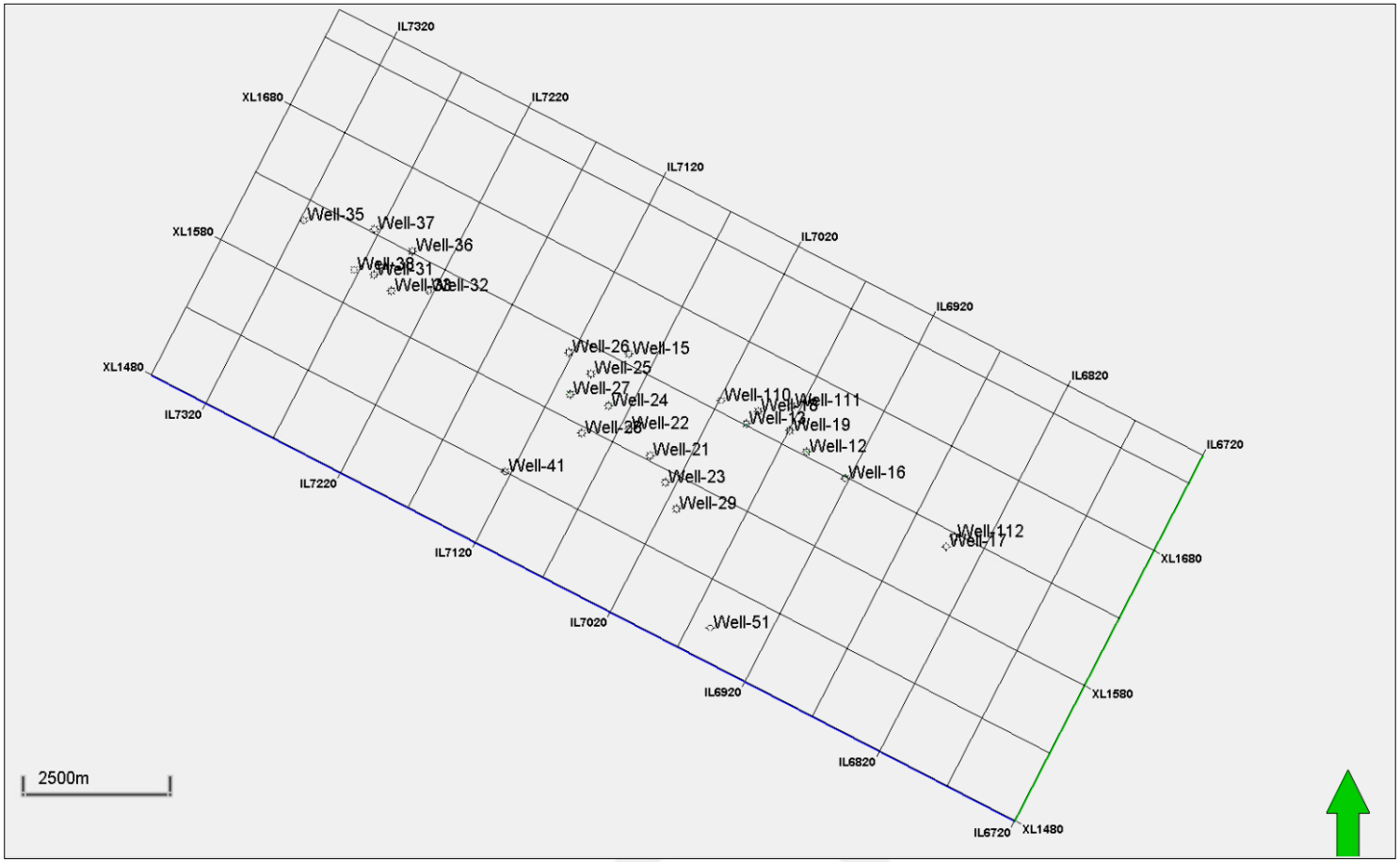

Figure 6.6. Geometry and location map of 3D seismic survey and wells.

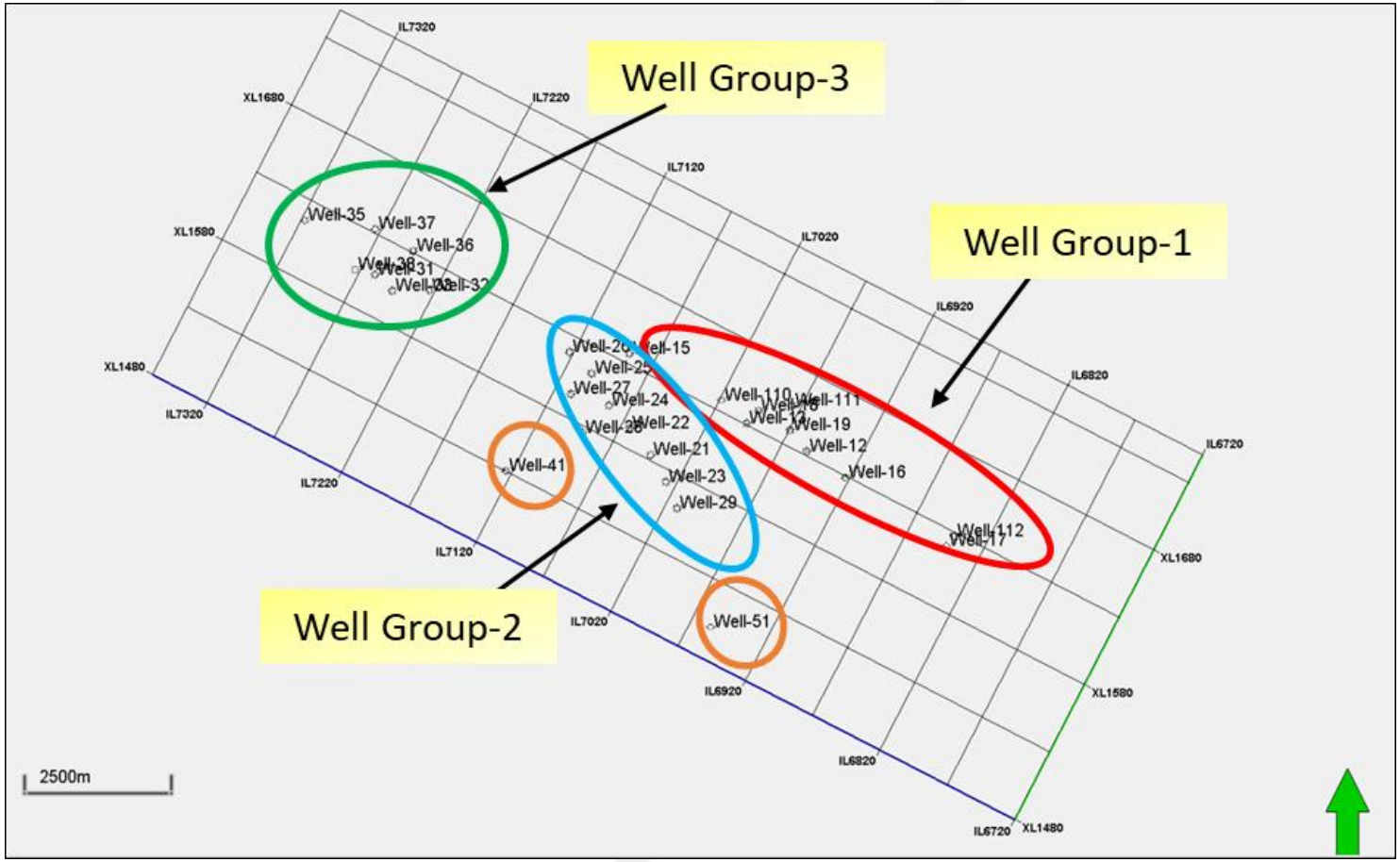

Figure 6.7. Well groups and locations in base map.

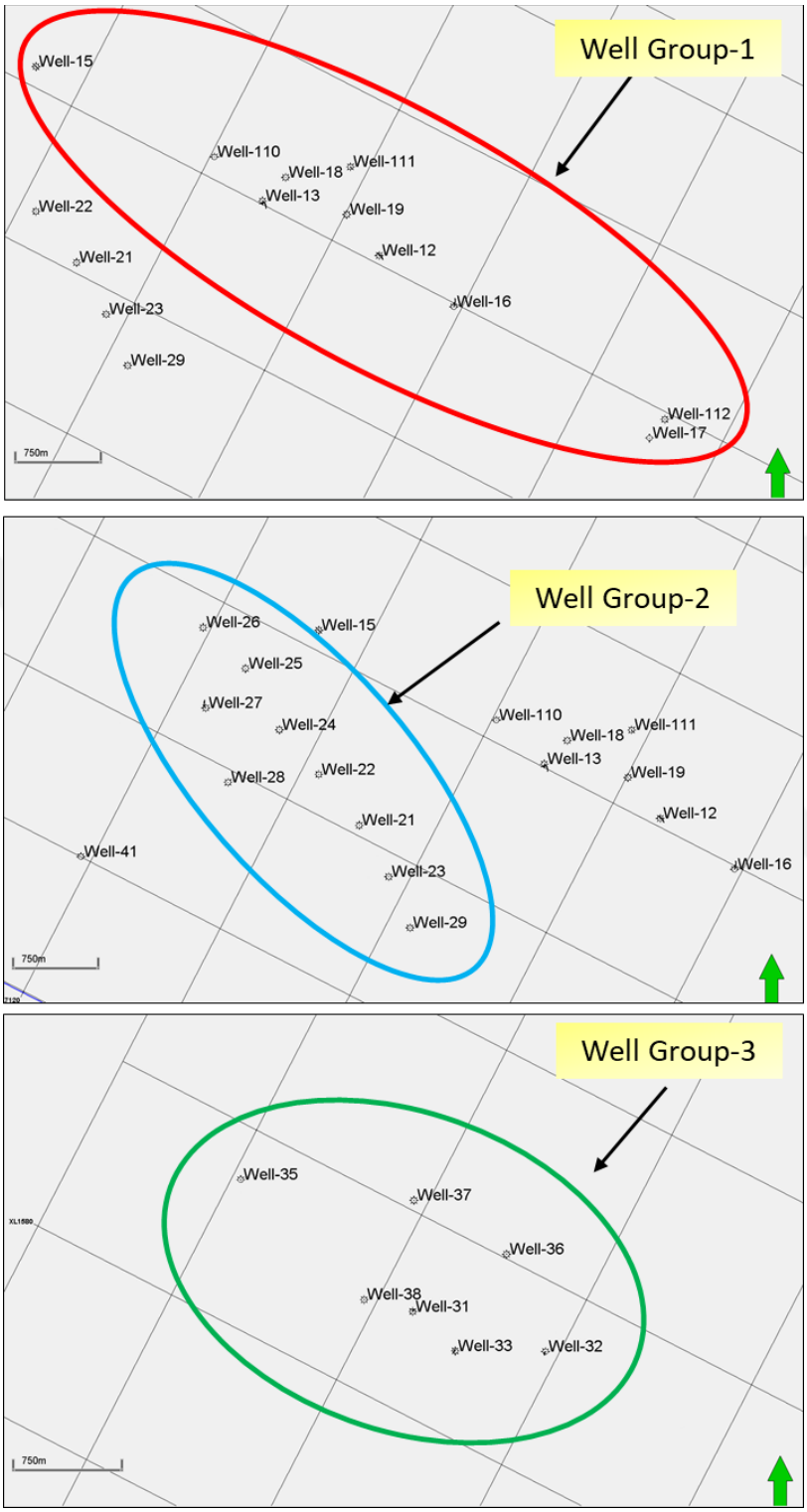

Figure 6.8. Zoomed display of well group-1 (top), group-2 (middle) and group-3 (bottom) wells.

Table 6.3 Available core plugs and depth intervals.

Well Name	Core No.	Depth Interval
Well-12	1	1347-1351.5
Well-13	1	1305-1314
	2	1489-1497.5
Well-15	1	1360.7-1369
	2	1404.5-1413.5
Well-16	1	1527-1531
Well-21	1	1651-1654
	2	1706-1714
Well-32	2	1798-1805.7

In addition to available data sets, a detailed Thrace Basin report, well reports and sedimentology report provide insight into studied problem. These reports will be listed in reference section at the end of this study.

CHAPTER 7

SEDIMENTOLOGY

7.1 Introduction

Clastic sediments are the result of the weathering and erosional processes of the rocks. Grain sizes and the content of the sediments are the significant elements for the classification of those clastic rocks. For a detailed classification and analysis of sedimentary rocks, a petrographic analysis is necessary (Nichols, 2009).

Udden (1914) and Wentworth (1922) classified clastic sediments according to grain sizes, which a detailed classification is given in Figure 7.1. According to this classification, 4 categories can be given as below:

- Clay (<4 μm),
- Silt (4 μm to 63 μm),
- Sand (63 μm to 2 mm),
- Gravel (>2 mm).

Sand can be defined as sediments consisting of grain sizes varying between 0.063 mm to 2 mm. Sedimentary rock formed from sand sized particles is called as sandstone. Sand and sandstone are composed of two categories: (1) Detrital grains containing quartz, feldspar, mica, heavy minerals and miscellaneous minerals and (2) fragments including lithic fragments, biogenic fragments, authigenic minerals and matrix. On the other hand, clay and silt can be defined as very small grain sized sediments which can be generally determined using optical techniques. Sedimentary rocks formed from clay or silt are called as claystone or siltstone (Nichols, 2009).

if a petrographic analysis is available, Pettijohn et al. (1987)'s classification is used (Figure 7.2) which is also called as "Toblerone Pilot". This scheme is helpful to discriminate whether the type of sandstone is closer to feldspar, quartz or lithic fragment. According to matrix content, facies can be classified as arenite, wacke or mudrock.

Sedimentary structures are significant features referring characteristic of depositional environment. Although these features can be observed in the field, some features are detectable on core plugs.

One aspect of this chapter is the examination of sedimentary features using core plugs to evaluate depositional environment. Another important topic is the petrographic analysis using available thin sections to reveal facies type, content and properties.

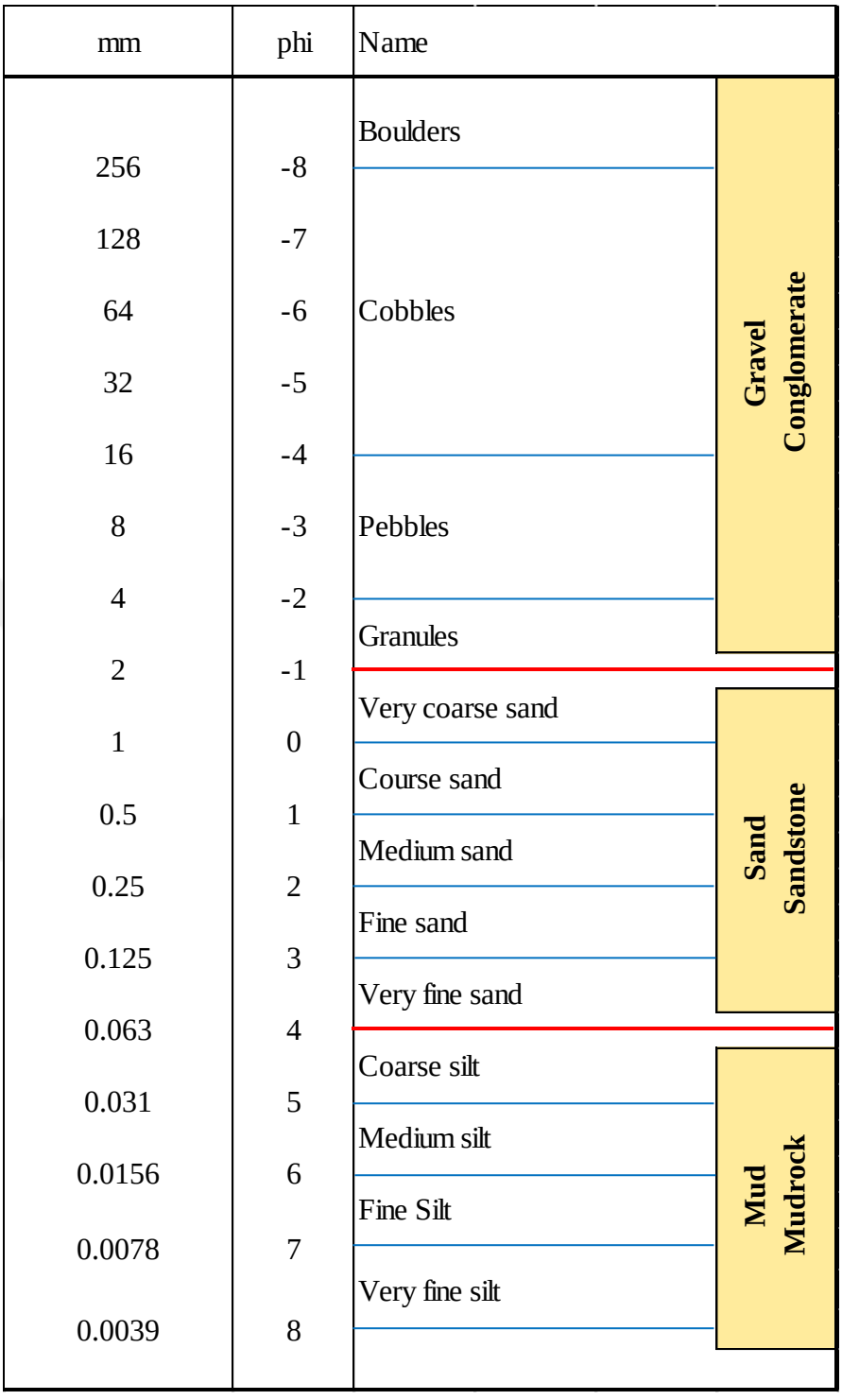

Figure 7.1. The Udden-Wentworth (Udden 1914; Wentworth 1922) scale according to grain sizes of clastic sediments.

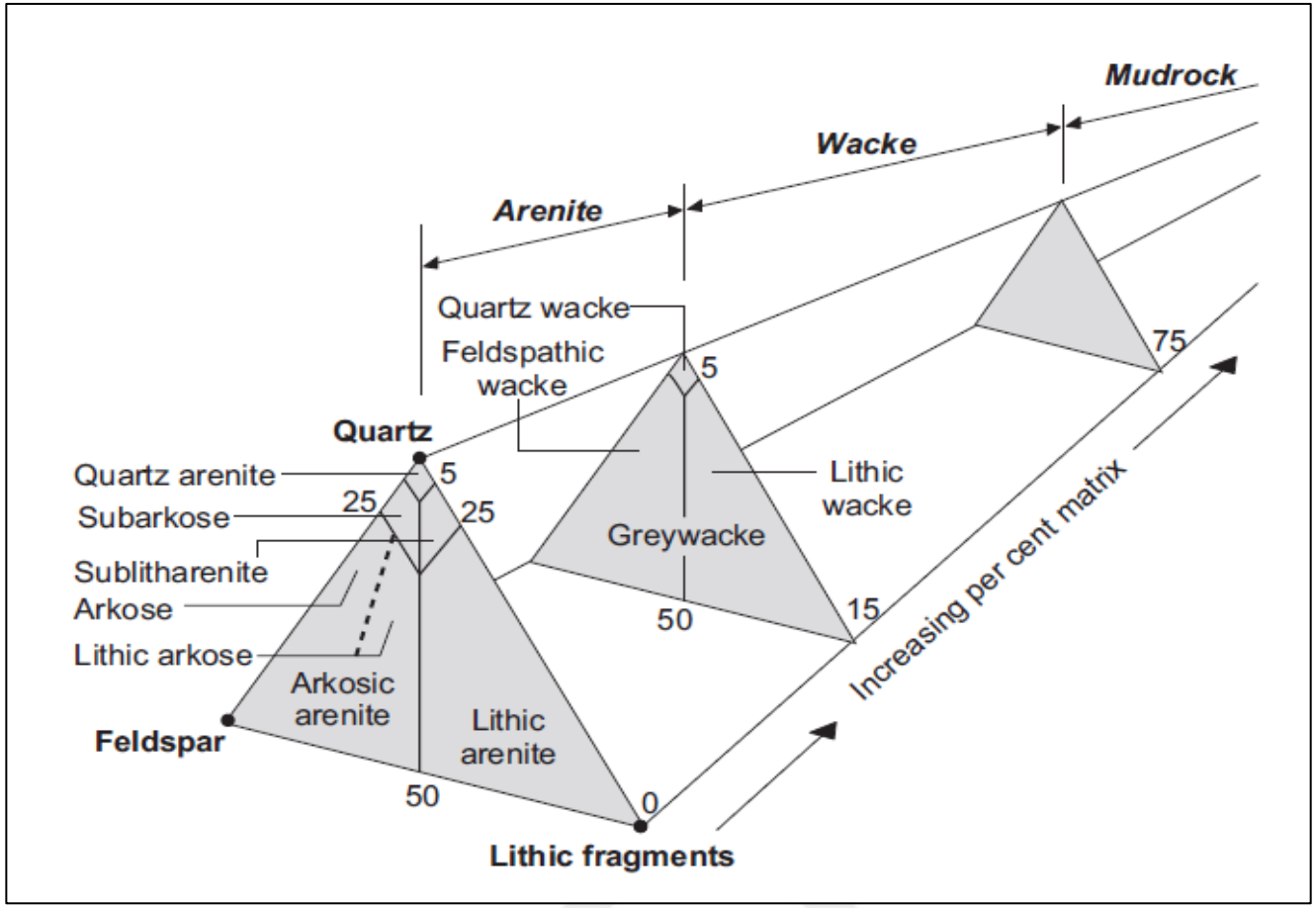

Figure 7.2. The Pettijohn classification (1975).

7.2 Evaluation of the Core Samples

Core samples taken from wells in the field of Karaçalı-Yulaflı are from deeper Osmancık Formation. As it was given in Table 6.3, core data from six wells were studied; namely, well-12, 13, 15, 16, 21 and 32. Location of these wells are demonstrated in Figure 7.3.

7.2.1 Well-12

Well 12 was drilled in 1995. This well is one of the deepest wells among Well Group-1 with a 2200-meter drilling depth. The Osmancık Formation includes alternating sandstone and shale. Shale thickness increases towards the Mezardere Formation. One core plug was taken out from the well between 1347-1351.5 meters. Core indicates sandstone, shale and siltstone interbeds. Fining upward sequence, rip-up shale clasts and weak current ripples are observed. Burrowing is very common in these sandstones composed of distribution channel deposits. Shale laminations are in the form of horizontal, parallel lamina. Charred root crumbs are also observed (Uygur et al. 2000). Core is not preserved well; however, horizontal shale laminae and some wavy structures are observed (Figure 7.4). Core descriptions are given below:

0-3 m. Shale: Grey colored, sand interbedded, consolidated, with abundant varves,

3-4.5 m. Sandstone: Light grey colored, unconsolidated, fine/medium grained, moderately sorted, weak carbonate cemented, with low interparticle porosity.

7.2.2 Well-13

Well-13 was drilled in 1997 with a 2125-meter drilling depth. In the well, cores from two different depth intervals, 1305-1314 and 1489-1497.5 meters, were taken out.

Core definitions are given below:

Core Number 1 (1305-1314.60 m.): Dominantly sandstone-siltstone alternation was observed (Figure 7.5).

0-0.30 m. Sandstone: Grey-light grey colored, mostly hard-brittle quartz, micaceous, fine grained, angular, poorly/medium sorted, weak carbonate cemented, with low interporosity.

0.30-0.55 m. Siltstone: Light grey colored, hard-brittle carbonated, sandstone-shale interbedded.

0.55-4 m. Sandstone-Siltstone Alternation: 10-30 cm thickness variation of sandstone-siltstone alternation.

4-9 m. Sandstone-Siltstone Alternation: 1-10 cm thickness variation of sandstone-siltstone alternation.

Core Number 2 (1489-1497.50 m.): Sandstone-shale alternation was observed (Figure 7.6).

0-0.40 m. Shale: Grey-dark grey colored, partly hard brittle carbonated, micaceous with varves.

0.40-0.70 m. Sandstone: Grey-light grey colored, mostly hard-brittle quartz, micaceous, carbonate cemented fine/medium grained, angular, weakly/medium sorted, with low interporosity.

0.70-0.85 m. Shale.

0.85-1.30 m. Sandstone.

1.30-1.50 m. Laminated sandstone-shale alternation (1-5 cm or less).

1.50-4.40 m. Sandstone.

4.40-4.50 m. Sandstone-shale alternation.

4.50-4.90 m. Sandstone

4.90-5.40 m. Sandstone-shale alternation.

5.40-6.90 m. Shale.

6.90-8.50 m. Sandstone

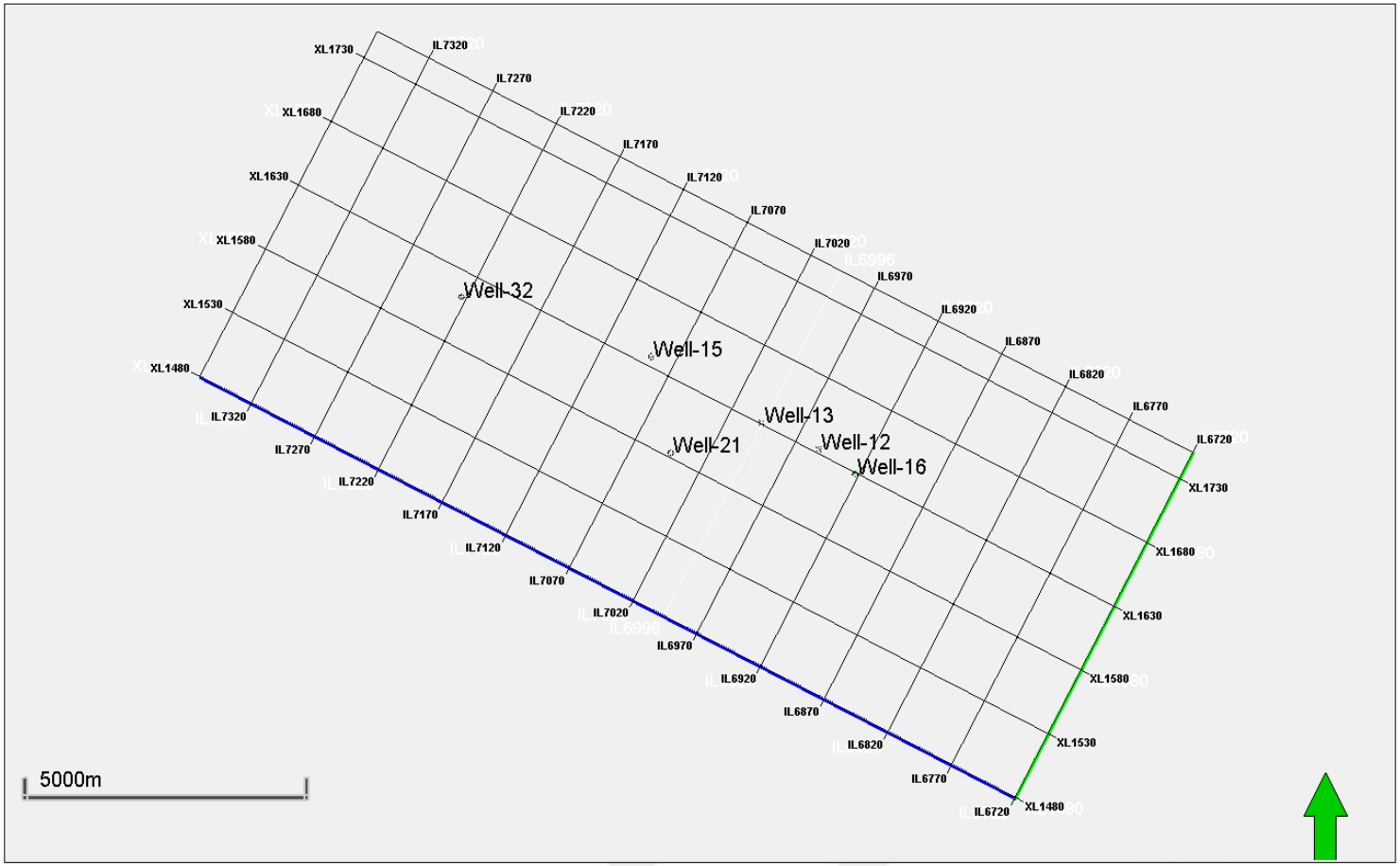

Figure 7.3. Location of the wells with core samples. Well 12, 13, 15 and 16 are group-1 wells, Well-21 is group-2 well and well 32 belongs to group-3.

Figure 7.4. Core-1 from Well-12 (1347-1351.5 meters). Horizontal shale lamina and convolute lamination are observed in core plugs.

Figure 7.5. Core-1 from Well-13 (1305-1314.60 meters). Sandstone-siltstone alternations are illustrated.

Figure 7.6. Core-2 from Well-13 (1489-1497.50 meters). Laminated shale-sandstone alternations with varying thickness are indicated.

7.2.3 Well-15

Well 15 was drilled in 1997 with a drilling depth of 1784 meters and ended inside the Osmancık Formation. Two core plugs were taken out of the well. The first core was drilled out from 1361-1369 meters. Distribution channels are dense in the core. Rip-up shale clasts are observed at the base of the core. Going upwards; fining upward sequence, groove marks within shale and siltstones, stratification without layering, cross stratification and climbing ripples, slumps and parallel lamination are observed (Figure 7.7 and and 7.8). The depth interval of the 2nd core is between 1404.5-1413.5 meters and mostly composed of channel sands. Moving upwards, fining upward sequence, shale rip-up clasts, bioturbation, parallel and wavy laminations, cross-stratification and climbing ripples, loading structures are observed (Figure 7.9). Core descriptions are shown below:

Core Number 1 (1361-1369 m.): Dominantly sandstone-siltstone alternation was observed.

0-1.79 m. Sandstone: Off-white, light greenish colored, mostly quartz, sparsely limestone, chert, magmatic and metamorphic micaceous, hard brittle, fine/medium grained, sub-angular, moderately sorted, carbonate cemented, with low interparticle porosity

1.79-2.27 m. Siltstone: Grey and green colored, laminated, shale interbedded,

2.27-4.64 m. Sandstone,

4.64-5.99 m. Siltstone,

9.99-6.12 m. Sandstone,

6.12-6.18 m. Siltstone,

6.18-8.10 m. Sandstone.

Core Number 2 (1404.5-1413.5 m.): Dominantly sandstone-shale alternation was defined.

0-1.52 m.: Shale: Dark grey-greenish colored, hard, fine dissipated pyrite and micaceous carbonated,

1.52-1.84 m.: Shale: Grey and green colored, with hard brittle sand, fine dissipated pyrite and micaceous carbonated, sandstone interbedded (fine grained, with low interparticle porosity),

1.84-2 m.: Sandstone: Off-white, grey, and light green colored, mostly quartzite, fine grained, sub-angular, moderately sorted, carbonate cemented, with low interparticle porosity, thin shale interbedded,

2-2.35 m.: Sandstone,

2.35-3.85 m. Sandstone: Course grained, sub-angular/angular, poorly sorted,

3.85-6 m. Sandstone: Grey colored shale interbedded,

6-6.40 m. Shale: Dark grey, greenish colored, carbonated sandstone interbedded,

6.40-7 m. Sandstone: grey and green colored shale interbedded,

7-7.65 m. Shale: Grey and green colored, hard brittle sand included,

7.65-9 m. Sandstone: shale interbedded.

7.2.4 Well-16

Well 16 was drilled in 1998 with a drilling depth of 1658 meters and ended inside Osmancık Formation. There is no gas production; therefore, the well was abandoned. Core plug was drilled out between 1527-1531 meters inside Osmancık Formation. However, core was not well preserved at later stages (Figure 7.10). In the core, Sandstone-shale alternation is observed. Core description regarding increasing depth is given below.

0-0.16 m. Sandstone-Shale: Thin beds with sandstone-shale alternation.

0.16-2.06 m. Sandstone: off-white, light green-greenish grey colored, polygenic, hard-brittle and medium grained, angular, poorly sorted, carbonate cemented, shale interbedded, with low inter-porosity.

2.06-2.72 m. Shale: green-greenish grey, off-green colored, hard-brittle low carbonated, thin dissipated pyrite and micaceous, charred plant clastic, with abundant varve.

2.72-3.16 m. Sandstone: 2-6 cm thick shale interbedded and fragments.

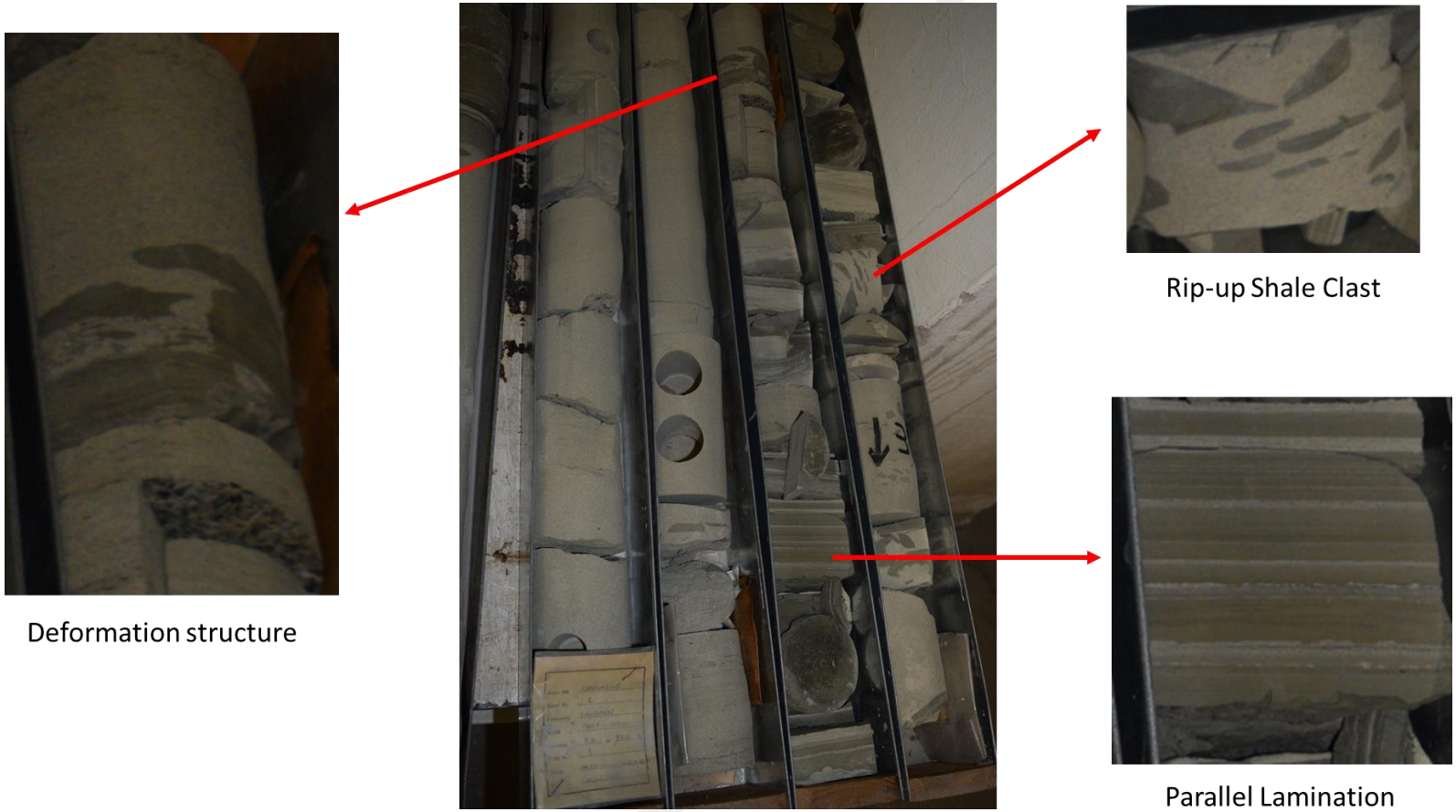

Figure 7.7. Shallower part of Core-1 between 1361-1364 meters from Well-15. Parallel lamination, rip-up shale clast and deformation structures observed.

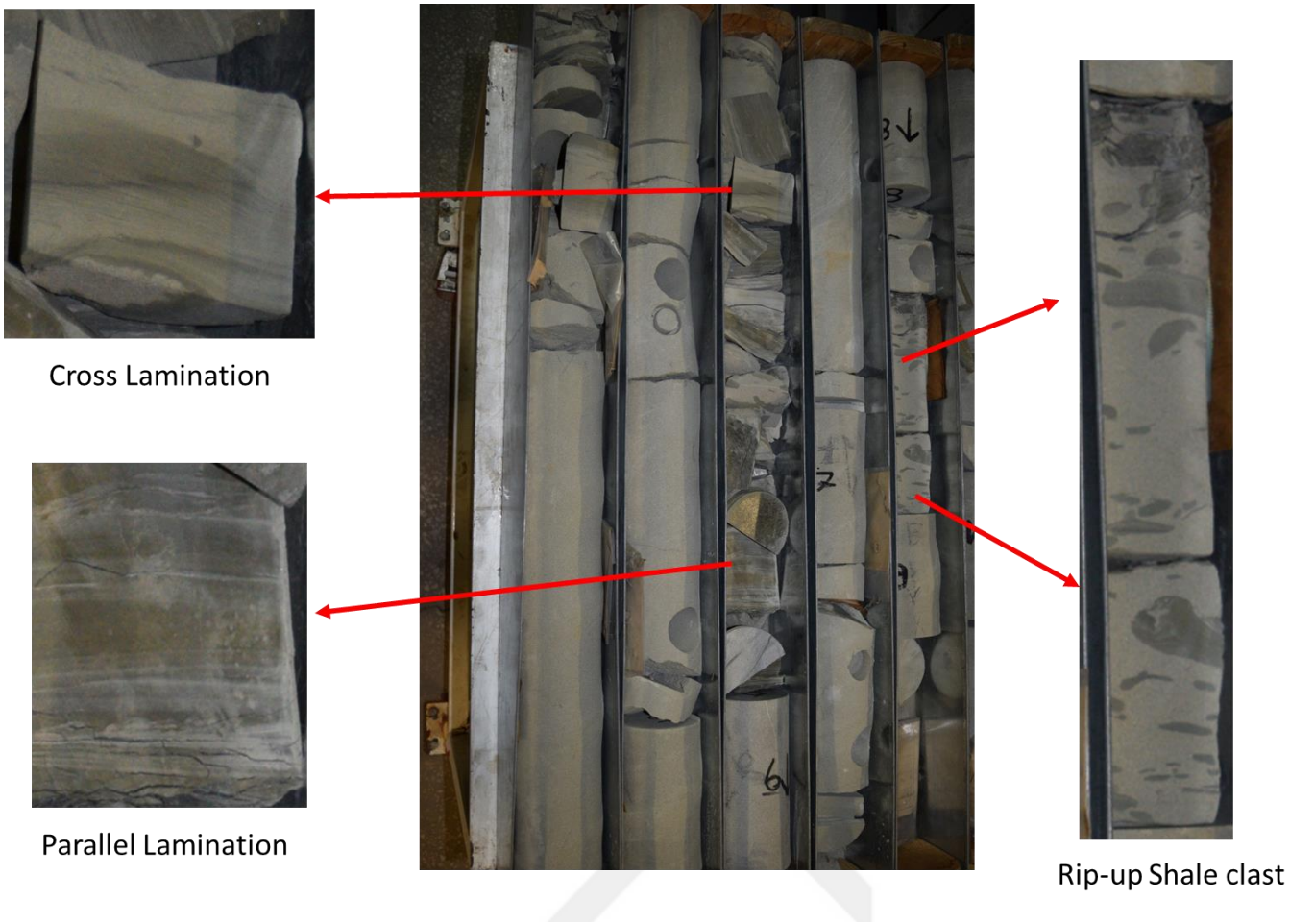

Figure 7.8. Deeper part of Core-1 between 1365-1369 meters from Well-15. Rip-up shale clast, parallel and cross laminations are observed in this section.

Figure 7.9. Core-2 between 1404.5-1413.5 meters from Well-15. Parallel and wavy laminations, load structures-frame structures and thick sandstones are observed in this core.

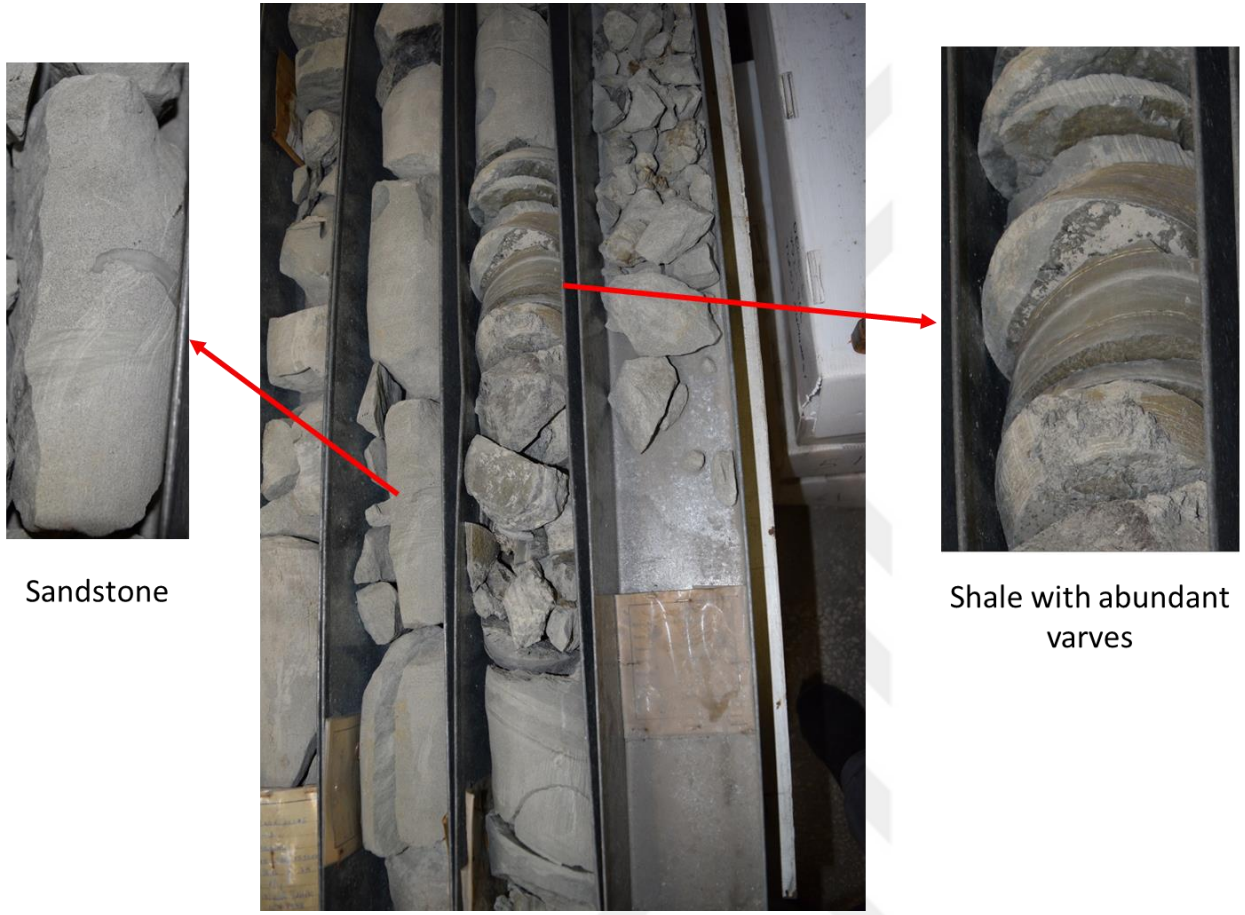

Figure 7.10. Core sample between 1527-1531m. from Well-16. Core plug is not well preserved. Alternating sandstone and shale is observed. Shale with abundant varves is also shown in the figure.

7.2.5 Well-21

Well-21 was drilled in 2001 and it was the first drilled well among the wells in well group 2. Additionally, this well is the only one having core data among well group-2. The drilling depth for Well-21 is 1840 meters. Two core plugs, between 1706-1714 and 1651-1654.60 meters, are available. Figure 7.11 demonstrates core samples between 1706-1714 m. Deformation structures, parallel and wavy laminations are observed on the core-2. Core descriptions are shown below:

Core Number 1 (1651-1654.60 meters): Dominantly sandstone with interbedded siltstone and shale.

0-2.64 m. Sandstone: Whitish grey, light grey colored, unconsolidated, fine/medium grained, angular, poorly sorted, weakly carbonate cemented, intergranular low porosity.

2.64-2.88 m. Sandstone, Siltstone, Shale alternated:

Sandstone: Similar properties with sandstone between 0-2.64 meters.

Siltstone: Light grey colored, brittle carbonated, abundant fine micaceous, charred plant clastic.

Shale: Greenish grey, light grey colored, carbonated, dispersed fine pyrite and charred plant clastic and with varves.

2.88-3.60 m. Sandstone: Whitish grey, light grey colored, unconsolidated, fine/medium grained, angular, poorly sorted, including charred plant clastic, weakly carbonate cemented, low interparticle porosity.

Core Number 2 (1706-1714 meters): Sandstone and shale alternation.

0-7.25 m. Sandstone: Light grey off-white colored (mostly quartz), mainly medium-rarely fine grained, angular, medium sized, charred plant clastic and laminated,

weakly carbonate cemented, 1-4 cm thick, dark grey - greyish - green colored, shale interbedded.

7.25-8 m. Shale: Dark grey, greenish grey colored, hard-brittle carbonated, abundant fine micaceous, charred plant clastic, thin sandstone interbedded.

Figure 7.11. Core sample between 1706-1714 m. from Well-21. Sandstone and shale alternation with deformation structure, parallel and wavy laminated sandstone.

7.2.6 Well-32

Well-32 was drilled in 1996 with 1857-meter total depth. There is no hydrocarbon production with this well. Two cores were taken out from both shallower (1463-1470 m.) and deeper (1798-1805.7 m.) parts of the Osmancık Formation. For the shallower part, 42.5% of the core, which is 3 m., was recovered and this part consists of shale lithology. Therefore, analysis was carried out only from core-2 which was taken between 1798-1805.7 meters depth. Core 1 and 2 displays are given in Figure 7.12. Core descriptions are given below:

Core Number 1 (1463-1470 meters): This core consists of only shale lithology.

0-3 m. Shale: Grey-dark grey colored, hard, abundant micaceous, rich in organic matter.

Core Number 2 (1798-1805.7 meters): This core includes sandstone-shale alternated lithology.

0-.30 m. Shale: Dark grey-grey colored, hard, few carbonated, laminated, with varve.

0.30-0.50 m. Sandstone: Grey colored, hard, sub-angular, poorly sorted, consisting of mostly quartz, fine-medium grained, carbonate cemented, with plant remnant, low interparticle porosity.

0.50-0.55 m. Shale.

0.55-3.25 m. Sandstone.

3.25-4.70 m. Sandstone-Shale alternation.

4.70-5.70 m. Sandstone: Very fine-fine grained.

5.70-6.40 m. Sandstone-Shale alternation.

Figure 7.12. On the left, core-1 between 1463-1470 m. is shown. Totally, shale with high amount of organic matter is observed. On the right, core-2 between 1798-1805.7 m. is shown. Core-2 consists of sandstone-shale alternation and parallel and wavy lamination can be observed.

7.3 Examination of Thin Sections

Thin section preparation and evaluation are the crucial aspects to conduct sedimentology studies. Type of facies, properties and content of grains, matrix and pore volume assist to interpret geological environment. Especially, for the modeling studies, all aspects of sedimentology should be integrated and understood to implement a detailed research.

Thin sections have been prepared from core data from Well-12, 13, 15 16 and 32. However, thin section from Well-21 is missing. Therefore, thin section evaluation was not implemented for this well. Nevertheless, other wells are very helpful to define facies type and properties of thin sections.

7.3.1 Thin sections from Well-12

Well-12 has been producing between 1341-1365 m. intervals. This interval is the most productive one among the producing intervals of wells in group-1. Three thin sections from this productive interval are available (1348.25 m., 1349 m. and 1351.25 m.).

Due to the lack of point counter which is used to analyze thin sections, an image tool was utilized to specify areal distribution of grain, matrix and pores (when blue dyed section is available). Threshold method was used to calculate percentage of each element in the thin section. An example of the areal calculation using this image tool is given in Figure from 7.13 to 7.18. Figure 7.13 and 7.14 indicate PPL and XPL displays of thin sections in the drilling depth of 1351.25 m. Figure 7.15 illustrates evaluation of the thin sections in terms of quartz, matrix and lithic fragment displays. Feldspar and polycrystalline quartz are detectable in XPL section shown in Figure 7.16. According to observations on PPL and XPL displays, facies in this depth is described as lithic arenite with coarse silt sized to medium sand sized particles, moderately-poorly sorted, sub-rounded/sub-angular grains. Figure 7.17 and 7.18

indicate calculation of areal distribution of elements of the thin section. Histograms and thresholds of each member of the facies such as grain, matrix, lithic fragment and pores are shown in Figure 7.17 (upper panel). After the application of threshold (middle panel) and coloration (lower panel) of each element, separation of each parameter is given in the same figure. Combination of the colored sections and calculation of the percentage of each component are demonstrated in Figure 7.18.

Facies at 1351.25 m depth is identified as lithic arenite due to matrix percentage less than 15% and dominant quartz content. Feldspar covers only 0.35% of the grains. Quartz content is approximately 30.35% of the grains covering 30.7% of the thin section. Facies consists of coarse silt sized to medium sand sized particles, moderately-poorly sorted, sub-rounded/sub-angular grains. Porosity values are around 22% confirming good reservoir quality.

PPL and XPL displays of thin section from depth of 1348.25 m. are given in Figure 7.19 and 7.20. Interpreted thin section is shown in Figure 7.21. A clear shale lamina is observed in the thin section, which possibly causes a flow barrier resulting a non-productive interval. Grains cover 22.3% of the area while lithic fragments are estimated as 0.95% and feldspar is about 0.3% resulting around 21.05% quartz. Matrix volume is around 55% in this thin section (Figure 7.22). Due to the presence of less than 75% quartz and more than 15% matrix, facies is described as lithic wacke (see Figure 7.2). In the relative depth, facies composed of medium/coarse silt sized (4 μm to 63 μm) to fine/very fine sand sized (63 μm to 2 mm) particles, moderately sorted, sub-angular / angular grains.

PPL and XPL displays of thin section from depth of 1349 m. are illustrated in Figure 7.23 and 7.24. and evaluated section is given in Figure 7.25. Grain content is almost equal to quartz percentage which is almost 21.2%. Matrix content is about 55%. Similar to thin section formed from 1348.25 m., facies type of the thin section from 1349 m. is described as lithic wacke. Facies consists of fine to coarse sand sized particles (63 μm to 2 mm), moderately sorted, sub-angular / angular grains.

Interval of 1351.25 m. which is identified as lithic arenite is a productive zone while intervals of 1348.25 and 1349 m. identified as lithic wacke are non-productive (Figure 7.26).

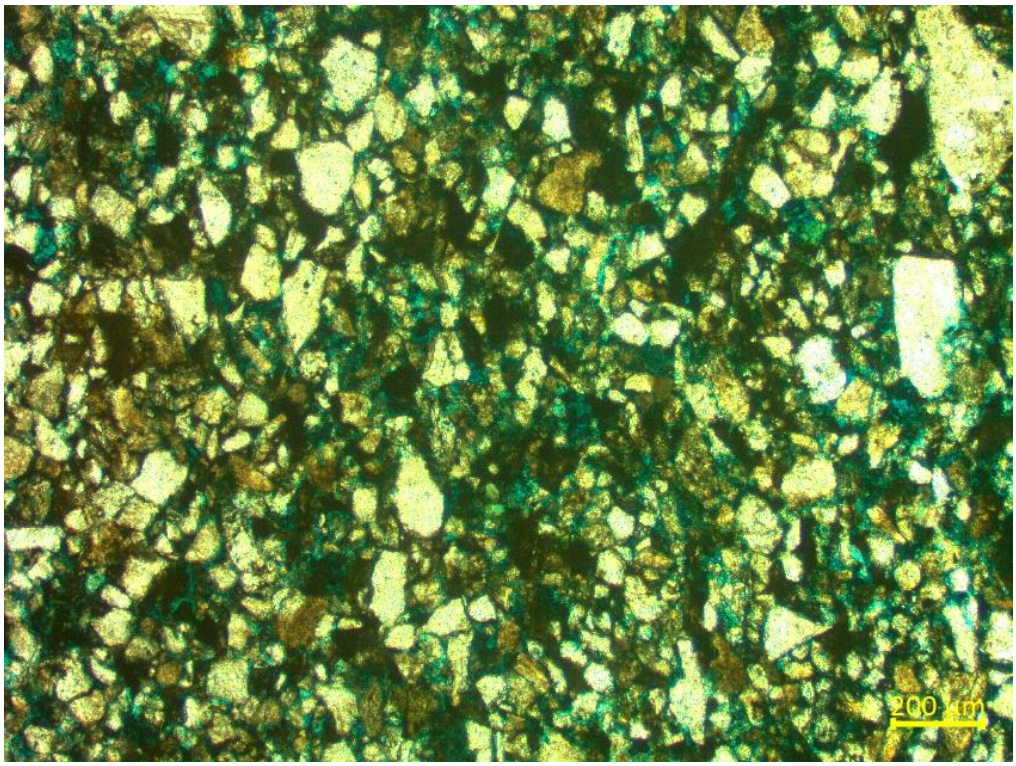

Figure 7.13. PPL display of thin section from 1351.25 m.

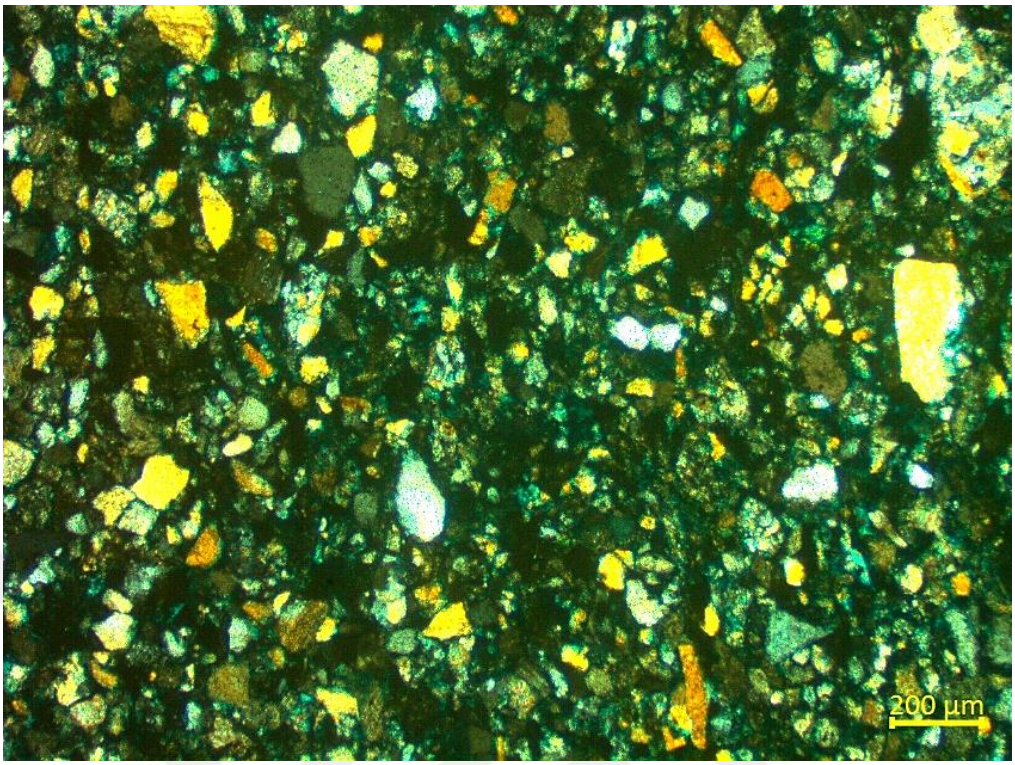

Figure 7.14. XPL display of thin section from 1351.25 m.

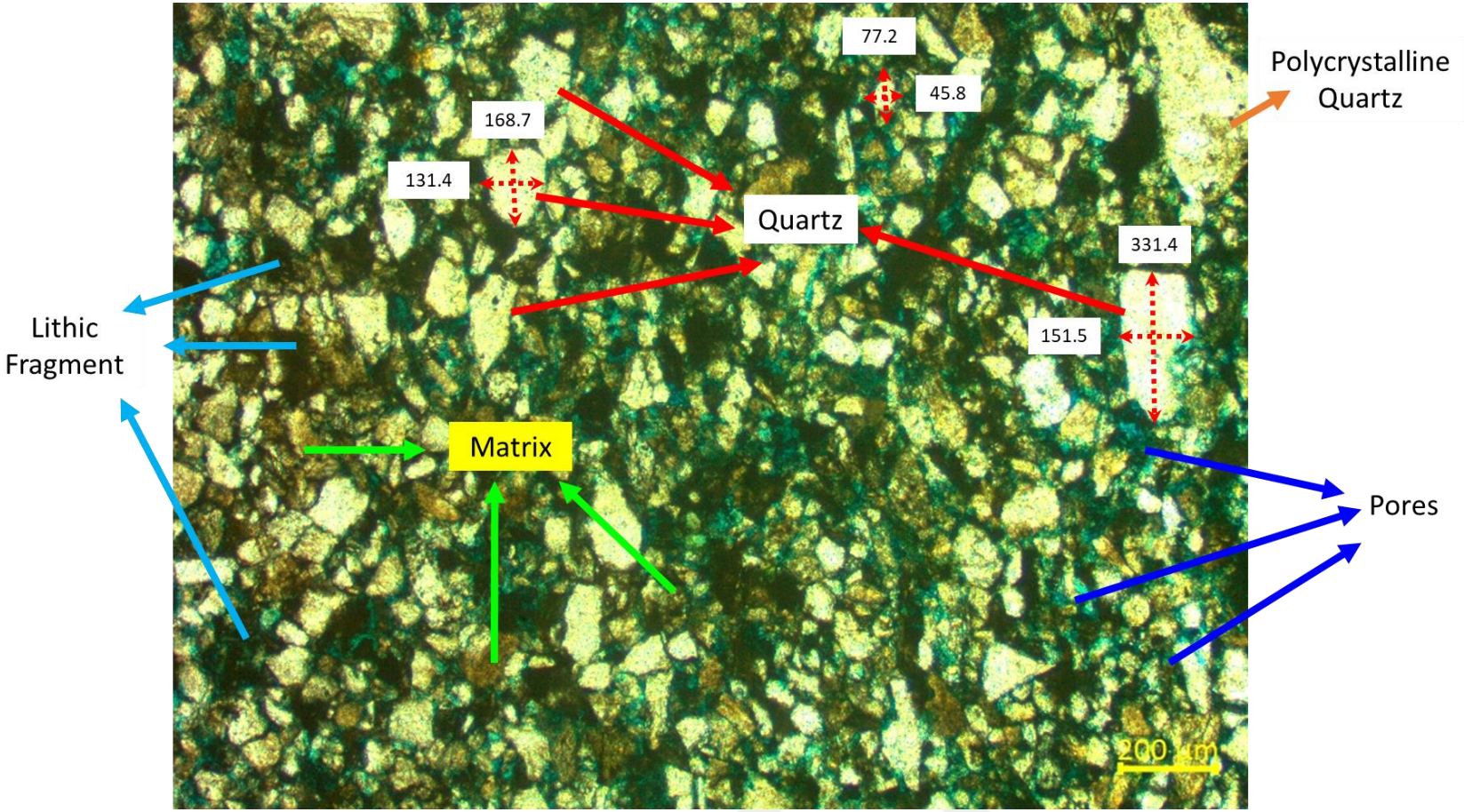

Figure 7.15. Evaluation of thin section from 1351.25 m. Numbers indicate length of grains, which are shown with dashed red lines. The scale of the thin section is 200 µm.

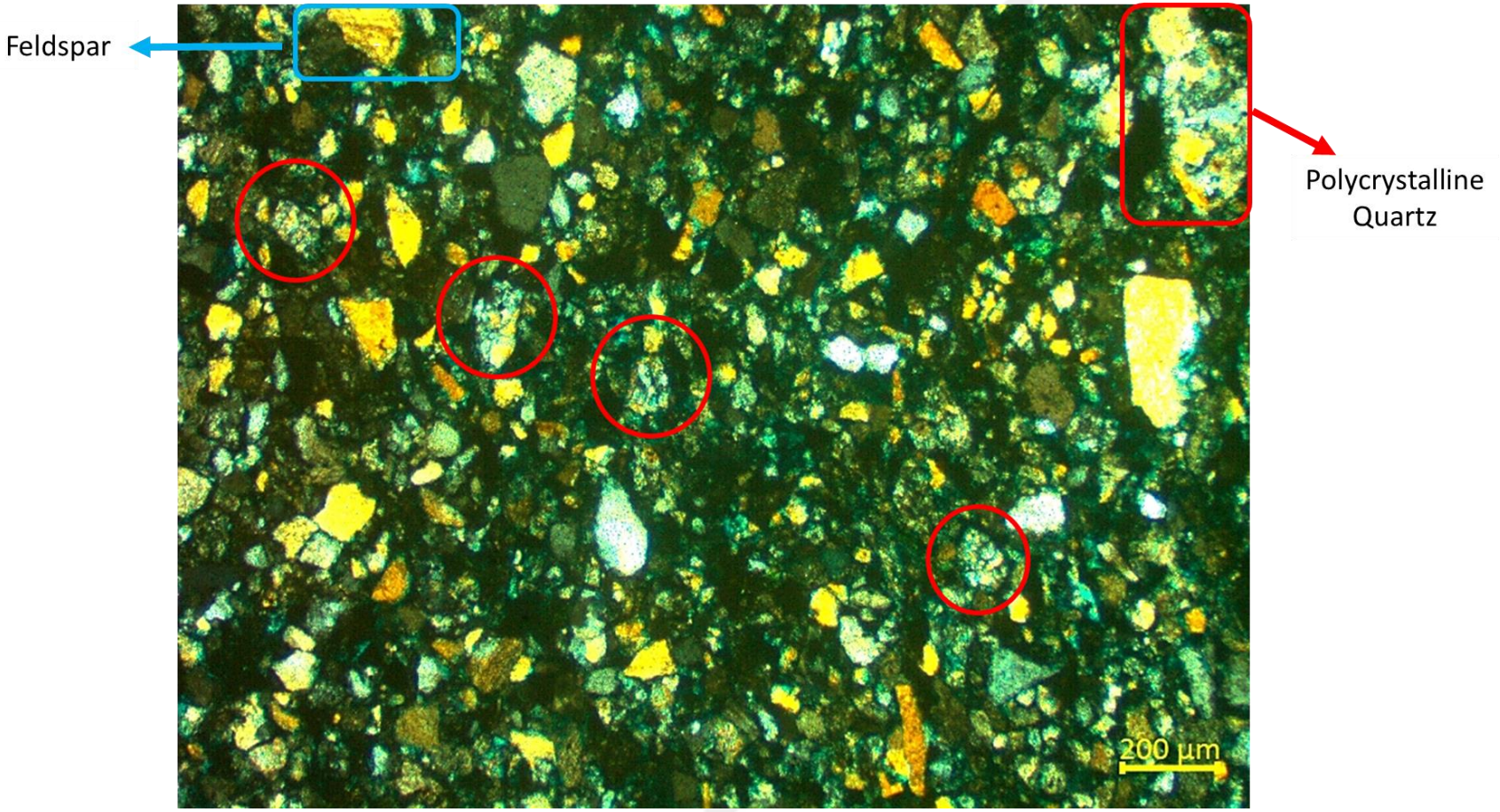

Figure 7.16. Evaluation of thin section using XPL view from 1351.25 m. Blue rectangle indicates feldspar while red circles demonstrate polycrystalline quartz.

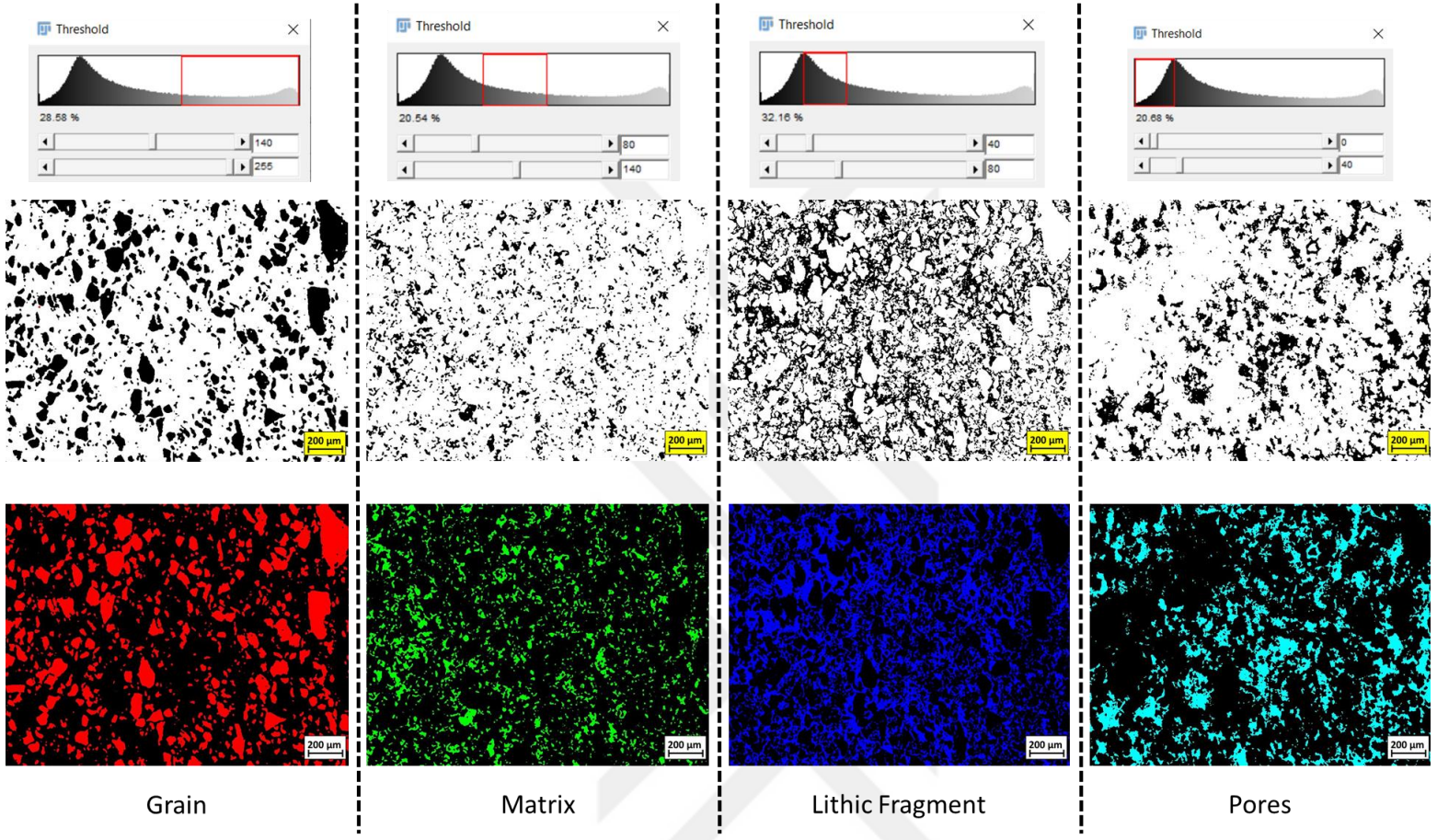

Figure 7.17. Histograms and regarding thresholds of each component are pointed out on the top of the figure. After the application of thresholds (middle) and coloration of each display (below) for grain, matrix, lithic fragment and pores are displayed in the figure.

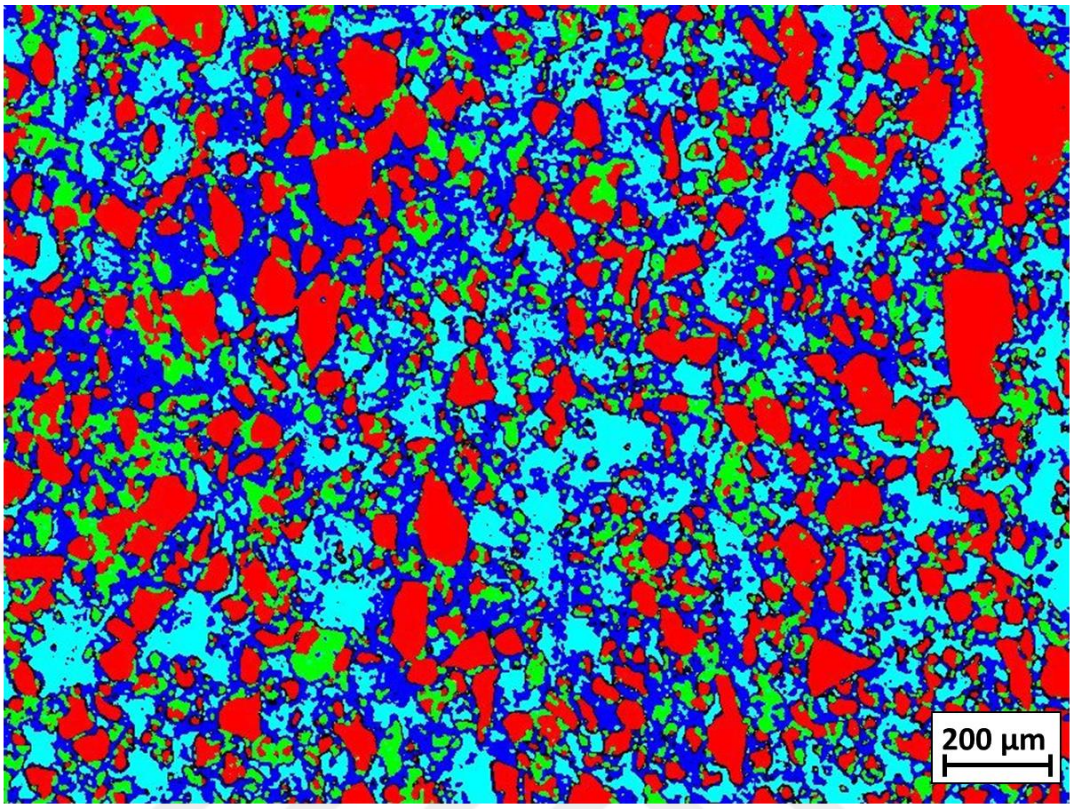

Type	Area	Mean	Min	Max	Circ.	Skew	%Area	Round
Grain	4373306.122	68.154	140	255	1	1.052	30.727	0.75
Matrix	4373306.122	79.070	80	140	1	2.234	12.745	0.75
Lithic F.	4373306.122	59.258	40	80	1	0.821	31.008	0.75
Pores	4373306.122	50.341	0	40	1	1.520	22.741	0.75

Figure 7.18. Merged colors of each component and calculated statistical values. Note that matrix percentage is less than 15 % and grain percentage is around 30 %.

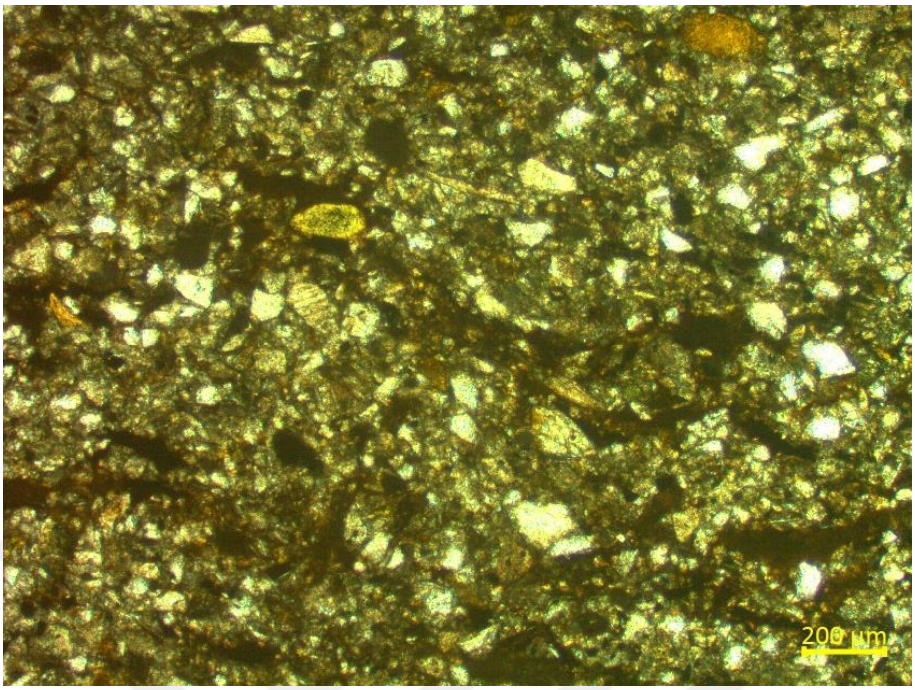

Figure 7.19. PPL display of thin section from 1348.25 m.

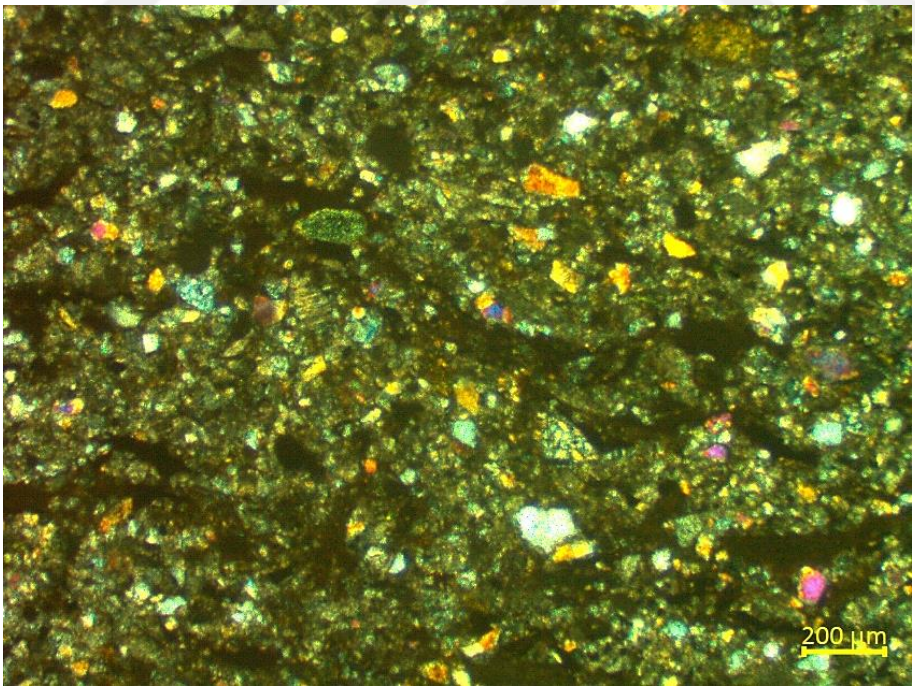

Figure 7.20. XPL display of thin section from 1348.25 m.

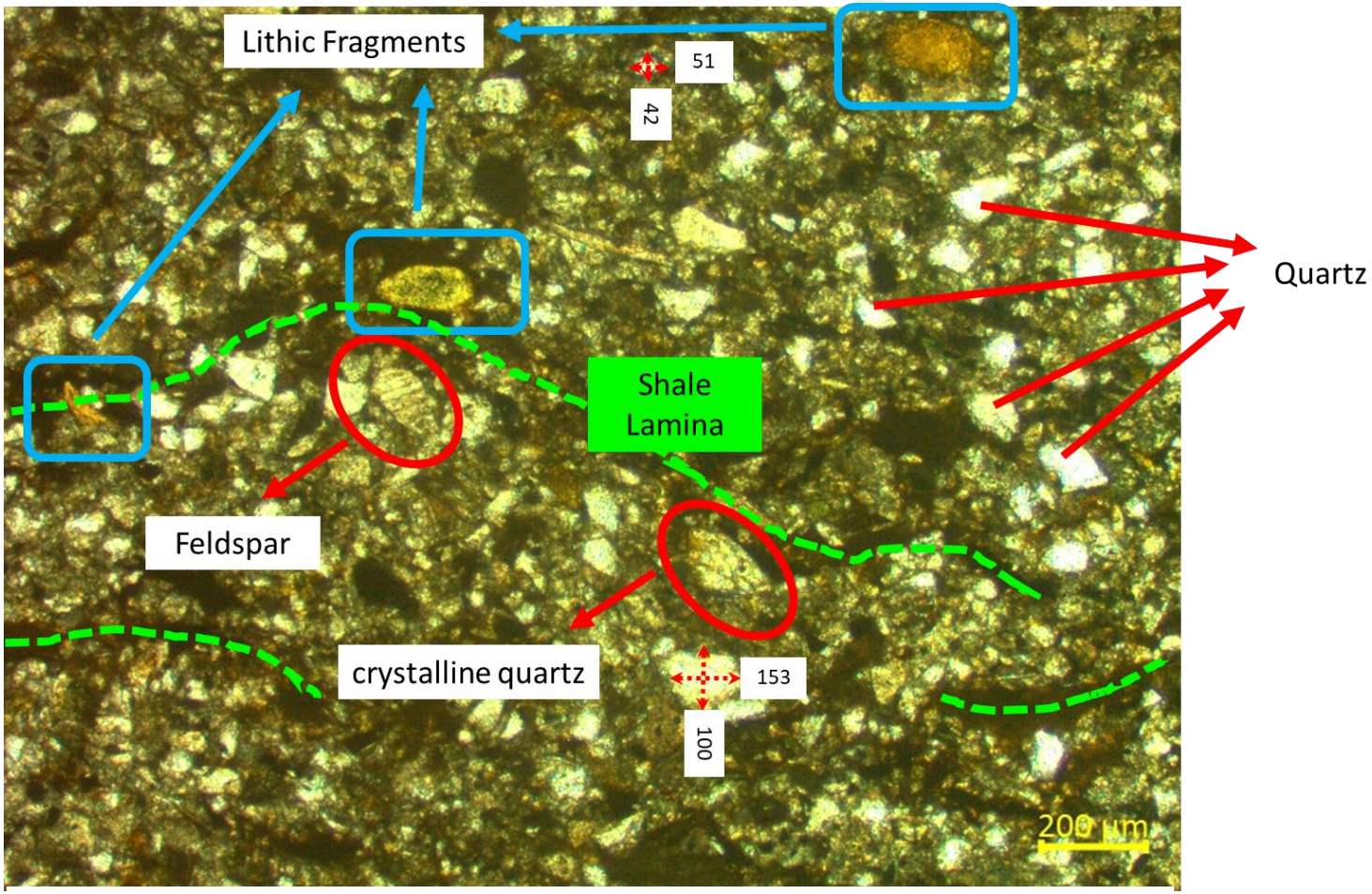

Figure 7.21. Evaluation of thin section from 1348.25 m. Numbers indicate length of grains, which are shown with dashed red lines. The scale of the thin section is 200 µm. A clear shale lamina is observed and drawn with green dashed line.

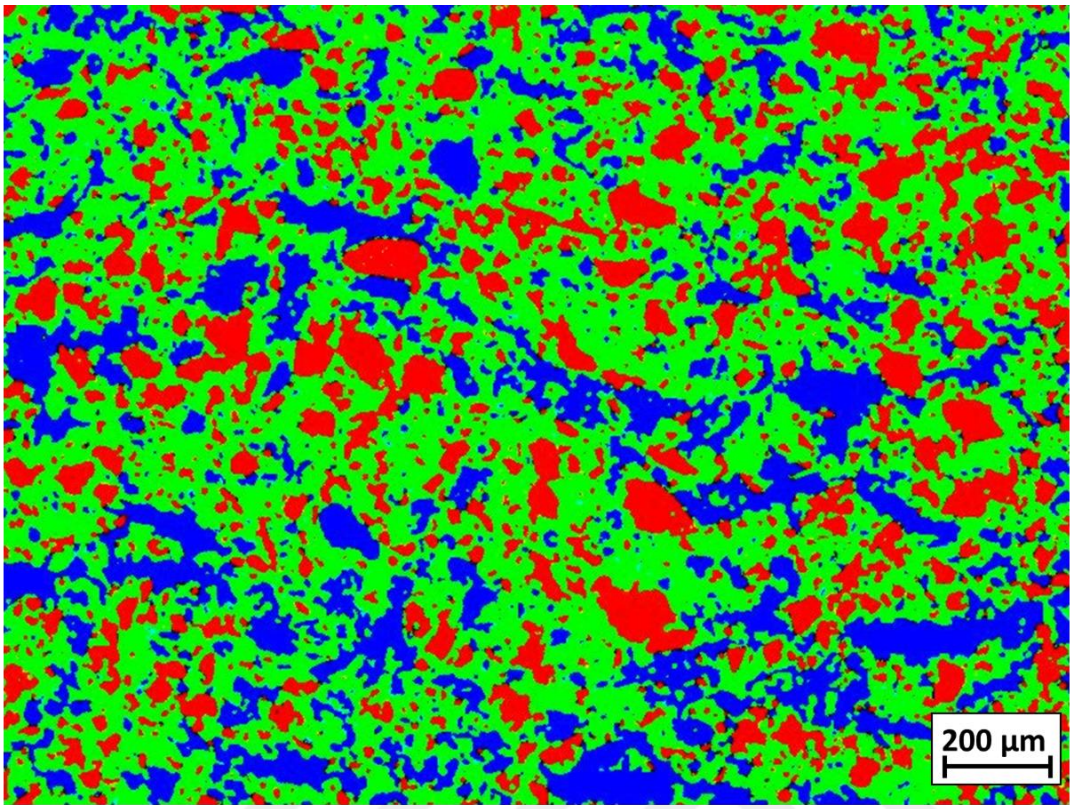

Type	Area	Mean	Min	Max	Circ.	Skew	%Area	Round
Grain	4373306.122	56.881	120	255	1	1.330	22.306	0.75
Matrix	4373306.122	140.482	60	120	1	-0.205	55.091	0.75
Lithic F.	4373306.122	57.665	0	60	1	1.309	22.614	0.75

Figure 7.22. Merged colors of each component and calculated statistical values in depth of 1348.25. Note that matrix percentage is more than 15 % and grain percentage is around 55 %.

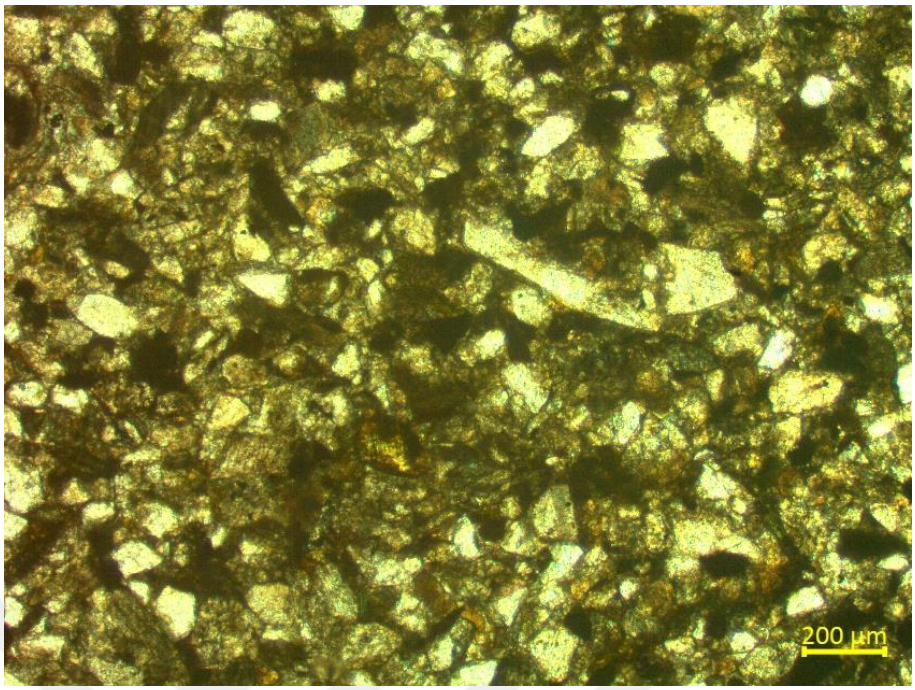

Figure 7.23. PPL display of thin section from 1349 m.

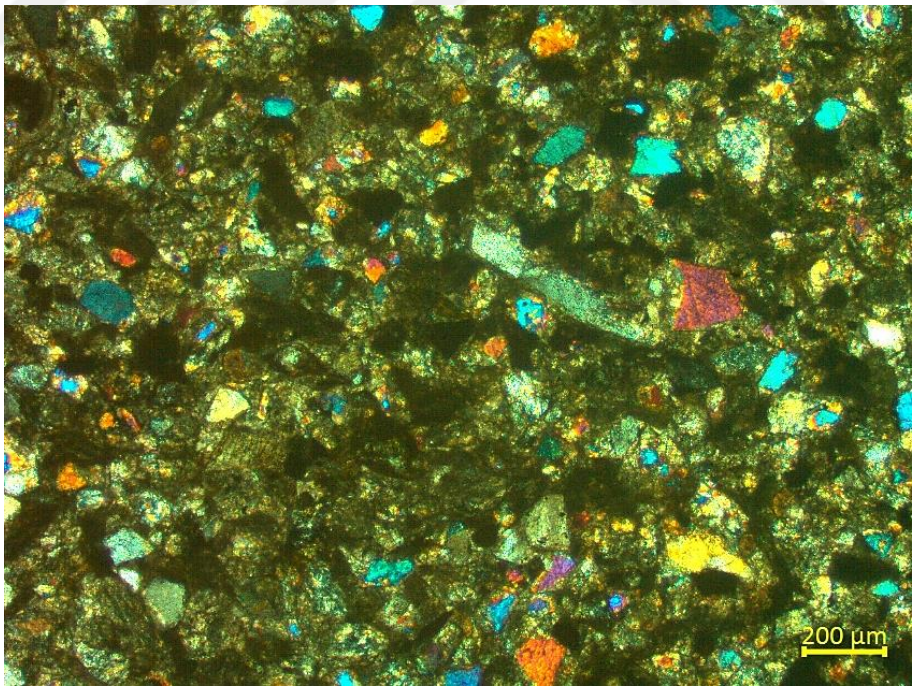

Figure 7.24. XPL display of thin section from 1349 m.

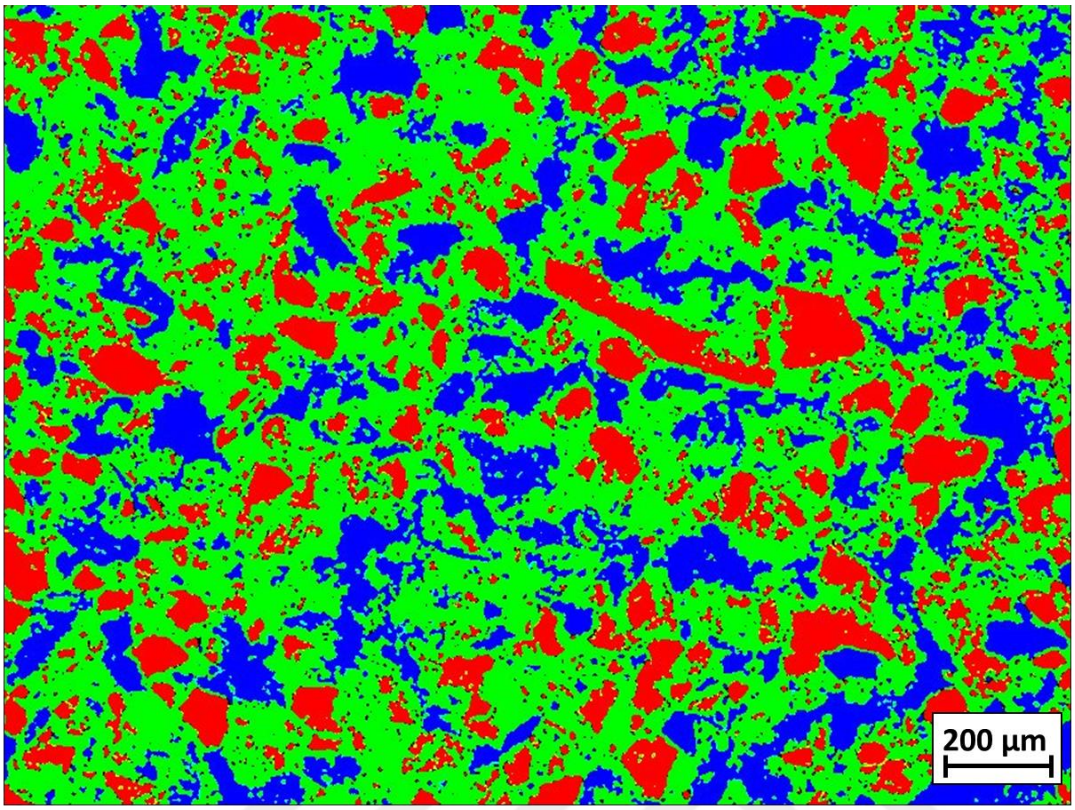

Type	Area	Mean	Min	Max	Circ.	Skew	%Area	Round
Grain	4373306.122	53.997	160	255	1	1.411	21.175	0.75
Matrix	4373306.122	141.1	80	160	1	-0.215	55.333	0.75
Lithic F.	4373306.122	59.258	0	80	1	1.267	23.238	0.75

Figure 7.25. Merged colors of each component and calculated statistical values in depth of 1349 m. Note that matrix percentage is more than 15 % and grain percentage is around 55 %. Percentage of components in depth of 1349 m. is similar to 1348.25 m.

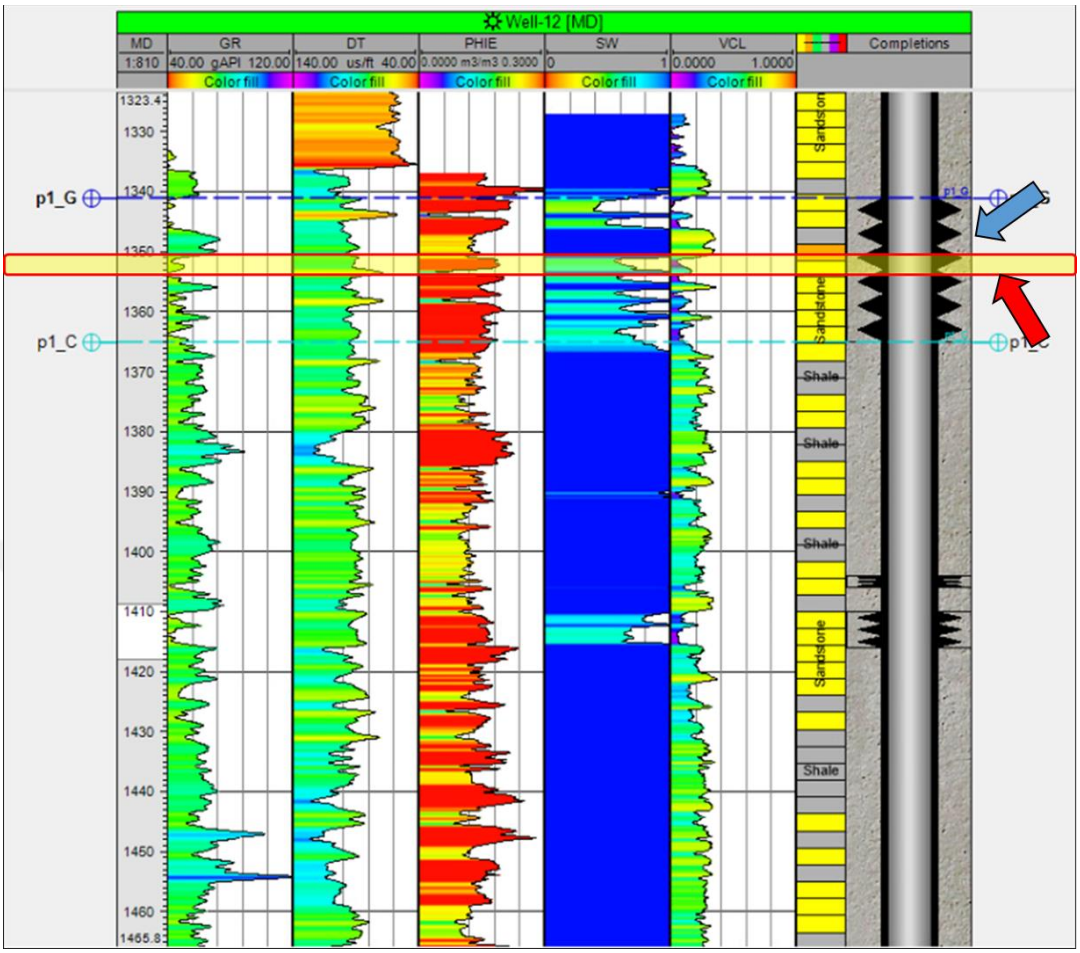

Figure 7.26. From left to right: GR, DT, PHIE, SW, VCL, upscaled facies and completions. The most productive interval, between 1341-1365 m., among group 1 wells are displayed within p1_G and p1_C tops. Blue arrow indicates non-producing depths (1348.25 m. and 1349 m.), which is evaluated as lithic wacke. Red arrow points out producing depth, which is shown with yellow rectangle and evaluated as lithic arenite facies (1351.25 m.).

7.3.2 Thin sections from Well-13

In this well, 2 cores are available including intervals of 1305-1314 m. and 1489-1497.5 m.

7.3.2.1 Thin Sections: Core-1

The core interval between 1305 and 1314 m. in this well was low productive and due to dropping pressure to 0 PSI, it is not productive anymore. PPL display of thin sections within the interval are given in Figure 7.27 and evaluation of these thin sections are illustrated in Figure 7.28. In these figures, depths of the thin sections are (A) 1305.25 m., (B) 1308.75 m., (C) 1310.05 m., (D) 1312.55 m. and (E) 1313.65 m. Some measured length of grains is given in Figure 7.28 with red dashed arrows. A common property for each thin section is that grain sizes are too small changing from medium silt sized to very fine sand sized (0.0156 to 0.125 mm.) or medium to coarse silt sized (0.0156 to 0.63 mm.) particles. Descriptions of each thin section are given below:

(A) 1305.25 m.: Lithic-wacke facies (matrix per. 59.2%, quartz per approximately 27%, see Figure 7.29), medium silt sized to very fine sand sized particles (btw 0.0156 to 0.125 mm.), moderately sorted, rounded/subrounded grains. A clear matrix lamination is observed and may cause a possible flow barrier.

(B) 1308.75 m.: Lithic-wacke facies (matrix per. 56.37%, quartz per approximately 25%, see Figure 7.29), medium silt sized to very fine sand sized particles (btw 0.0156 to 0.125 mm.), moderately sorted, rounded/sub-rounded grains.

(C) 1310.05 m.: Lithic-wacke facies (matrix per. 52.820 %, quartz per approximately 20%, see Figure 7.29), medium silt sized to very fine sand sized particles (btw 0.0156 to 0.125 mm.), moderately sorted, angular/sub-angular grains.

(D) 1312.55 m.: Lithic-wacke facies (matrix per. 52.128 %, quartz per approximately 30%, see Figure 7.29), medium silt sized to coarse silt sized particles (btw 0.0156 to 0.63 mm.), moderately sorted, angular/sub-angular grains.

(E) 1313.65 m.: Lithic-wacke facies (matrix per. 66.7 %, quartz per approximately 11%, see Figure 7.29), medium to course silt sized particles (btw 0.0156 to 0.063 mm.), moderately sorted, angular/sub-angular grains. Shale lamina at the top and bottom of the thin section is observed possibly causing a flow barrier.

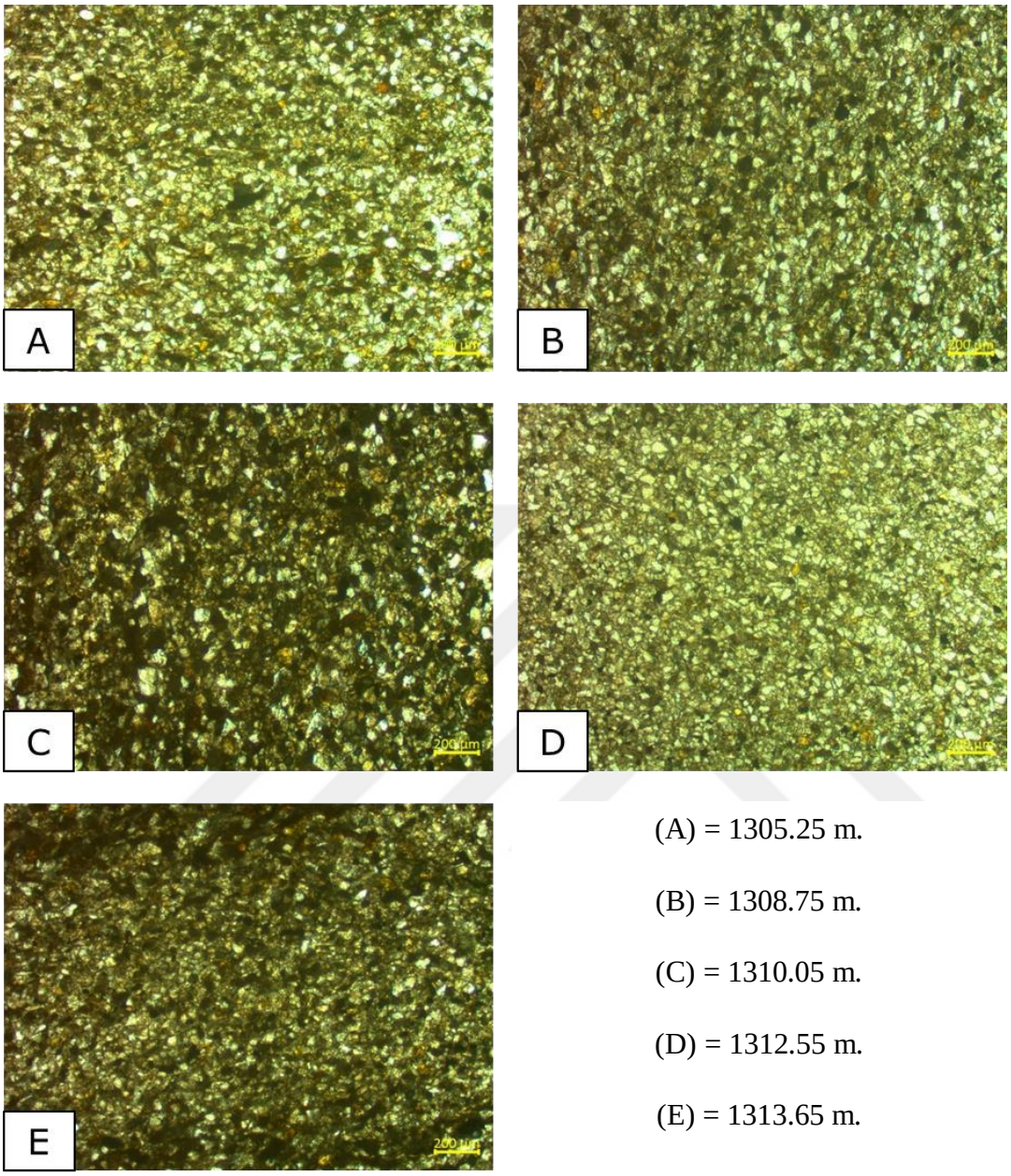

Figure 7.27. PPL display of thin sections regarding each sample of depth between 1305 m. and 1314 m.

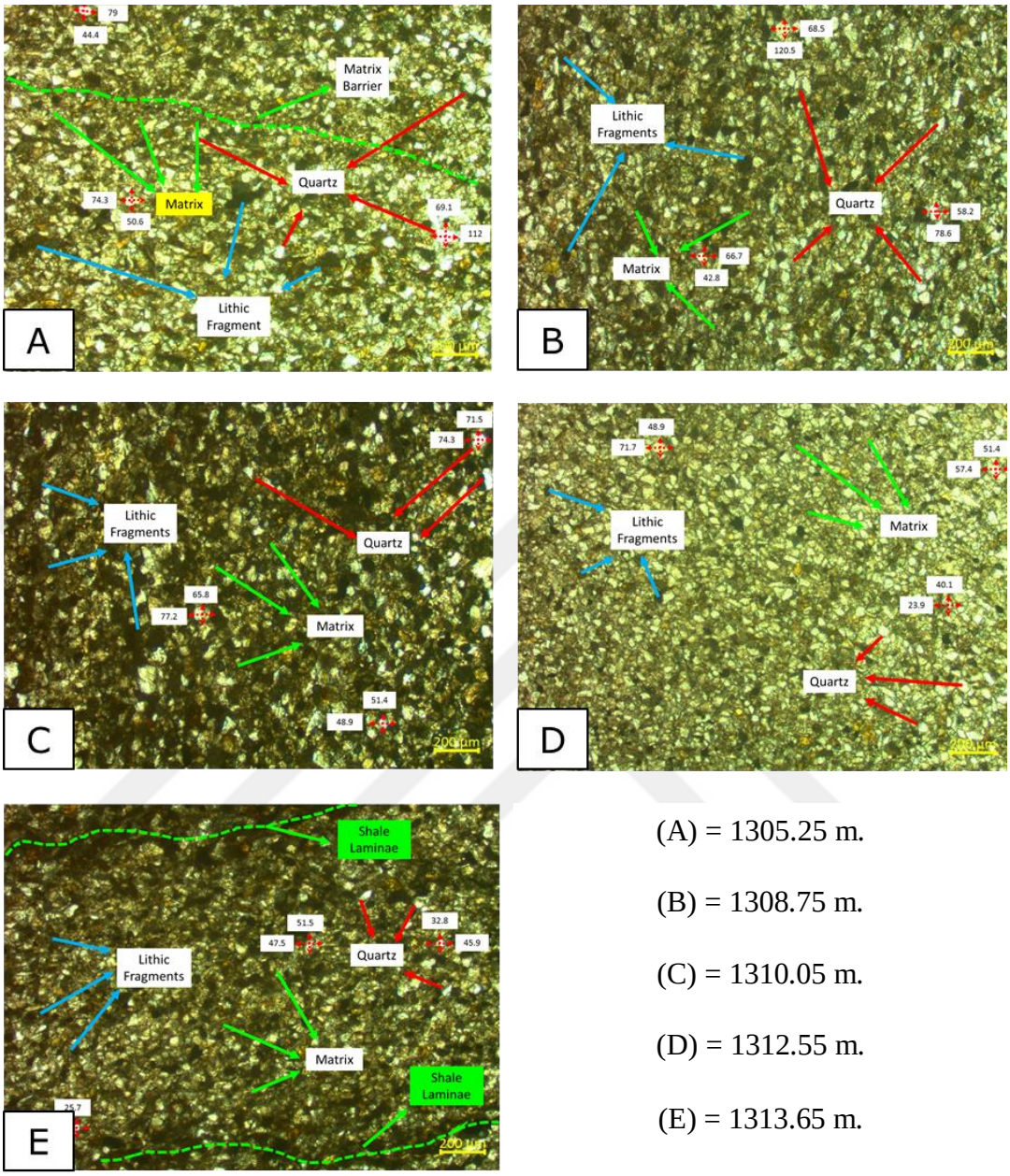

(A) = 1305.25 m.

(B) = 1308.75 m.

(C) = 1310.05 m.

(D) = 1312.55 m.

(E) = 1313.65 m.

Figure 7.28. Evaluated PPL displays of thin sections regarding each sample. Quartz, lithic fragments, matrix and length of grains are illustrated on the figures A, B, C, D and E. Common property of each section is observed as small grain sizes and high amount of matrix.

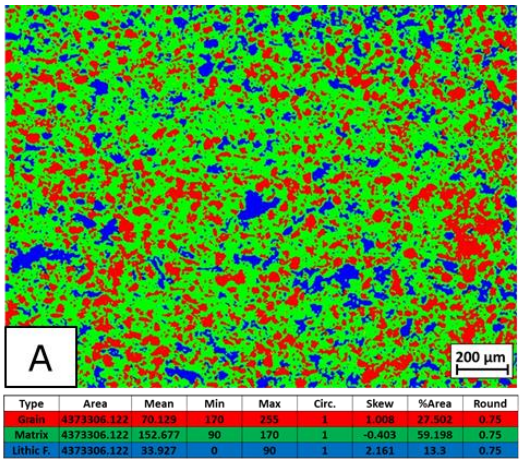

Type	Area	Mean	Min	Max	Circ.	Skew	%Area	Round
Grain	4373306.122	70.129	170	255	1	1.008	27.502	0.75
Matrix	4373306.122	152.677	90	170	1	-0.403	59.198	0.75
Lithic F.	4373306.122	33.927	0	90	1	2.161	13.3	0.75

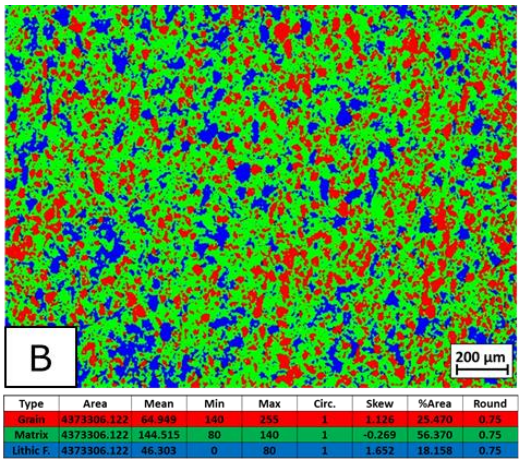

Type	Area	Mean	Min	Max	Circ.	Skew	%Area	Round
Grain	4373306.122	64.949	140	255	1	1.126	25.470	0.75
Matrix	4373306.122	144.515	80	140	1	-0.269	56.370	0.75
Lithic F.	4373306.122	46.303	0	80	1	1.652	18.158	0.75

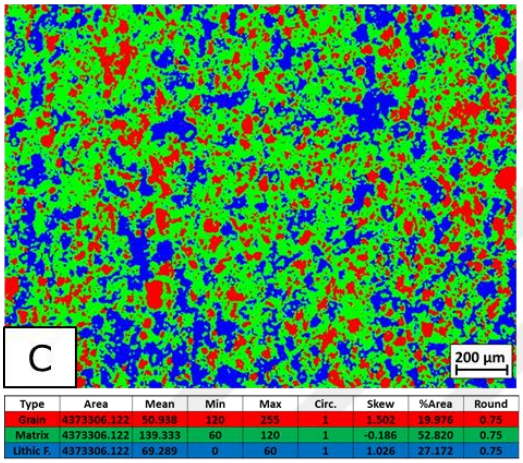

Type	Area	Mean	Min	Max	Circ.	Skew	%Area	Round
Grain	4373306.122	50.938	120	255	1	1.502	19.976	0.75
Matrix	4373306.122	139.333	60	120	1	-0.186	52.820	0.75
Lithic F.	4373306.122	69.289	0	60	1	1.026	27.172	0.75

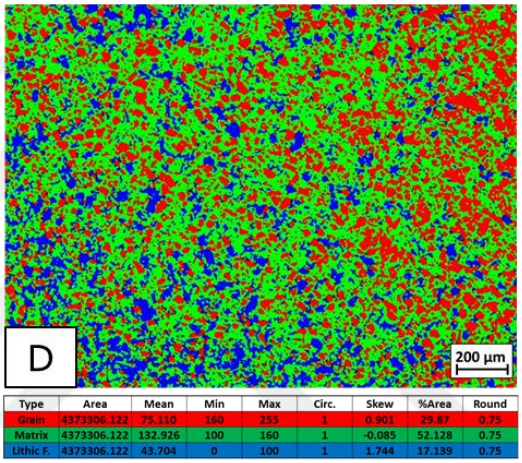

Type	Area	Mean	Min	Max	Circ.	Skew	%Area	Round
Grain	4373306.122	75.110	160	255	1	0.901	29.87	0.75
Matrix	4373306.122	132.926	100	160	1	-0.085	52.128	0.75
Lithic F.	4373306.122	43.704	0	100	1	1.744	17.139	0.75

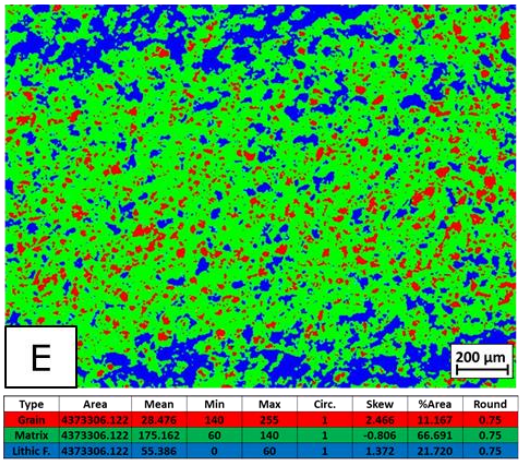

Type	Area	Mean	Min	Max	Circ.	Skew	%Area	Round
Grain	4373306.122	28.476	140	255	1	2.466	11.167	0.75
Matrix	4373306.122	175.162	60	140	1	-0.806	66.691	0.75
Lithic F.	4373306.122	55.386	0	60	1	1.372	21.720	0.75

(A) = 1305.25 m.

(B) = 1308.75 m.

(C) = 1310.05 m.

(D) = 1312.55 m.

(E) = 1313.65 m.

Figure 7.29. Merged colors of each component and calculated statistical values. Note that matrix percentage is higher than 50% for each sample and grain percentage varies from 10% to 30%.

Due to very small grain sizes, it is not possible to digitize the percentage of quartz. However, it can be said that the percent of the quartz approximates the percent of grains. Calculated percentages for grain, matrix and lithic fragments are illustrated in Figure 7.29. At these thin sections, it is possible to state that small grain sizes and high percentage of matrix as well as the type of facies are effective parameters resulting non-productive zone.

7.3.2.2 Thin Sections: Core-2

The core interval between 1489 and 1497.5 m in this well is a productive zone. This interval has produced 13,000,000 m^3 with pressure of 2270 PSI. Only two thin sections were utilized to interpret facies properties. Figure 7.30 illustrates of (A) PPL display, (B) XPL display and (C) evaluated thin section at 1489.45 m. Quartz area covers 27.3% of the grains (29.34%). Matrix percentage is calculated as approximately 58.3% and lithic fragments comprise of 12.12% of the section (Figure 7.31). Facies in this thin section is described as lithic-wacke facies, very fine to fine sand sized particles (btw 0.063 mm. to 0.25 mm.) (Figure 7.30 C), moderately sorted, angular/sub-angular grains.

Second thin section in this core was generated from the depth of 1490.95 m. PPL and XPL displays are given in Figure 32 A and B. In this section, addition to grains, matrix and lithic fragment, opaque minerals are also observed. Some section defects are also present as it is seen in Figure 7.32 C. Figure 7.33 shows the calculated areal distribution of the components of facies. Grain covers only 19.7% of the section. 18.8% of the grains are composed of quartz minerals. Almost 47% of the area consists of matrix and 33% of the area is the lithic fragments. Facies at this depth is described as lithic-wacke facies, fine to medium sand sized particles (btw 0.125 mm. to 0.5 mm.) (Figure 7.32 C), moderately sorted, angular grains.

Two core intervals are shown in Figure 7.34. Grain sizes are evaluated as key parameter in this well. In other words, grain sizes controls on production amount:

Small grain sizes and high matrix content narrow pore throat, so reduces porosity which is crucial for reservoir properties. On the other hand, although matrix content is similar in both intervals, facies with higher grain sizes is much more productive.

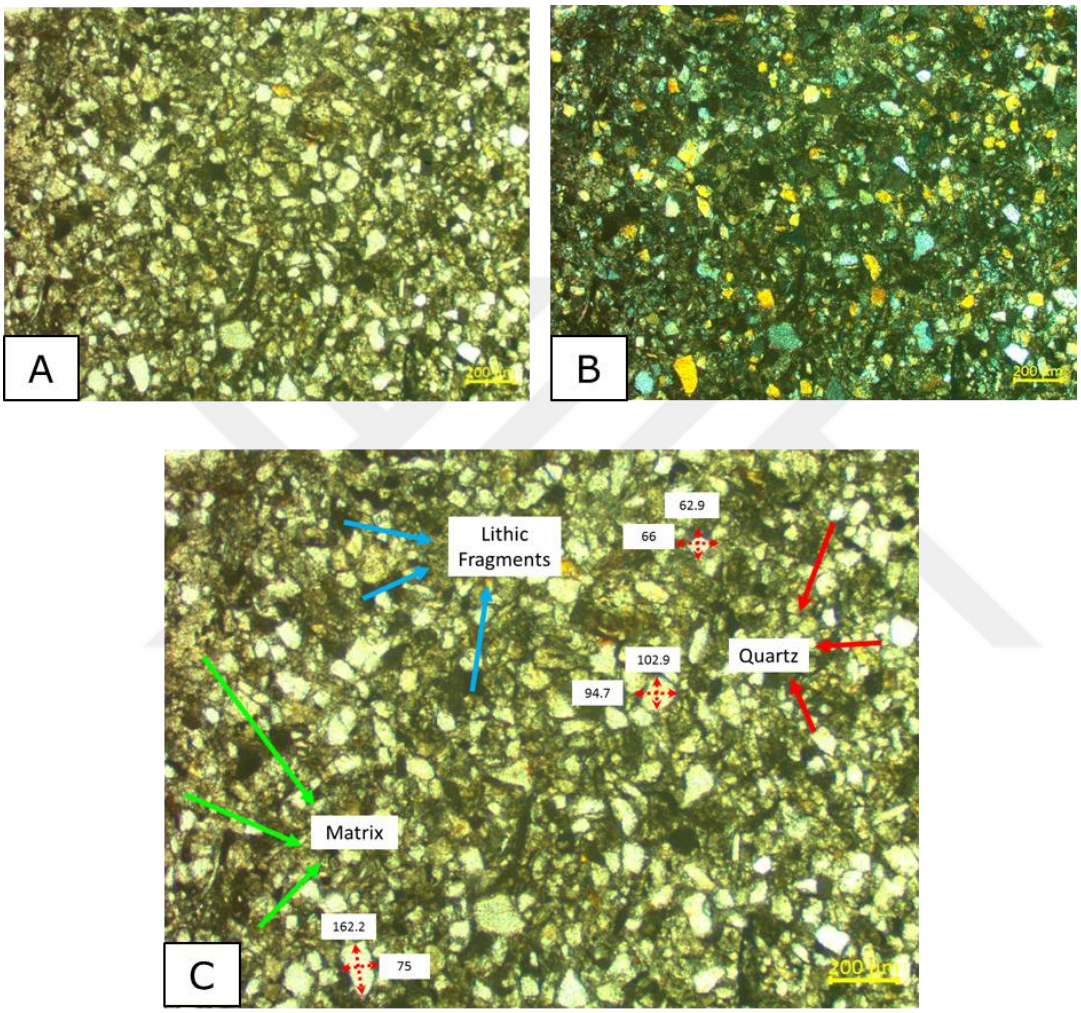

Figure 7.30. (A) PPL and (B) XPL displays of the thin section and (C) evaluated section. Calculated length of three different grains are illustrated with red dashed lines. The scale of the thin section is 200 µm. Quartz minerals covers a high range of grains.

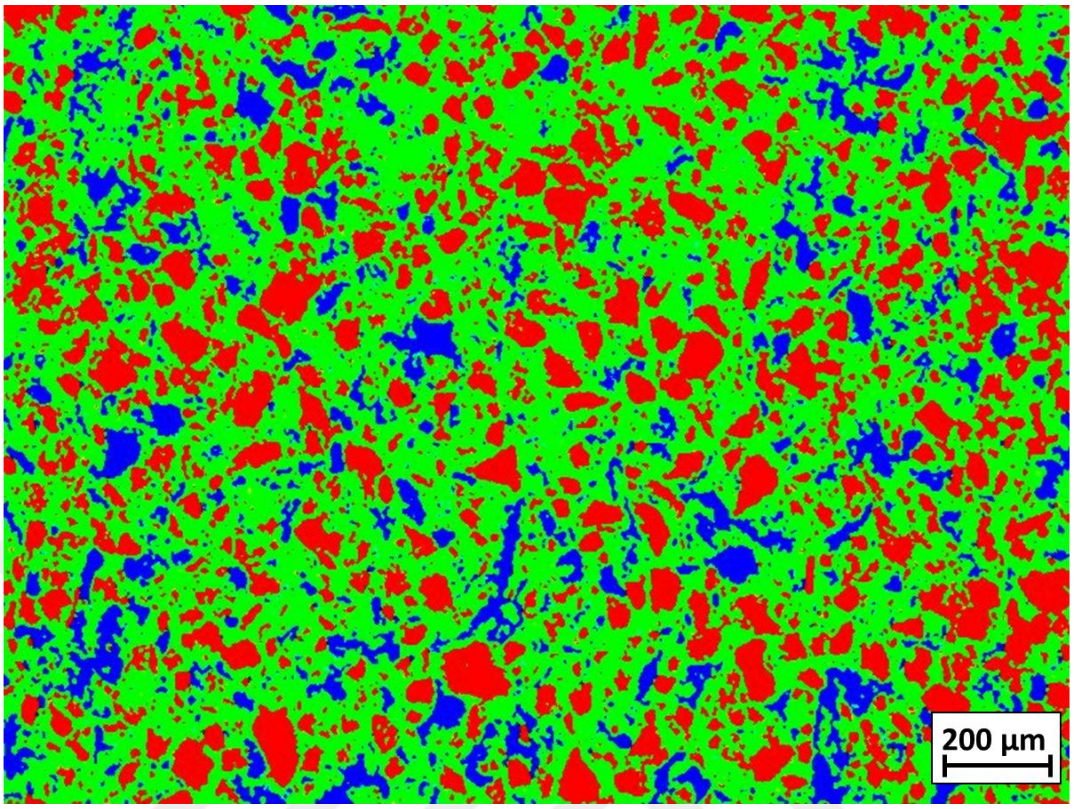

Type	Area	Mean	Min	Max	Circ.	Skew	%Area	Round
Grain	4373306.122	74.826	160	255	1	0.907	29.344	0.75
Matrix	4373306.122	151.844	80	160	1	-0.389	58.272	0.75
Lithic F.	4373306.122	31.019	0	80	1	2.315	12.164	0.75

Figure 7.31. Merged colors of each component and calculated statistical values. Note that matrix percentage is higher than 50% and grain percentage is almost 29.34%.

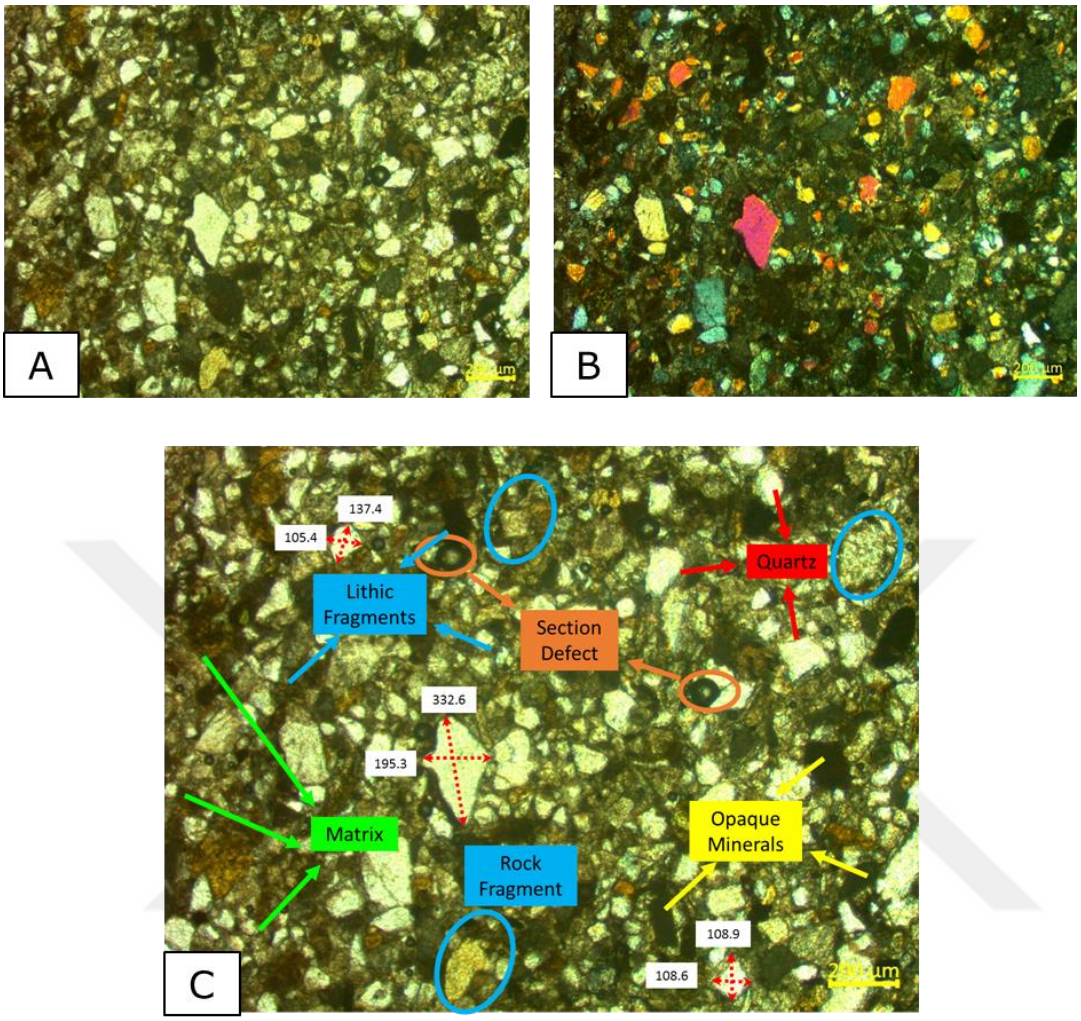

Figure 7.32. (A) PPL and (B) XPL displays of the thin section and (C) evaluated section. Calculated length of three different grains are illustrated with red dashed lines. Grain sizes are variable. The scale of the thin section is 200 μm. Quartz minerals covers a high range of grains similar to the thin section at depth of 1489.45 m.

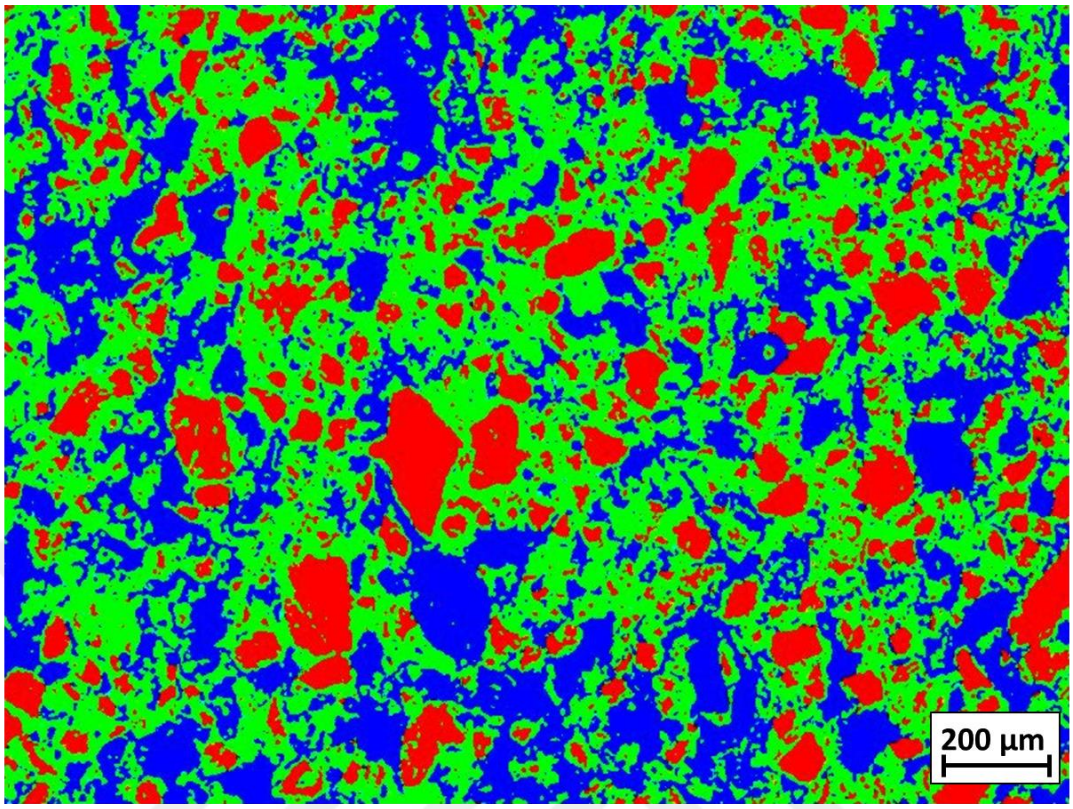

Type	Area	Mean	Min	Max	Circ.	Skew	%Area	Round
Grain	4373306.122	50.257	160	255	1	1.523	19.709	0.75
Matrix	4373306.122	122.333	80	160	1	-0.081	46.974	0.75
Lithic F.	4373306.122	84.380	0	80	1	0.719	33.090	0.75

Figure 7.33. Merged colors of each component and calculated statistical values. Note that matrix percentage is higher than 50% and grain percentage is almost 19.7%.

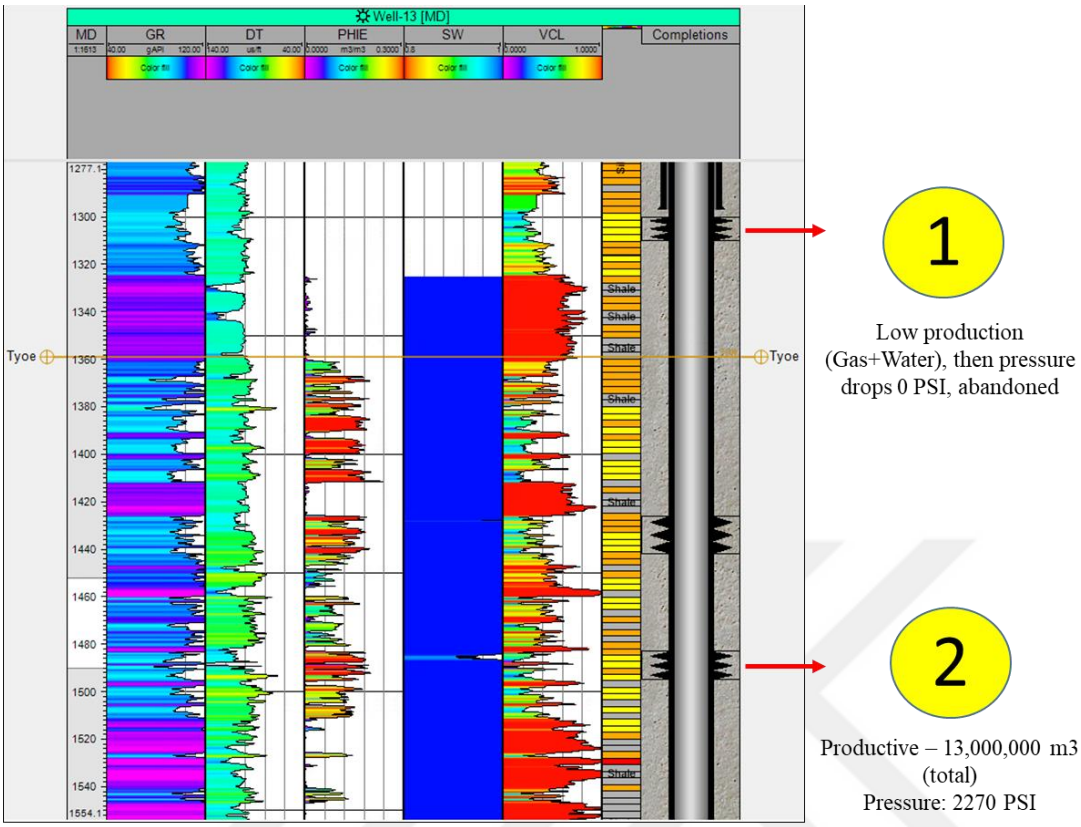

Figure 7.34. From left to right: Gamma-ray (GR), p-slowness (DT), effective porosity (PHIE), water saturation (SW), volume of clay (VCL), facies log and completions for well-13. Number 1 shows low producing, then, abandoned zone in which core-1 is drilled out. Grain sizes vary between very fine to fine sand particles. Number 2 indicates productive zone where core-2 is taken out. Although matrix content is similar to each other, grain size of core-2 interval changes from fine to medium sand size particles, resulting higher porosity and better reservoir condition.

7.3.3 Thin sections from Well-15

In this well, 2 cores are available within intervals of 1360.7-1369 m. and 1404.5-1413.5 m.

7.3.3.1 Thin Sections: Core-1

The core interval between 1360.7-1369 m. in this well is non-productive due to lack of pressure. 5 samples of thin section were studied and evaluated within core-1 of Well-15. PPL and XPL displays and interpreted thin sections are given in Figure from 7.35 to 7.39.

The first sample is from 1360.85 m. drilling depth. Mainly quartz and minor feldspar grains are observed in this section (Figure 7.35). Calculated percentage of area for those grain, matrix, lithic fragments and porosity is illustrated in Figure 7.40 A. Grains cover 34.6% of the section (Figure 7.40 A). 30.95% of the grains are quartz and 0.4% is the unstable feldspar. Thin section is composed of Matrix with 14.71% percentage. Facies of this sample is described as lithic arenite facies (matrix per. 14.71 %, quartz per approximately 31%), very fine to medium sand sized particles (between 0.063 and 0.5 mm., Figure 7.35 C), moderately sorted, sub-rounded/sub-angular grains with moderate porosity which is approximately 7% (Figure 7.40 A) of the section.

The second sample is from 1365.5 m. drilling depth. Mainly quartz and minor feldspar and accessory mineral grains are observed in this section (Figure 7.36). Calculated percentage of area for each component is shown in Figure 7.40 B. Grains cover 48.7% of the section (Figure 7.40 B). 43.1% of the grains is composed of quartz and 0.4% is the feldspar. Thin section is composed of matrix with 41.2% percentage. Facies of this sample is described as lithic wacke facies (matrix per. higher than 15%, quartz per approximately 43.1%), very fine to fine sand sized

particles (between 0.063 and 0.25 mm., Figure 7.36 C), moderately sorted, angular/sub-angular grains with low porosity approximately 2.5% (Figure 7.40 B).

The third sample is from 1366.35 m. drilling depth. Most of the grains are composed of quartz mineral (Figure 7.37). Percentage of the area for each component is given in Figure 7.40 C. Grains cover 22.1% of the section (Figure 7.40 C). 21.1% of grains is the area of quartz mineral. Some accessory minerals are available in the section (Figure 7.37 C, purple ellipses). Facies of this sample is described as lithic wacke facies (matrix per. higher than 15%, quartz per approximately 21.1%), very fine to fine sand sized particles (between 0.063 and 0.25 mm., Figure 7.37 C), moderately sorted, angular/sub-angular grains with low porosity approximately 5% (Figure 7.40 C).

The fourth sample is from 1367.35 m. drilling depth. The thin section includes mainly quartz mineral with minor accessory minerals (shown with purple ellipse) (Figure 7.38). Figure 7.40 D indicates the percentage of each element in the section. Grains cover 27% of the section (Figure 7.40 D), which 24.35% includes area of quartz mineral. Blue dyed stain for the purpose of porosity estimation is not available. However, high matrix content (61.8%, Figure 7.40 D) is expected to decrease the porosity. Additionally, a shale lamina is observed, which is estimated as possible flow barrier (Figure 7.38 C). Dominant mineral is the quartz, similarly to thin sections from different sample depths. Some accessory minerals are available. Facies of this sample is described as lithic wacke facies (matrix per. is around 61.8%), very fine to fine sand sized particles (between 0.063 and 0.25 mm., Figure 7.38 C), moderately sorted, angular/sub-angular grains with expected low porosity.

The last sample is from 1368.50 m. drilling depth. A large amount of the grains consists of quartz mineral. Calculation of the percentage of each component is given in Figure 7.40 E. Grains cover 22.17% of the section (Figure 7.40 E), which 20.54% of the grains includes quartz mineral. The highest percentage of porosity is calculated in this sample (Figure 7.40 E). Facies of this sample is described as lithic wacke

facies (matrix per. is around 31.25%), coarse silt sized to fine sand sized particles (between 0.031 and 0.25 mm., Figure 7.39 C), moderately sorted, angular/sub-angular grains with medium porosity (approximately 11.8%) (Figure 7.40 E).

Two core intervals are shown in Figure 7.41. Grain sizes are evaluated as key parameter in this well. In other words, grain sizes controls on production amount: Small grain sizes and high matrix content narrow pore throat, so reduces porosity which is crucial for reservoir properties. On the other hand, although matrix content is similar in both intervals, facies with higher grain sizes is much more productive.

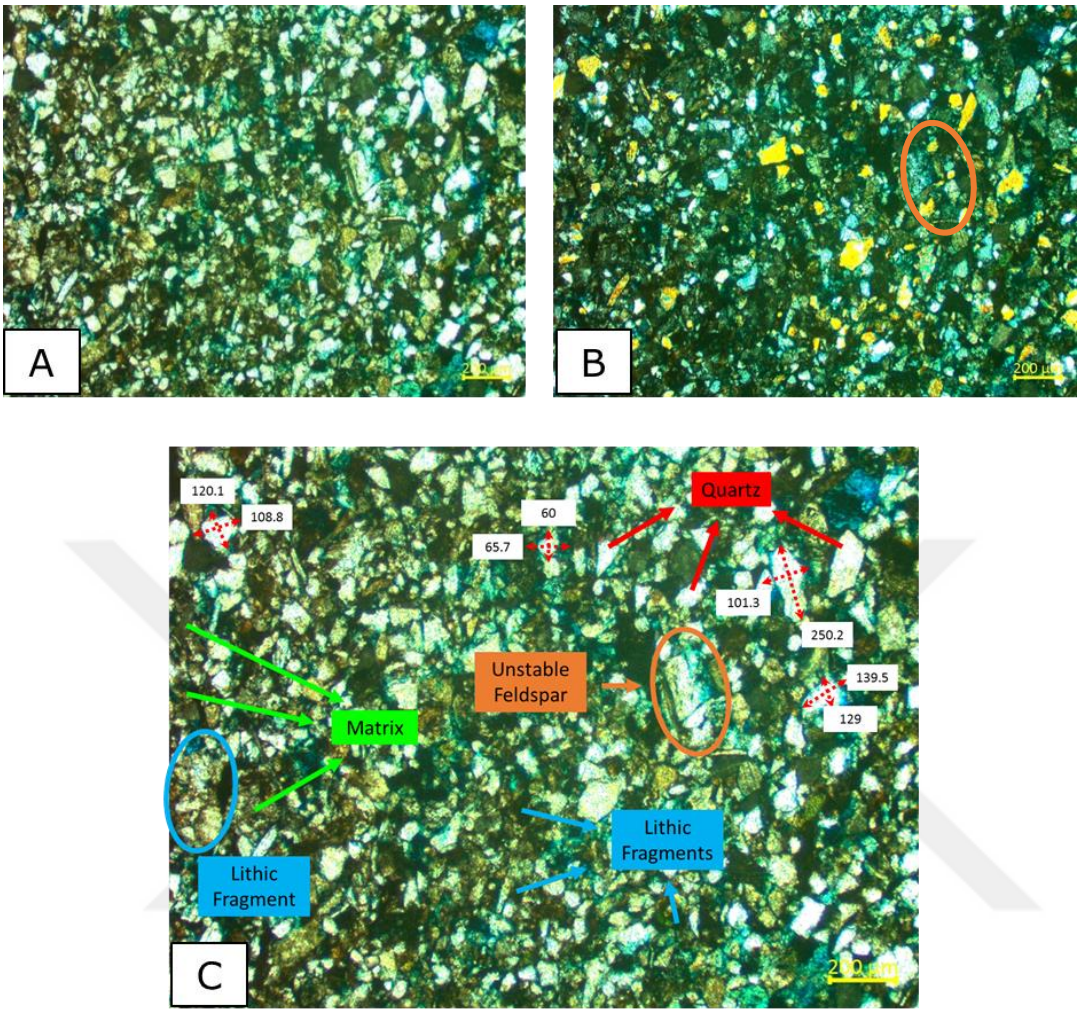

Figure 7.35. (A) PPL display, (B) XPL display and (C) interpretation of thin section at a sample depth of 1360.85 m. Mainly quartz mineral is observed in the section. An unstable feldspar mineral covering 0.4% is observed and illustrated with an orange ellipse. (B) XPL section assits to evaluate the feldspar grain. Red dashed lines display the length of different quartz grains. Blue dyed stain in the sections indicates porous areas.

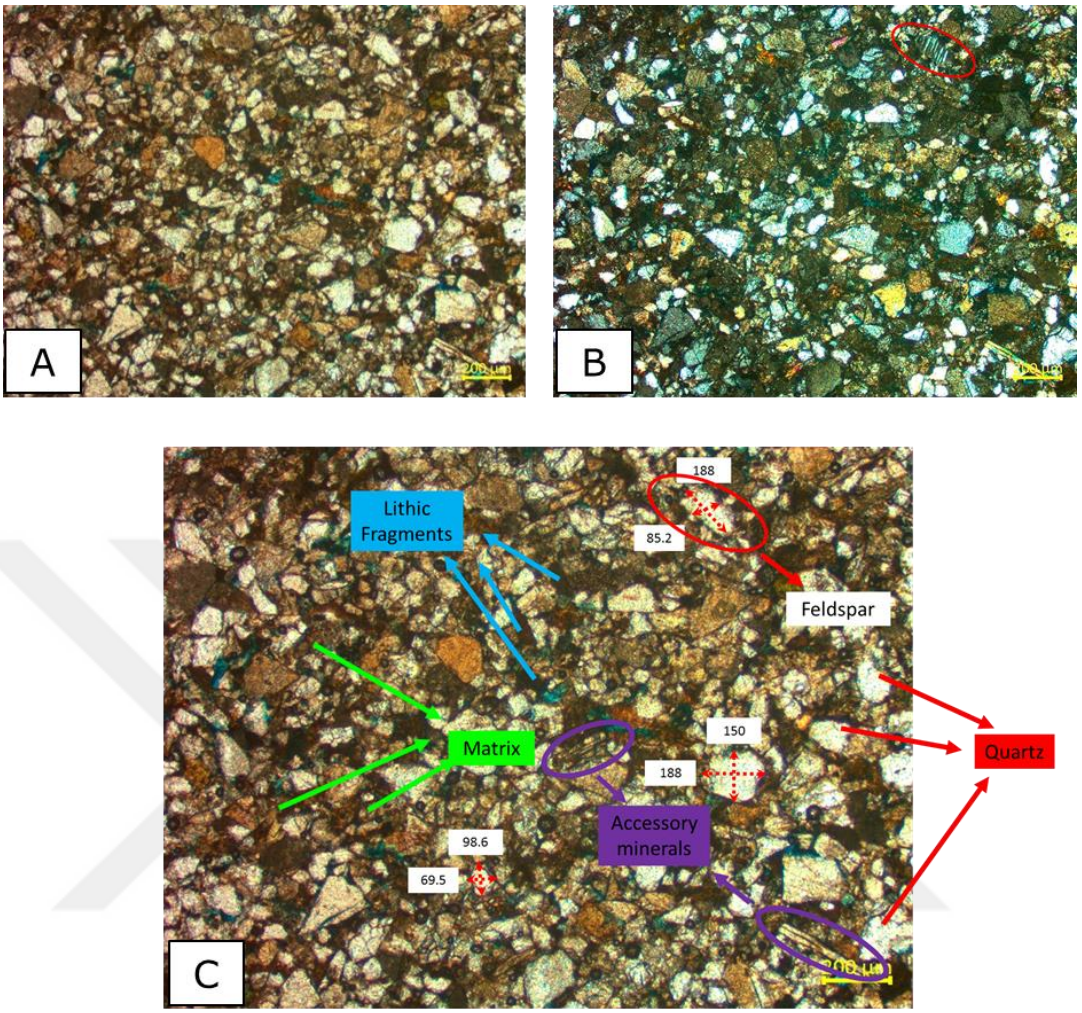

Figure 7.36. (A) PPL display, (B) XPL display and (C) interpretation of thin section at a sample depth of 1365.54 m. Mainly quartz mineral is observed in the section, which some of them are pointed out with red arrows. Purple ellipses indicate accessory minerals, which have a direction and distinctive color in (B) XPL section. Red ellipse points out feldspar mineral in (B) XPL display clearly. Red dashed lines display the length of different grains. Blue dyed stain in the sections indicates porous areas.

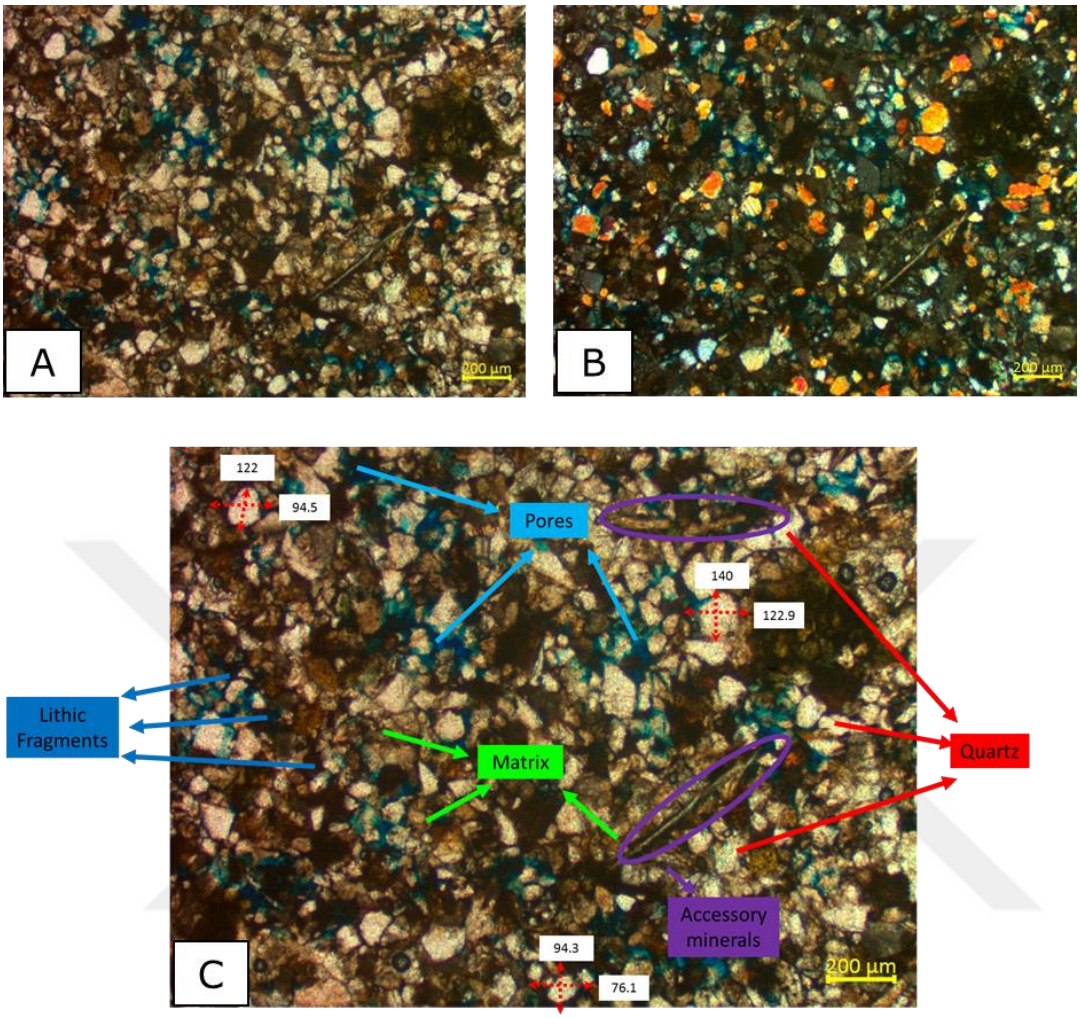

Figure 7.37. (A) PPL display, (B) XPL display and (C) interpretation of thin section at a sample depth of 1366.35 m. Mainly quartz mineral is observed in the section, which some of them are pointed out with red arrows. Purple ellipses indicate accessory minerals. Red dashed lines display the length of different quartz grains. Blue dyed stain in the sections indicates porous areas.

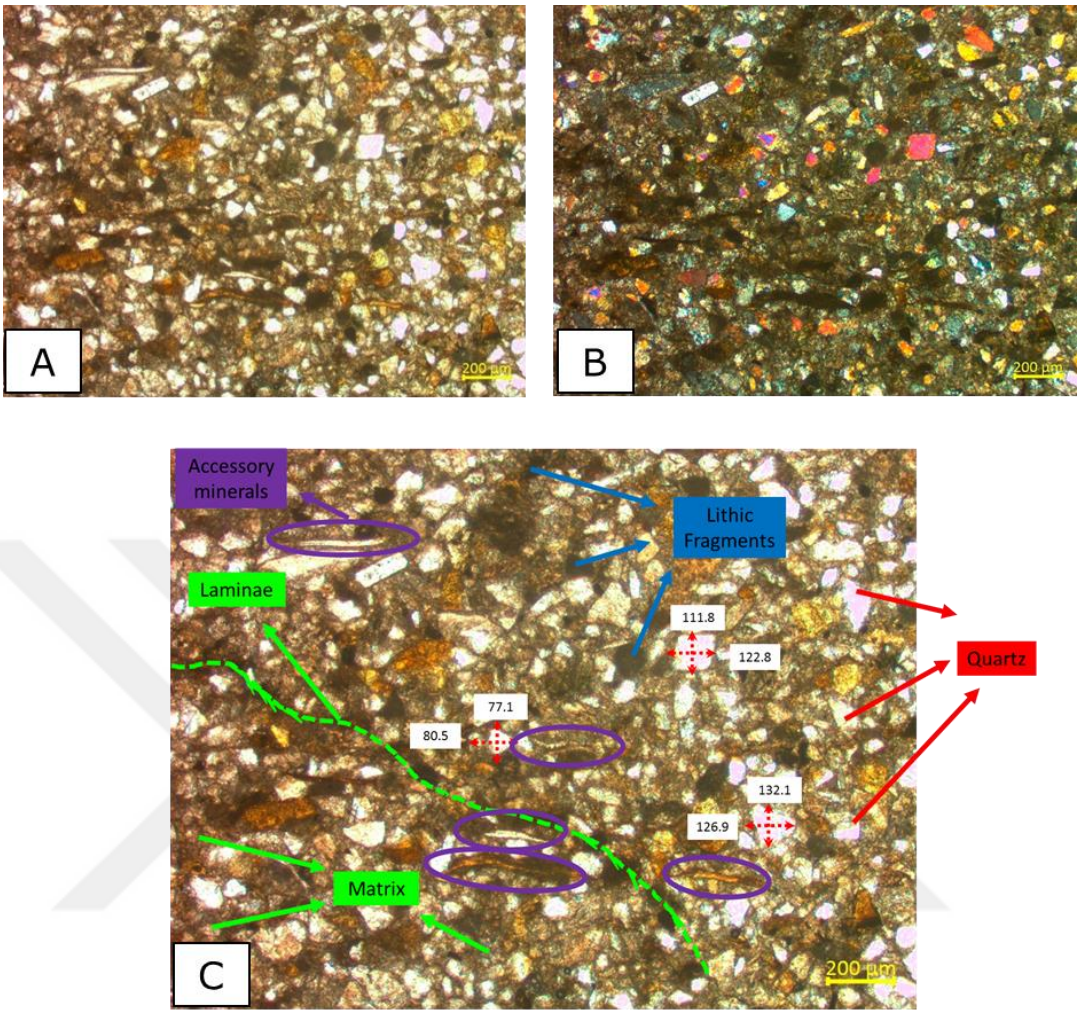

Figure 7.38. (A) PPL display, (B) XPL display and (C) interpretation of thin section at a sample depth of 1367.35 m. High percent of matrix is detected in this sample. Shale lamina is shown and drawn with dashed green line. This lamina is evaluated as possible flow barrier, which worsens reservoir condition. Purple ellipses indicate accessory minerals. Red dashed lines display the length of different quartz grains. Blue dyed stain is absent in this section.

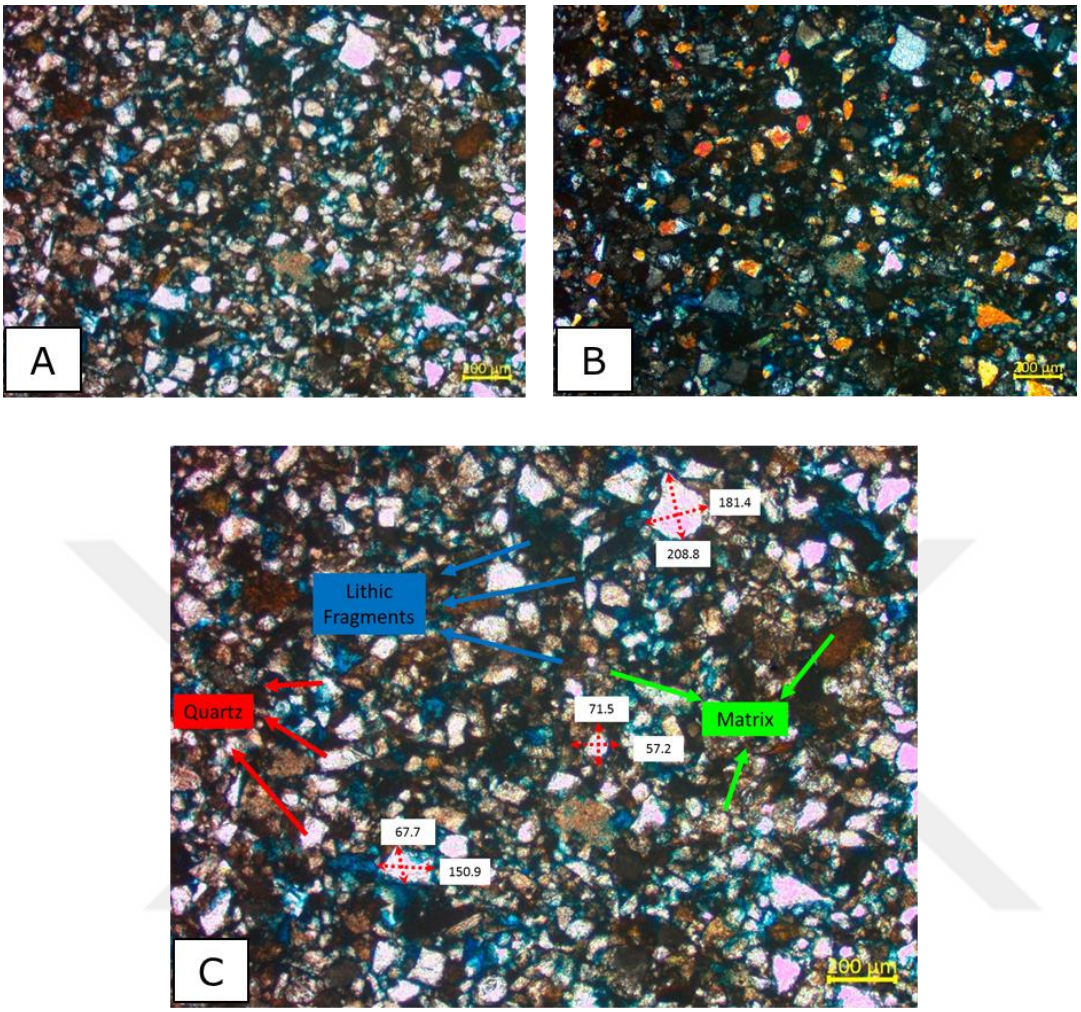

Figure 7.39. (A) PPL display, (B) XPL display and (C) interpretation of thin section at a sample depth of 1368.5 m. Higher percent of pores comparing other sections is seen and calculated values are given in Figure 7.40. Red dashed lines display the length of different quartz grains.

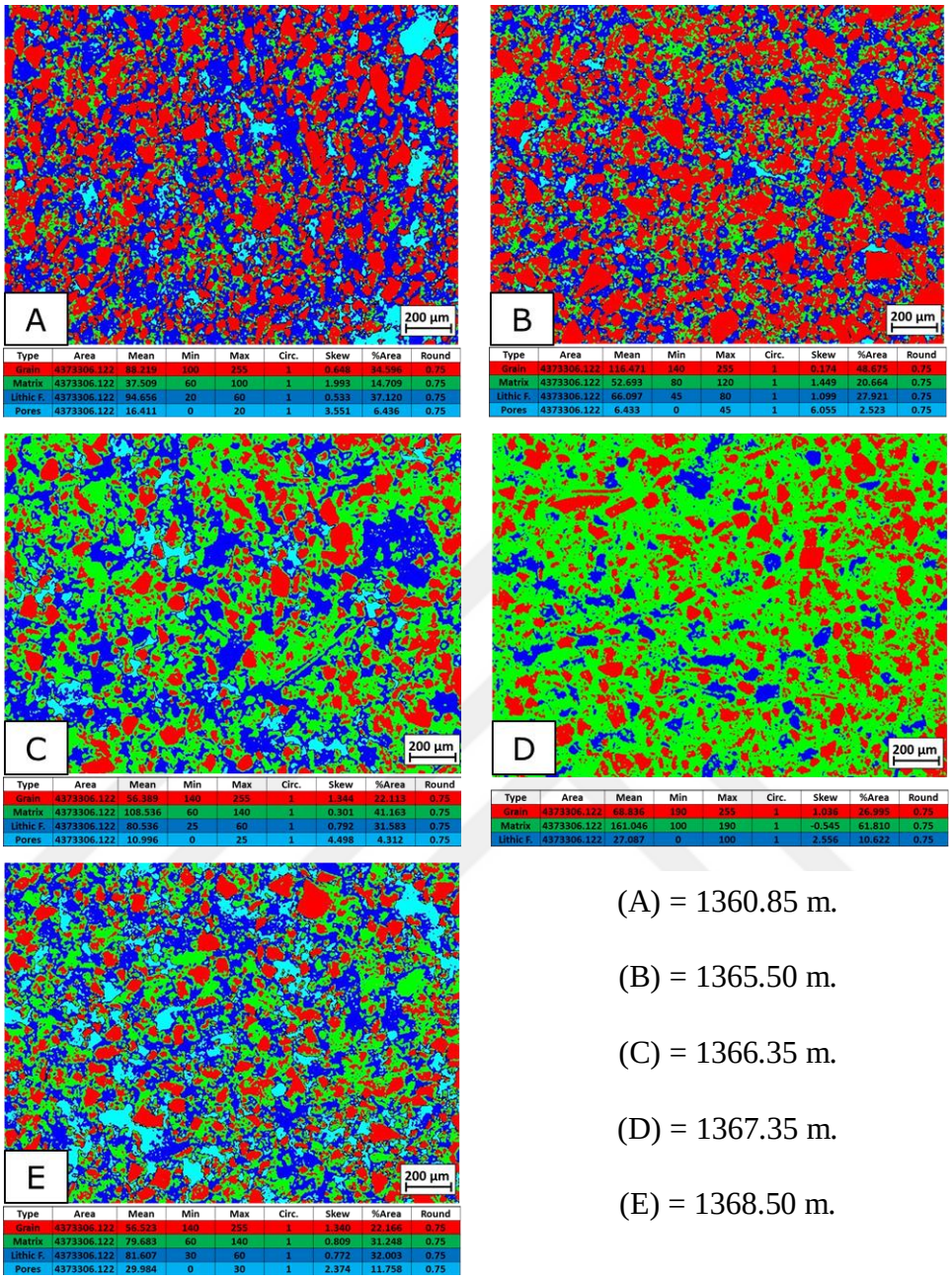

(A) = 1360.85 m.

(B) = 1365.50 m.

(C) = 1366.35 m.

(D) = 1367.35 m.

(E) = 1368.50 m.

Figure 7.40. Estimation of the percentage for different depth of samples; (A) 1360.85 m., (B) 1365.50 m., (C) 1366.35 m., (D) 1367.35 m. and (E) 1368.50 m. Approximate porosity values are calculated, except for 1367.35 m. due to lack of blue dyed stain. The highest matrix content is seen in the fourth sample (D) with 1367.35 depth. Sample 1 and 2 (A and B) have the highest percent of grain values. The fifth sample (E) indicates the highest porosity among thin sections of core-1. Percentage of lithic fragments for each sample are closer, except the sample 4 which includes high amount of matrix.

7.3.3.2 Thin Sections: Core-2

The core interval between 1404.5-1413.5 m. in this well has been produced 13,300,000 m^3. This well is the most second productive well in deeper Osmancık Formation among the wells of group-1. 5 samples of thin section, similarly core-1, were studied and evaluated within core-2 of Well-15. PPL and XPL displays and interpreted thin sections are given in Figure from 7.41 to 7.45.

The first sample is from 1405.4 m. drilling depth. Mainly quartz minerals and a clear cement development are observed in this section (Figure 7.41). Calculated percentage of area for those grain, matrix, lithic fragments and porosity is illustrated in Figure 7.46 A. Grains cover 23.5% of the section (Figure 7.46 A). 21.4% of the grains are quartz. Thin section is composed of matrix with 28.25% percentage. Facies of this sample is described as lithic wacke facies (matrix per. more than 15%, quartz per approximately 21.4%), very fine to medium sand sized particles (between 0.063 and 0.5 mm, Figure 7.41 C), moderately sorted, angular/sub-angular grains with high porosity which is approximately 16.3% (Figure 7.46 A), including cement development resulting decrease in porosity through upper part of the thin section.

The second sample is from 1406.55 m. drilling depth. Mainly quartz minerals are observed in this section (Figure 7.42). Calculated percentage of area for each component is illustrated in Figure 7.46 B. Grains cover 24% of the section (Figure 7.46 B). 22% of the grains is composed of quartz. Thin section is composed of Matrix with 28.9% percentage. Facies of this sample is described as lithic wacke facies (matrix per. 28.9 %, quartz per approximately 22%), very fine to fine sand sized particles (between 0.063 and 0.25 mm, Fig 7.42 B), poorly sorted, angular/sub-angular grains with high porosity which is almost 18.6% (Figure 7.46 B).

The third sample is from 1407.55 m. drilling depth. Most of the grains are composed of quartz mineral (Figure 7.43). Percentage of the area for each component is shown in Figure 7.46 C. Grains cover 33.2% of the section (Figure 7.46 C), which 32.6% includes area of quartz mineral. Facies of this sample is described as lithic wacke

facies (matrix per. higher than 15%, quartz per approximately 32.6%, Figure 7.46 C), fine to medium sand sized particles (between 0.125 and 0.5 mm, Figure 7.43 C), poorly sorted, rounded/subrounded grains with moderate porosity which is almost 7.3% (Figure 7.46 C).

The fourth sample is from 1408.55 m. drilling depth. The thin section includes mainly quartz mineral with minor feldspar (orange ellipse) and chert (blue ellipse) presence (Figure 7.44 B and C). Figure 7.46 D indicates the percentage of each element in the section. Grains cover 23.3% of the section (Figure 7.40 D), which 20.8% includes area of quartz mineral. Matrix percentage is about 14.5. Facies of this sample is described as lithic arenite facies (matrix per. lower than 15%, quartz per. 20.8%, Figure 7.46 D), fine to medium sand sized particles (between 0.125 and 0.5 mm., Figure 7.44 C), poorly sorted, angular/sub-angular grains with high porosity around 20.7% (Figure 7.46 D).

The last sample is from 1410.25 m. drilling depth. A large amount of the grains consists of quartz mineral (Figure 7.45). Additionally, high rate of matrix and lithic fragment is also available. Blue dyed stain is missing; therefore, porosity calculation cannot be achieved. Calculation of the percentage of each component is shown in Figure 7.46 E. Grains cover 39.8% of the section (Figure 7.46 E), and it is not possible to differentiate quartz and other possible minerals due to poor quality of the thin section. Facies of this sample is described as lithic wacke facies (matrix per. is 41%, Figure 7.46 E), fine to medium sand sized particles (between 0.125 and 0.5 mm., Figure 7.45 C), moderately sorted, angular/sub-angular grains including possibly low porosity due to high content of matrix.

Two core intervals from Well-15 are shown in Figure 7.47. Facies properties are closer to each other for core-1 and core-2 intervals while porosity values are higher in core-2 samples in this well. Only one lithic arenite type of facies is present in each core. When these samples are compared to each other, sample from core-2 has higher porosity (~20%) than the sample of core-1 (~6.5%). However, the main difference

between producing and non-producing intervals seems as reservoir pressure rather than facies properties.

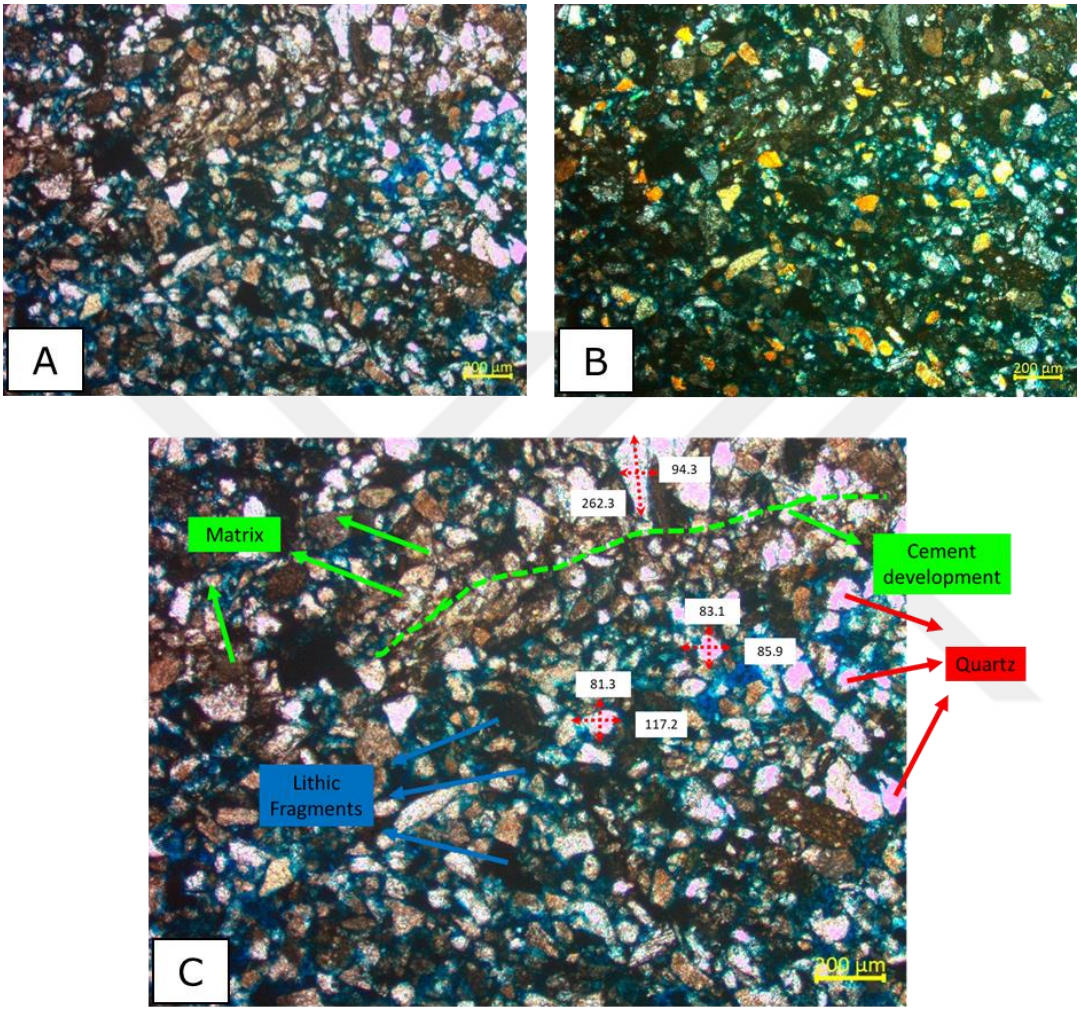

Figure 7.41. (A) PPL display, (B) XPL display and (C) interpretation of thin section at a sample depth of 1405.4 m. Mainly quartz mineral is observed in the section. Cement development is illustrated with a green dashed line, which causes preventing porosity development. Red dashed lines display the length of different quartz grains. Blue dyed stain in the sections indicates porous areas.

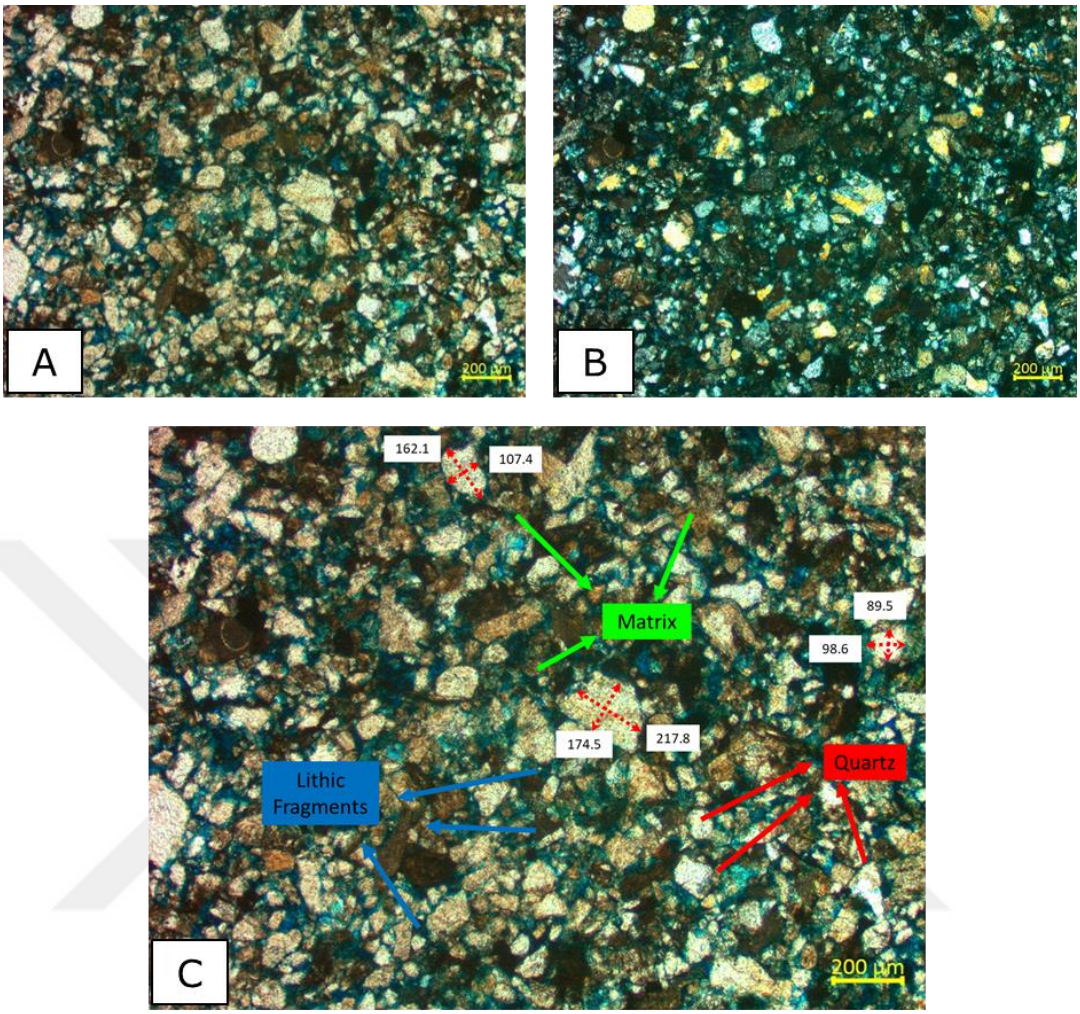

Figure 7.42. (A) PPL display, (B) XPL display and (C) interpretation of thin section at a sample depth of 1406.55 m. Mainly quartz mineral is observed in the section. Red dashed lines illustrate the length of different quartz grains. Blue dyed stain in the sections indicates porous areas.

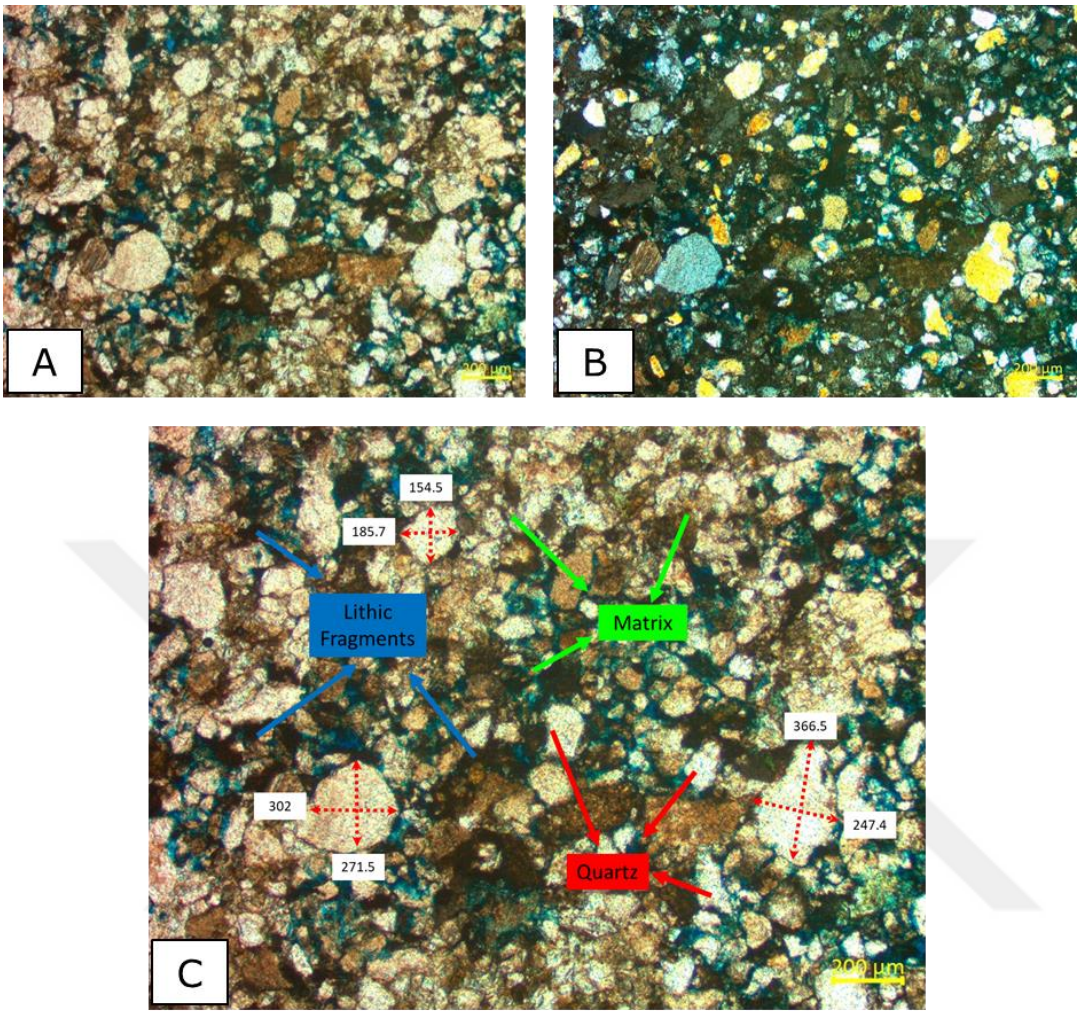

Figure 7.43. (A) PPL display, (B) XPL display and (C) interpretation of thin section at a sample depth of 1407.55 m. Mainly quartz minerals with different sizes are observed in the section. Red dashed lines demonstrate the length of different quartz grains. Blue dyed stain in the sections indicates porous areas.

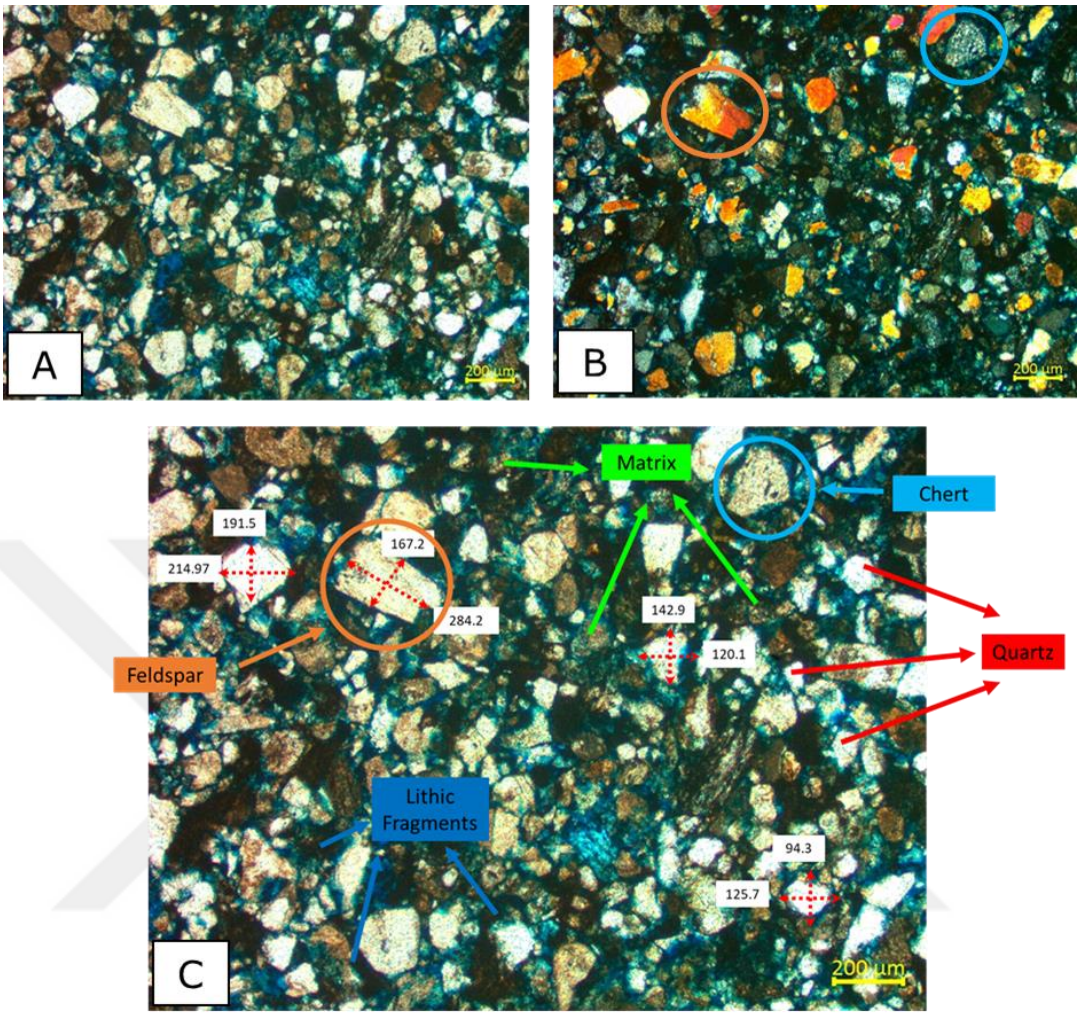

Figure 7.44. (A) PPL display, (B) XPL display and (C) interpretation of thin section at a sample depth of 1408.55 m. Addition to quartz minerals, feldspar and chert grains (with the aid of XPL (B)) are also illustrated in the section. Red dashed lines indicate the length of different grains. Blue dyed stain in the sections indicates porous areas.

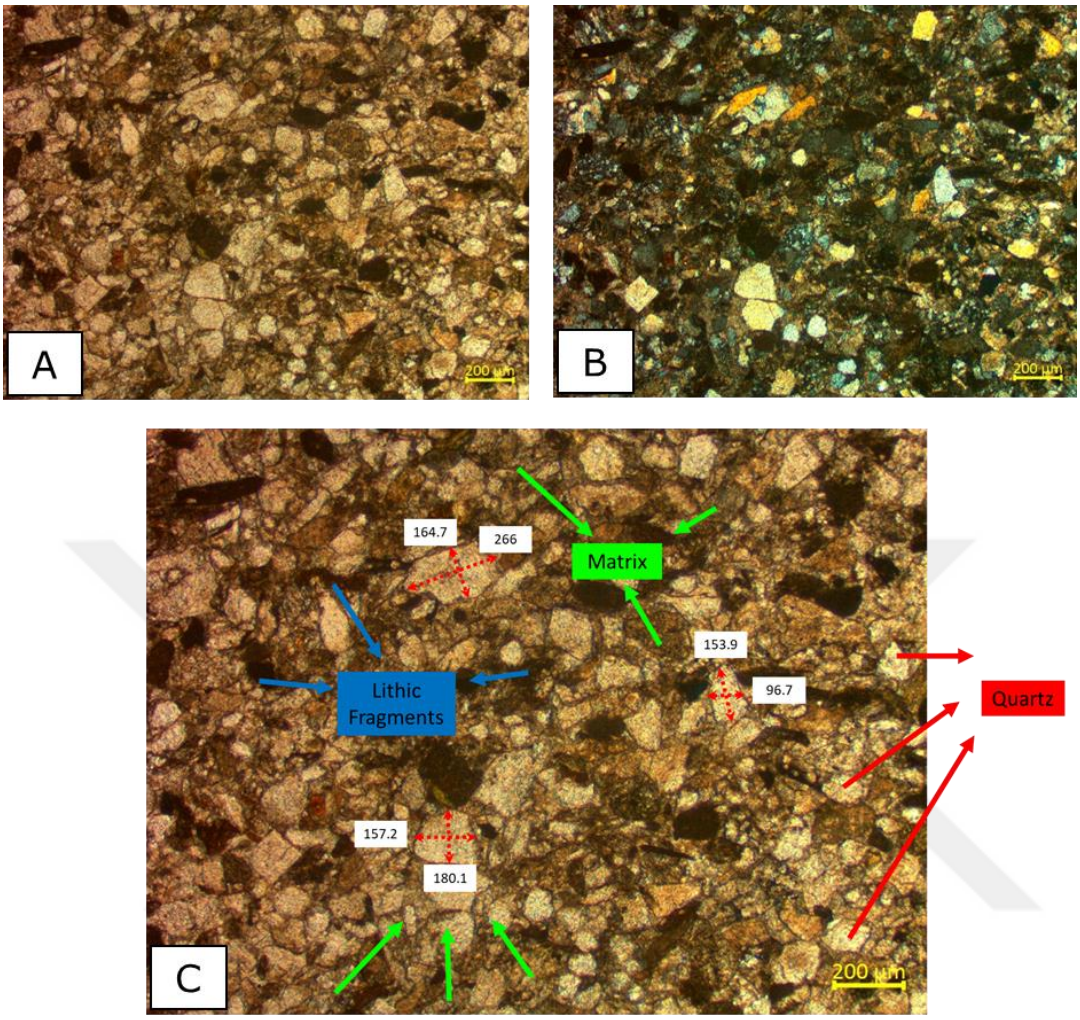

Figure 7.45. (A) PPL display, (B) XPL display and (C) interpretation of thin section at a sample depth of 1410.25 m. Mainly quartz grains with high rate of lithic fragments and matrix are observed. Red dashed lines indicate the length of different grains. Blue dyed stain is missing in this section, which is expected to be used for the evaluation of pores.

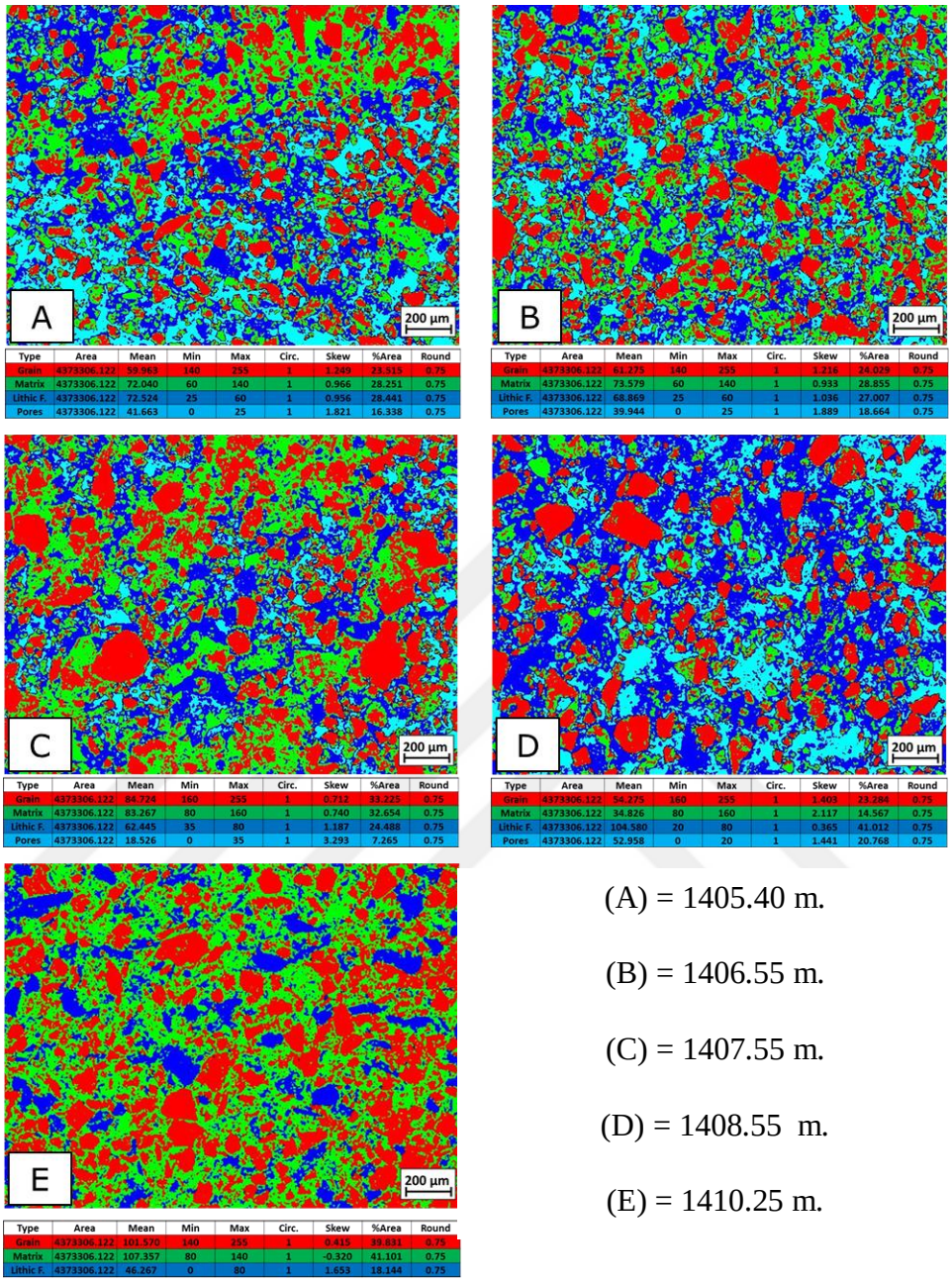

Figure 7.46. Estimation of the percentage of different components for five samples; (A) 1405.40 m., (B) 1406.55 m., (C) 1407.55 m., (D) 1408.55m. and (E) 1410.25 m. Approximate porosity values are calculated, except for 1410.25 m. (E) due to lack of blue dyed stain. The highest matrix content is seen in the fifth sample (E) with 1410.25 depth. Although this sample has the highest percent of grain values, quality of the thin section is weak, which is not very reliable. The fourth sample (E) indicates the highest porosity among thin sections of core-2.

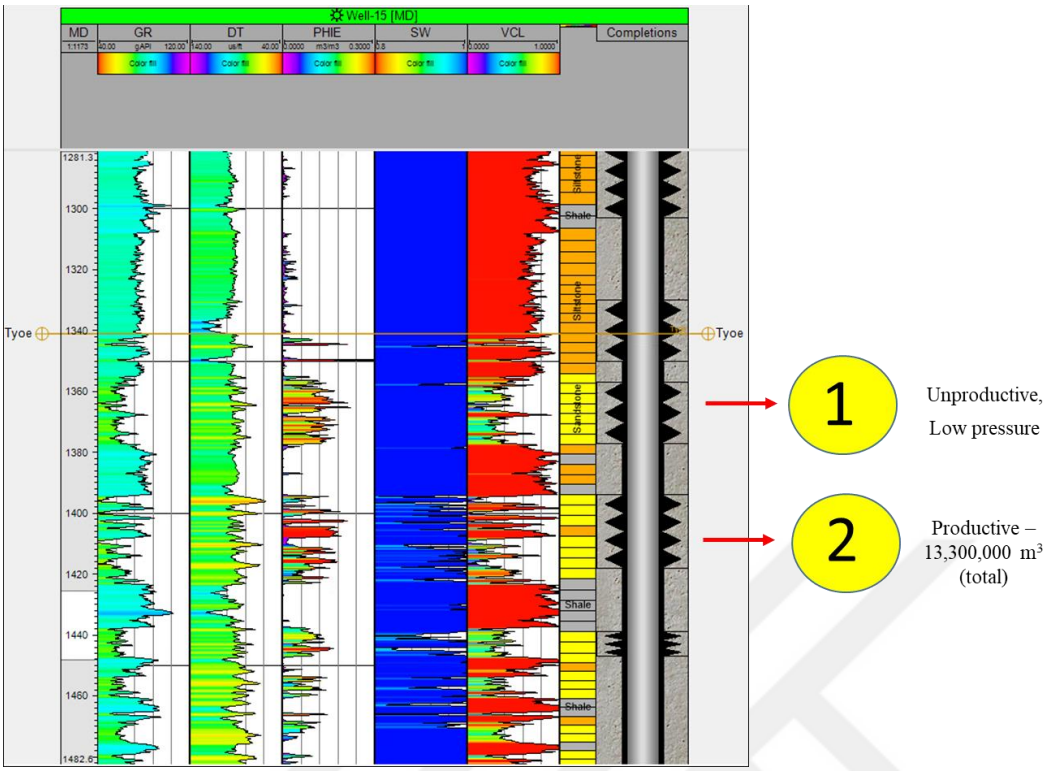

Figure 7.47. From left to right: Gamma-ray (GR), p-slowness (DT), effective porosity (PHIE), water saturation (SW), volume of clay (VCL), facies logs and completions for well-15. Number 1 is non-productive interval from core-1 although this zone has high effective porosity and low amount of clay volume. Number 2 indicates productive zone where core-2 is drilled out. Water saturation is 100% for number-1 interval, which means that the zone is lack of hydrocarbon presence. However, number-2 interval includes lower water saturation dropping around 50%, resulting the presence of hydrocarbon.

7.3.4 Thin sections from Well-16

The core was drilled out from the interval between 1527-1531 m. in this well. Well-16 is a non-productive well. 3 samples of thin section were studied and evaluated within the relevant core. PPL and XPL displays and interpreted thin sections are given in Figures from 7.48 to 7.50.

The first sample has a drilling depth of 1527.35 m. Mainly quartz and minor accessory minerals are observed in this section (Figure 7.48). Calculated percentage of area for those grain, matrix, lithic fragments and porosity is illustrated in Figure 7.51 A. Grains cover 29.5% of the section. Around 29% of the grains are composed of quartz minerals. 37.6% of the section consists of matrix (Figure 7.51 A). Facies of this sample is described as lithic wacke facies (matrix per. 37.6%, quartz per. is about 29%, Figure 7.51 A), very fine to medium sand sized particles (between 0.063 and 0.5 mm., Figure 7.48 C), moderately sorted, angular/sub-angular grains with low porosity around 4.3% (Figure 7.51 A). Pores in the thin section are not connected resulting as low effective porosity.

The second sample is from drilling depth of 1527.85 m. Mainly quartz minerals are observed in this section (Figure 7.49). Calculated percentage of area for each component is shown in Figure 7.51 B. Grains cover 20% of the section (Figure 7.51 B). Percentage of the quartz minerals nearly equal to percentage of grains. Thin section is composed of matrix with 27.6% percentage of the area. Facies of this sample is described as lithic wacke facies (matrix per. 27.6%), very fine to medium sand sized particles (between 0.063 and 0.5 mm., Figure 7.49 C), moderately-poorly sorted, angular/sub-angular grains with low porosity around 5.7% (Figure 7.51 B).

The last sample is from 1528.85 m. drilling depth. Most of the grains are composed of quartz mineral (Figure 7.50). Percentage of the area for each component is given in Figure 7.51 C. Grains cover 21% of the section, which is almost equivalent to quartz content. Matrix covers 34.2% of the thin section. Lithic fragments dominate the thin section with a percentage of 34.4 (Figure 7.51 C). Facies of this sample is

described as lithic wacke facies (matrix per. 34.2%, quartz per approximately 21%), very fine to fine sand sized particles (between 0.063 and 0.25 mm., Figure 7.50 C), moderately sorted, sub-rounded /sub-angular grains with medium porosity approximately 9.4% (Figure 7.51 C).

Perforated zones in Well-16 did not produce. Well section representing the perforated interval that core was drilled out is given in Figure 7.52. Although a thick sandstone is available in the interval of perforation and effective porosity is about 10%, pressure does not appear in the zone, resulting a non-productive depth range. Water saturation is 100% except a very small interval. To sum up, although reservoir properties are compatible with producing wells, hydrocarbon is not accumulated in the location of the reservoir interval.

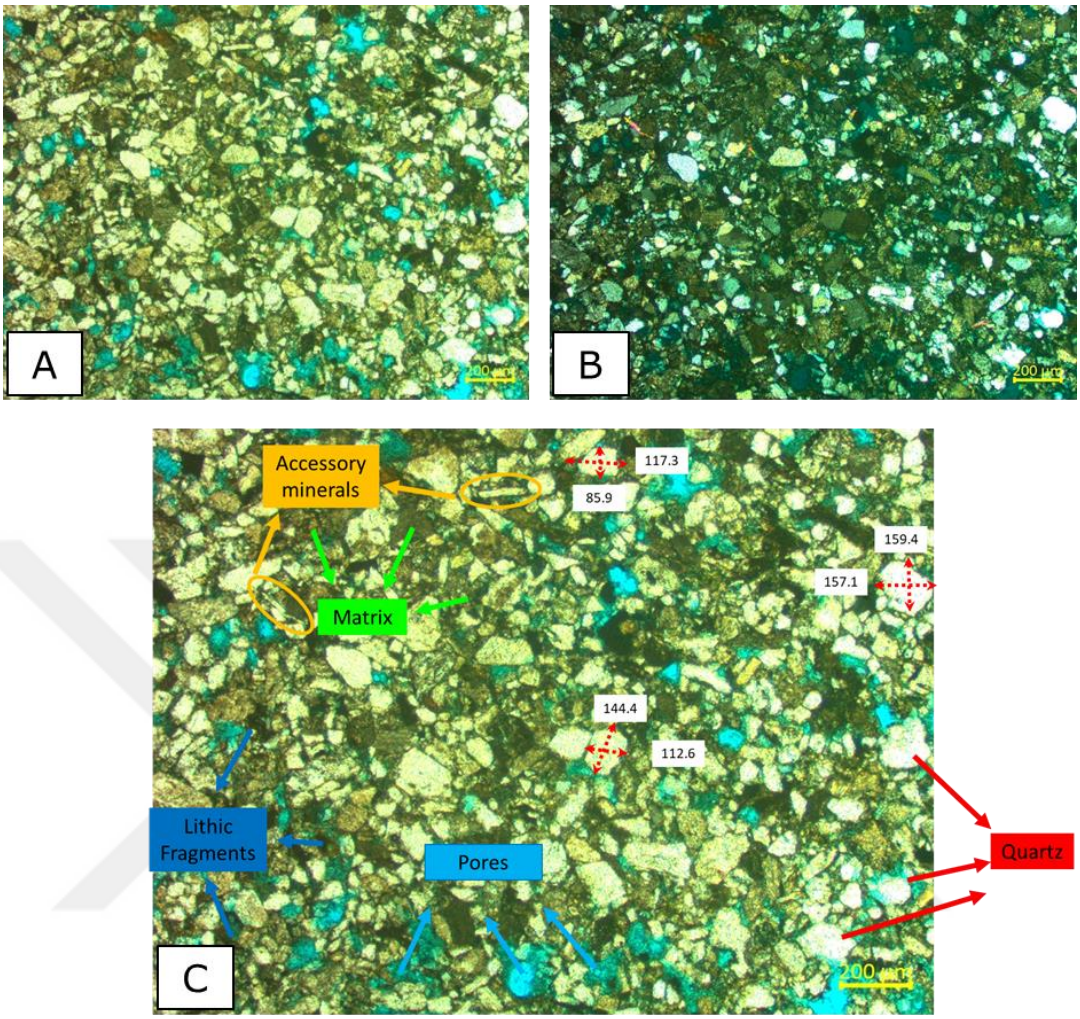

Figure 7.48. (A) PPL display, (B) XPL display and (C) interpretation of thin section at a sample depth of 1527.35 m. Mainly quartz mineral is observed in the section. Red dashed lines display the length of different quartz grains. Blue dyed stain in the sections indicates porous areas. Mostly, pores are not connected resulting low effective porosity.

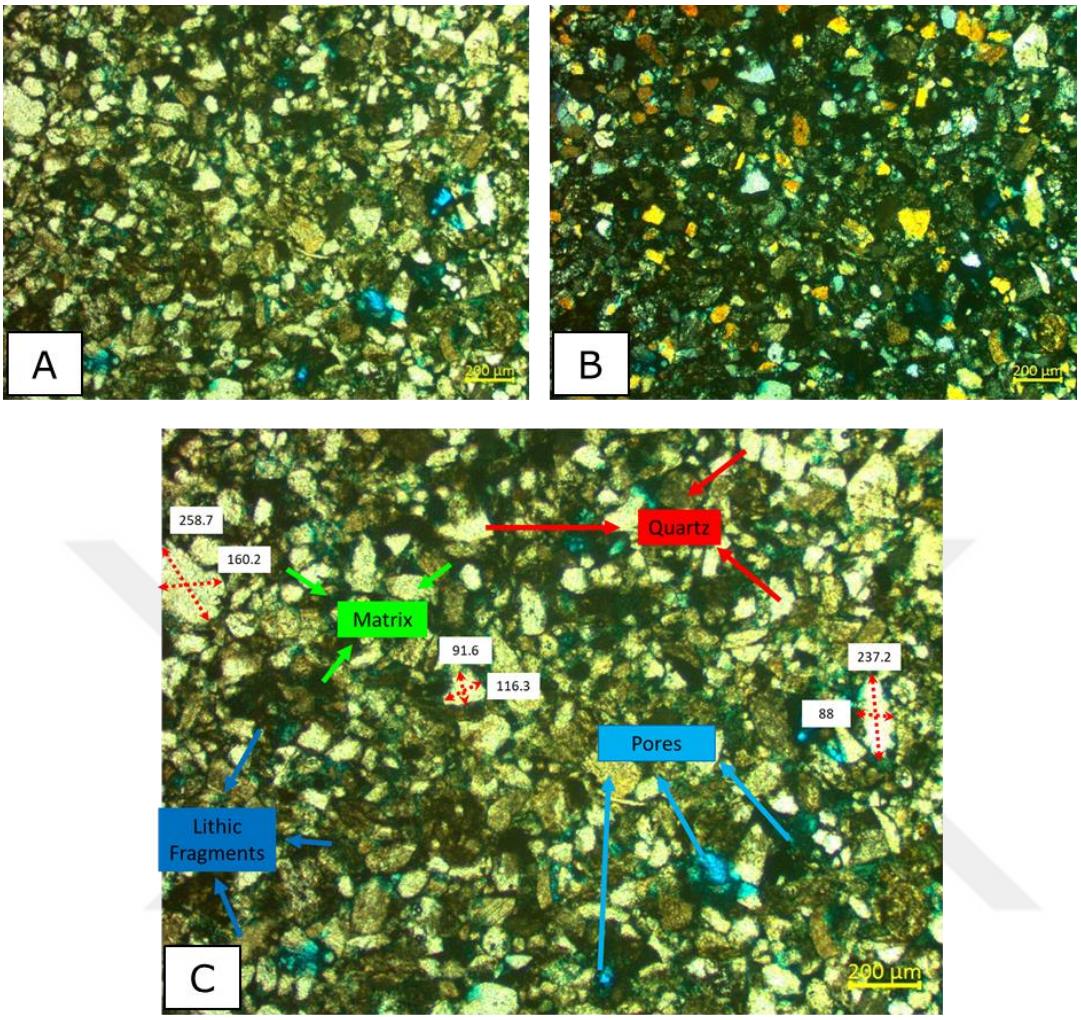

Figure 7.49. (A) PPL display, (B) XPL display and (C) interpretation of thin section at a sample depth of 1527.85 m. Mainly quartz mineral is encountered in the section. Red dashed lines display the length of different grains. Blue dyed stain in the sections indicates porous ones, which covers a small area.

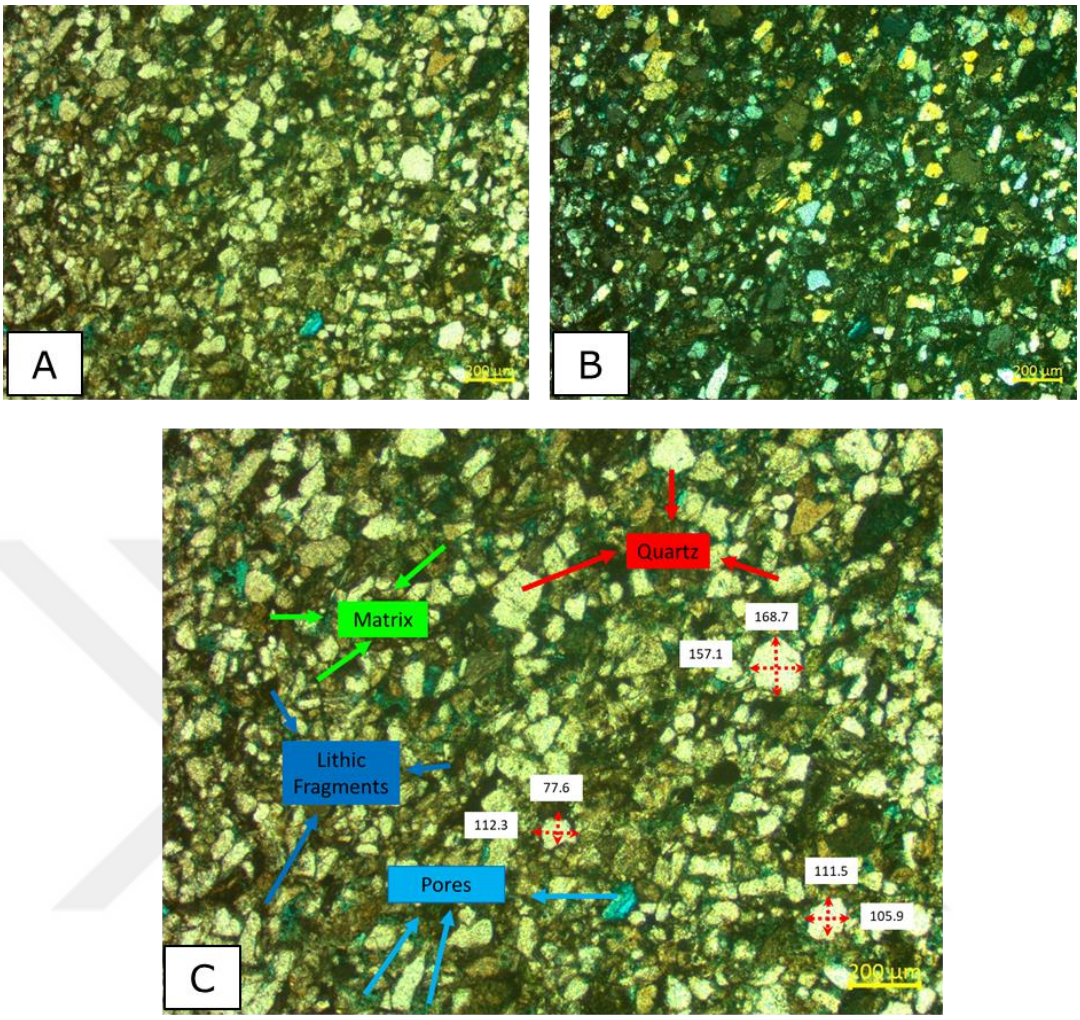

Figure 7.50. (A) PPL display, (B) XPL display and (C) interpretation of thin section at a sample depth of 1528.85 m. Similar to other thin sections in this well, quartz mineral is dominant. Red dashed lines display the length of different grains. Blue dyed stain in the sections shows porous area.

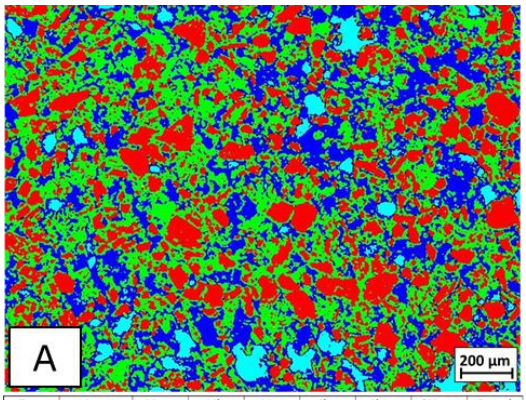

Type	Area	Mean	Min	Max	Circ.	Skew	%Area	Round
Grain	4373306.122	75.115	160	255	1	0.901	29.457	0.75
Matrix	4373306.122	95.835	80	160	1	0.513	37.582	0.75
Lithic F.	4373306.122	69.093	30	80	1	1.031	27.095	0.75
Pores	4373306.122	10.881	0	30	1	4.525	4.267	0.75

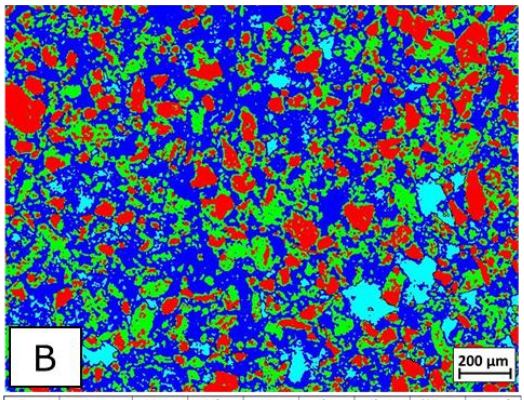

Type	Area	Mean	Min	Max	Circ.	Skew	%Area	Round
Grain	4373306.122	50.993	160	255	1	1.5	19.997	0.75
Matrix	4373306.122	70.474	80	160	1	1	27.637	0.75
Lithic F.	4373306.122	116.698	30	80	1	0.170	45.764	0.75
Pores	4373306.122	14.597	0	30	1	3.812	5.724	0.75

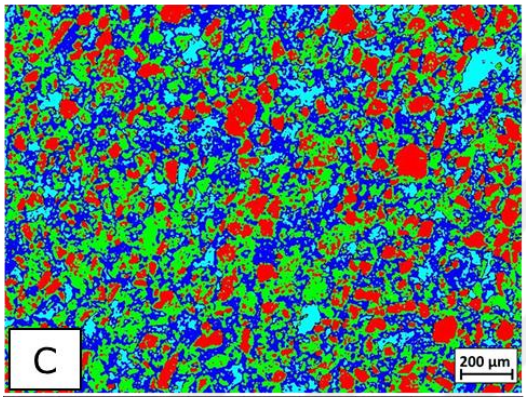

Type	Area	Mean	Min	Max	Circ.	Skew	%Area	Round
Grain	4373306.122	53.482	160	255	1	1.426	20.973	0.75
Matrix	4373306.122	87.272	80	160	1	0.665	34.224	0.75
Lithic F.	4373306.122	86.625	30	80	1	0.677	33.970	0.75
Pores	4373306.122	23.921	0	30	1	2.786	9.381	0.75

(A) = 1527.35 m.

(B) = 1527.85 m.

(C) = 1528.85 m.

Figure 7.51. Merged colors of each component and calculated statistical values in thin sections of Well-16. Matrix percentage is similar varying between 27-37% for each sample and grain percentage changes from 20% to 30%. Porosity is low in all sections, which the largest value is around 9.4% and the smallest one is about 4.5%.

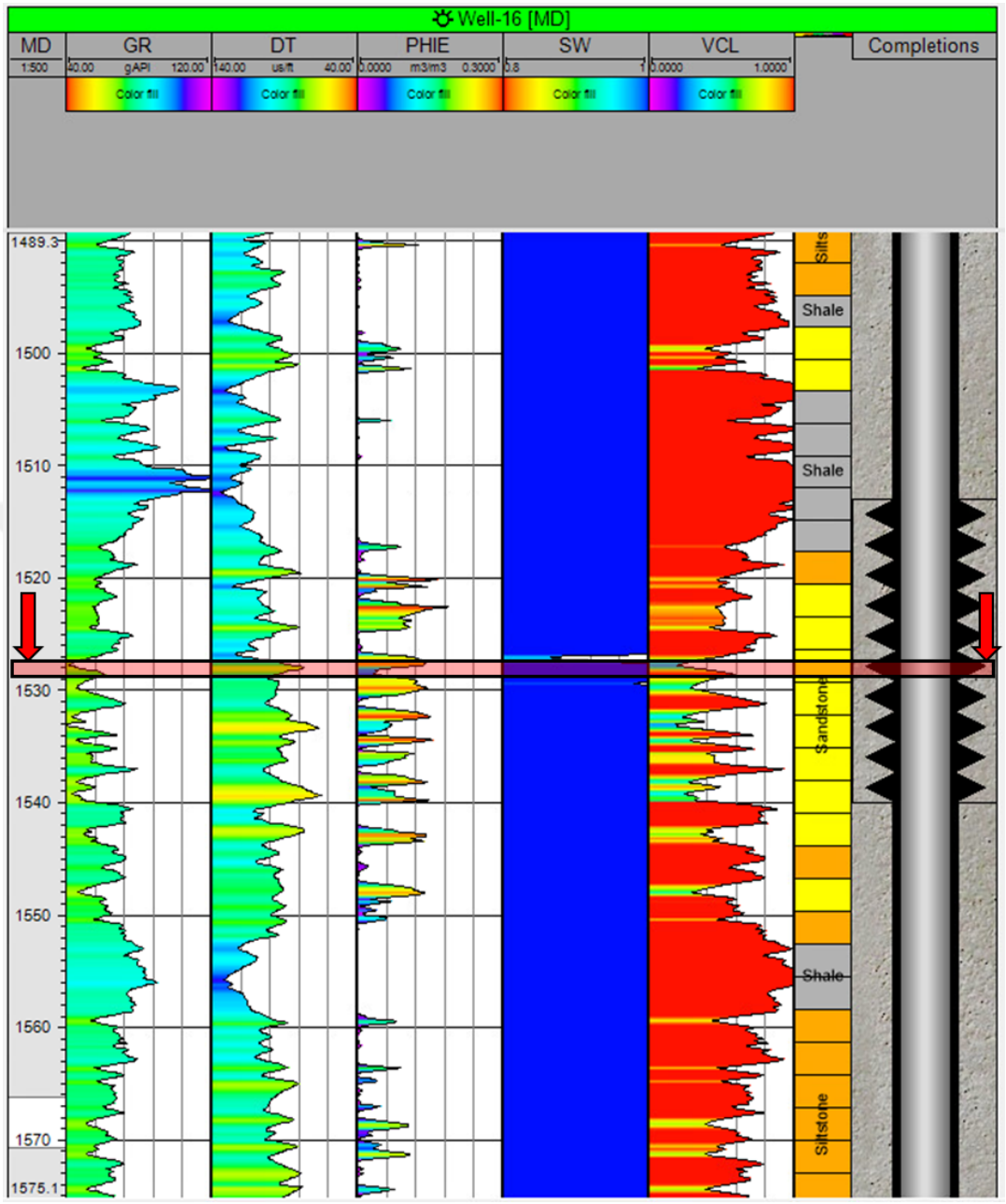

Figure 7.52. From left to right: Gamma-ray (GR), p-slowness (DT), effective porosity (PHIE), water saturation (SW), volume of clay (VCL), facies log and completions for well-16. Although, the presence of a thick sandstone column and relatively higher effective porosity, hydrocarbon is only available in an interval less than 1 m, which is observable in water saturation log values. Rest of the values for SW is 100%. Core interval is shown with red rectangle and is pointed out with red arrows.

7.3.5 Thin sections from Well-32

The core was drilled out from the interval between 1798-1805.7 m. in this well. Well-32 is another non-productive well similar to Well-16. 4 samples of thin section were studied and evaluated within the relevant core.

PPL and XPL displays of each section are illustrated in Figure 7.53. PPL sections are given on the left column and XPL sections are shown on the right column in this figure. Evaluation of the thin sections are demonstrated within Figures 7.54-7.57, respectively.

The first sample has a drilling depth of 1798.75 m. The amount of quartz mineral and lithic fragments are, relatively, close to each other. Matrix content is high allowing porosity loss. Because dyed blue stain is not available, porosity cannot be calculated. However, high amount of matrix gives some idea about low porosity values. Calculated percentage of area for each component is illustrated in Figure 7.58 A. Grains cover 28.6% of the section. Percentage of quartz mineral is evaluated as nearly equal to amount of grains. 48.2% of the section consists of matrix. Area of lithic fragments is about 25.6%. Facies of this sample is described as lithic wacke facies (matrix per. 48.2%, quartz per. is about 28.6%, Figure 7.58 A), very fine to fine sand sized particles (between 0.063 and 0.25 mm., Figure 7.54), moderately sorted, angular/sub-angular grains with possibly low porosity.

The second sample is from drilling depth of 1800.9 m. Both quartz minerals and lithic fragments are dominant in this section. Additionally, an opaque mineral is observed in the section (Figure 7.55). Grains cover 35.6% of the section and percentage of quartz is almost the same with grains. Thin section is composed of matrix with 32.9% percentage of the area. The percentage of lithic fragments is 30.3% (Figure7.58 B). Facies of this sample is described as lithic wacke facies (matrix per. 32.9%), very fine to fine sand sized particles (between 0.063 and 0.25 mm., Figure 7.55), moderately sorted, sub-rounded/sub-angular grains.

The third sample is from 1803.2 m. drilling depth. Most of the grains are composed of quartz mineral (Figure 7.56). Figure 7.58 C indicates that the area of grains, matrix and lithic fragments are close to each other. Grains are composed of 31.8%, matrix covers 32.6% and lithic fragments consist of 33.4% of the thin section (Figure 7.58 C). Facies of this sample is described as lithic wacke facies, very fine to coarse sand sized particles (between 0.063 and 1 mm., Figure 7.56), poorly sorted, angular/sub-angular grains with medium porosity approximately 9.4% (Figure 7.58 C).

The last sample is from drilling depth of 1804.35 m. Grains in the section include high content of quartz minerals. Additionally, minor opaque minerals and chert are observed in the section (Figure 7.57). 38% of the grains (38.7%) consists of quartz mineral. Lithic fragments cover a very small area which is 7.2%. Matrix content is the dominant and reaches 54.7%, which is the highest area among thin sections in Well-32. Although blue dyed stain is not available, porosity of the section is clearly very low (Figure 7.57) due to high matrix content. Facies of this sample is described as lithic wacke facies, very fine to fine sand sized particles (between 0.063 and 0.25 mm., Figure 7.55), moderately sorted, angular/sub-angular grains.

Processed logs such as effective porosity, water saturation and volume of clay were generated within depth range of 1593 m. and 1782 m. Additionally, competition information is not available at the core interval. Therefore, comparison between thin sections and well logs is missing for Well-32.

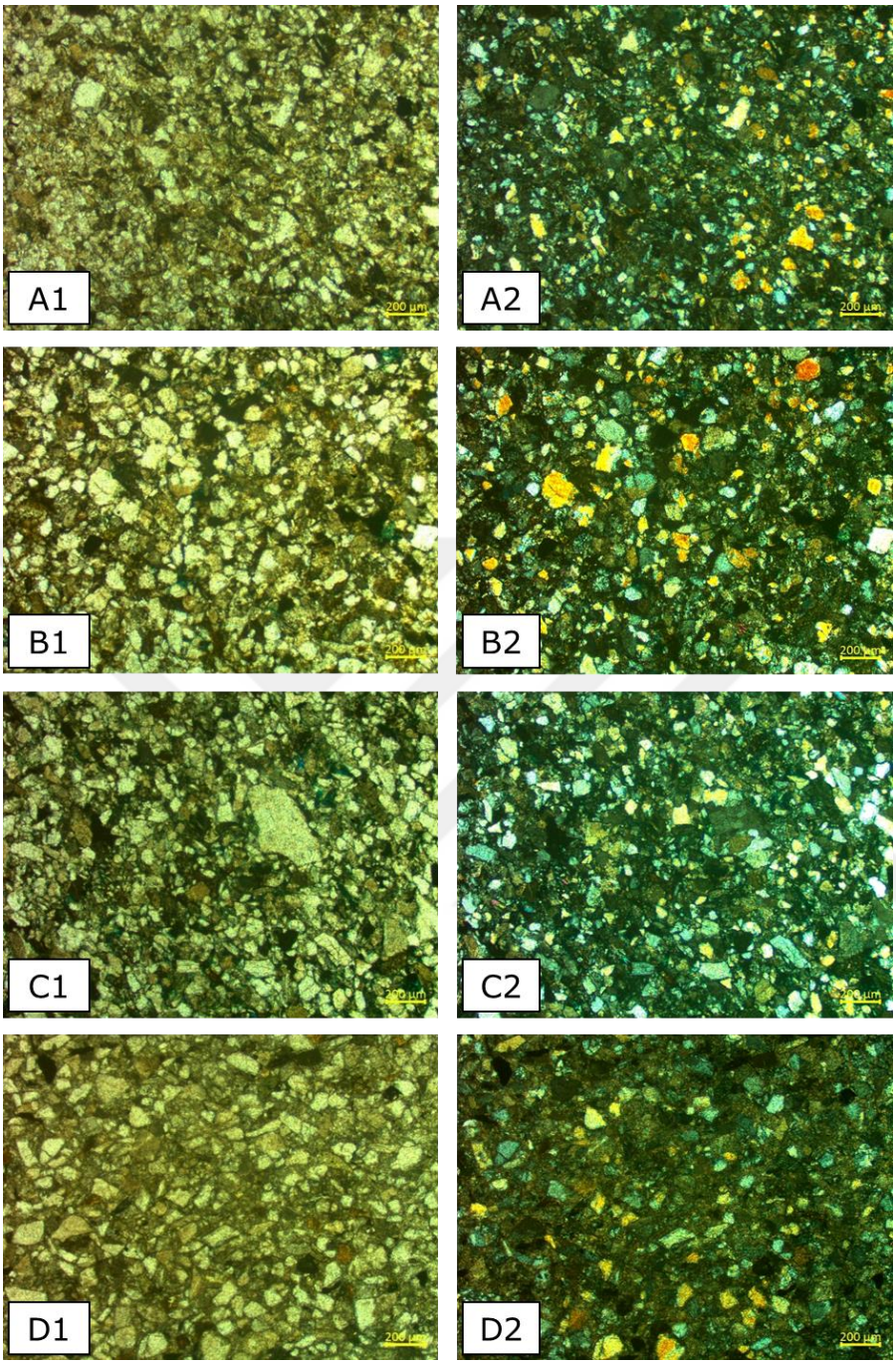

Figure 7.53. PPL displays (left panel) and XPL images (right panel) of each sample. A1, B1, C1 and D1 indicate PPL sections while A2, B2, C2 and D2 includes XPL sections of the sample depth with 1798.75, 1800.9, 1803.2 and 1804.35 m. are illustrated respectively.

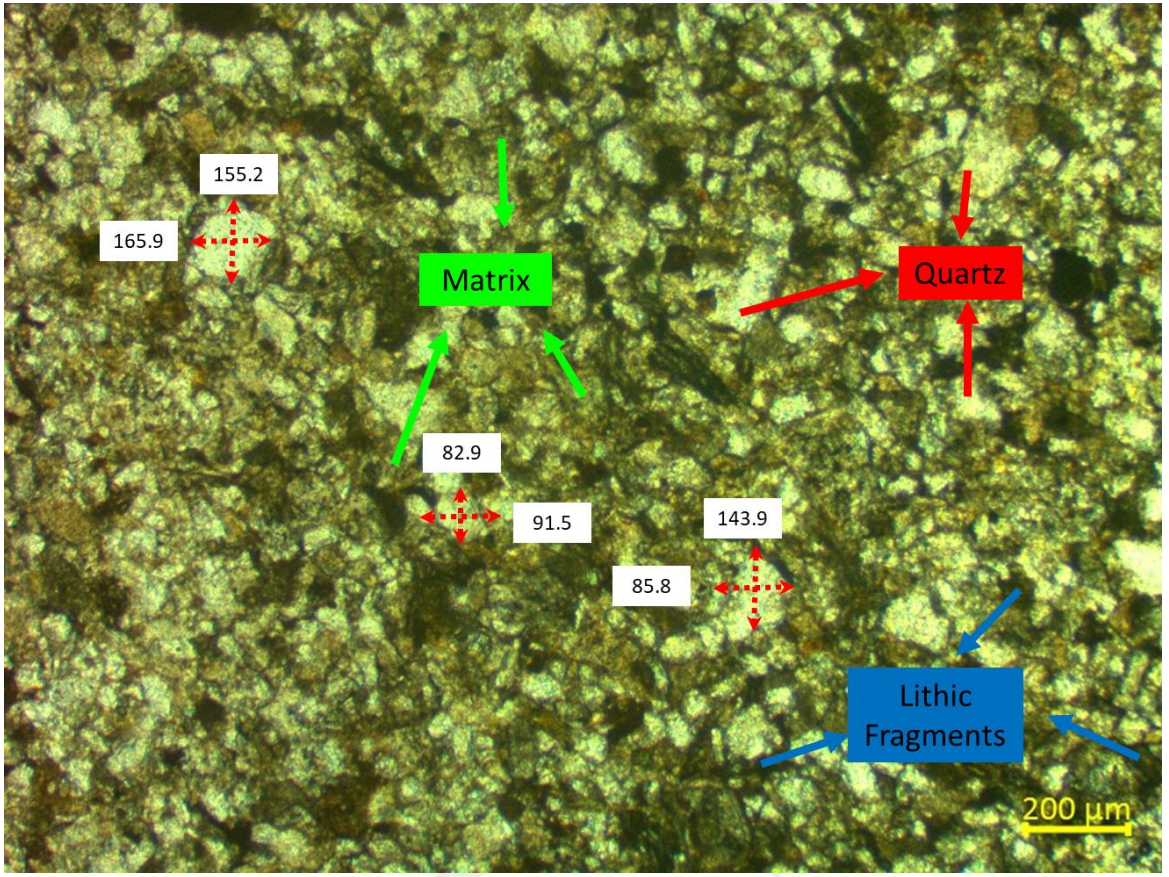

Figure 7.54. Evaluated thin section for the sample with a depth of 1798.75 m. Calculated length of three diffrent grains are illustarted with red dashed lines. The scale of the thin section is 200 µm. Quartz minerals covers a high range of grains. Matix is the dominant component of the section covering high amount of the area.

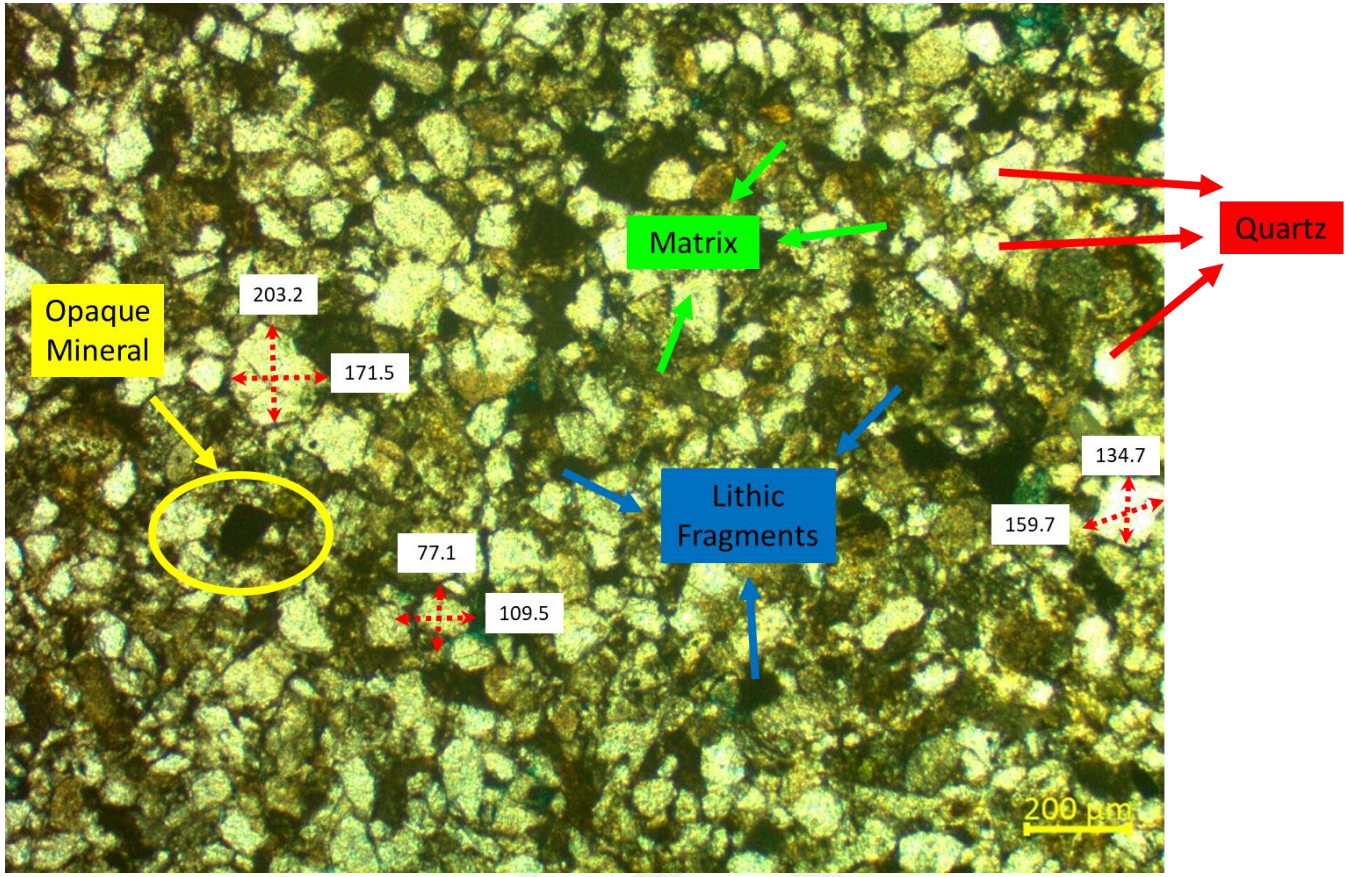

Figure 7.55. Evaluated thin section for the sample with a depth of 1800.9 m. Quartz mineral is dominant within grains. Additionally, opaque minerals are observed. Calculated length of three diffrent grains are illustarted with red dashed lines. The scale of the thin section is 200 µm.

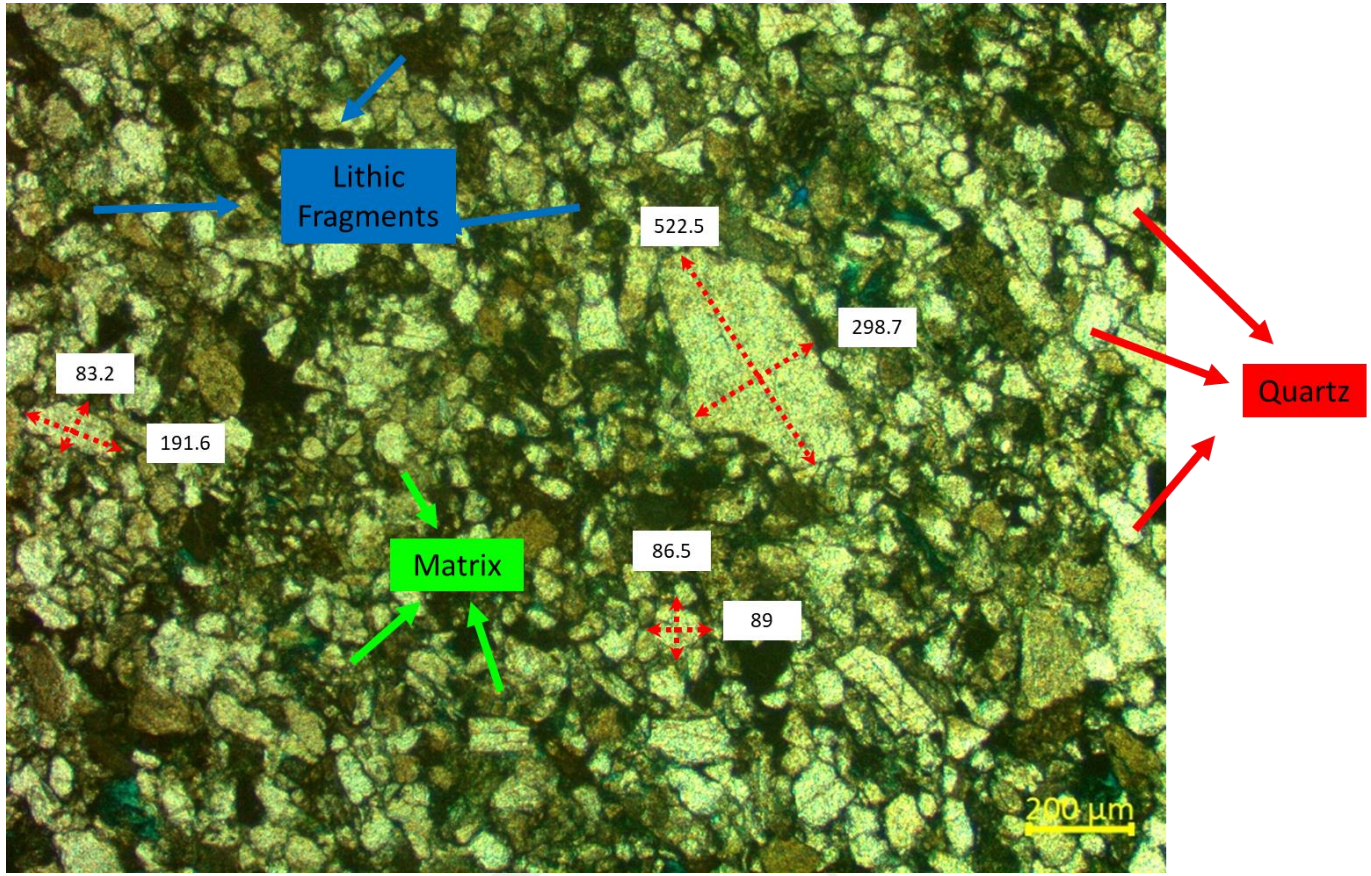

Figure 7.56. Evaluated thin section for the sample with a depth of 1803.2 m. Additionally, opaque minerals are observed. Mostly, quartz minerals are available. Calculated length of three diffrent grains are illustrated with red dashed lines. A coarse quartz mineral is observed, which is rare in thin sections of deeper Osmancık Formation. The scale of the

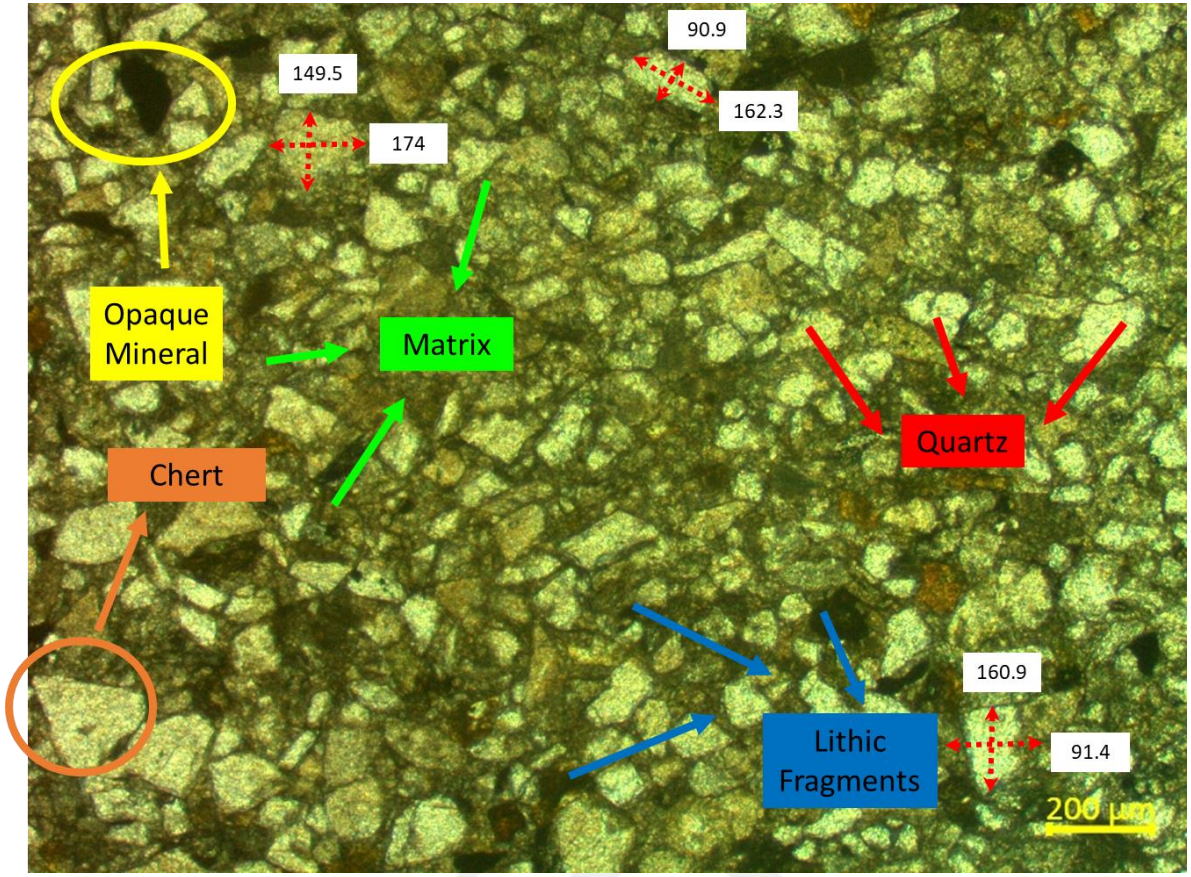

Figure 7.57. Evaluated thin section for the sample with a depth of 1804.35 m. Additionally, opaque minerals and chert are observed. Quartz minerals are dominant within grains. High content of matrix is available. Calculated length of three diffrent grains are illustrated with red dashed lines. The scale of the thin section is 200 µm.

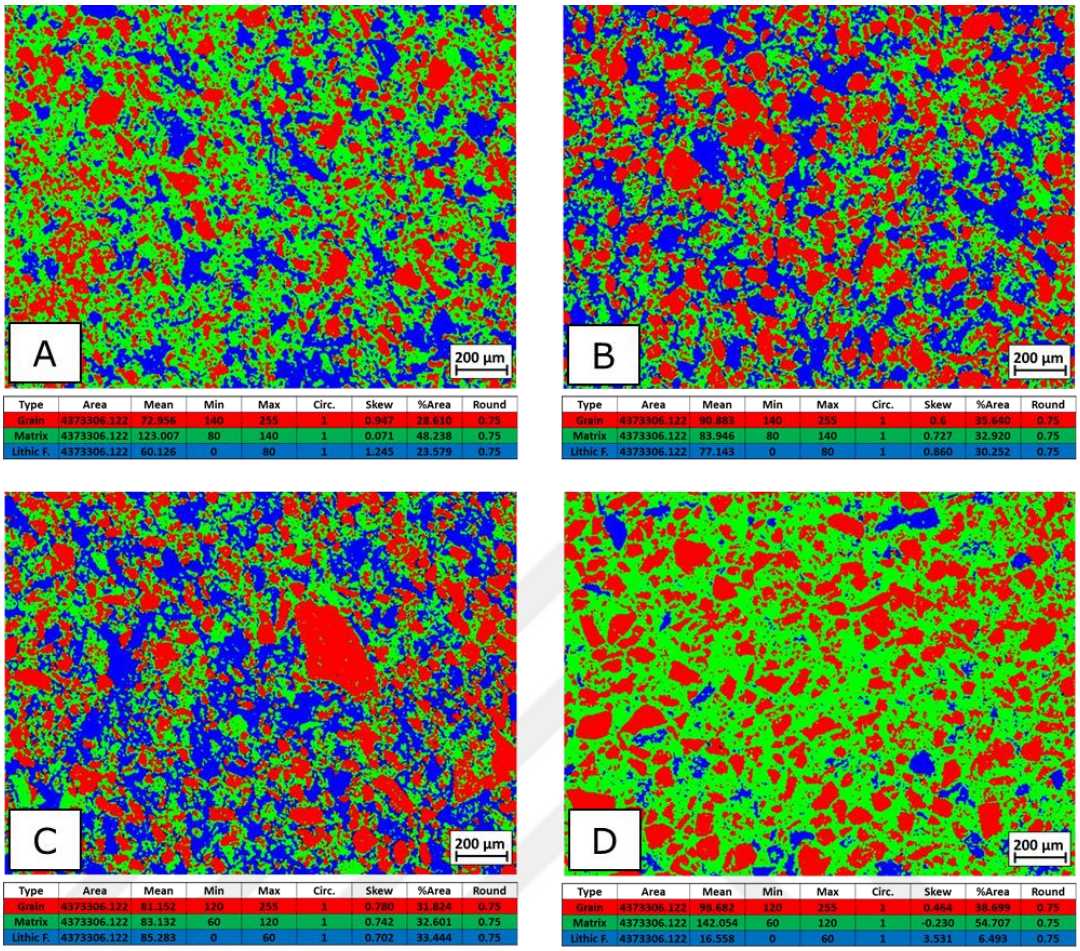

Figure 7.58. Merged colors of each component for the samples ((A): 1798.75 m., (B): 1800.9 m., (C): 1803.2 m. and (D): 1804.35 m.) and calculated statistical values in Well-32. Quatz content is similar for each sample while matrix show a big difference within these samples, varying from 32.6% to 54.7%.

7.3.6 Summary: The evaluation of the Thin Section

Well-12 is the most productive well in deeper Osmancık Formation among well group-1. Three samples were examined in this well. First two samples are not producers while the third one is productive. The main difference is the facies type of the samples. Type of the facies for the productive one is described as lithic arenite while facies type for other two zones is lithic wacke. Thus, facies type is a key parameter for this well.

Two core samples are available for Well-13. The first core at shallower depth produced a little and then pressure dropped zero while deeper core produced a large amount of gas. Grain size is a significant parameter between thin sections of each core data. When grain sizes are larger, reservoir properties such as porosity is also better. As a result, grain size is an effective property allowing producing or less/non-producing zones.

Well-15 has also two core data similar to Well-13. Each core has only one lithic arenite thin section and other sections are described as lithic wacke. Also, facies properties are similar. However, deeper core interval is productive while the shallower one is not. The main reason is evaluated as the pressure, which is low for the shallower part. Thus, the indicative parameter for the producing or non-producing zone is the pressure for this well.

Well-16 is a non-producing well. Porosity varies between 4%-9% and not well-connected each other according to evaluation of thin section. This well does not reflect good reservoir properties. The pressure of the perforated zones is very low. As a result, this well is not a hydrocarbon bearing one, which does not contribute to the evaluation of the thin sections.

Well-32, similar to Well-16, does not produce any hydrocarbon fluid. The main reason is that hydrocarbon was not accumulated in this well. Therefore, this well is

out of the evaluation, which does not give any information about key parameters affecting reservoir properties.

Another well which is not used for the evaluation is Well-21. Although this well the most productive one among the wells having core data, thin section for this well is missing.

A summary of the examination of each thin section is given in Table 7.1.

Table 7.1 Facies Properties of Thin Sections.

Well	Core	Depth	Facies Type	Grain %	Quartz %	Feldspar %	Matrix %	Lithic Fragment %	Pore %	Sorting	Grain Size	Roundness
Well-12	1	1348.25	Lithic Wacke	21.35%	21.05%	0.30%	55%	23.55%		moderately	coarse silt sized to fine sand sized	sub angular/angular
Well-12	1	1349	Lithic Wacke	21.18%	21.18%		55.30%	23.24%		moderately	fine to course sand sized	sub angular/angular
Well-12	1	1351.25	Lithic Arenite	30.70%	30.35%	0.35%	12.70%	33%	22.70%	moderately/poorly	coarse silt sized to medium sand sized	sub rounded/angular
Well-13	1	1305.25	Lithic Wacke	27.5	27.5		59.2	13.3		moderately	medium silt sized to very fine sand sized	rounded/subrounded
Well-13	1	1308.75	Lithic Wacke	25.5	25.5		56.4	18.1		moderately	medium silt sized to very fine sand sized	rounded/subrounded
Well-13	1	1310.05	Lithic Wacke	19.98	19.98		52.8	27.2		moderately	medium silt sized to very fine sand sized	angular/subangular
Well-13	1	1312.55	Lithic Wacke	29.87	29.62		52.1	17.4		moderately	medium to coarse silt sized	angular/subangular
Well-13	1	1313.65	Lithic Wacke	11.2	11.2		66.7	21.7		moderately	medium to coarse silt sized	angular/subangular
Well-13	2	1489.45	Lithic Wacke	29.3	27.3		58.8	12.3		moderately	very fine to fine sand sized	angular/subangular
Well-13	2	1490.95	Lithic Wacke	19.7	18.7		47	34		moderately	fine to medium sand sized	angular
Well-15	1	1360.85	Lithic Arenite	34.6	30.95	0.4	14.71	40.4	6.5	moderately	very fine to medium sand sized	sub rounded/sub-angular
Well-15	1	1365.5	Lithic Wacke	48.7	43.1	0.4	20.67	33.1	2.5	moderately	very fine to fine sand sized	angular/sub-angular
Well-15	1	1366.35	Lithic Wacke	22.1	21.1		41.2	32.6	4.3	moderately	very fine to fine sand sized	angular/sub-angular
Well-15	1	1367.35	Lithic Wacke	27	24.35		61.8	13.2		moderately	very fine to fine sand sized	angular/sub-angular
Well-15	1	1368.5	Lithic Wacke	22.17	20.54		31.25	33.6	11.8	moderately	coarse silt to fine sand sized	angular/sub-angular
Well-15	2	1405.4	Lithic Wacke	23.5	21.4		28.25	30.5	16.34	moderately	very fine to medium sand sized	angular/sub-angular
Well-15	2	1406.55	Lithic Wacke	24	22		28.9	29	18.7	poorly	very fine to medium sand sized	angular/sub-angular
Well-15	2	1407.55	Lithic Wacke	33.2	32.6		32.65	25	7.3	poorly	fine to medium sand sized	rounded/sub-rounded
Well-15	2	1408.55	Lithic Arenite	23.3	20.8		14.5	43.5	20.8	poorly	fine to medium sand sized	angular/sub-angular
Well-15	2	1410.25	Lithic Wacke	39.8	39.8		41.1	18.1		moderately	fine to medium sand sized	angular/sub-angular
Well-16	1	1527.35	Lithic Wacke	29.5	29.5		37.6	27.1	4.3	moderately	very fine to medium sand sized	angular/sub-angular
Well-16	1	1527.85	Lithic Wacke	20	20		27.6	45.8	5.72	moderately/poorly	very fine to medium sand sized	angular/sub-angular
Well-16	1	1528.85	Lithic Wacke	21	21		34.2	34.4	9.4	moderately	very fine to fine sand sized	sub rounded/sub-angular
Well-32	2	1798.75	Lithic Wacke	28.6	28.6		47.2	23.6		moderately	very fine to fine sand sized	angular/sub-angular
Well-32	2	1800.9	Lithic Wacke	35.6	35.6		32.9	30.25		moderately	very fine to fine sand sized	sub rounded/sub-angular
Well-32	2	1803.2	Lithic Wacke	31.8	31.8		32.6	33.4		poorly	very fine to coarse sand sized	angular/sub-angular
Well-32	2	1804.35	Lithic Wacke	38.7	38		54.7	7.2		moderately	very fine to fine sand sized	angular/sub-angular

7.4 Diagenesis in Deeper Osmancık Formation

Diagenetic processes have different stages such as early (eodiagenesis), late (mesodiagenesis) and up-lifted (telodiagenesis). In sandstones diagenesis processes can be either physical or chemical. Generally, development of authigenic minerals and precipitation of cement is a consequence of early diagenesis, later followed by lithification resulting of decreasing pore spaces and occurring grain packs. Some of these processes can be listed as cementation, compaction, mineral overgrowth such as quartz and feldspar, chloritization, dissolution, re-crystallization and replacement. Some chemical processes such mineral overgrowths of quartz and feldspar, recrystallization and chloritization take place in the late diagenetic stage. Calcitization, deformation and dissolution occur during up-lifted stage (Chima et al., 2018).

In deeper Osmacık Formation, physical processes such as compaction and cementation are clearly observed in core samples. Porosity and permeability values also diminish from shallower to deeper sections as it is tested in perforated zones.

Chemical processes such as quartz overgrowths and possible chloritization are also identified in SEM photos taken from core samples.

In Well-12, Intergranular/grain boundary microfractures and intragranular microfractures with weak quartz overgrowth were observed in SEM photomicrographs (Figure 7.59). Although chlorite damages porosity partly, it results in independent micro-porosity developments.

In Well-13, SEM photos show that in the sample of 1307.8 m. (Figure 7.60 A), clean and dense high interparticle porosities and lower intraparticle porosities are observed. Smectite is observed as covering grains in the sample from 1489.45 m. (Figure 7.60 B). Core analysis results support SEM photos.

In Well-15, SEM study of core 1 shows that interparticle porosities are very common between sandstone grains (Figure 7.61 A). Also, SEM photo for core 2 illustrates

inter-porosities between grains. Quartz overgrowths causes s decrease in porosity values and reduces size of pore throats. Additionally, chlorite developments are detected (Figure 7.61 B).

XRD Analysis for core-1 of Well-13 and Well-15 are given in Table 7.2. Lithology column in the table confirms the analysis of thin sections. Grain sizes are too small for core-1 of Well-13, which lithology is considered mostly siltstone while the lithology is defined as mostly sandstone and shale for core-1 of Well-15. The highest amount of mineral is quartz as it was mentioned earlier. Feldspar content varies between 10% and 30%. Carbonate content is very low to be negligible. The percentage of clay minerals are closer to each other except the chlorite. Chlorite is the highest amount of mineral among clay minerals, which is a result of possible diagenetic process.

Although XRD analysis of core-1 in Well-12 is not added on the Table 7.2, 50% quartz, 25% feldspar, 10% calcite, 15% clay plus mica, 50% chlorite, 10% kaolinite, 30% illite and 10% smectite was reported (Uygur et al. 2000).

To sum up, cemented and compacted grains resulting lower porosity and permeability as much as quartz overgrowth and probable chloritization are the result of diagenesis in sandstone, which are observed in the cores of Well-12, Well-13 and Well-15.

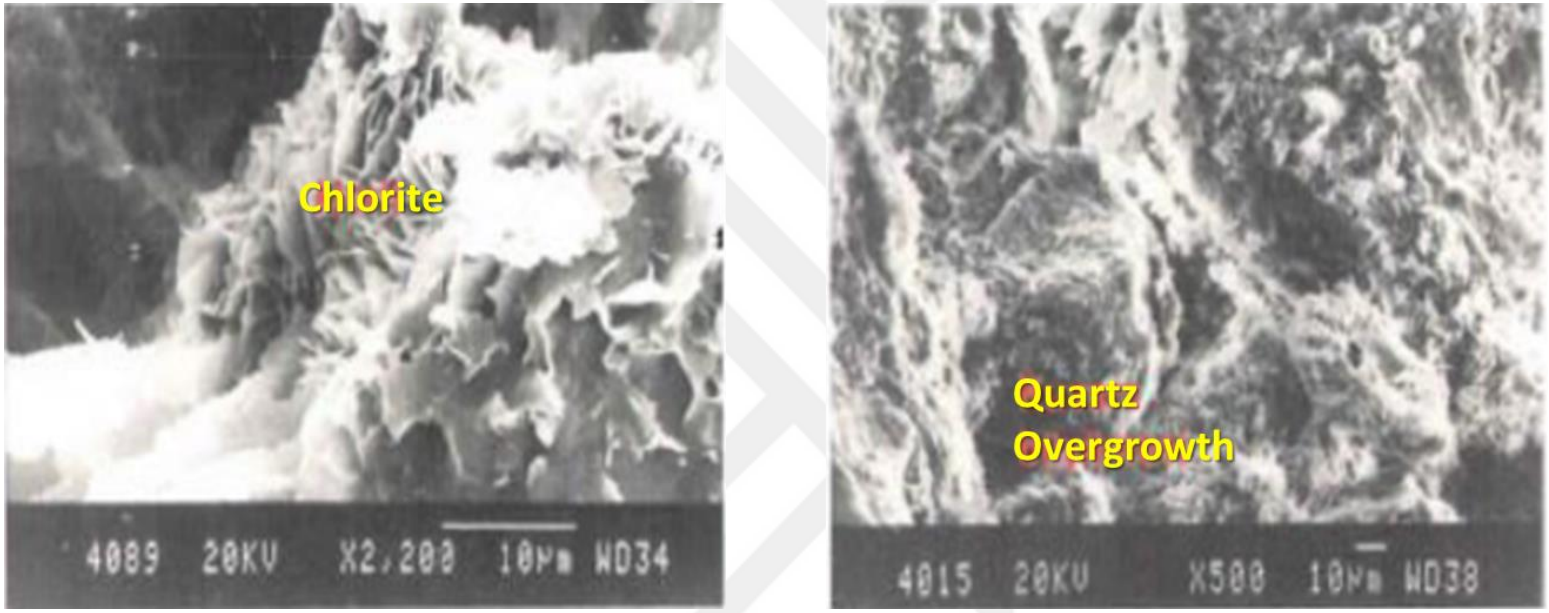

Figure 7.59. Well-12, Core-1, SEM photomicrographs between 1347 and 1351.5 m. On the left, chlorite development reducing porosity is illustrated. On the right side, another result of diagenesis process, quartz overgrowth, is detected.

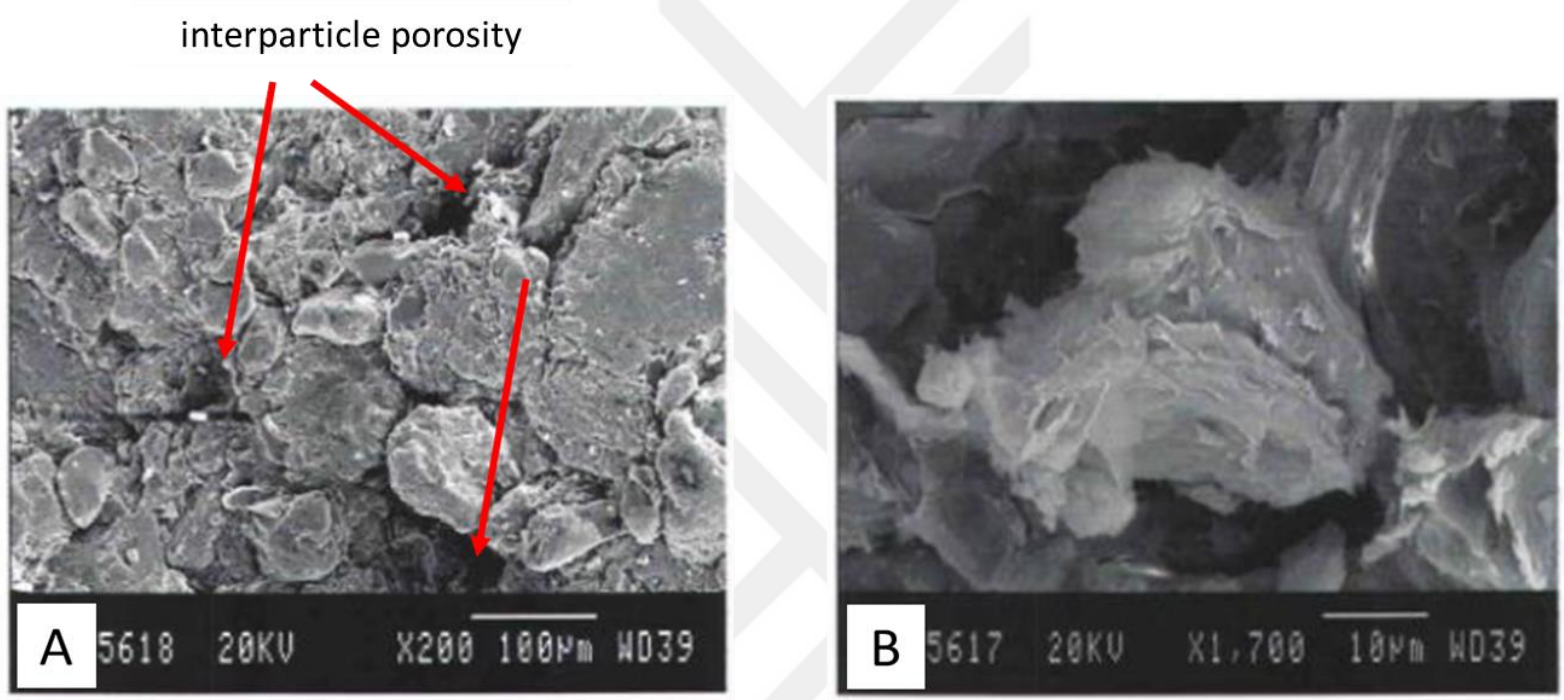

Figure 7.60. Well-13 SEM photomicrographs: (A) Clean section with high and dense interparticle porosity in 1307.8 m. of core 1 is illustrated. (B) Smectite mineral covering grains is detected in 1489.45 m. of core-2.

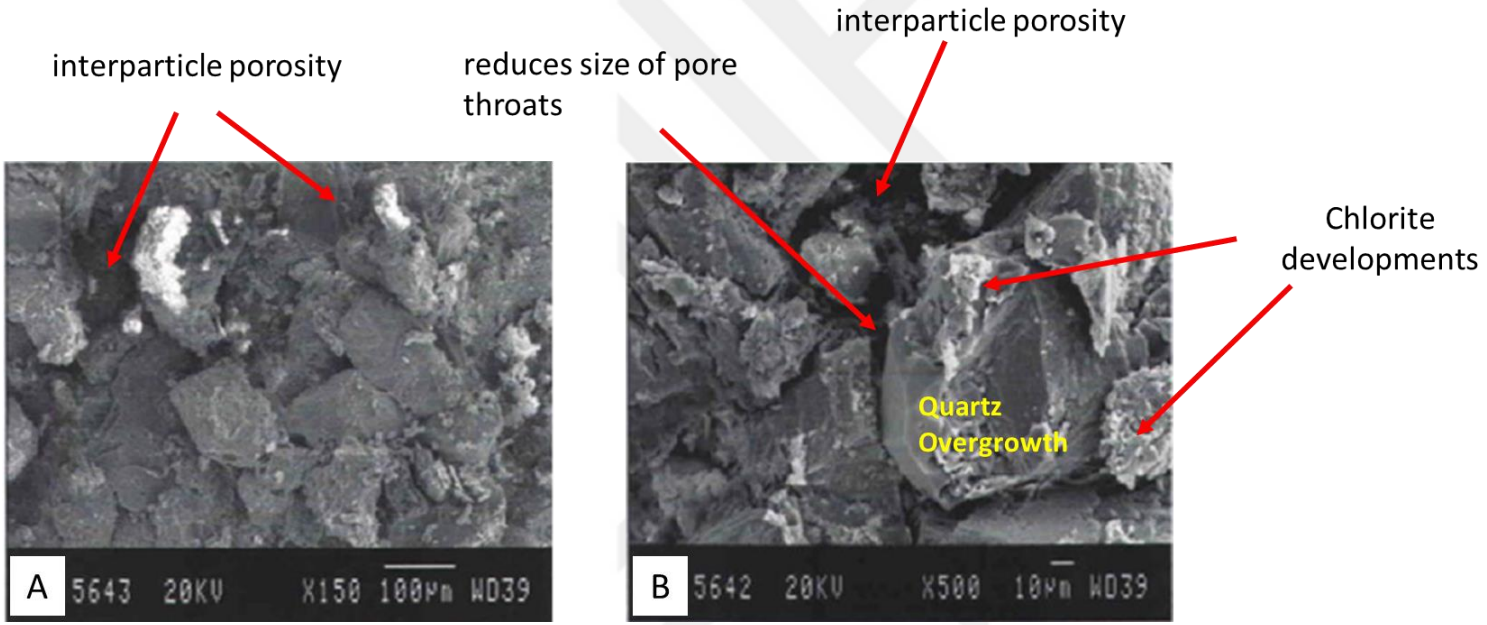

Figure 7.61. Well-15 SEM photomicrographs: (A) Interparticle porosities are observed in 1307.8 m. of core-1, (B) Interparticle porosities and quartz overgrowth resulting in reduction of pore throat sizes and chlorite development are displayed in 1489.45 m. of core-2.

Table 7.2 X-Ray diffraction analysis (XRD) for Core-1 of Well-13 and Well-15 (in percentage).

Well Name	Sample	Depth	Lithology	Quatz	Calcite	Feldspar	Dolomite	Clay+Mica	Chlorite	Kaolinite	Illite	Smectite
Well 13	1	0.50	Silty Shale	40	15	20	few	25	55	10	20	10
Well 13	2	1.65	Silty Shale	40	20	20	5	15	50	10	30	5
Well 13	3	2.35	Siltstone	40	20	15	5	20	60	20	10	5
Well 13	4	3.70	Siltstone	45	15	15	10	15	60	10	20	10
Well 13	5	4.55	Siltstone	50	15	15	5	15	65	10	25	5
Well 13	6	5.30	Sandstone	40	35	25	none	few	85	5	10	none
Well 13	7	6.60	Silty Shale	45	15	20	5	15	50	15	25	5
Well 13	8	7.25	Shale	35	25	15	5	20	70	5	25	none
Well 13	9	8.70	Siltstone	50	15	25	few	10	50	15	25	5
Well 15	1	0.65	Sandstone	50	15	20	few	15	55	20	10	10
Well 15	2	1.40	Sandstone	35	15	30	5	15	60	20	10	5
Well 15	3	2.25	Shale	40	20	15	few	25	55	20	10	10
Well 15	4	3.70	Shale	40	20	10	5	25	60	15	10	15
Well 15	5	4.85	Sandstone	45	25	30	none	few	50	15	20	10
Well 15	6	5.45	Sandstone	40	10	20	10	20	50	5	40	5
Well 15	7	6.30	Shale	45	25	10	5	15	50	15	25	5
Well 15	8	7.20	Sandstone	55	20	20	none	5	50	10	25	10
Well 15	9	8.35	Sandstone	45	20	25	few	10	50	15	15	15

CHAPTER 8

PETROPHYSICS

8.1 Introduction

Understanding petrophysical behavior of well logs and preparation of the data for reservoir modeling are an essential process to conduct a detailed reservoir characterization of the field. Core measurements, as well as measured and processed log responses, are very helpful to reveal relationships between porosity and permeability variations. Because these two parameters play an important role in detecting potential producing zones, a well-planned workflow is necessary. All these data sets are utilized and explained in this chapter.

8.2 Core Measurements: Porosity and Permeability

In this section, core measurements of porosity and permeability will be evaluated for Well-12, 13, 15, 16, 21 and 32.

8.2.1 Core Measurements for Well-12

As mentioned in Chapter 6, core measurements are available for specific wells. Core analysis results for Well 12 is given in Table 8.1. Measured porosity values are around 20%, which are also compatible with the calculated area of thin section for 1351.25 m. depth (Figure 7.18). Permeability changes between 1.91 and 4.79 md for the core interval.

The cross-plot regarding porosity and permeability measurement for Well-12 is given in Figure 8.1. This cross-plot indicates that porosity values change within a small percentage while permeability values show little variation. However, when the permeability values are considered, indeed, these changes are in a very small range, which means that permeability is also not variable too much. Well log section and core measurements within depth of 1347-1351.5 meters are given in Figure 8.2.

Table 8.1 Core Analysis of plugs in Well-12.

Core No.	**Depth Interval (m)**	**Sample Depth (m)**	**Porosity (%)**	**Permeability (md)**	**Grain Density (g/cc)**
1	1347-1351.5	1348	22.06	2.30	2.67
1	1347-1351.5	1349	21.84	4.79	2.69
1	1347-1351.5	1350	22.78	1.96	2.71
1	1347-1351.5	1351	21.36	4.94	2.67
1	1347-1351.5	1351.3	21.28	1.91	2.67
1	1347-1351.5	1351.5	21.87	2.35	2.67

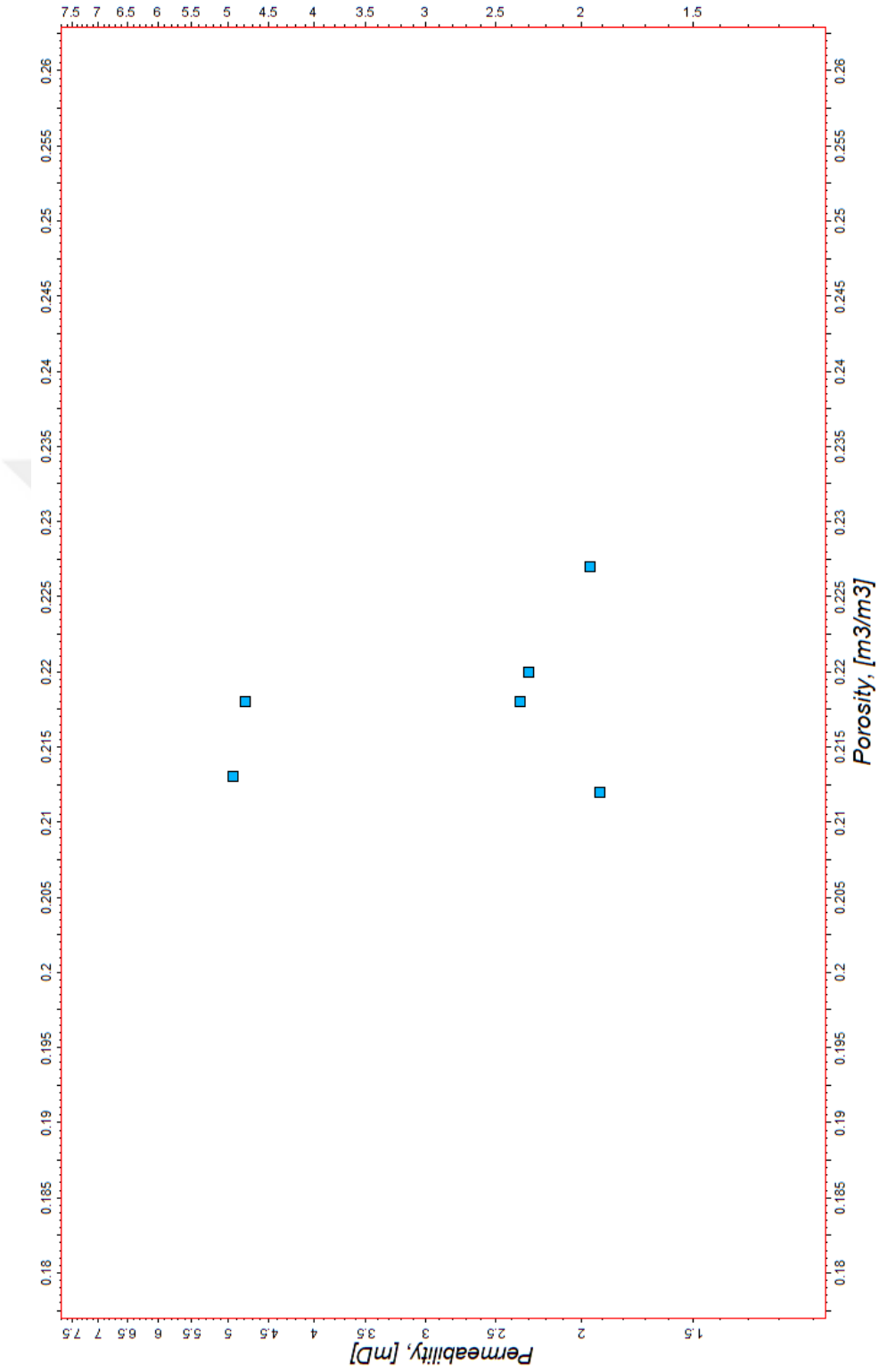

Figure 8.1. Porosity versus permeability cross-plot of the core sample of Well-12.

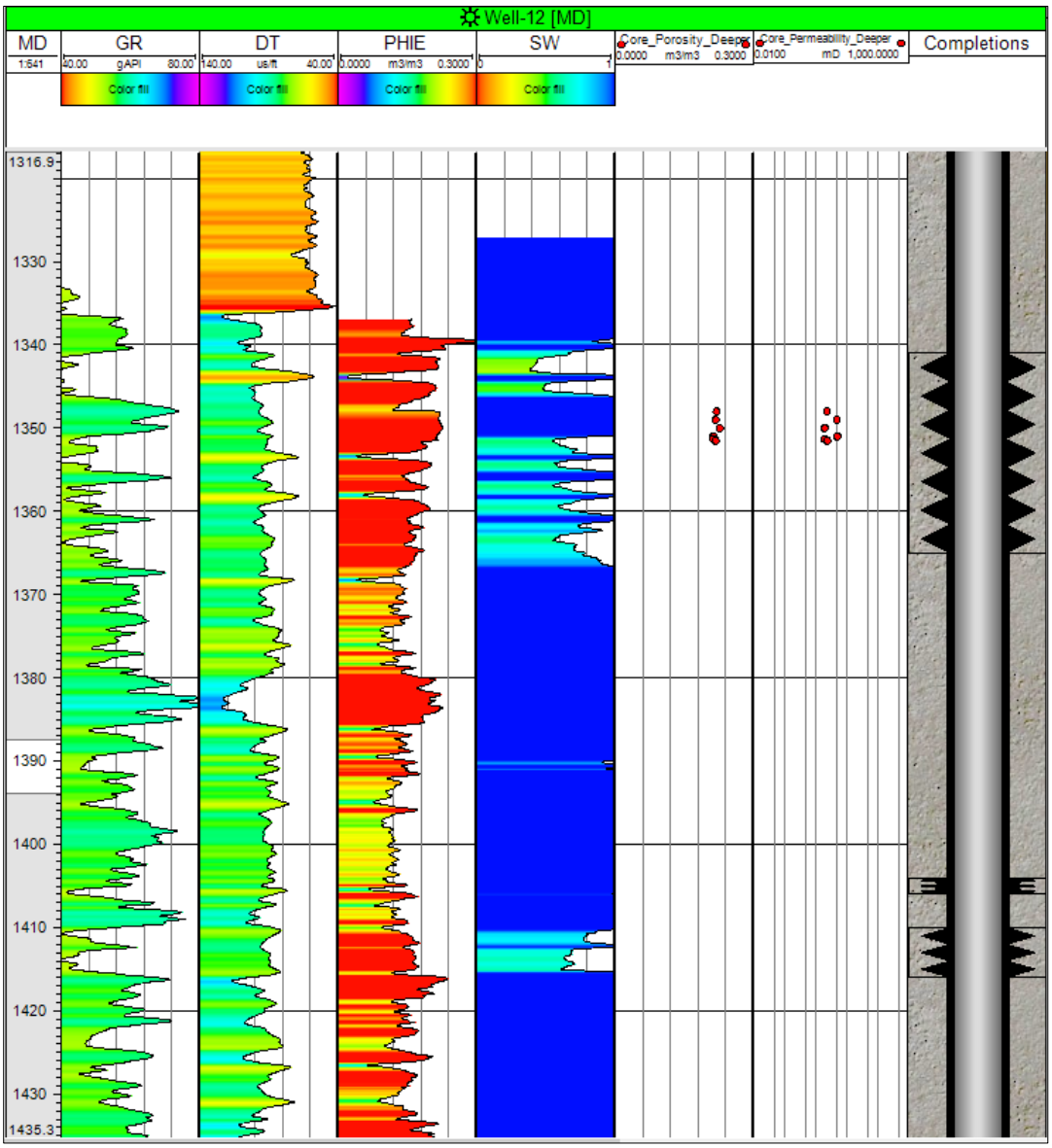

Figure 8.2. Measured-processed logs and core measurements of Well-12. From Left to right: Tack 1: Gamma-Ray Track 2: P-sonic; Track 3: Effective porosity; Track 4: Water saturation; Track 5: Core porosity; Track 6: Core permeability; Track 7: Well completion.

8.2.2 Core Measurements for Well-13

Core measurements for Well-13 cover two different intervals. Measured porosity and permeability parameters are given in Table 8.2. Core-1 measurements between 1305-1314 m. indicate that porosity and permeability vary in a wide range while core-2 measurements between 1489-1497.5 m. are stable showing lower porosity and permeability. Although core-1 has higher values, small grain sizes and variable petrophysical properties result in a low production zone. On the other hand, core-2 was drilled out below a productive zone, which indicates larger grains even though the zone has lower porosity and permeability. Cross-plot of porosity and permeability is given in Figure 8.3. Variations in zone of core-1 measurements are seen in the figure.

Well log section and core measurements within depth of 1305-1314 m. and 1489-1497.5 m. are given in Figure 8.4. Processed logs are not available for the depth range of core-1. Water saturation for the productive interval right above core-2 is around 80% although this interval is more productive. In general, Well-13 is the lowest productive well among the ones producing in deeper Osmancık Formation.

Table 8.2 Core Analysis of plugs in Well-13.

Core No.	Depth Interval (m)	Sample Depth (m)	Porosity (%)	Permeability (md)	Grain Density (g/cc)
1	1305-1314	1305.3	4.75	0.18	2.63
1	1305-1314	1306.8	23.71	42.11	2.67
1	1305-1314	1307.7	25.7	58.12	2.67
1	1305-1314	1307.8	23.27	41.45	2.67
1	1305-1314	1307.9	24.53	39.04	2.66
1	1305-1314	1307.9	23.27	39.22	2.66
1	1305-1314	1308.8	5.52	0.1	2.63
1	1305-1314	1312.6	3.09	0.08	2.64
1	1305-1314	1313.7	4.49	0.14	2.63
2	1489-1497.5	1489.5	2.62	0.08	2.67
2	1489-1497.5	1492.3	1.38	0.08	2.63
2	1489-1497.5	1492.5	3.05	0.12	2.63
2	1489-1497.5	1493.7	7.52	0.47	2.56

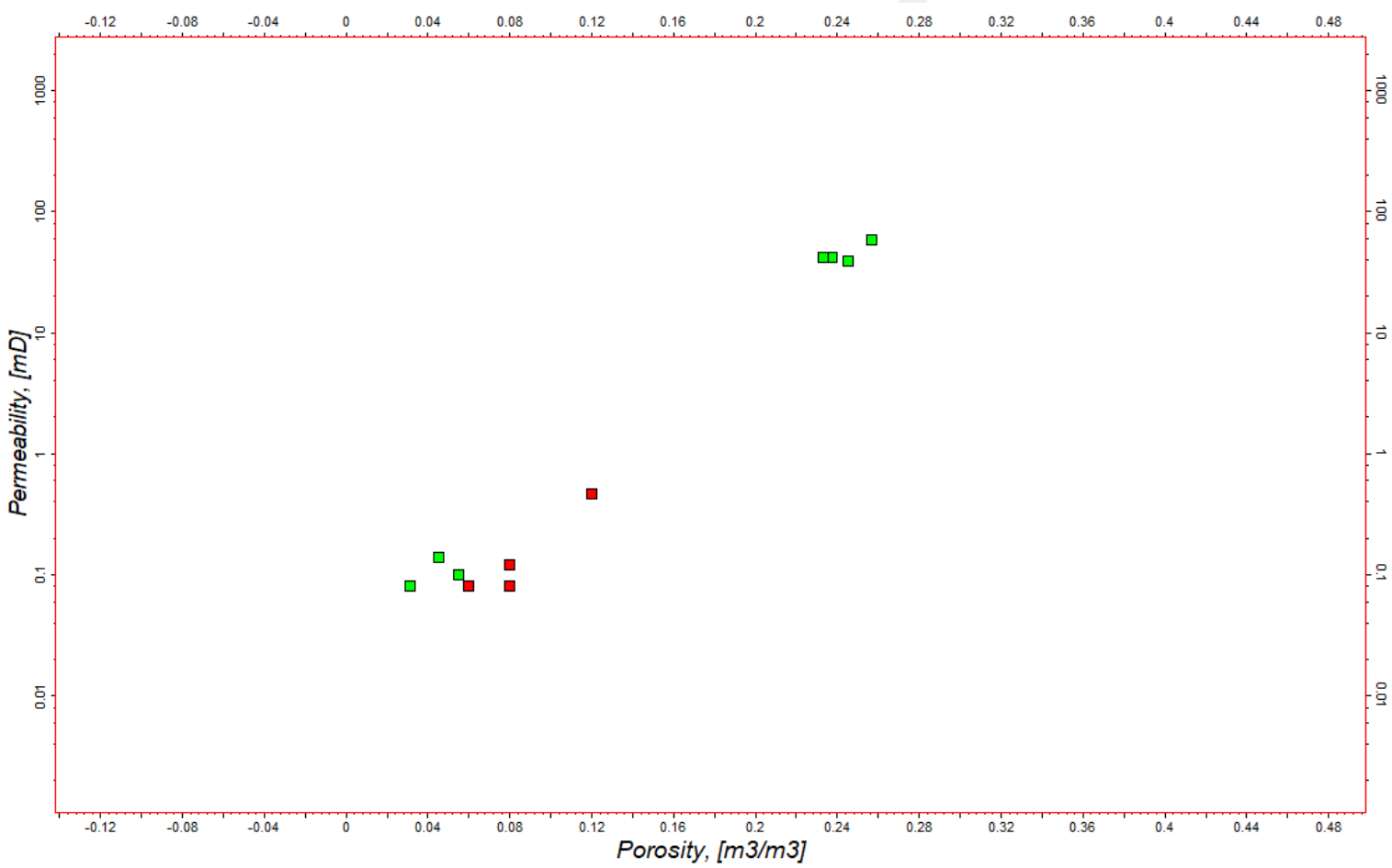

Figure 8.3. Porosity versus Permeability cross-plot of the core sample of Well-13. Green data points represent measured data for core-1 (1305-1314 m.) and red points are the data for core-2 (1489-1497.5 m.).

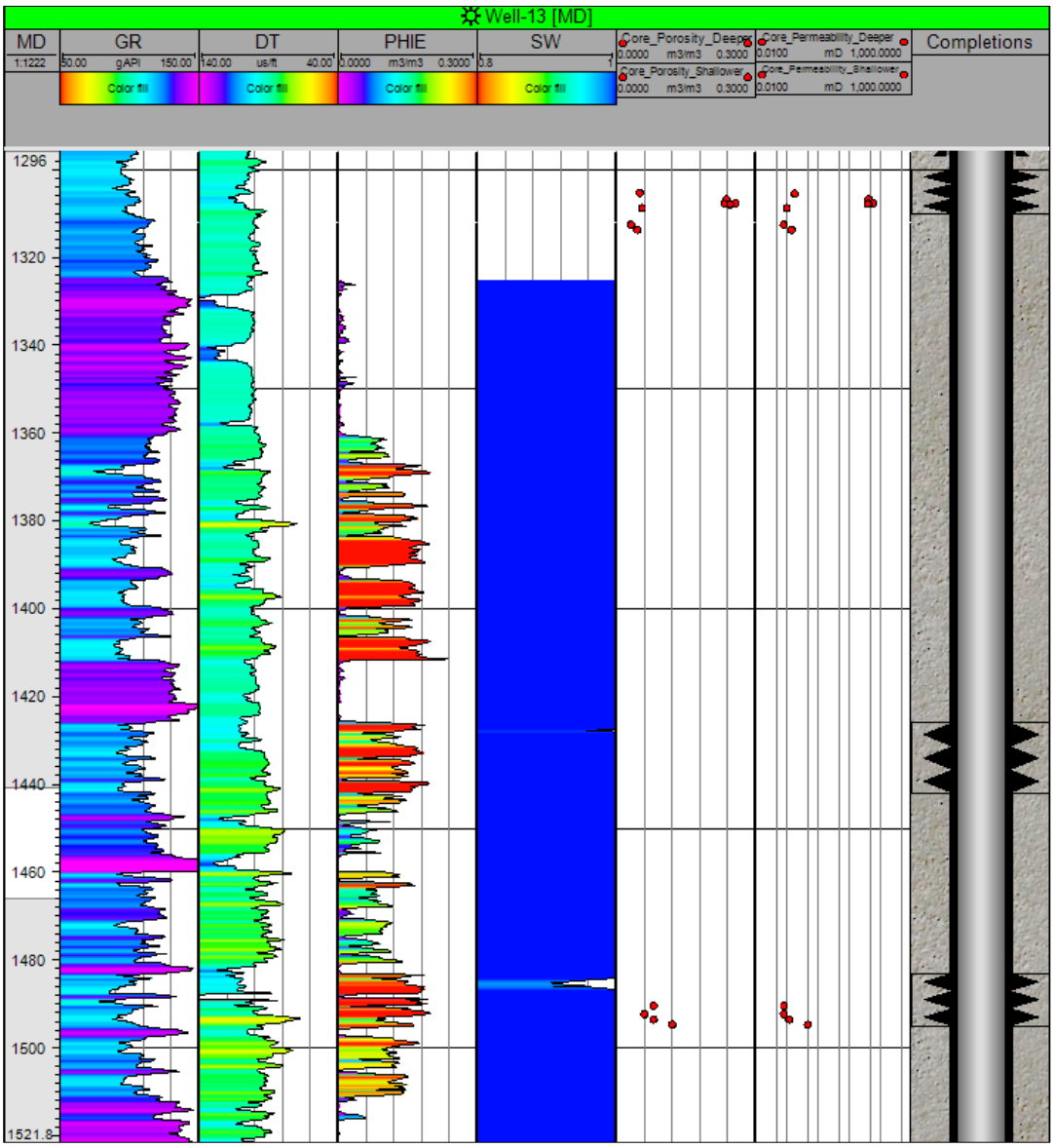

Figure 8.4. Measured-processed logs and core measurements of Well-13. From Left to right: Tack 1: Gamma-Ray; Track 2: P-sonic; Track 3: Effective porosity; Track 4: Water saturation; Track 5: Core porosity; Track 6: Core permeability; Track 7: Well completion.

8.2.3 Core Measurements for Well-15

In this well, two cores are available within range of 1360.7-1369 and 1404.5-1413.5 meters. Core porosity and permeability values are variable for both depth ranges. Because the reservoir pressure is very low, the interval of core-1 is not productive. However, the zone of core-2, which tends to have higher porosity and permeability values, has been produced more than 13,000,000 m^3. Table 8.3 shows core measurements. A cross-plot of porosity versus permeability is also given, which confirms the higher tendency of petrophysical properties for core-2 (Figure 8.5).

Well log section and core measurements are indicated in Figure 8.6. Calculated water saturation log values are about 80% for the productive interval while these values are 100% for the non-productive zone. Well-15 is the second highest productive well among the ones producing in deeper Osmancık Formation, in group-1.

Table 8.3 Core Analysis of plugs in Well-15.

Core No.	Depth Interval (m)	Sample Depth (m)	Porosity (%)	Permeability (md)	Grain Density (g/cc)
1	1360.7-1369	1361.3	16.43	0.7	2.6
1	1360.7-1369	1362	11.83	3.4	2.56
1	1360.7-1369	1362.5	15.01	0.21	2.56
1	1360.7-1369	1364	13.09	0.1	2.58
1	1360.7-1369	1365	18.3	0.87	2.65
1	1360.7-1369	1365.2	8.92	0.3	2.6
1	1360.7-1369	1366	7.27	0.19	2.66
1	1360.7-1369	1366	14.84	0.13	2.52
1	1360.7-1369	1366.4	16.5	0.67	2.65
1	1360.7-1369	1366.9	0.71	0	2.64
1	1360.7-1369	1367.2	7.79	0.01	2.57
1	1360.7-1369	1367.5	3.56	0.05	2.66
1	1360.7-1369	1367.7	13.54	0.51	2.55
1	1360.7-1369	1368	18.82	1.37	2.64
1	1360.7-1369	1368.2	15.39	0.41	2.6
2	1404.5-1413.5	1404.7	18.11	1.22	2.68
2	1404.5-1413.5	1405	14.62	0.31	2.61
2	1404.5-1413.5	1405	1.55	0	2.67
2	1404.5-1413.5	1405.3	15.12	0.99	2.59
2	1404.5-1413.5	1405.4	14.48	1.19	2.67
2	1404.5-1413.5	1406.1	18.09	1.23	2.67
2	1404.5-1413.5	1407	16.11	1.29	2.65
2	1404.5-1413.5	1407.5	19.25	5.28	2.68
2	1404.5-1413.5	1407.7	14.68	0.84	2.62
2	1404.5-1413.5	1408.2	1.99	0.05	2.66
2	1404.5-1413.5	1410	1.27	0	2.68
2	1404.5-1413.5	1410.3	3.53	0.05	2.67
2	1404.5-1413.5	1411	21.12	21.6	2.67
2	1404.5-1413.5	1411.1	5.21	0.05	2.66

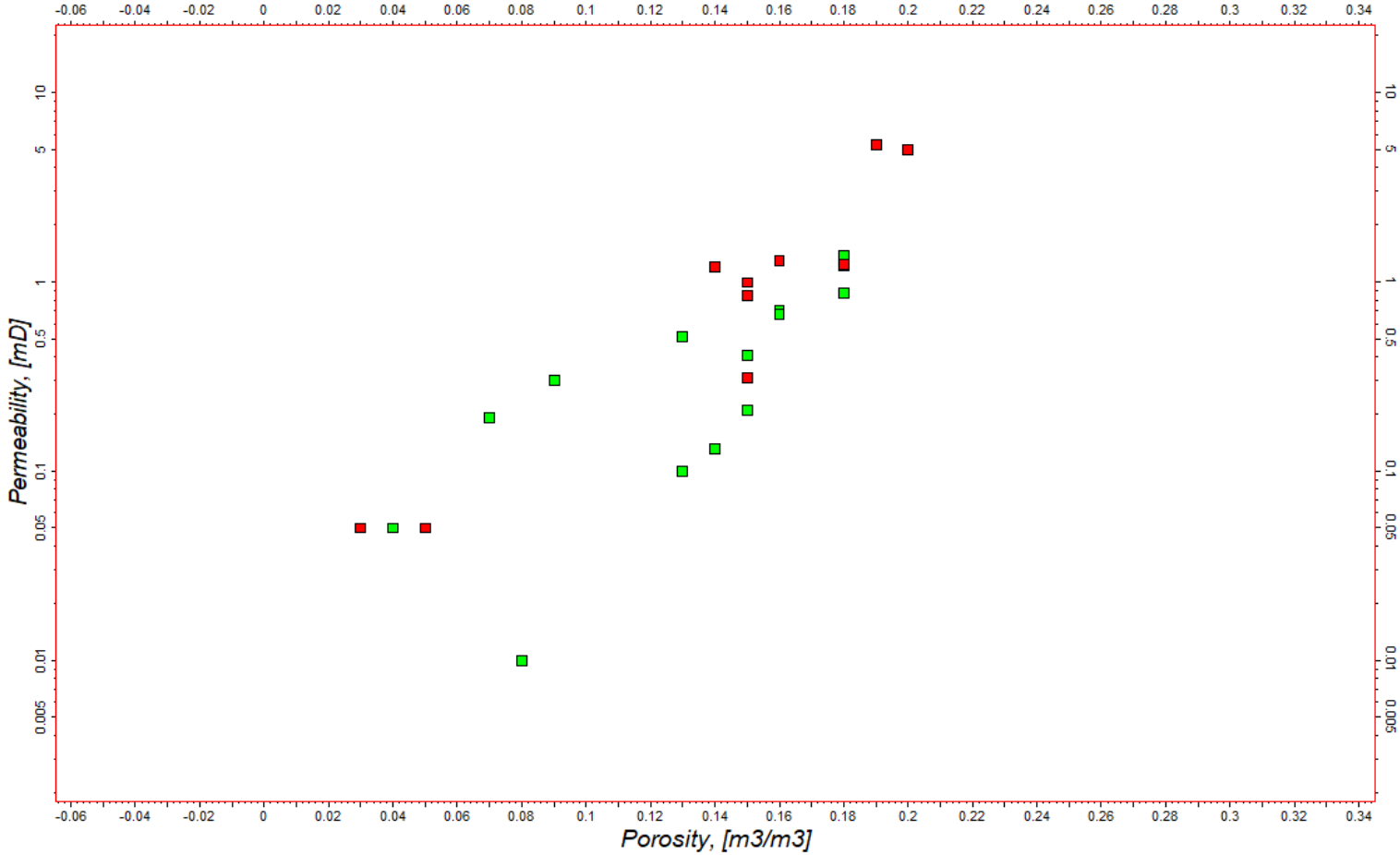

Figure 8.5. Porosity versus Permeability cross-plot of the core sample of Well-15. Green data points represent measured data for core-1 (1360.7-1369 m.) and red points are the data for core-2 (1404.5-1413.5 m.).

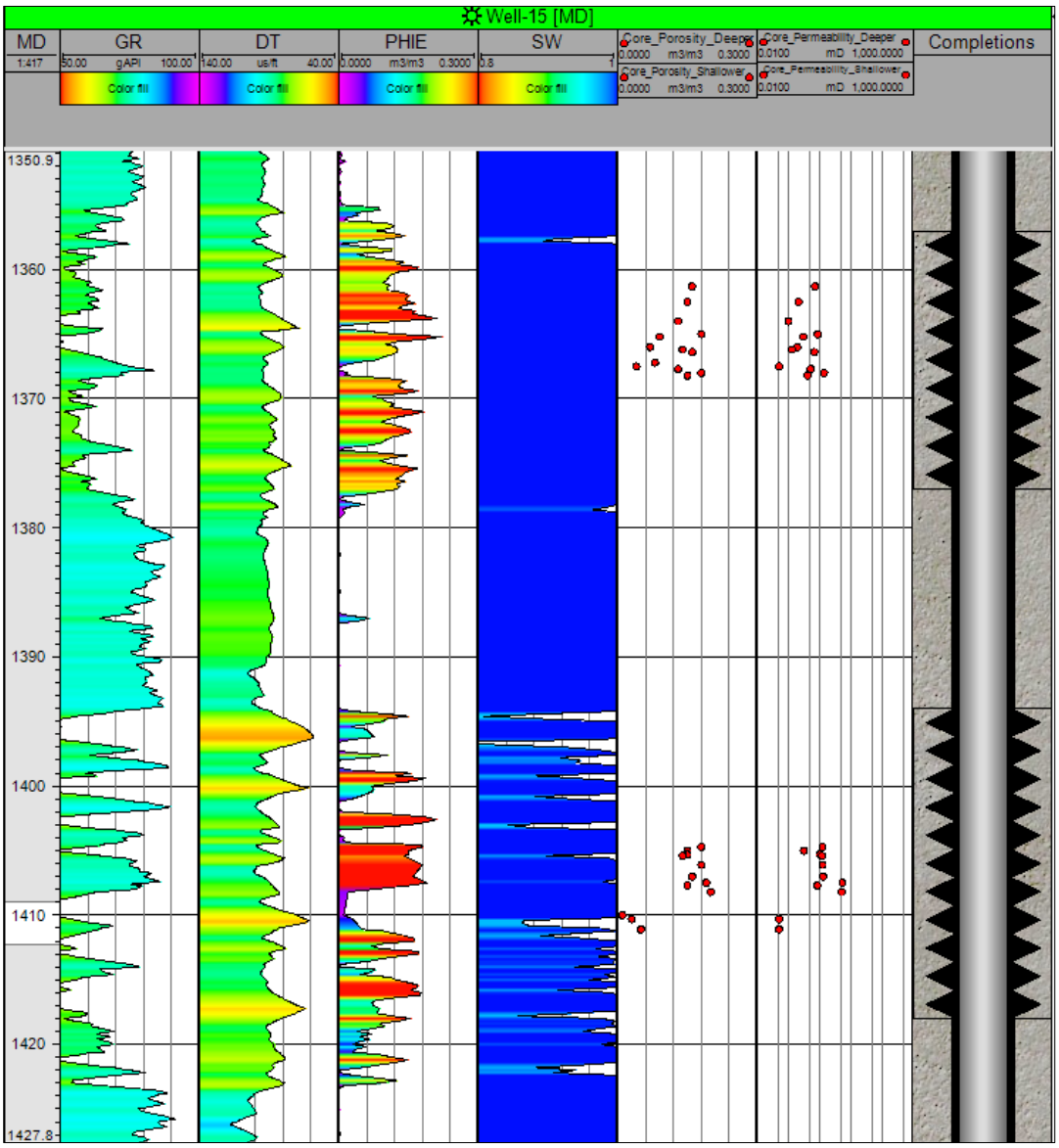

Figure 8.6. Measured-processed logs and core measurements of Well-15. From Left to right: Tack 1: Gamma-Ray; Track 2: P-sonic; Track 3: Effective porosity; Track 4: Water saturation; Track 5: Core porosity; Track 6: Core permeability; Track 7: Well completion.

8.2.4 Core Measurements for Well-16

In this well, core data is available between 1527-1531 m. This well has not been produced from either shallower or deeper Osmancık Formation. Porosity measured from cores is relatively high, which is mostly around 20% while permeability values are changing from 0.26 to 2.16 (Table 8.4). Although reservoir properties for the well is competitive with producing intervals among the wells of group-1, hydrocarbon fluid is not filled within the zone. A cross-plot of porosity and permeability is shown in Figure 8.7.

Well log section and core measurements are illustrated in Figure 8.8.
Approximately an interval of 30 meters was perforated without any production in this well.

Table 8.4 Core Analysis of plugs in Well-16.

Core No.	Depth Interval (m)	Sample Depth (m)	Porosity (%)	Permeability (md)	Grain Density (g/cc)
1	1527-1531	1528.2	13.47	0.26	2.68
1	1527-1531	1528.7	19.97	2.16	2.67
1	1527-1531	1529.1	20.17	1.66	2.68
1	1527-1531	1529.7	19.39	1.61	2.66
1	1527-1531	1529.9	20.3	2.11	2.67

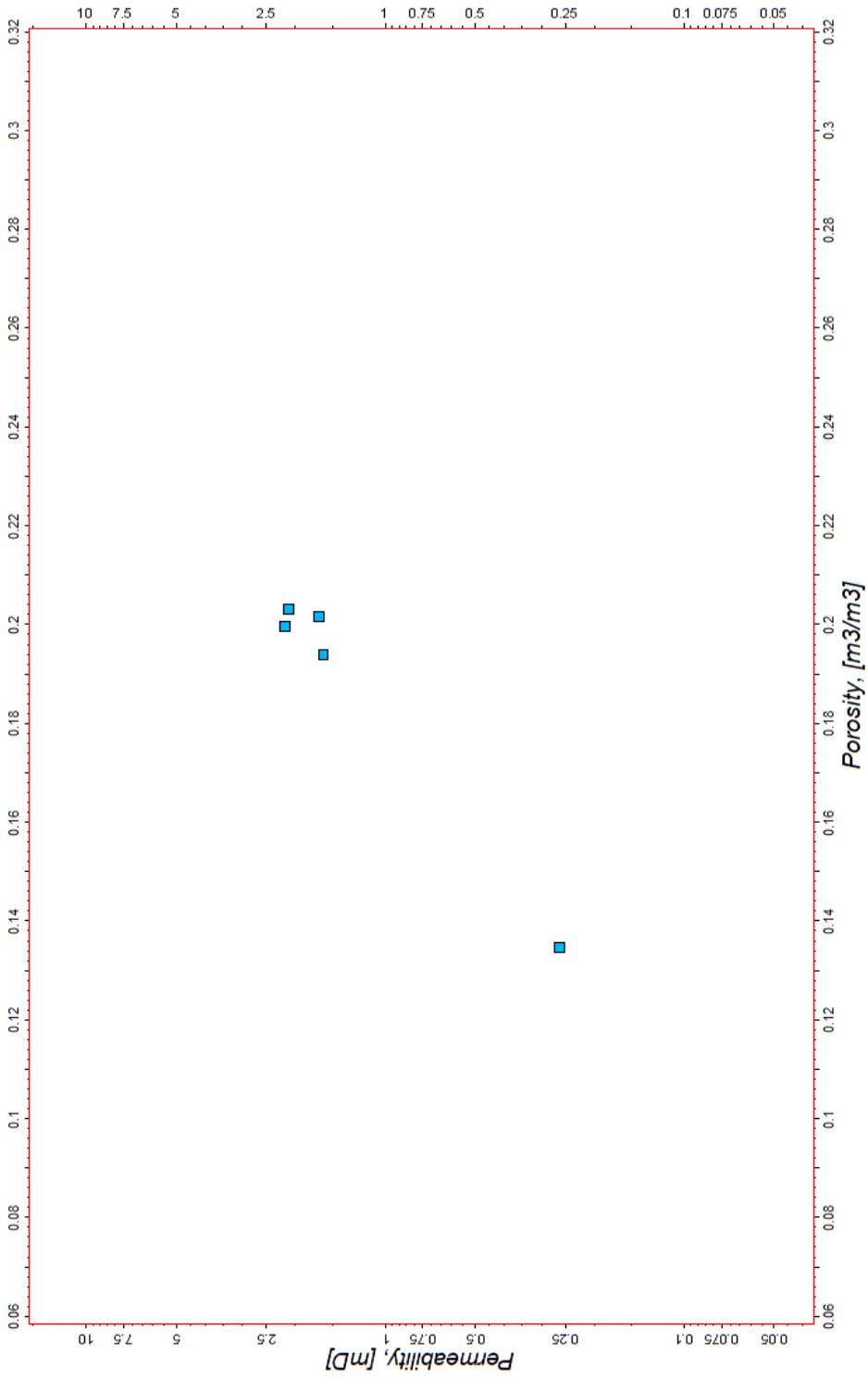

Figure 8.7. Porosity versus Permeability cross-plot of the core sample of Well-16.

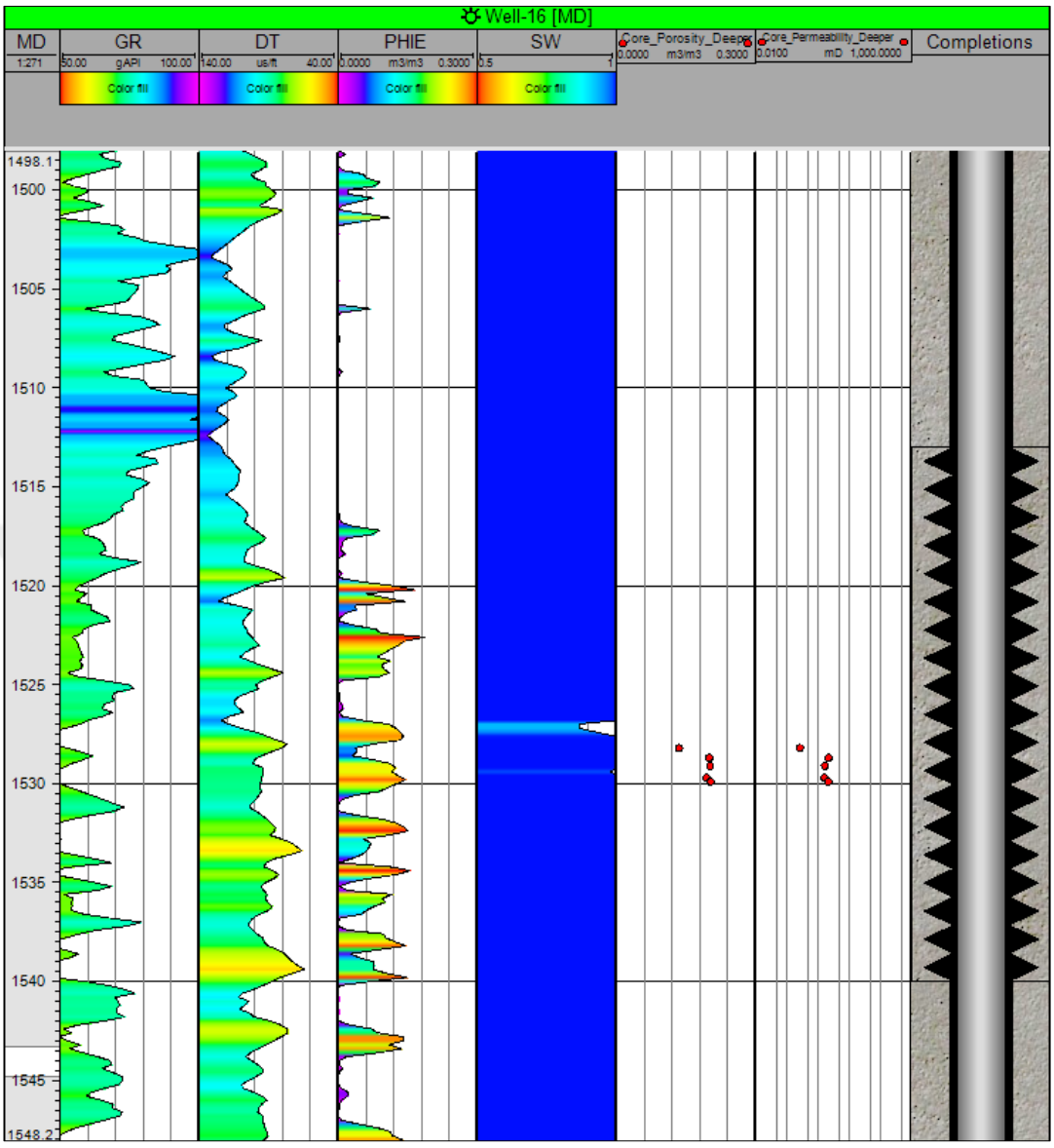

Figure 8.8. Measured-processed logs and core measurements of Well-16. From Left to right: Tack 1: Gamma-Ray; Track 2: P-sonic; Track 3: Effective porosity; Track 4: Water saturation; Track 5: Core porosity; Track 6: Core permeability; Track 7: Well completion. Note that there is no production in this well.

8.2.5 Core Measurements for Well-21

Well-21 is the most productive one among the wells with core measurement. Two core plugs, between 1706-1714 and 1651-1654.60 meters, were drilled out and analyzed. Analysis results are given in the Table 8.5. Both zones have high porosity and permeability values. Each interval is productive with a total production more than 100,000,000 m3 gas reservoir. Cross-plot of porosity versus permeability show that values for core-1 has very high petrophysical values. With increasing depth, porosity and permeability decrease while values for core-2 are still enough for high amount of production (Figure 8.9).

Well log section and core measurements are displayed in Figure 8.10. Gamma-ray log indicates the presence of clear sandstone intervals. Perforated intervals show that effective porosity changes between 20%-25% and water saturation is around 50%.

Table 8.5 Core Analysis of plugs in Well-21.

Core No.	Depth Interval (m)	Sample Depth (m)	Porosity (%)	Permeability (md)	Grain Density (g/cc)
1.00	1651-1654	1651.15	18.80	17.40	2.67
1.00	1651-1654	1651.60	19.30	14.73	2.67
1.00	1651-1654	1652.05	20.26	34.06	2.67
1.00	1651-1654	1652.15	21.00	40.07	2.67
1.00	1651-1654	1652.95	20.45	35.85	2.67
1.00	1651-1654	1653.00	20.62	25.37	2.66
1.00	1651-1654	1653.25	20.05	21.61	2.67
2.00	1706-1714	1706.45	19.69	1.77	2.67
2.00	1706-1714	1706.80	16.03	0.15	2.68
2.00	1706-1714	1707.60	17.37	0.41	2.67
2.00	1706-1714	1708.50	19.52	4.47	2.67
2.00	1706-1714	1708.75	20.26	3.83	2.66
2.00	1706-1714	1709.60	17.30	0.72	2.67
2.00	1706-1714	1710.55	18.72	2.50	2.66
2.00	1706-1714	1711.40	15.22	0.17	2.68
2.00	1706-1714	1712.10	17.79	0.58	2.67
2.00	1706-1714	1712.50	17.91	0.64	2.66
2.00	1706-1714	1713.05	18.09	0.45	2.67

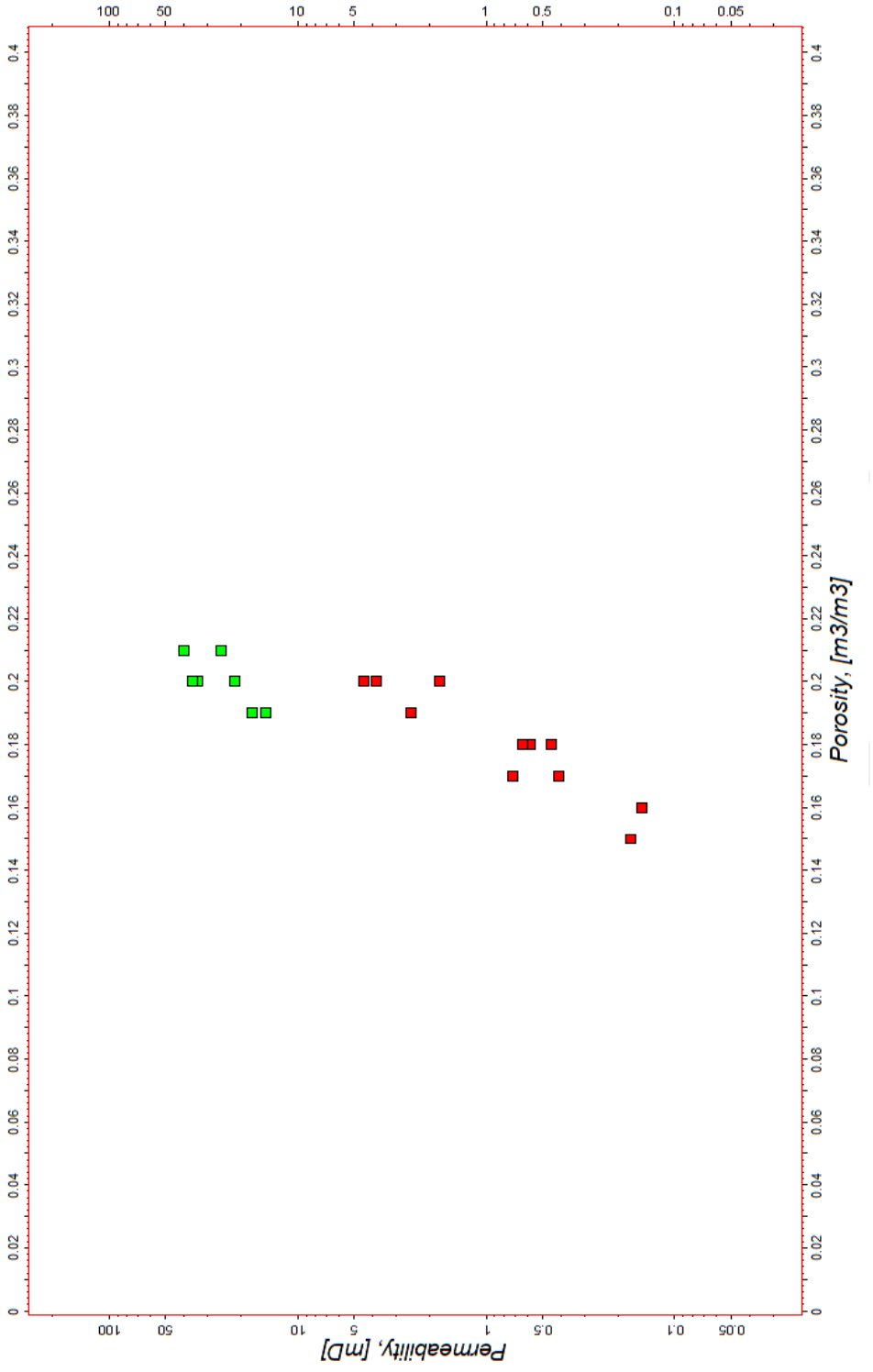

Figure 8.9. Porosity versus Permeability cross-plot of the core sample of Well-21. Green data points represent measured data for core-1 (1651-1654 m.) and red points are the data for core-2 (1706-1714 m).

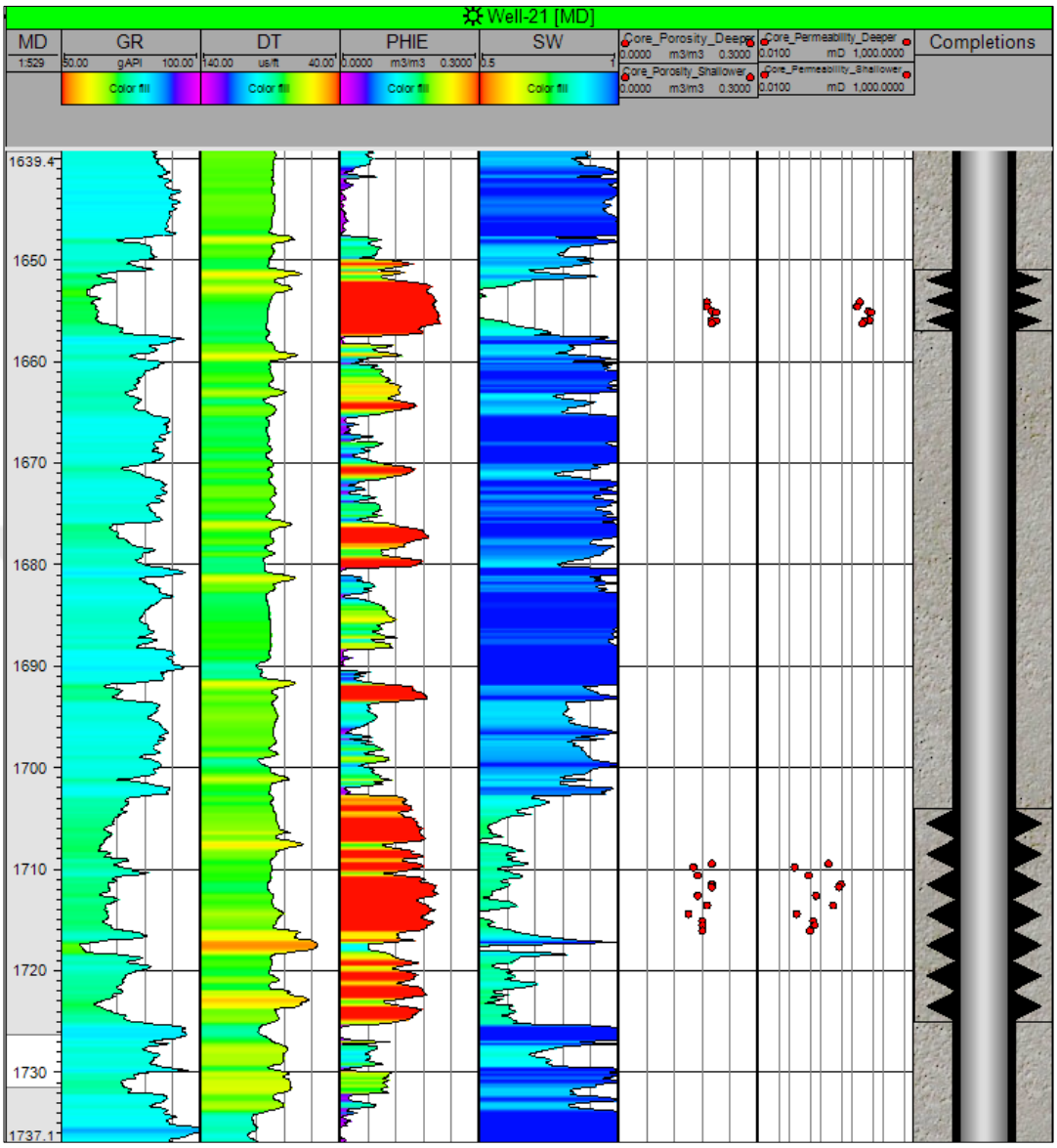

Figure 8.10. Measured-processed logs and core measurements of Well-21. From Left to right: Tack 1: Gamma-Ray; Track 2: P-sonic; Track 3: Effective porosity; Track 4: Water saturation; Track 5: Core porosity; Track 6: Core permeability; Track 7: Well completion. Note that both intervals in which cores cutting out are highly productive in this well.

8.2.6 Core Measurements for Well-32

In this well, core data is available between 1463-1470 m. and 1798-1805.7 m. For the shallower part, 42.5% of the core, which is 3 m., was recovered and this part consists of shale. Therefore, analysis was carried out only from core-2. This well has not been produced from deeper Osmancık Formation. Porosity measured from cores is moderate varying between 3.7% and 13%. Permeability values are very low compared to producing intervals (Table 8.6). Hydrocarbon fluid is not filled within the zone, so the pressure is zero. A cross-plot of porosity and permeability is shown in Figure 8.11.

Well log section and core measurements are demonstrated in Figure 8.12. Unfortunately, processed logs are not available. Therefore, this well is not used for the evaluation and modeling purposes.

Table 8.6 Core Analysis of plugs in Well 32.

Core No.	Depth Interval (m)	Sample Depth (m)	Porosity (%)	Permeability (md)	Grain Density (g/cc)
2	1798-1805.7	1798.8	12.93	0.44	2.67
2	1798-1805.7	1801	9.64	0.23	2.66
2	1798-1805.7	1803.2	11.72	0.63	2.67
2	1798-1805.7	1804.5	3.69	0.14	2.68

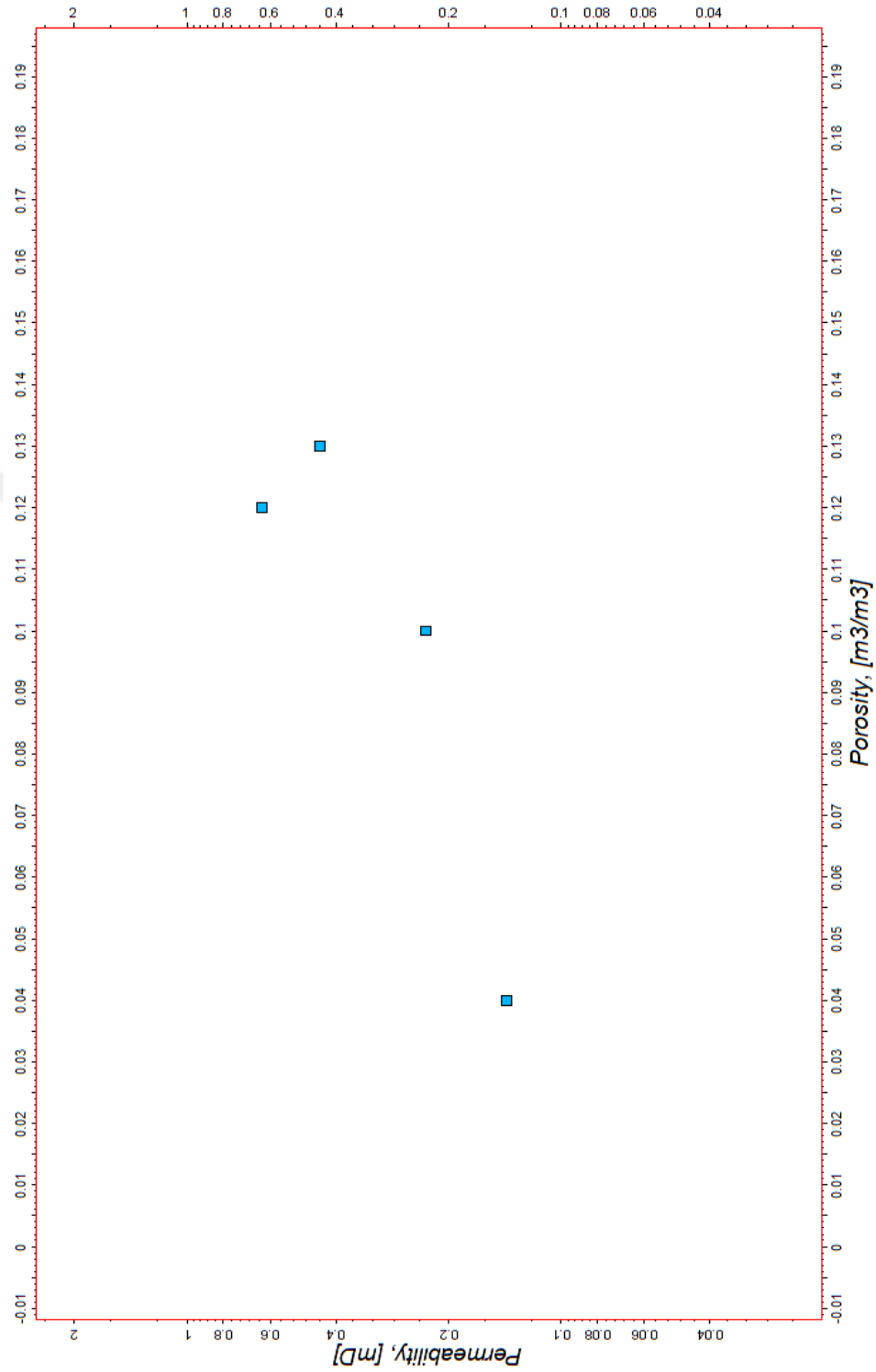

Figure 8.11. Porosity versus Permeability cross-plot of the core sample of Well-32.

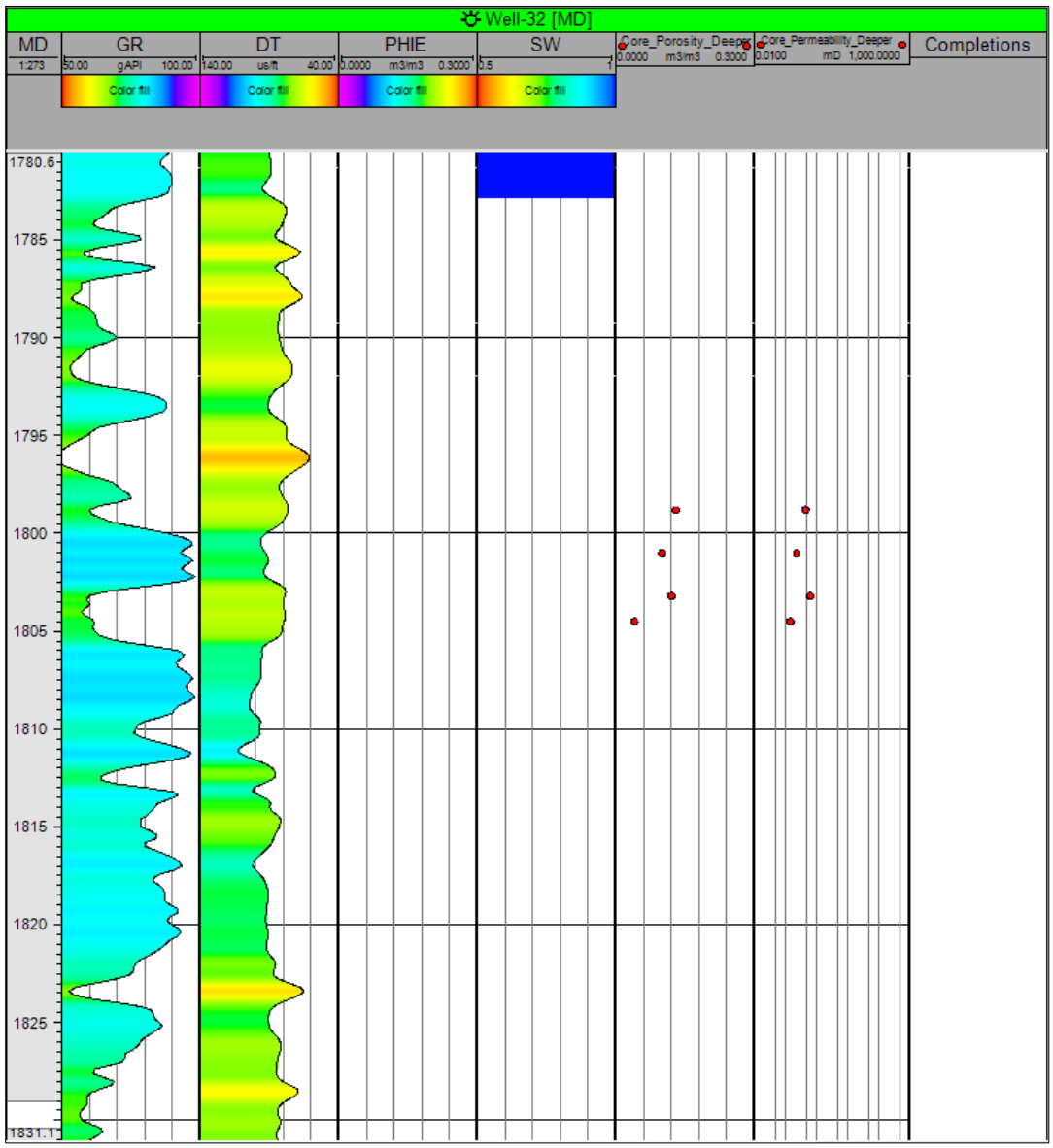

Figure 8.12. Measured-processed logs and core measurements of Well-32. From Left to right: Tack 1: Gamma-Ray; Track 2: P-sonic; Track 3: Effective porosity; Track 4: Water saturation; Track 5: Core porosity; Track 6: Core permeability; Track 7: Well completion. Note that log curves except GR and DT are not available within the range of the core data.

8.2.7 Compilation of Core Measurements

Six wells include core measurements as mentioned above. Four wells; Well-12, 13, 15 and 16 belong to well group-1, one well, Well-21, is from well group-2 and the last one, Well-32, is from well group-3. Well-21 is the most productive one among the wells having core data. Well-12 produces the highest amount of gas within well group-1. Wells 13 and 15 produce moderately. Well-16 is a dry well and Well-32 produces only from shallower Osmancık Formation. All available core data were drilled out from deeper Osmancık Formation.

Cross-plot of porosity and permeability variations including all available core data is given in Figure 8.13. Core measurements for Well 12 and 21 are clearly detected in the zone of the highest data points, which are shown with green and red color, respectively. Well 13 and 15 show variations in the cross-plot, which are illustrated with pink and dark blue color. Core porosity and permeability variations for Well 32 in the cross-plot, which are given with black color, are located in a zone with lower values. Well-16 is the only well with good reservoir properties. However, hydrocarbon fluid is not available in this well.

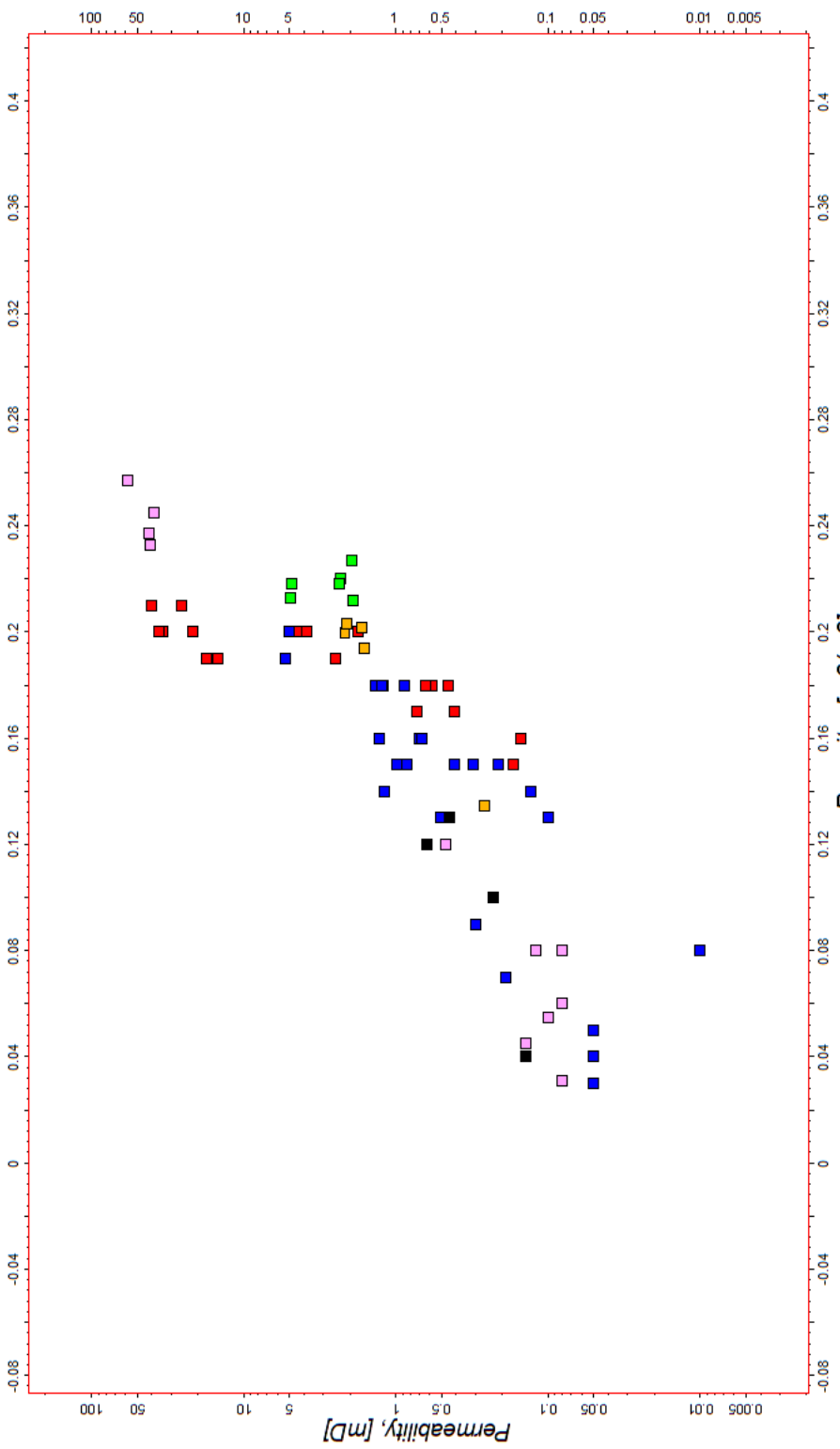

Figure 8.13. All available core measurements for porosity and permeability are shown. In the crossplot, all data points for Well-12, 13, 15, 16, 21 and 32 are shown in order with green, pink, dark blue, orange, red and black color.

8.3 Estimation of Permeability Curve

Permeability values are only available for core measurements because permeability is not a directly measured or processed reservoir property using well logs. To create a 3D permeability model using geostatistical modeling, generation of permeability log curves are necessary. In this respect, core porosity and permeability cross-plots were used to create permeability logs. To implement permeability curves, both statistical and theoretical models were utilized.

8.3.1 Statistical Permeability Estimation

To estimate permeability curve for each well, at first, a common porosity-permeability relationship was aimed to reveal. All core porosity and permeability data were cross-plotted. A general equation was obtained from the trend of data set using a linear regression line (Figure 8.14). The linear equation is given as below:

$$Log(K) = 12.5 * \Phi - 1.96 \quad 8.1$$

where K is the permeability and Φ is the porosity.

However, Well-21 is very productive and porosity and permeability values are higher compared to other cores. Therefore, data trend of porosity versus permeability is different in Well-21 from the rest of the wells (Figure 8.15), another linear equation was fitted using only core data from this well (Figure 8.16). This equation is given as below:

$$Log(K) = 43.3 * \Phi - 7.6 \quad 8.2$$

After the core data of Well-21 was extracted from general cross-plot of porosity versus permeability, a new regression line was fitted to be used for Well group-1 wells (Figure 8.17). The linear equation is also given below:

$$Log(K) = 11.4 * \Phi - 1.83 \quad 8.3$$

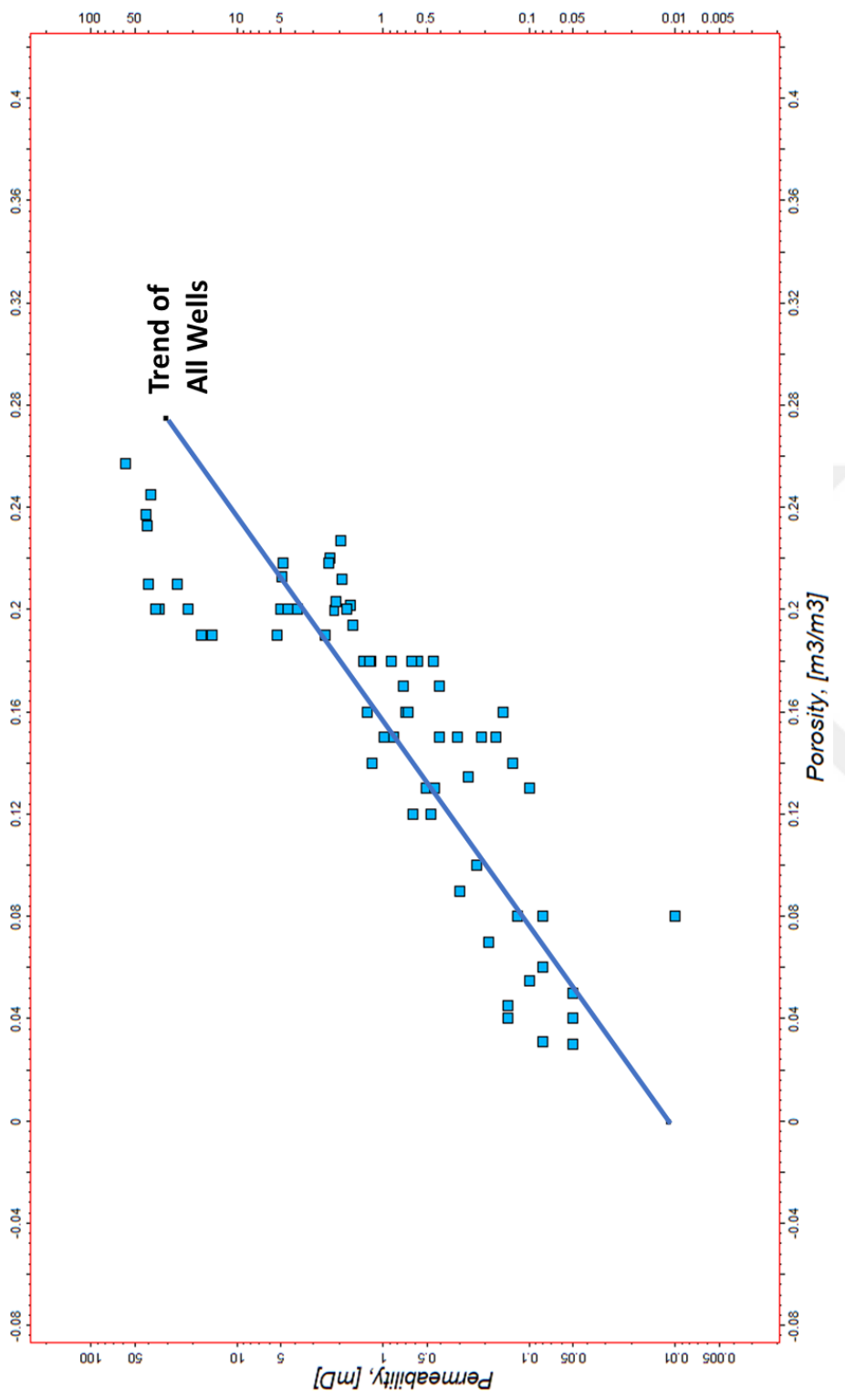

Figure 8.14. Porosity versus permeability cross-plot of core measurements including all wells.

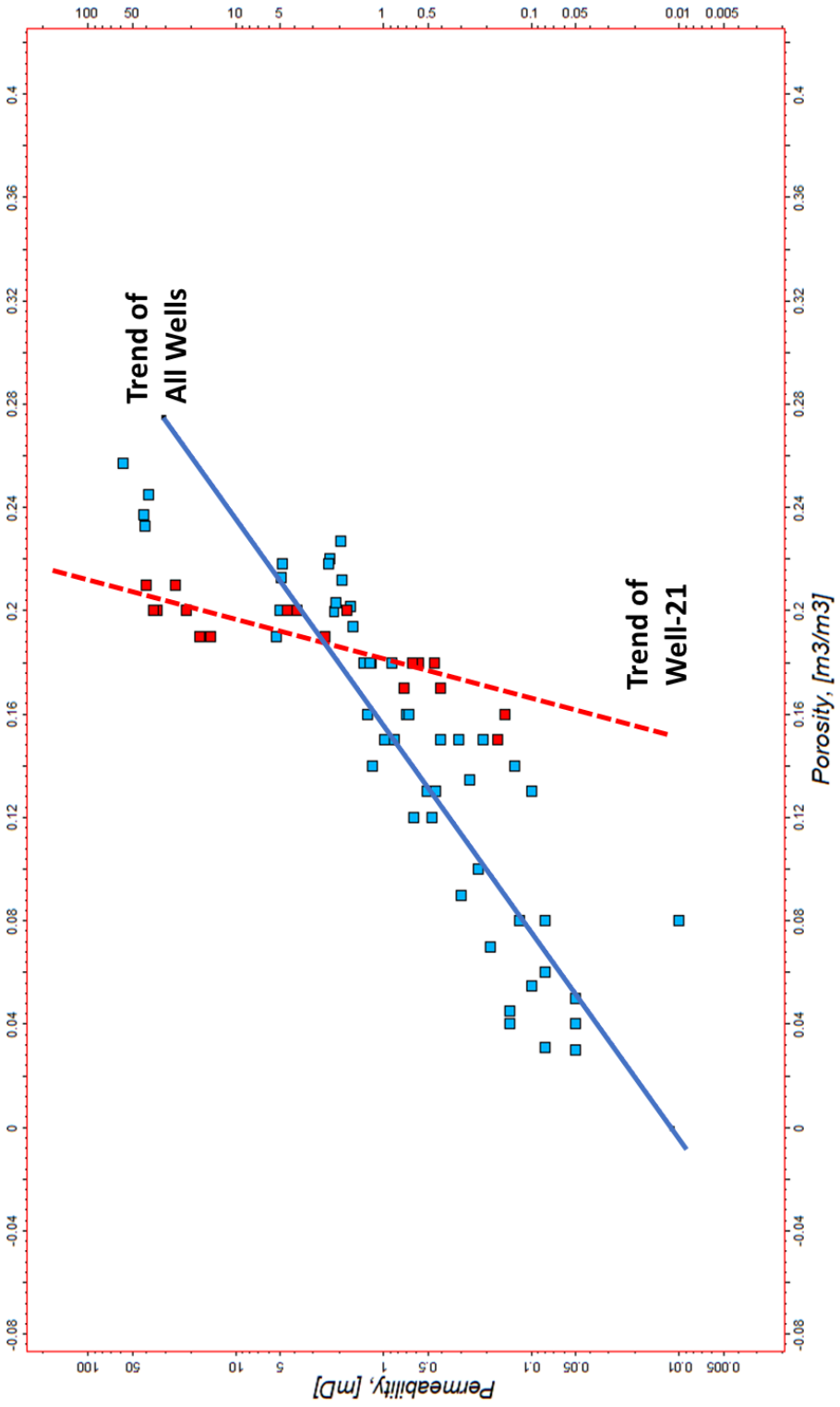

Figure 8.15. Discrimination of porosity versus permeability trend of Well-21 from the trend of all wells.

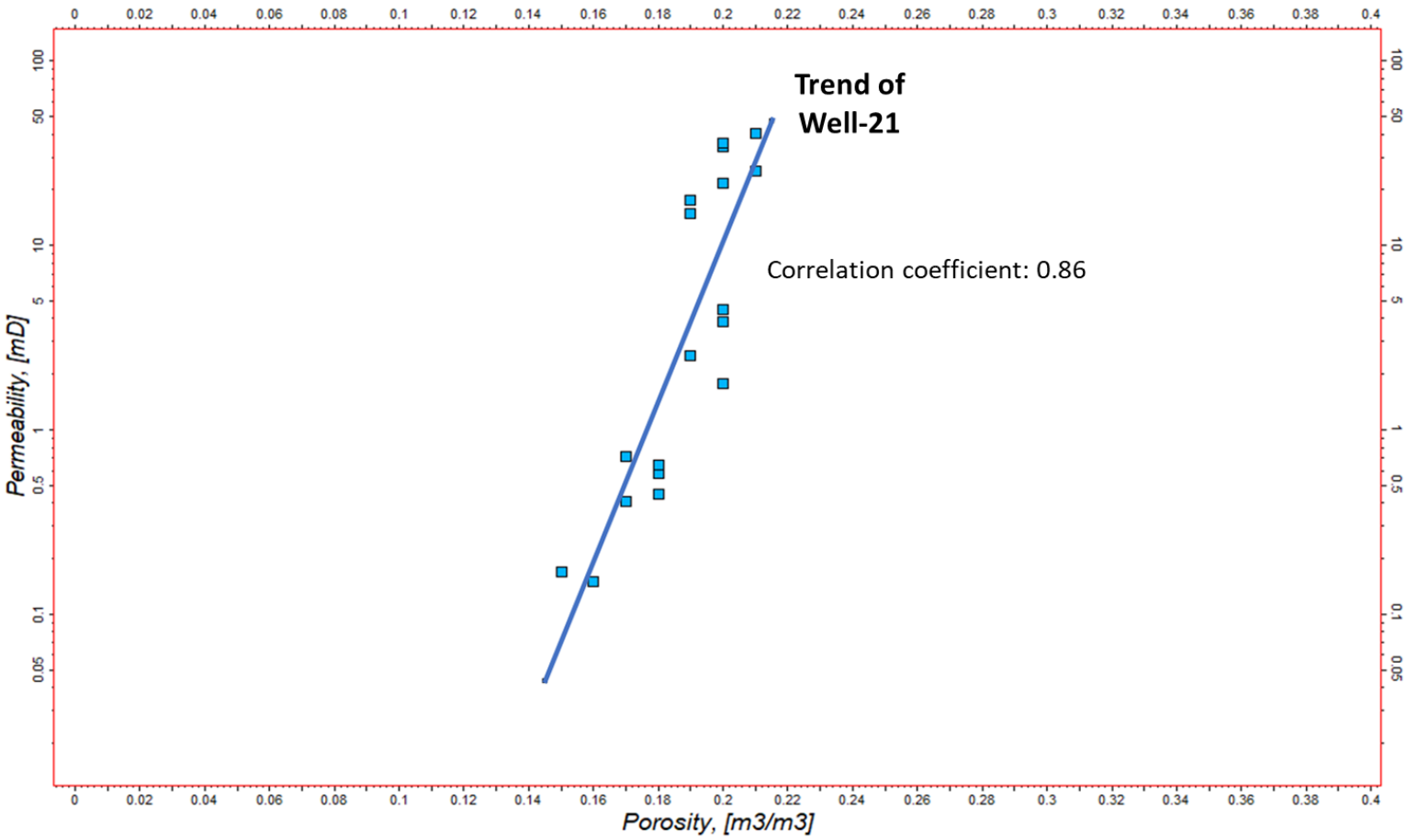

Figure 8.16. Porosity versus permeability cross-plot of core measurements, revealing a distictive trend for Well-21.

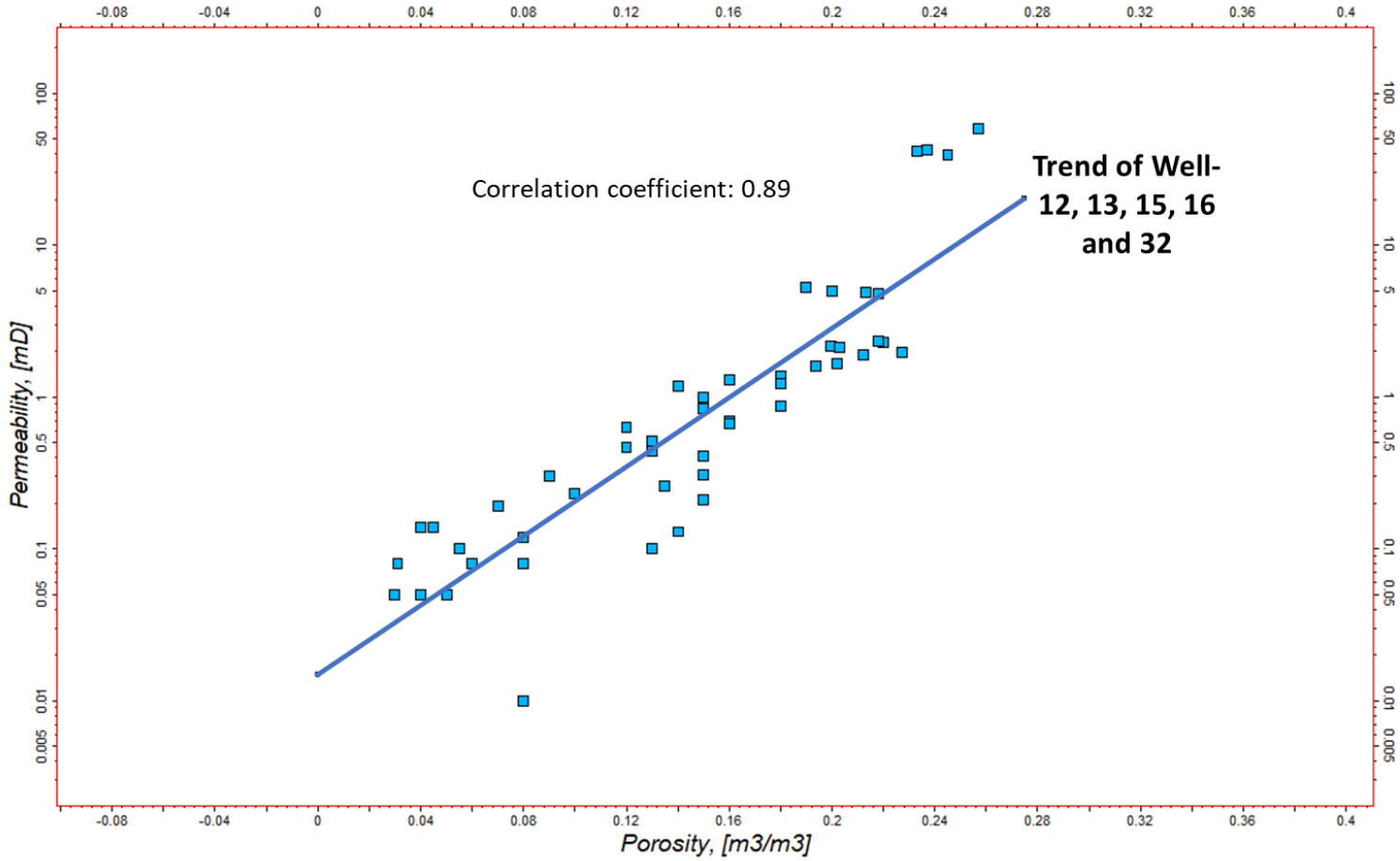

Figure 8.17. Porosity versus permeability cross-plot of core measurements. A different trend of measurement from Well-21 is observed.

8.3.2 Theoretical Permeability Estimation

Several theoretical methods for the calculation of permeability from porosity have been applied from many scientists (Tixier, 1949; Wylie and Rose, 1950; Timur, 1968; Coats and Dumanior, 1974; Berg, R. R.,1975; Van Baaren, J., 1979; Glover et al., 2006). Some of these theoretical models were utilized to create permeability curves. Results of a publication, including the same theoretical approximations, and of this research will be explained.

8.3.2.1 Previous Study

Davies et all. (2019) published a paper showing differences of four different models; Van Baaren (1979), Berg (1975), RGPZ (Glover et al., 2006) and Timur (1968) models. In the paper, sandstone reservoirs covering some parts of Niger Delta were studied. A number of core measurements from two reservoir zones at one well were utilized.

Four different equations used in generating permeability curves are given below:

RGPZ model (Glover et al., 2006);

$$k_{RGPZ}(mD) = \frac{1013 d^2 \Phi^{3m}}{4am^2} \qquad 8.4$$

where Φ represents porosity, d is the weighted mean grain size (in microns), m is the cementation exponent and a is equal to 8/3 assuming grains are spherical (Schwartz et al., 1989),

Timur's Model (1968);

$$k_{TM}(mD) = 0.136 \frac{\Phi^{4.4}}{S_{wi}^2} \qquad 8.5$$

where Φ is porosity and Sw is irreducible water saturation,

Berg's Model (1975);

$$k_{BM}(mD) = 8.4x10^{-2}\Phi^{5.1}D^2 \quad 8.6$$

where Φ represents porosity, D is the median grain size,

Van Baaren's Model (1979);

$$k_{VBM}(mD) = 10D_d^2\Phi^{3.64+m}C^{-3.64} \quad 8.7$$

where Φ is Porosity, Dd is the dominant grain size, m is the cementation exponent (m=1.65), C is the sorting index. Sorting index table is below:

Table 8.7 Sorting index.

SORTING	SORTING INDEX
Extremely well to very well sorted	0.70
Very well to well sorted	0.77
Well Sorted	0.84
Well to moderately sorted	0.87
Moderately Sorted	0.91
Moderately to poorly sorted	0.95
Poorly sorted	1

Janssen and Heuberger (1995) defined a mathematical expression of Root Mean Square Error (RMSE) indicating model error calculation as shown below:

$$RMSE = \sqrt{\frac{\sum_{i=1}^{N}(X_{i,\ model} - X_{i,\ observed})^2}{N}} \quad 8.8$$

where $X_{i,\ observed}$ is the measured core permeability and $X_{i,\ model}$ is the estimated permeability of i^{th} sample.

The normalized root mean square error, NRMSE, is also mathematically expressed as;

$$NRMSE = \frac{RMSE}{\overline{X_{observed}}} \tag{8.9}$$

where $\overline{X_{observed}}$ is the average value of measured (core) data.

The results of RMSE and NRMSE for two reservoirs interval are given in Table 8.8.

Table 8.8 RMSE and NRMSE for RESERVOIR I and RESERVOIR II (m=1.65).

	RESERVOIR I		RESERVOIR II	
	RMSE	NRMSE	RMSE	NRMSE
RGPZ Model	1577.42	4.95	2172.96	4.28
Timur's Model	9675.94	30.38	12527.03	24.69
Berg's Model	590.12	1.85	790.08	1.56
Van Baaren's Model	382.91	1.2	554.69	1.09

According to estimated permeability values for both reservoir levels, the best resulted equation predicting the actual core permeability is Van Baaren's model while Timur's model is the least acceptable one. Permeability calculated from Berg's model is also close to the results of Van Baaren's model. The first ten samples of the observed and calculated variables for reservoir I and II are given in Table 8.9 and 8.10, respectively.

Table 8.9 Observed and estimated permeabilities of the first ten samples for RESERVOIR I.

Depth (Ft)	Core Permeability (mD)	KRGPZ (mD)	KTM (mD)	KBM (mD)	KVBM (mD)
7874	21.46	2630.03	13909.93	5.1	585.86
7882	1625	6895.49	32765.57	13.77	1641.16
7888	2166	6180.17	29726.12	12.3	1459.89
7898	1115	1654.7	9213.9	3.16	357.05
7906	515.5	2847.97	14929.95	5.54	637.89
7908	89.71	4272.95	21412.81	8.41	984.1
7910	2003	3075.54	15985.81	5.99	692.51
7922	65.61	2104.07	11407.55	4.05	461.57
7924	550	2904.87	15194.78	5.65	651.52
7926	25.91	2847.97	14929.95	5.54	637.89

Table 8.10 Observed and estimated permeabilities of the first ten samples for RESERVOIR II.

Depth (Ft)	Core Permeability (mD)	KRGPZ (mD)	KTM (mD)	KBM (mD)	KVBM (mD)
8340	4.62	2630.03	13909.93	5.1	585.86
8342	213.5	1565.56	8771.37	2.99	336.53
8348	772.2	1658.21	9231.29	3.17	357.86
8350	1306	2125.82	11512.26	4.1	466.67
8360	455	1726.23	9567.13	3.31	373.57
8364	1887	8505.84	39485.91	17.1	2053.83
8366	1873	1877.42	10308.43	3.6	408.64
8370	88.49	2104.07	11407.55	4.05	461.57
8372	159.3	3968.73	20052.16	7.79	909.41
8384	95.97	1081.21	6312.05	2.04	226.58

8.3.2.2 Permeability Estimation Using Theoretical Models for Karaçalı-Yulaflı Field

Similar to previous work, four theoretical models; Van Baaren (1979), Berg (1975), RGPZ (Glover et al., 2006) and Timur (1968) were used to predict permeability curves in the study field. As porosity inputs, two reservoir intervals were utilized from Well-21 (Table 8.3).

Although two cores which are drilled out from Well-21 do not have any thin sections, dominant and median grain sizes were used as 100 microns. The reason for this is that median grain sizes of thin sections prepared from available cores for deeper Osmancık are around 100 microns. Additionally, production of Well group-2 wells are much higher, therefore, sorting index was selected as well sorted. Once several empirical permeability curves calculated from these different theoretical models, it can be understood that assumptions for Well-21 work pretty well (Figure 8.18). The best fitted models are observed as Van Baaren's and Berg's models. Curves obtained from these two models are very similar. Nelson (1994) stated that both models show high similarity; however, because Van Baaren's model have two additional parameters (cementation factor and sorting index), this model is more flexible.

Additionally, root mean square error (RMSE) and normalized root mean square error (NRMSE) were calculated for two reservoir intervals from Well-21. A simple code using MATLAB software was written to calculate these errors as below:

```
clc;clear all;
Data1=load('Permeability-Models_Core-1.dat');
Data2=load('Permeability-Models_Core-2.dat');
N1=numel(Data1(:,1));
Mean1=mean(Data1(:,1));
for i=1:4
    Sum_RMSE(:,i)=(Data1(:,i+1)-Data1(:,1)).^2;
```

```
    RMSE1=sqrt(sum(Sum_RMSE)/N1);
    if i==4
        RMSE1=sqrt(sum(Sum_RMSE)/N1)
    end
end
N2=numel(Data2(:,1));
Mean2=mean(Data2(:,1));
for i=1:4
    Sum_RMSE2(:,i)=(Data2(:,i+1)-Data2(:,1)).^2;
    RMSE2=sqrt(sum(Sum_RMSE2)/N2);
    if i==4
        RMSE2=sqrt(sum(Sum_RMSE2)/N2)
    end
end

NRMSE1=RMSE1/Mean1
NRMSE2=RMSE2/Mean2

Data_Output=[RMSE1(:),RMSE2(:),NRMSE1(:),NRMSE2(:)];
save Data_Output.dat Data_Output -ascii
```

Observed and estimated results of permeability for Well-21 including shallower and deeper reservoirs are given in Table 8.11 and 8.12, respectively. According to results of RMSE and NRMSE (Table 8.13), RGPZ calculates the most erroneous results for both reservoir intervals. Timur's equation also fails to calculate permeability and underestimates the values for the reservoir interval of core-1 while this approximation is the most successful one to generate permeability curve for the deeper reservoir where the core-2 was drilled out. On the other hand, Van Baaren's and Berg's models are successful to calculate permeability of shallower zone while these two models generate optimum values for deeper reservoir zone.

Table 8.11 Observed and estimated permeabilities for the shallower reservoir.

Depth (m)	Core Permeability (mD)	KRGPZ (mD)	KTM (mD)	KBM (mD)	KVBM (mD)
1651.15	17.4	130	5.6	29.7	24.7
1651.6	14.7	133.4	5.6	30.5	25.3
1652.05	34.1	143.4	6	33.2	27.3
1652.15	40.1	157.7	6.5	37	30.1
1652.95	35.9	160	4.6	37.5	30
1653	25.4	161.4	4.5	38	30.8
1653.25	21.6	177.1	4.4	42.2	33.9

Table 8.12 Observed and estimated permeabilities for the deeper reservoir.

Depth (m)	Core Permeability (mD)	KRGPZ (mD)	KTM (mD)	KBM (mD)	KVBM (mD)
1706.45	1.77	46.7	1.07	9.1	8.5
1706.8	0.15	69.9	2.1	14.5	13
1707.6	0.41	10.9	0.3	1.7	1.92
1708.5	4.5	120	3	25	23
1708.75	3.8	136	3.6	31	26
1709.6	0.7	133.4	4.2	30.5	25.3
1710.55	2.5	90	2.2	20	17.6
1711.4	0.2	91.4	4.3	19.2	17.1
1712.1	0.6	100	3.4	20	22
1712.5	0.6	100	3	20	18
1713.05	0.5	57	1.5	11.5	10.6

Table 8.13 RMSE and NRMSE for both reservoir intervals of Well-21.

	Shallower Reservoir		Deeper Reservoir	
	RMSE	NRMSE	RMSE	NRMSE
RGPZ Model	125.71	4.6	92.6	64.8
Timur's Model	23.45	0.89	2.1	1.5
Berg's Model	11.9	0.44	18.7	13.1
Van Baaren's Model	8.7	0.32	16.6	11.6

As a result, two models, Van Baaren's and Berg's, generate more realistic permeability curves among four different empirical models. Because Van Baaren's model is also more flexible, this model was chosen for the purpose of modeling. Using Van Baaren's model, permeability curve of Well-12 is given in Figure 8.19.

Using Van Baaren's model, permeability curves for Well-13 and Well-15 were estimated and results are evaluated as relatively close to permeability values generated from cores (Figure 8.20). To increase the accuracy at deeper cores, Van Baaren's Model was edited as below, which is shown in Figure 8.20 and 8.21:

$$k_{VBM}(mD) = 10D_d^2\Phi^{4.5+m}C^{-4.5} \quad 8.10$$

Comparison of estimated permeability values, using Van Baaren's Model and modified version of this model, are given in Table 8.14 and 8.15 for Well-15. Calculated errors are shown in Table 8.16 for both models.

Table 8.14 Observed and estimated permeabilities for the shallower reservoir (Well-15).

Depth (m)	Core Permeability (mD)	KVBM (mD)	Modified KVBM (mD)
1362.300	0.7000	4.5	0.85
1363.500	0.2100	6.7	1.3
1365.000	0.1000	1.9	0.3
1366.000	0.8700	0.3	1.7
1366.200	0.3000	2.2	0.3
1367.000	0.1900	0.23	0.02
1367.200	0.1300	0	0
1367.400	0.6700	0	0
1368.200	0.0100	0	0
1368.500	0.0500	0.6	0.08
1368.700	0.5100	4.4	0.8
1369.000	1.3700	2.1	0.4
1369.200	0.4100	3	0.5

Table 8.15 Observed and estimated permeabilities for the deeper reservoir (Well-15).

Depth (m)	Core Permeability (mD)	KVBM (mD)	Modified KVBM (mD)
1404.700	1.2200	13.8	3.1
1405.000	0.3100	5.2	1
1405.300	0.9900	5.2	1
1405.400	1.1900	3.6	0.7
1406.100	1.2300	13.8	3.1
1407.000	1.2900	7.4	1.5
1407.500	5.2800	18.4	4.4
1407.700	0.8400	5.2	1
1408.200	5.0000	0	0
1410.000	0.0000	0	0
1410.300	0.0500	0	0
1411.100	0.0500	0.05	0.04

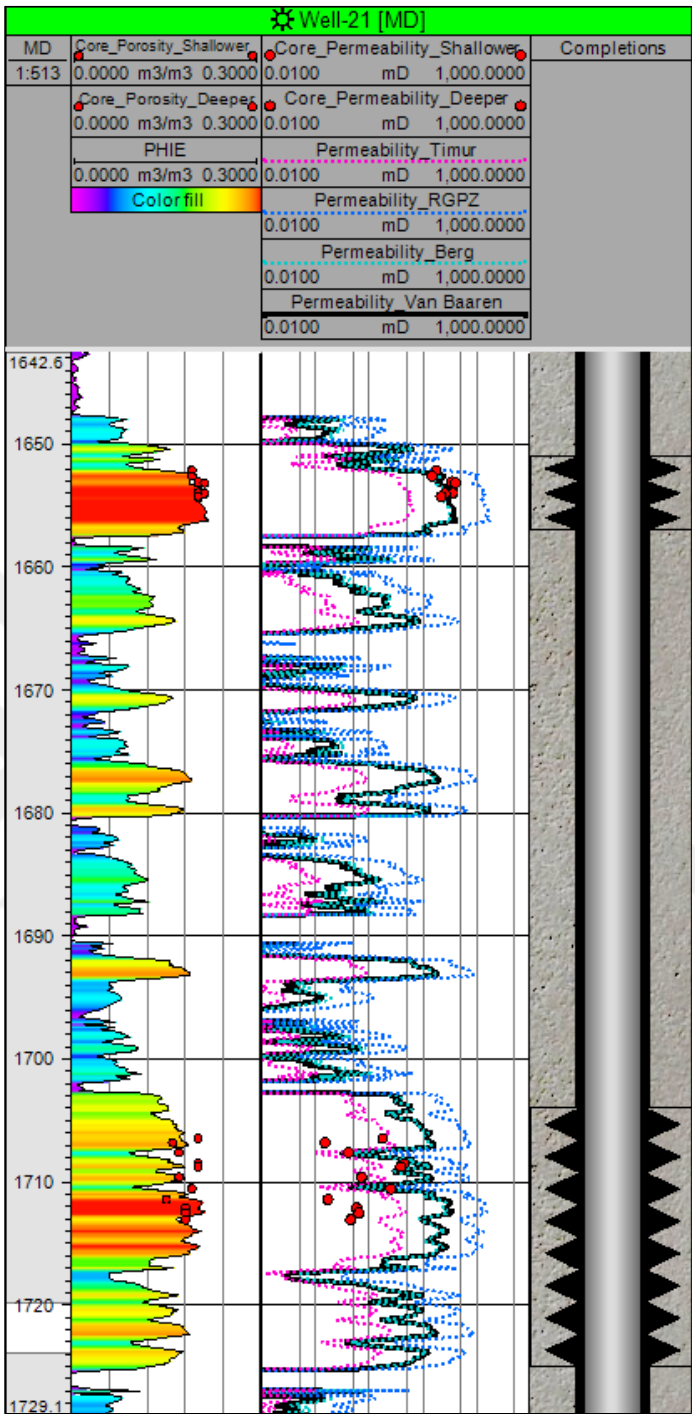

Figure 8.18. From left to right: Effective porosity log, theoretical permeability curves and completions are given for Well-21. Core porosity and permeability measurements are displayed with red circles. Four models; Van Baaren's (black line), Berg's (dashed green line), RGPZ (dashed blue line) and Timur's (dashed pink) equations are shown on the permeability curve track.

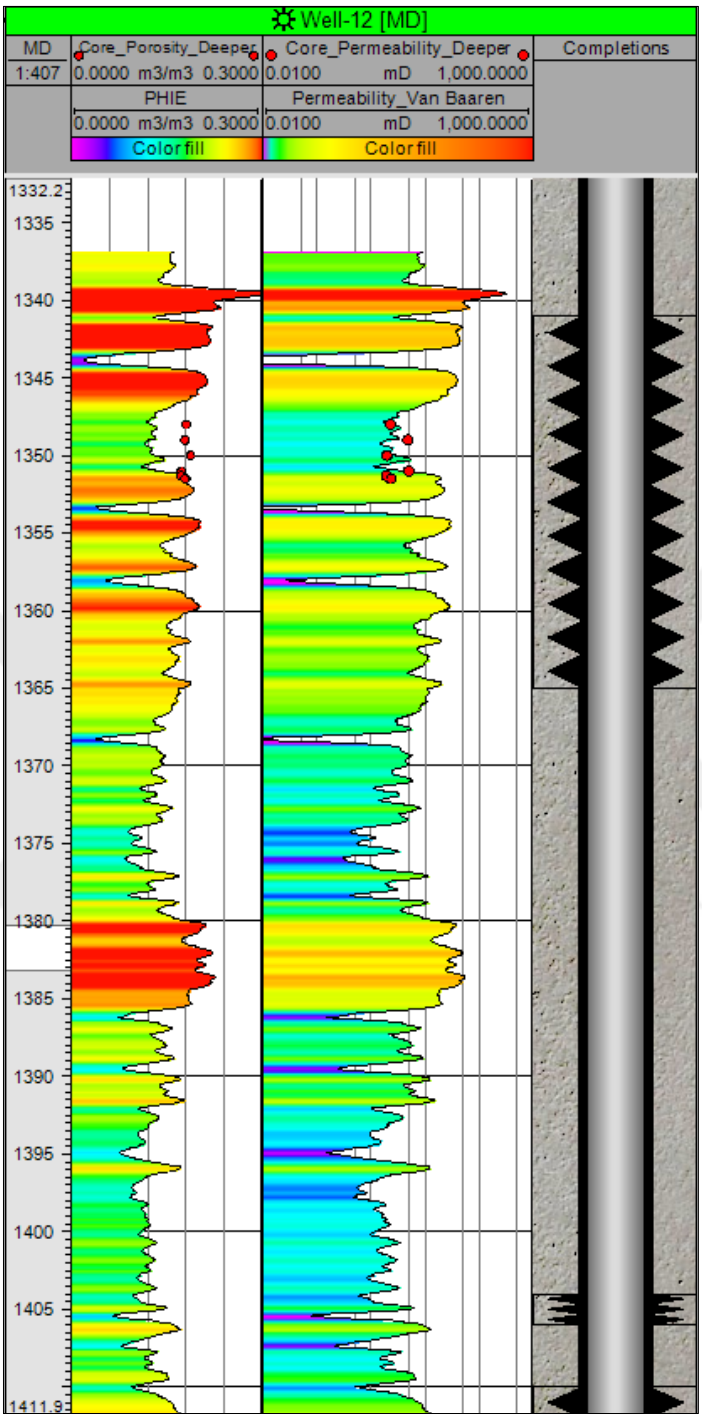

Figure 8.19. From left to right: Effective porosity, theoretical permeability curve and completions are given for Well-12. Van Baaren's model was used to estimate permeability from porosity. Core permeability and theoretical permeability curve show a good match.

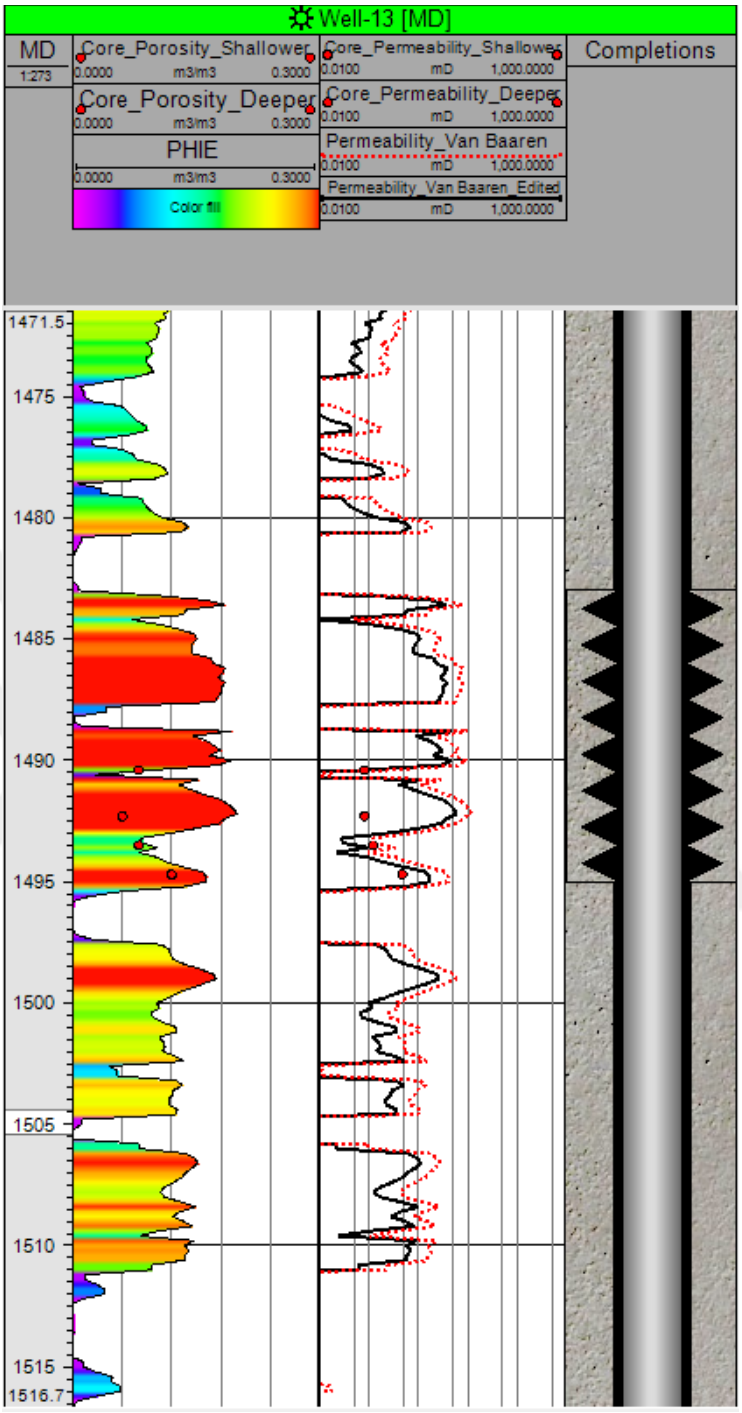

Figure 8.20. From left to right: Effective porosity log, theoretical permeability curves and completions are given for Well-13. The results of Van Baaren's model (dashed red curve) and edited Van Baaren's model (black line) are compared. These results are similar. However, edited model is closer core permeability.

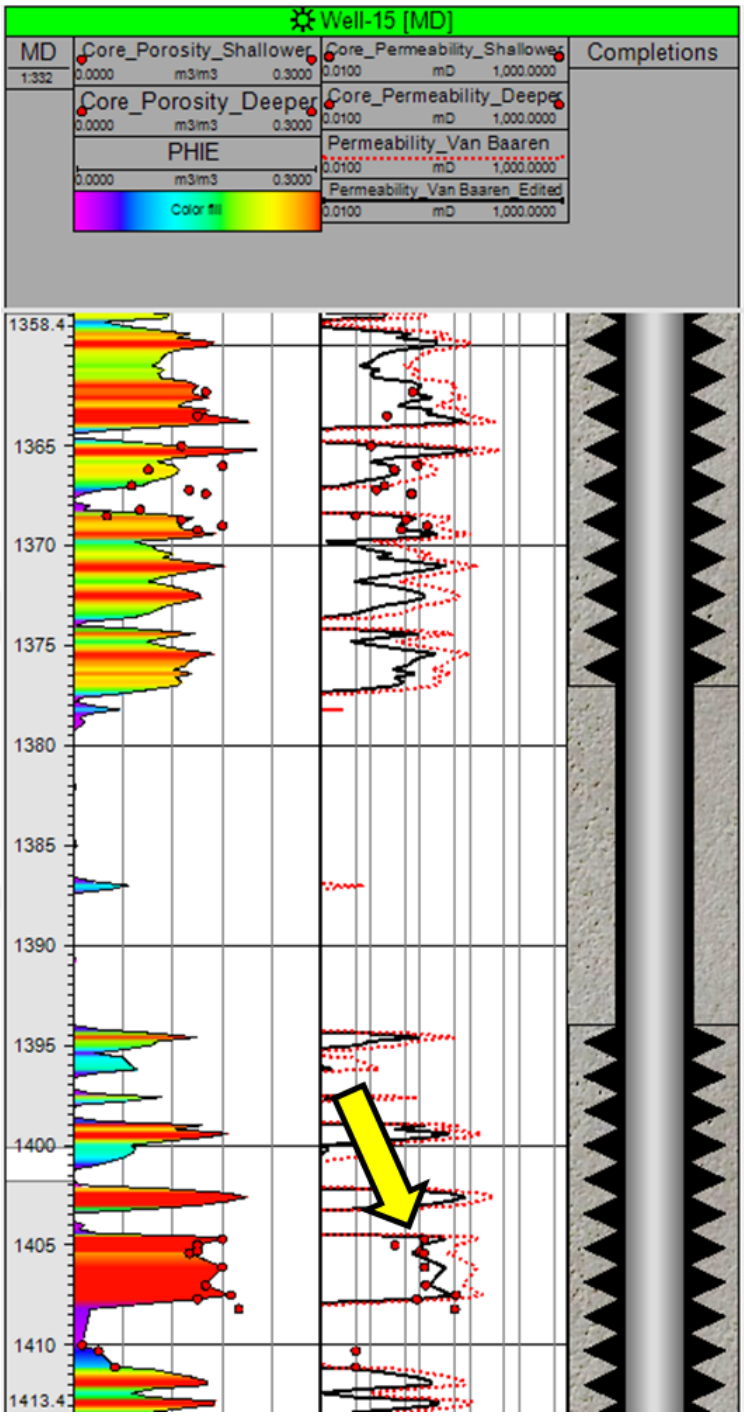

Figure 8.21. From left to right: Effective porosity log, theoretical permeability curves and completions are given for Well-15. The results of Van Baaren's model (dashed red curve) and edited Van Baaren's model (black line) are compared. At shallower zone, results are similar. However, edited model curve shows a clear match with core permeability at deeper zone and predicts these values more accurately.

Table 8.16 RMSE and NRMSE for both reservoir intervals of Well-15.

	Shallower Reservoir		Deeper Reservoir	
	RMSE	NRMSE	RMSE	NRMSE
Van Baaren's Model	7.17	4.93	2.59	6.1
Modified Van Baaren's Model	1.7	1.15	0.51	1.2

8.3.3 Results

Permeability estimation using both statistical (Equation 8.2) and theoretical methods were conducted. A comparison between resulted curves for Well-21 are given in Figure 8.22. According to these results, the estimation of statistical curve is more successful. However, if this relation is used for other wells in well group-2, statistically generated permeability curves fail because when porosity decreases, permeability show a higher proportional decrease resulting zero permeabilities at productive zones. Results for randomly selected wells, Well-25 and Well-28, are illustrated in Figure 8.23.

For Well group-1, permeability curve was statistically generated as well (Equation 8.3). Unfortunately, core measurements only available at deeper Osmancık, in which porosities and permeability values much lower than the values in shallower Osmancık. Thus, the use of statistical relation causes low permeability curves although shallower Osmancık reservoirs in the field are expected to be much higher. Randomly selected wells, Well-18 and Well-15, are given in Figure 8.24.

To sum up, theoretical estimation of permeability is found to be more realistic and accurate. Using Van Baaren’s original and edited versions, permeability of other

wells was created. These generated curves are utilized as inputs for the permeability modeling of Karaçalı-Yulaflı field.

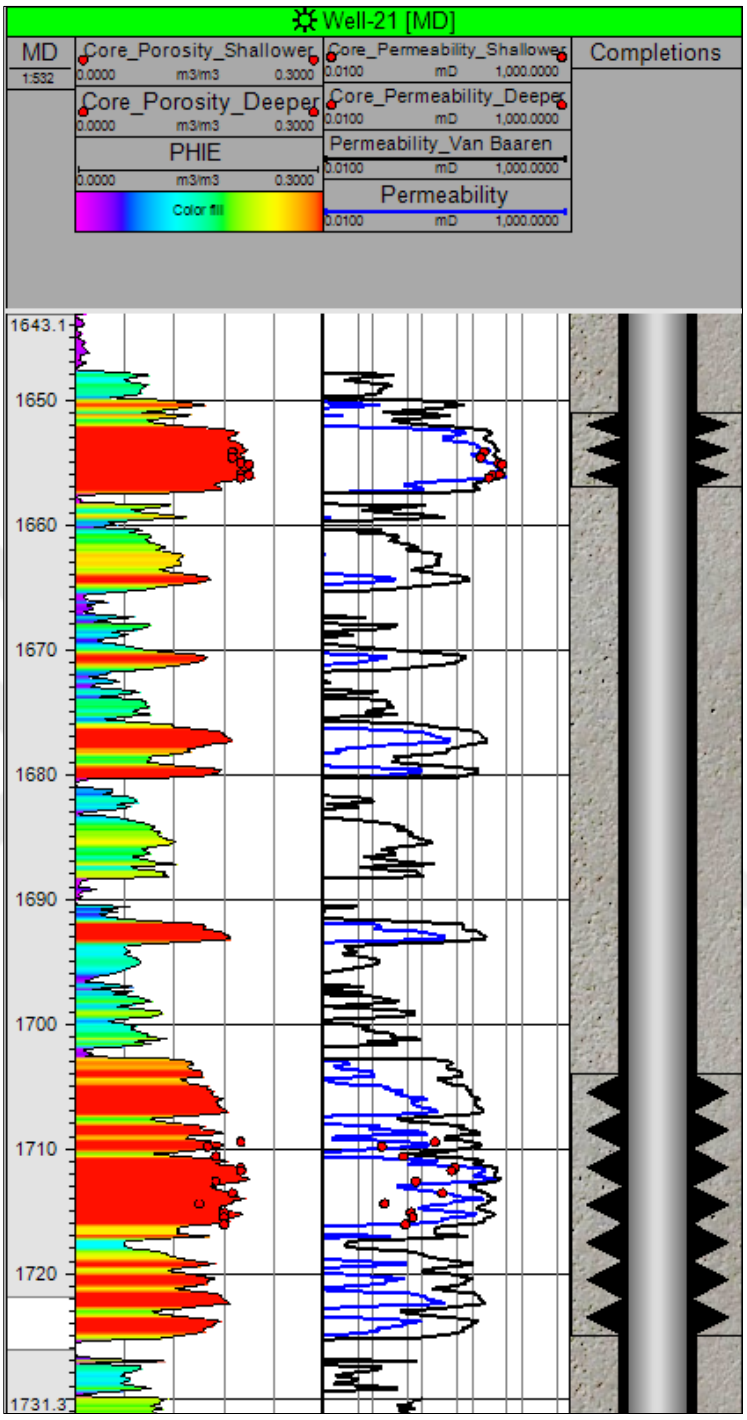

Figure 8.22. From left to right: Effective porosity log, calculated permeability curves and completions are given for Well-21. Comparison of statistical and theoretical estimations shows that statistical method results are more compatible for this well.

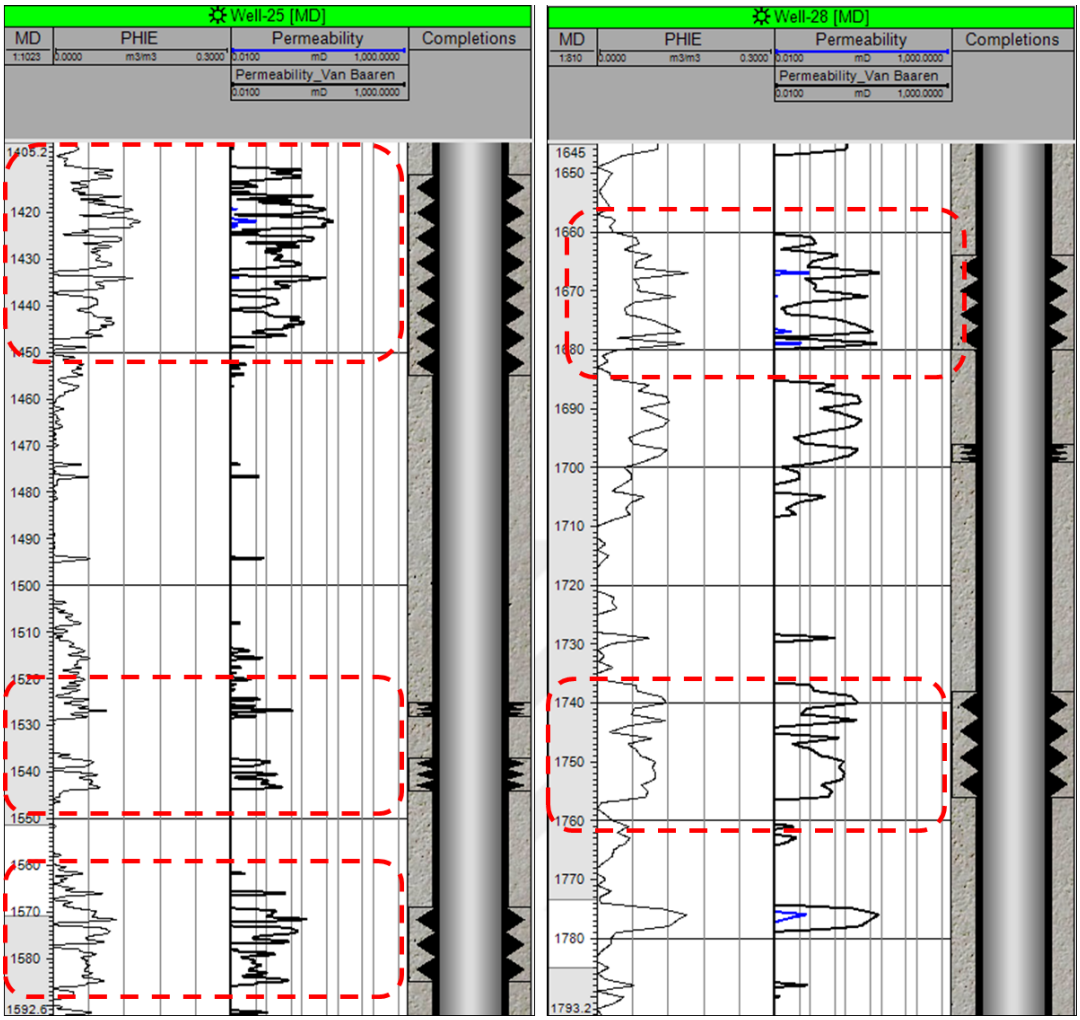

Figure 8.23. From left to right: Effective porosity log, calculated permeability curves and completions are given for Well-25 and 28. Comparison of statistical and theoretical estimations shows that permeability curves generated by using statistical approach fails in deeper sections in the case porosity values are very low.

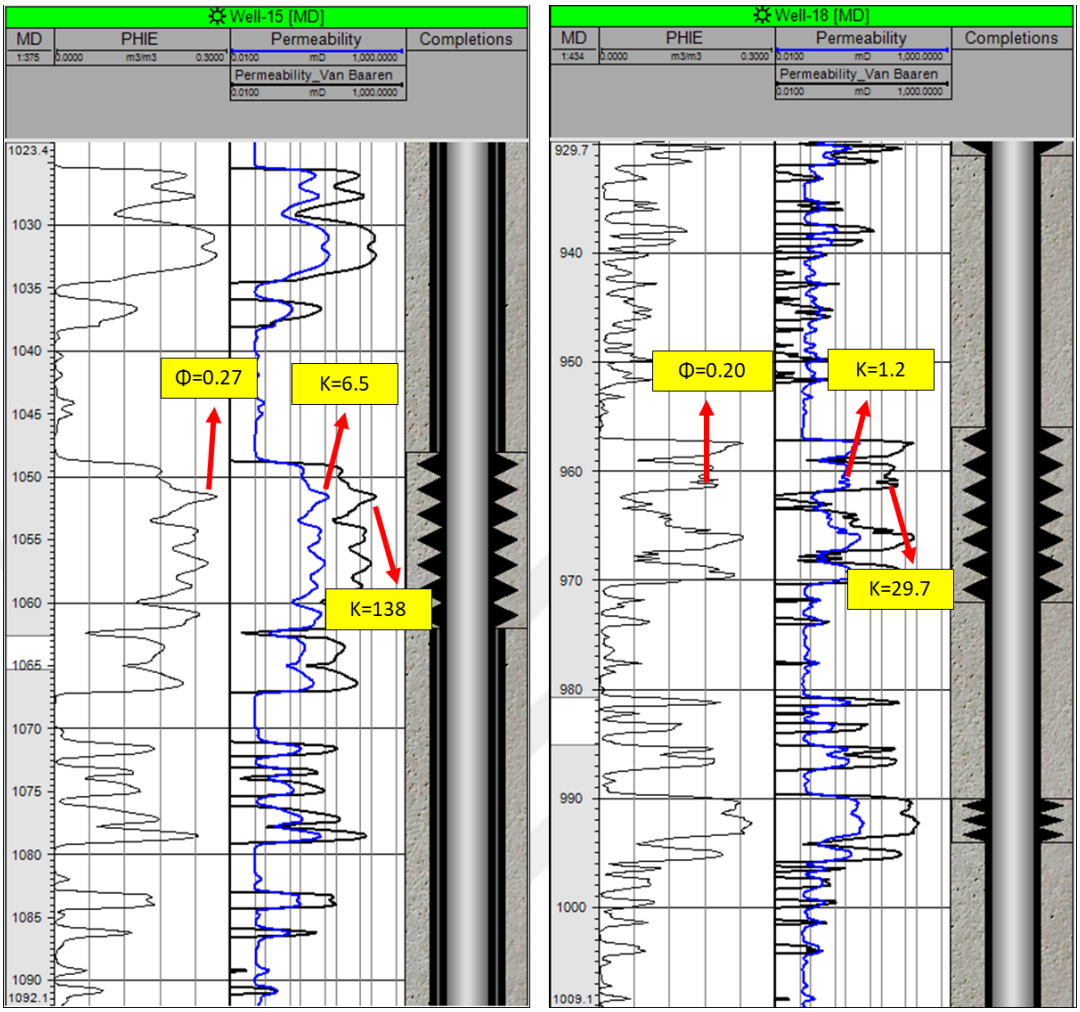

Figure 8.24. From left to right: Effective porosity log, calculated permeability curves and completions are given for Well-15 and 18. Comparison of statistical and theoretical estimations shows that permeability curves estimate very low values in shallower producing zones although both porosity and permeability should be much higher.

CHAPTER 9

GEOPHYSICS

9.1 Introduction

The purpose of this chapter is to explain both qualitative and quantitative seismic interpretation of the study field. Qualitative or conventional seismic interpretation is significant in terms of understanding structural behavior of the field while quantitative interpretation provides detailed information about fluid content of the reservoir zones. These methods are used for reservoir characterization of the field in terms of seismic perspective.

9.2 Conventional (Qualitative) Seismic Interpretation

Seismic signal propagating through a reflector with an angle of incidence is reflected and refracted due to impedance contrast between two layers. When the angle of incidence is higher than zero, P wave energy is converted into P and S waves. (Burianyk, 2000) (Figure 9.1). Seismic reflection is described as the wave coming out form a source and reflected back, which is called as a reflector, due to acoustic impedance contrast as a result of geological difference in terms of velocity and density between two layers (Sheriff, 2022). The more impedance contrast causes the more strength of a reflection. When the seismic wave hits on a reflection boundary, a part of energy is reflected, a part of it is absorbed and rest of the energy continues into subsurface as transmitted wave.

The main goal of the qualitative interpretation for this study is to identify structural geometry of the field using seismic reflections by picking events laterally continued

(horizons) and faults forming the structural architecture. Furthermore, a accurate velocity modeling and time to depth conversion is a key aspect to evaluate structural behavior of this field. Finally, a structural model is aimed to be created for modeling studies.

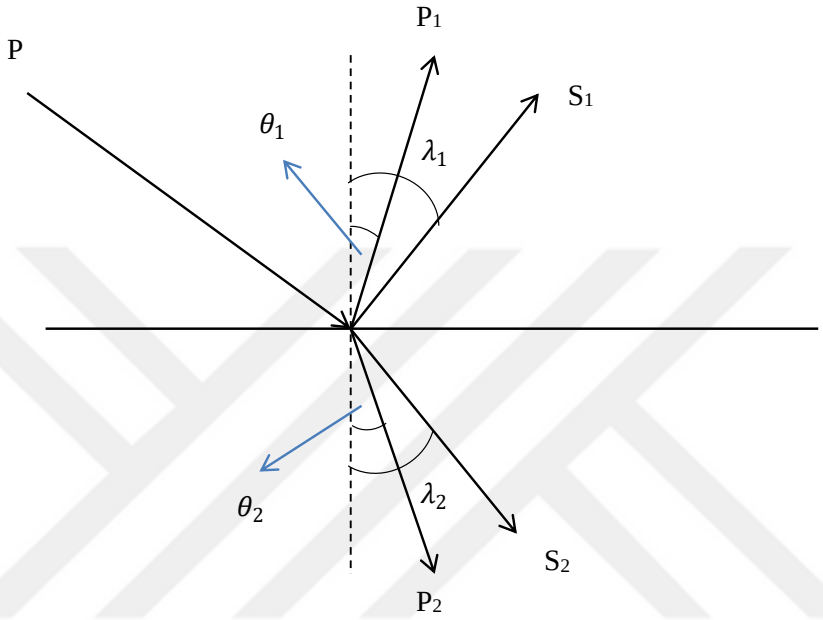

Figure 9.1. Reflected/refracted P and S waves when a P wave is partitioned. P1 and P2 are the reflected and refracted P waves. S1 and S2 are the reflected and refracted S waves. θ_1 is the angle of reflected P wave, θ_2 is the angle of refracted P wave, λ_1 is the angle of reflected S wave, and λ_2 is the angle of refracted S wave.

9.2.1 Seismic Wavelet Extraction and Well-to-Seismic Tie

Seismic signals are measured as a function two-way travel time (TWT). On the other hand, well logs are measured in depth domain. To interpret seismic reflections appropriately well logs and seismic reflections are necessary to be correlated, which is also referred as well-to-seismic tie.

The first step of well-to-seismic tie is extraction of a seismic wavelet. Seismic wavelet is defined as the mathematical expression of a signal coming out from a source (Stone, 1984). When the signal hits a surface boundary and reflects back to

the receiver, both wavelet and seismic information of a reflector (also called as reflection coefficient) reaches receivers as convolved. (Figure 9.2). In other words, seismic signals include both the information coming from subsurface and wavelet coming out from a source and changing shape and frequency going through deeper.

For stacked seismic data, a statistical zero phase wavelet was extracted by autocorrelation of seismic traces (Figure 9.3).

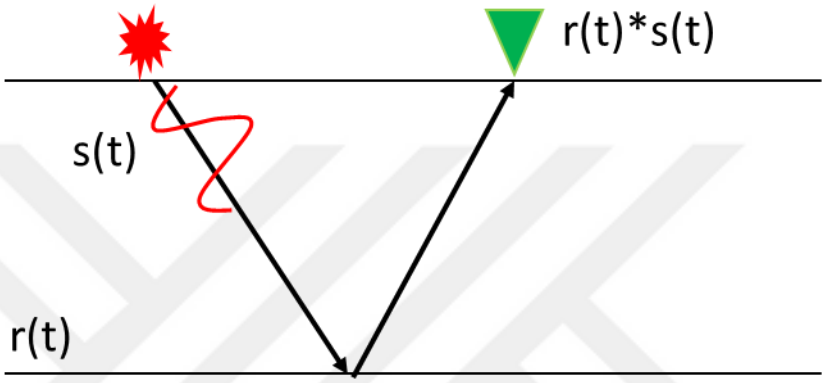

Figure 9.2. An illustration of convolution of seismic reflection and wavelet. s(t) is wavelet, r(t) is reflection coefficient and r(t)*s(t) is the convolved signal reaching a receiver.

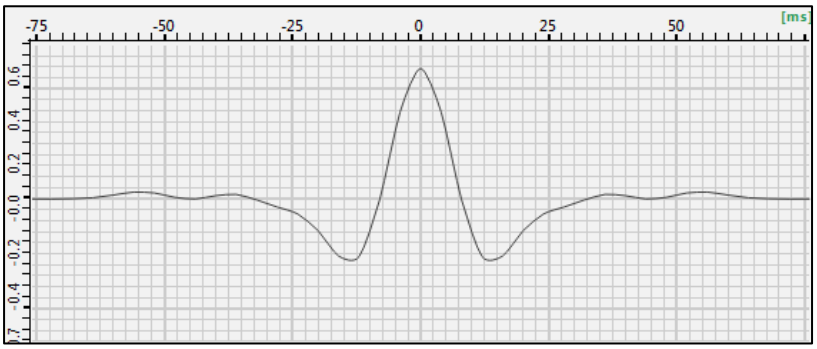

Figure 9.3. A statistical seismic wavelet extracted by autocorrelation of seismic traces.

When a proper wavelet is extracted, reflection coefficients are calculated as the formula below to represent suitable seismic traces (e.g., Morozov and Ma, 2009).

$$R_i = \frac{Z_{i+1} - Z_i}{Z_{i+1} + Z_i} \quad 9.1$$

where R is the zero offset P wave reflectivity, i is the related layer, and Z is the acoustic impedance which is:

$$Z_i = V_{pi} * \rho_i \quad 9.2$$

where Vp is the P-wave velocity and ρ is the density at i^{th} layer.

To correlate well logs and seismic reflections, synthetic gathers are created using well logs to match with real seismic data. Using P-sonic and density logs, acoustic impedances of each layer are calculated (Equation 9.2). Then, using Equation 9.1, reflection coefficients are computed. Log measurements have higher resolution compared to seismic data. Therefore, log data should be upscaled into seismic resolution. To achieve this, obtained coefficients are convolved with a seismic wavelet extracted from seismic data to upscale log measurements (Figure 9.4).

A composite line for each well group was generated. The map views of each line are given in Figure. 9.4. After generation of these composite lines for each well group, displays of corelated real seismic stack data and synthetics calculated from well logs are illustrated for well group-1, 2 and 3 in Figure 9.5, 9.6 and 9.7, respectively.

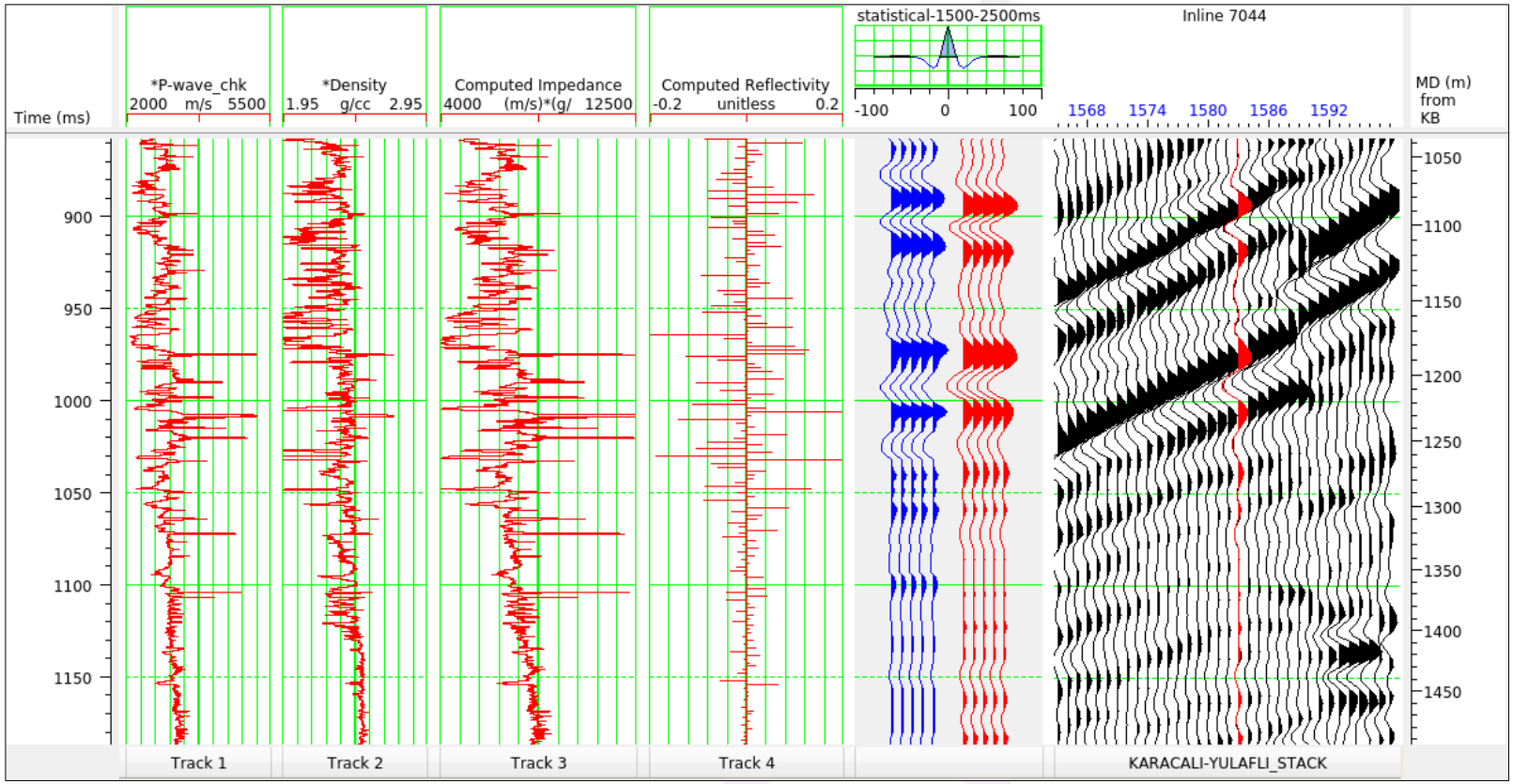

Figure 9.4. Well correlation window for Well-21. From left to right: P-sonic log, density log, computed impedances, computed reflectivities, synthetic traces (blue colored), extracted composite traces from seismic data and seismic section are displayed. Synthetic and real data show a clear match after well-to-seismic tie process.

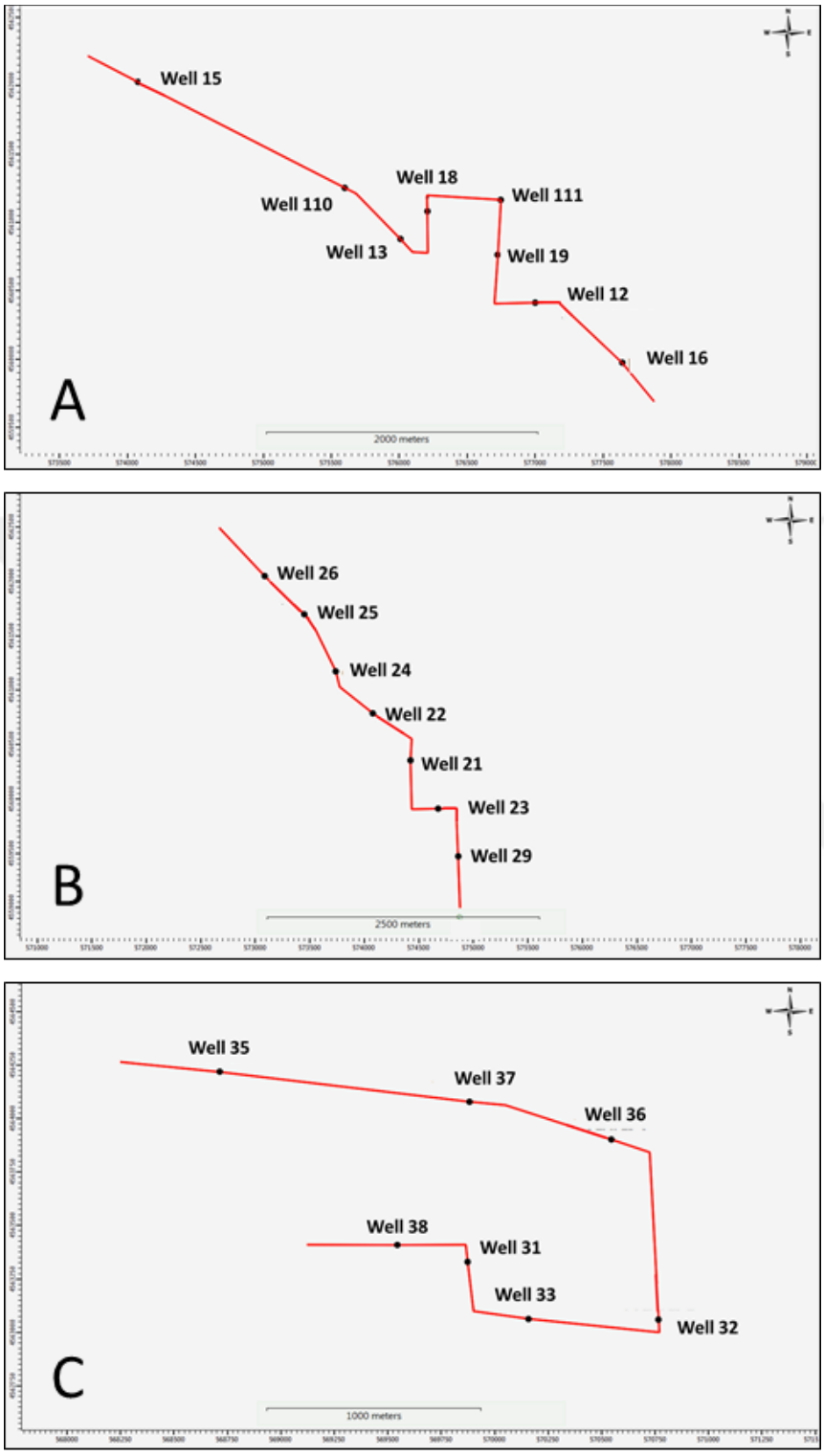

Figure 9.5. Composite line views of (A) well group 1, (B) well group 2 and (C) well group 3.

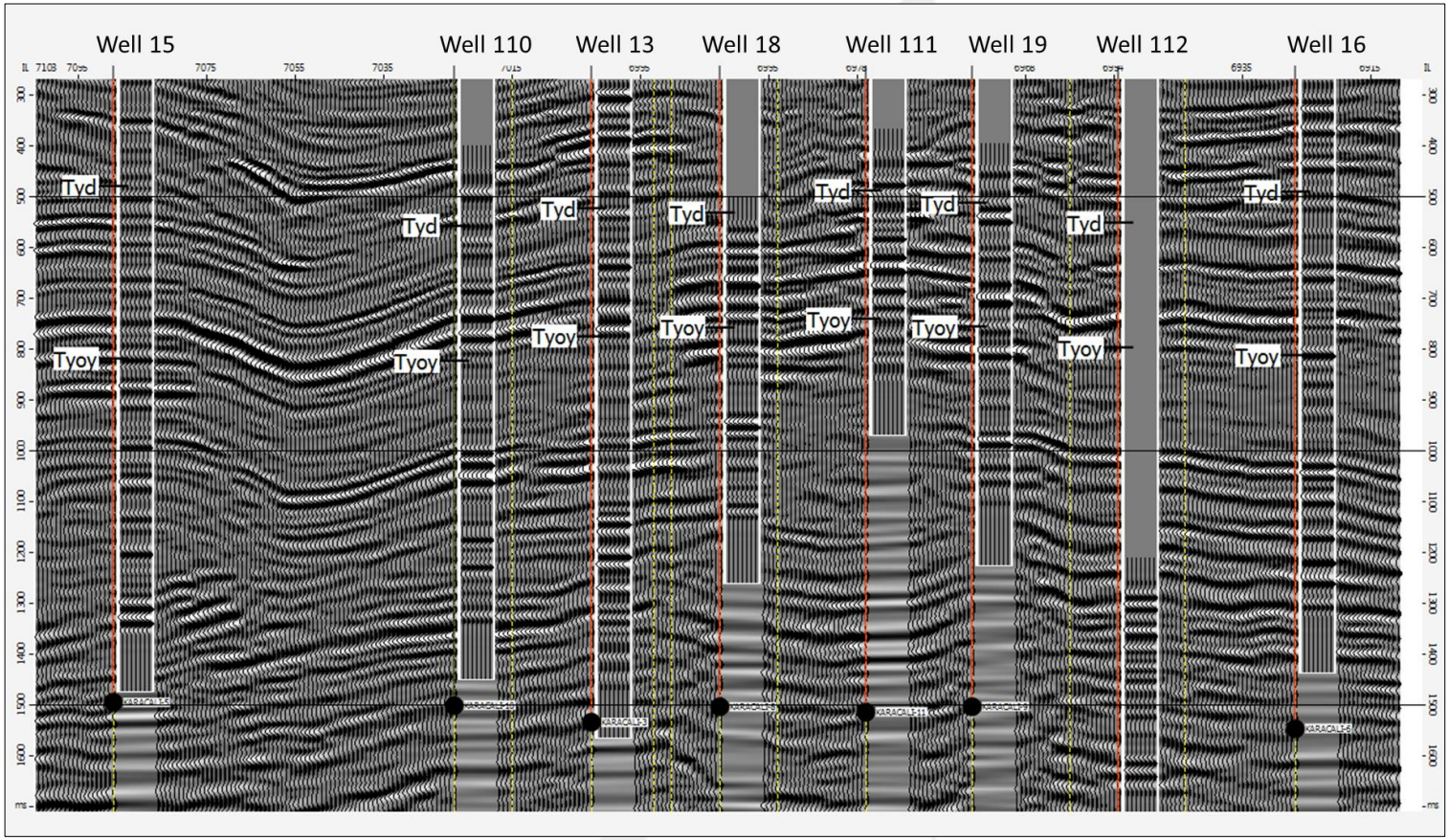

Figure 9.6. Correlation between synthetic traces obtained from logs and real seismic data for well group 1 composite section (see Figure 9.5 A) are given. Traces along the wellbores represent synthetic traces and rest of the data are real one. There is a high correlation between real and synthetic traces.

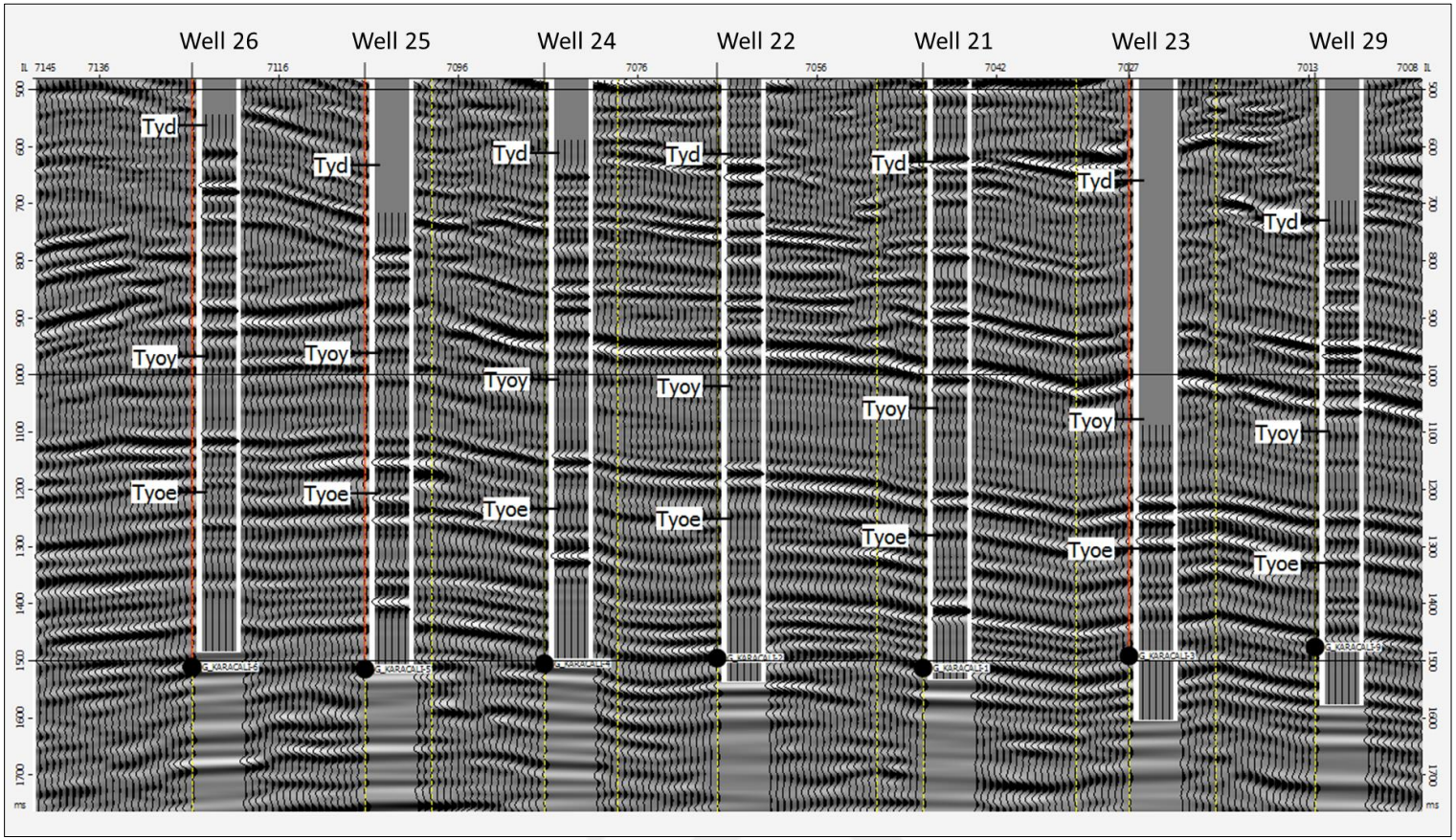

Figure 9.7. Correlation between synthetic traces obtained from logs and real seismic data for well group 2 composite section (see Figure 9.5 B) are given. Traces along the wellbores represent synthetic traces and rest of the data are real one. There is a high correlation between real and synthetic traces.

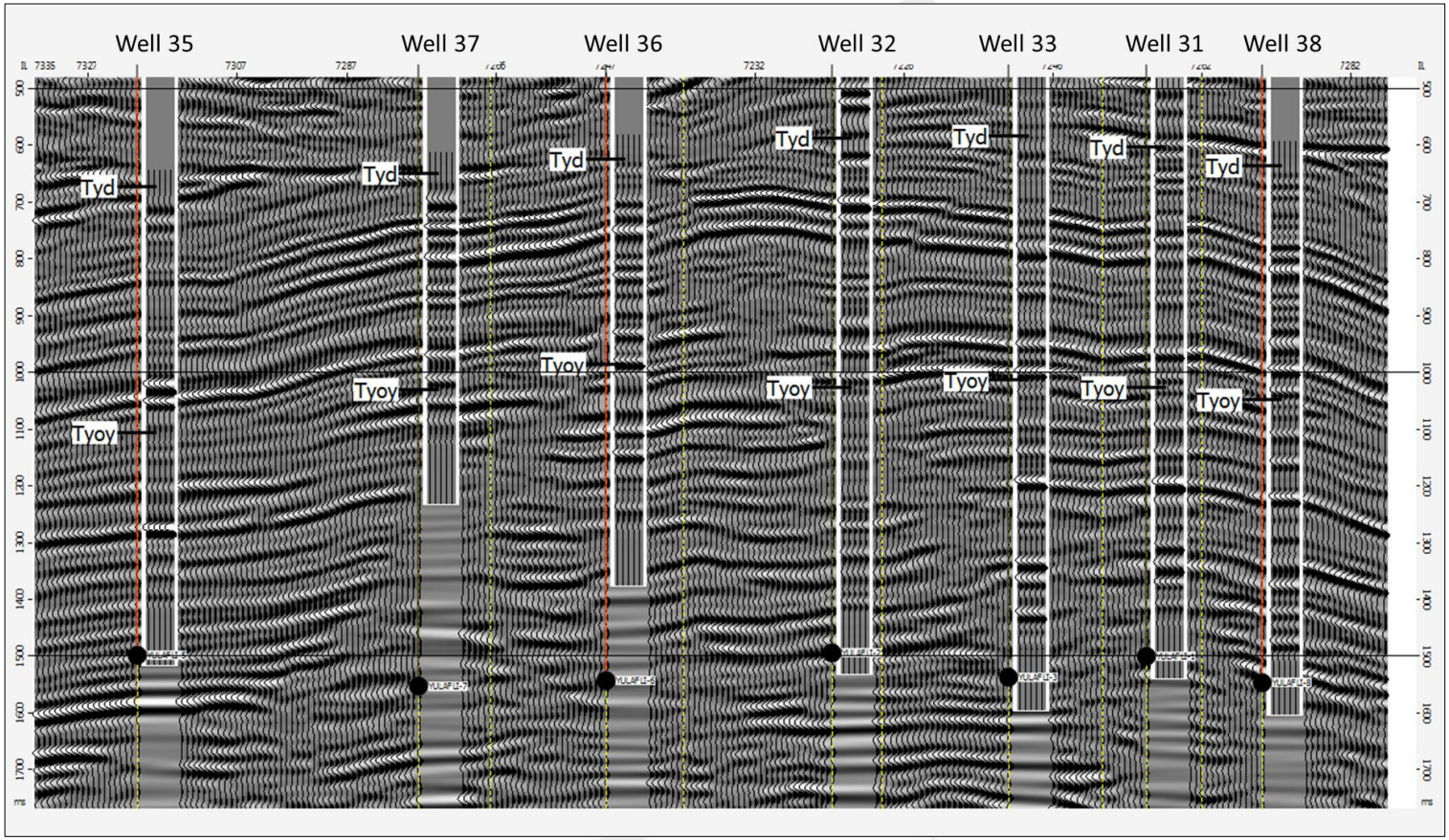

Figure 9.8. Correlation between synthetic traces obtained from logs and real seismic data for well group 3 composite section (see Figure 9.5 C) are given. Traces along the wellbores represent synthetic traces and rest of the data are real one. There is a high correlation between real and synthetic traces.

9.2.2 Fault and Horizon Interpretation

The north branch of the Terzili Fault Zone (TFZ) splay (Turgut et al., 1991) divides the field into two halves. Antithetic and synthetic faults of the north branch of the TFZ are frequently observed on the Karaçalı-Yulaflı field, which results in tectonically very complex area.

To reveal structural geometry of the field, firstly, faults were interpreted. During interpretation, chaos attribute which is also a type of structural attribute was utilized Chaos attribute is defined as a measure of chaotic texture within seismic data. It is a dip and azimuth estimation method and can be used to identify reflector distribution such as faults and discontinuous surfaces (Koson et al., 2014).

Fault interpretation was followed by horizon interpretation of formation tops. The entrance of three formations; named as Danişmen, Osmancık and Mezardere Formations and a level inside Osmancık Formation representing almost top of deeper Osmancık Formation were interpreted. Horizons and faults were interpreted every 10 inline and crossline except Osmancık Formation. Because this formation is the ultimate target in this research, the top of the formation was picked in every 5 inline and crossline for a more detailed study. Randomly selected inline sections from west to east direction and interpretation displays are given in Figure from 9.9 to 9.12.

Fault planes on a base map including main and all faults are given in Figure 13 A and B. The main faults are observed from west to east direction of the field. Additionally, horizon picks, and grids obtained by the interpolation of these horizons are indicated in Figure 14. Within the boundary of Karaçalı-Yulaflı Field (Fig 14 B), the entrance of the Osmancık Formation rises up through the middle-east region of the field and is trapped with the main faults resulting in prospective and producing reservoirs around the location of group-1 wells.

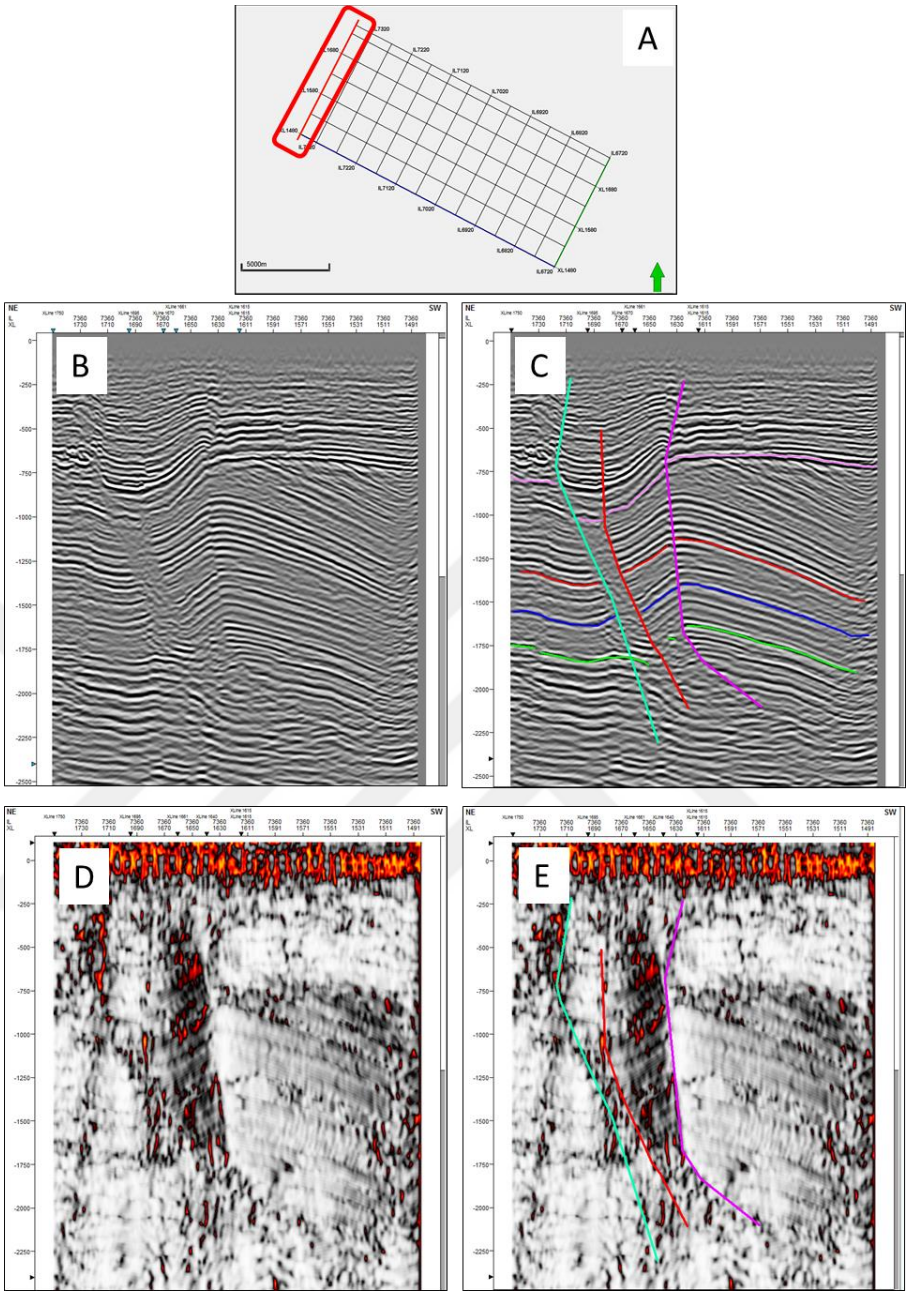

Figure 9.9. Location map of the field indicating inline 7360 (red line), (B) seismic section without interpretation, (C) seismic section after fault and horizon interpretation, (D) chaos structural attribute and (E) chaos attribute with fault interpretation are shown. Green and red faults are north branches of Terzili Fault Zone. Purple horizon indicates the top of the Danişmen Formation, red one is the Osmancık Formation and green one is the Mezardere Formation. Blue horizon is a level inside deeper Osmancık Formation.

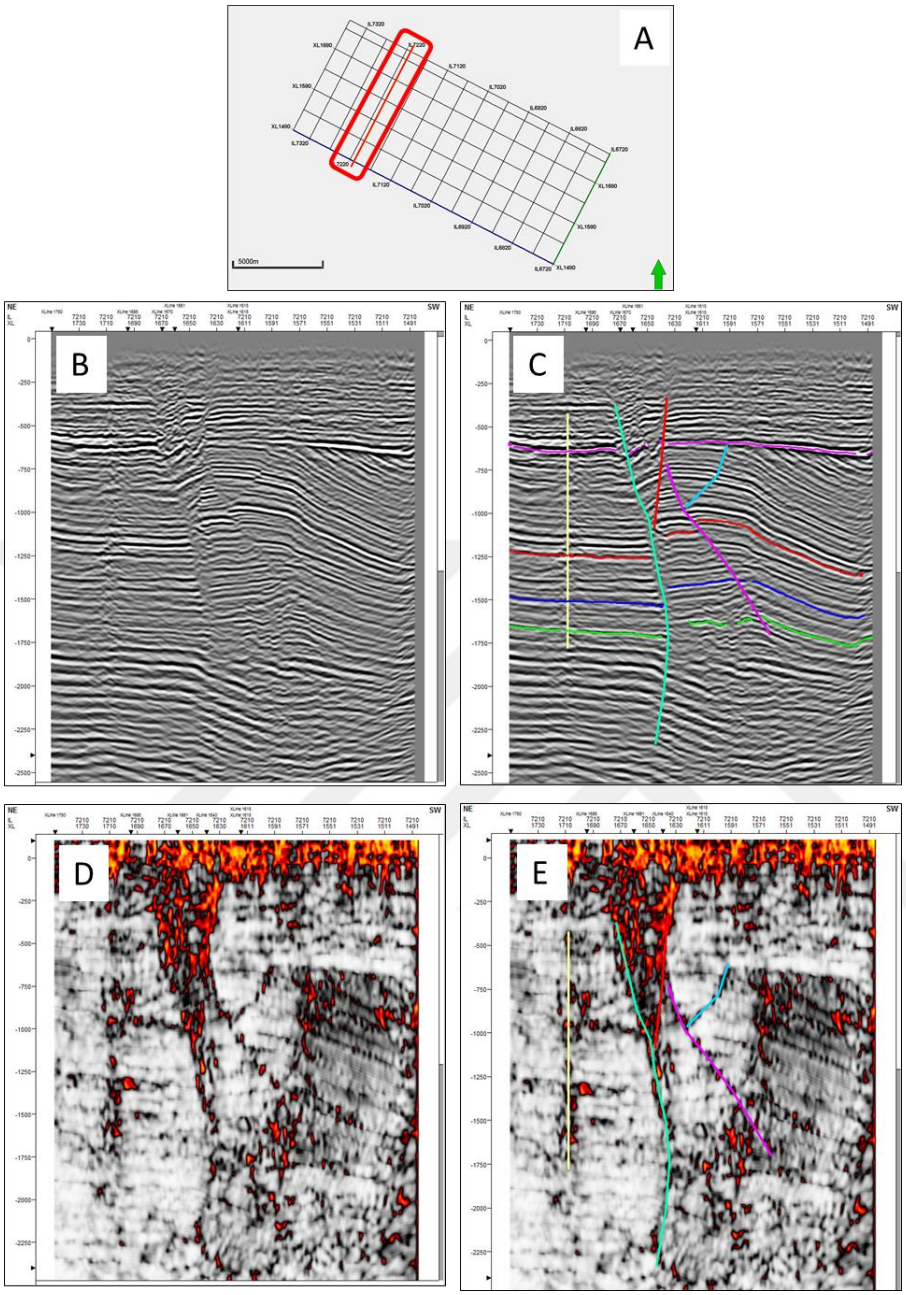

Figure 9.10. Location map of the field indicating inline 7210 (red line), (B) seismic section without interpretation, (C) seismic section after fault and horizon interpretation, (D) chaos structural attribute and (E) chaos attribute with fault interpretation are shown. Green and red faults are north branches of Terzili Fault Zone. Purple horizon indicates the top of the Danişmen Formation, red one is the Osmancık Formation and green one is the Mezardere Formation. Blue horizon is a level inside deeper Osmancık Formation.

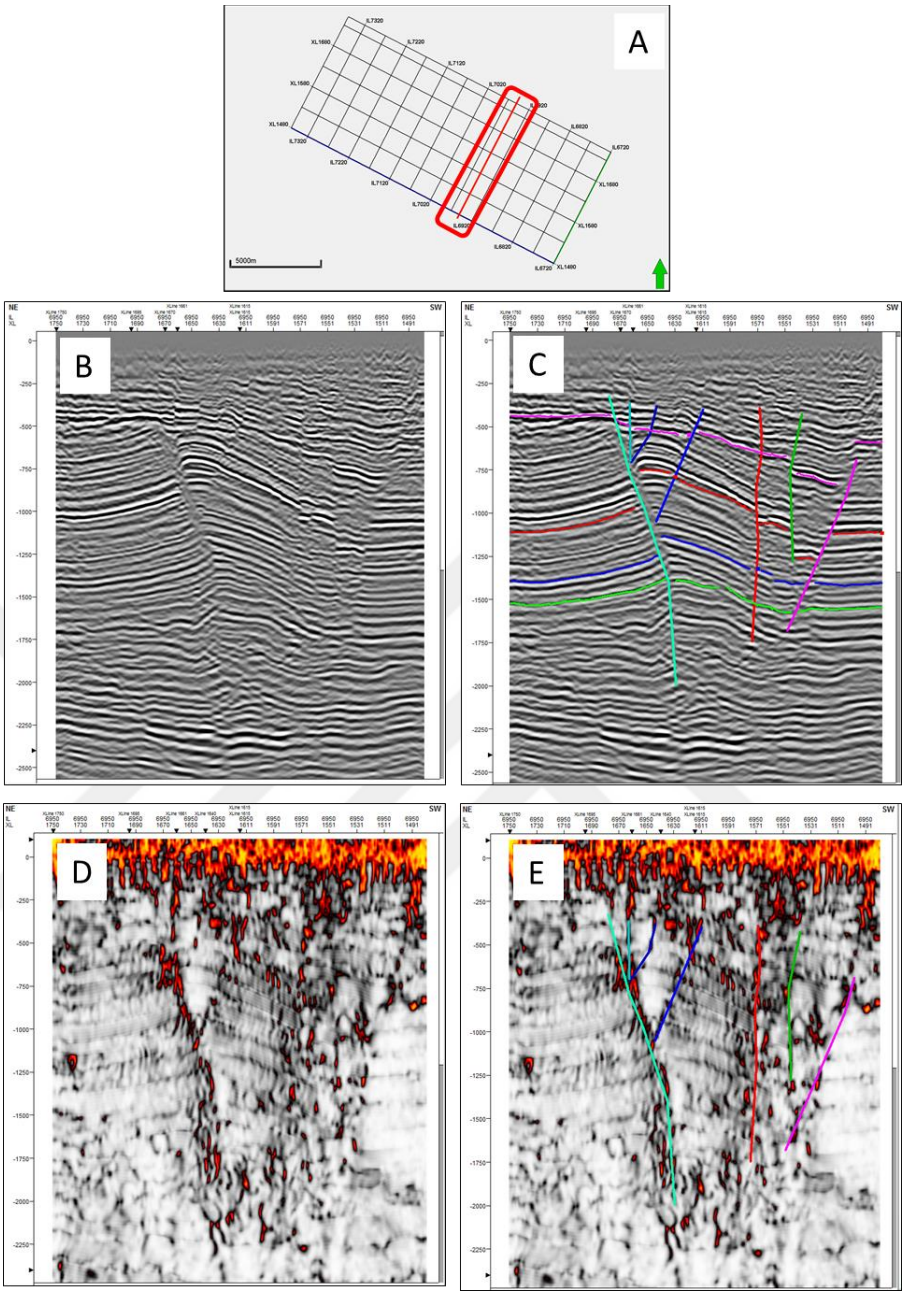

Figure 9.11. Location map of the field indicating inline 6950 (red line), (B) seismic section without interpretation, (C) seismic section after fault and horizon interpretation, (D) chaos structural attribute and (E) chaos attribute with fault interpretation are shown. Green and red faults are north branches of Terzili Fault Zone. Purple horizon indicates the top of the Danişmen Formation, red one is the Osmancık Formation and green one is the Mezardere Formation. Blue horizon is a level inside deeper Osmancık Formation.

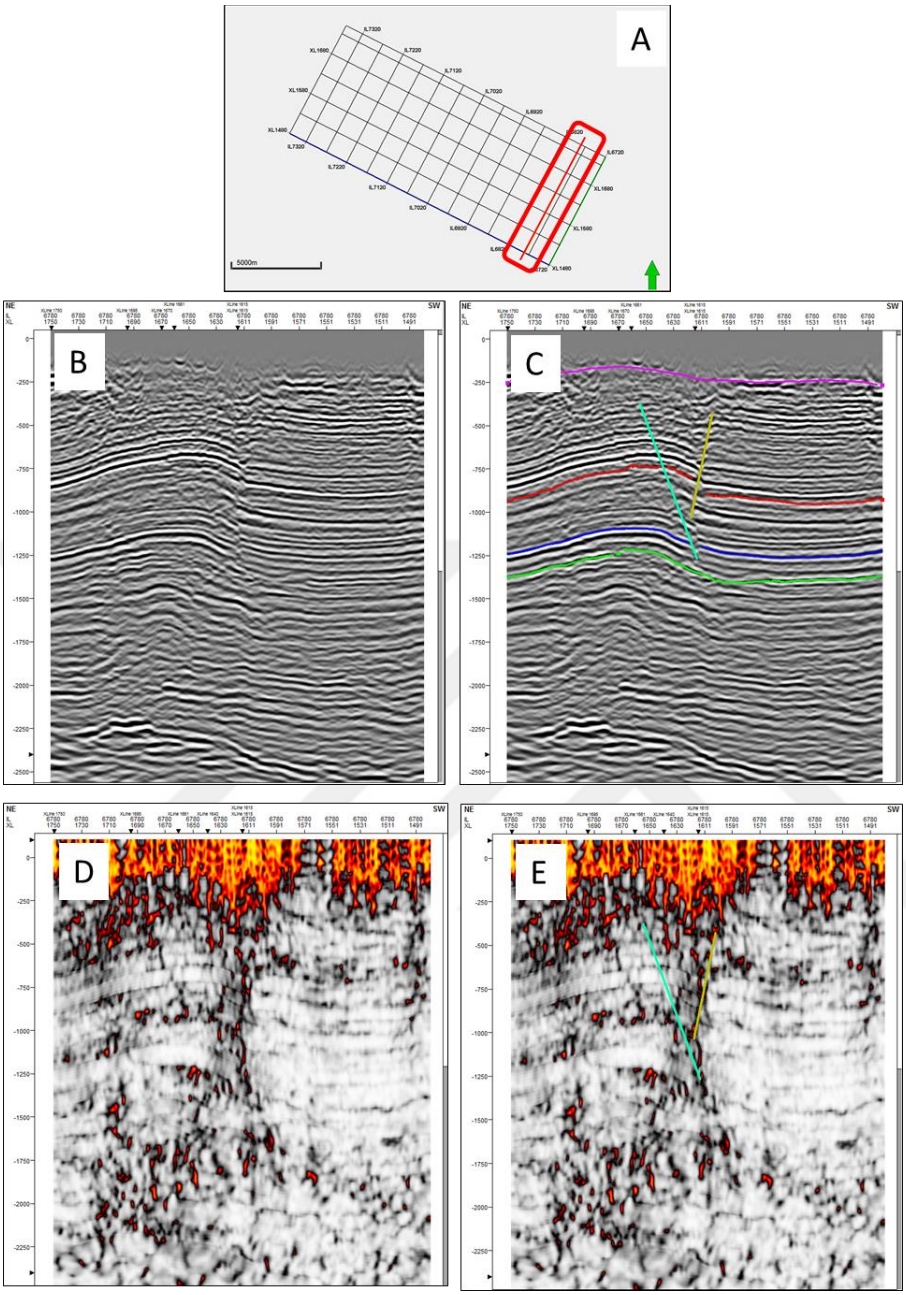

Figure 9.12. Location map of the field indicating inline 6950 (red line), (B) seismic section without interpretation, (C) seismic section after fault and horizon interpretation, (D) chaos structural attribute and (E) chaos attribute with fault interpretation are shown. Green and red faults are north branches of Terzili Fault Zone. Purple horizon indicates the top of the Danişmen Formation, red one is the Osmancık Formation and green one is the Mezardere Formation. Blue horizon is a level inside deeper Osmancık Formation.

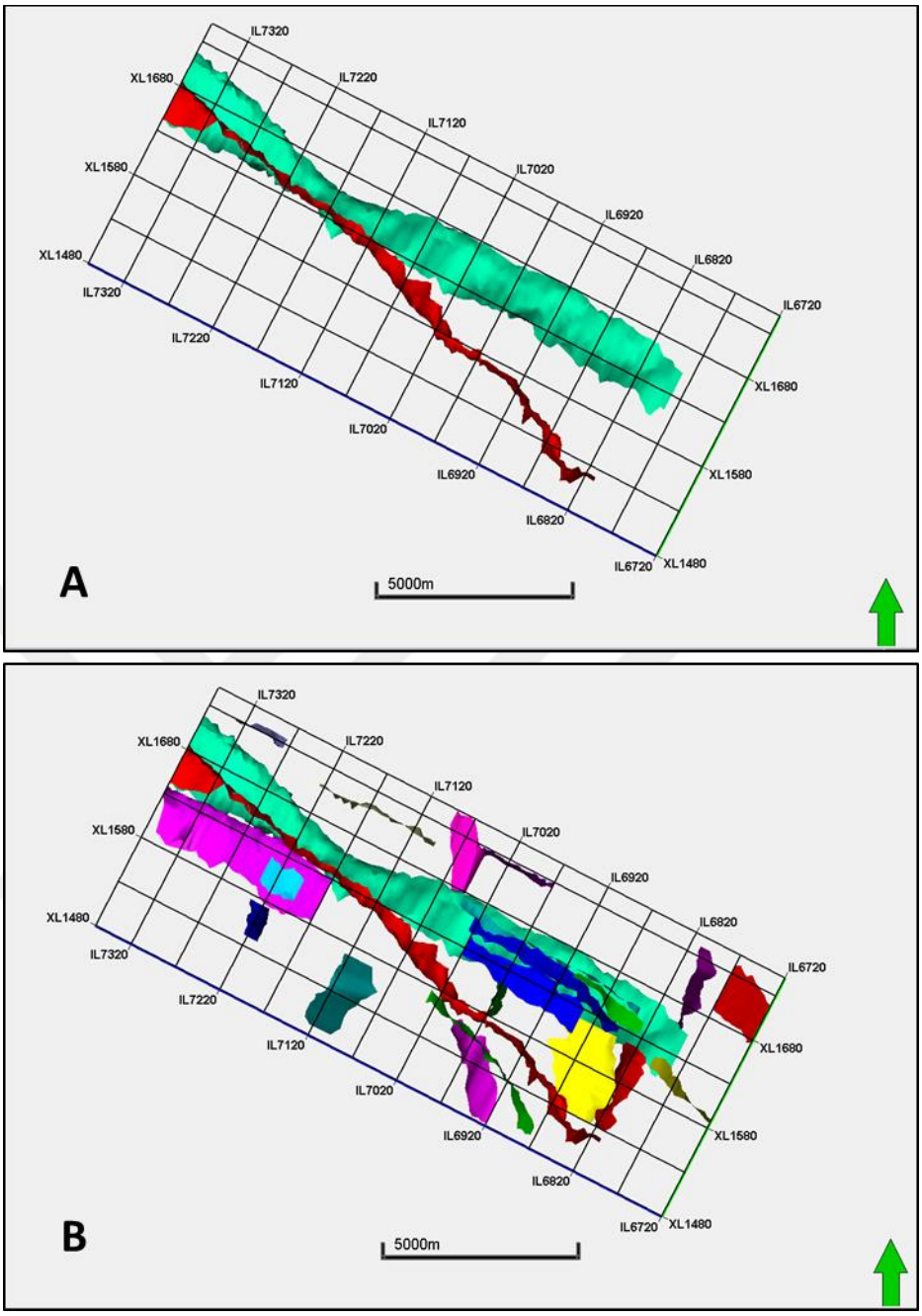

Figure 9.13. (A) Main fault plains on a base map and (B) all picked faults together are seen in this figure. Main faults are the north branches of Terzili Fault Zone.

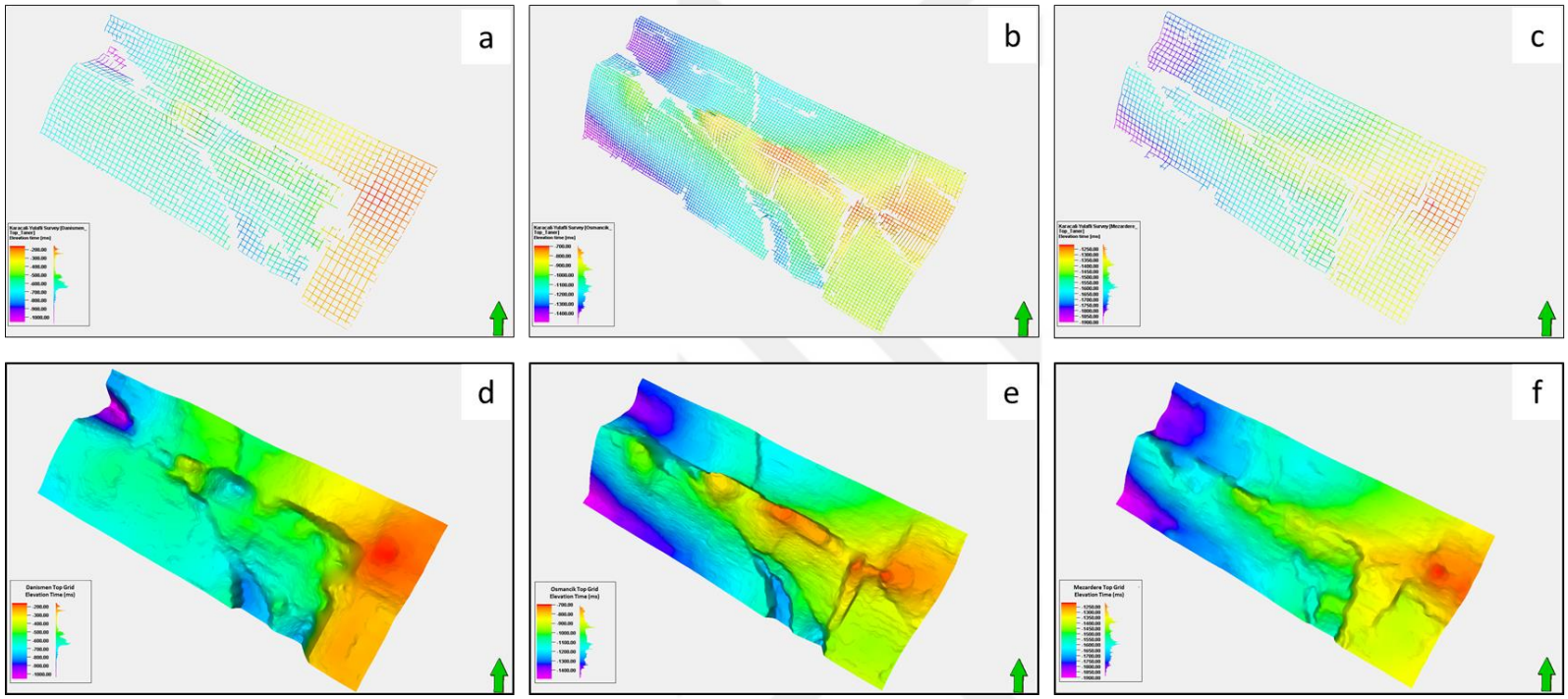

Figure 9.14. Horizon picks of (a) Danişmen, (b) Osmancık, (b) Mezardere and grids of (d) Danişmen, (e) Osmancık, (f) Mezardere Formations are illustrated. Note that the intensity of picked horizon for the Osmancık Formation is greater. Red colors show the shallowest time ranges while purple one indicates deeper areas in time.

9.2.3 Velocity Model Building and Time to Depth Conversion

Traveling of a seismic wave can be measured as a function of travel time. Because of its nature, Seismic data is measured in time scale. To obtain relative depths of the reflections, a velocity model should be built. There are several methods to generate a velocity model. One could be using directly "root mean square velocities" calculated during seismic processing. These may be useful to evaluate general depth variations; however, exact depths cannot be estimated by this way. Another way is the use of the combination of well logs with these RMS velocities. Embedded measured sonic logs into velocity lead to generate more reliable velocity distribution of the field. Well-to-seismic tie summarized in previous section enables the correlate time and depth domain between seismic reflections and well logs. Generated velocity model from the combination of seismic and log data on formation surfaces are illustrated in Figure 9.15. A well-known and simple equation can be used to calculate surfaces in depth domain, which is a function of velocity and travel time given below:

$$X = V * t \qquad 9.3$$

where X is the converted depth, V is the velocity in m/sec and t is two-way travel time in sec. The resulted surfaces in depth domain are demonstrated in Figure 9.16. Additionally, interpreted faults in time domain should be converted into depth scale using the same equation (Equation 9.3). A merged display of interpreted horizons and faults are given in Figure 9.17.

9.2.4 Structural Model Building

The last step of the qualitative interpretation for this research is building a structural model in depth domain. For this research, the main purpose of the structural model is to generate an initial input for facies and petrophysical modeling. Using formation surfaces and fault framework, a depth-related structural model was created. Each zone in this model and a complete model display is illustrated in Figure 9.18.

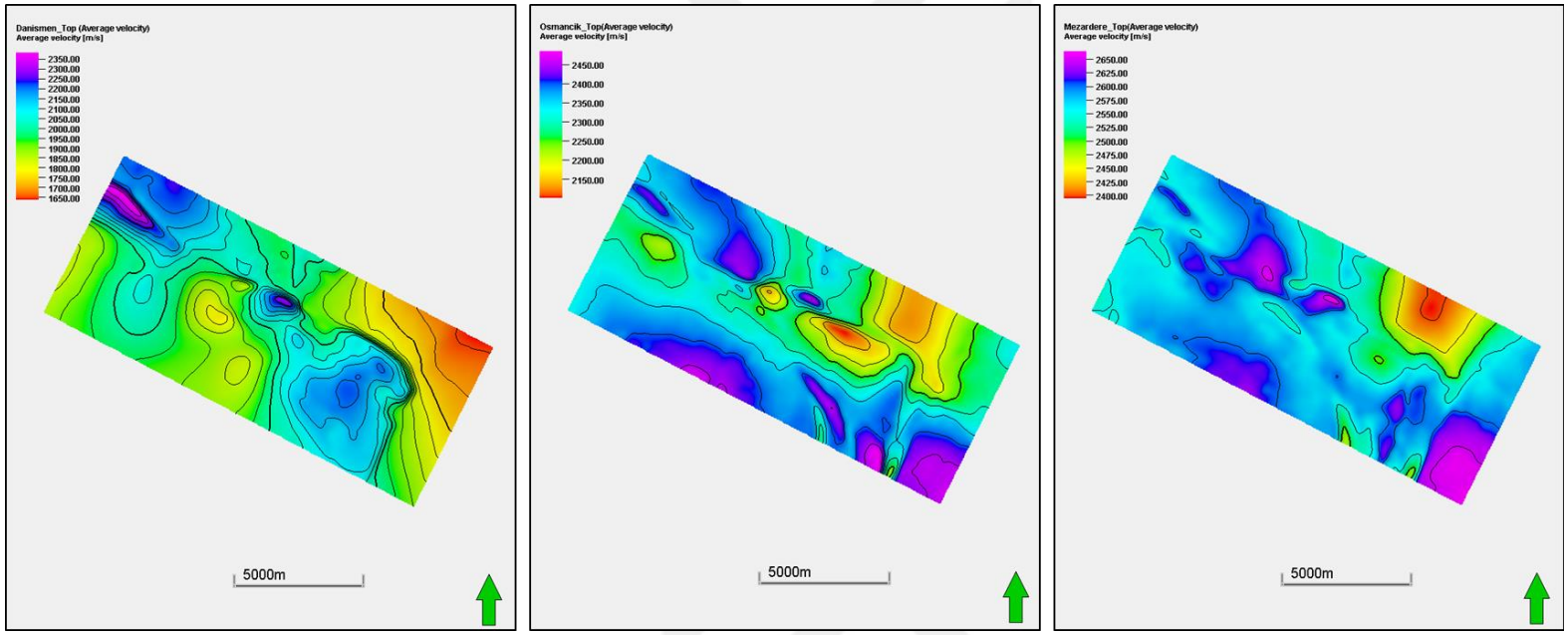

Figure 9.15. Average velocities for each formation surface. From left to right; average velocities of the Danişmen, Osmancık and Mezardere Formation tops are given. Red color indicates lower velocities and purple color is higher ones. The surfaces were contoured in every 50 m/s.

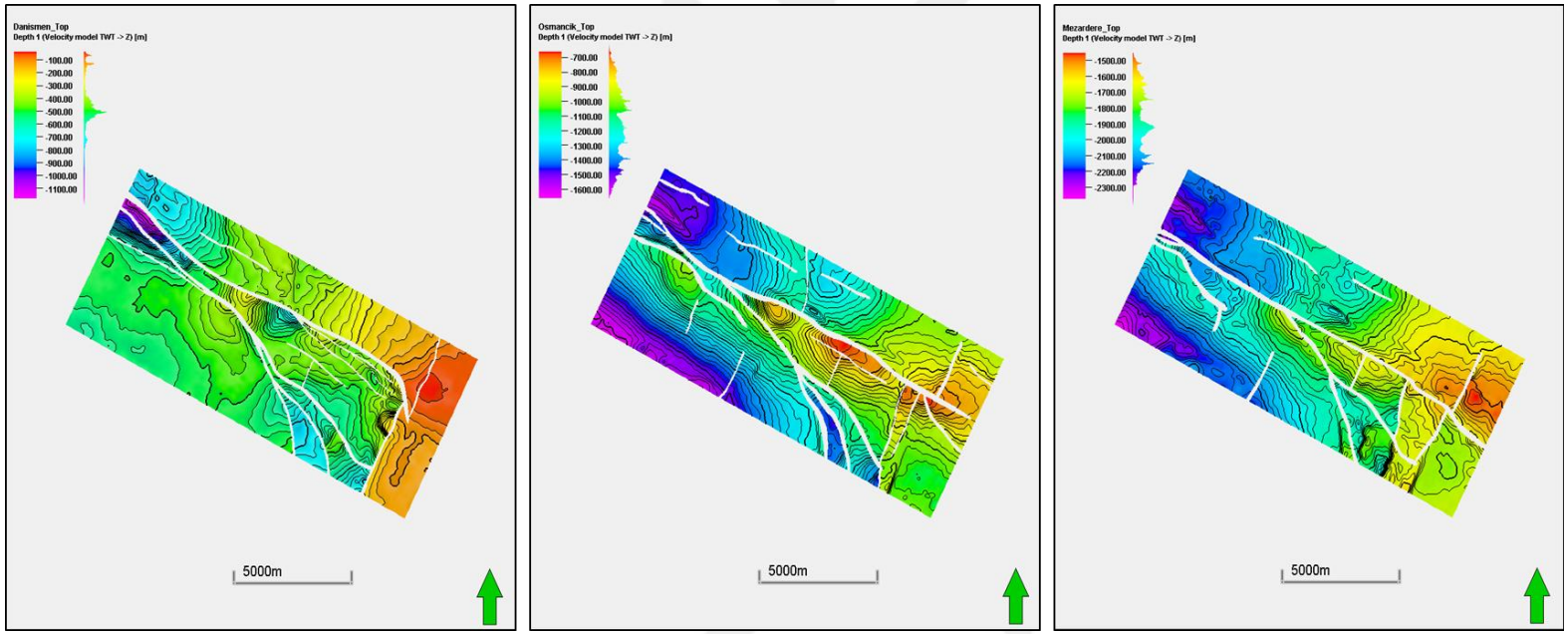

Figure 9.16. Danişmen (left), Osmancık (middle) and Mezardere (right) top surfaces in depth. The unit is meter. White lines show faults.

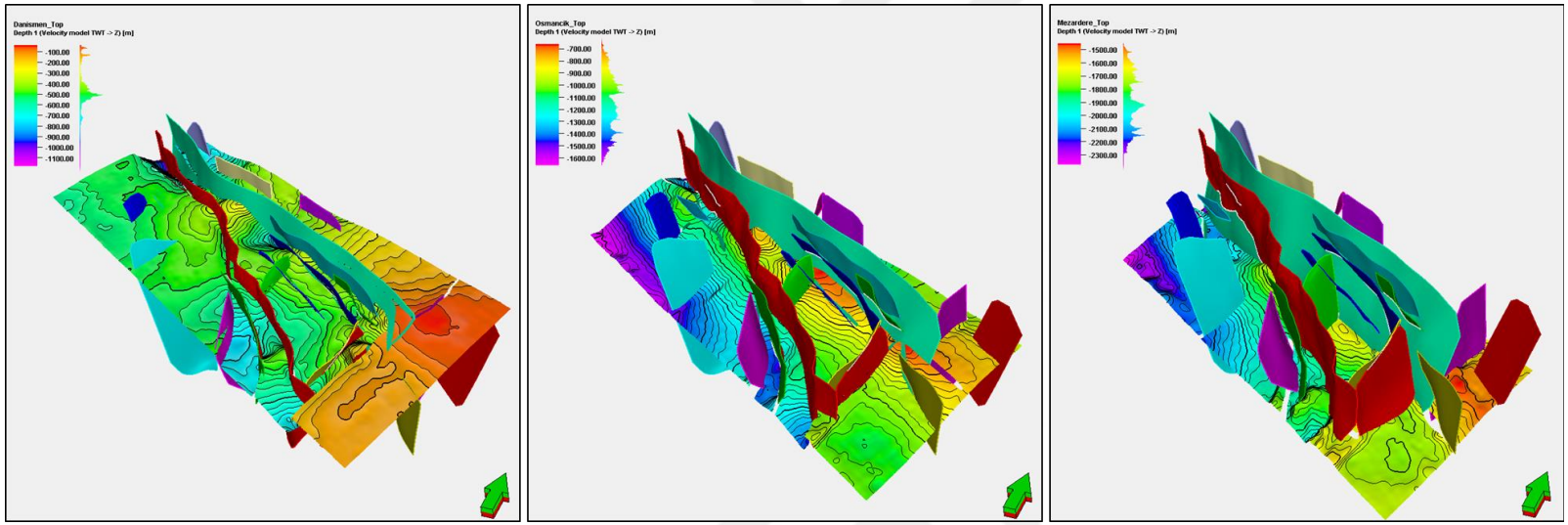

Figure 9.17. This figure demonstrates converted faults in depth domain. From left to right; Danişmen, Osmancık and Mezardere formation surfaces (in depth) were embedded.

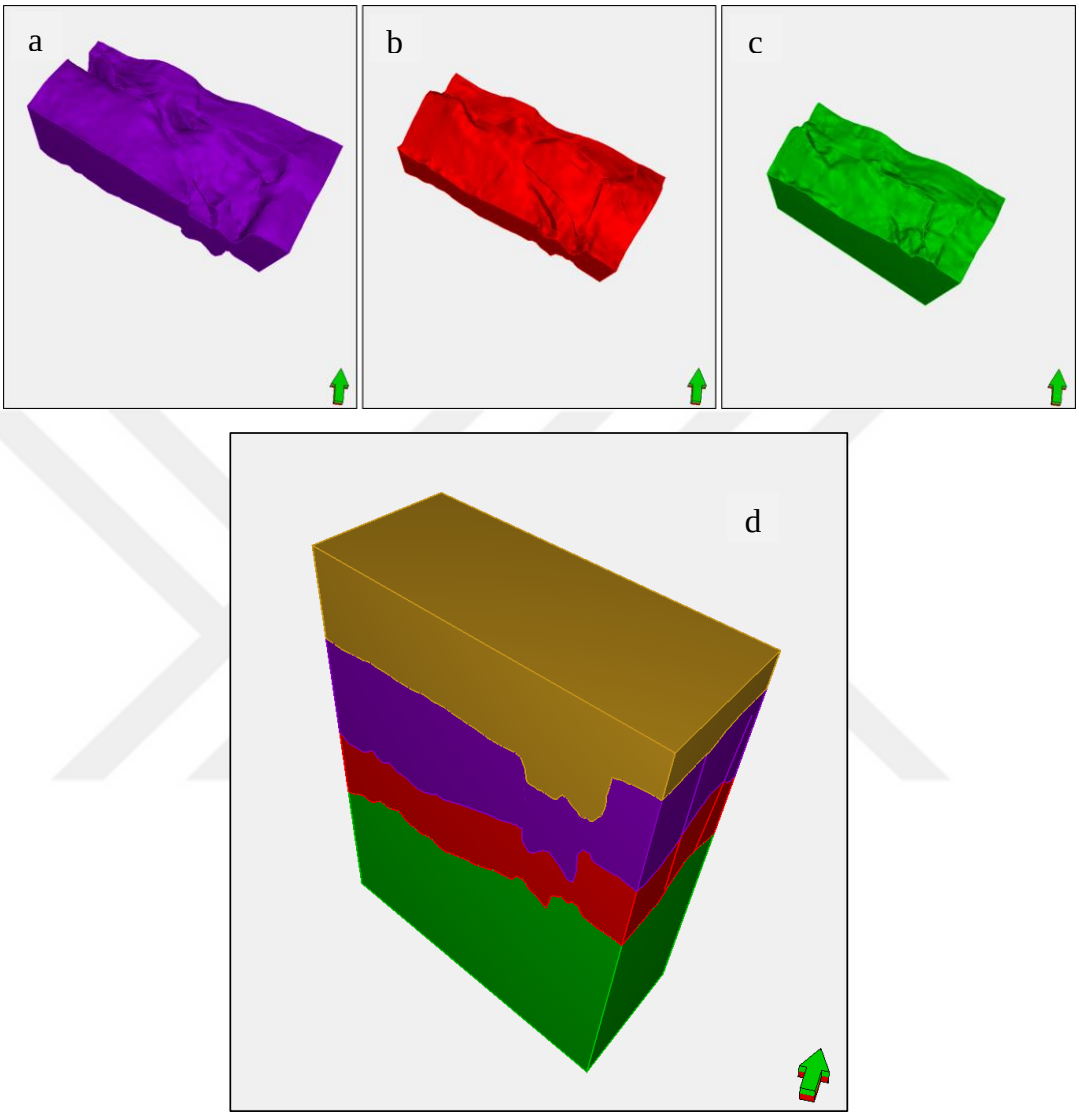

Figure 9.18. Zones of created structural model (from left to right; the Danişmen (a), Osmancık (b) and Mezardere (c) Formations) and the whole display (d) of this model are given. Faulting structures are clearly identified.

9.3 Quantitative Seismic Interpretation

Quantitative seismic inversion, referred as reservoir geophysics as well, is a widely used method to reveal reservoir properties and fluid indications of a formation. Many aspects are available in this technique. Amplitude-versus-offset (AVO), pre-stack seismic inversion and application of neural network to understand reservoir properties are mainly utilized in this research. To implement these methodologies, seismic and log data are necessary to be conditioned.

9.3.1 Seismic Data Preconditioning

Pre-stack seismic gathers are used for the application reservoir geophysics techniques. This type of data has a lower signal-to-noise ratio compared to stack seismic data used in qualitative interpretation. To obtain more reliable and robust results, seismic data should be conditioned before implementation of the relative techniques.

In the theory of seismic techniques, all available reflections are assumed as horizontal while reflectors are shifted residually in reality. To flatten the gathers, two approaches may be utilized such as velocity- and statics-based (Singleton, 2009). In this study, a statics-based method called as “trim statics” was benefited. The CDP gathers before and after flattening process are given in Figure 9.19. Another method used for eliminate parabolic noises is “parabolic radon transform”. Unwanted noises especially in far offsets were eliminated as it is illustrated in Figure 9.20.

Because CDP gathers are sorted to offsets, amplitude variations with angles should be calculated using RMS velocities (Figure 9.21). Angle gathers and angle stacks are the main inputs for pre-stack seismic inversion method. Since we need to know the angle of the traces, a relationship between angle, time, and amplitudes is required. A relationship between velocity and angle could be revealed by using iterative ray tracing by means of Snell Law which is given below:

$$\frac{\sin\theta_1}{V_1} = \frac{\sin\theta_2}{V_2} \qquad 9.4$$

9.3.2 Well Log Data Editing and Shar Wave Estimation

One of the main outputs for pre-stack seismic inversion is V_P/V_S ratio. While P-sonic log is measured at all wells, S-sonic log is rarely measured. S-velocity is calculated from other wells using a relationship between P-velocity and S-velocity from measured ones. In this area, three wells have measured S-sonic log. These wells are well-36, well-111 and well-112. From log measurements, while V_P/V_S ratios of well-36 and well-111 are between 2.4 and 3.0, this ratio is between 1.5 and 2.5 for well-112. This difference will cause an unbalanced distribution of elastic properties. To ensure which values are in a correct range, V_P/V_S ratio from surrounding wells were also compared to the wells which measured S-velocity is available in the field (Figure 9.22). The comparison shows that V_P/V_S ratio varies between 1.5 and 2.5, which also represents the theoretical ranges. Using all wells with measured S-velocities, P-S velocity cross-plots were generated and a relation was obtained for each (Figure 9.23). These cross-plots show that well-36 and well-111 have lower S velocities (Figure 9.24). Therefore, S-velocities were normalized an optimum range for these wells (Figure 9.25) with the equation below and the results were compared (Figure 9.26).

$$Norm_Log = Norm_Log_{min} + (Norm_Log_{max} - Norm_Log_{min}) * (Log - Log_{\min})/(Log_{max} - Log_{\min}) \qquad 9.5$$

where $Norm_Log$ is the normalized log curves and $Log_{\min}$ and Log_{max} are the minimum and maximum log values.

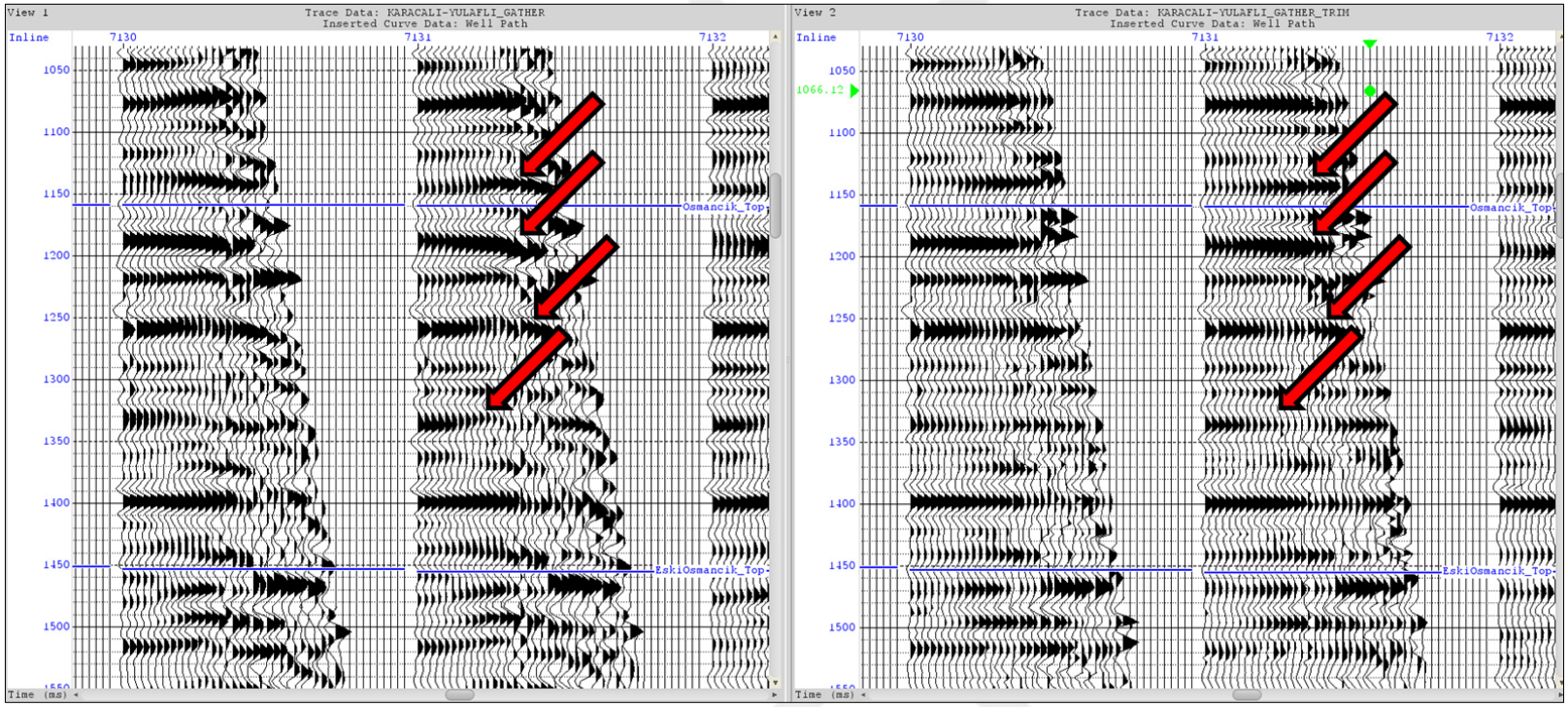

Figure 9.19. Raw offset gathers (on the left) are flatten (on the right) using trim statics.

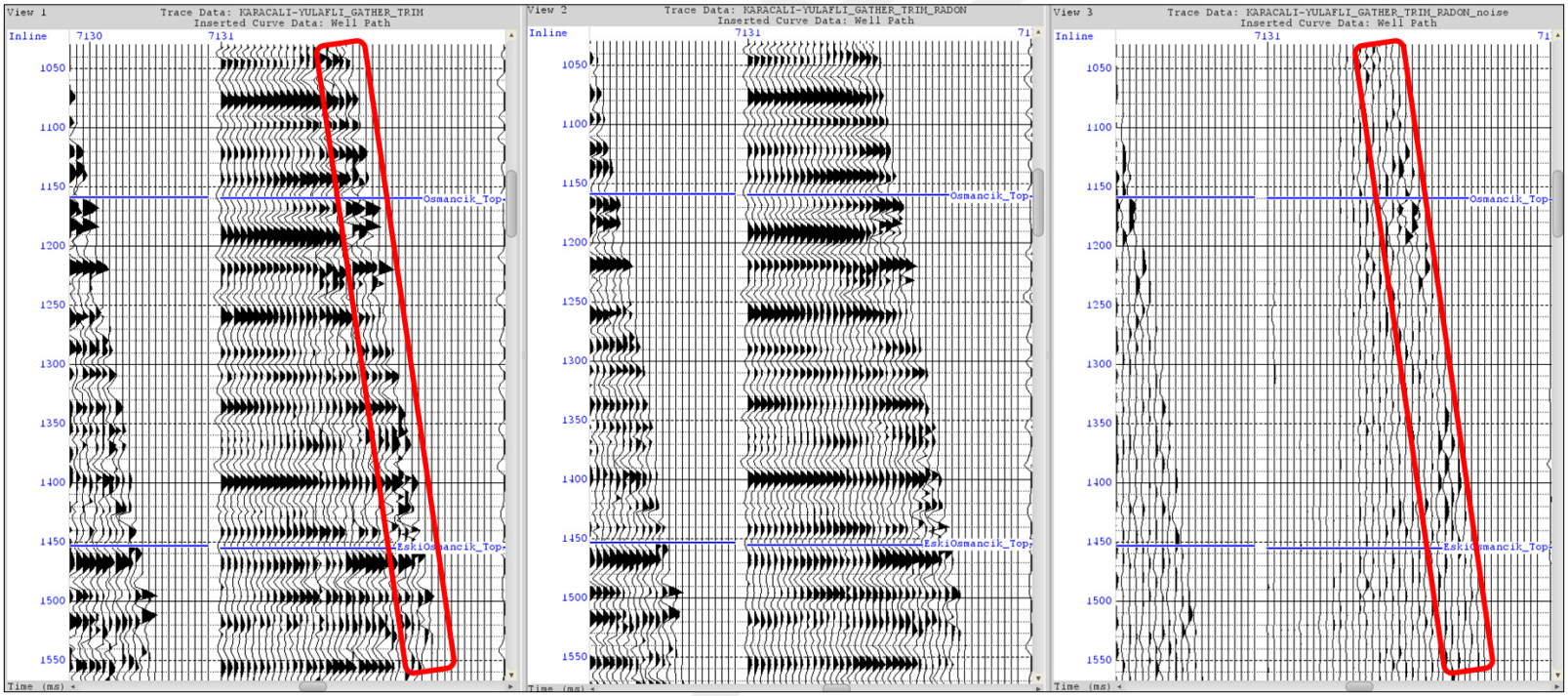

Figure 9.20. To increase signal to noise ratio, bad signals at far offsets were eliminated using parabolic radon transform. Offset gathers before parabolic radon transform (left), after the application of the process (middle) and eliminated random noises (right) are displayed on the right side of this figure.

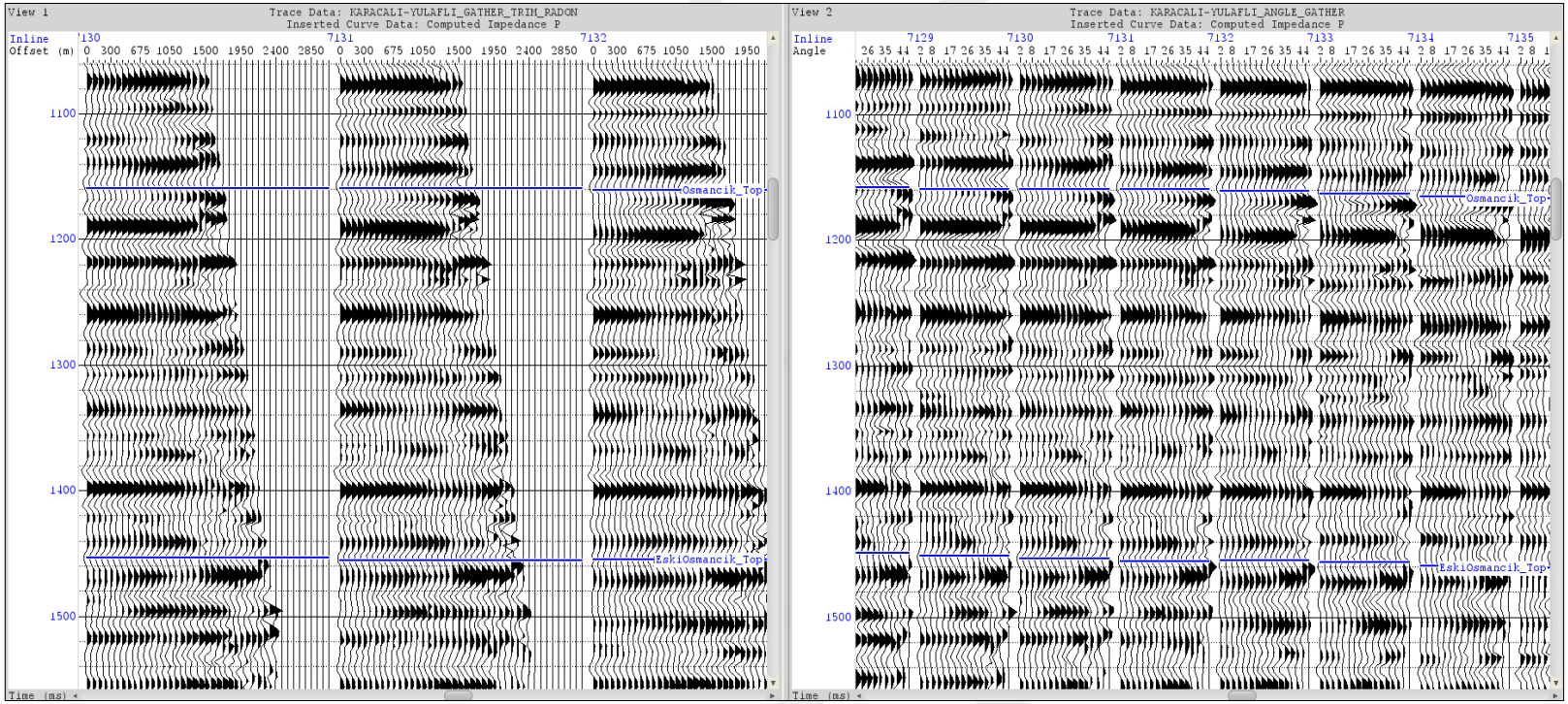

Figure 9.21. Using iterative ray tracing, offset dependent gathers were converted to angle dependent gathers. These angle gathers are used as AVO and pre-stack seismic input for seismic inversion.

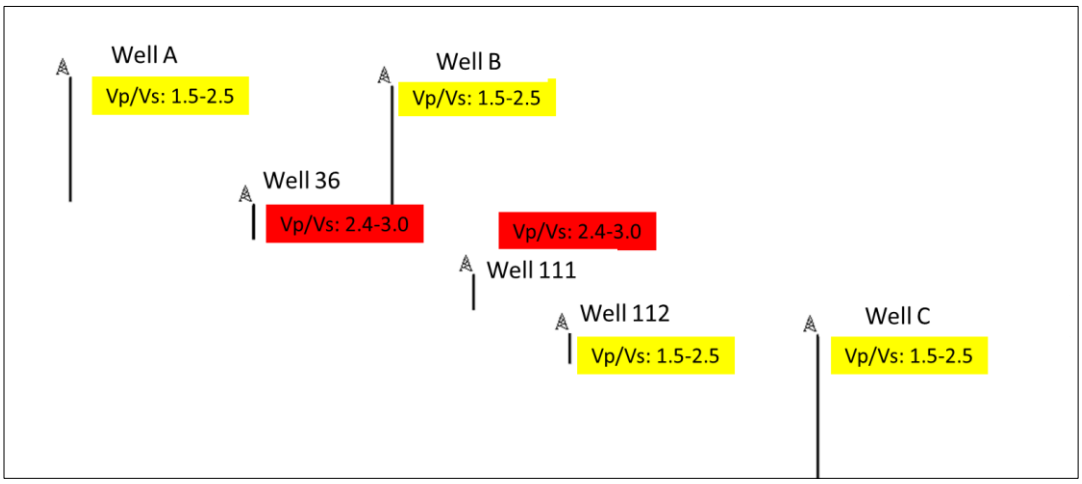

Figure 9.22. V_P/V_S ratio of the wells with measured S-velocity. Well A, B and C represent the wells from other fields. Surrounding wells confirm that the optimum ratio in the area changes from 1.5 to 2.5.

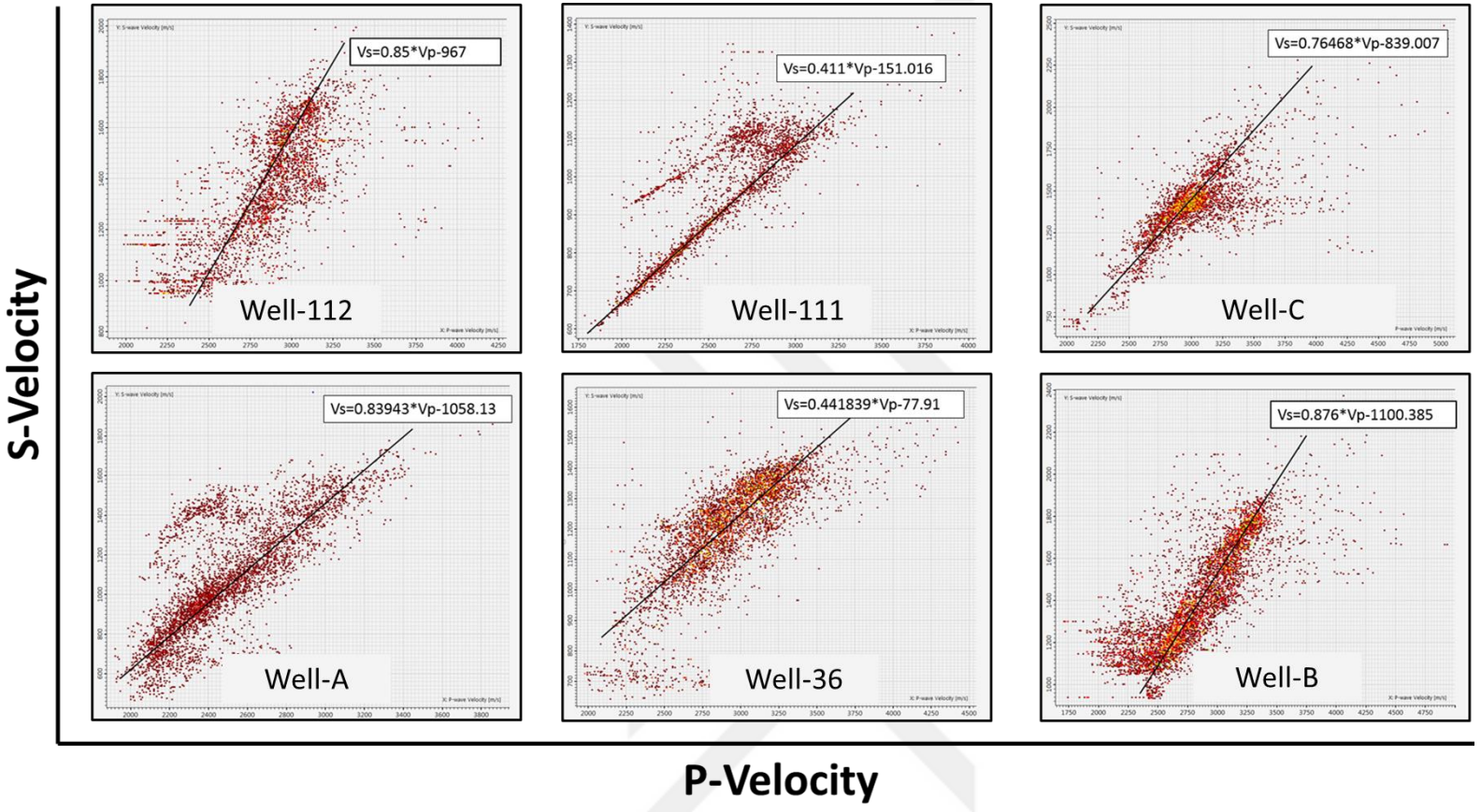

Figure 9.23. Mathematical relationships of P-wave versus S-wave velocities for each well are shown.

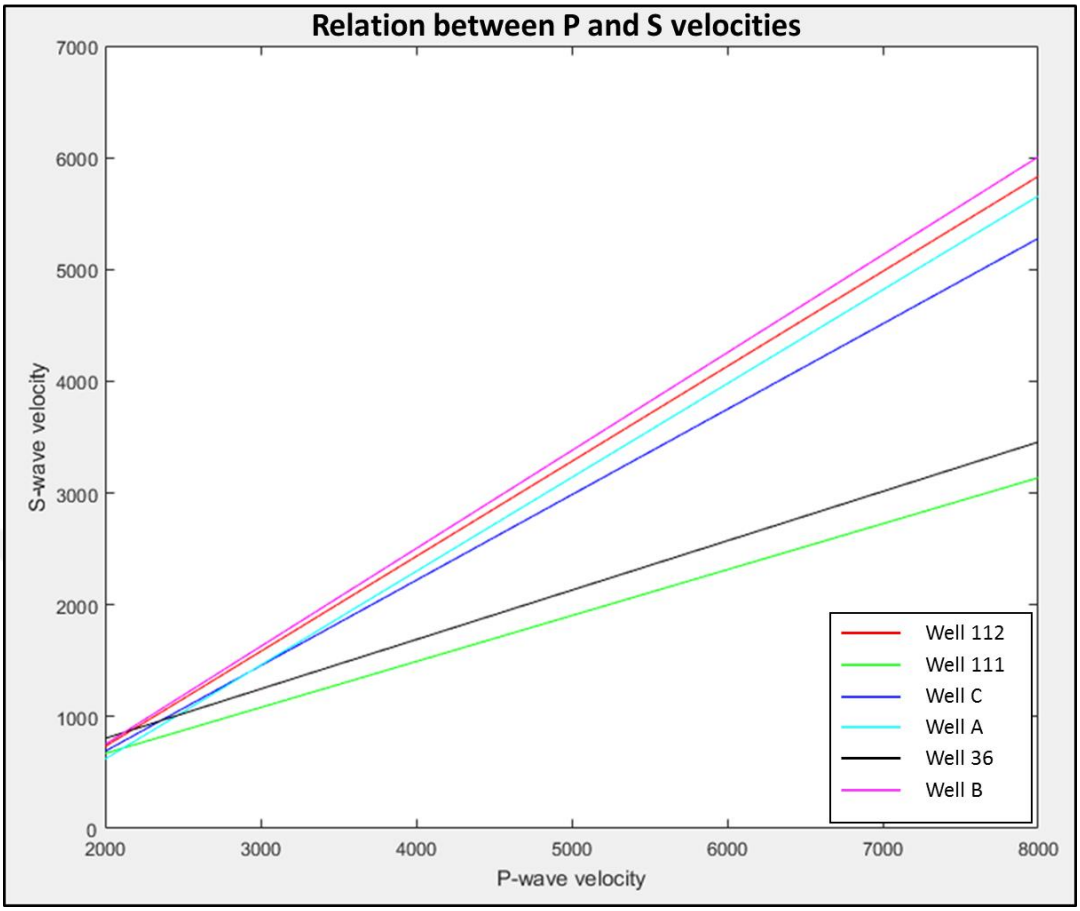

Figure 9.24. P-velocity versus S-velocity cross-plot of the wells used for comparison. Well-36 (black color) and Well-11 (green color) have lower S-velocities than the rest of the wells resulting higher V_P/V_S ratio.

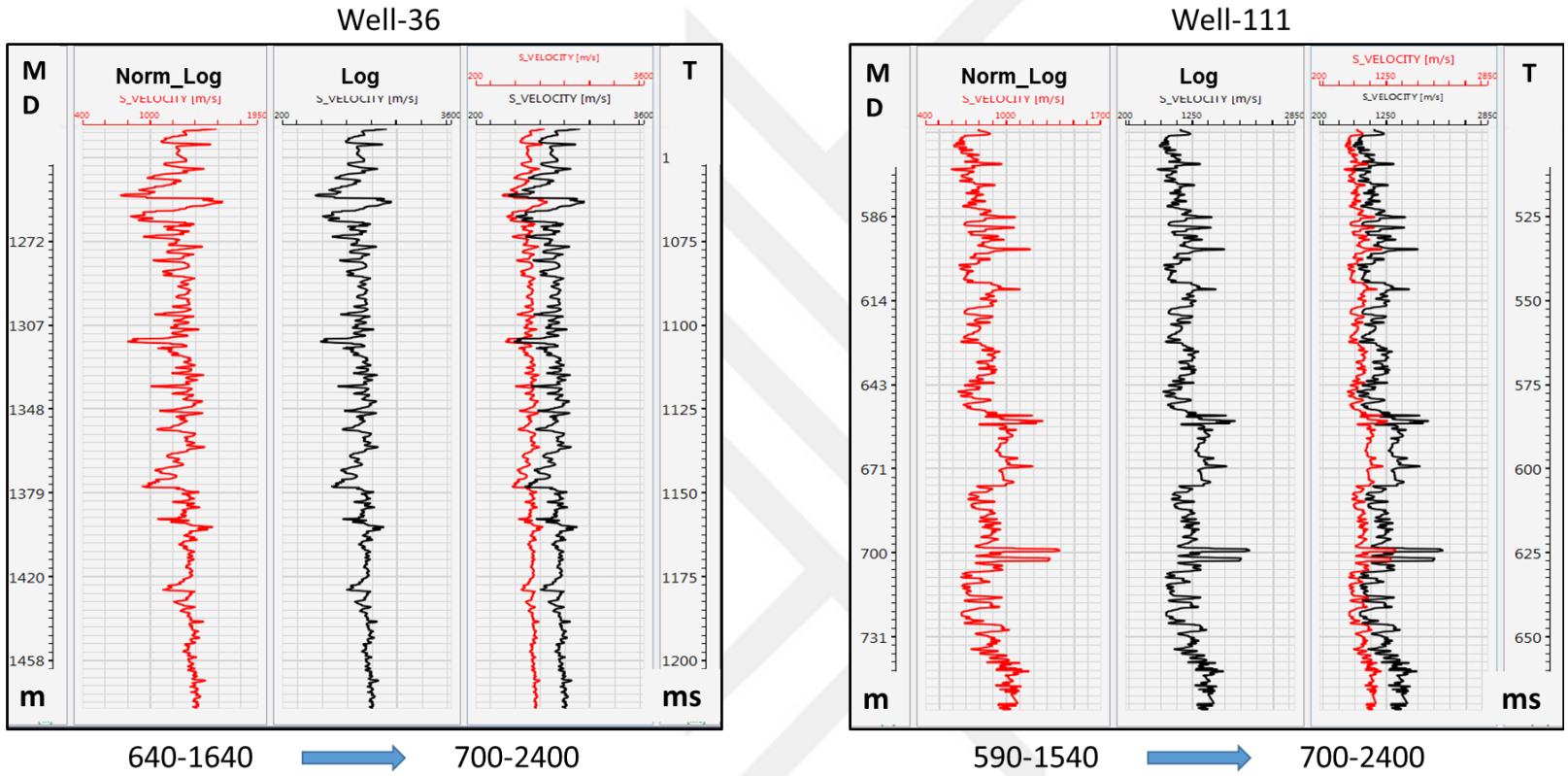

Figure 9.25. After normalization of s-velocities for Well-36 (on the left) and Well-111 (on the right). From left to right for each well: Normalized s-velocities (red color), original logs (black color) and comparison of both curves are given.

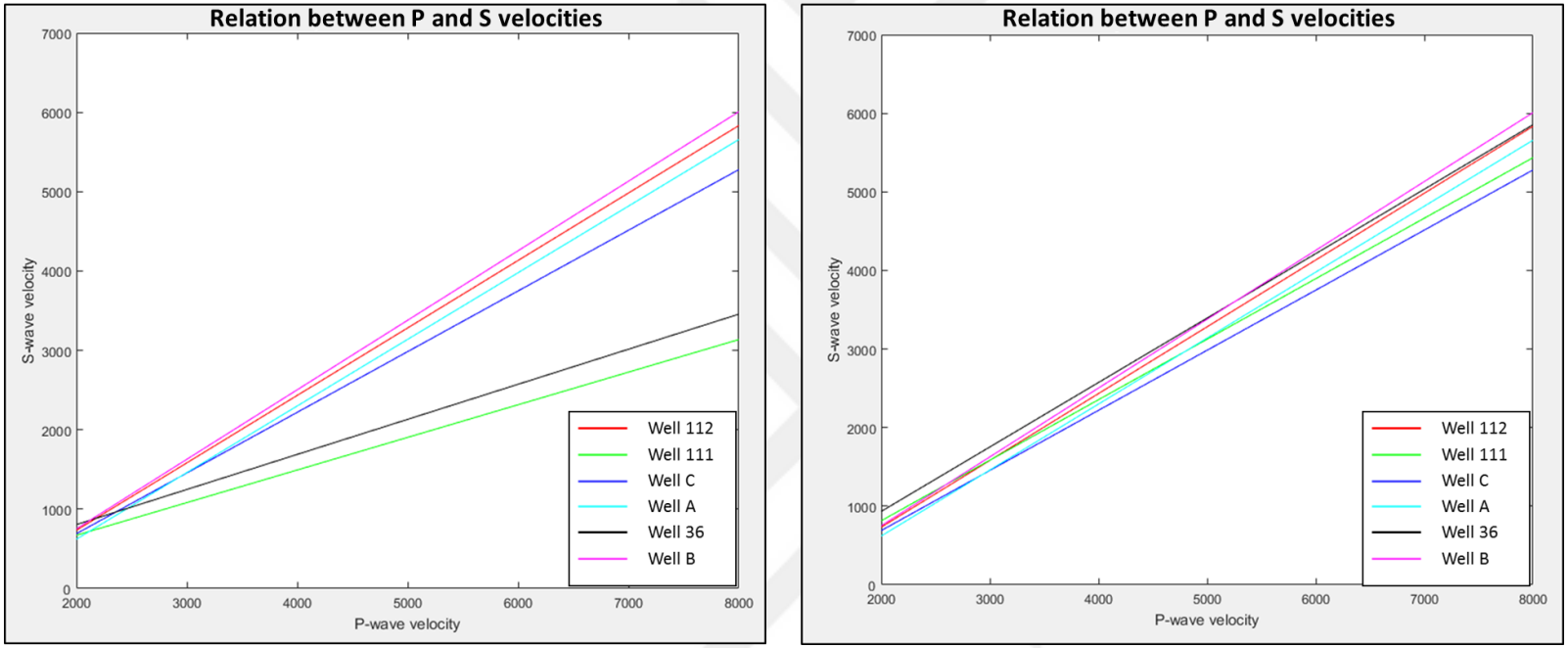

Figure 9.26. Comparison of the cross-plots of P-velocity versus S-velocity before (left) and after (right) normalization of S-velocity values for Well-111 and Well-36. Note that after the normalizations, P-S relationship for all wells fit on almost at the same trend.

9.3.3 Amplitude Versus Offset/Angle Analysis

Depending on the energy content, seismic amplitudes varies with increasing offset or angle of incidence. The main target of AVO studies is to detect amplitude variations with changing offset (Castagna, 2001). To achieve this analysis, firstly, reflection coefficients are necessary to be calculated. Since offset information is available in CDP gathers, reflection coefficients are computed in a different way than the calculation of zero offset coefficient which are useful only for stack data. Calculation of reflection coefficients depending on offset can be obtained by Zoeppritz's (1919) equations. Unfortunately, these equations are very complex to apply real CDP gathers, some approximations are done to Zoeppritz's (1919) equations (Lavaud, 1999). Therefore, in practical AVO studies, these approximations are used instead of Zoeppritz's equations (Burianyk, 2000).

9.3.3.1 Zoeppritz's Equations

Zoeppritz (1919) achieved to calculate reflection coefficients for pre-stack CDP gathers in. However, these equations have been found very complex and complicated to use in practice (Lavaud, 1999). Especially, when the geology of the study area, the use of these equations become more difficult to apply. Hilterman (2001) reproduced these equations given below:

$$A_1 \cos\theta_1 - B_1 \sin\lambda_1 + A_2 \cos\theta_2 + B_2 \sin\lambda_2 = A_0 \cos\theta_1 \quad 9.6$$

$$A_1 \cos\theta_1 - B_1 \sin\lambda_1 + A_2 \cos\theta_2 + B_2 \sin\lambda_2 = A_0 \cos\theta_1 \quad 9.7$$

$$A_1 Z_1 \cos 2\lambda_1 - B_1 W_1 \sin 2\lambda_1 - A_2 Z_2 \cos 2\lambda_2 - B_2 W_2 \sin 2\lambda_2 = -A_0 Z_1 \cos 2\lambda_1 \quad 9.8$$

$$A_1 \gamma_1 W_1 \sin 2\theta_1 + B_1 W_1 \cos 2\lambda_1 + A_2 \gamma_2 W_2 \sin 2\theta_2 - B_2 W_2 \cos 2\lambda_2 = -A_0 \gamma_1 W_1 \sin 2\theta_2 \quad 9.9$$

$$\gamma_i = \frac{\beta_i}{\alpha_i} \quad 9.10$$

$$Z_i = \rho_i * \alpha_i \quad 9.11$$

$$W_i = \rho_i * \beta_i \quad 9.12$$

where α is P wave velocity, β is S wave velocity, and ρ is density. A1 and B1 are reflected and A2 and B2 are refracted compressional and shear wave coefficients (see Figure 9.1).

9.3.3.2 Approximations to Zoeppritz's Equations

To avoid the difficulties of Zoeppritz's equations, some approximations such as Aki and Richards (1980) and Shuey (1985). are used in practice. These approximations cannot calculate true amplitude variations at far angles; however, these are still very useful to study in practice.

Aki and Richards (1980) simplified Zoeppritz's equations as below:

$$R(\theta) = \frac{1}{2}\left(1 - 4\frac{{V_s}^2}{{V_p}^2}sin^2\theta\right)\frac{\Delta\rho}{\rho} + \left(\frac{1}{2cos^2\theta}\right)\left(\frac{\Delta V_p}{V_p}\right) - 4\frac{{V_s}^2}{{V_p}^2}sin^2\theta\frac{\Delta V_s}{V_s} \quad 9.13$$

where ρ, V_P, and V_S are the average of and Δρ, ΔV_P and ΔV_S are the differences of densities, P wave velocities, and shear wave velocities between two layers respectively. θ indicates the angle of incidence and is calculated as $\theta = (\theta_1+\theta_2)/2$ (see Figure 9.1).

Shuey's simplified Zoeppritz's equation using Aki and Richard's approximation (Burianyk, 2000). This method is also not very successful to calculate reflection coefficients at high incidence angle. However, it is very practical to use in real data sets. Shuey's approximation is given below:

$$R(\theta) = \frac{1}{2}\left[\frac{\Delta V_p}{V_p} + \frac{\Delta \rho}{\rho}\right] + \frac{1}{2}\left[\left(\frac{\Delta V_p}{V_p}\right) - 2\left(\frac{V_s}{V_p}\right)^2\right]\left[2\frac{\Delta V_s}{V_s} + \frac{\Delta_\rho}{\rho}\right] sin^2\theta + \frac{1}{2}\left(\frac{\Delta V_p}{V_p}\right)(tan^2\theta - sin^2\theta) \quad 9.14$$

This equation can be written as a simpler form:

$$R(\theta) = A + Bsin^2\theta + C(tan^2\theta - sin^2\theta) \quad 9.15$$

The first term, A, refers to reflectivity at normal incidence (θ=0), which is also called as "*intercept*". The second term, B, characterizes reflectivities with increasing angle of incidence R(θ), which is called as "*gradient*". The third term, C, describes an approach to the critical angle and called as "curvature", which is also ignorable for practical studies.

9.3.3.3 AVO Classification

Rutherford and Williams (1989) proposed a classification including class I, II and III based on impedance contrast of two layers. Then, Castagna and Swan (1997) revealed class IV as an addition the first three-class type. AVO class type can be specified according to cross-plot of intercept versus gradient.

AVO classes are valid for gas sands with encasing shale lithology. When gas-bearing sandstone has higher impedances than the encasing medium including shale lithology, AVO response is called as class I type. This type of reservoirs has positive reflection coefficient at zero offset. With increasing offset or angle of incidence, reflection coefficient becomes smaller. At a certain degree is reached, it changes polarity and increases in magnitude negatively (Figure 9.27). These classes appear in very compacted and consolidated reservoir (Rutherford and Williams, 1989).

When the impedance contrast between two layers is near zero, AVO response is identified as Class II reservoir. This type of AVO class occurs in compacted reservoirs as well (Rutherford and Williams, 1989). This type of class may either

have very low positive or negative reflection coefficient. A class II type starting with a positive reflection firstly decreases in magnitude and changes polarity in a certain angle, then increases negatively (Figure 9.27). A class II type starting with a negative reflection increases in magnitude negatively (Figure 9.27) (Rutherford and Williams, 1989).

Class III type of gas-bearing sandstones have lower impedances than encasing medium. This kind of reservoirs are mostly unconsolidated and not compacted. At zero offset, reflection coefficients are high and negative. With increasing offset, these coefficients become larger in magnitude negatively (Figure 9.27) (Rutherford and Williams, 1989).

Class IV type reservoirs are also referred as low impedance reservoirs similar to class III type (Castagna and Swan, 1997). Class IV type reservoir starts with high negative reflection coefficient and decreases in magnitude with increasing offset (Figure 9.27).

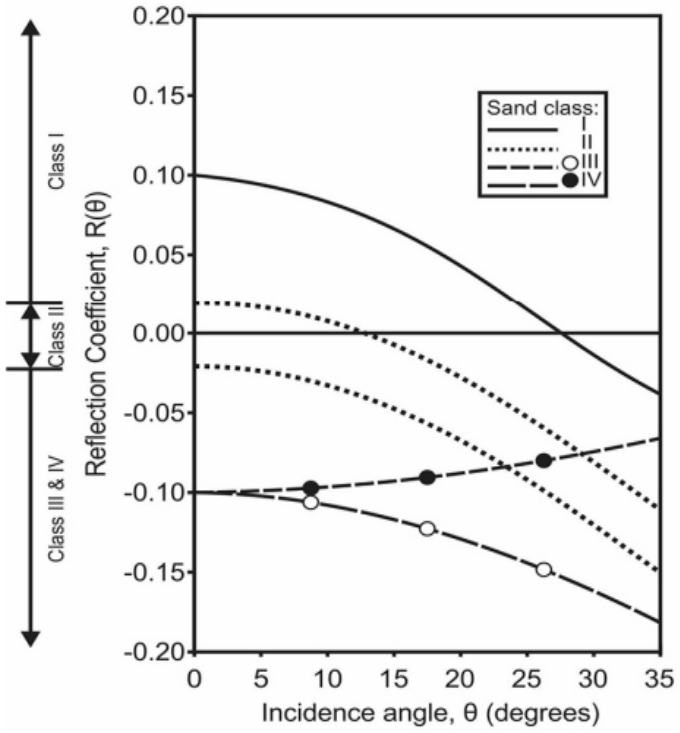

Figure 9.27. Reflection coefficients indicating different class types of gas-sands with increasing angle of incidence (Castagna et al., 1998).

9.3.3.4 AVO Classification in Karaçalı-Yulaflı Field

AVO anomalies are generally observed in producing Osmancık sands in the Thrace Basin. Especially, class-III AVO anomalies causing bright sports are clearly identified, and most of the production is done from these sweat spots. However, going deeper, bright spot reflections lose their strength and locating hydrocarbon-bearing sands becomes harder.

One of the producers from shallower Osmancık Formation, such as Well-18, shows AVO class-III anomalies at reservoir zones (Figure 9.28). Stack seismic data at Well-18 location indicates a bright spot at reservoir zone (Figure 9.29). On the other hand, highly productive zone in Well-12 has Class-II type AVO anomalies showing polarity changes (Figure 9.30); therefore, this interval has almost no reflection

(Figure 9.31) The most distinctive feature in terms of seismic data between shallower and deeper Osmancık Formation is relevant AVO classes because each class type represents different acoustic impedance relation. Since AVO class III type reservoirs are low impedance zones, these producing intervals show high impedance contrast with encasing shale. However, because AVO class-II indicates near zero impedance contrast between producing sand and shale, impedances of each lithology are so closed to each other resulting weakly detected impedance difference. Thus, impedances and reflections are not distinctive for deeper Osmancık Formation.

AVO studies reveal that sediments in producing intervals at shallower zones are unconsolidated while the sediments deposited in deeper sections are compacted.

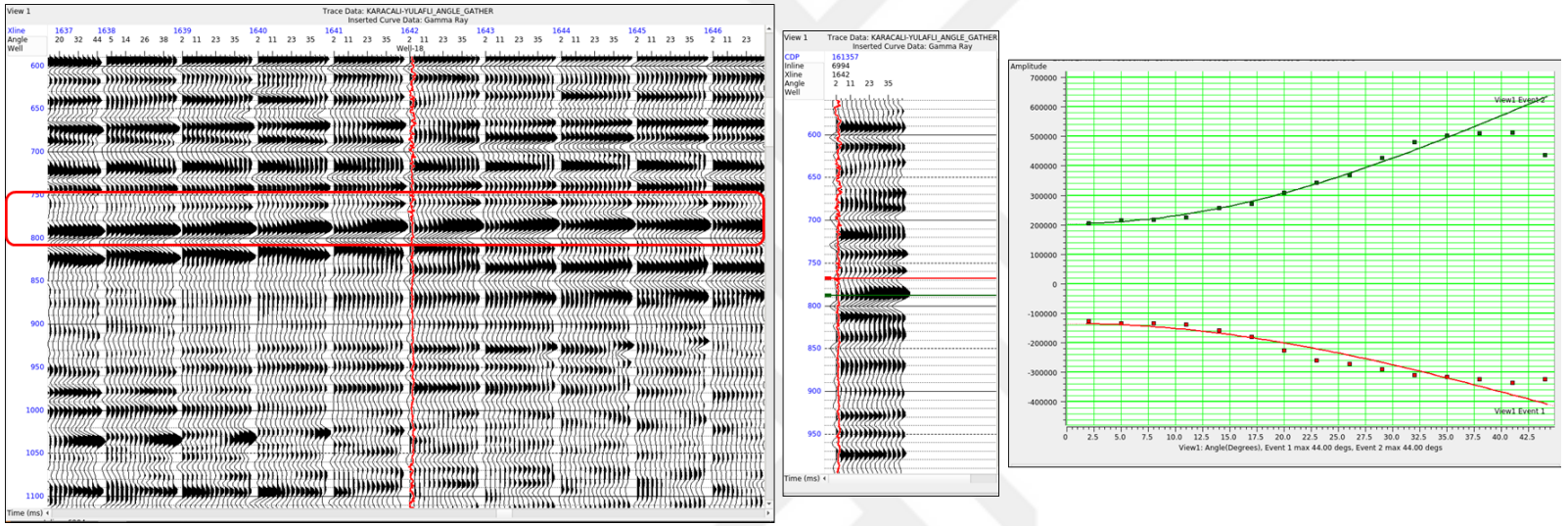

Figure 9.28. From left to right panels: Angle gathers (2-42 degrees), individual angle gather with picked top (red) and base (green) of the reservoir and amplitude versus angle of incidence for the picked events are shown. Red rounded rectangle on the left panel illustrates the producing reservoir zone for Well-18. For the top of reservoir (red curve), amplitudes start with high negative values and increase in amplitude with changing incidence angle, which represents A class III type of AVO anomaly (right panel).

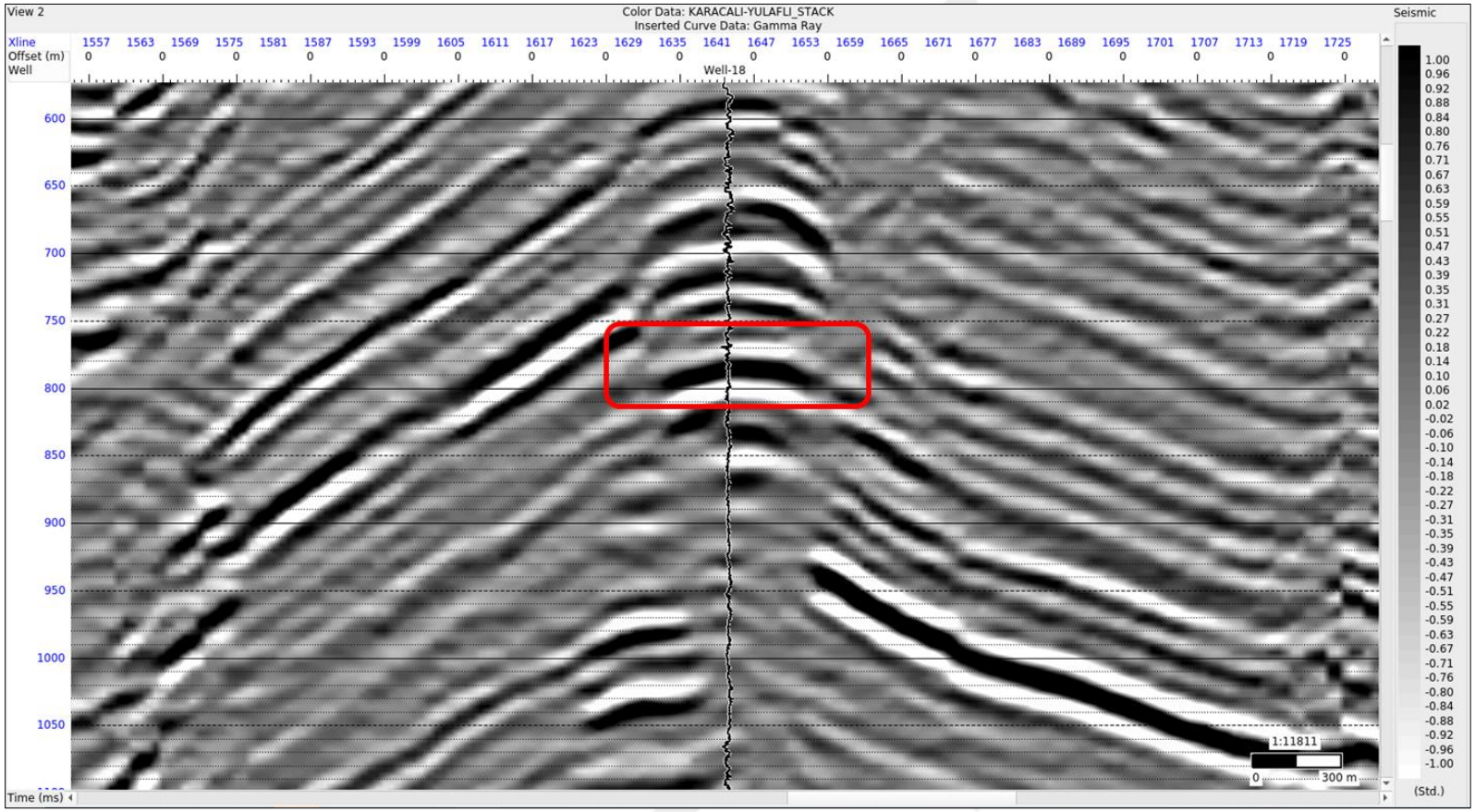

Figure 9.29. Stack seismic section at the location of Well-18 is given. Producing interval is pointed out with rounded rectangle. A clear bright spot as a result of class-3 AVO type is observed.

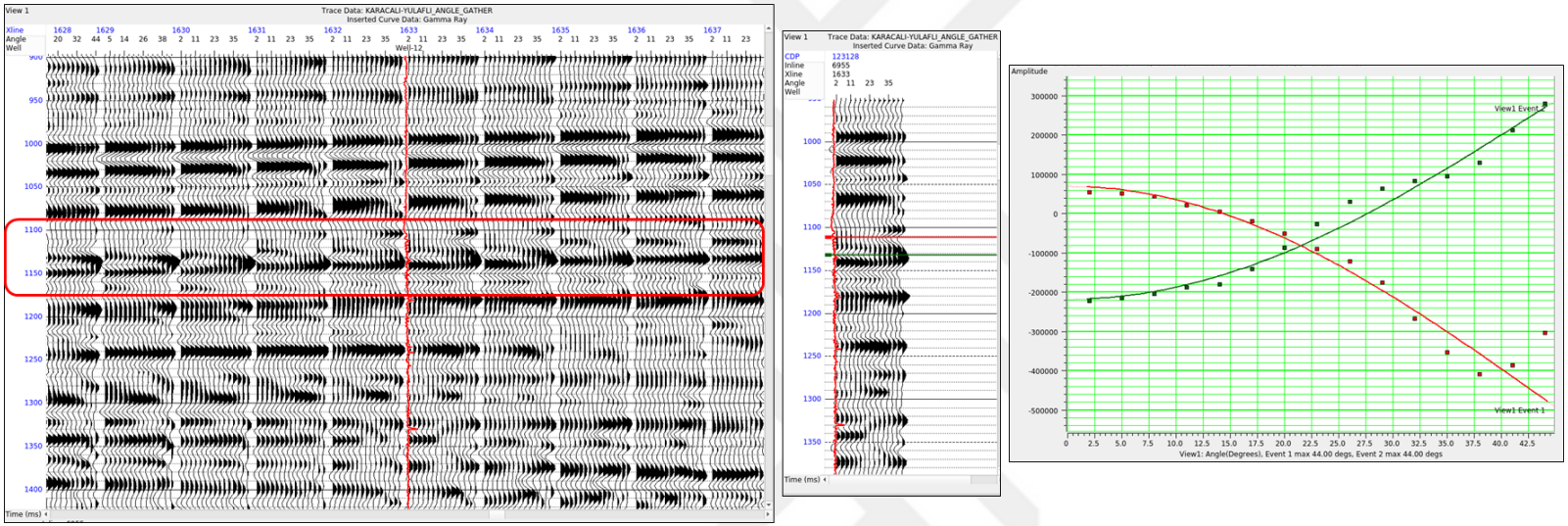

Figure 9.30. From left to right panels: Angle gathers (2-42 degrees), individual angle gather with picked top (red) and base (green) of the reservoir and amplitude versus angle of incidence for the picked events are shown. Red rounded rectangle on the left panel illustrates the producing reservoir zone for Well-12. For the top of the reservoir (red curve), amplitudes start with low positive values and drop until reaching a certain angle of incidence. Then, the polarity changes and start to increase in magnitude at negative side, which represents A class III type of AVO anomaly (right panel).

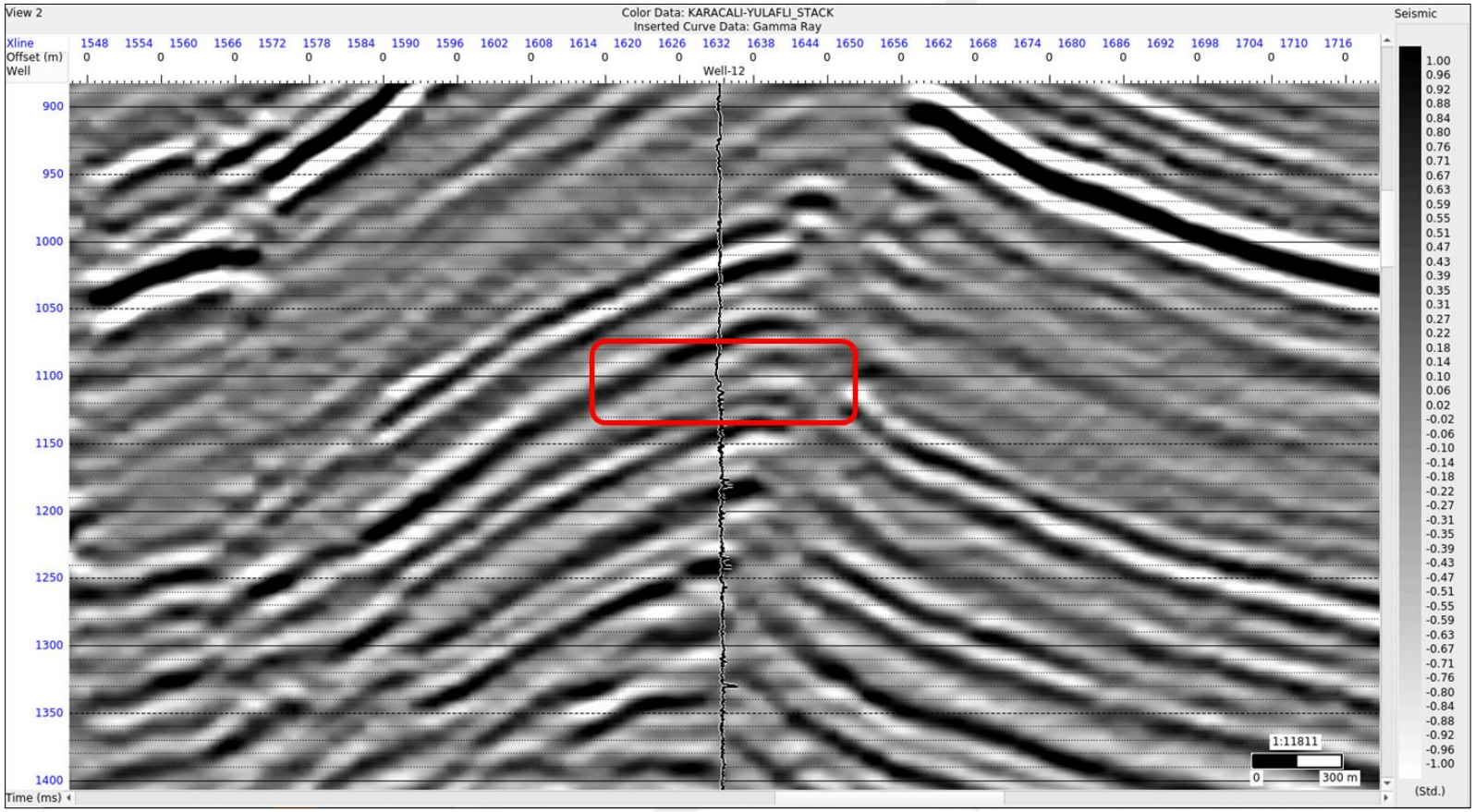

Figure 9.31. Stack seismic section at the location of Well-12 is given. Producing interval shown rounded rectangle. Seismic reflection is too weak to be detected, as a result of polarity changing AVO anomaly.

9.3.4 Seismic Inversion

Seismic inversion is a significant method used for the quantitative analyses and reservoir geophysics. This technique is widely used to infer fluid content and lithology. The main importance of using this tool is that interface attributes are transformed into formation attributes (Pendrel, 2001). Instead of interpretation of reflections showing formation top or bottom, interval attributes are much easier to evaluate (Morozov and Ma, 2009).

Barclay et al. (2008) described inversion technique as the inverse of forward modeling. Forward modeling can be defined as the mathematical expression of the earth response. In contrast, inversion converts real data into the model. When the real and modelled data are similar, it means that the results of the inversion is acceptable. (Barclay et al., 2008).

Forward modeling is achieved by the convolution of the reflection and wavelet while inverse modeling is the deconvolution of a wavelet from real seismic data (Figure 9.32).

Workflow of an inversion of pre-stack gathers are illustrated in Figure 9.33.

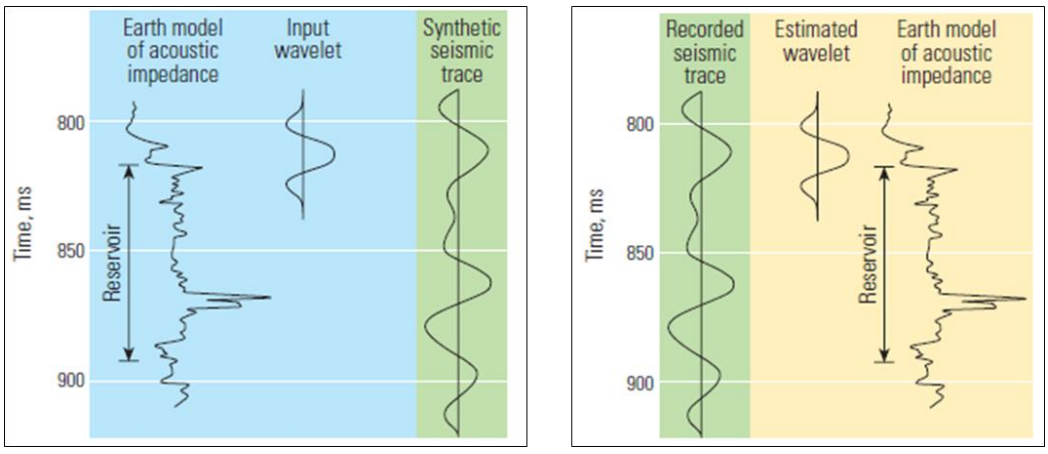

Figure 9.32. On the left side, the convolution of an earth model with an extracted wavelet to calculate synthetics is shown. On the right side, the inversion process by deconvolution of an extracted wavelet from recorded seismic traces to calculate earth model is displayed (Barclay et al., 2008).

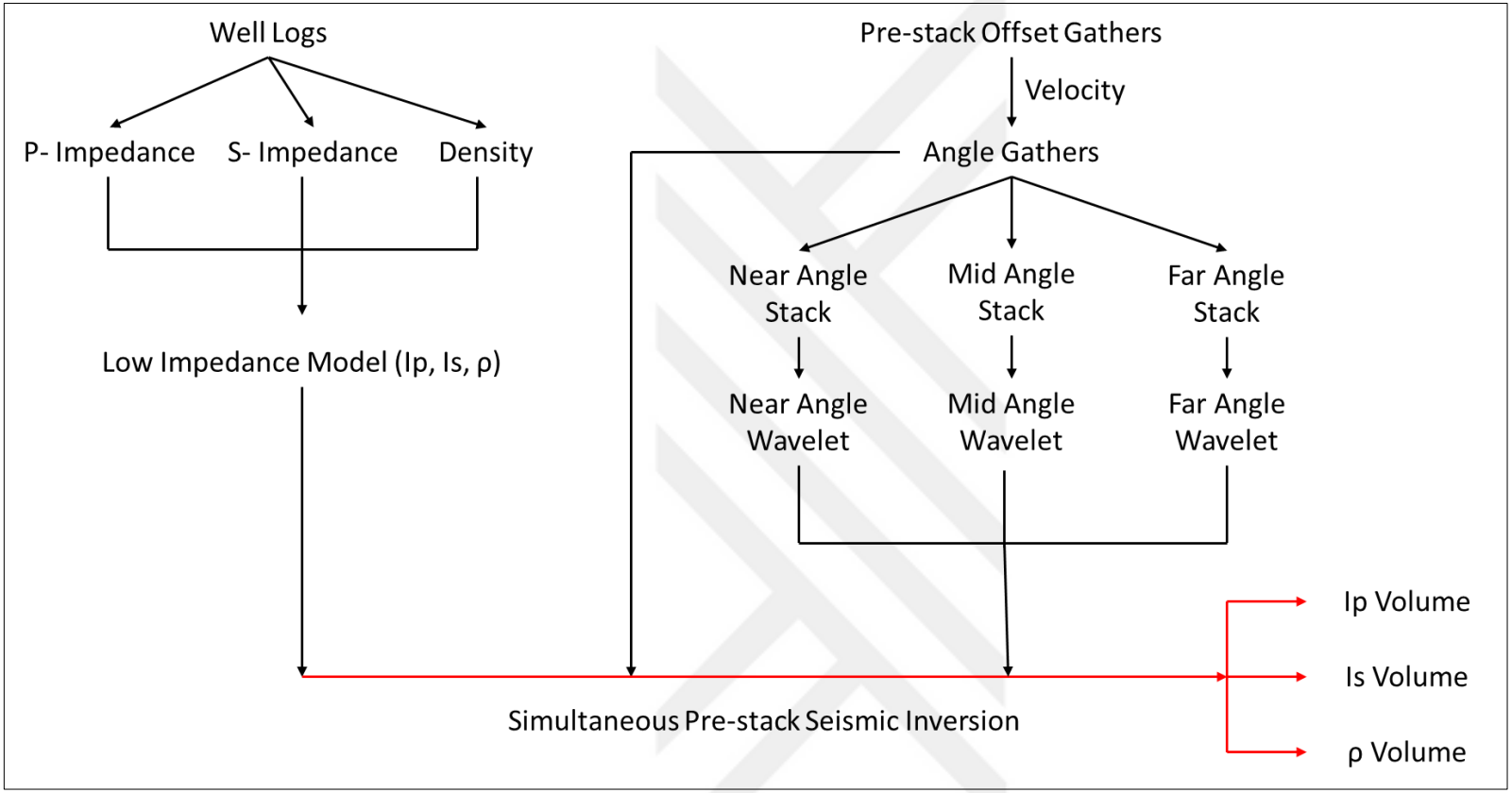

Figure 9.33. Workflow of pre-stack seismic inversion

Offset gathers converted into angle domain using RMS velocities are utilized as input for the pre-stack seismic inversion. Since both compressional and shear velocities are considered, the results include 3D volumes of impedances, I_P and I_S. These elastic parameters can be used also to calculate V_P/V_S ratio, which is an important parameter for the estimation of the presence of hydrocarbon. When hydrocarbon is encountered, I_P shows a decrease while I_S shows little variation resulting low V_P/V_S ratio.

9.3.4.1 Forward Modeling

To implement model based seismic inversion, a forward model is essential to be created using P-sonic, S-sonic and density (ρ) logs. Because acquired seismic data does not cover frequencies lower than 10 Hz, low frequency content of log data is utilized for model building.

Simple kriging was utilized to create initial models. These models were filtered between 0-12 Hz to obtain low frequency content of well log data. To calculate the max filter range of minimum frequency content, Nyquist frequency was computed (Eq. 9.16) using seismic spectrum (Fig. 34). Three diverse models are necessary to be generated and filtered as a guidance for pre-stack seismic inversion. Created I_P, I_S and ρ models are shown Figure 9.35, 9.36 and 9.37 for group 1 wells in a composite section, respectively. These models do not consist of detailed information because a model should be developed. Iteration of seismic inversion will be stopped when it reaches chosen misfit error or maximum iteration number.

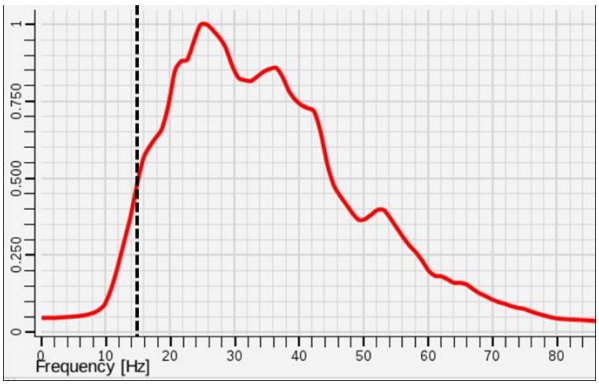

Figure 9.34. Amplitude Spectrum of the seismic data. Maximum low frequency is 15 Hz.

$$f_N = \frac{fmin}{1/(2 * \Delta t)} \tag{9.16}$$

where f_N is Nyquist frequency, $fmin$ is minimum frequency, Δt is the sampling rate which is 4 ms.

9.3.4.2 Pre-Stack Seismic Inversion Results

The inverted p-impedance and V_P/V_S ratio volumes were calculated. Impedance contrast in shallower depths of the Osmancık Formation is mostly greater than the contrast in deeper Osmancık Formation. Therefore, decrease in impedances at shallower Osmancık Formation is clearly observed. Reflections are stronger in these levels. On the other hand, lower impedance contrast between sand and shale lithology results in weaker reflections and similar impedance values which are hardly detectable for each well group. Figure 9.38 and 9.39 indicate composite stack sections while Figure 9.40 and 9.41 display p-impedance variations for well groups 1 and 2, respectively.

Calculated V_P/V_S ratio volumes are independent of impedance contrast because an increase or decrease in P-impedance is also similar for the variation in S-impedance. Therefore, both shallower and deeper Osmancık Formation sands and shales are easier to be detected. Especially, when the pores are filled with a hydrocarbon fluid,

differentiation of V_P/V_S ratio between sand and shale becomes clearer. V_P/V_S ratio for well group 1 and 2 are given in Figure 9.41 and 9.42.

Using p- and s-impedance volumes, approximations such as lambda*rho (λρ) and mu*rho (μλ) can be also calculated. While λρ provides information about fluid content of the zones similar to V_P/V_S ratio, μλ is a lithology indicator which generally shows a little increase in the presence of hydrocarbon, similar to s-impedance. These two elastic parameters are computed using the equations below:

$$\lambda\rho = Ip^2 - 2 * Is^2 \quad 9.17$$

$$\mu\rho = Is^2 \quad 9.18$$

Where Ip represents the p-impedance and Is is the s-impedance. λρ and μρ sections for well group-1 (Figure 9.42 and 9.43) and well group-2 (Figure 9.44 and 9.45) were generated to reveal fluid and lithology indication. While λρ decreases at producing intervals, μρ remains almost still or shows a little bit increase.

Figure from 9.40 to 9.45 showing calculated and evaluated results of inversion outputs, for well group 1 and 2, such as acoustic (P) impedance, shear (S) impedance, V_P/V_S ratio, lambda*rho (λρ) and mu*rho (μρ) indicate that producing intervals have been detected successfully. Additionally, compacted zones are discriminated form unconsolidated lithology.

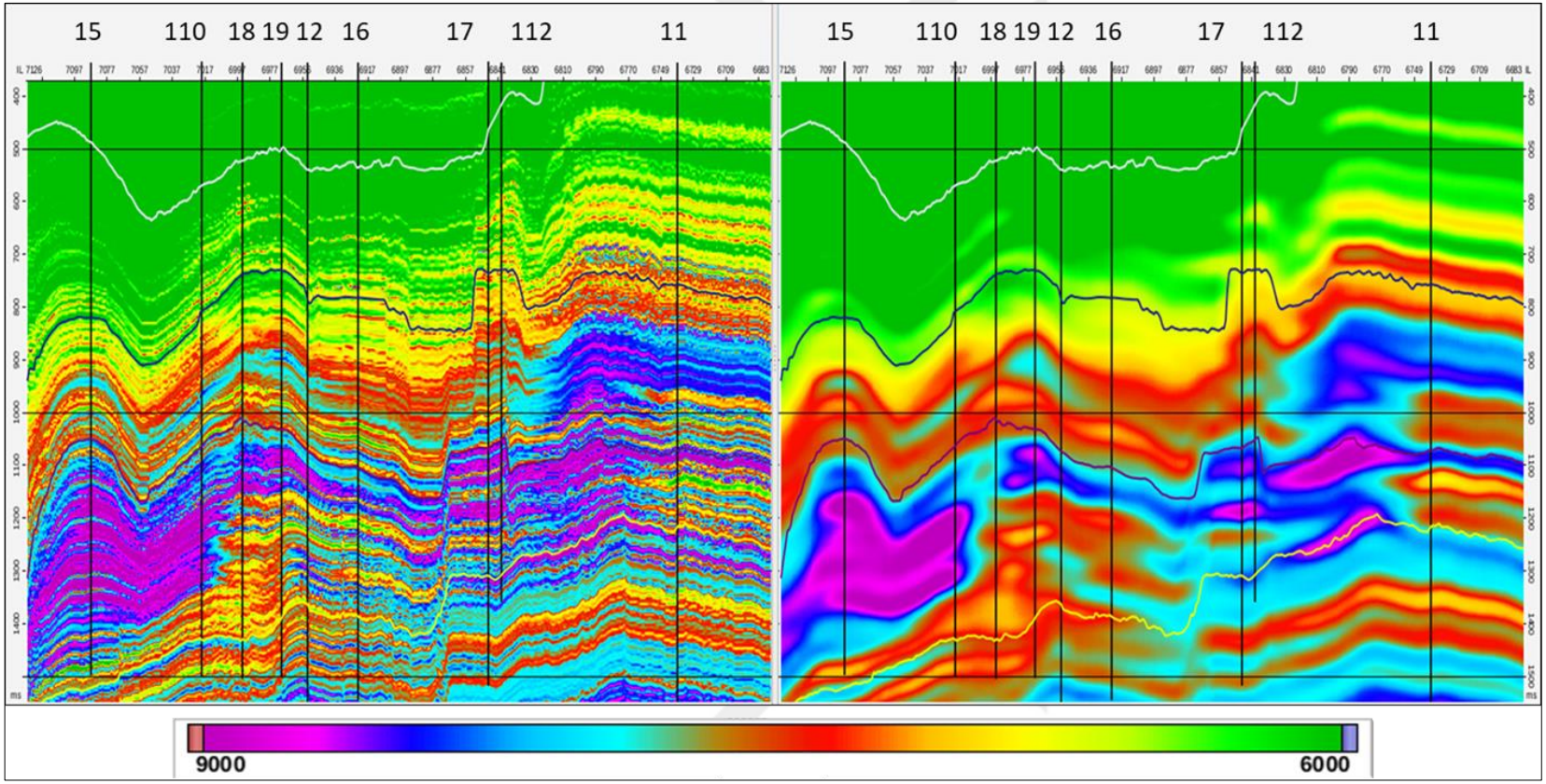

Figure 9.35. P-impedance model calculated from the product of p-sonic and density logs using kriging method (on the left) and the filtered model (on the right) are given.

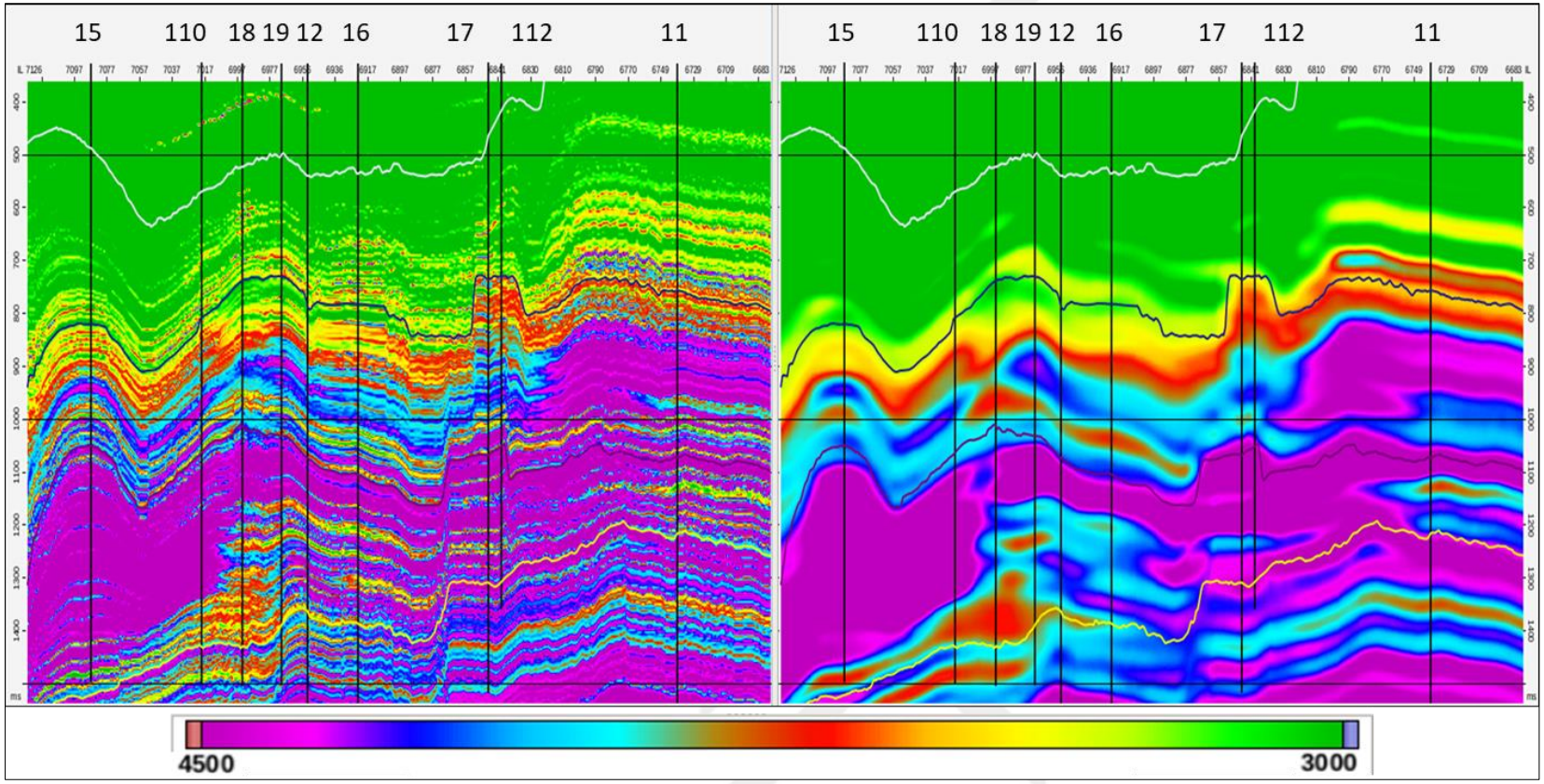

Figure 9.36. S-impedance model calculated from the product of estimated s-sonic and density logs using kriging method (on the left) and the filtered model (on the right) are given.

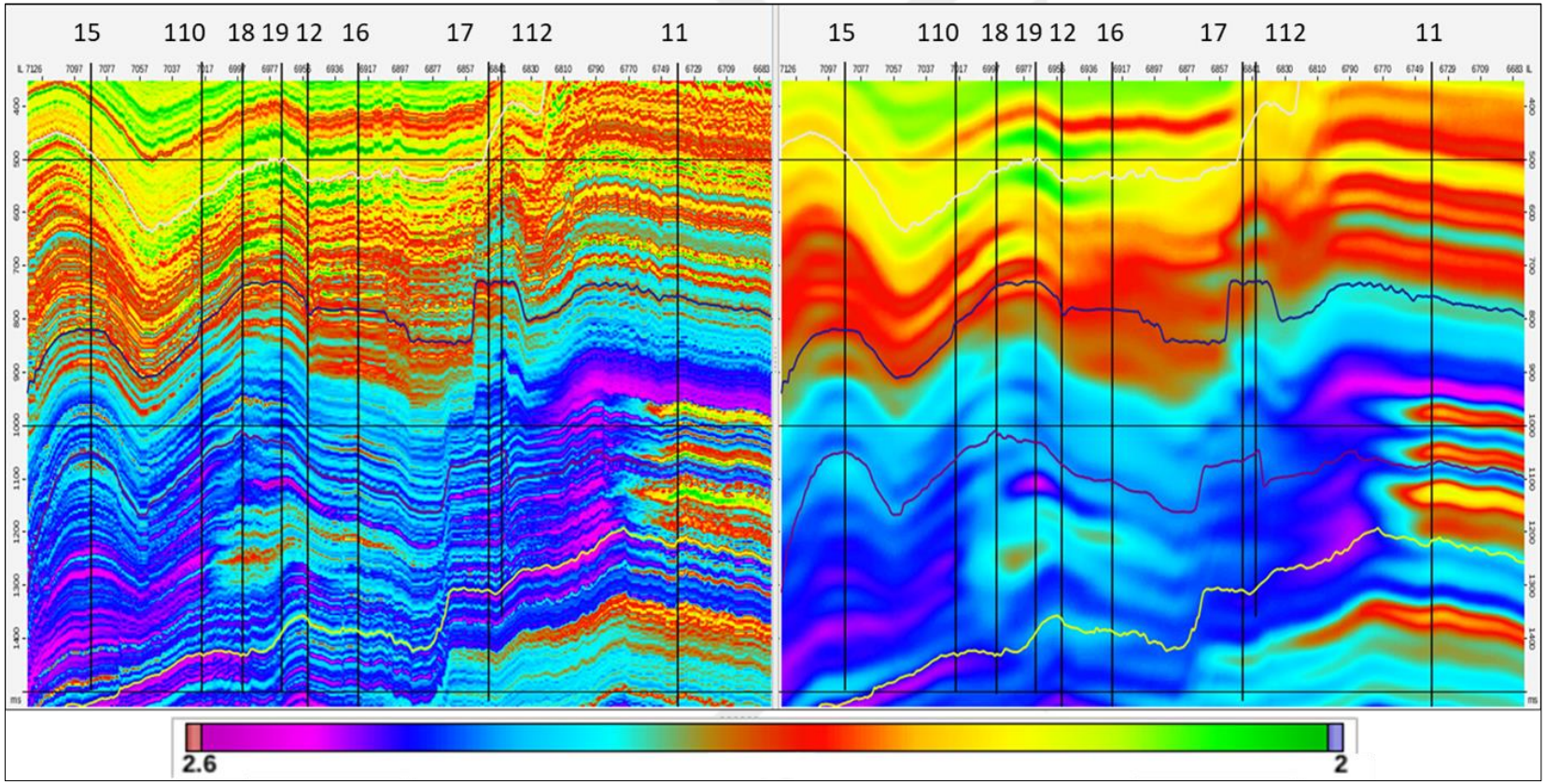

Figure 9.37. Density model using measured density logs using kriging method (on the left) and the filtered model (on the right) are given.

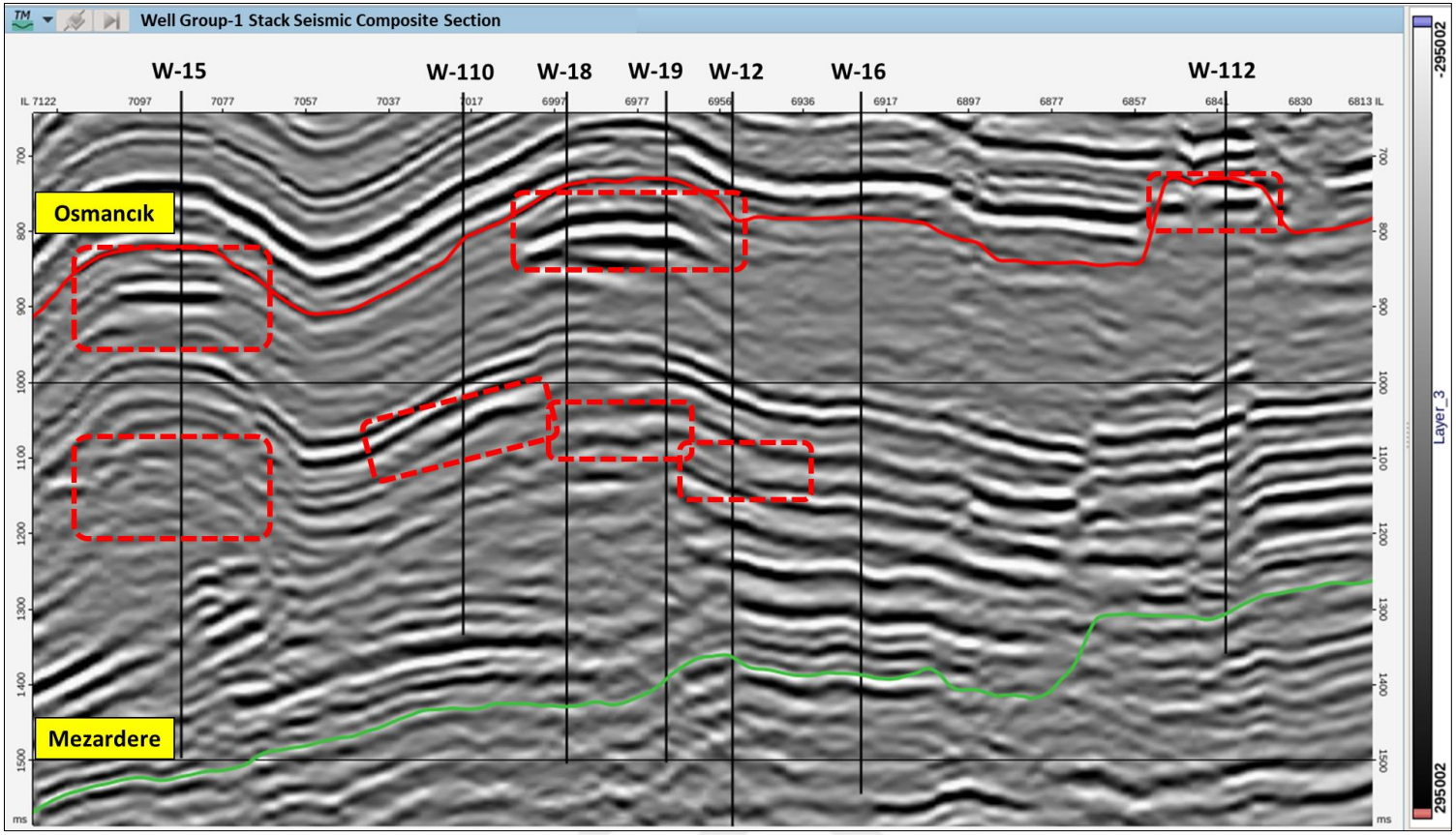

Figure 9.38. Seismic composite section (see Figure 9.5 A) from well group-1. Dashed rounded rectangles represent hydrocarbon producing intervals. Producing zones right below the entrance of the Osmancık Formation are clearly identified as bright spots showing strong reflections. Going deeper, the reflections of the producing zones become weaker due to low impedance contrast between layers resulting of increasing compaction of the lithology.

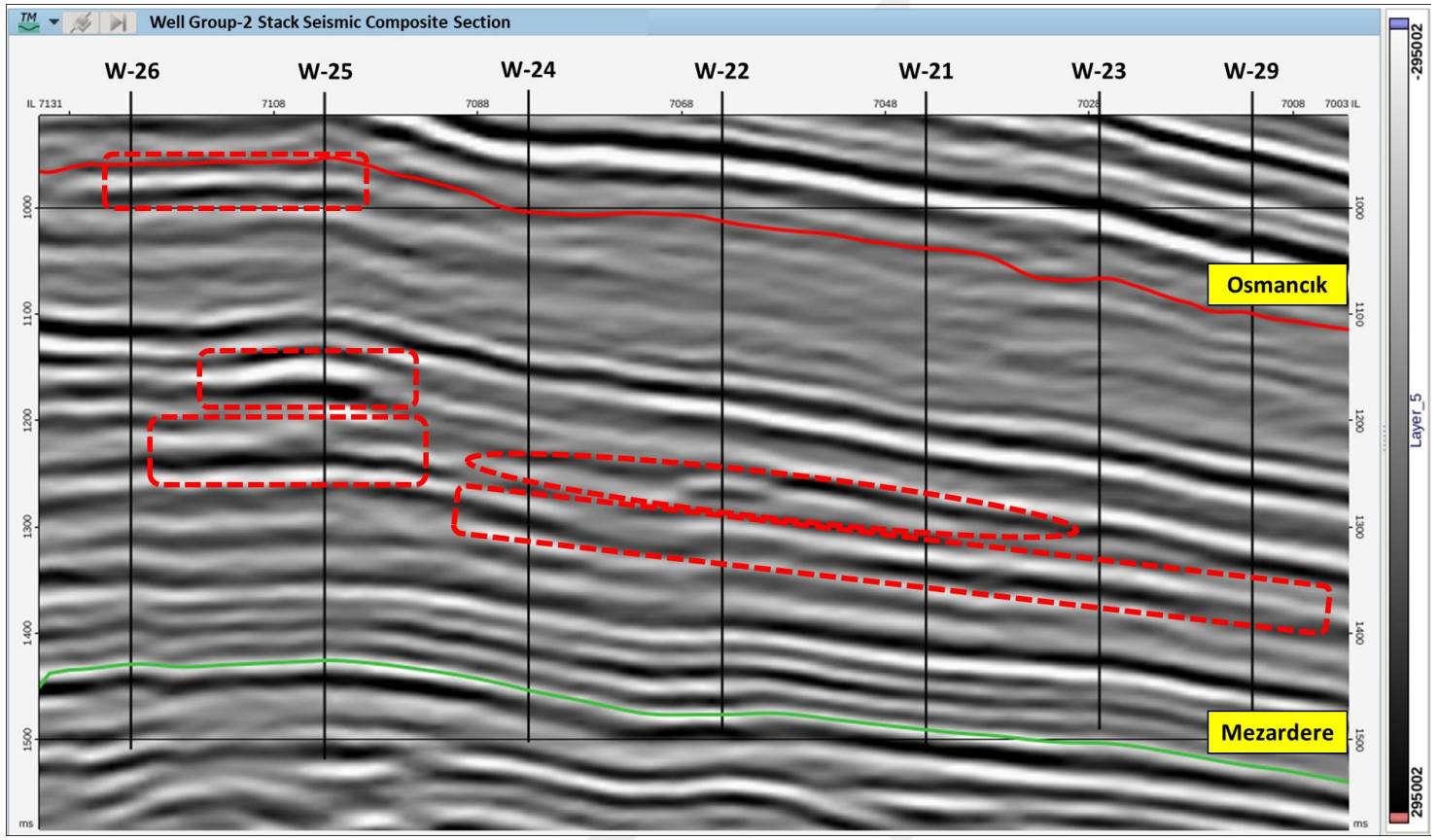

Figure 9.39. Seismic composite section (see Figure 9.5 B) from well group-2. Dashed rounded rectangles and ellipse represent hydrocarbon producing intervals. Producing two shallow zones between 950 and 1200 ms at well-25 are easily detected due to lower impedances of sand reservoirs while highly productive intervals below 1200 ms are not differentiated from other. Going deeper, the reflections of the producing zones become weaker due to low impedance contrast between layers resulting of increasing compaction of the lithology.

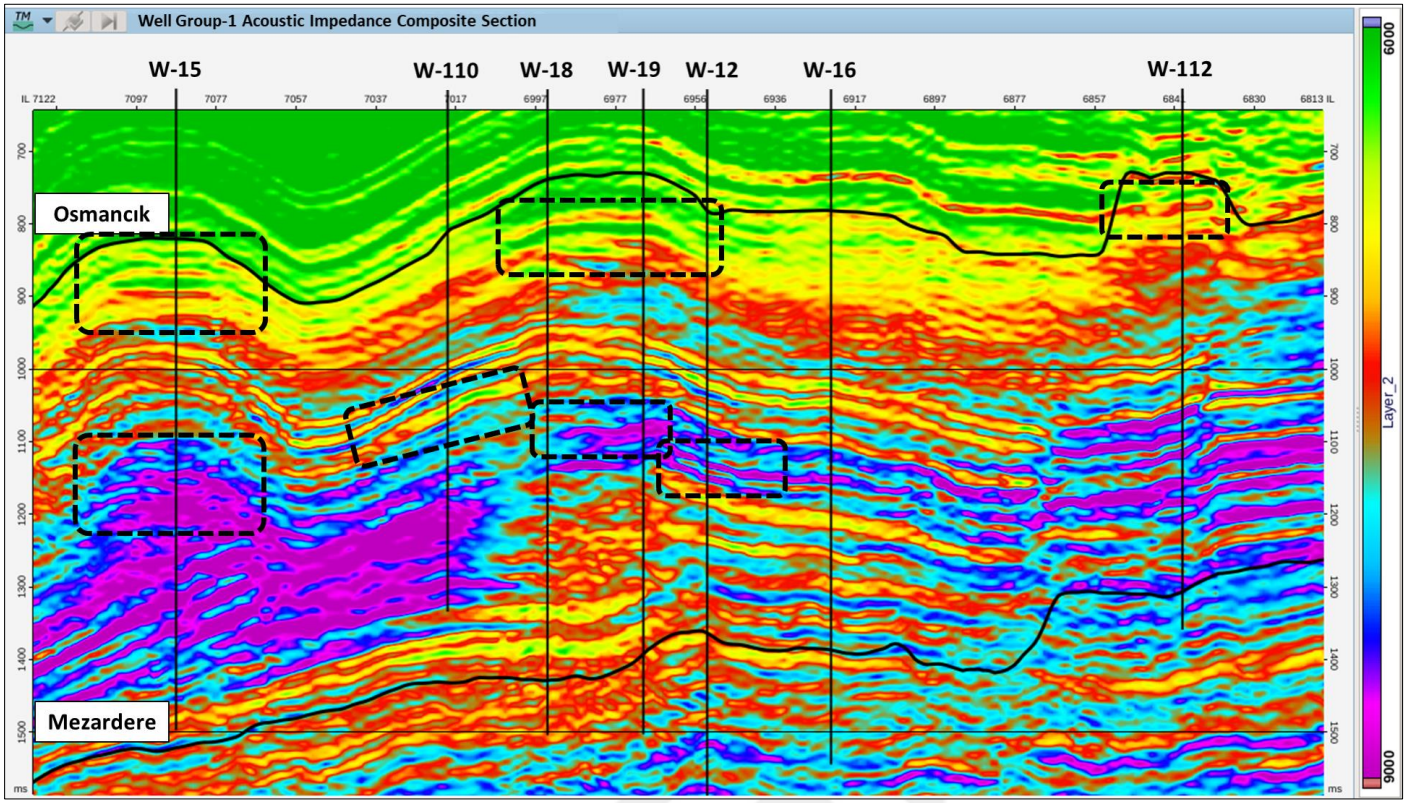

Figure 9.40. A composite section (see Figure 9.5 A) showing acoustic impedance variations for well group 1. The shallowest gas bearing zones of Well-10, 12, 15, 18, and 19 have distinctive lower impedance values as a result of class-III AVO responses. The lithology consists of mainly uncompacted sandstone and shale alternation. At deeper productive zones, impedances become higher as a result of class-II responses because of compacted reservoirs. The impedance contrast is too low to differentiate sand and shale lithology at deeper zones.

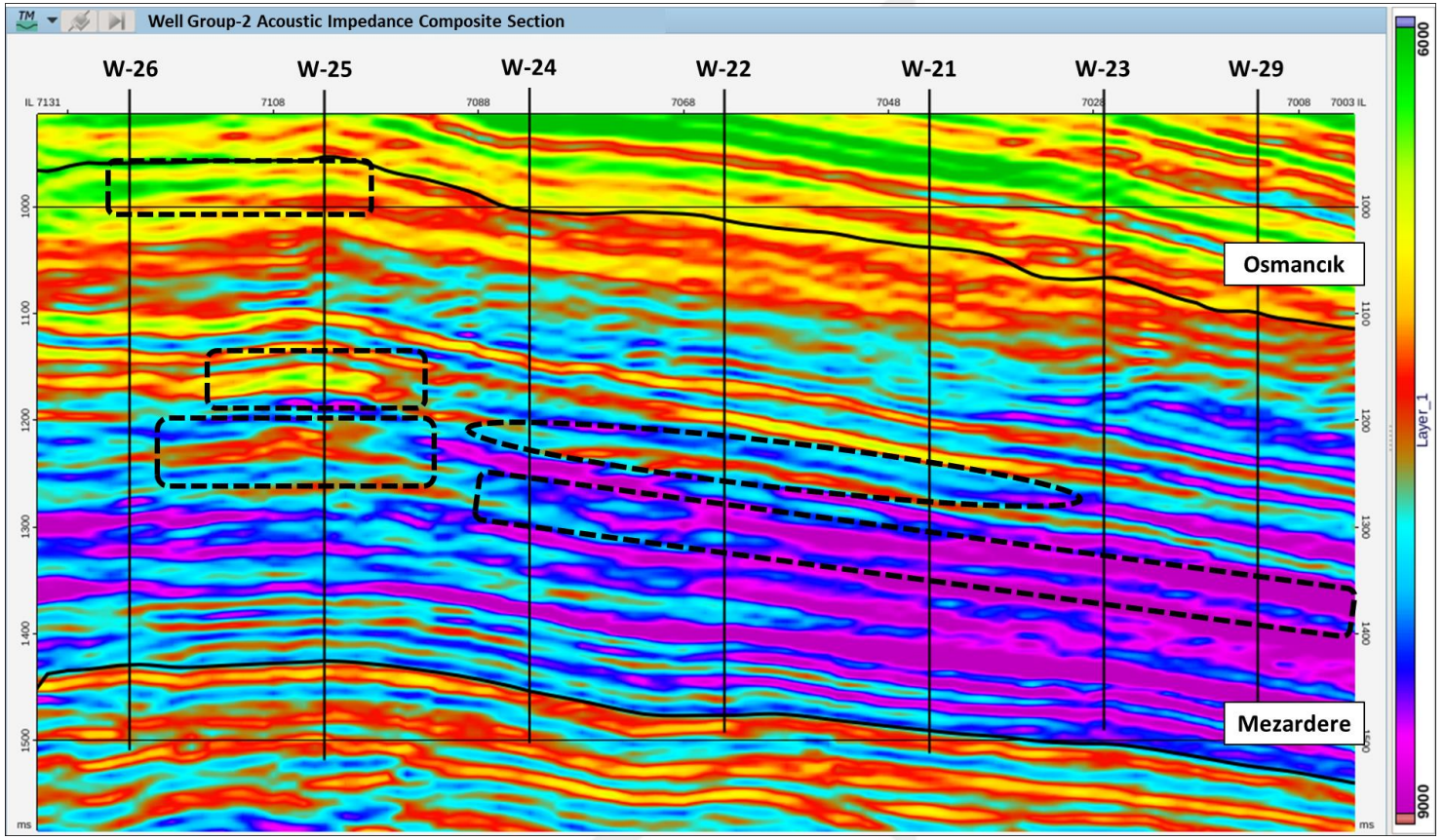

Figure 9.41. A composite section (see Figure 9.5 B) showing acoustic impedance variations for well group 2. Acoustic impedances of two shallow gas bearing zones at Well-25 can be distinguished as a result of class-III AVO responses. The lithology consists of mainly uncompacted sandstone and shale alternation similar to well group 1. At deeper productive zones, impedances become higher and harder to be detected as a result of class-II responses due to compacted lithologies.

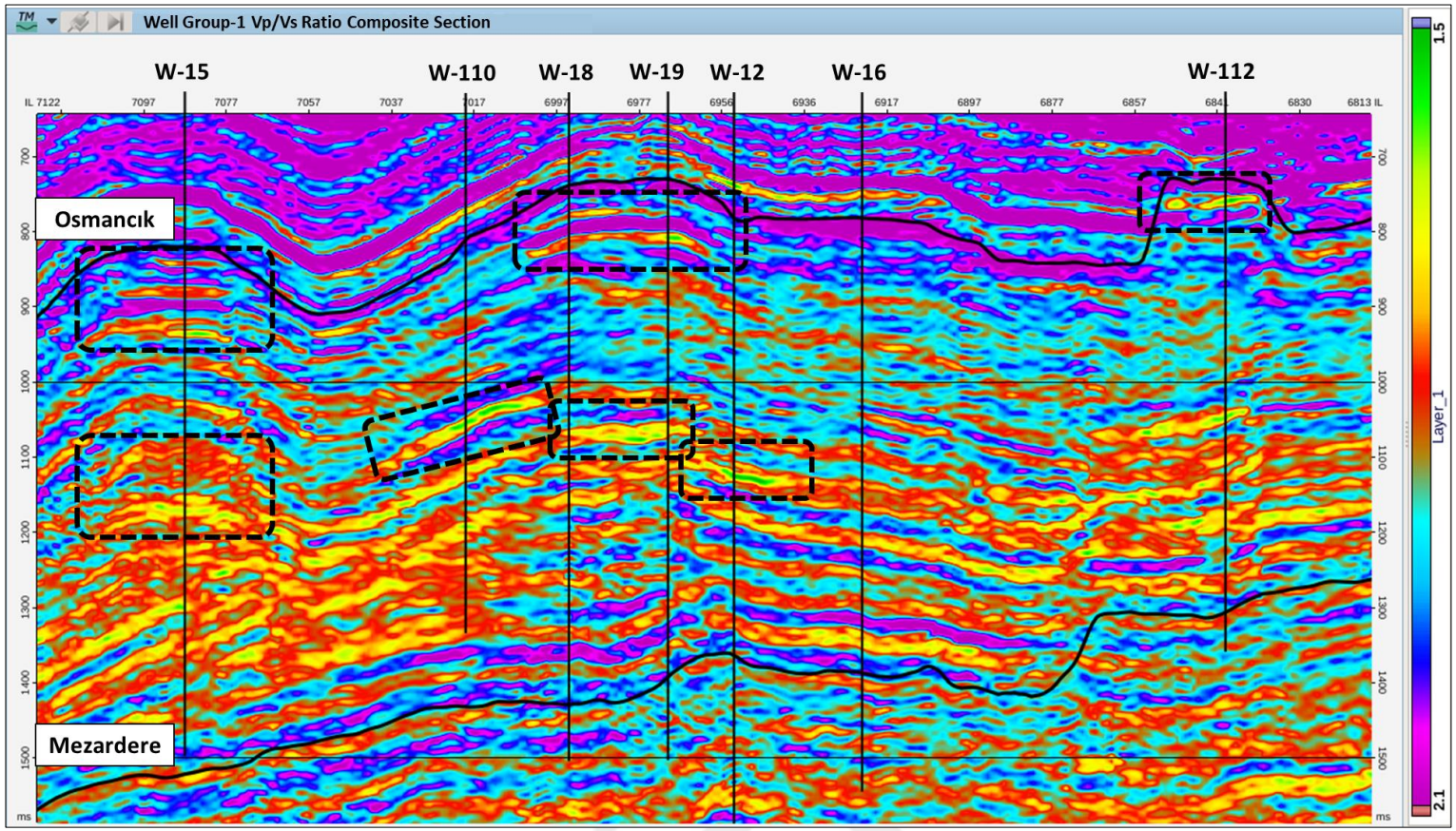

Figure 9.42. A composite section (see Figure 9.5 A) indicating V_P/V_S ratio for well group 1. Low values (green and yellow color) indicate producing zones. Due to similar behavior of P- (acoustic) and S-impedances, this ratio is not affected by compaction or impedance contrast.

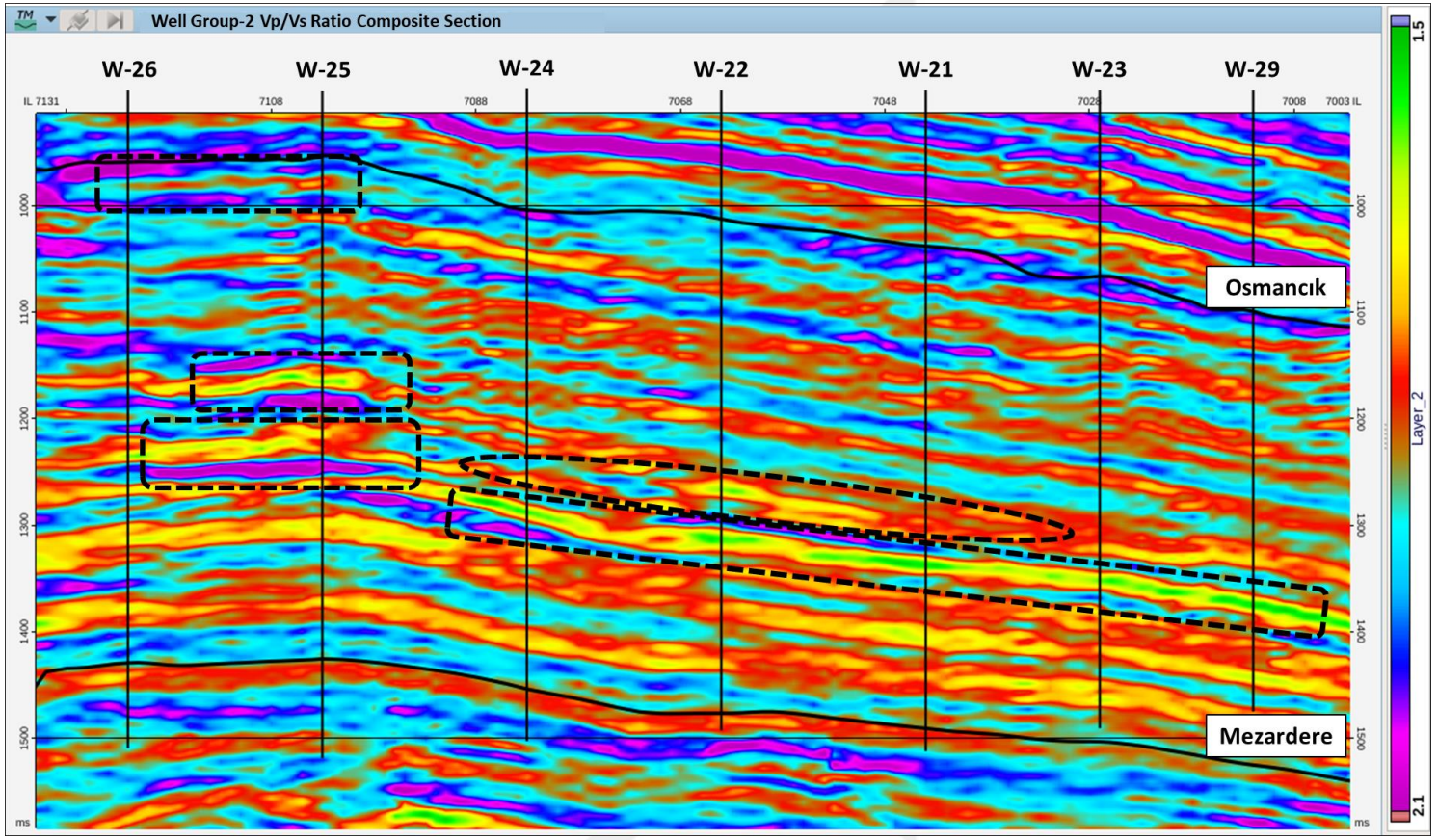

Figure 9.43. A composite section (see Figure 9.5 B) indicating V_P/V_S ratio for well group 2. Low values (green and yellow color) indicate producing zones. Similar to well group-1, V_P/V_S ratio is not affected from compaction or impedance contrast. Mostly, the lowest values which are color-coded as green are productive sandstones and low values color-coded as yellow and red are non-productive sandstones. Shale lithology have higher V_P/V_S ratio (blue-purple colors).

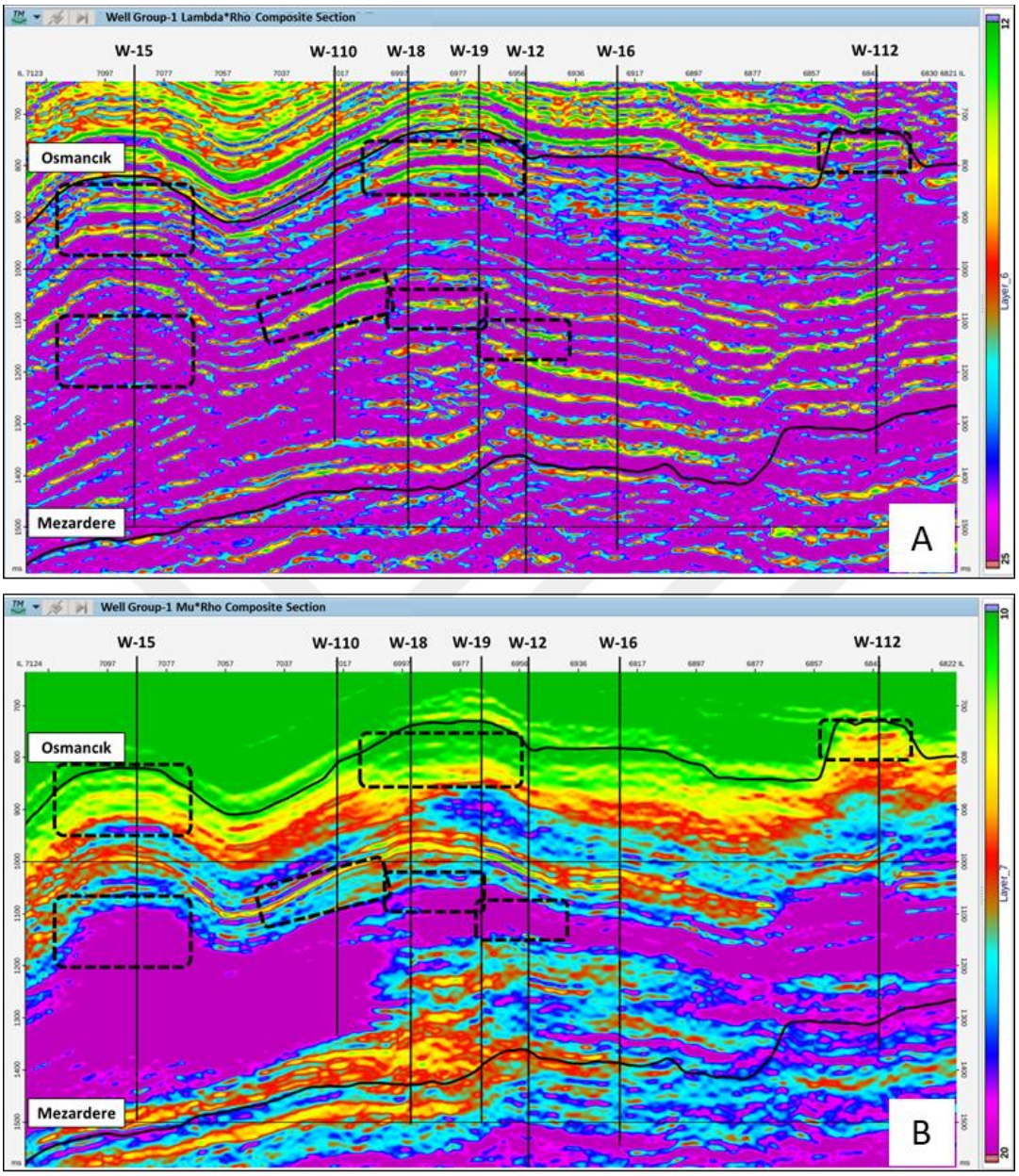

Figure 9.44. A composite section (see Figure 9.5 A) indicating (A) λρ and (B) μρ for well group 1. Lower values for λρ are hydrocarbon indicators while μρ are used as lithology indicator. The intervals showing decrease in λρ values and remaining still or increasing in μρ are evaluated as producing or potential hydrocarbon bearing zones. Due to the impedance contrast, optimum color scale was selected. Reservoir zones have higher μρ values compared to encasing lithology.

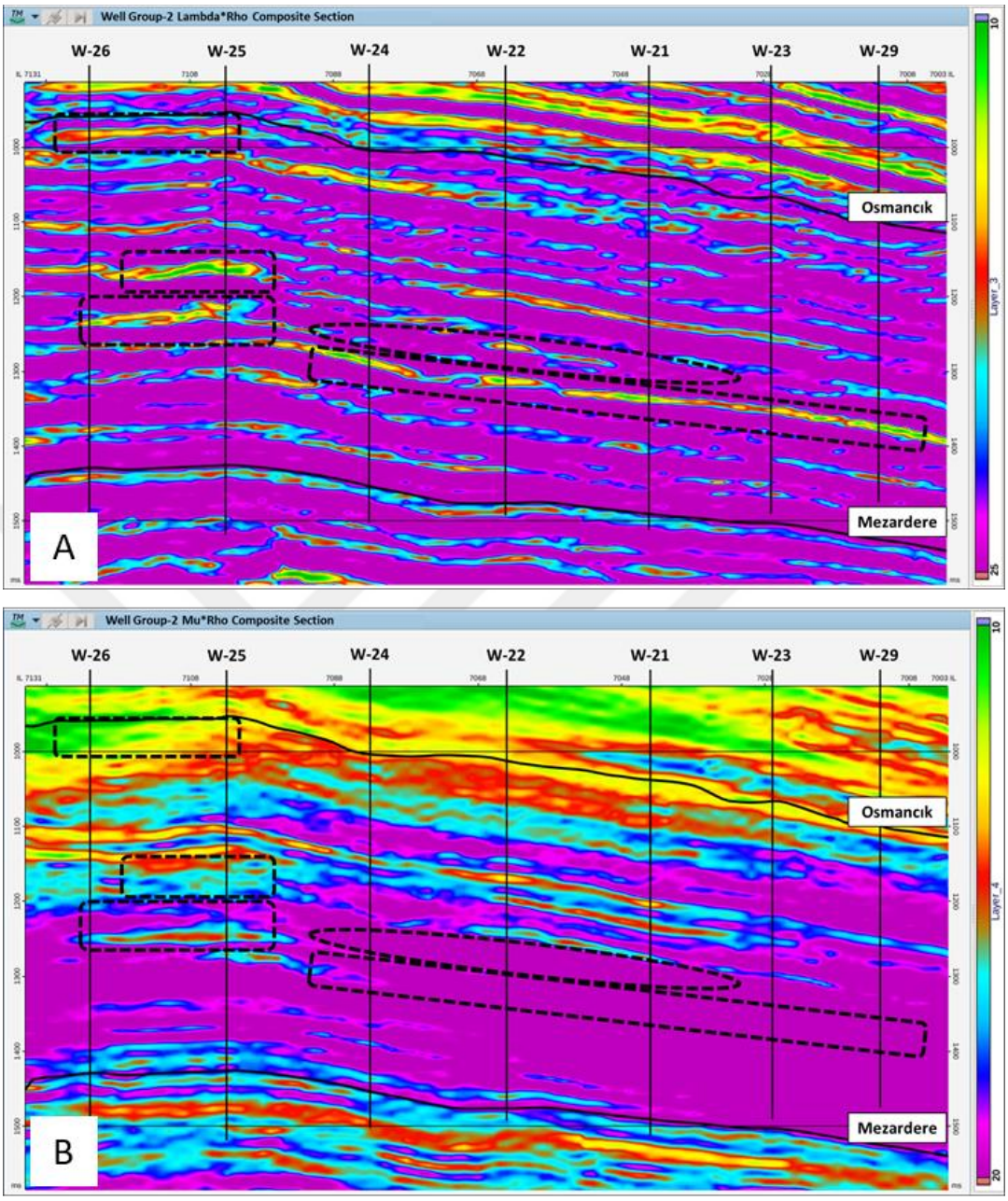

Figure 9.45. A composite section (see Figure 9.5 B) indicating (A) λρ and (B) μρ for well group 2. Lower values for λρ are hydrocarbon indicators while μρ are used as lithology indicator. The intervals showing decrease in λρ values and remaining still or increasing in μρ are evaluated as producing or potential hydrocarbon bearing zones. Due to the impedance contrast, optimum color scale was selected. Reservoir zones have higher μρ values compared to encasing lithology.

9.3.5 Neural Network Applications

The use of neural network techniques in geophysics initiated early 1990s and This method was used for the prediction of lithology of a well (McCormack, 1991). Recent development of technologies lead to predict reservoir properties (Cersósimo et. al., 2016). The aim of the use of this method in this study is to elaborate lithology variations and to provide a secondary and meaningful parameter for facies modeling.

9.3.5.1 Gamma-Ray Distribution

Probabilistic Neural Network (PNN) applications generate a non-linear relationship between reservoir properties and seismic data set (Othman et al., 2022). Any log data can be distributed on the study area, in the case, number and the quality of the data sets are good enough.

Three type of data sets are used in the application of PNN: (1) Type of the log curve representing the parameter aimed to be distributed, (2) seismic stack data as an internal attribute, (3) seismic inversion outputs and attributes generated from the seismic data as external attributes. (Figure 9.46).

A workflow of the PPN application is given in Figure 9.47. Selected log parameter is correlated with seismic attributes using a signal operator. Length of the operator is tested during the implementation of this method. All data sets are trained and cross-correlated to obtain optimum data sets. During this process, several error plots are utilized.

In this research, gamma-ray (GR) distribution of the 3D seismic field was targeted. Firstly, multiple attribute list was created to be trained. A step wise regression technique was applied to find the best fitted attributes with GR log. After the training of data sets, well logs from each group was selected and the ones which are not suitable were extracted. The error plot of the selected wells is shown in Figure 9.48.

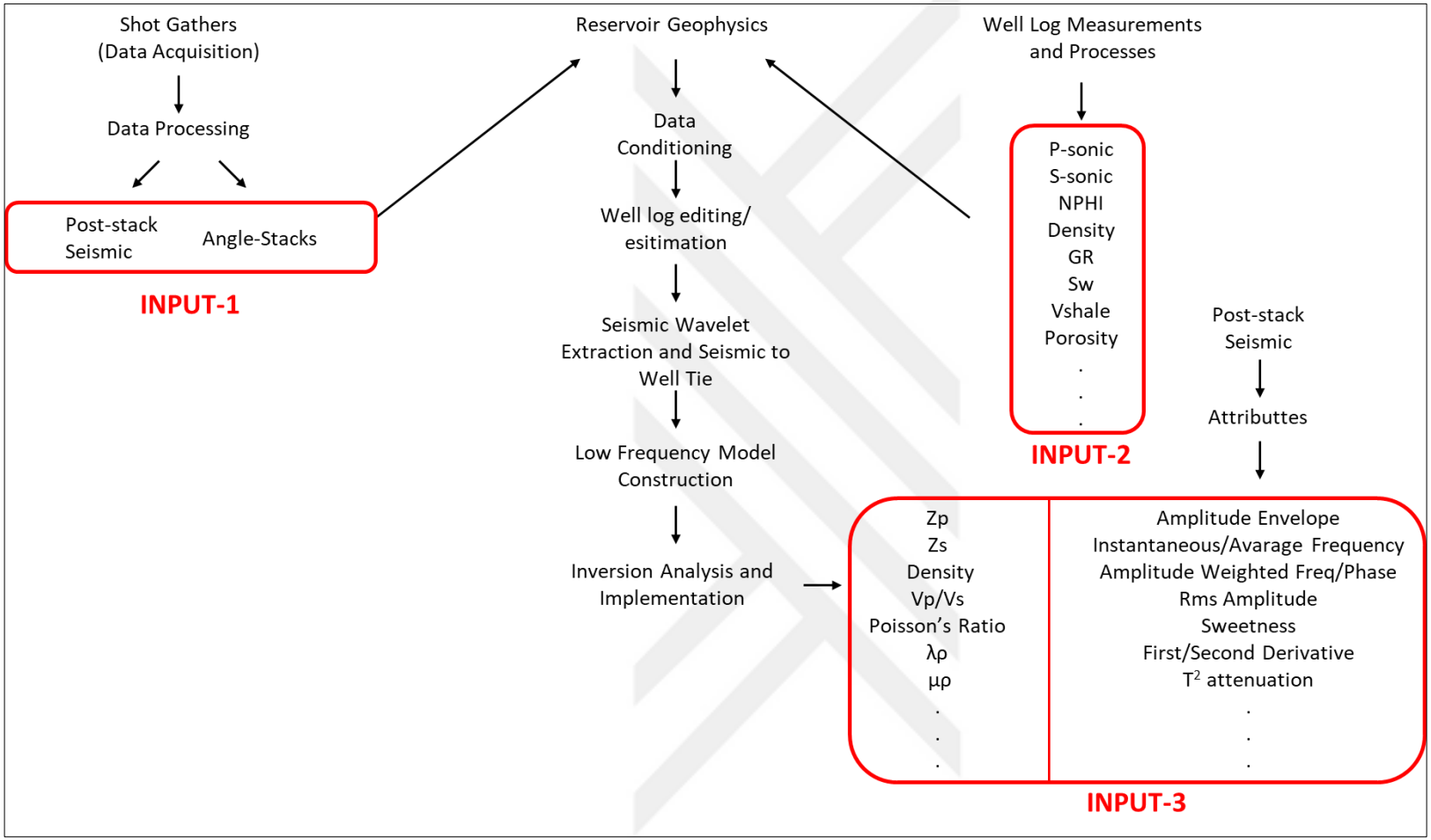

Figure 9.46. Input data sets used for probabilistic neural network is given in this figure.

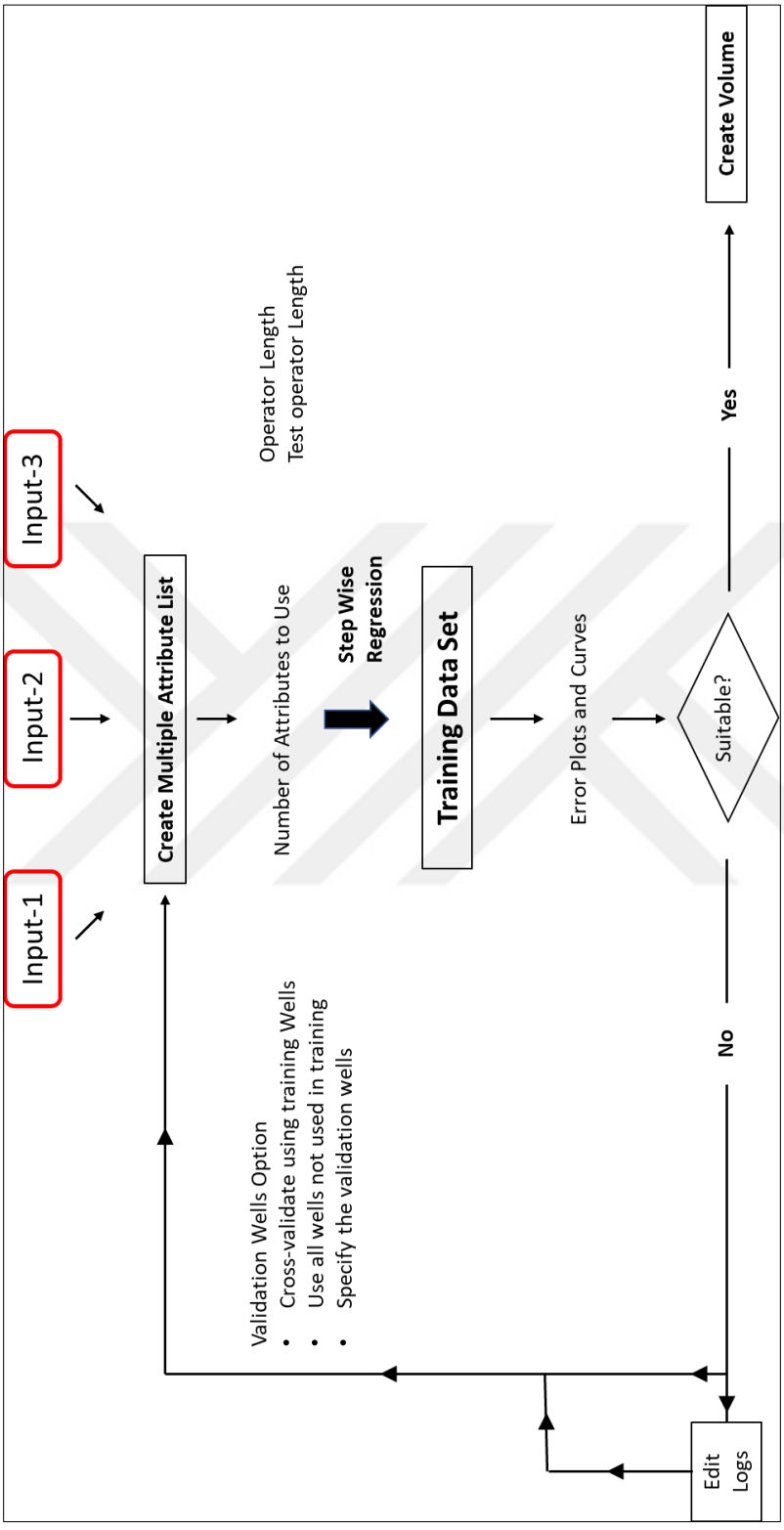

Figure 9.47. Workflow of probabilistic neural network (PNN) using inputs illustrated in Figure 9.46.

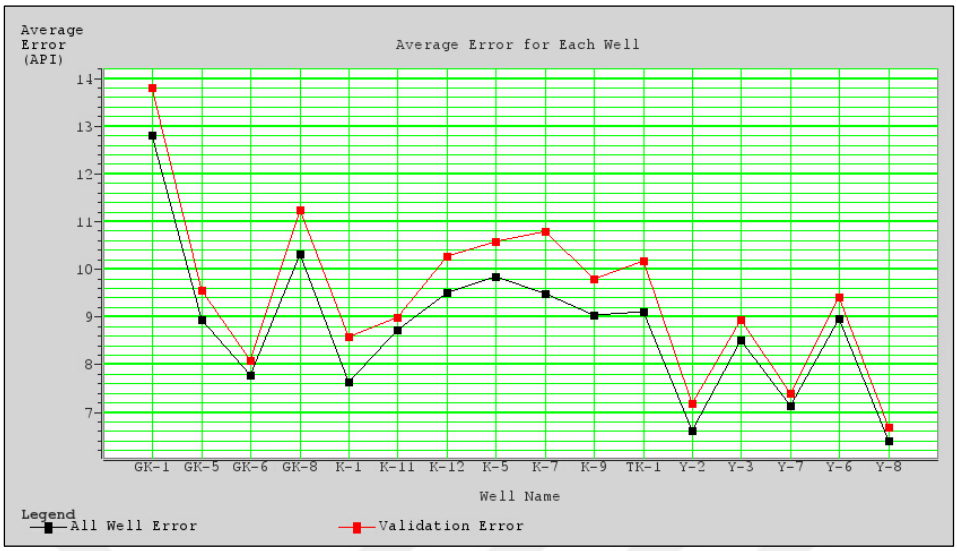

Figure 9.48. Training and validation errors for each well determined to be used.

Next, training and validation errors were calculated. To achieve this calculation, initially, all logs used for the prediction of GR were trained together and the error of each well was computed. Real and estimated curves are given in Figure 9.49 for group-2 and 3, separately. A cross-plot of these actual and computed GR values are also shown in Figure 9.50. The correlation of this cross-plot is almost 82%.

The misfit error obtained from real and calculated log data at well locations is called as training error. To calculate validation error, each well was extracted one by one, and other wells were used to calculate GR curve at the well location of the extracted one. This process was implemented to each well, in orderly. Finally, both training and validation errors were compared to pick the number of attributes chosen. These cross-plots assisted to determine the number of seismic attributes to be used to apply the data (Figure 9.51). The selected final attributes for PNN is shown in figure 9.52.

When the data sets used for PNN was determined, this method was applied to the 3D seismic volume. An average GR map approximately covering only deeper section of the Osmancık Formation is illustrated in Figure 9.53. This map indicates that shaleness increases towards north-east of the field in deeper Osmancık Formation.

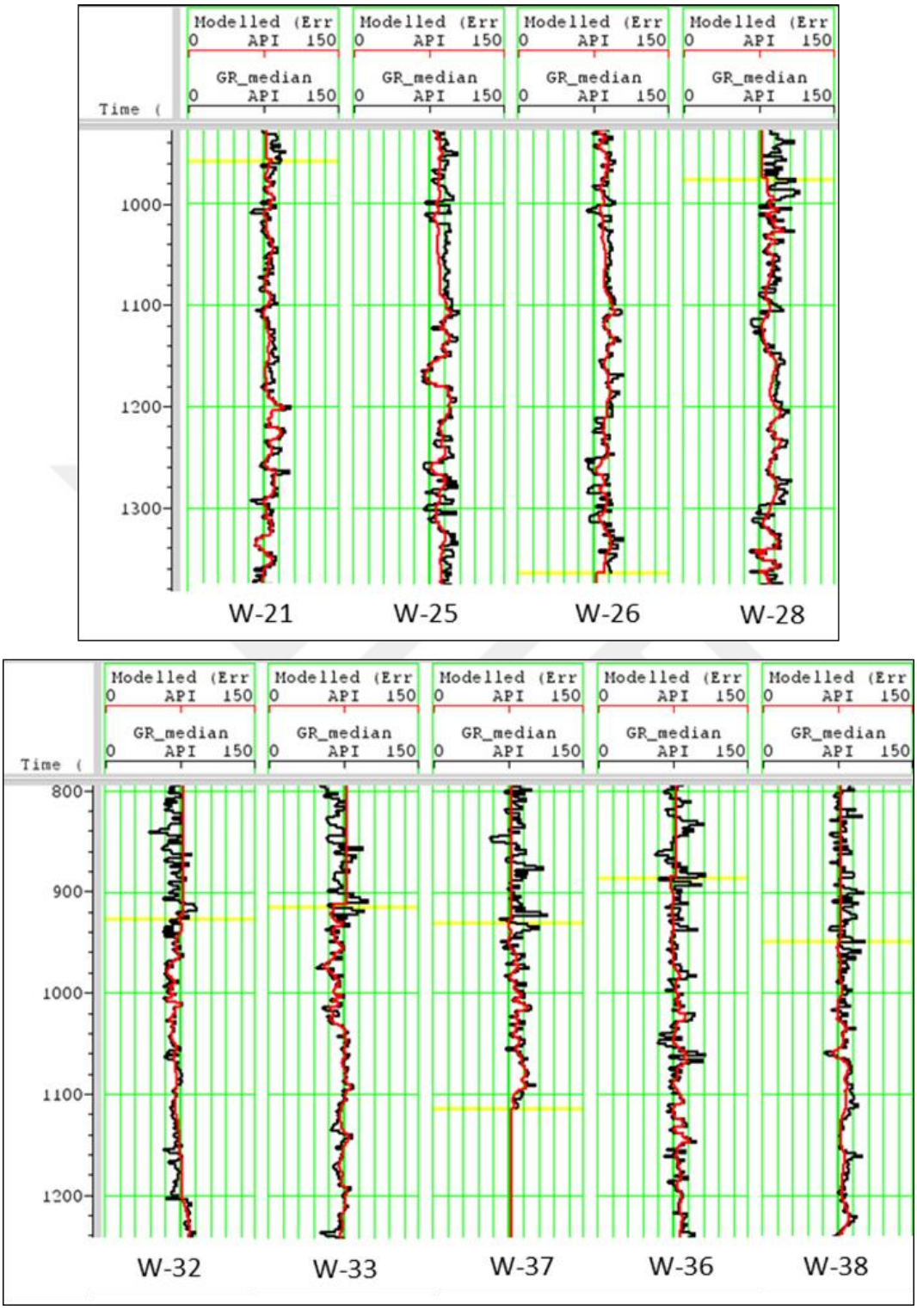

Figure 9.49. The comparison of actual GR (black curve) and estimated GR (red curve) logs for well group 2 (lower panel) and well group-3 (upper panel) are given.

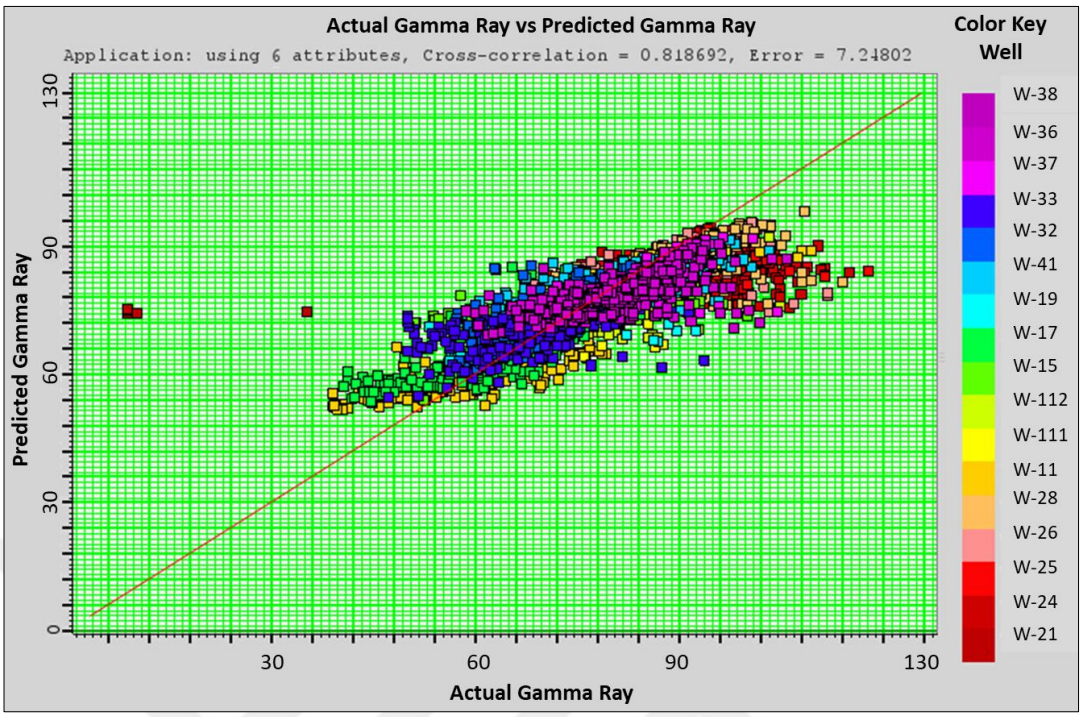

Figure 9.50. The cross-plot of actual versus predicted gamma ray logs is given in this Figure. Correlation coefficient was calculated as 82%.

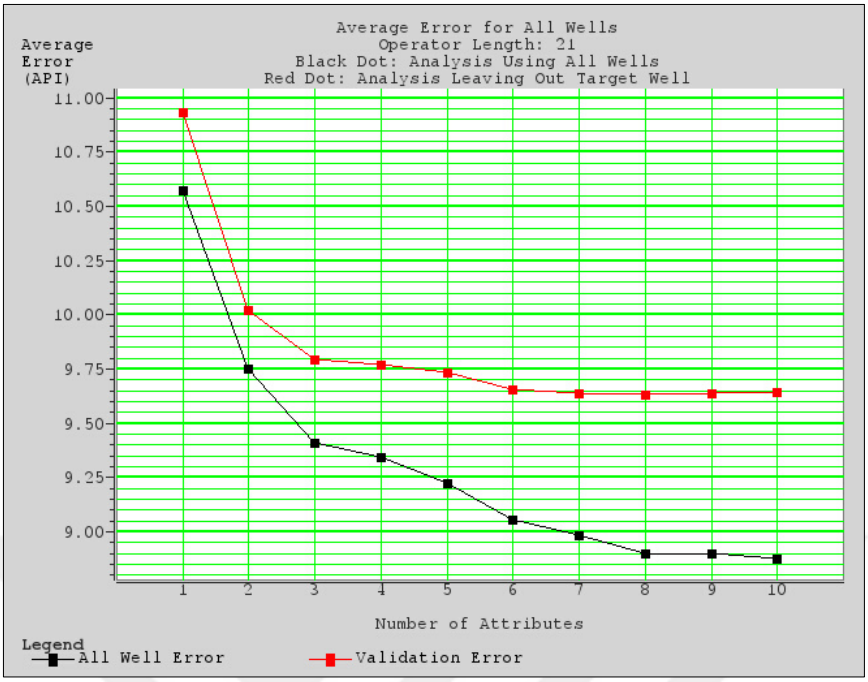

Figure 9.51. Training error (black curve) and validation error (red cure) are given. Until the 6th attribute is reached, both errors decrease. Then, validation remains still.

Multi-Attribute List: Multi Attribute List 2

	Target	Final Attribute	Training Error	Validation Error
1	Gamma Ray	Average Frequency	10.576183	10.937623
2	Gamma Ray	(PHD_KARACALI-YULAFLI_S-IMP)**2	9.756786	10.026673
3	Gamma Ray	Dominant Frequency	9.411467	9.796096
4	Gamma Ray	Filter 15/20-25/30	9.345363	9.774169
5	Gamma Ray	(PHD_KARACALI-YULAFLI_DENSITY)**2	9.230007	9.735395
6	Gamma Ray	(PHD_KARACALI-YULAFLI_LR)**2	9.058519	9.657761
7	Gamma Ray	Amplitude Weighted Frequency	8.989257	9.641079
8	Gamma Ray	PHD_KARACALI-YULAFLI_P-IMP	8.903605	9.637573
9	Gamma Ray	PHD_KARACALI-YULAFLI_MR	8.902754	9.643032
10	Gamma Ray	Filter 5/10-15/20	8.880982	9.651060

Figure 9.52. The selected 10 attributes after step wise regression. The first six attributes displayed with yellow color were used. After the 6th attribute, contribution of the attributes is neglectable.

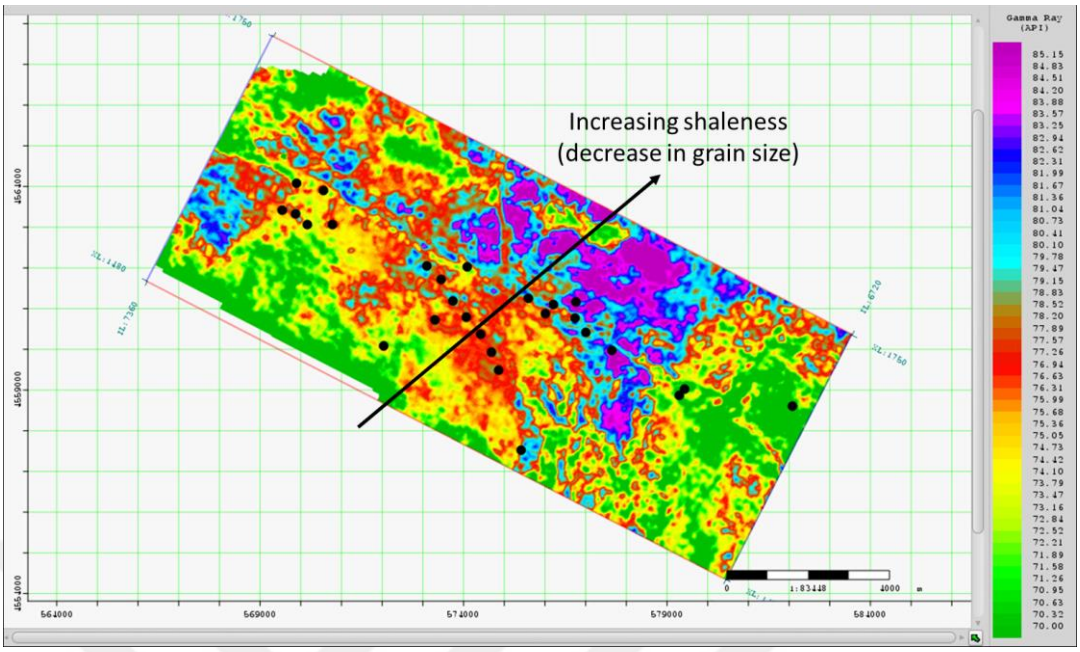

Figure 9.53. Gamma-Ray distribution representing the deeper section of the Osmancık Formation is given. GR values are higher in the north-east of the field. Well group-3 sands (on the west of the area) seem to be clearer than the sediments of other two groups. Well group 2 and 3 wells are very productive while well group 1 wells are not as it was discussed in previous chapters.

9.3.5.2 Seismic Trace Based Classification

Seismic facies classification method is an advanced statistical technique benefiting artificial intelligence, particularly, neural network applications. This method uses seismic data and attributes as input and classifies seismic waveform. It is an unsupervised method because well log information is not included to classify seismic facies. Principle component method is used for the purpose of dimension reduction to select proper number of seismic attributes. Neural network is utilized to determine classes and propagate these classes.

9.3.5.2.1 Inputs

Seismic facies classification is an unsupervised method due to lack of the use of well logs as input. Post-stack seismic data, output cubes of seismic inversion and calculated or measured attributes are the main inputs. Table-1 shows input cubes for seismic facies classification.

9.3.5.2.2 Volume Reduction by Principle Component Analyses

Principle Component Analysis (PCA) is a common method used in neural network applications for the purpose of dimension reduction. This method is benefited to decide the number of attributes to use. Reducing volume will assist to decrease computation cost because after a certain number of attributes is reached, the rest of the attributes do not contribute the accuracy of the result. The first step is to analyze data sets and define relations between each attribute. Addition of each attribute will result in decreasing this value and approximate a more reliable result. Figure 9.54 indicates a cross-plot of components (number of attribute) versus Eigen values. Note that after reaching a certain number of attributes, the contribution of additional inputs becomes minimal. In this study, six components were determined to be used. Attributes and their relevant contributions are given in Figure 9.55.

Table 9.1 Input list for seismic facies classification.

Attribute	**Source**
Post-stack Seismic Data	Seismic Data Itself
P-impedance	Seismic Inversion
S-impedance	Seismic Inversion
Poisson's Ratio	Seismic Inversion
Vp/Vs Ratio	Seismic Inversion
Lambda*Rho	Seismic Inversion
Mu*Rho	Seismic Inversion
Density	Seismic Inversion
Amplitude-weighted instantaneous frequency	Seismic Attributes
Amplitude-weighted instantaneous phase	Seismic Attributes
Average Frequency	Seismic Attributes
Dominant Frequency	Seismic Attributes
Signal Envelope	Seismic Attributes
RMS Amplitude	Seismic Attributes
Instantaneous Frequency	Seismic Attributes
Instantaneous Phase	Seismic Attributes
Envelope Derivative	Seismic Attributes
Second Derivative of Envelope	Seismic Attributes
Weighted Mean Frequency	Seismic Attributes
Sweetness	Seismic Attributes

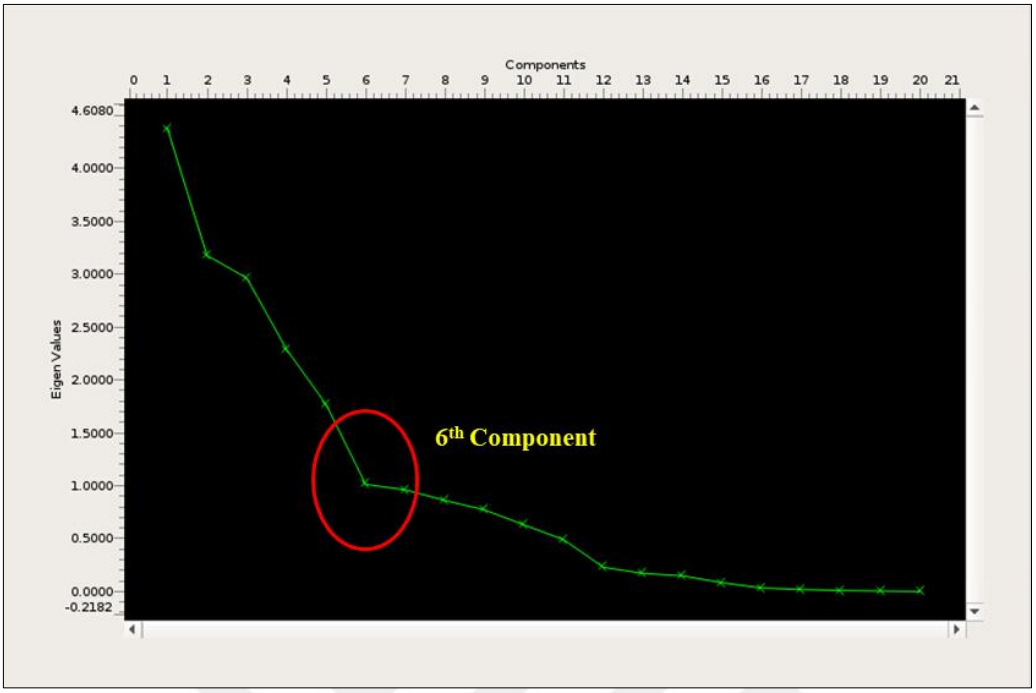

Figure 9.54. Cross-plot of components versus Eigen Values. 20 attributes were calculated. After 6th component, any significant improvement was not observed.

	Eigen values	Contributions		Cumulated
Component 1	4.378152	21.890761	From Seismic Files - PhD_ Density	21.890761
Component 2	3.176274	15.881371	From Seismic Files - PhD_ Lambda * Rho	37.772132
Component 3	2.963208	14.816042	From Seismic Files - PhD_ Mu * Rho	52.588174
Component 4	2.290546	11.452731	From Seismic Files - PhD_ P-wave Impedance	64.040906
Component 5	1.768065	8.840325	From Seismic Files - PhD_ Poisson's Ratio	72.881231
Component 6	1.013217	5.066084	From Seismic Files - PhD_ S-wave Impedance	77.947315
Component 7	0.960660	4.803300	From Seismic Files - PhD_ Vp_Vs Ratio	82.750614
Component 8	0.861215	4.306076	From Seismic Files - PhD_Amp-Weighted Inst Freq	87.056691
Component 9	0.771576	3.857881	From Seismic Files - PhD_Amp-Weighted Inst Phase	90.914572
Component 10	0.629557	3.147785	From Seismic Files - PhD_Average Frequency	94.062357
Component 11	0.490088	2.450439	From Seismic Files - PhD_Dominant Frequency	96.512796
Component 12	0.228618	1.143092	From Seismic Files - PhD_Envelope Derivative	97.655888
Component 13	0.171321	0.856604	From Seismic Files - PhD_Instantaneous Frequency	98.512492
Component 14	0.147896	0.739481	From Seismic Files - PhD_Instantaneous Phase	99.251973
Component 15	0.082798	0.413992	From Seismic Files - PhD_KARACALI-YULAFLI_STACK	99.665965
Component 16	0.033570	0.167852	From Seismic Files - PhD_RMS Amplitude	99.833817
Component 17	0.018938	0.094691	From Seismic Files - PhD_Second Deriv of Envelope	99.928508
Component 18	0.009283	0.046414	From Seismic Files - PhD_Signal Envelope	99.974923
Component 19	0.004371	0.021856	From Seismic Files - PhD_Sweetness	99.996779
Component 20	0.000644	0.003221	From Seismic Files - PhD_Weighted Mean Frequency	100.000000

Figure 9.55. After the 6th attribute, contribution of additional ones is minimal. After the 12th attribute, additional ones are even neglectable. Optimum number of components was specified as 6.

9.3.5.2.3 Class Determination

Seismic facies classification uses seismic waveforms to create classification. In other words, different waveforms are classified and propagated for facies classification. To test the number of classes, input data sets are trained. In this research, number of classes was selected as 5 within the Osmancık Formation. Lithofacies classification cross-plot using PCA is given in Figure 9.56 A. Each square on the cross-plot is responsible for one class or different waveform shape. A histogram showing the intensity of color is displayed in Figure 9.56 B.

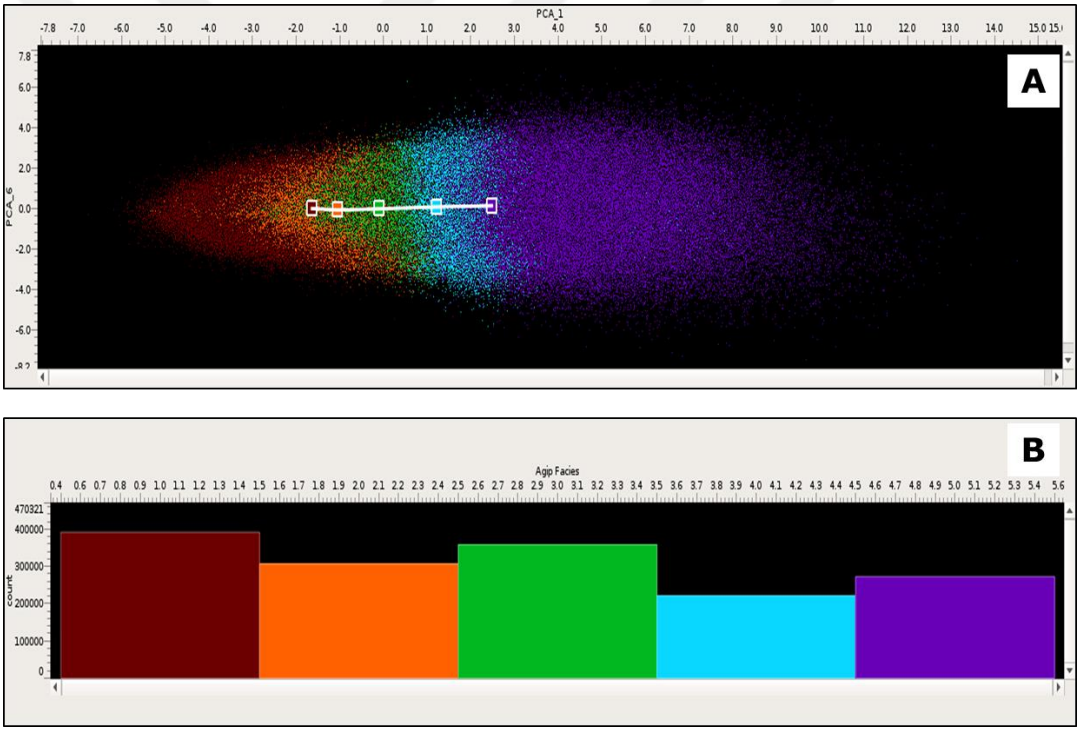

Figure 9.56. (A) Classification of waveforms, (B) histogram showing frequency of colors representing each class. (A) Five classes were selected. Purple and blue colors represent sandy intervals while brown and orange ones are mostly shaly or silty lithology. Green is mostly mix facies. (B) Histogram view showing frequency of color used for classification. This figure shows that colors have similar counts which means sand and shale alternation is very intensive.

9.3.5.2.4 Propagation of Seismic Facies

Analyzed colors were correlated with well responses to identify quality of the results. Figure 9.57, 9.58 and 9.59 show composite sections created from each well group, which indicate seismic facies. Purple and blue colors represent sandy and coal lithologies, green one is mostly mixed facies consisting of sand and shale lithology and orange and brown colors are shaly, silty or fine grain sized sand facies. Results of the seismic trace-based classification confirm the changing behavior of lithology through deeper sections.

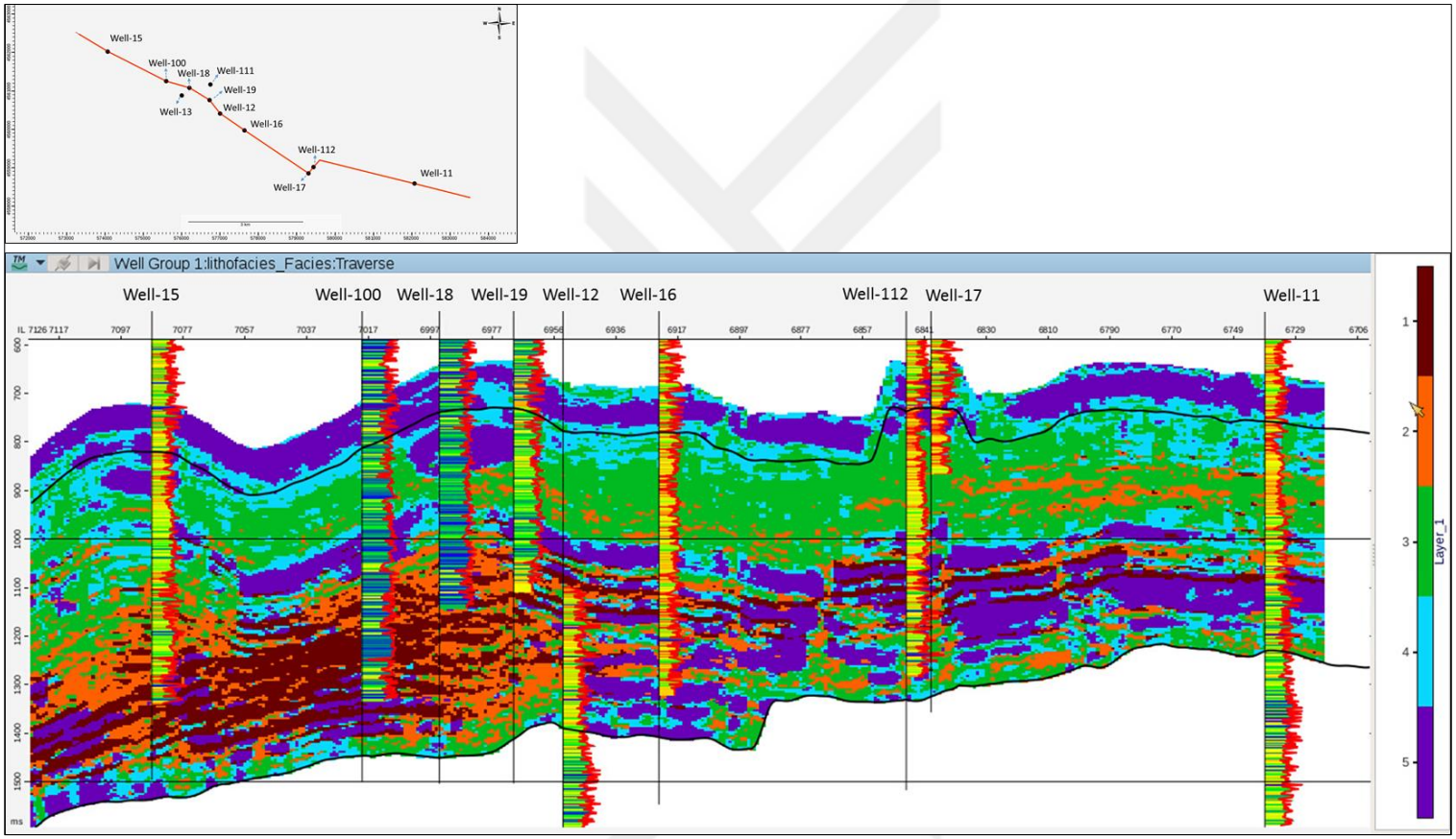

Figure 9.57. Location map of the composite section related to Well Group 1 is shown on the top and seismic facies classification section is on the bottom in this figure. Gamma-ray log curves are inserted. Purple and blue ones are mostly sandy while orange and brown colors mostly small grain sized sand/shale/silt lithologies. Green color represents mixed facies of sand and shale.

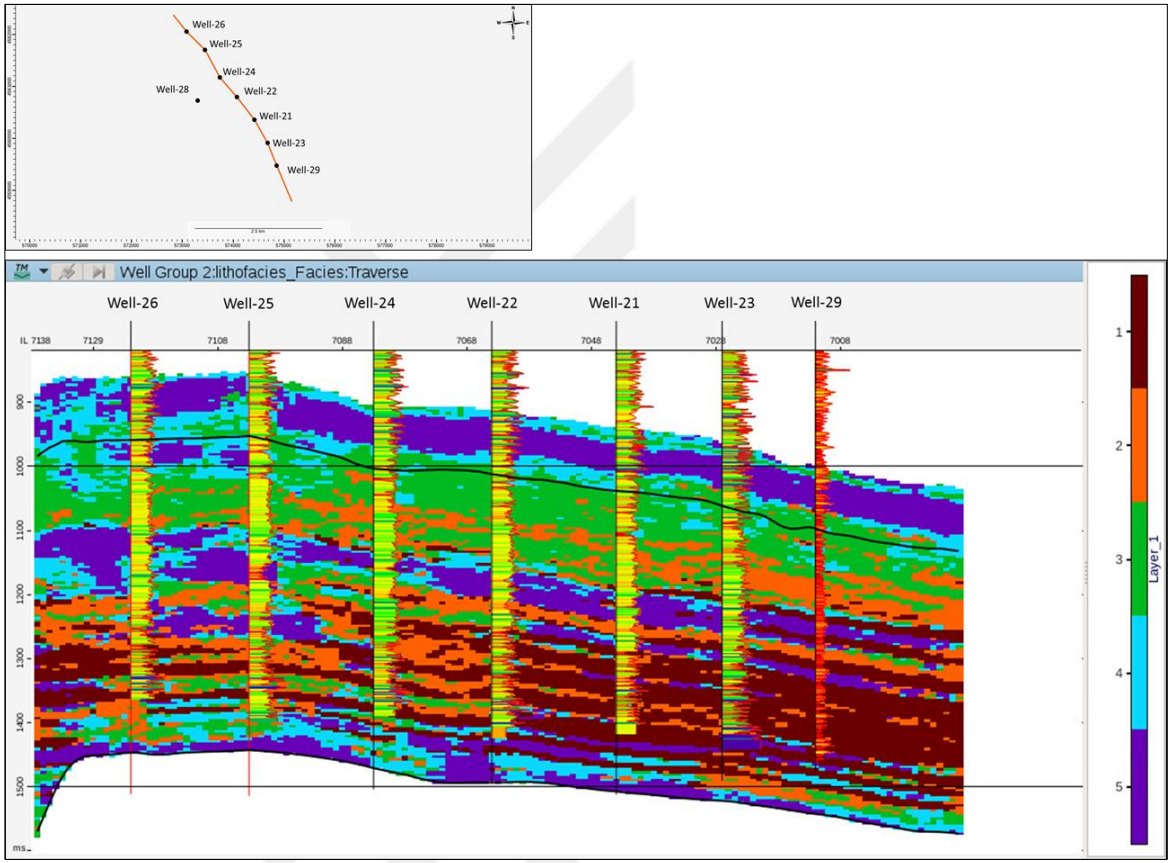

Figure 9.58. Location map of the composite section related to well group 2 is shown on the top and seismic facies classification section is on the bottom in this figure. Gamma-ray logs inserted. Purple and blue ones are mostly sandy while orange and brown colors mostly small grain sized sand/shale/silt lithologies. Green color represents mixed facies of sand and shale.

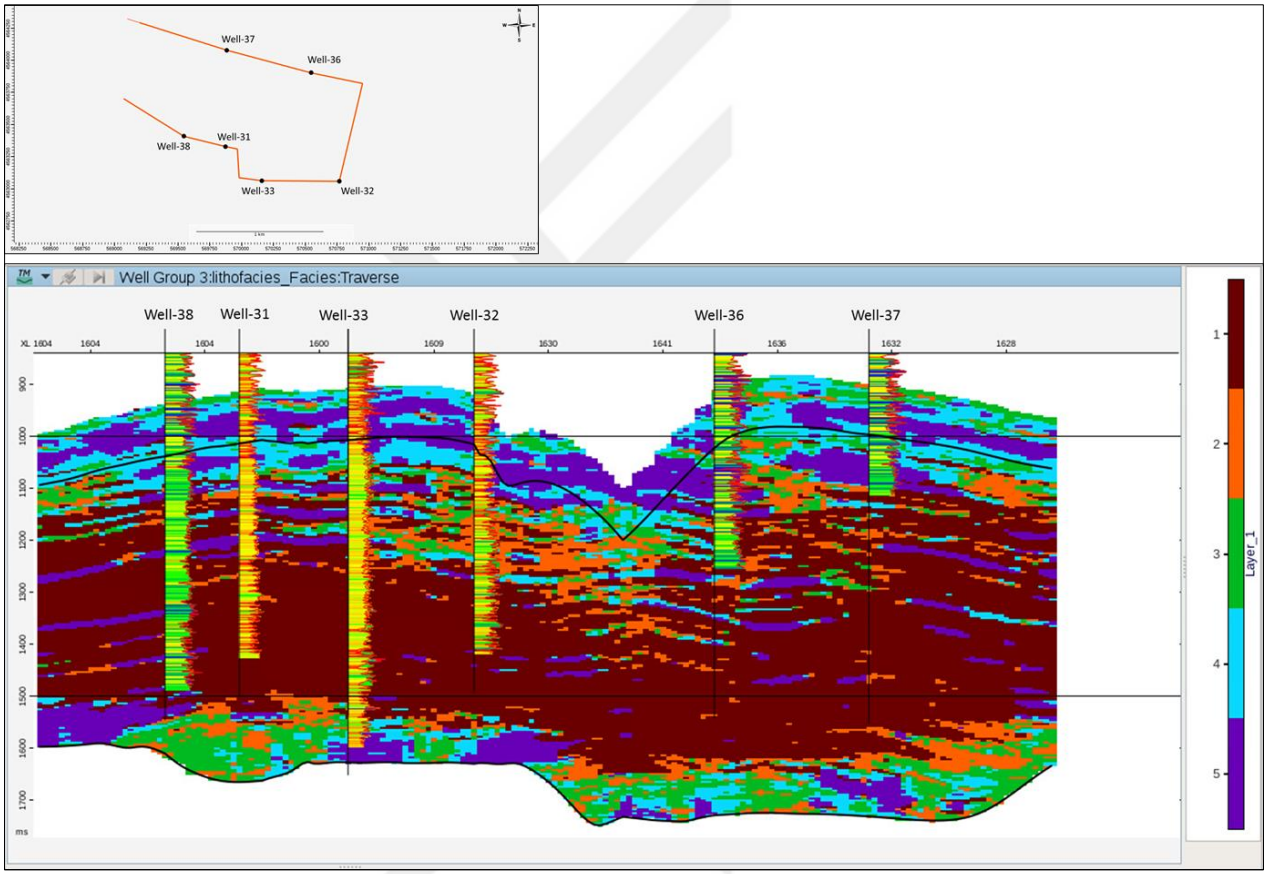

Figure 9.59. Location map of the composite section related to well group 3 is shown on the top and seismic facies classification section is on the bottom in this figure. Gamma-ray logs inserted. Purple and blue ones are mostly sandy while orange and brown colors mostly small grain sized sand/shale/silt lithologies. Green color represents mixed facies of sand and shale.

CHAPTER 10

GEOSTATISTICAL RESERVOIR MODELING

10.1 Introduction

The main target of geostatistical reservoir modeling is to generate 3D numerical models honoring a range of disciplines such as geoscience, petroleum and engineering data sets. Therefore, one of the key aspects of geostatistics is the integration of multiple data set to construct a 3D geostatistical model (Pyrcz and Deutsch, 2014). In this study, several data sets and disciplines were studied and a database was created for the purpose of modeling.

In this research, facies variability and petrophysical properties, such as total porosity, effective porosity and permeability, were modeled to characterize the Osmancık Formation in Karaçalı-Yulaflı field. Advanced simulation techniques such as Sequential Indicator Simulation (SIS) and Sequential Gaussian Simulation (SGS) were used for spatially modeling the field.

10.2 Conceptual Model

A structural framework is described as a well-identified concept, which is used to add structural explanation of a geological model (Piessens et al., 2020). Qualitative (Conventional) interpretation (Chapter 9) led the generate a constrained structural model for the study field. This model was used as a conceptual model, forming to base of geostatistical modeling (Figure 10.1). For cell-based simulation techniques such as SIS and SGS this structural model was honored.

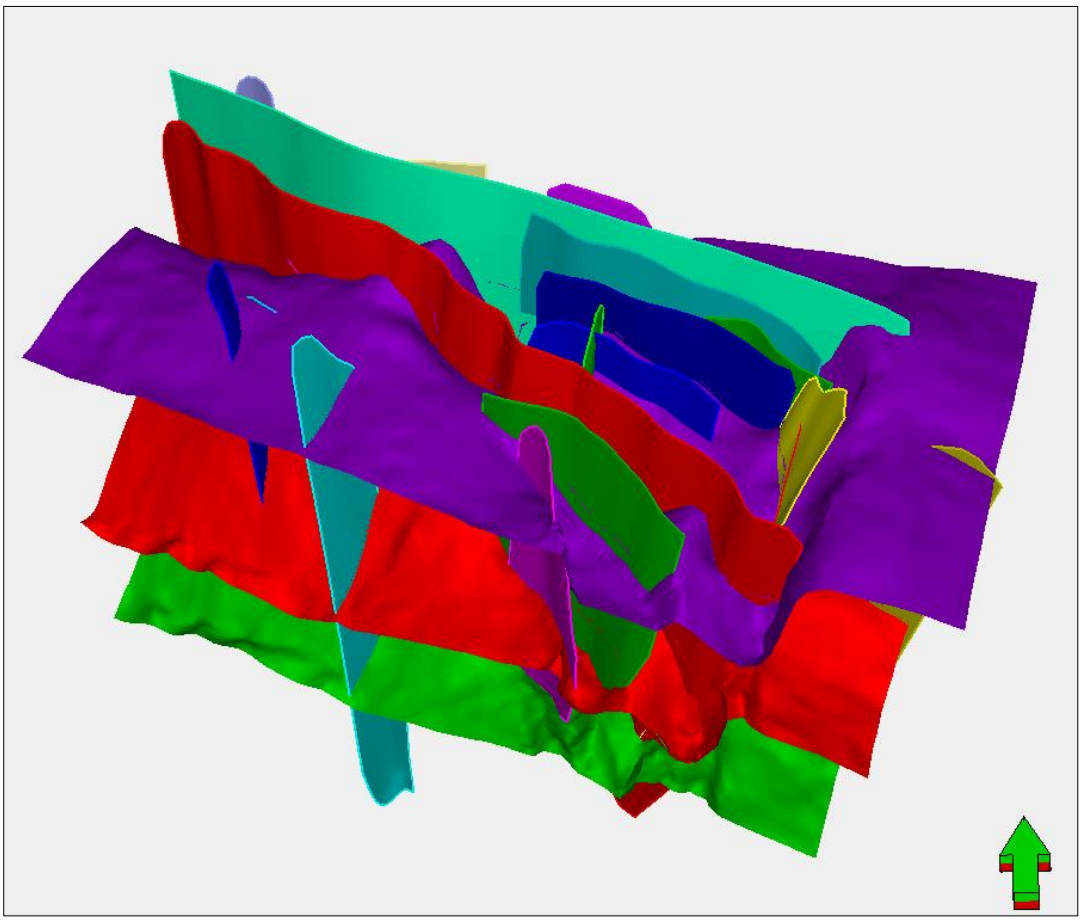

Figure 10.1. A 3D display of structural framework including the Danişmen Formation (purple color), Osmancık Formation (red color) and Mezardere Formation (green color) horizons with the combination of fault framework.

10.3 Gridding

Very early stage of the advance modeling is to grid structural model into the cells. To specify the number of grids, the thickness of the Osmancık Formation was mapped (Figure 10.2). The thickest part of formation mostly covers the middle part of the field from west to east direction between main fault zones. The maximum thickness is defined as 1200 meter and the minimum is around 200 m. Sampling rate of the seismic data is 4 ms. To benefit from the seismic data, structural model was

divided 300 layer (Z), allowing to calibrate maximum thickness as 4 m and minimum thickness as 0.65 m. The number of the horizontal grid was defined as 120 for both directions (X-Y) which is the half distance of the closest two wells in the field. The Osmancık Formation was gridded using 300 to 600 cell numbers. Cell numbers between 300-450 represent shallower Osmancık Formation, wheares 450-600 represent deeper Osmancık formation approximately. The gridded model of the zone of the Osmancık Formation and gridded fault planes are given in Figure 10.3.

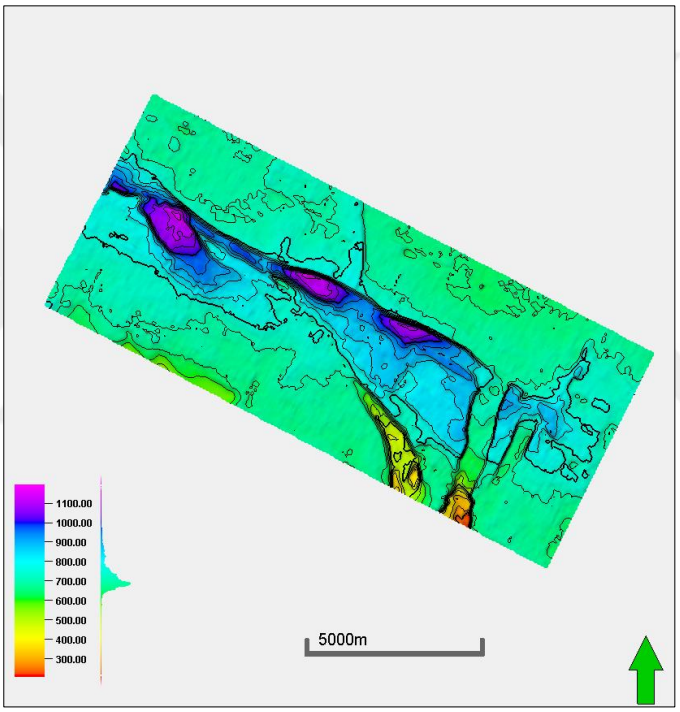

Figure 10.2. Thickness map of the Osmancık Formation. The maximum thickness (purple color) is 1200 m. and minimum thickness is 200 m (red color).

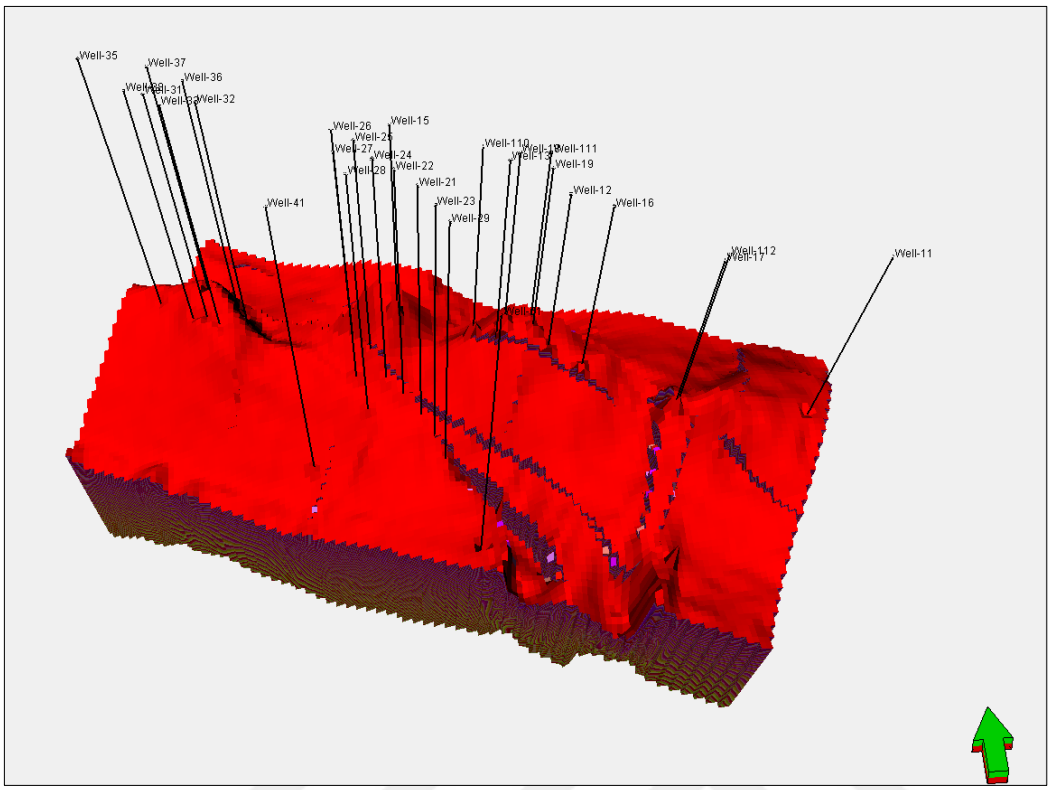

Figure 10.3. Gridded structure volume (120x120x300) of the Osmancık Formation zone.

10.4 Experimental and Model Variograms

The semivariance measures the spatial difference of a variable between two observed locations. How rate of the variable changes in a specified orientation is the main concern of this method. Even though a variable is continuous spatially, known values are restricted only an area with a small boundary. The values of the variable can be measured only by observation of the samples collected from diverse locations (Davis, John C., 2002).

The semivariance is calculated as below:

$$\gamma_h = \frac{\sum\left\{(x_i - x_{i+h}) - \frac{\sum(x_i - x_{i+h}}{n}\right\}^2}{2n} \qquad 10.1$$

For practical computation, sample spacing is assumed to constant. In the case, this spacing of the observations is different from each other, semivariogram is computed as given:

$$\gamma_h = \sum_i^{n-h} (x_i - x_{i+h})^2 / 2n \qquad 10.2$$

where x_i is a measurement of the variable at i^{th} location, $i + h$ is the next observation with h distance, n is the number of points and $n - h$ represents number of comparisons between the points.

10.4.1 Experimental Variogram

When semivariances at different observation distances are computed, the resulted semivariogram can be plotted, which is also called as experimental variogram. The values of semivariance are dependent of the spacing distance (Δh) between observations. The more Δh results in the higher semivariance values or vice versa.

When a certain distance is reached, the data points will not be related to each other. In this in this situation, the semivariance will not increase any more, resulting a flat region. This region is called as “Sill”. When lag distance in a semivariogram is zero, the value of the semivariance is referred as “Nugget”. The lag distance from zero to sill is called as “Range” (Davis, John C., 2002) (Figure 10.4).

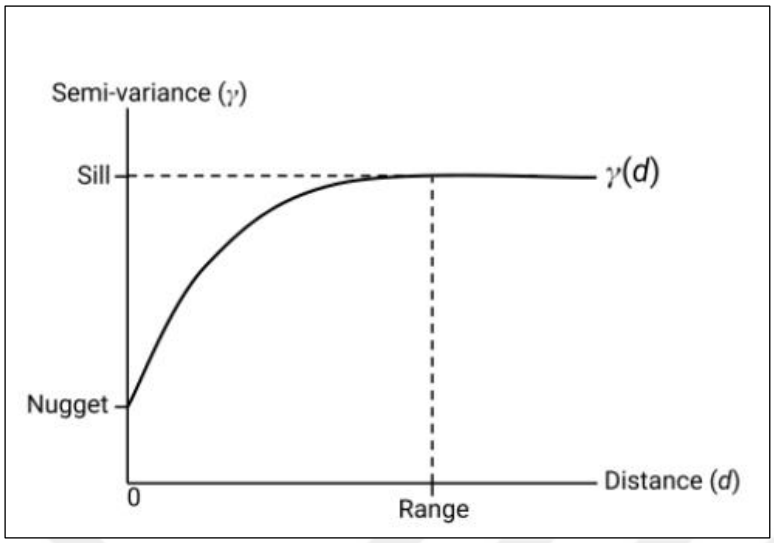

Figure 10.4. Chart of a semi-variogram showing terms.

10.4.2 Variogram Modeling

Experimental variogram only shows the points measured at given lag distance. However, measuring variables in each location is not possible. Therefore, locations without any measurement are necessary to be modelled. Several fitting techniques are available. An example of modelled variograms is illustrated in Figure 10.5.

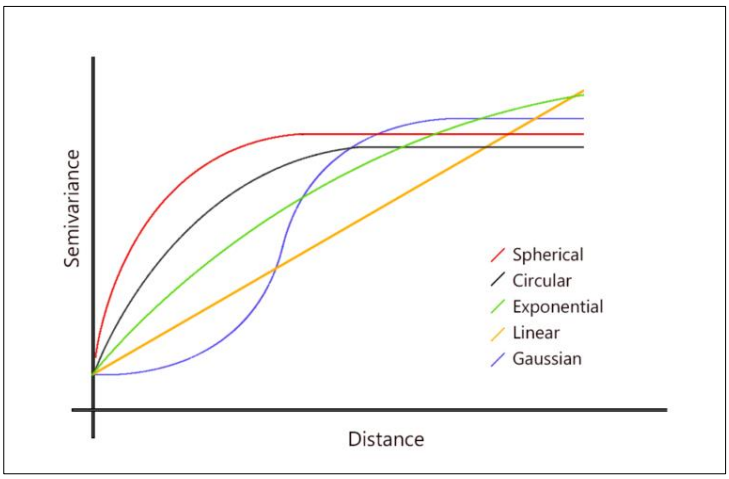

Figure 10.5. Illustration of fitting techniques for variogram modeling (Tolosana-Delgado and Mueller, 2021).

Well-known and frequently used variogram models can be listed as are spherical, exponential and Gaussian models. Equations of each model is given as below:

Spherical model:

$$\gamma h = c\left(\frac{3h}{2a} - \frac{h^3}{2a^3}\right) \quad 10.3$$

Exponential model:

$$\gamma h = c\left(1 - e^{-3h/a}\right) \quad 10.4$$

Gaussian model:

$$\gamma h = c\left(1 - e^{-3h^2/a^2}\right) \quad 10.5$$

Where h is the lag distance, a is the range and c is the sill.

10.5 Geostatistical Methods for Modelling

For spatially distribution of facies, sequential indicator simulation (SIS) method was run. This method is frequently used for the distribution of highly variable facies (Deutsch, 2006). This is one of the variogram-based methods. If it is assumed that M facies categories are available, the indicator transform at a location with specified facies (s_m) represents probability of those facies at that location.

$$s_m, m = 1, \dots\dots, M \qquad 10.1$$

Depending the number of categorical facies, M, indicator transforms with M number is available at each of the data location. Each facies assigned into the grids using SIS. Each grid node is placed with following: (1) Locating nearby data and previous simulation location, (2) calculation of the probability of each facies specified to be distributed by kriging; $p_m, m = 1, \dots\dots, M$, and (3) simulation facies using a number of probabilities. Multiple realizations are created by the re-run of the randomly selected seeds (Pyrcz and Deutsch, 2014).

Sequential Gaussian Simulation (SGS) method has been frequently utilized for reservoir property modelling (Hu and Ravalec-Dupin, 2005; Isaaks, 1991). SGS algorithm may be explained as:

(1) Transformation of the data to normal distribution,

(2) Place of transformed data into the grids,

(3) Kriging the data and estimation the variance between previously simulated one,

$$Y(u) = \sum_{\beta=1}^{n} \lambda_\beta * Y(u_\beta) \qquad 10.2$$

$$\sigma_{SK}^2(u) = C(0) - \sum_{\alpha=1}^{n} \lambda_\alpha C(u, u_\alpha) \qquad 10.3$$

where $\gamma(u)$ is the kriged estimate, σ_{SK}^2 is the simple kriging variance, λ_α is the kriging weight, $C(u, u_\alpha)$ is the nonstationary covariance and C(0) is the stationary variance between randomly assigned variables,

(4) Specification of a random residual and addition to estimated variable by kriging to obtain a value which is simulated,

$$Y_s(u) = Y(u) + R(u) \quad (10.4)$$

where $R(u)$ is the residual, $Y(u)$ is the estimated value at location u and $Y_s(u)$ is the simulated variable,

(5) Application of the simulation randomly to all locations,

(6) Back transform data after the simulation,

(7) Generation of multiple realization.

10.6 Seismic Data Resampling

Modeling of property or facies can be achieved in a more reliable way using a secondary variable as a constraint. The outputs of quantitative seismic interpretation or reservoir geophysics are not only beneficial to characterize the reservoirs but also a guidance for the purpose of modeling as a secondary variable. Thus, these volumes were resampled into the grids. The gridded resampled volumes of seismic inversion and artificial intelligence are illustrated in orderly in Figures 10.6 and 10.7.

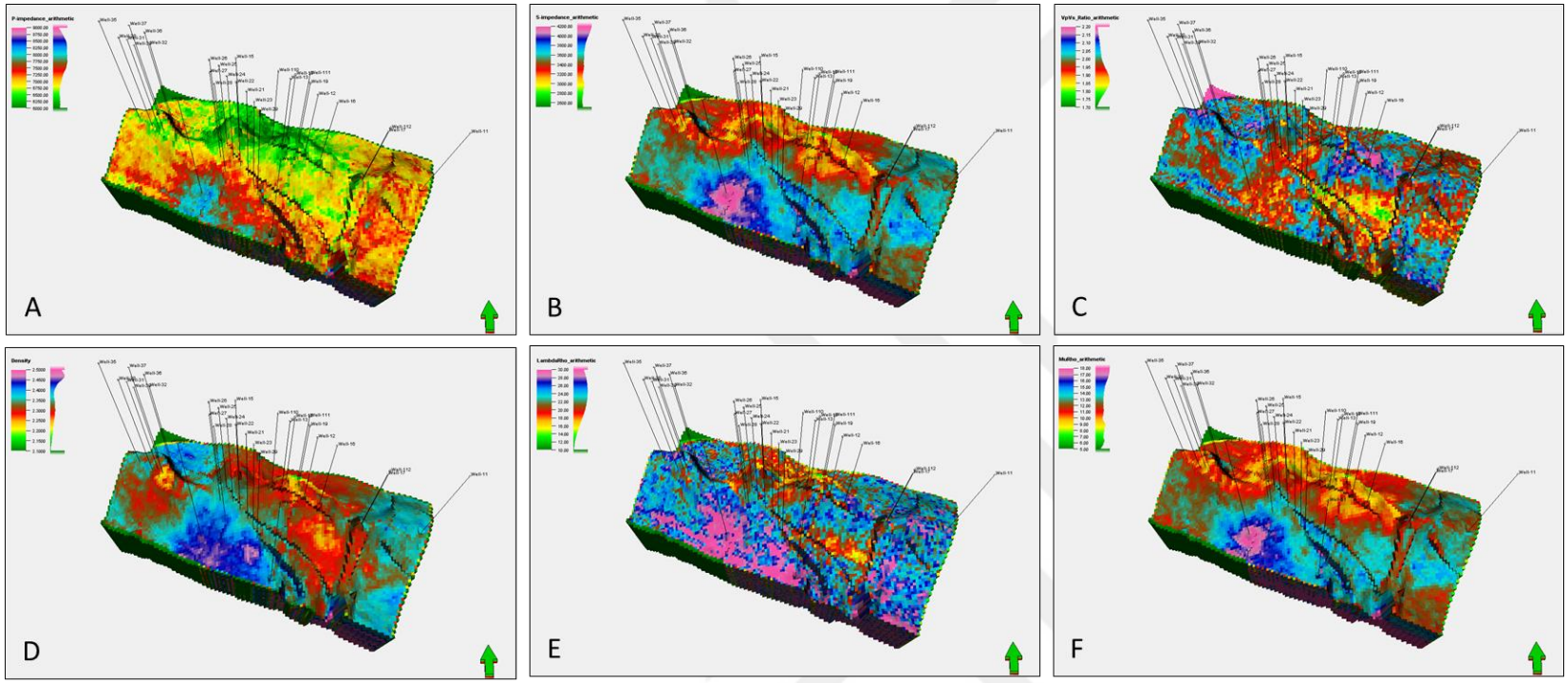

Figure 10.6. Resampled (A) acoustic impedance, (B) shear impedance, (C) V_P/V_S ratio, (D) density, (E) $\lambda\rho$ and (F) $\mu\rho$ cubes.

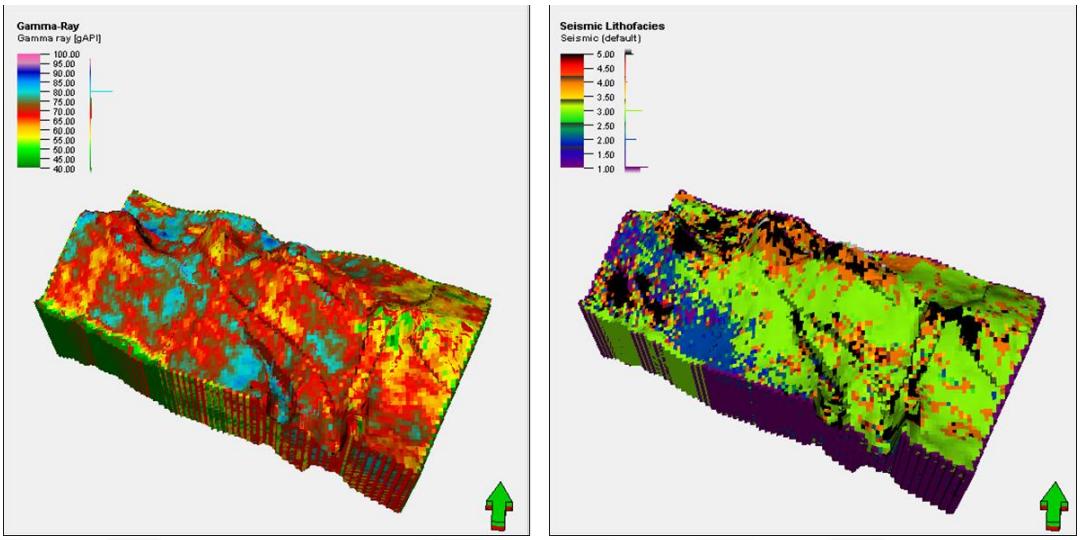

Figure 10.7. Gridded GR volume (left) and gridded seismic facies volume (right) are shown. GR volume was generated by supervised PNN and seismic facies volume was created from only seismic trace differences using unsupervised neural network.

10.7 Modeling Workflow

A general workflow of modeling may include the (1) specification of a goal, (2) conceptual model development, (3) inference of necessary statistical parameters, (4) estimation of a value in unsampled locations, (5) simulation and (5) post-process of the generated models (Pyrcz and Deutsch, 2014).

The first step of the modeling is the specification of the goal. In this study, facies and petrophysical properties of deeper Osmancık Formation are not well-known due to worsen reservoir conditions compared to shallow depths. Therefore, these parameters at unknown locations are targeted to be modelled covering the area of 3D volume. The second step includes the development of a conceptual model restricting study area with a known geometry. A structural model generated by seismic interpretation was used in this study. Then, required statistical parameters were inferred such as histograms, spatially continuous volumes (volumes created by seismic inversion and artificial intelligence), correlations and so on. Next, unsampled values were estimated using data trends, variograms, relations. The last

process covers the implementation of multiple realizations to find out best representative models. Finally, the resulted models were validated using blind wells (post-process).

10.8 Validation of the Modelling Results

When facies or petrophysical modeling is applied, generated volumes also should be validated. This process could be achieved by using blind well test. Because modeling results at well locations will be the same with the utilized wells, it is an important step to confirm the results at locations of a known well without utilized as an input. Two later drilled wells Well-12T and Well-210 were replaced in the field (Figure 10.8). Well section displays of the blind wells, Well-12T and Well-210, are shown in Figure 10.9 and 10.10, respectively. The validation of the illustrative results will be given in Chapters 10.9.3 (Figures 10.19 and 10.21) and 10.10.4 (Fgures 10.34 and 10.35).

10.9 Facies Modeling

Facies distribution of deeper Osmancık Formation is not well defined in the field due to frequent changes in sand and shale alternation. Horizontal and vertical extension of the facies in the field are not continuous and variable in thickness. Therefore, facies show uncertainty, especially, for hydrocarbon bearing reservoirs. In this respect, facies distribution was modelled to detect potential sand facies.

10.9.1 Well Log Upscaling

The earliest step of the facies modeling is to upscale facies logs at wells into the grids. For this purpose, interpreted facies logs, generated from the combination of composite facies logs and seismic data, were selected.

Facies logs are discrete variables meaning that continuum does not exist between two variables. In other words, as an example, if sand and shale alternation is observed in a facies log, other lithologies cannot be available in between these two facies. The result after upscaling process could be shale, sand or both. Discrete variables are only defined with histogram, not a continuous curve (Pyrcz and Deutsch, 2014).

Several methods are available to achieve this process. To upscale facies logs, "the most of" option was preferred. In this technique, the dominant facies falling into the grid dimension is upscaled. An example of the use of this method for Well- 21 is given in Figure 10.11. A 3D display of all upscaled logs is displayed in Figure 10.12.

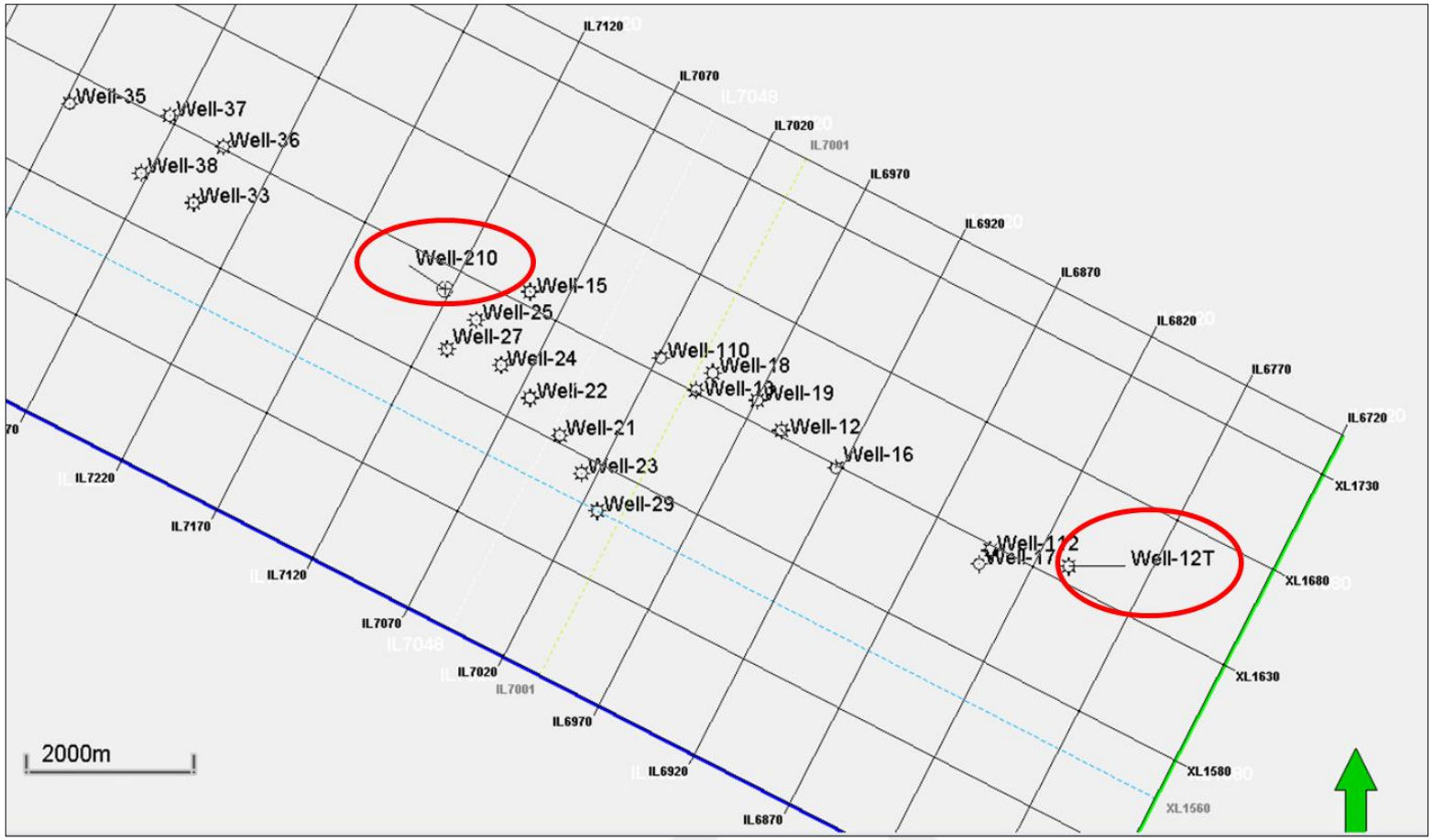

Figure 10.8. Base map indicating the input and validation wells. The wells used as a blind are shown with red ellipse.

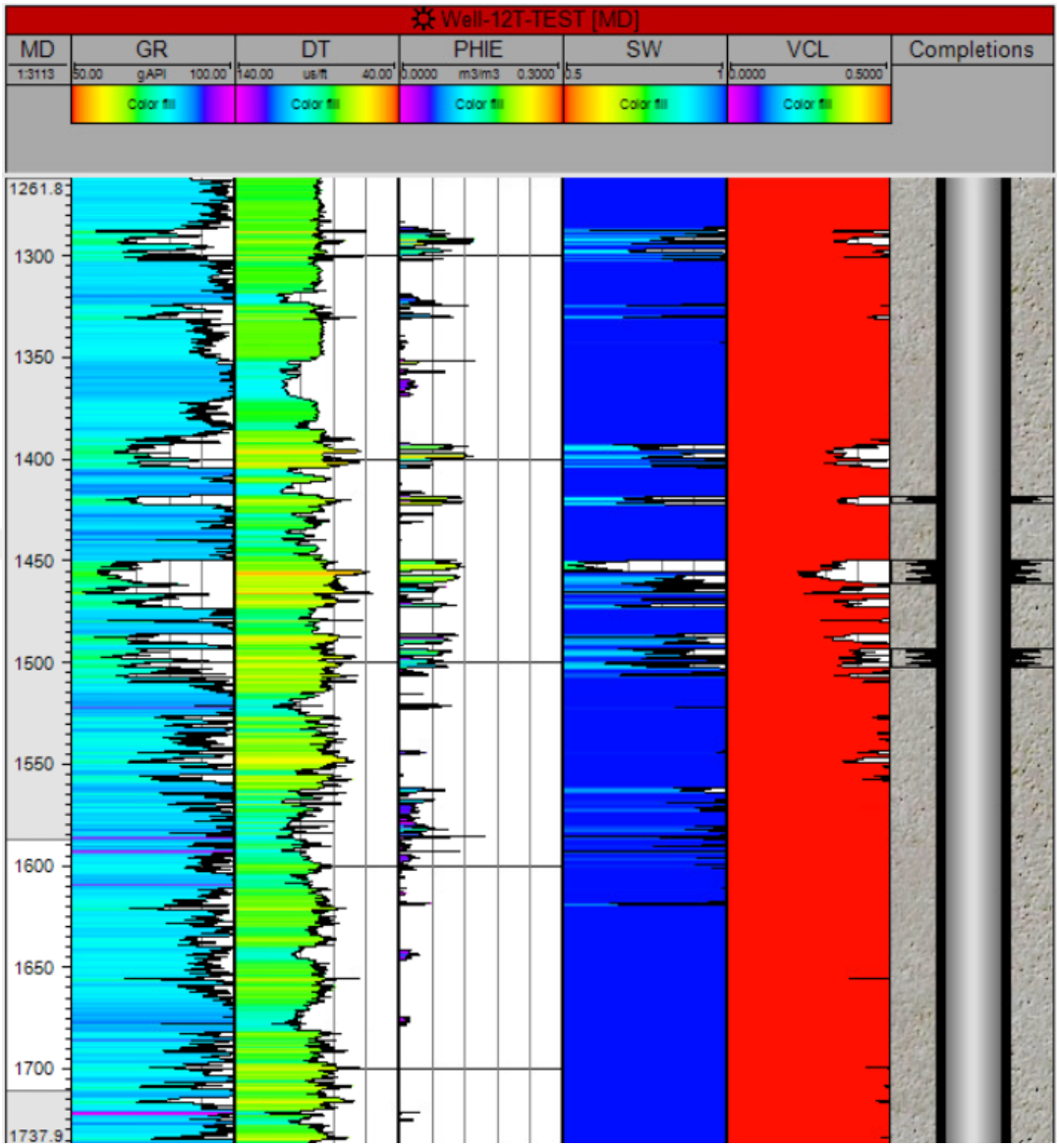

Figure 10.9. Well section display of the blind well, well-12T. From left to right: Gamma-Ray (GR), p-sonic (DT), effective porosity (PHIE), water saturation (SW), volume of clay (VCL) and completions are illustrated.

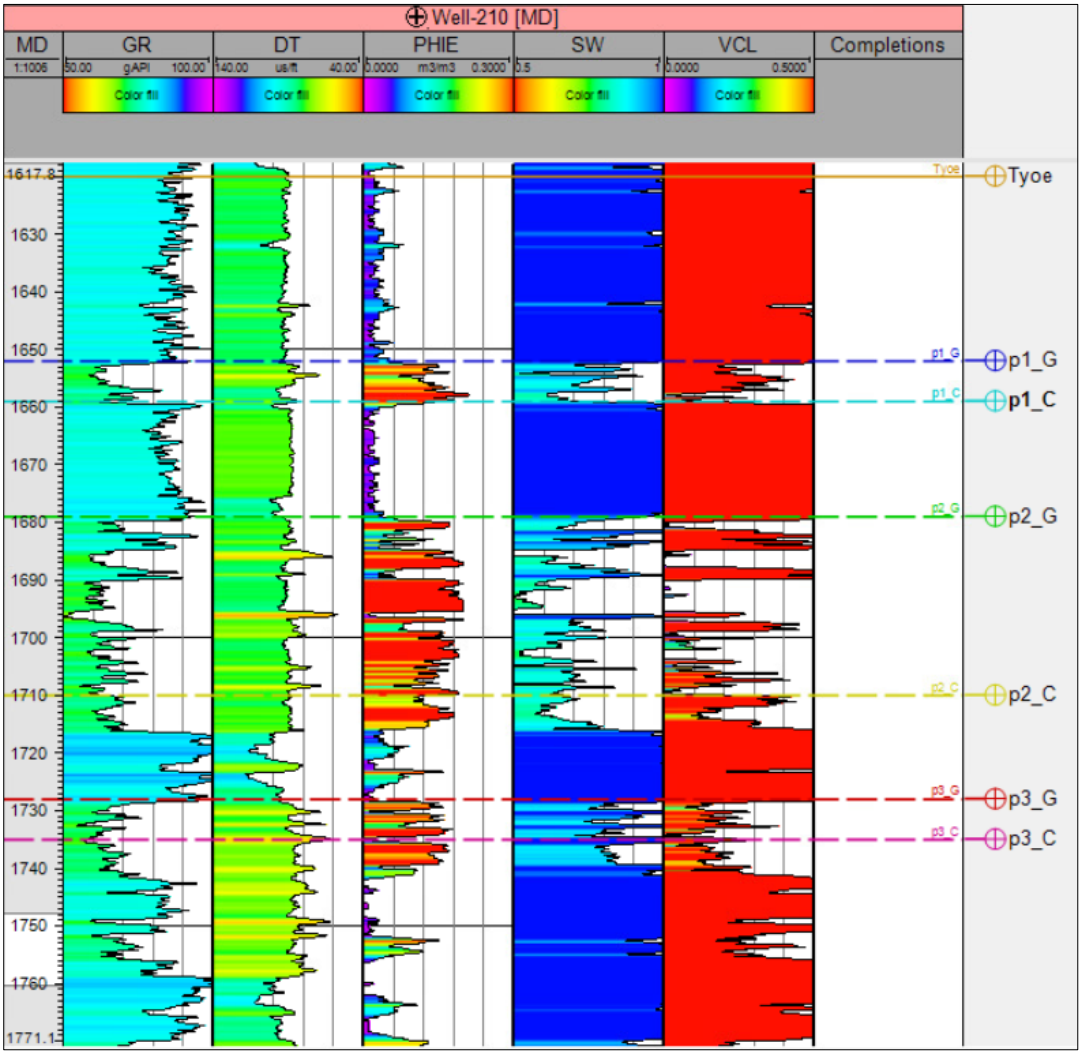

Figure 10.10. Well section display of the blind well, Well-210. From left to right: Gamma-Ray, p-sonic (DT), effective porosity (PHIE), water saturation (SW), volume of clay (VCL) and perforation tops are given.

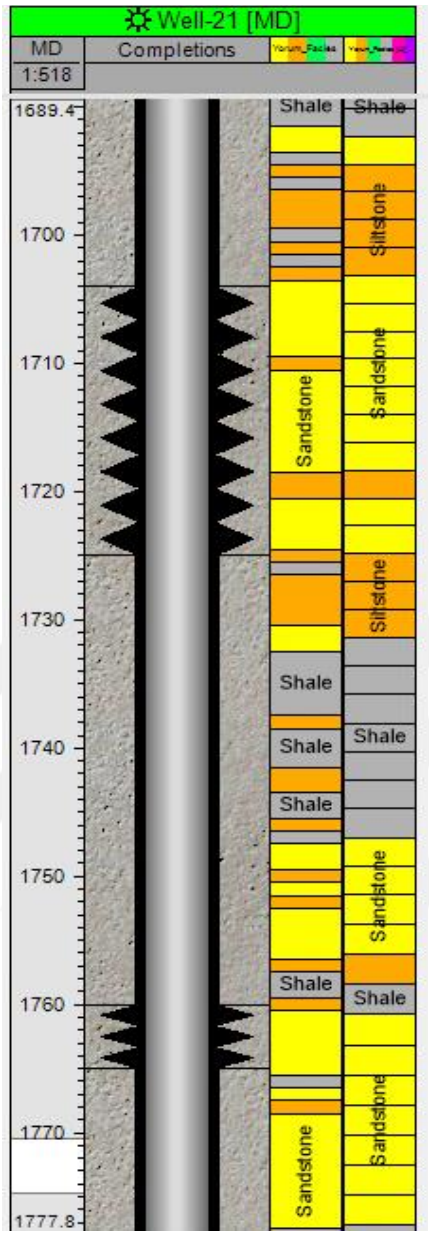

Figure 10.11. Facies log of Well-21 on the left column represents original facies. On the right column, upscaled facies are shown created by "most of the facies" method. As an example, approximately, between 1730 and 1745 m., shale-siltststone alternation is observed. Because siltstone thickness is very low in this interval, dominant shale facies is assigned into the structural grid.

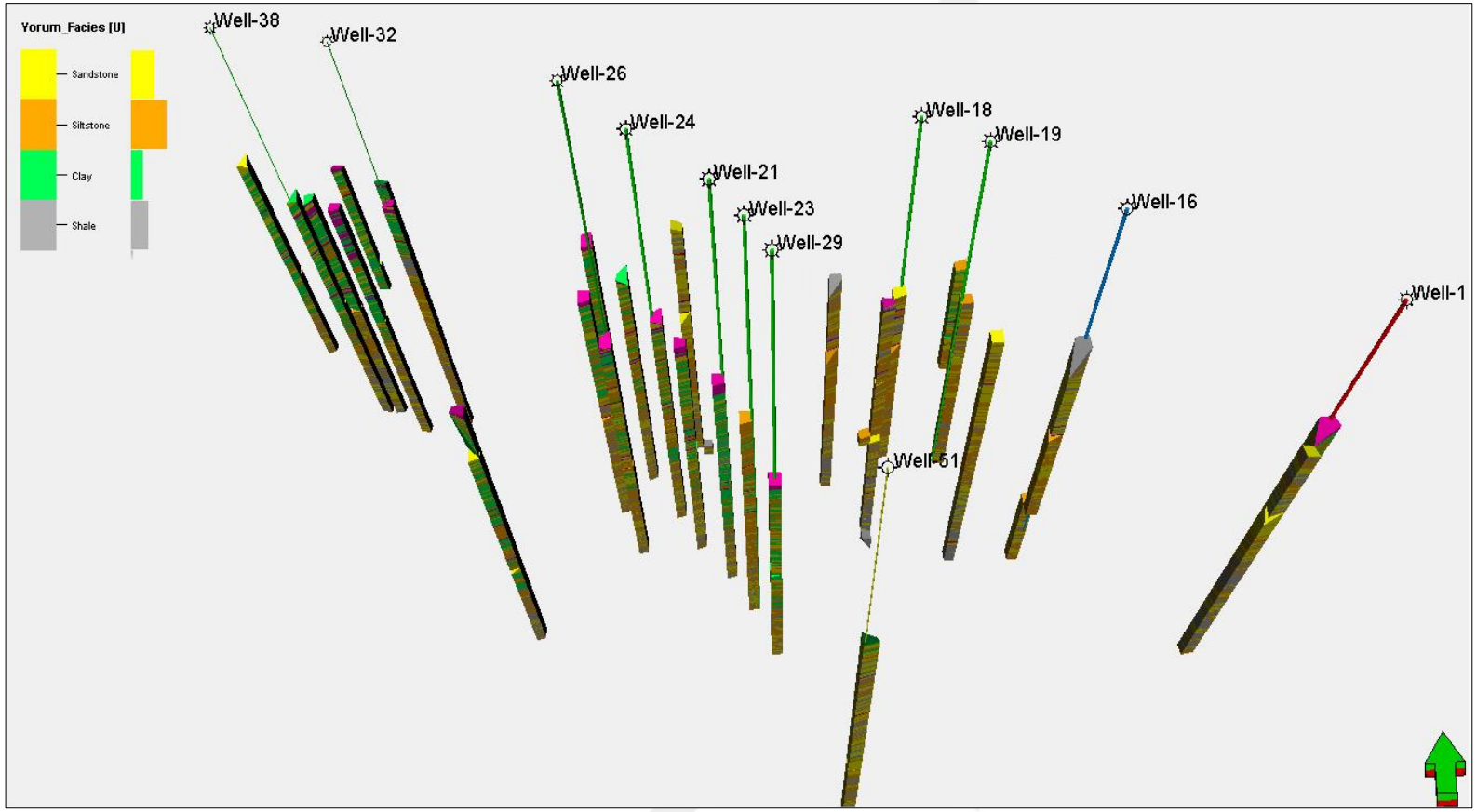

Figure 10.12. Upscaled facies logs in a 3D window.

10.9.2 Data Analysis

Data analysis of facies is a critical part for the preparation data set to facies modeling. Data analysis is performed to constrain data set and guide for spatial distribution.

10.9.2.1 Estimated Facies Proportions and Proportion Curves

Vertical proportion curve is calculated using facies logs and defined as the cross-plot of the percentage of lithology versus drilling depth. This curve provides a vertical constraint and controls on the distribution of each facies during facies modeling processes (Pranter, 2008). Estimated facies proportions and resulted proportional curves (Figure 10.13) indicate that the dominant facies of the formation are siltstone. Percent of the shale facies diminishes with increasing depth because energy of the depositional environment decreases towards pro-delta.

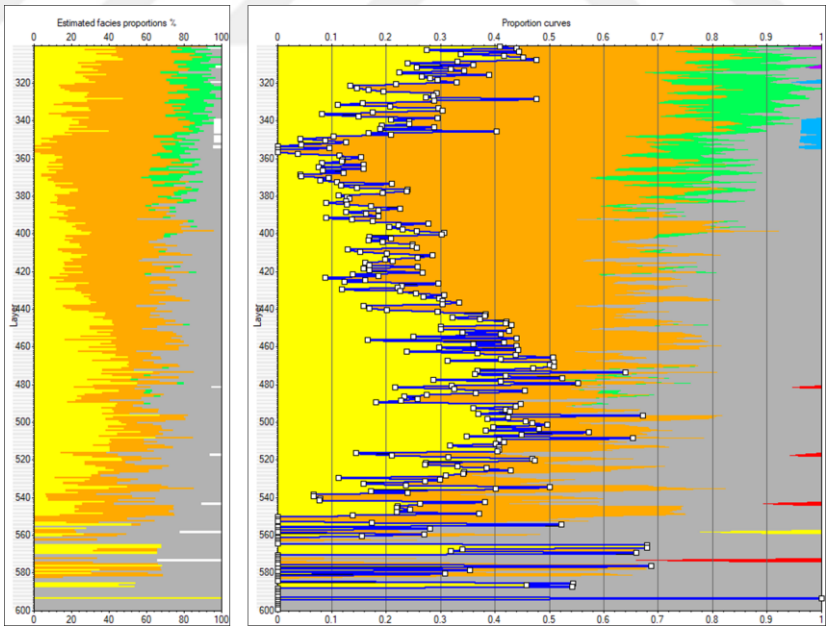

Figure 10.13. Estimated facies proportion (left) and proportion curves (right). Sandstone (yellow): 25.2%; siltstone (orange): 38.22%; clay (green): 3.8% and shale: (grey) 32.27%.

10.9.2.2 Probability Attribute

Output volumes of seismic inversion and attributes can be used as a secondary constraint for facies modeling. Each attribute was run and the best resulted one found as mu*rho (μρ) calculated from shear impedance volume. The results will be shown in the following sections. Probability display of this attribute is given for each facies in Figure 10.14. When μρ reaches the maximum value, sand probability (yellow color) becomes 100% (Figure 10.14 A) and silt probability (orange) becomes 0% At low values of mu*rho, siltstone has the highest probability (Figure 10.14 B). A strict relationship between mu*rho and clay probability (green color) is not observed. However, clay amount is too low, which can be ignorable (Figure 10.14 C). Increasing mu*rho results in an increase in shale probability (grey color). After a certain value (where sand probability is close to 100 %), shale probability decreases sharply (Figure 10.14 D).

10.9.2.3 Variogram Modeling

Variogram controls the spatially distribution of facies during modelling process. Orientation of facies patterns are specified using modelled variograms. Exponential type of variogram was determined to use for modelling purposes. For each facies type (sand, silt, clay and shale) variograms were modelled separately. Modelled variograms representing vertical, major and minor directions for each facies are given in Figure from 10.15 to 10.18. Used parameters for variogram modelling are listed in Table 10.1. Relative information of orientation and lag distance is also given in Table 10.2.

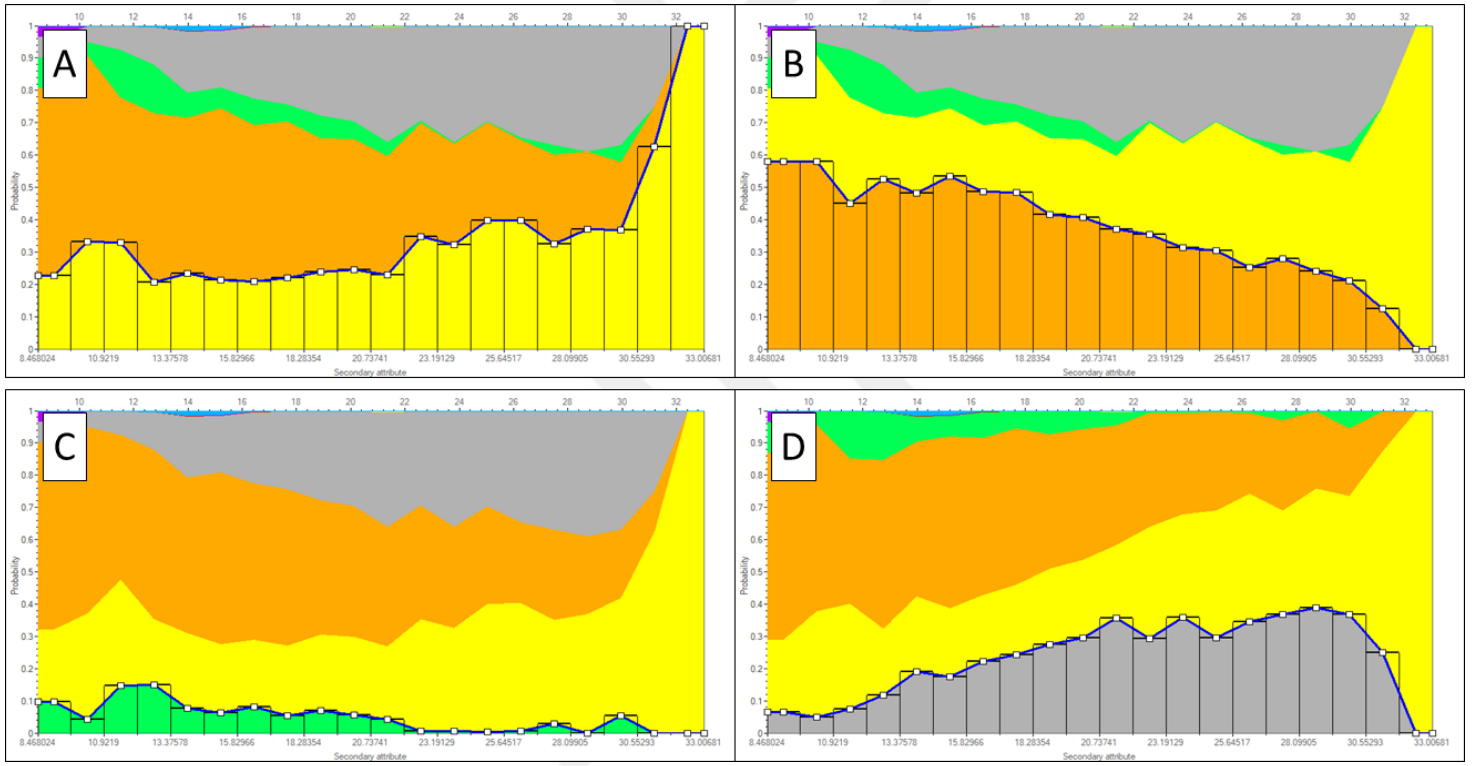

Figure 10.14. Relations between mu*rho values and (A) sand probability with yellow color, (B) silt probability with orange color, (C) clay probability with green color, (D) shale probability with grey color are illustrated.

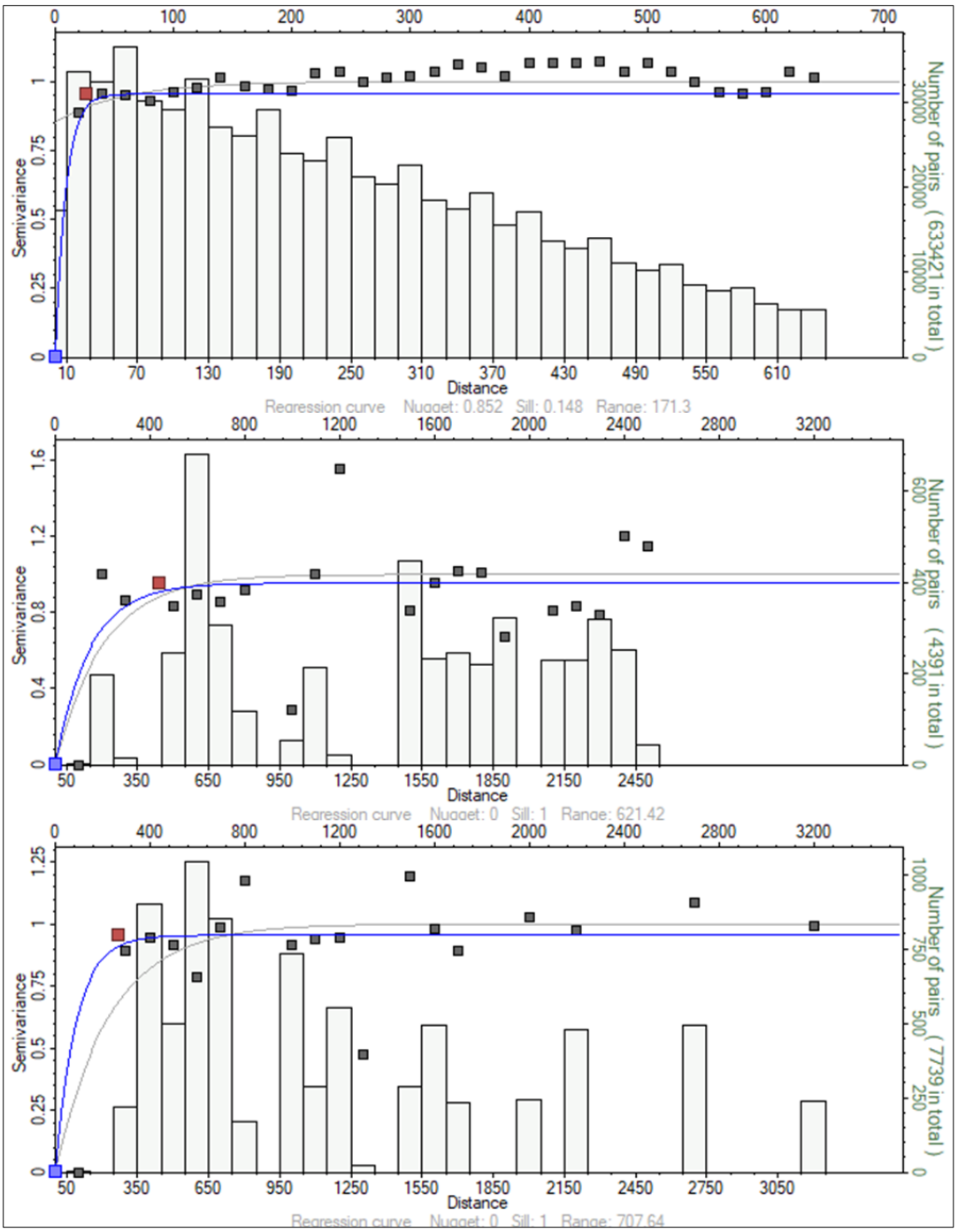

Figure 10.15. Experimental and modelled variograms of sand facies. Vertical (top), major (middle) and minor (bottom) variograms are shown.

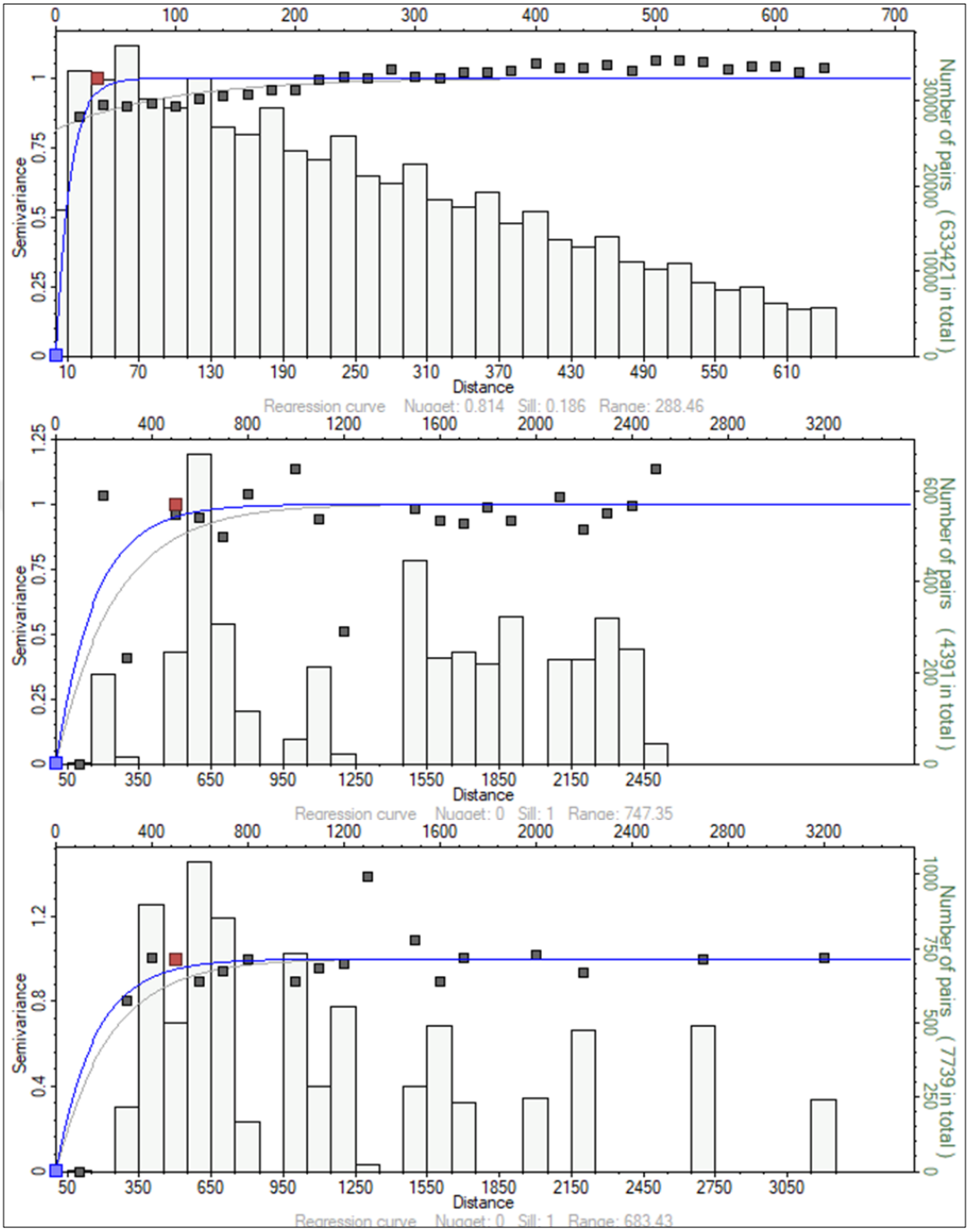

Figure 10.16. Experimental and modelled variograms of silt facies. Vertical (top), major (middle) and minor (bottom) variograms are given.

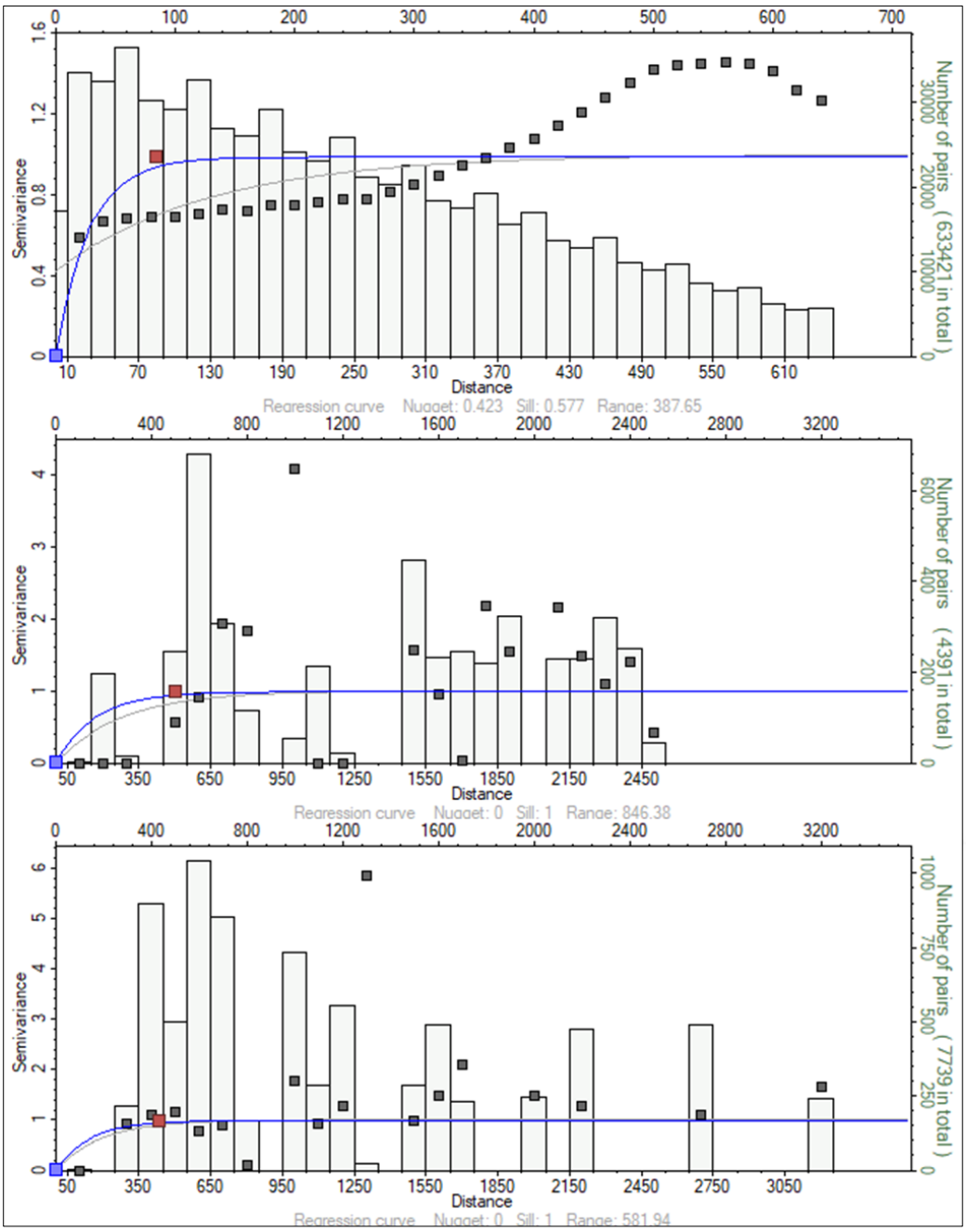

Figure 10.17. Experimental and modelled variograms of clay facies. Vertical (top), major (middle) and minor (bottom) variograms are illustrated.

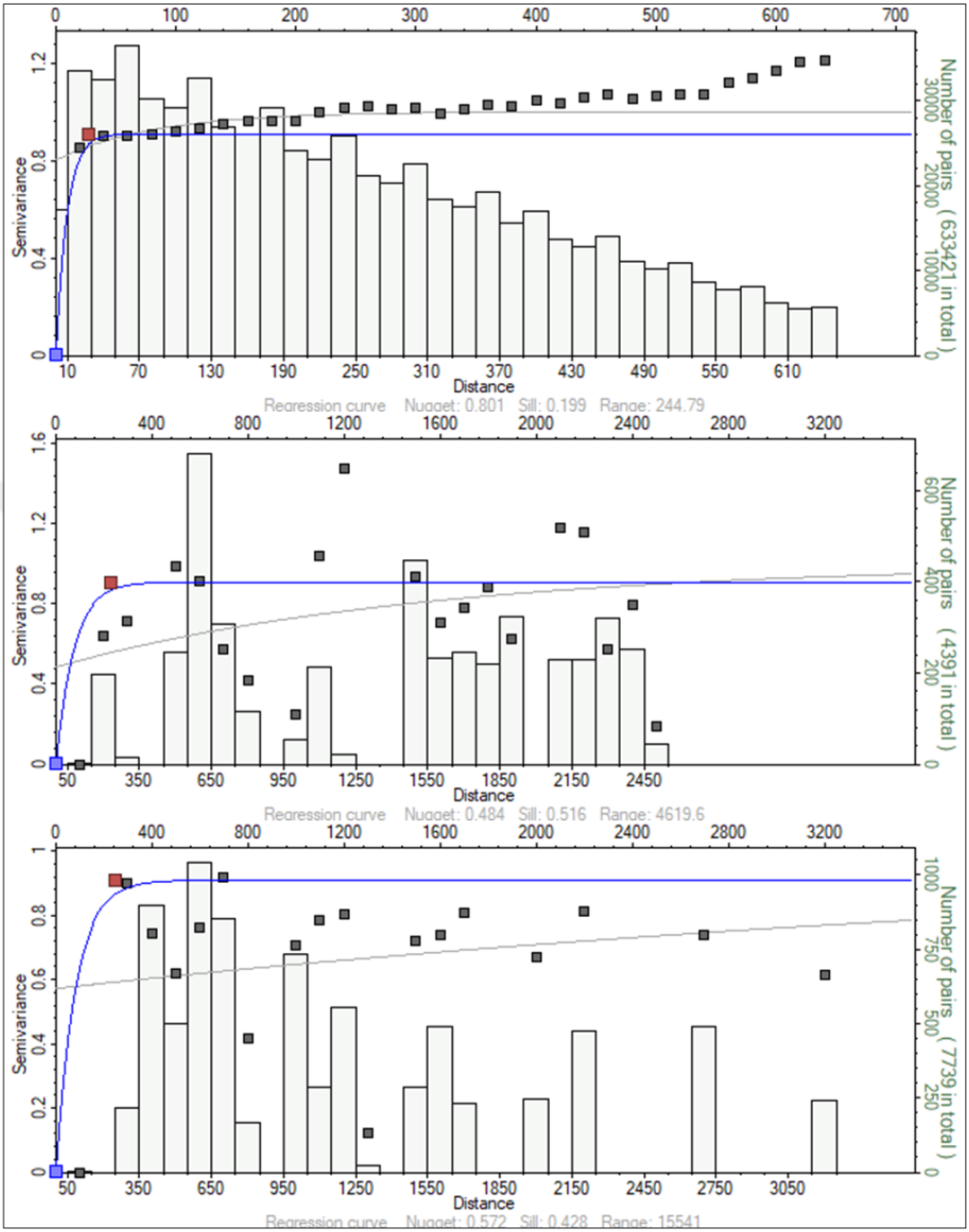

Figure 10.18. Experimental and modelled variograms of shale facies. Vertical (top), major (middle) and minor (bottom) variograms are indicated.

Table 10.1 Modelled variogram parameters.

Facies	Sand	Silt	Clay	Shale
Type	Exponential	Exponential	Exponential	Exponential
Sill	0.955	0.99	0.98	0.91
Major Range	442.4	500	500	229.1
Minor Range	267.6	500	433.2	249.5
Vertical Range	26.9	35.4	84.2	27.4

Table 10.2 Orientation and lag distance of the modelled variogram.

Direction	Azimuth	Dip	Number Lags	Lag Distance
Vertical	NA	90	32	20
Major	60	0	32	100
Minor	330	0	32	100

10.9.3 Facies Distribution

Facies including sand, silt, clay and shale were modeled using SIS method in Karaçalı-Yulaflı field. Computed μρ volume from shear impedances generated from seismic inversion was utilized as a co-kriging volume. Calibrated facies logs are not available for those blind test wells, Well-12T and well-210. For validation of the final facies model in deeper Osmancık Formation, different realizations of diverse inputs were compared for Well-12T by the interpretation of several logs. (Figure 10.19). The combination of variogram and μρ are found the most successful results. Ten versions of the inputs are listed below:

1- Only variogram,
2- Variogram + proportional facies curve,
3- Variogram + proportional and estimated facies,
4- Variogram + P-impedance + estimated facies,
5- Variogram + P-impedance,
6- Variogram + Vp/Vs Ratio,

7- Variogram + GR volume,
8- Variogram + Seismic Lithofacies,
9- Variogram + S-impedance,
10- Variogram + Mu*Rho.

Gamma-Ray (GR) log measures organic matter in a formation. Therefore, GR is a useful lithology tool to evaluate the presence of sandstone and shale. Especially, very low values indicate sandstone lithology while higher values represent shaleness, mostly. Processed tools can also be utilized to interpret variations in type of facies. Effective porosity (PHIE) log value is expected to be very low for shale in contrast to total porosity. Thus, PHIE can also be used to discriminate facies. Water saturation (SW) log is calculated by using resistivity logs. Therefore, decrease in SW is only related to zones with effective porosity. Volume of clay (VCL), in this study, is equivalent to volume of shale. In this respect, rising values in VCL are directly related to increase in shaleness. Using all these logs, facies can be predicted in the absence of facies log. A composite facies section for Well group-1 is shown in Figure 10.20.

The resulted facies model at well-210 location is also given in Figure 10.21. For this well, especially producing zones are detected as siltstone while producing intervals at other wells, among well group-2, are described as sandstone. Indeed, this is an expected situation because seismic data and outputs from seismic inversion reveal that facies properties changes from south-east to north-west of the field. A composite facies section for well group-2 is demonstrated in Figure (10.22).

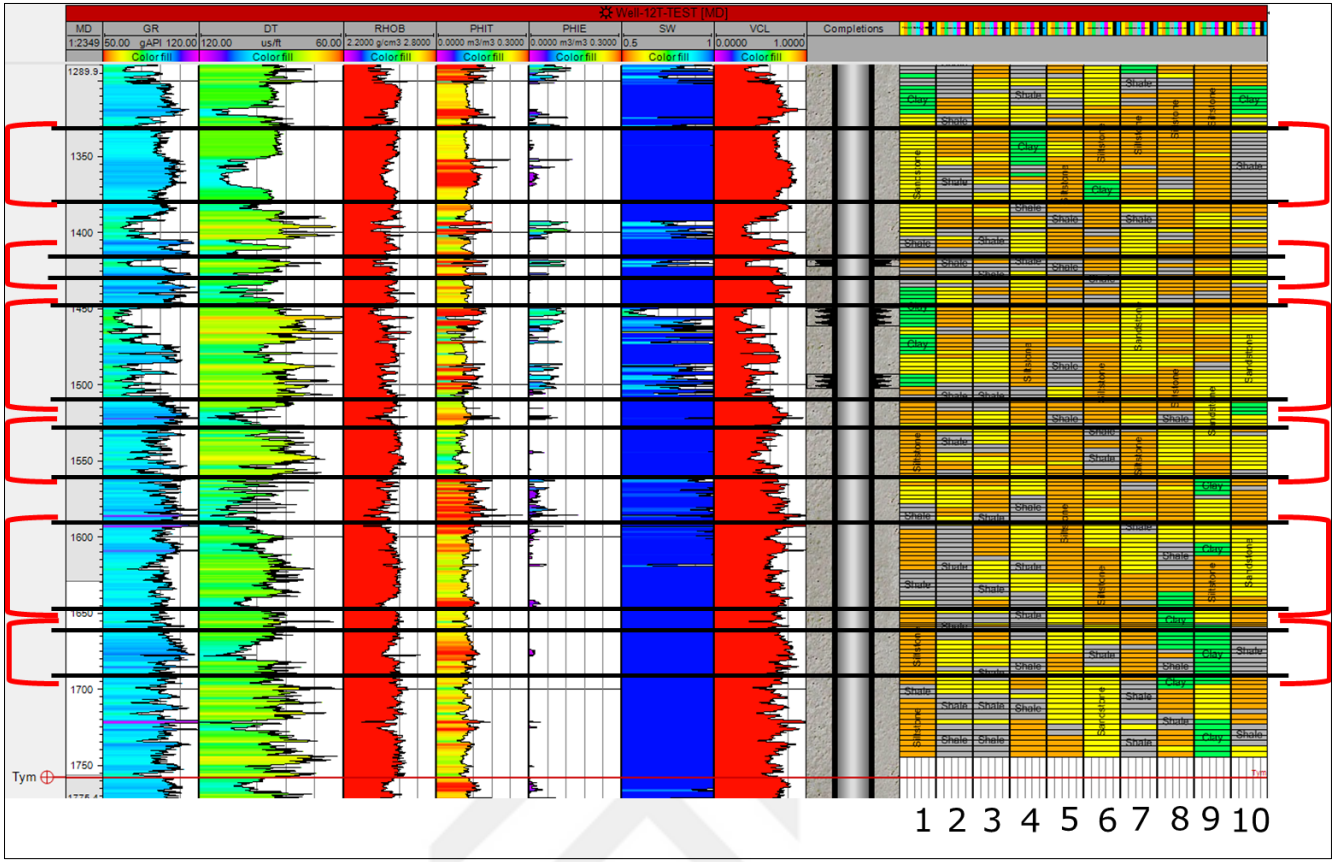

Figure 10.19. Well section of Well-12T is given. From left to right: GR, DT, RHOB, PHIT, PHIE, SW and VCL logs, completions and modelled facies at the well location are demonstrated. The facies column shown with number 10 represents the best fitted facies model generated by the combination of variogram and μσ attribute. Black lines restricted with red brackets indicate the clearly identified facies types by the interpretation of given logs.

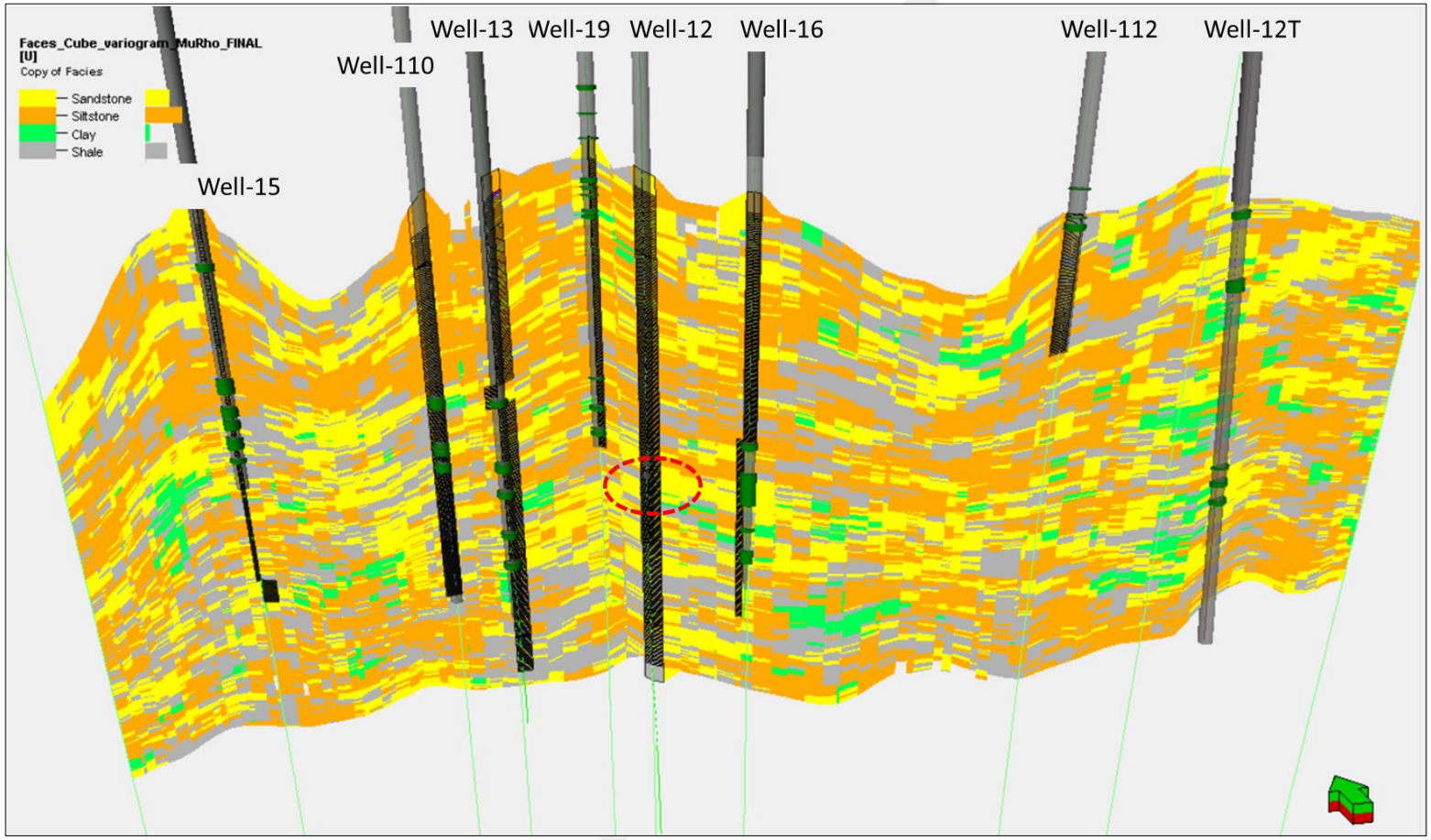

Figure 10.20. Composite facies representing well group 1 wells. Dashed red ellipse indicates the facies from the best producing interval among well group 1.

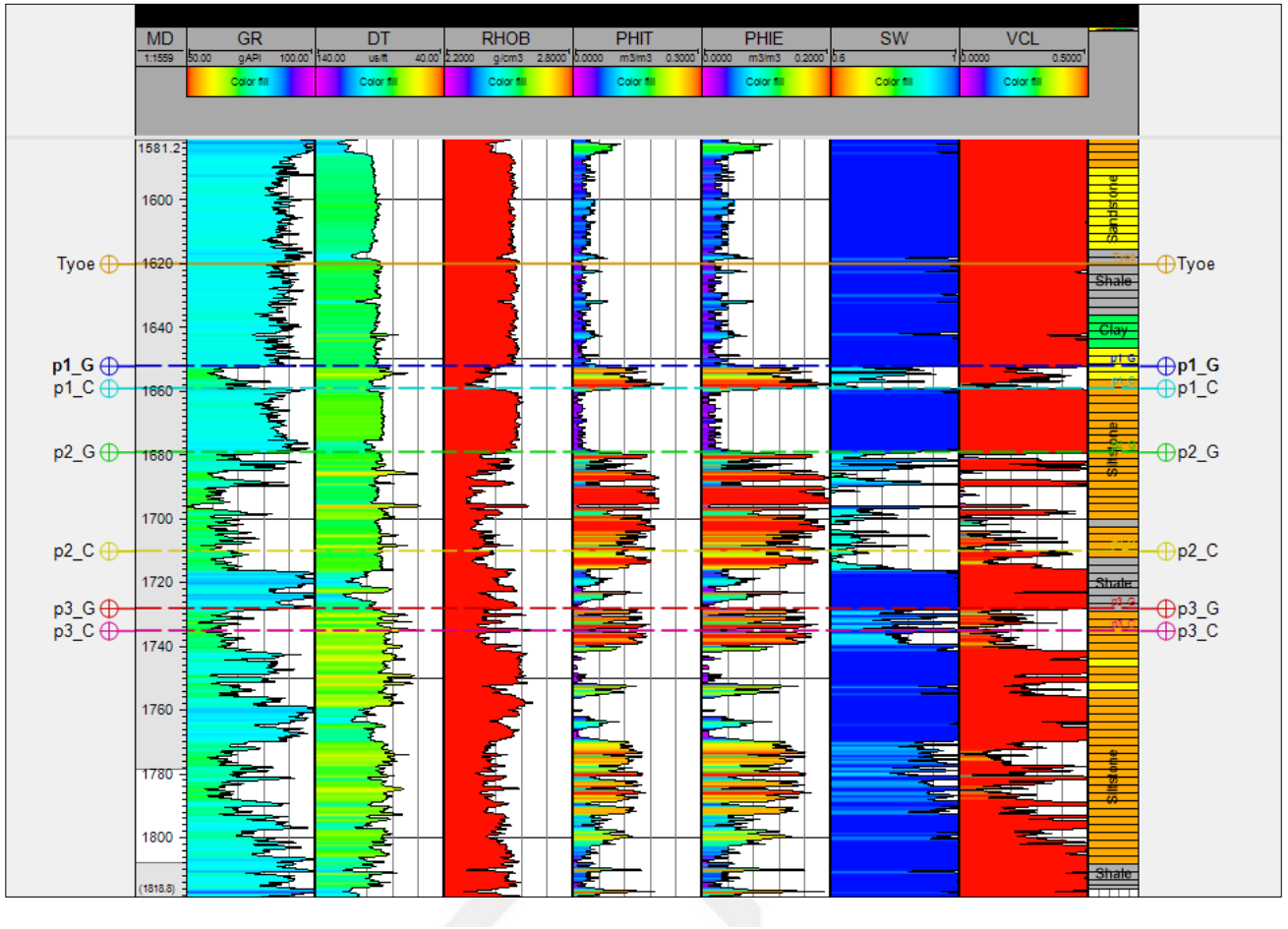

Figure 10.21. Well section of Well-210 is shown. From left to right: GR, DT, PHIE, SW and VCL logs and modelled facies are replaced. p1, p2 and p3 tops represent perforated intervals. Note that p3 interval does not produce while p1 and p2 are active producers.

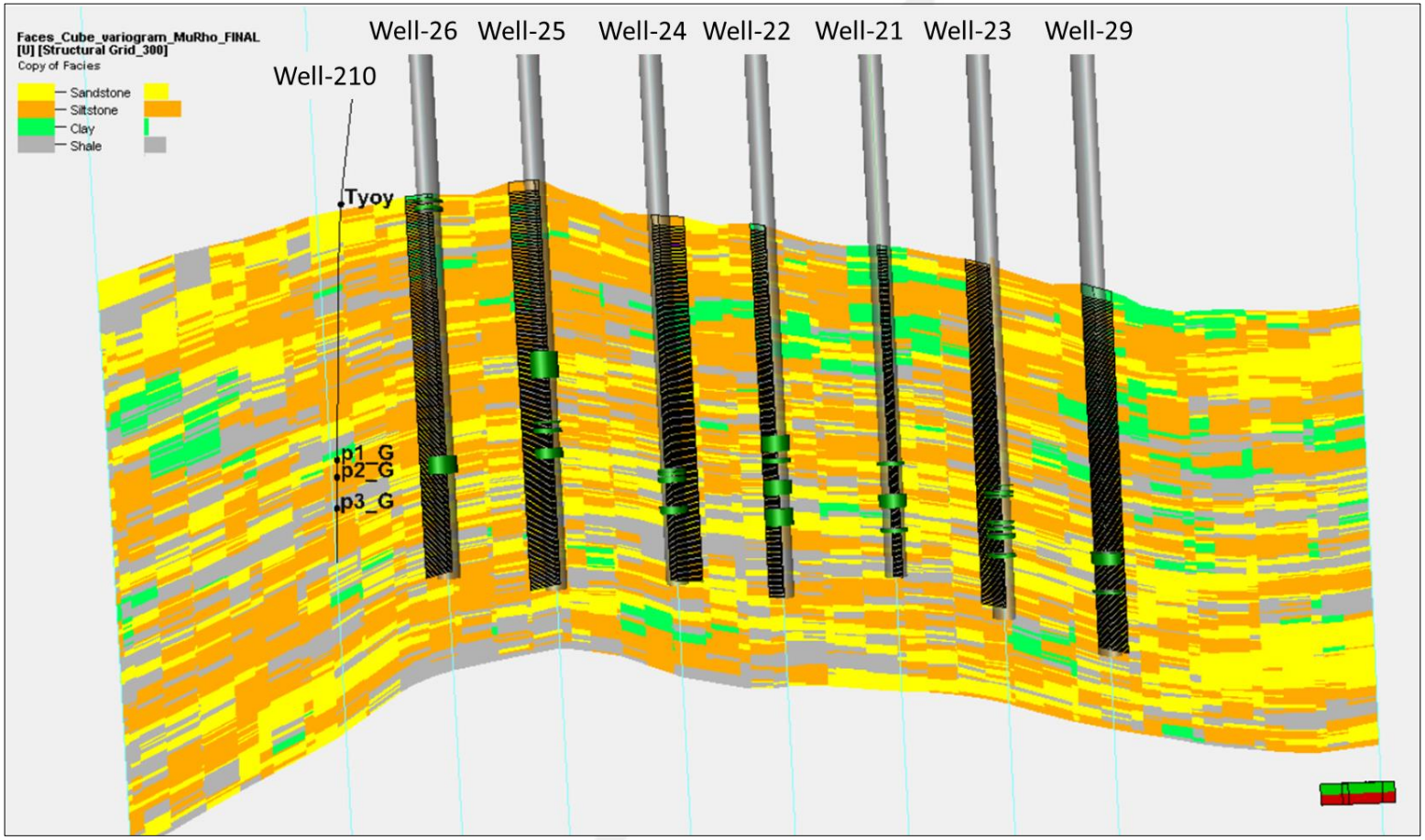

Figure 10.22. Composite facies section of well group 2 is shown. From right to left (SE-NW) sand facies become thinner and decrease in grain sizes except the most westernmost part of shallower Osmancık Formation.

10.10 Property Modeling

Reservoir properties of Karaçalı-Yulaflı field control hydrocarbon accumulation in the reservoir rock. Porosity and permeability distributions are two of the significant properties controlling potential hydrocarbon zones. Spatial distribution of both porosity and permeability were achieved using SGS method.

10.10.1 Well Log Upscaling

The first step of the property modeling is upscaling porosity and permeability logs into the grids. An averaging method among different techniques was selected to succeed upscaling properties. For this purpose, processed porosity logs and estimated permeability curves were utilized. Input logs and upscaled versions at Well-21 is given in Figure 10.23.

10.10.2 Data Analysis

Upscaled logs were conditioned before the application of SGS method to distribute properties in a more reliable way. Two important aspects are data transformation and variogram modelling to create robust inputs for the modelling purpose.

10.10.2.1 Data Transformations

Data transformation is a crucial step applied to input parameters before property modeling. In this study, there are some extreme points from well logs and these values affect property distribution negatively. Therefore, an input truncation was applied to obtain more stable results. Cut-offs as 30% for total porosity and 20% for effective porosity were applied.

Another aspect used for data transformation is the determination of the directional trend for each property. In the data, directional trends are used to constrain data points to prevent from scattering (Figure 10.24).

Reservoir properties are defined as continuous variables and these variables are described with a continuous curve (Pyrcz and Deutsch, 2014). Because Gaussian simulation methods use normal distributed data sets as inputs, selected input data are necessary to transform into normal score (Figure 10.25).

10.10.2.2 Variogram Modeling

Variograms were modelled using Gaussian technique for total and effective porosity. A comparison of vertical variograms using Gaussian, exponential and spherical models for effective porosity is given in Figure 10.26. Figure 10.27 and 10.28 illustrate vertical, major and minor directions for both properties.

Variogram was modelled using exponential method for permeability modeling. Exponential model is the best fitted one among three different models (Figure 10.29). A comparison between modelled variograms is shown in Figure 10.30.

Table 10.3 list variogram modeling parameters for each property. Orientation and lag distance information is given in Table 10.4.

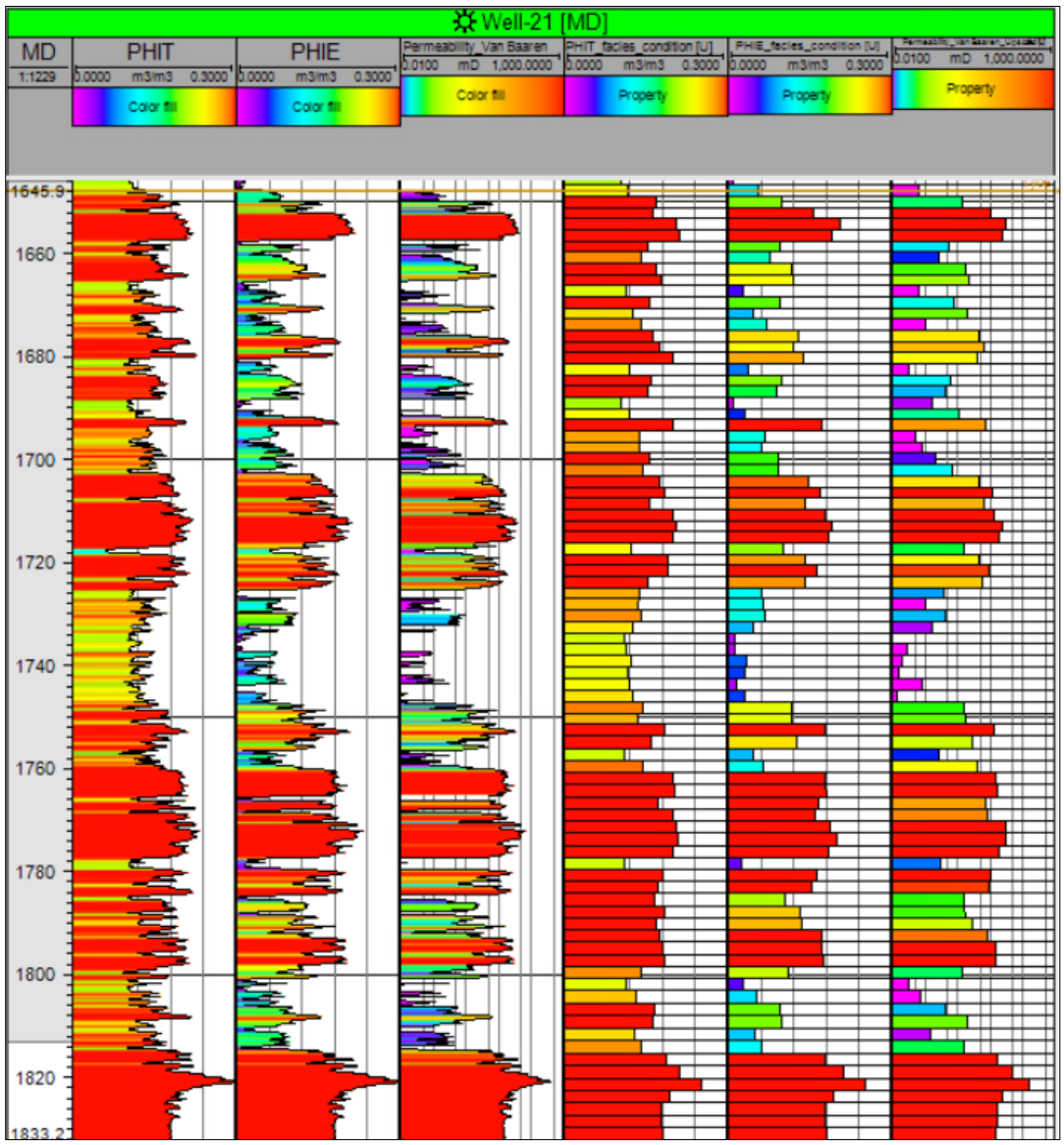

Figure 10.23. Property logs and upscaled versions at Well-21 are illustrated. First three tracks include processed total porosity, effective porosity and estimated permeability curves. Last three tracks represent upscaled log versions, in orderly.

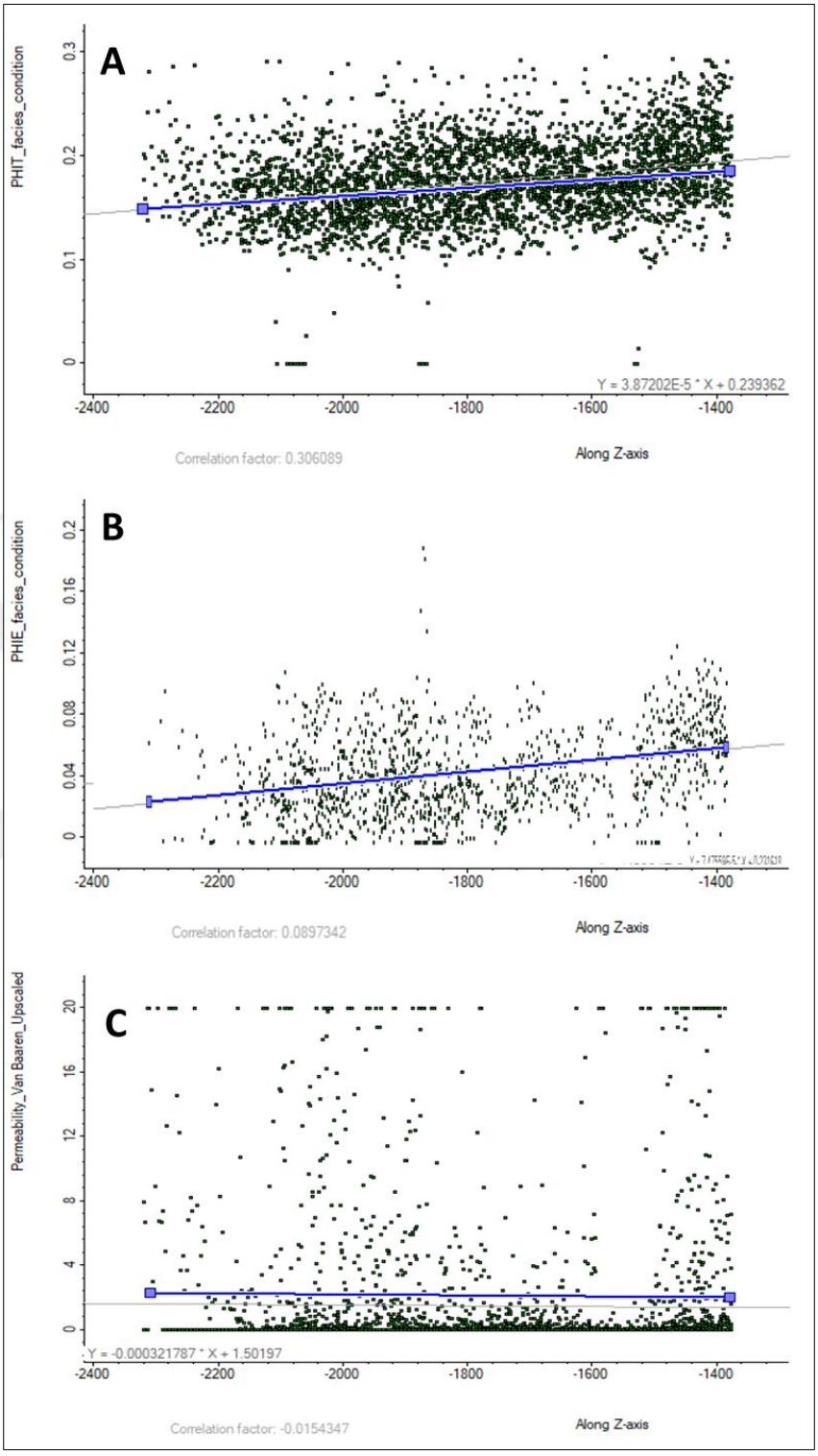

Figure 10.24. Data trends of (A) total porosity, (B) effective porosity and (C) permeability.

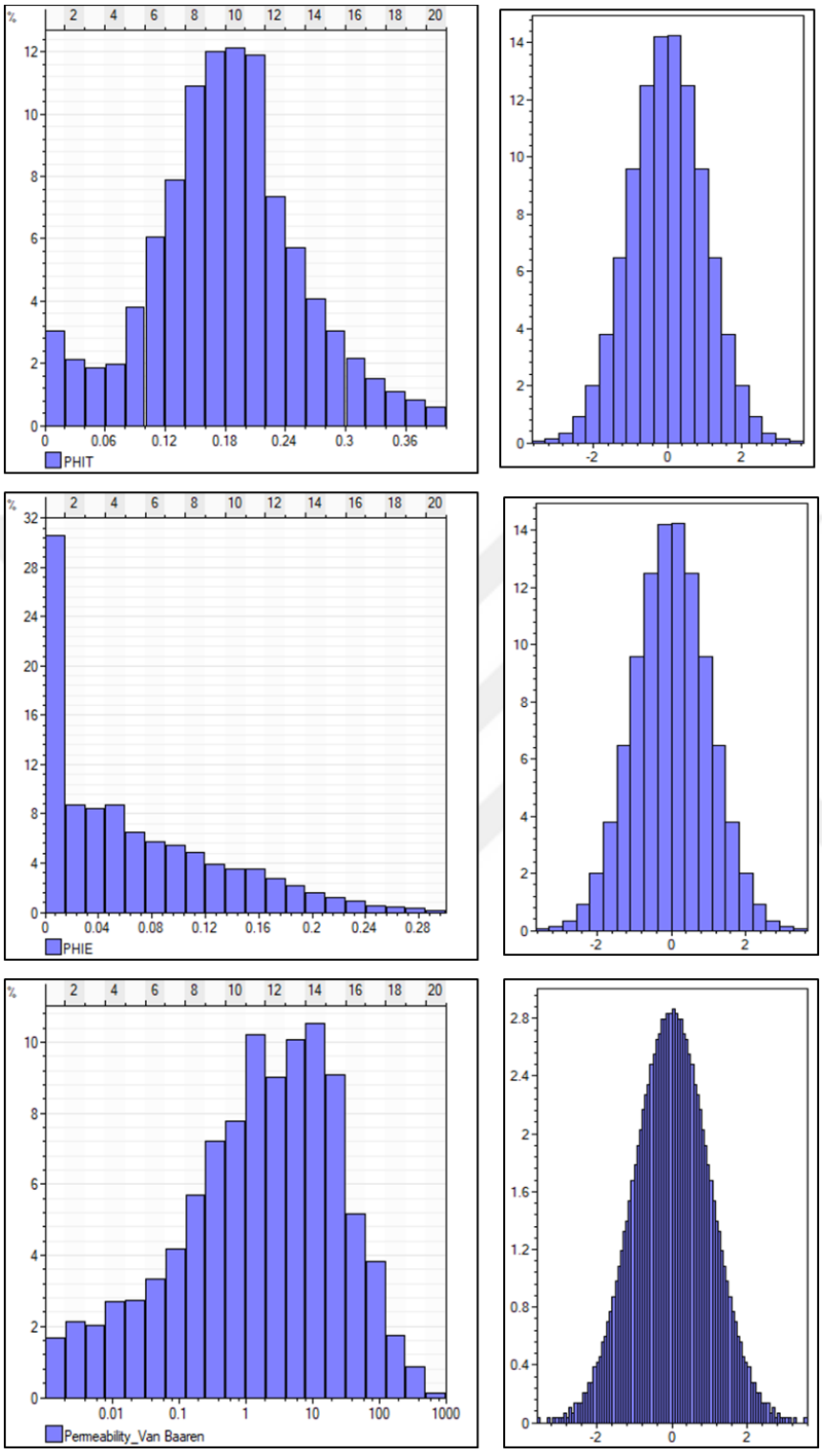

Figure 10.25. Histograms (left column) and normal distribution (right column) of PHIT, PHIE and permeability from top to bottom are displayed, respectively.

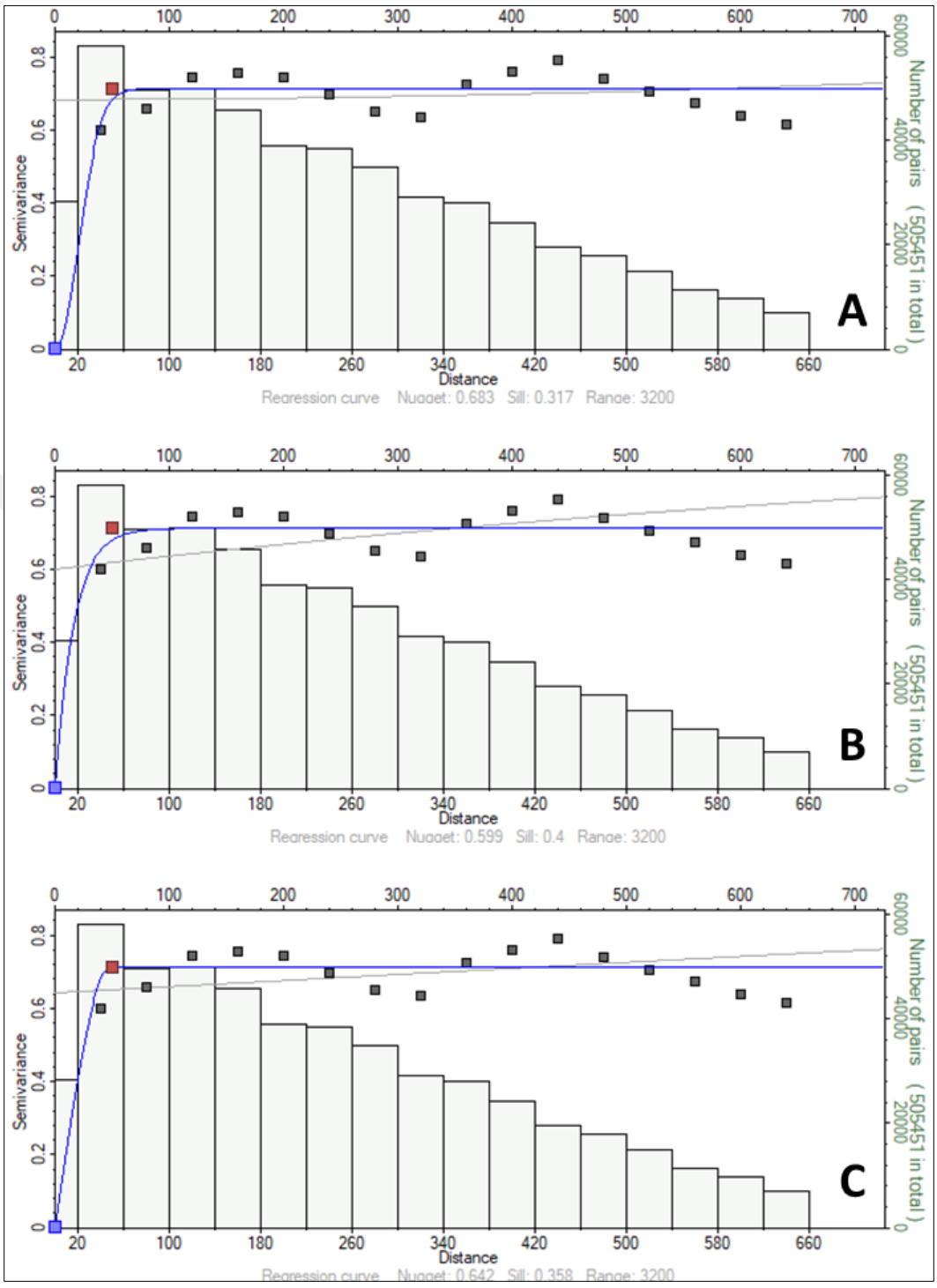

Figure 10.26. Vertical variograms calculated by using upscaled effective porosity logs are given. The compared methods are (A) Gaussian, (B) Exponential and (C) Spherical models.

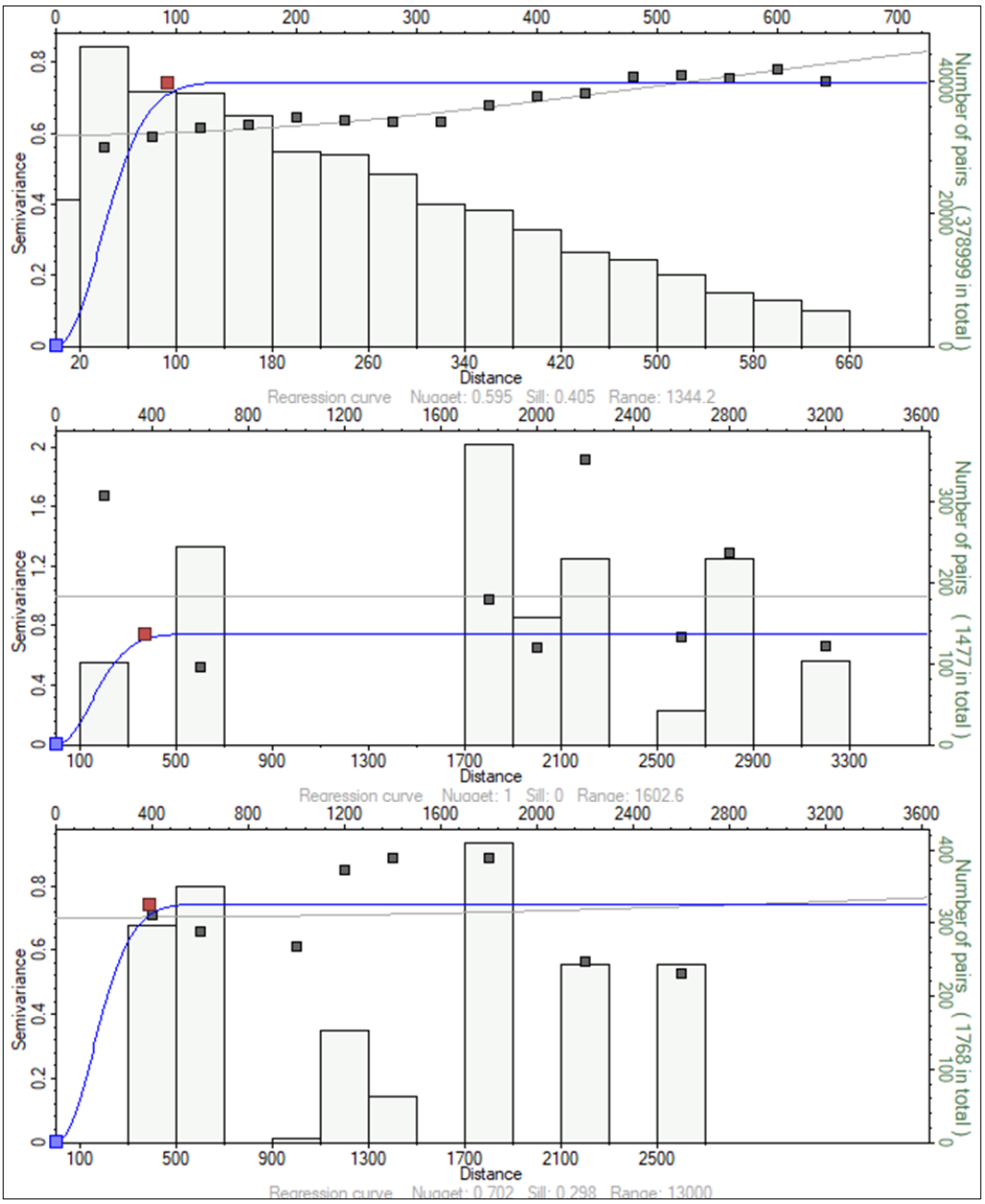

Figure 10.27. Experimental and modelled variograms for vertical (top), major (middle) and minor directions of total porosity.

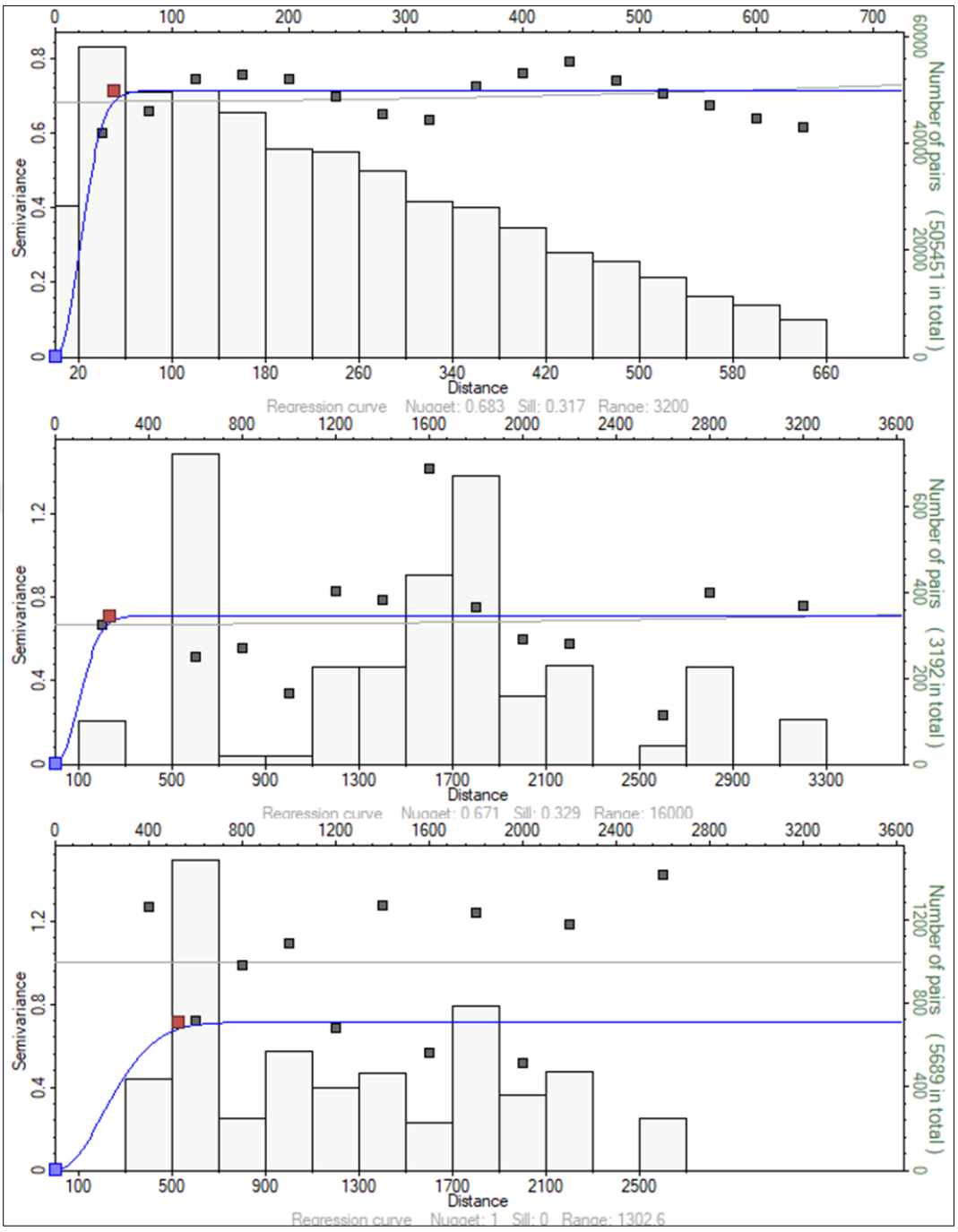

Figure 10.28. Experimental and modelled variograms for vertical (top), major (middle) and minor directions of effective porosity.

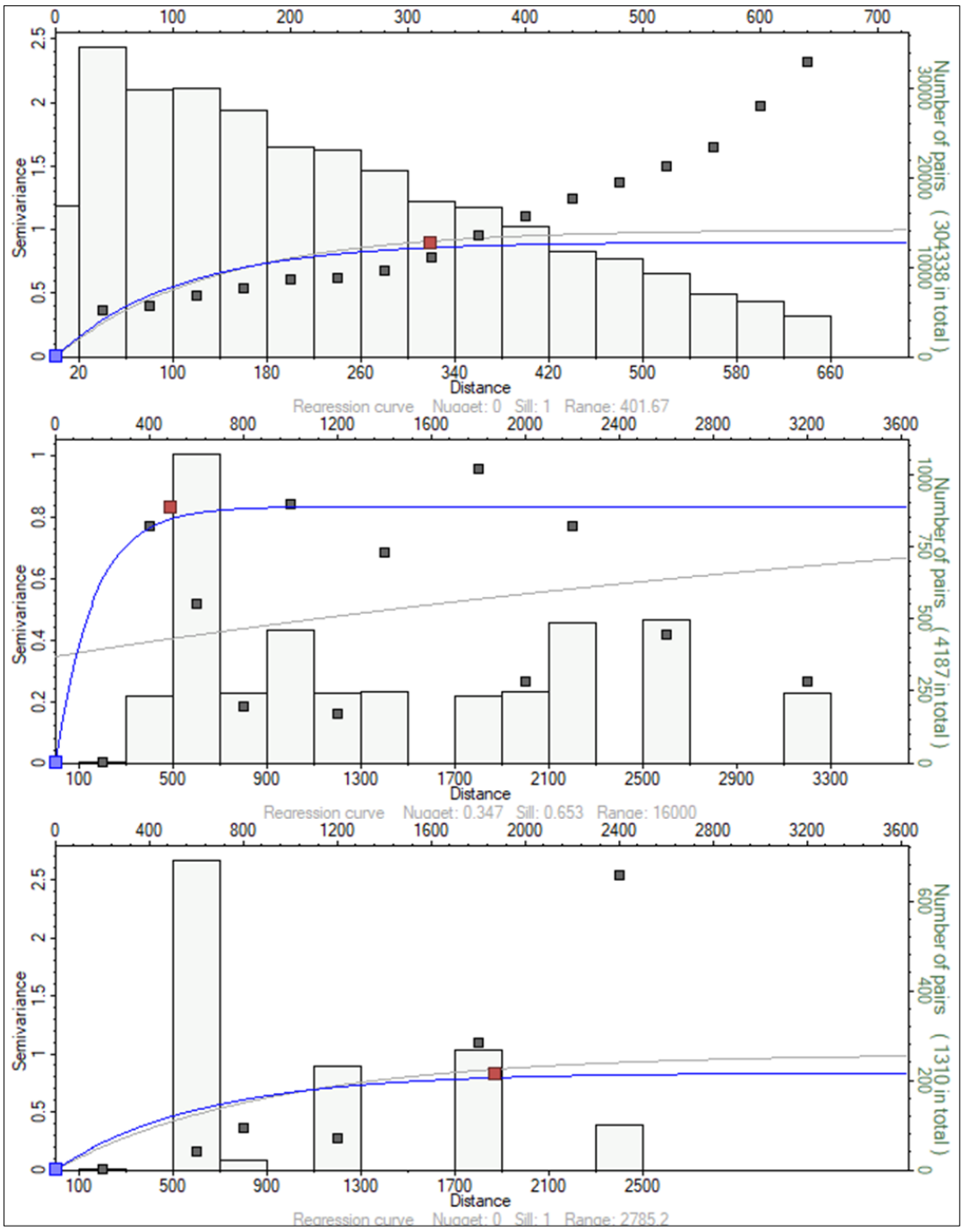

Figure 10.29. Experimental and modelled variograms for vertical (top), major (middle) and minor directions of permeability.

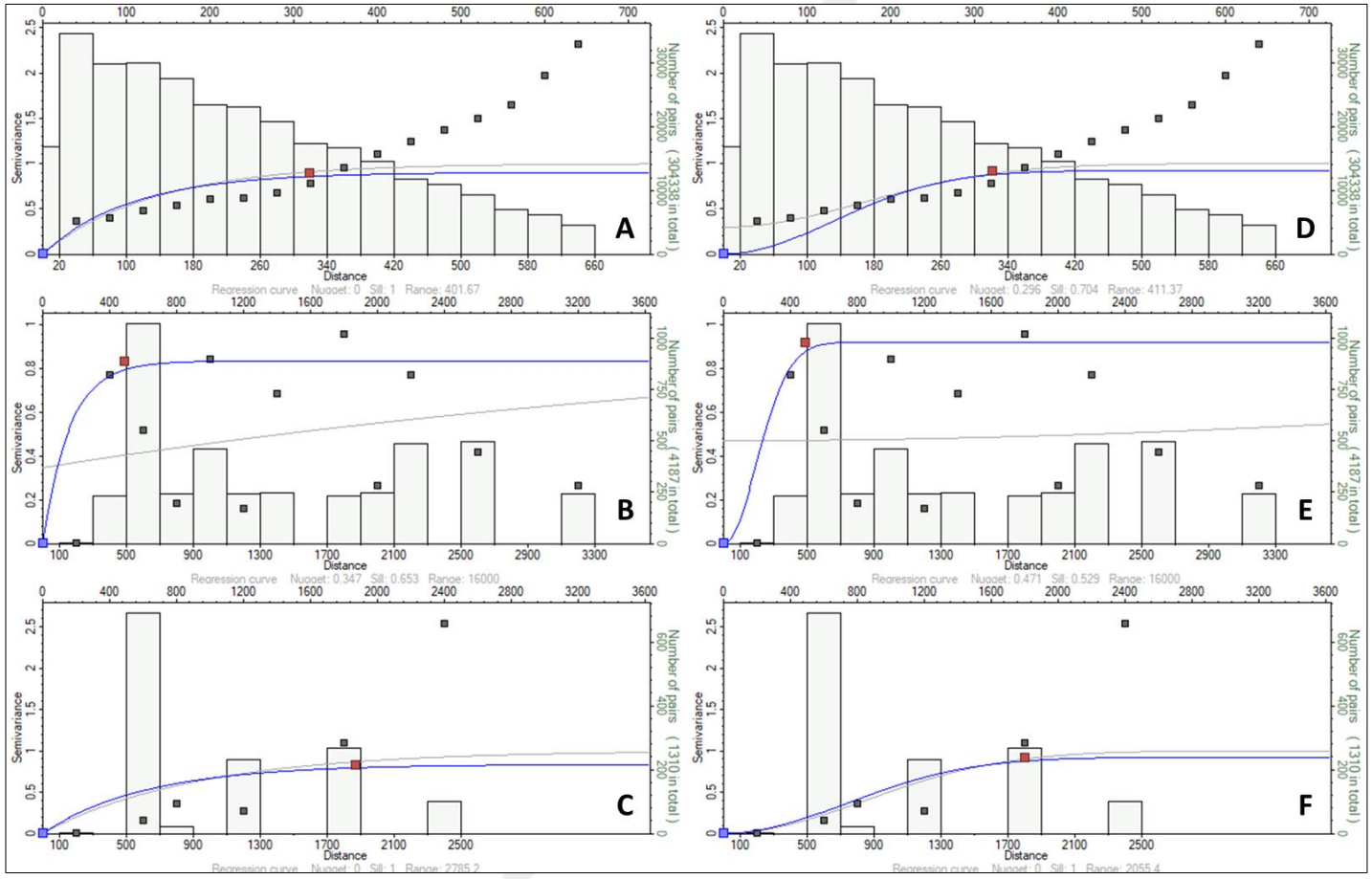

Figure 10.30. A comparison between (A) vertical, (B) major and (C) minor directions of exponential modelled variograms and (D) vertical, (E) major and (F) minor directions of Gaussian modelled variograms of upscaled permeability logs is given.

Table 10.3 Modelled variogram parameters.

Property	PHIT	PHIE	K
Type	Gaussian	Gaussian	Exponential
Sill	0.74	0.71	0.92
Major Range	373.8	237.2	490.9
Minor Range	390.4	525.4	1800
Vertical Range	92.6	50	321.5

Table 10.4 Orientation and lag distance of the modelled variogram.

Direction	Azimuth	Dip	Number Lags	Lag Distance
Vertical	NA	90	16	40
Major	45	0	16	200
Minor	315	0	16	200

10.10.3 Secondary Volumes for Porosity and Permeability

A recently drilled well, Well-210, was implemented into the field model as it was discussed previously. The advantage of using this well is the presence of measured s-sonic velocity which is missing for other group 2 wells.

P-impedance is commonly used as co-kriging parameter during modeling process. However, it is clearly observed that increasing porosity causes a little variation for p-impedance values (Figure 10.31) while V_P/V_S ratio is more sensitive to changes in porosity in deeper Osmancık Formation (10.32). Comparison of these cross-plots for Well-210 are given in Figure 10.33. Consequently, V_P/V_S ratio was utilized as co-kriging parameter.

Permeability variations within siliciclastic facies is generally directly proportional to porosity changes. Thus, effective porosity model was utilized as co-kriging parameter.

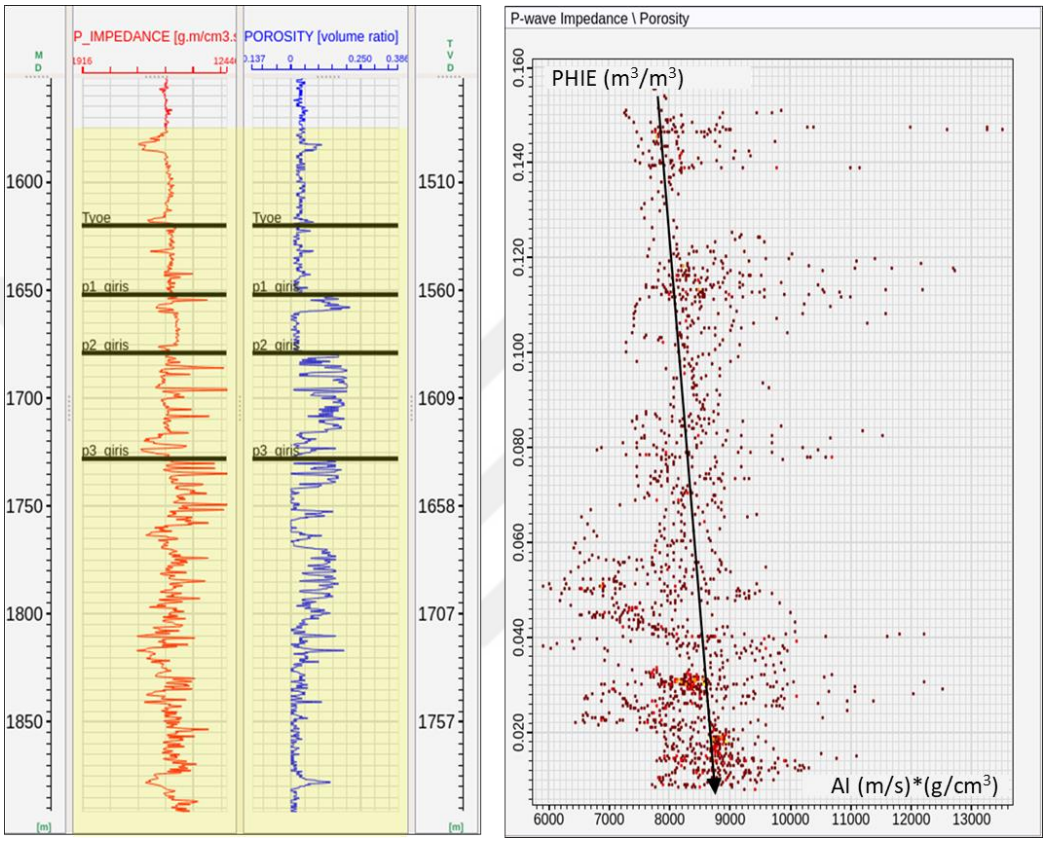

Figure 10.31. P-impedance (Acoustic) and effective porosity logs (on the left) and cross-plot of these parameters (on the right) are demonstrated.

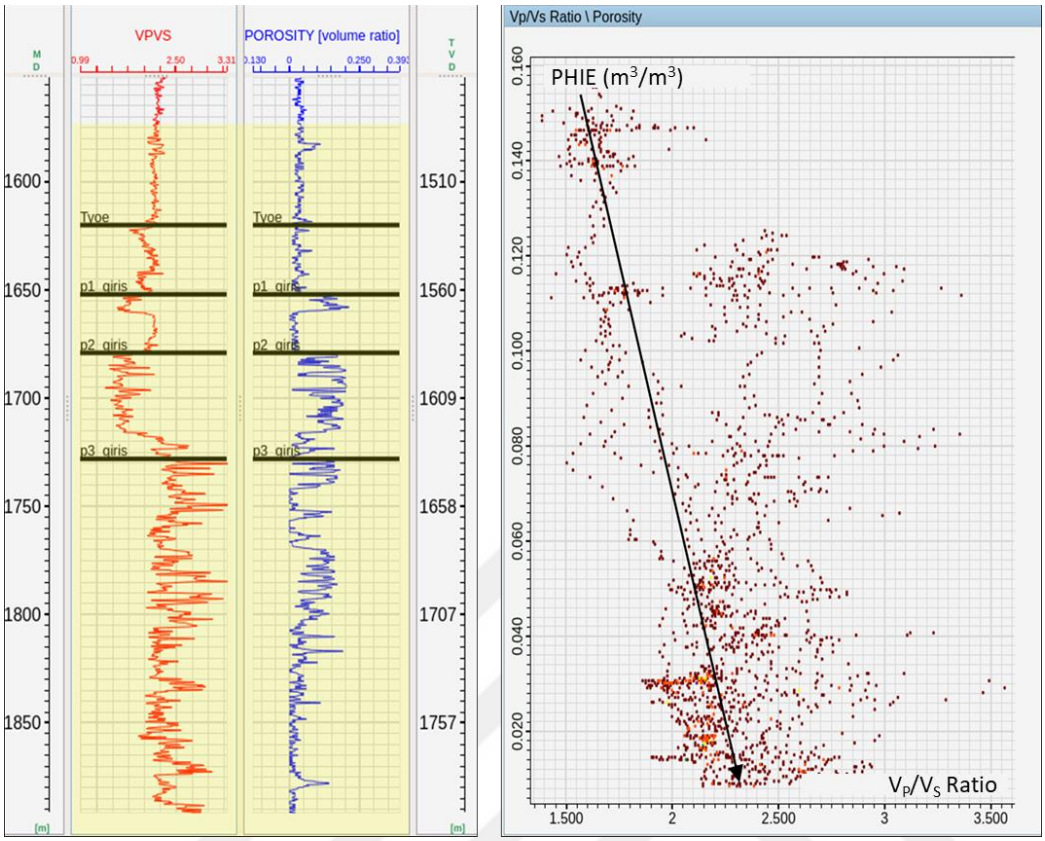

Figure 10.32. V_P/V_S ratio and effective porosity logs (on the left) and cross-plot of these parameters (on the right) are demonstrated.

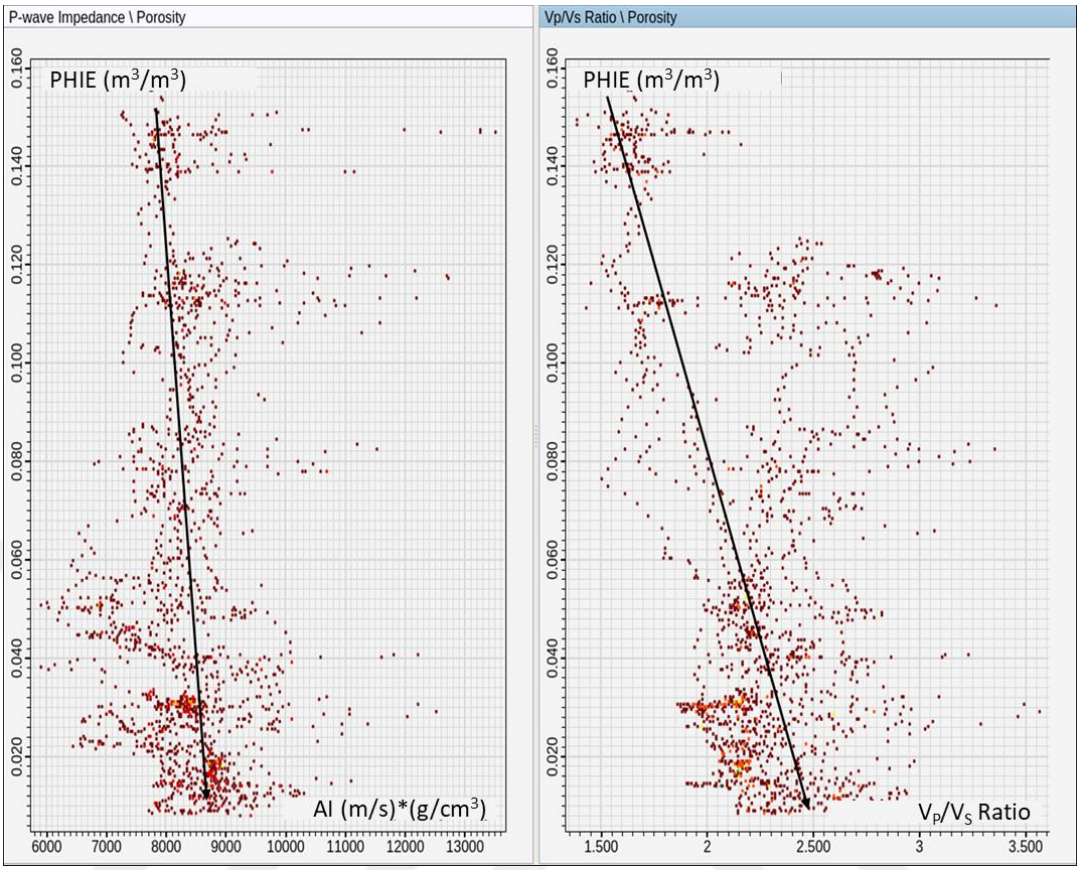

Figure 10.33. For deeper Osmancık Formation, acoustic impedance changes little with increasing porosity (on the left) while V_P/V_S ratio is more sensitive to changes in porosity variations (on the right).

10.10.4 Property Distribution

Three reservoir models for the distribution of total porosity, effective porosity and permeability properties were built using SGS method. V_P/V_S ratio calculated from impedance volumes were used as co-kriging parameter to model both total and effective porosities. Modelled effective porosity was utilized as co-kriging parameter to model permeability distribution of the field. To validate these results, estimated properties at Well-12T (Figure 10.34) and Well-210 (Figure 10.35) locations were

investigated. Resulted models are evaluated as compatible with the measured and process logs.

Intersections of group 1 wells representing total porosity model (Figure 10.36), effective porosity model (Figure 10.37) and permeability model (Fig 10.38) reveal that reservoir properties from east to west direction is worsen. The middle part in which the Osmancık Formation is the thickest has more potential zones. Similarly, intersections indicating total porosity (Figure 10.39), effective porosity (Figure 10.40) and permeability (Figure 10.41) models for well group 2 reveal that the reservoir conditions are also worsen. To sum up, eastern part of Karaçalı Formation is more potential compared to the western part.

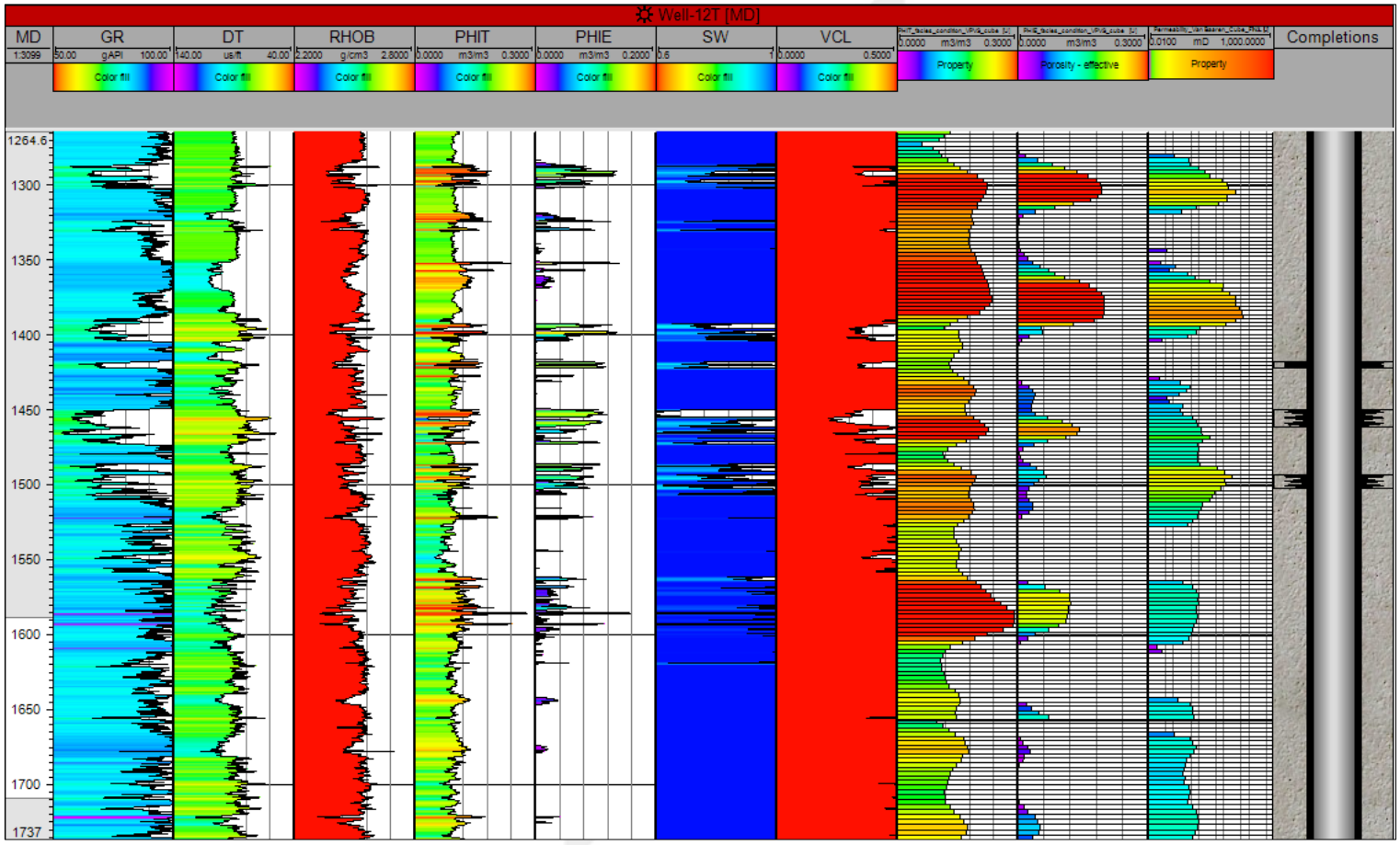

Figure 10.34. Well section of Well-12T is given. From left to right: GR, DT, RHOB, PHIT, PHIE, SW and VCL logs, total porosity, effective porosity and permeability models and completions at the well location are given. Except the interval between 1350 and 1400 m. modelled properties are reasonable.

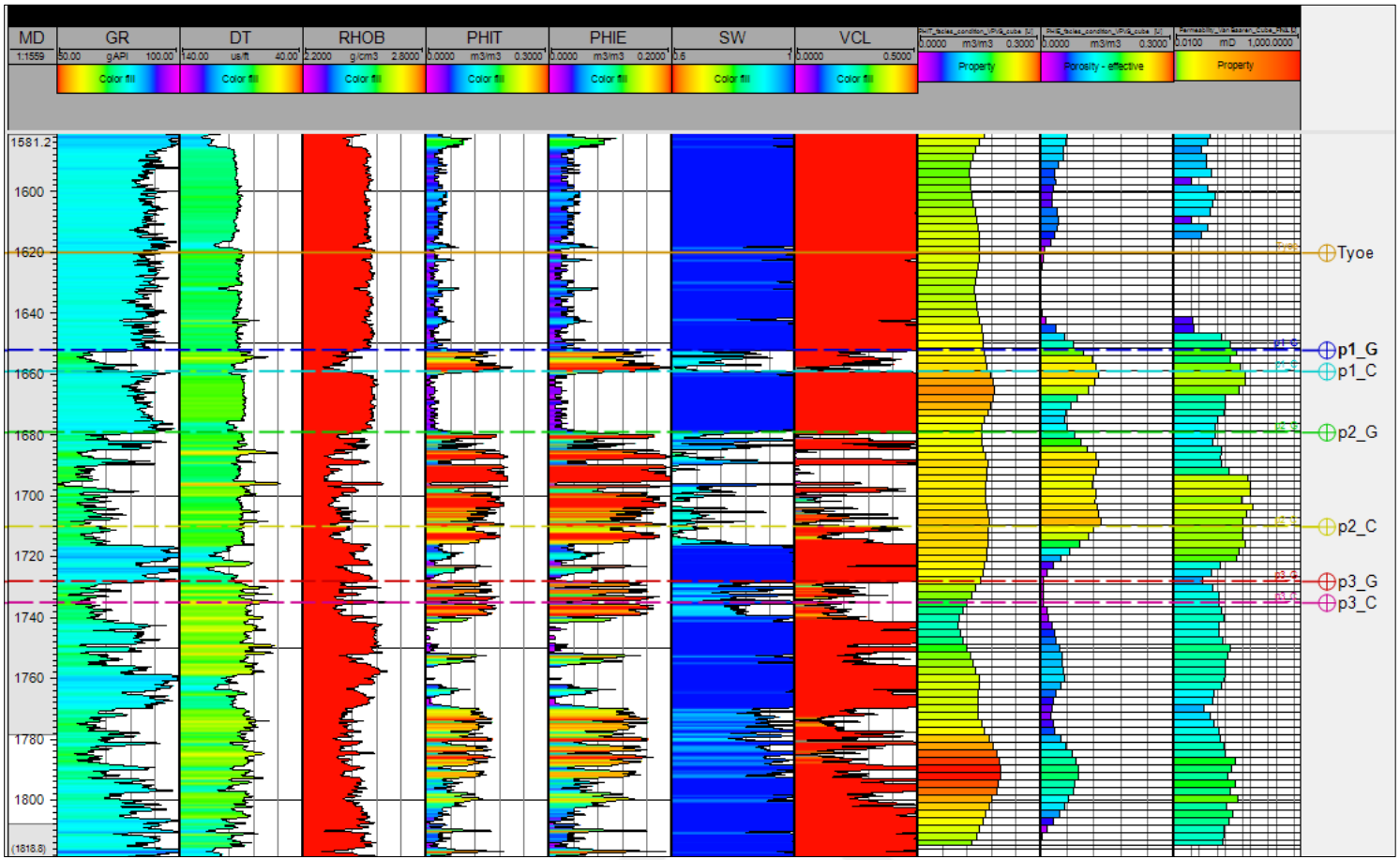

Figure 10.35. Well section of Well-210 is shown. From left to right: GR, DT, RHOB, PHIT, PHIE, SW and VCL logs, total porosity, effective porosity and permeability models and tops of perforated intervals at the well location are given. P1 and p2 intervals are producers while p3 interval does not produce.

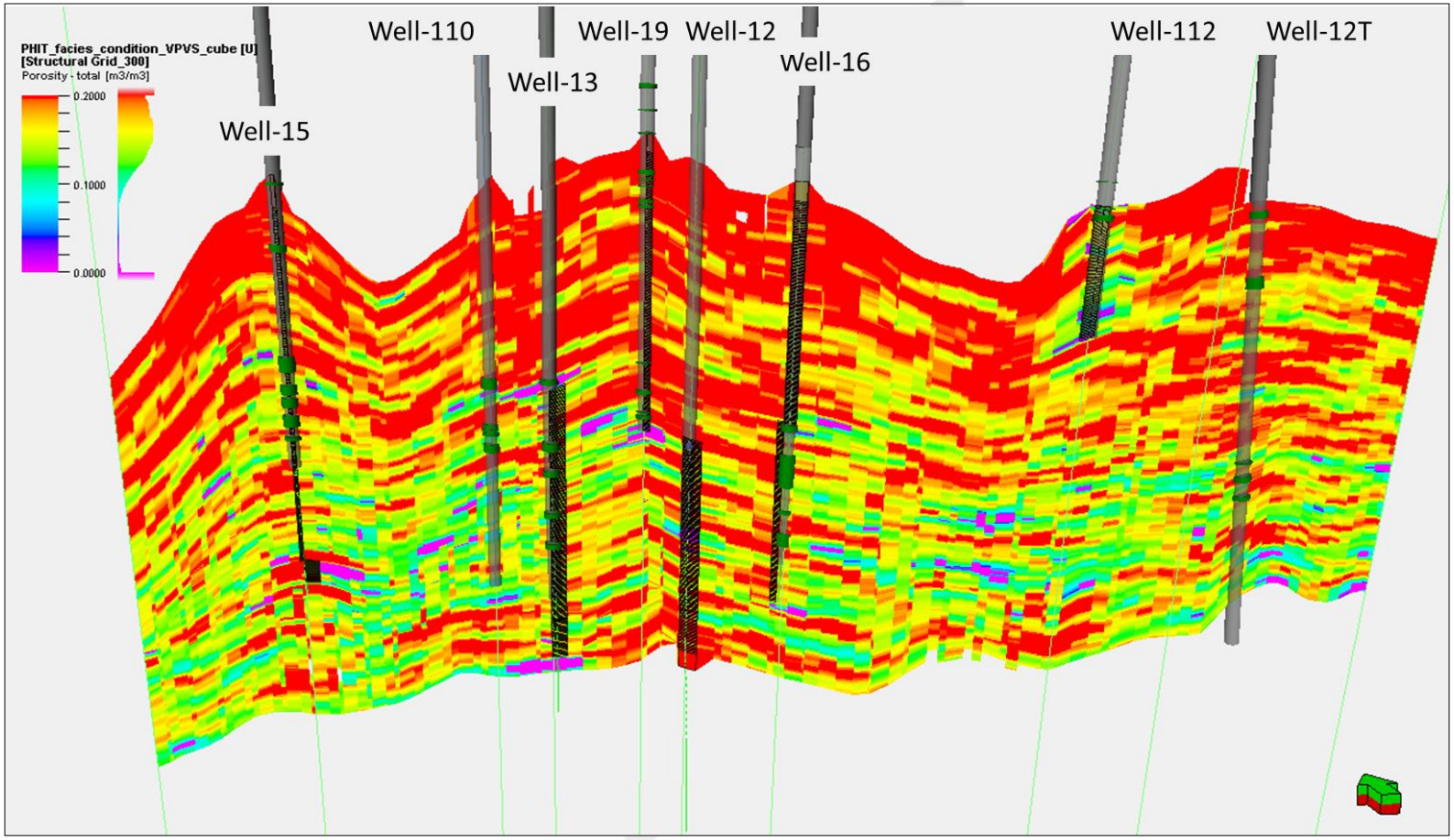

Figure 10.36. Composite total porosity model representing well group 1 wells. Total porosity values for shallower depths are higher due to unconsolidated facies while a clear decrease in total porosity is observed in deeper levels.

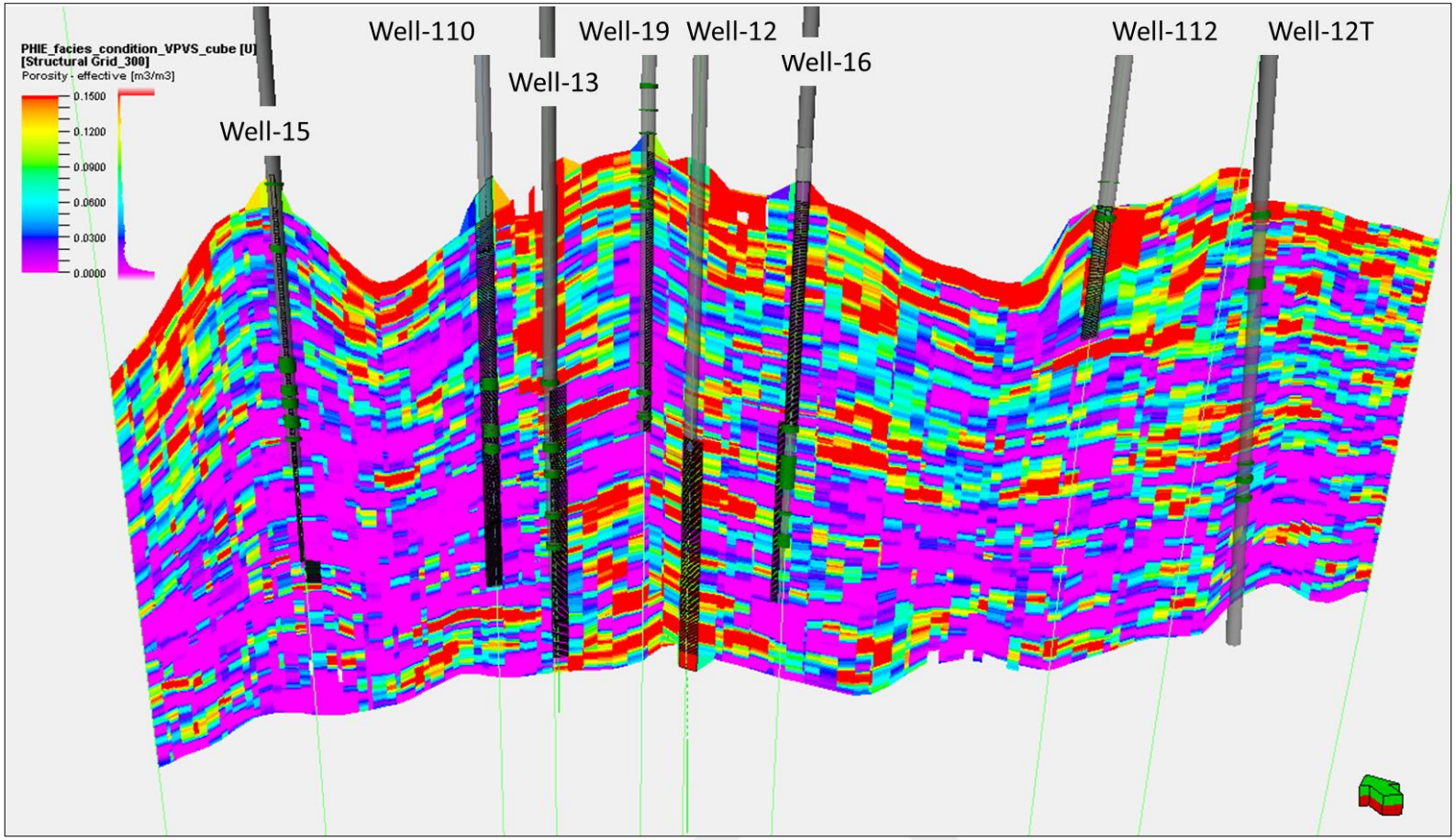

Figure 10.37. Composite effective porosity model representing well group 1 wells. Effective porosity values are high enough especially in hydrocarbon bearing zones. Effective porosity properties on the east direction are better in terms of reservoir potential.

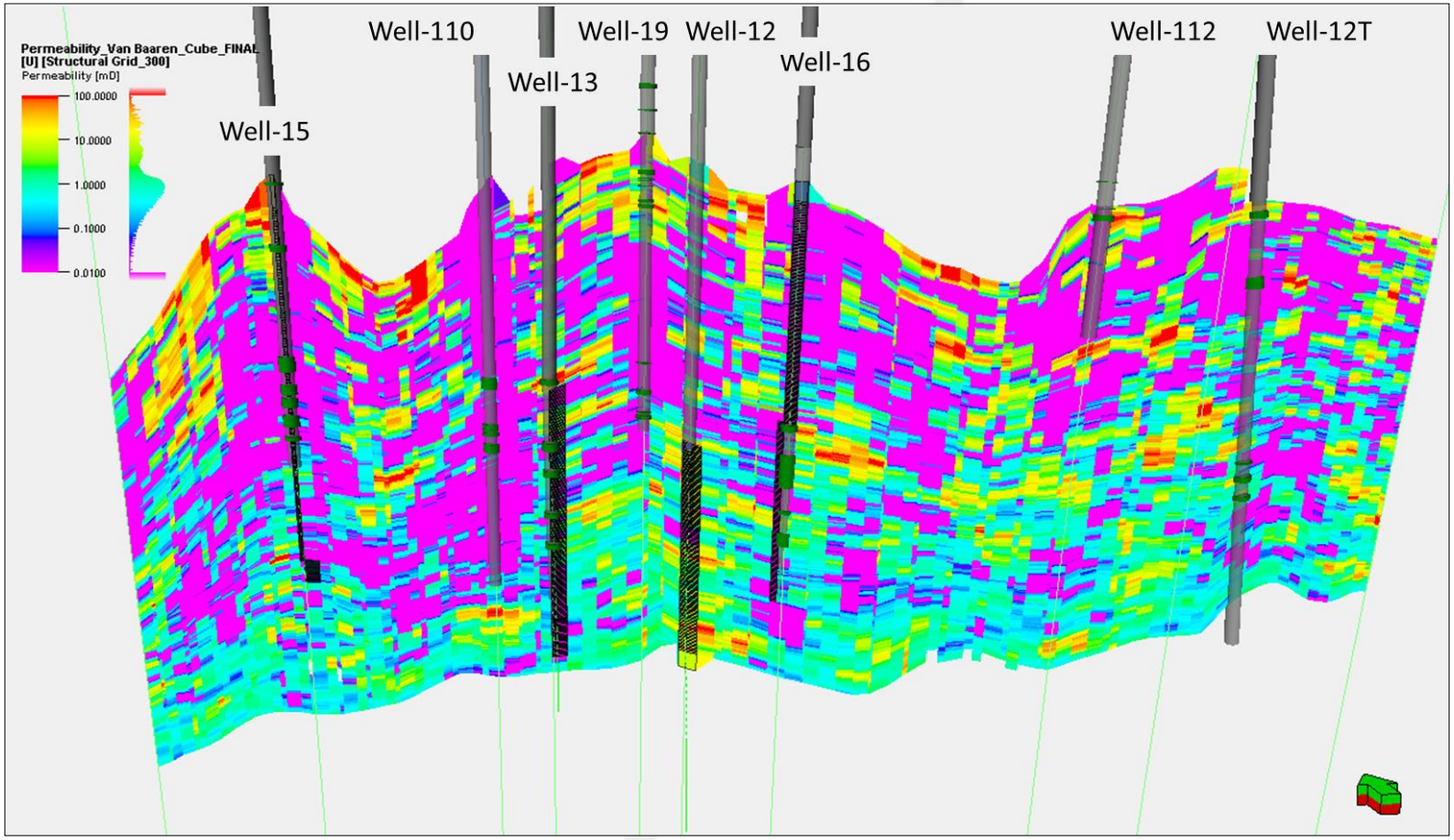

Figure 10.38. Composite permeability model representing well group 1 wells. Permeability values on the east direction are higher in similar to effective porosity variations.

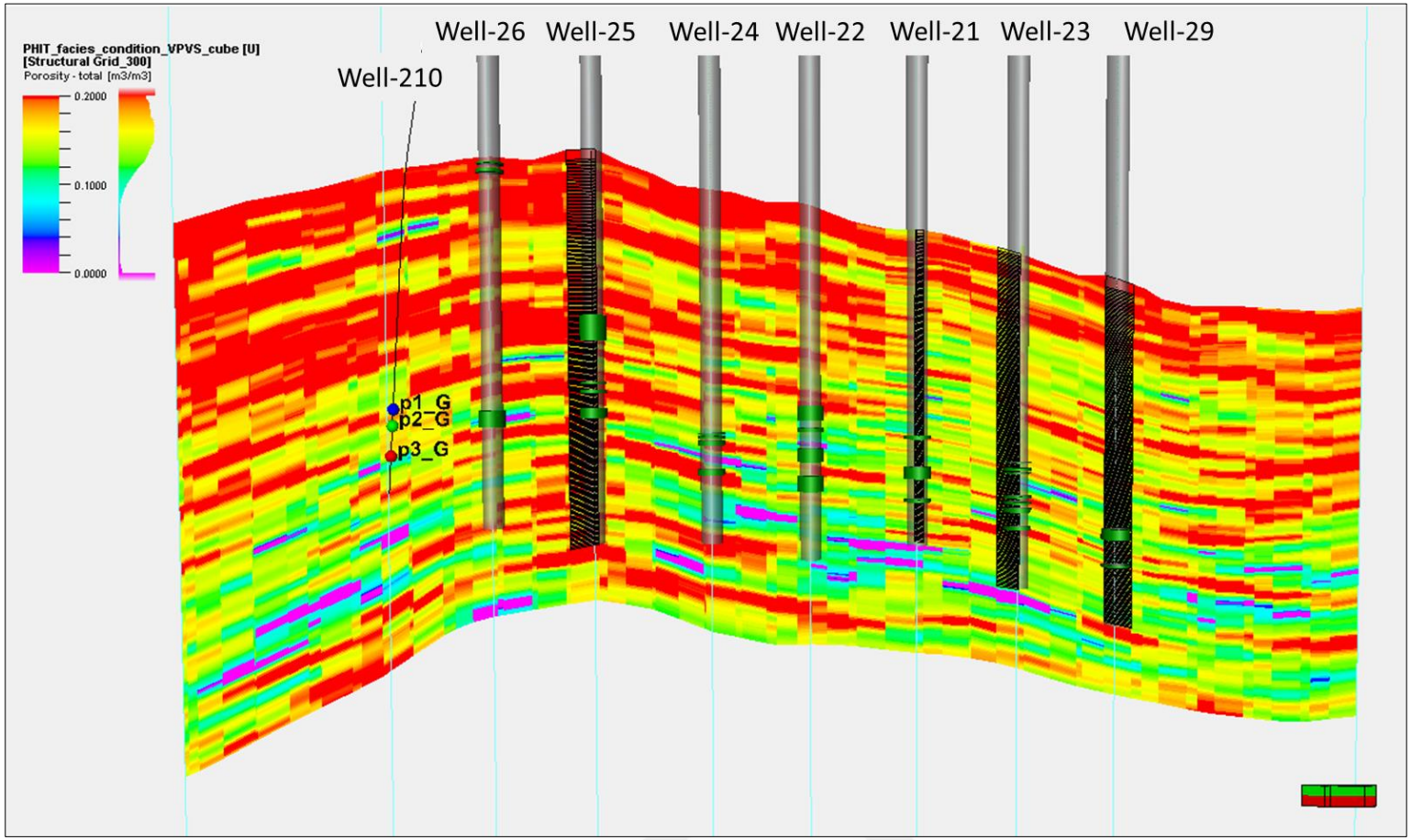

Figure 10.39. Composite total porosity model representing well group 2 wells. Similar to well group 1, total porosities are higher in shallower depths.

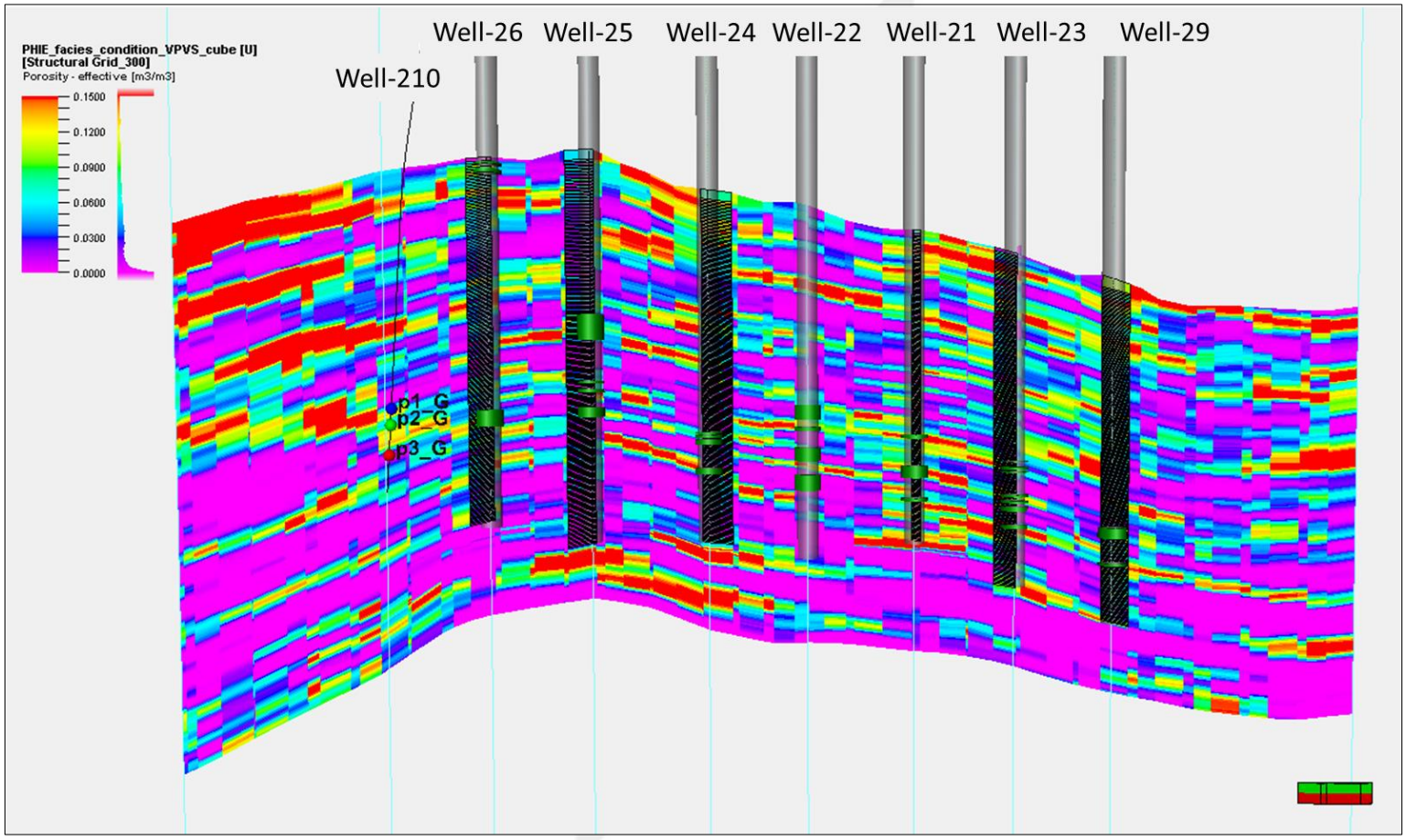

Figure 10.40. Composite effective porosity model representing well group 2 wells. Effective porosity values are in balanced at entire intersection. The westernmost part includes some intervals in shallower Osmancık Formation, which indicate potential reservoir zones.

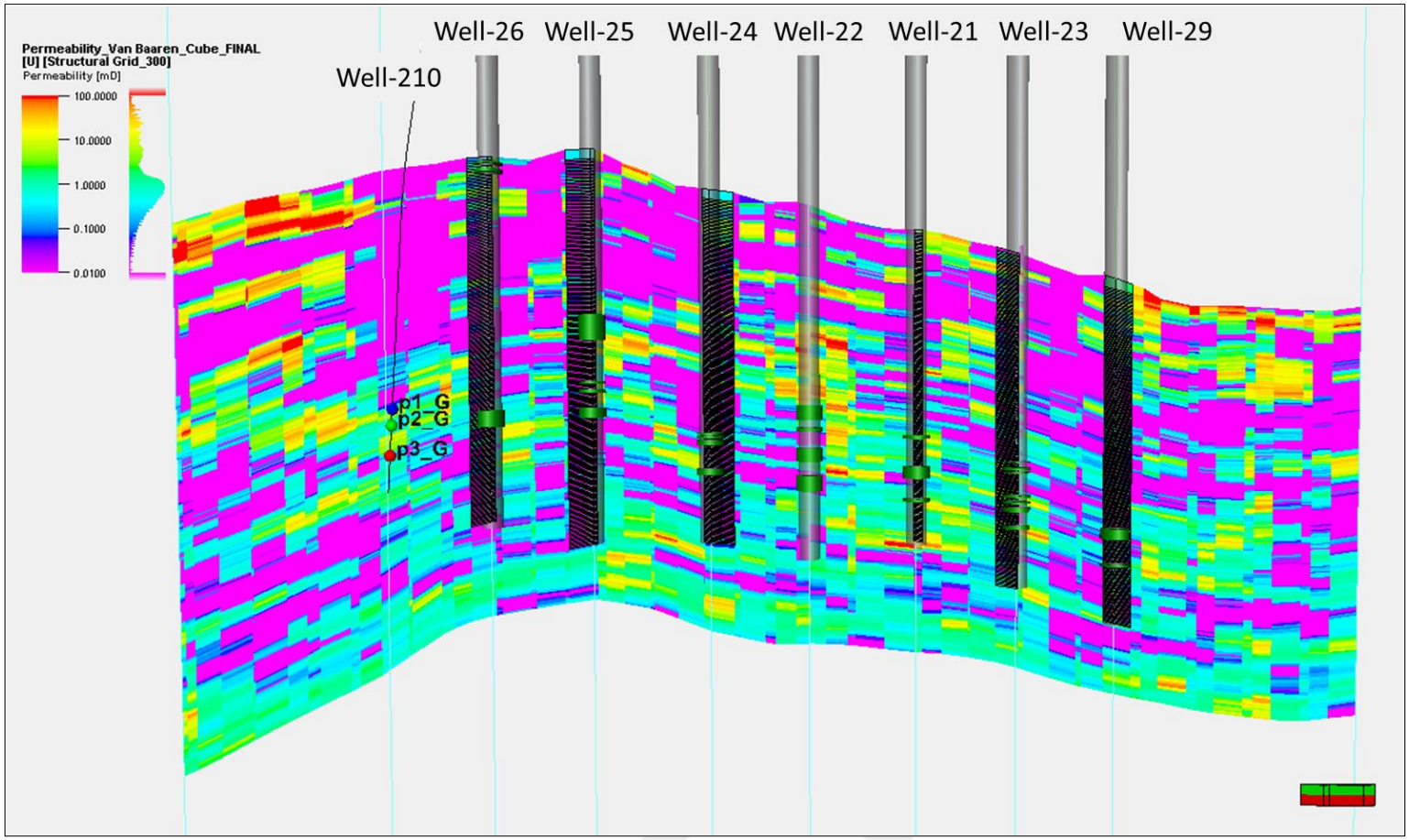

Figure 10.41. Composite permeability model representing well group 2 wells. Similar to effective porosity variations, permeability values are in balanced at entire intersection. Increase in permeability in the westernmost part is clearly observed, which can be considered as potential reservoir intervals.

10.10.5 Comparison of Facies and Property Models

Facies and property models were evaluated separately in the previous sections. 3D distributions of the built models will be compared and evaluated around specific producing areas.

Horizontal distribution of facies and property variations of a productive zone (cell-324) at shallower Osmancık Formation is shown in Figure 10.42. Producing area is indicated with a black ellipse for each model. In this area, sand facies are dominantly observed (Figure 10.42 A). Although total porosity values mostly change between 20%-30% covering 3D boundary, producing zone shows a distinctive increase, which can be detected easily (Figure 10.42 B). Effective porosity and permeability distributions are clearly detectable and distinguished from neighbor zones (Figure 10.42 C and D). Figure 10.42 includes group 1 wells placed into the models.

Three wells in group-1 are producers. While gas-bearing zone in Well-12 produces high amount of volume around 80,000,000 m^3, total gas production of the zones from well-13 and well-15 is around 26,000,000 m^3. Figure 10.43 indicates distribution of facies and properties for the productive zone in Well-12 (Cell-463). This zone includes widely distributed sandstone facies (10.44, top) with high amount of effective porosities (10.44, middle) and permeability values (Figure 10.44, bottom).

Wells in group 2 produce from several intervals. Some reservoir zones are widely spread, and these zones are consumed from several wells together. Facies and property models of one of these zones are displayed in Figure 10.43 and 10.44 (Cell-452). This zone is shown with a black ellipse and consists of sand and silt facies (Figure 10.43 A). Total porosity values are similar or lower compared to neighbor lithologies (Figure 10.43 B). However, effective porosities are distinguished and follow a certain pattern (Figure 10.43 C). A similar pattern is observed in permeability values (10.43 D). Figure 10.44 indicates the variation of these facies and properties with included wellbores of group-2. Another producing wide spread reservoir showing similar pattern in well group 2 is illustrated in Figures 10.44 and

10.45. Although the lithology consists of mainly sand facies (Figure 10.44 A), increasing depth (cell 470) results in decreasing porosity (Figure 10.44 B and C) and permeability (Figure 10.44 D) values. Wellbores embedded into these facies and property models are given in Figure 10.45.

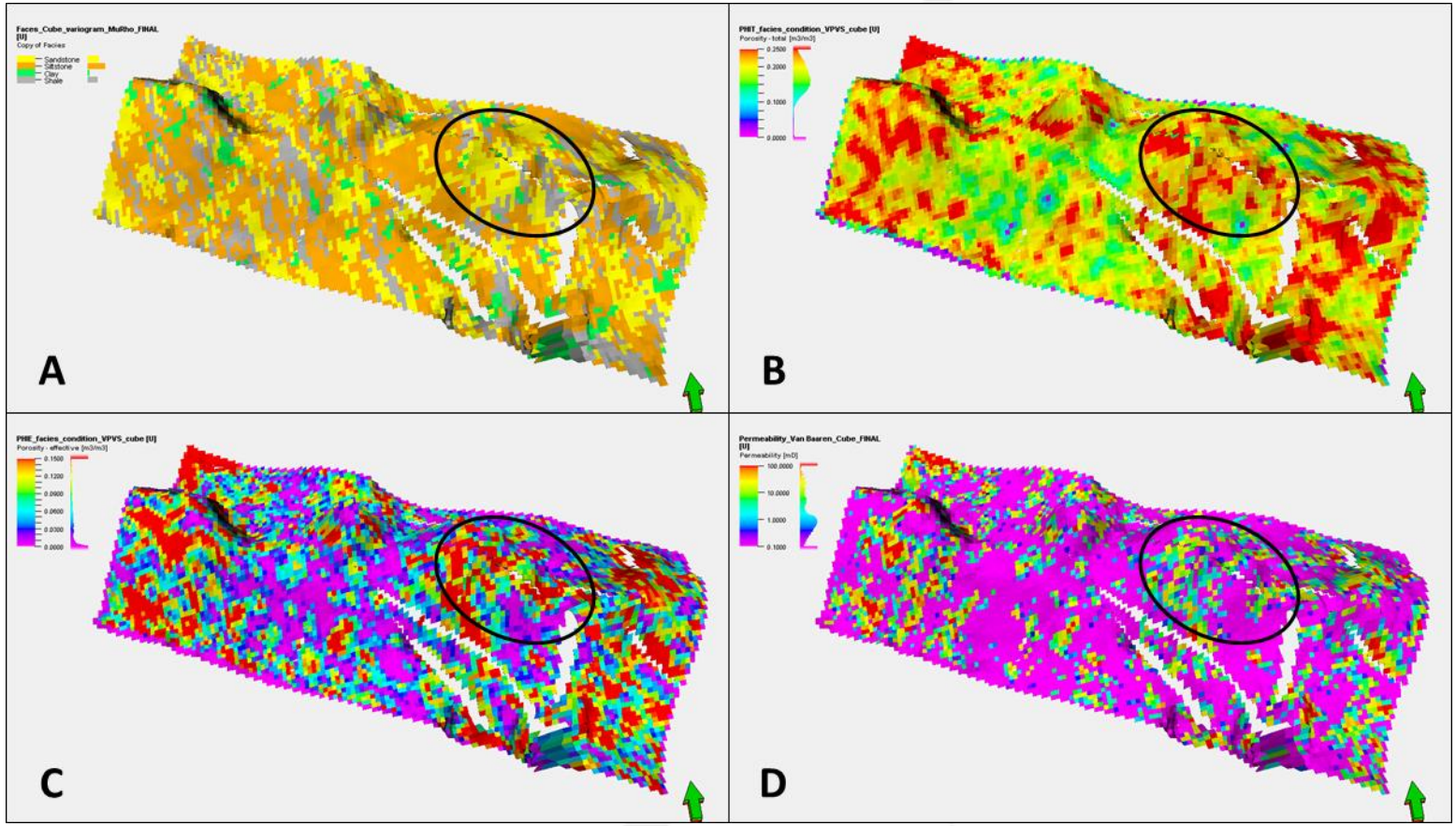

Figure 10.42. (A) Facies, (B) total porosity, (C) effective porosity and (D) permeability models representing a producing zone in shallower Osmancık Formation. Sand facies with good reservoir quality is observed in the zone shown with an ellipse.

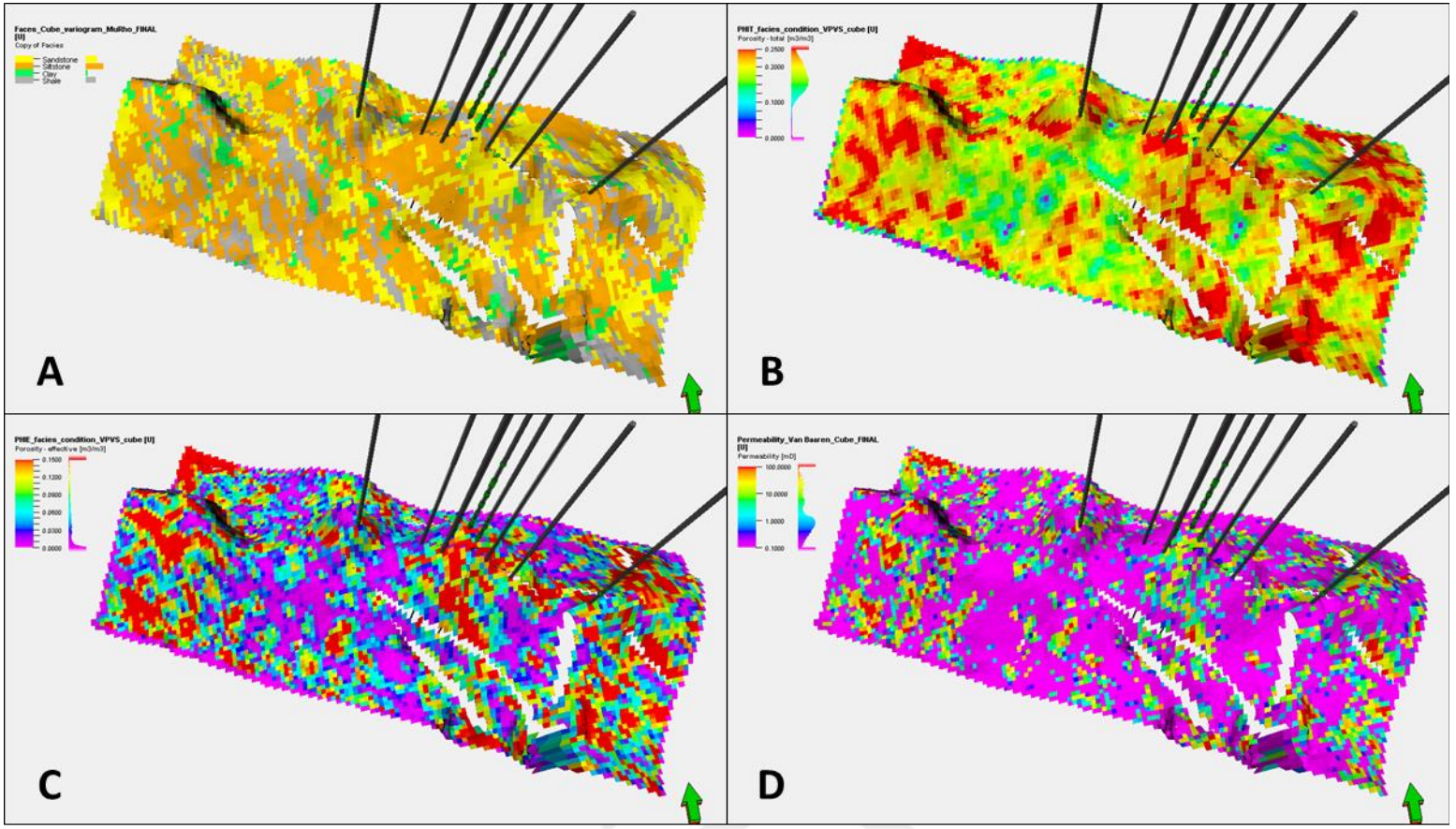

Figure 10.43. (A) Facies, (B) total porosity, (C) effective porosity and (D) permeability models in figure 10.42 include available wells in group-1.

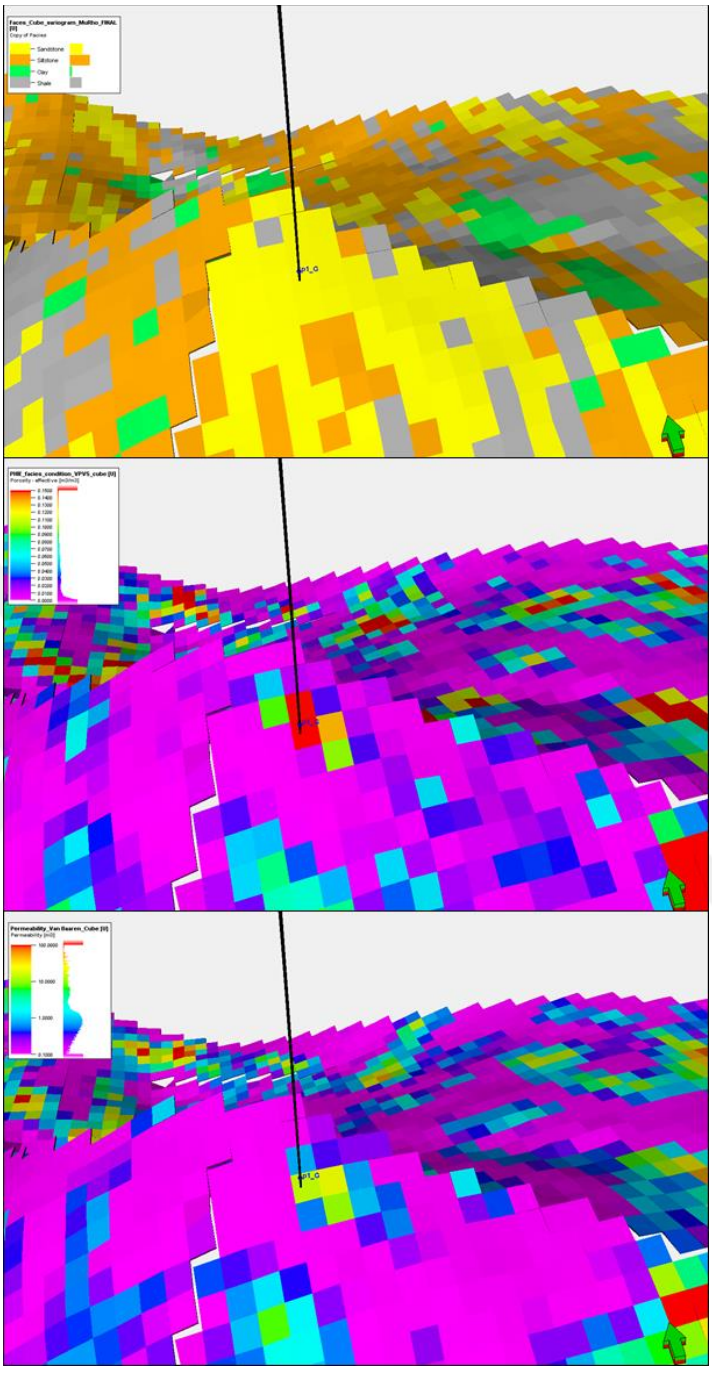

Figure 10.44. Total porosity (top), effective porosity (middle) and permeability (bottom) models for the best productive interval in deeper Osmancık Formation among group 1 wells.

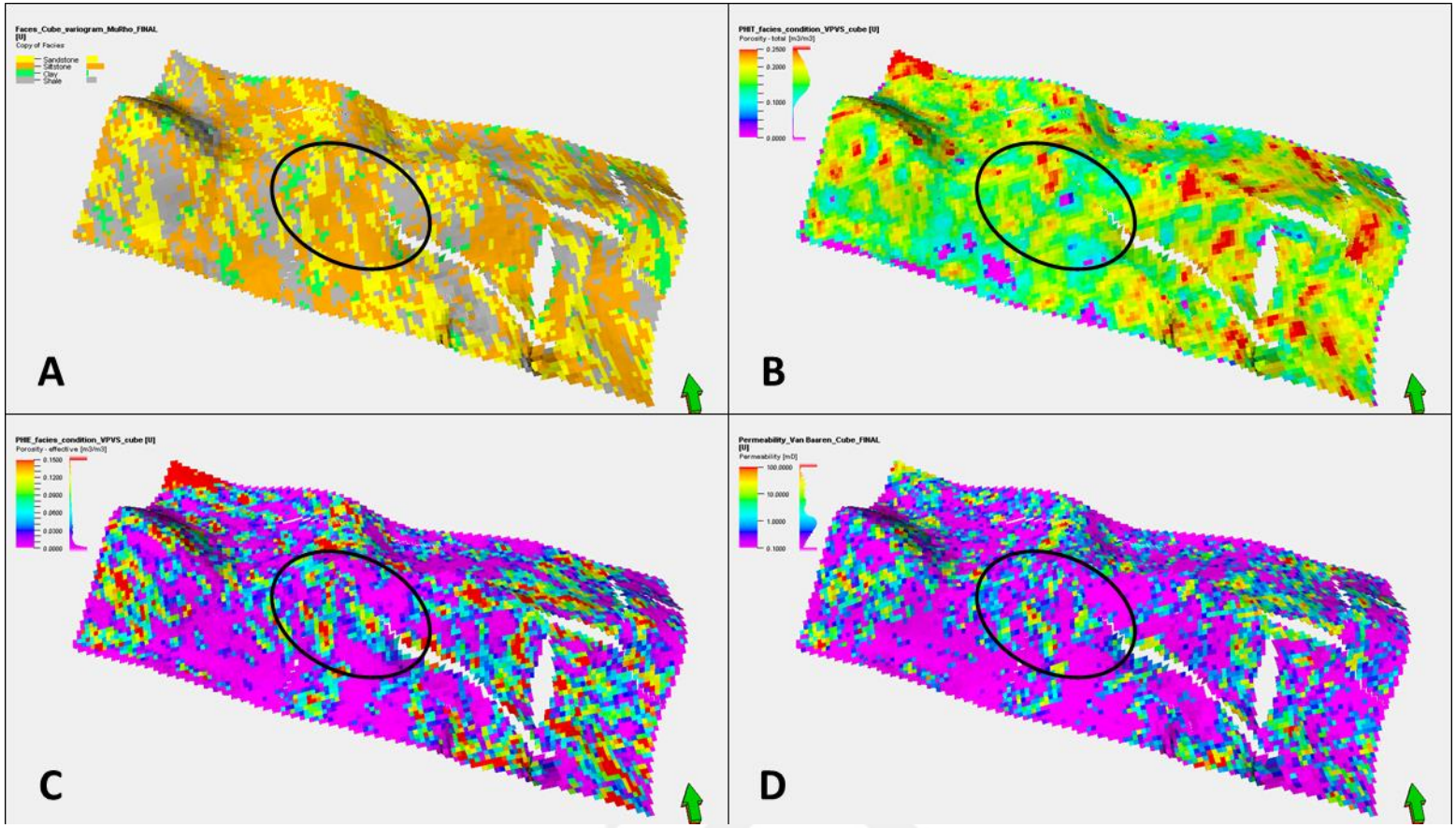

Figure 10.45. (A) Facies, (B) total porosity, (C) effective porosity and (D) permeability models of a productive reservoir interval (shown with a black ellipse), in which wells in group 2 are the producers.

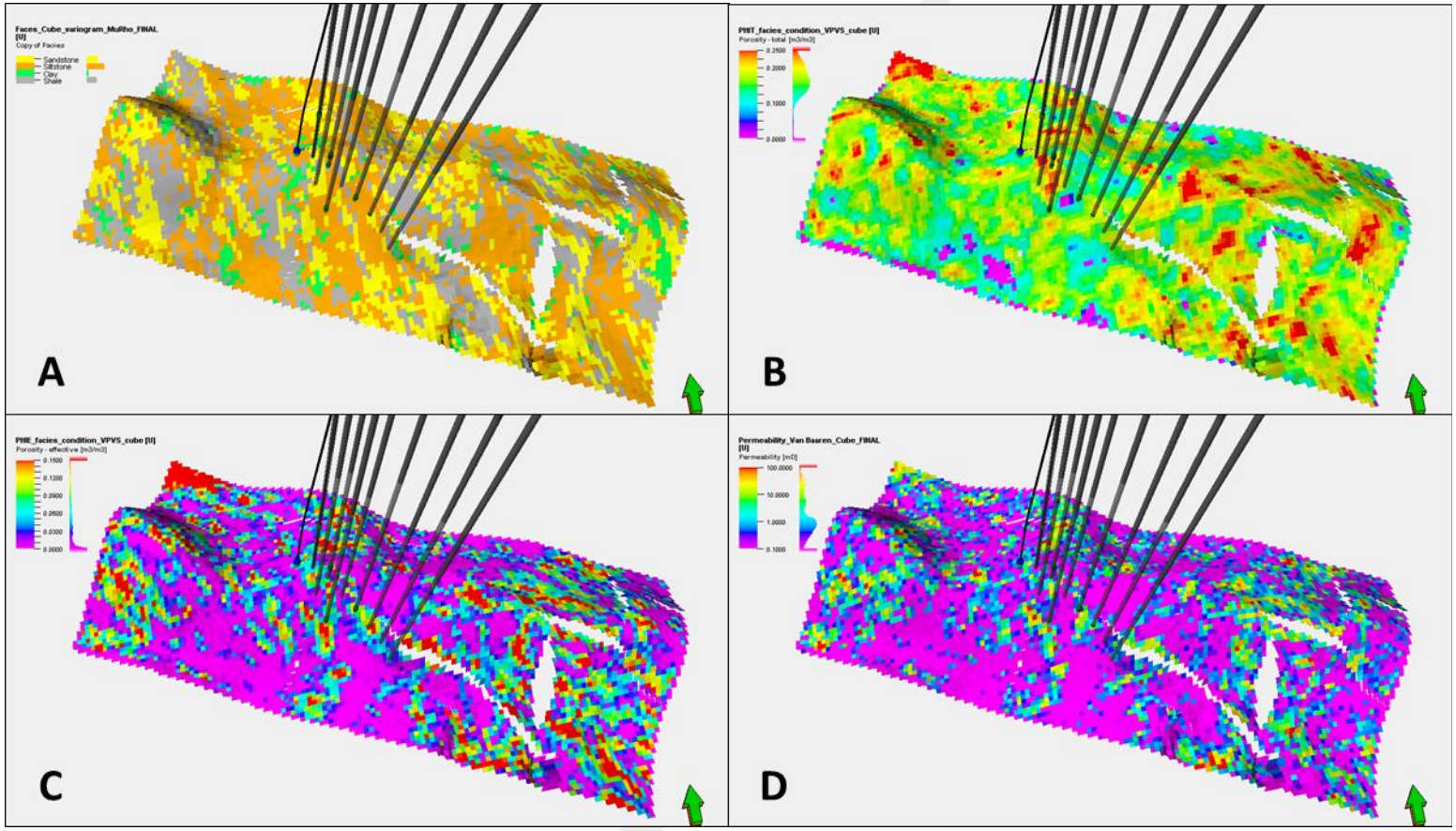

Figure 10.46. (A) Facies, (B) total porosity, (C) effective porosity and (D) permeability models in figure 10.45 with available wells in group-2.

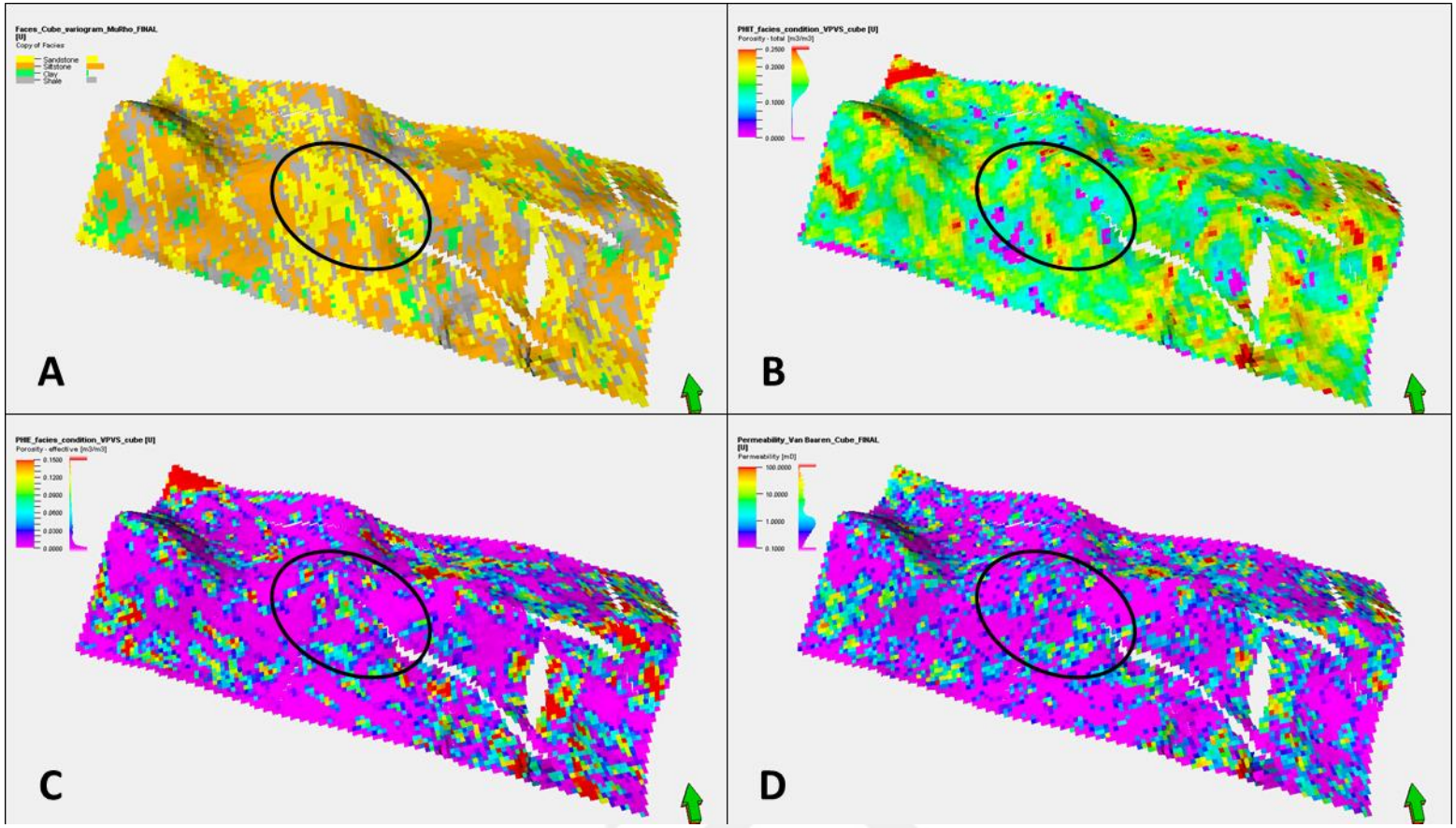

Figure 10.47. (A) Facies, (B) total porosity, (C) effective porosity and (D) permeability models of a deeper productive reservoir interval (shown with a black ellipse), in which wells in group 2 are the producers. Note that increasing depth causes a decrease in porosity and permeability values.

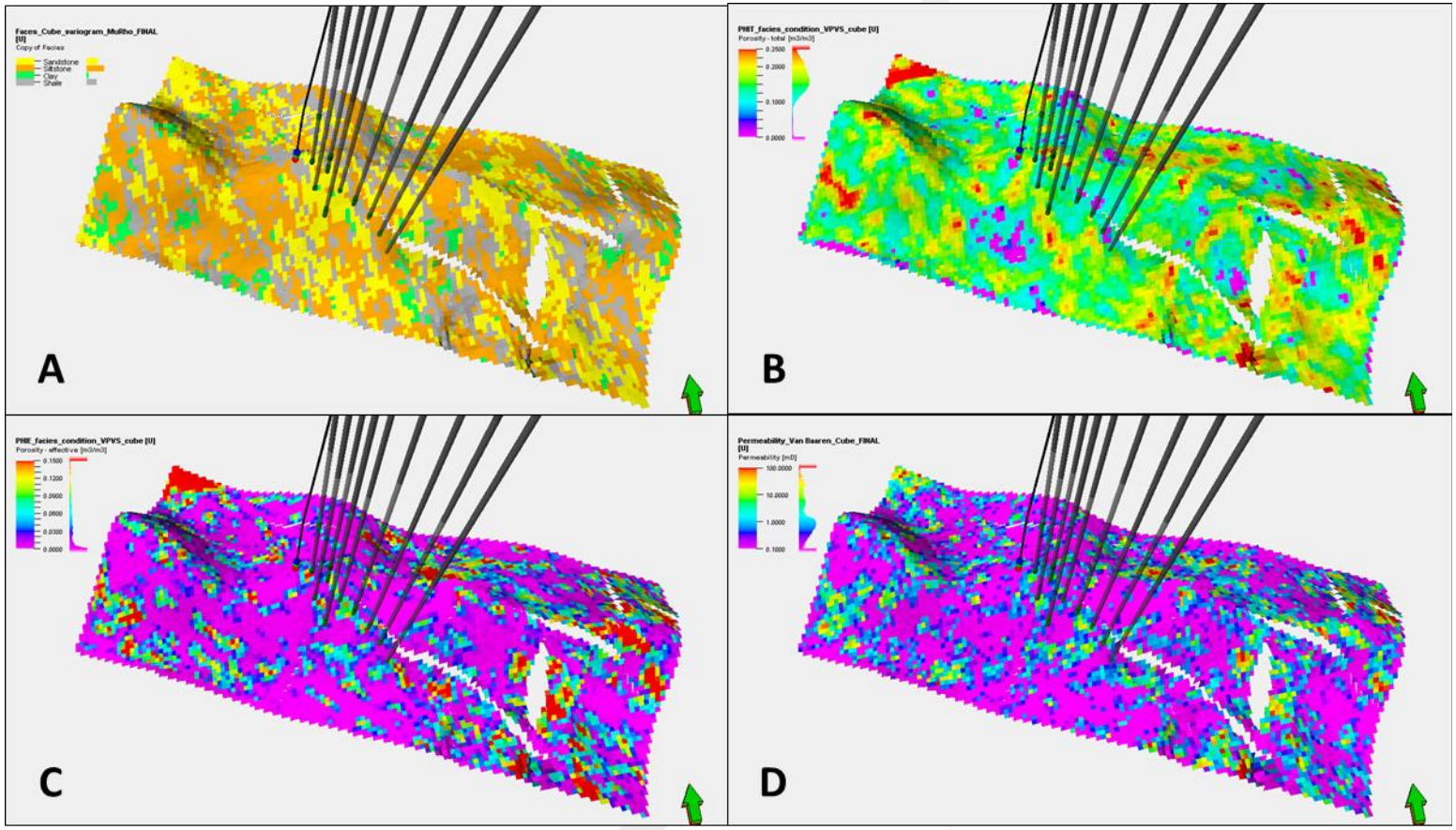

Figure 10.48. (A) Facies, (B) total porosity, (C) effective porosity and (D) permeability models in figure 10.47 contain available wells in group-2.

CHAPTER 11

DISCUSSION

It has always been a main concern to answer the questions about the reservoir potential of deeper Osmancık Formation. Drilling risk of a dry well in shallower depths of this formation is in a small range when optimum conditions are provided, which can be listed but not limited to geological structure, trap mechanism, seismic reflections (bright spots), seismic attributes. On the other hand, there is a big uncertainty at deeper parts of the formation even though all possible conditions are ensured. To understand the reason why deeper sections of the Osmancık Formation differs from shallower parts, facies and petrophysical properties of deeper zones were investigated. In this respect, an integrated study of several disciplines was conducted to reveal facies and property distribution of deeper Osmancık Formation.

Available wells were grouped into three categories according to the drilling location. (Figure 6.5). A north branch of Terzili Fault zone splits up well group 1 and 2 with a reverse fault. Well-group 1 is located on the hanging-wall while well group-2 is on the footwall of this system. The reason differentiating Karaçalı-Yulaflı field among the fields in the Thrace Basin is that well-producers of deeper Osmancık Formation belongs to well-group 2 located on the footwall part of this reverse faulting system.

Six wells out of twenty-eight wells (Table 6.2 and 6.3) contain core data from deeper Osmancık Formation while core data is not available for shallower parts. However, it is well-known from producing zones that productive intervals include mostly sand facies with high porosities. Thin sections from different depth intervals were examined. Unfortunately, thin section is not available in Well-21 which is one of the most productive ones in deeper Osmancık Formation. Measurements from the thin sections point out that dominant facies are lithic-wacke due to the presence of high

percentage of matrix. Only three of them were evaluated as lithic arenite facies, one is from Well-12 and other two belong to Well-15 (Table 7.1).

Three thin sections were used in Well-12. Two shallow thin sections (1348.25 m. and 1349 m.) have lithic wacke facies while the deepest one (1351.25 m) is lithic-arenite. GR, PHIE, SW and VCL logs confirm that lithic-arenite facies belongs to clear, productive, low water saturated sandstone while the other two facies show an increase of shaleness with unproductive and water saturated siltstone and shale (Figure 7.26). This finding provides an insight about how the type of facies plays an important role in production.

Well-13 includes two available core data ranging between (1) 1305-1304 and (2) 1489-1497.5 meters. The reservoir interval of the first core data does not produce although natural gas came out at first. The second reservoir where deeper core data was drilled out was produced low amount of natural gas (Figure 7.34). In other words, deeper level was producer while shallow part is not. It is obvious that the grain size for the shallower zone is very low approximately ranging from 40 to 70 microns (Figure 7.28). Low production from deeper zone could be because of facies type due to high matrix percent. It is clear that grain size is a significant indicator for hydrocarbon production because low grain sizes result in lower porosity and narrower pore throat, so permeability.

Well-15 is another well with two core data available at different depth ranges 1360.7-1369 m and 1404.5-1413.5 m) (Figure 7.47). The interval where deeper core was drilled out (Core-2) produced low amount of gas volume around 13,000,000 m^3. However, unproduced shallower interval (Core-1) has similar reservoir properties with deeper one. The productivity is a consequent of available gas pressure. In other words, the gas pressure of the unproductive interval is very low. This observation shows that another important parameter affecting to productivity is the availability of pressure.

Diagenesis has a great influence on deeper Osmancık Formation. Lower porosity and smaller grain sizes in deeper sections compared to shallower depths are the results of compaction and consolidation. Possible chlorization and quartz overgrowths are also observed in SEM photos (Figure 7.59 and 7.61). XRD analysis of Core-1 for Well-13 and 15 is also another evidence indicating high amount of chlorite percentage (Table 7.2).

Quantitative seismic interpretation methods such as AVO/AVA analysis and inverted acoustic impedance volumes confirm the evaluation of sedimentological inferences. Class II type of AVO anomalies for reservoir zones, which are encountered in deeper Osmancık Formation (Figure 9.30), are the result near zero impedance contrast between gas bearing sandstone and shale. This anomaly appears on compacted and consolidated reservoirs (Rutherford and Williams, 1989) as it was discussed in Chapter 9.3.3.3. Additionally, low impedance contrast results in decreasing strength of seismic reflections of stack seismic data as it is observed in deeper Osmancık Formation (Figure 9.31). Therefore, bright spots do not appear in deeper levels of the Osmancık Formation, so discrimination of gas bearing zones and other lithologies become harder. Controversially, gas-producing zones in shallower depths indicate AVO class III anomalies because of unconsolidated gas bearing sandstone as it is given in Figure 9.28. As a result of Class III type of AVO responses, bright spots are easily detected in shallower zones (Figure 9.29).

Addition to AVO variations in deeper Osmancık Formation, acoustic impedances calculated by seismic inversion show an abrupt increase after a certain depth which can be followed laterally on the seismic section (Figure 9.40 and 9.41). This increase indicates a change from high to low porosity leading compacted lithology indication towards deeper section.

Permeability parameter of a reservoir cannot be measured or processed by common well logs directly. Therefore, to create a permeability model, suitable permeability curves are necessary to be calculated. In clastic lithology, estimation of permeability

curve is possible and can be achieved by many suggested equations (Tixier, 1949; Wylie and Rose, 1950; Timur, 1968; Coats and Dumanior, 1974; Berg, R. R.,1975; Van Baaren, J., 1979; Glover et al., 2006). Several formulas have been implemented and the best fitted one, Van Baaren's (1979), was selected. Furthermore, the selected equation was edited to obtain a better representative permeability curve based on core permeability measurements.

Facies distribution of the field was achieved by using SIS method. This method only uses categorical variables, such as facies logs. Upscaled facies logs calibrated with seismic data were used as input for facies modeling. To implement property modeling, SGS method was utilized. This method uses continuous variables such as porosity logs. Upscaled porosity and permeability logs were utilized as input for property modeling. Two blind wells, Well-12T and Well-210, were utilized to validate each modeling result (Figure 10.19, 10.21, 10.34 and 10.35). The confirmation results are satisfactory at blind well locations.

There are also other methods for modeling of facies and property variations. For facies modeling, MPS is another practice as it was mentioned in Chaper 3. However, training images are required. Because of the unavailability of this data, this method was not applied during this research. For property modeling, Gaussian Rondom Function Simulation (GRFS) is another useful method. This method was also applied to generate porosity and permeability models. The results of SGS found more successful in deeper Osmancık Formation for the calculated porosity and permeability distribution in this study area than the results of GRFS.

Producing zones in shallower and deeper sections of the Osmancık Formation clearly suggest that facies are dominantly sandstone in shallower zones while grain sizes are variable in deeper sections. Effective porosity and permeability are the main parameters influencing reservoir conditions. Also, these property values show a decrease with increasing depth of drilling. However, these two parameters follow a specific pattern allowing the production of deeper reservoir zones.

Due to the compaction of the lithology, difference in total porosity between shallower and deeper parts is distinguished. This situation is another evidence how compaction trend changes with increasing depth (Figure 10.42 B, 10.45 B, 10.47 B).

For the following researches related to reservoir conditions of Karaçalı-Yulaflı field, several suggestions are listed to below:

In the absence of a point counter, area of the components of each thin section was calculated using an image tool. Therefore, area of the elements in thin sections were estimated approximately. For the following studies, a point counter should be utilized to obtain more precise measurements.

Core data is available at only deeper part of the formation. To make a more reliable comparison between shallower and deeper zones, especially in terms of grain sizes and distributions, it is proposed that core samples to be drilled from shallower depths as well. Additionally, the number of the measured porosity and permeability values in each core sample is inadequate to predict permeability from porosity. To increase the accuracy of the estimated values, more samples from each core should be measured. Also, it is suggested that cores should be drilled out at more wells to make a more robust distribution of the reservoir properties in the field. More core data leads more accurate process and interpretation of reservoir properties.

All plugs were cut out from available cores horizontally. However, due to the presence of highly shale lithology, anisotrophy should be taken into consideration. Therefore, it is suggested that core plugs should be cut out vertically and measured to evaluate porosity and permeability variations due to anisotrophy.

Porosity and permeability distribution of the study field are modelled. Dry wells could be detected also using water saturation variation in the field. Therefore, for the future studies, water saturation distribution is also suggested to be modelled.

The computed elastic parameters from seismic inversion allow each reservoir zone to be detected successfully. Evaluating reservoir models and inversion results

simultaneously will bring an insight to locate gas-bearing reservoir zones. Thus, this research could be used for commercial purposes as much as academic researches.

Due to the unbalanced results of acoustic impedances, shallower and deeper parts of the Osmancık Formation act as two different formations from a geophysical perspective. Although the use of acoustic impedances as a co-kriging parameter in porosity modeling in practice is a frequent application, these impedances did not work well for deeper Osmancık Formation contrary to the expectation. Instead, V_P/V_S ratio was utilized, which is an inversion output not affected by compaction trend. In this study, this ratio was a representative attribute discriminating sandstone and shale lithology. However, it is not always the case, so it might calculate erroneous models for different fields. Therefore, it is suggested that shallower and deeper sections of the Osmancık Formation should be studied separately to obtain more reliable and representative models in other fields.

CHAPTER 12

CONCLUSION

- Sedimentological studies on thin sections indicate that more than one parameter affects productivity in deeper Osmancık Formation. Well-12, which is the best productive group-1 well from deeper Osmancık Formation, shows that the type of facies (lithic arenite) is one of the parameters affecting the productivity.
- Considering a low productive group-1 well, Well-13, grain size is the second parameter influencing gas production. When grain sizes are too small about silt sized, due to worsen reservoir condition such as decreasing porosity and permeability, related zone cannot be produced. When grains reach at least fine to medium sizes, then production can be succeeded.
- The third parameter affecting the productivity is gas pressure. When pressure does not exist, facies type, grain size or any other facies or property related variables do not control on the productivity.
- Acoustic impedances computed from seismic inversion discriminate shallower and deeper parts of the Osmancık Formation clearly. Another important output calculated from seismic inversion is the V_P/V_S ratio. All productive reservoir zones can be detected using V_P/V_S ratio. When a gas-bearing sandstone is encountered, p velocity decrease while s velocity is little affected, so V_P/V_S ratio drops. These two elastic parameters were utilized for reservoir characterization.
- Because of the low acoustic impedance contrast in deeper Osmancık Formation, acoustic impedances do not vary significantly with porosity

changes. On the other hand, V_P/V_S ratio is sensitive to porosity changes in deeper sections.

- Shallower productive reservoir zones indicate class III AVO anomalies representing unconsolidated sandstones while class II AVO anomalies are encountered in deeper sandstone reservoirs resulting of compacted lithology.
- GR variations calculated by supervised neural network application demonstrates that shaleness increases towards north of the field.
- Lithofacies classification using unsupervised neural network confirms that an abrupt change in lithology appears at the boundary of deeper Osmancık Formation.
- Facies model built by SIS method indicates that productive zones in shallower depths are mostly sandstone dominated while facies are variable between sandstone and siltstone in deeper Osmancık Formation.
- Reservoir properties such as total porosity, effective porosity and permeability were generated using SGS method. Modelled total porosities change significantly from shallower to deeper sections. While the total porosity values in lower depths are around 25-30%, these values decrease to 15-20% in deeper sections. This is evaluated as a result of compaction rather than shale intrusion.
- Core measurements were used to estimate a relationship between porosity and permeability leading prediction of permeability curves using empirical equations. Also, core porosity and permeability cross-plots show that most productive ones, Well-12 and Well-21, among the wells with core data have higher porosity and permeability variations. Only a part of unproductive core-1 in Well-13 has high porosity and permeability values. However, these properties at deeper part of the same core are lower. This may cause a flow barrier preventing the fluid to flow upward.
- The modelled effective porosity and permeability parameters reveal that increasing depth causes a decrease in values as a result of compacted

sediments. A certain pattern for the distribution of porosity and permeability is observed in producing deeper sediments at well group-2.

- Diagenesis in sandstone is one of the most significant parameters playing role on both facies and property variations. With increasing drilling depth, compaction and consolidation also increase. Core plugs with compacted sandstone, high matrix content and low grain size particles in thin sections, possible chloritization, quartz overgrowth, and low interparticle porosities observed in SEM photomicrographs, XRD analysis of Well-13 and 15, abrupt increase in acoustic or P-impedances, class II type AVO anomalies, weaken reflections from seismic data, lessen total porosity values in deeper sections calculated by property modeling are the evidence of diagenesis in sandstone in the Karaçalı-Yulaflı field, Thrace Basin.

REFERENCES

Abdelmaksoud, A., Amin, A.T., El-Habaak, G.H. and Ewida, H.F., 2019, Facies and petrophysical modeling of the Upper Bahariya Member in Abu Gharadig oil and gas field, north Western Desert, Egypt. Journal of African Earth Sciences, 149, pp.503-516.

Aki, K., and Richards, P. G., 1980, Quantitative seismology: Theory and methods: W. H. Freeman and Co.

Akyol, E., ve Akgün, F., 1995, Trakya karasal Tersiyeri'nde yaş tayinleri, Trakya Havzası Jeolojisi Sempozyumu Bildiriler Kitabı, 28-29.

Alabert, F. G.,1987, Stochastic imaging of spatial distributions using hard and soft information.Master's thesis, Stanford University, Stanford, CA.

Ali, A.M., Radwan, A.E., Abd El-Gawad, E.A. and Abdel-Latief, A.S.A., 2022, 3D integrated structural, facies and petrophysical static modeling approach for complex sandstone reservoirs: A case study from the Coniacian–Santonian Matulla formation, July Oilfield, Gulf of Suez, Egypt. Natural Resources Research, 31(1), pp.385-413.

Ali, M., Abdelmaksoud, A., Essa, M.A., Abdelhady, A. and Darwish, M., 2020, 3D structural, facies and petrophysical modeling of C member of six hills formation, Komombo Basin, Upper Egypt. Natural Resources Research, 29, pp.2575-2597.

Al-Khalifah, M. and Makkawi, M., 2002, The impact of data integration on geostatistical porosity modelling: A case study from the Berri Field, Saudi Arabia. Journal of Petroleum Geology, 25(4), pp.485-498.

Arpacı, T. and Özdemir, H., 2020, Step-out well positioning using hydrocarbon indicators from seismic inversion: a case study. First Break, 38(1), pp.43-51.

Arpacı, T., 2018, Karaçalı-12 Kuyusu Rezervuar Jeofiziği Değerlendirme Raporu. TPAO, Ankara, pp. 1–32.

Arpacı, T., 2021, Karaçalıtepe 1 ve 2 Kuyuları Öncesi ve Sonrası Rezervuar Jeofiziği ve Kantitatif Yorumlar Sonuç Değerlendirme Raporu,

Arpaci, T. and Ozdemir, H., 2016, Step-out well position optimisation using inverted hydrocarbon indicators. In 78th EAGE Conference and Exhibition 2016 (Vol. 2016, No. 1, pp. 1-5). EAGE Publications BV.

Atalık, E., 1992, Depositional systems of the Osmancık Formation in the Thrace Basin: METU, The Graduate School of Natural and Applied Sciences, Ph. D. Thesis, 366 p.

Bai, T. and Tahmasebi, P., 2022, Sequential Gaussian simulation for geosystems modeling: a machine learning approach. Geoscience Frontiers, 13(1), p.101258.

Barclay, F., Bruun, A., Rasmussen, K. B., Alfaro, J. C., Cooke, A., Cooke, D., Salter, D., Godfrey, R., Lowden, D., McHugo, S., Ozdemir, H., Pickering, S., Pineda, F. G., Herwanger, J., Volterrani, S., Murineddu, A., Rasmussen, A., Roberts., R., 2008, Seismic Inversion: Reading Between the Lines: Oilfield Review, 20(1), 42-63.

Barka, A.A., Gülen, L., 1988, New constrains on age and total offset of the North Anatolian Fault Zone: Implications for tectonics of eastern Mediterranean region. Spec. Publ. Middle- East Tech. Univ. Ankara, Turkey, pp. 39–65.

Barka, A.A., Hancock, 1985, Tectonic interpretation of enigmatic structures in the North Anatolian Fault Zone. J. Struct. Geol. 5, 217–220.

Batı, Z., Alişan, C., Ediger, V.Ş., Teymur, S., Akça, N., Sancay, H., Ertuğ, K., Kirici, S., Erenler, M., ve Aköz, Ö., 2002, Kuzey Trakya Havzası'nın Palinomorf, Foraminifer ve Nannoplankton Biyostratigrafisi, Türkiye Stratigrafi Komitesi Çalıştayı (Trakya Bölgesi'nin Litostratigrafi Adlamaları) Özleri, s. 14.

Batı, Z., Erk, S. ve Akça, N., 1993, Trakya Havzası Tersiyer birimlerinin palinomorf, foraminifer ve nannoplankton biyostratigrafisi, TPAO Araştırma Grubu Arşivi, rapor no, 1947, 92s., Ankara.

Baytok, S., Selek, B. and Özdemir, H., 2017, Cross-equalization and prestack seismic inversion of time-lapse land seismic data, Central Thrace Basin, Turkey. The Leading Edge, 36(7), pp.588-597.

Beer, H. ve Wright, J.A., 1960, Stratigraphy of the Ganosdağ, Korudağ and Keşan Hills, District I, TPAO Arama Grubu Arşivi, yayınlanmamış teknik rapor, 736, 42 s.

Berg, R. R., 1975, Capillary pressures in stratigraphic traps. AAPG bulletin, 59(6), 939-956.

Boer, N.P. de, 1954, Report on a geological reconnaissance in Turkish Thrace: September, December G.A. 25373.

Burianyk, Michael, 2000, Amplitude-vs-Offset and Seismic Rock Property Analysis: A Primer: Canadian Society of Exploration Geophysicists, 25(11), 4-14.

Bürkan, K., 2010, Trakya'nın Jeoloji Haritası, Jeolojisi, Tektonik Evrimi ve Hidrokarbon Potansiyeli, TP Raporu.

Büyükutku, A. and Geçer, A., 2020, Trakya Havzası Kuzeybatısında Hamitabat Formasyonu Denizaltı Yelpaze Kumtaşlarının Rezervuar Potansiyeli. Gümüşhane Üniversitesi Fen Bilimleri Dergisi, 10(1), pp.174-189.

Castagna, J. P., 2001, AVO Analysis: Canadian Society of Exploration Geophysicists, 29-34.

Castagna, J. P., and Swan, H.W., 1997, Principles of AVO Crossplotting: The Leading Edge, 16, 337-344.

Castagna, J. P., and Swan, H.W., and Foster, D. J., 1998, Framework for AVO gradient and intercept interpretation: Geophysics, 63, 948–956.

Cersósimo, D.S., Ravazzoli, C.L. and Martínez, R.G., 2016, Prediction of lateral variations in reservoir properties throughout an interpreted seismic horizon using an artificial neural network. The Leading Edge, 35(3), pp.265-269.

Chima, P., Baiyegunhi, C., Liu, K. and Gwavava, O., 2018, Diagenesis and rock properties of sandstones from the Stormberg Group, Karoo Supergroup in the Eastern Cape Province of South Africa. Open Geosciences, 10(1), pp.740-771.

Coats, G.R. and Dumanoir, J.L., 1974, A New Approach to Improved Log-Derived Permeability. The Log Analyst, 15, 17-31.

Coşkun, B., 1997, Oil and gas fields –transfer zone relationships, Thrace Basin, NW Turkey, Marine and Petroleum Geology 14 (4): 401-416, Ankara.

Çetinkaya, C., Akpınar, M., Mağara, F.S. and Karakeçe, Y.Ş., 2011, May. Integrated Geostatistical Reservoir Characterization And 3D Geological Modelling Study of Yulaflı Field. In 18th International Petroleum and Natural Gas Congress and Exhibition of Turkey (pp. cp-377). European Association of Geoscientists & Engineers.

Davies, O., 2019, Permeability Modelling of a Sandstone Reservoir in Parts of the Niger Delta. Available at SSRN 3424667.

Davis, John C., 2002, Statistics and Data Analysis in Geology.

de Carvalho, P.R.M., da Costa, J.F.C.L., Rasera, L.G. and Varella, L.E.S., 2017, Geostatistical facies simulation with geometric patterns of a petroleum reservoir. Stochastic environmental research and risk assessment, 31, pp.1805-1822.

Dell'Arciprete, D., Bersezio, R., Felletti, F., Giudici, M., Comunian, A. and Renard, P., 2012, Comparison of three geostatistical methods for hydrofacies simulation: a test on alluvial sediments. Hydrogeology Journal, 20(2), p.299.

Deutsch C.V., Journel A.G., 1998, GSLIB: Geostatistical Software Library: and User's Guide Oxford University Press, New York, 2nd Ed.

Deutsch, C. V., 1992, Annealing Techniques Applied to Reservoir Modeling and the Integration of Geological and Engineering (Well Test) Data. PhD thesis, Stanford University, Stanford, CA.

Deutsch, C.V., 2006, A sequential indicator simulation program for categorical variables with point and block data: BlockSIS. Computers & Geosciences, 32(10), pp.1669-1681.

Deutsch, Clayton V., 2002, Geostatistical Reservoir Modeling. Oxford University Press.

Dickinson, W.R., 1995, Forearc basins, in Busby, C.J., and Ingersoll, R.V., eds., Tectonics of sedimentary basins: blackwell Science, Oxford, p.221-261.

Duman TM, Keçer M, Ateş Ş, Emre O, Gedik İ, Karakaya F, Durmaz S, Olgun Ş, Şahin H and Gökmenoğlu O, 2004, İstanbul metropolü batısındaki (Küçükçekmece-Silivri-Çatalca) kentsel gelişme alanlarının yer bilim verileri, Özel Yayın Serisi-3, Maden Tetkik ve Arama Müdürlüğü, Ankara.

Edigbue, P., Olowokere, M.T., Adetokunbo, P. and Jegede, E., 2015, Integration of sequence stratigraphy and geostatistics in 3-D reservoir modeling: a case study of Otumara field, onshore Niger Delta. Arabian journal of geosciences, 8, pp.8615-8631.

Ediger, V.Ş. and C. Alişan, 1989, Tertiary fungal and algal palynomorph biostratigraphy of the northern Thrace basin, Turkey. Review of Palaeobotany and Palynology, v. 58, p. 139-161.

Elmas, A., 2012, The Thrace Basin: stratigraphic and tectonic-palaeogeographic evolution of the Palaeogene formations of northwest Turkey. International Geology Review, 54(12), pp.1419-1442.

Erarslan, C. and Örgün, Y., 2017, Mineralogical and geochemical characterization of the Saray and Pınarhisar coals, Northwest Thrace Basin, Turkey. International Journal of Coal Geology, 173, pp.9-25.

Fatti, Jan L., Smith G. C., Vail P. J., Strauss P. J., and Levitt P. R., 1994, Detection of Gas in Sandstone Reservoirs Using AVO Analysis: a 3-D Seismic Case History Using the Geostack Technique: Geophysics, 59, 1362-1376.

Foley, J.E., 1938, Memorandum on the geology of the vicinity of Tekirdağ. M.T.A. Rep. no. 769 (unpublished), Ankara.

Glover, P.W., Zadjali, I.I. and Frew, K.A., 2006, Permeability prediction from MICP and NMR data using an electrokinetic approach. Geophysics, 71(4), pp.F49-F60.

Gómez-Hernández, J.J. and Srivastava, R.M., 1990, ISIM3D: An ANSI-C three-dimensional multiple indicator conditional simulation program. Computers & Geosciences, 16(4), pp.395-440.

Goovaerts, P., 1994, Comparative performance of indicator algorithms for modeling conditional probability distribution functions. Mathematical Geology.

Goovaerts, P., 1997, Geostatistics for Natural Resources Evaluation. Oxford University Press, New York.

Gökçen, L.S., 1967, Keşan bölgesinde Eosen-Oligosen sedimantasyonu, Güneybatı Türkiye Trakyası: MTA Bulletin, v. 69, p. 1-10.

Gökçen, N., 1971, Güneydoğu Trakya'nın Paleojen stratigrafisinde ostrakodlar açısından yeni görüşler, Türkiye 1. Petrol Kongresi Bildiriler Kitabı, 81-85.

Görür, N. and Okay, A.I., 1996, Fore-arc origin of the Thrace basin, northwest Turkey. Geologische Rundschau, 85, 662-668.

Görür, N., Çağatay, M.N., Sakınç, M., Sümengen, M., Şentürk, K., Yaltırak, C., Tchapalyga, A., 1997, Origin of the Sea of Marmara as deduced from the Neogene to Quaternary palaeogeographic evolution of its frame. Int. Geol. Rev. 39, 342–352.

Güçtekin, A., 2017, Geochemical and Petrologic Properties of Intermediate and Acidic Rocks of Hisarlıdağ (Enez-Trakya)Volcanism." Bulletin of the Earth Sciences Application and Research Centre of Hacettepe University, vol. 38, no. 2, p. 141-160.

Güldürek, M., 2019, Trakya Havzası Güneybatı ve Güneydoğusu Senozoyik Çökellerin Mikropaleontolojik İncelemesi ve Tetis-Paratetis İlişkisi. Çukurova Üniversitesi, Ph. D. Thesis, pp. 303p.

Gürcan, Ç. et al.,, 2016, Trakya ve Çevresi Arazi Rehberi, TPAO Raporu.

Gürgey, K., 2009. Geochemical overview and undiscovered gas resources generated from Hamitabat petroleum system in the Thrace Basin, Turkey. Marine and Petroleum Geology, 26(7), pp.1240-1254.

Gürgey, K., Philp, R.P., Clayton, C., Emiroğlu, H. and Siyako, M., 2005, Geochemical and isotopic approach to maturity/source/mixing estimations for natural gas and associated condensates in the Thrace Basin, NW Turkey. Applied Geochemistry, 20(11), pp.2017-2037.

Hilterman, F.J., 2001, Seismic Amplitude Interpretation: No. 4 in Distinguished Instructor Series, Soc. of Expl. Geophys.

Holmes, A.W., 1961, A stratigraphic review of Thrace: TPAO Exploration Group Archieve, unpublished technical report, no: 368.

Hosseini, E., Gholami, R. and Hajivand, F., 2019, Geostatistical modeling and spatial distribution analysis of porosity and permeability in the Shurijeh-B reservoir of Khangiran gas field in Iran. Journal of Petroleum Exploration and Production Technology, 9(2), pp.1051-1073.

Hoşgörmez, H., Yalçın, M.N., 2005, Gas-source rock correlation in Thrace basin, Turkey. Marine and Petroleum Geology 22, 901–916.

Hu, L.Y. and Ravalec-Dupin, M.L., 2005. On some controversial issues of geostatistical simulation. Geostatistics Banff 2004, pp.175-184.

Huvaz, O., Sarikaya, H. & Nohut, Ö.M., 2005, Nature of a regional dogleg pattern in maturity profiles from Thrace basin, northwestern Turkey: A newly discovered unconformity or a thermal anomaly. AAPG Bulletin, 89, 1373-1396.

Iltaf, K.H., Yue, D., Wang, W., Wan, X., Li, S., Wu, S., Liu, R., Weijia, Z., Mehboob, S., Shah, S.A. and Awan, R.S., 2021, Facies and petrophysical modeling of Triassic Chang 6 tight sandstone reservoir, Heshui oil field, Ordos basin, China. Lithosphere, 2021(Special 1).

Isaaks, E. H. and Srivastava, R. M, 1989, An Introduction to Applied Geostatistics.Oxford University Press, New York.

Isaaks, E.H., 1991. The application of Monte Carlo methods to the analysis of spatially correlated data. Stanford University.

Islam, M.A., Yunsi, M., Qadri, S.T., Shalaby, M.R. and Haque, A.E., 2021. Three-dimensional structural and petrophysical modeling for reservoir characterization of the Mangahewa formation, Pohokura Gas-Condensate Field, Taranaki Basin, New Zealand. Natural Resources Research, 30, pp.371-394.

İmik M, 1988, Kırklareli-C2–3 paftası ve İzahnamesi, 1: 100,000 ölçekli Türkiye Jeoloji Haritaları, Maden Tetkik ve Arama Genel Müdürlüğü, 10 s., Ankara

Janssen, P., & Heuberger, P., 1995), Calibration of process-oriented models. Ecological Modelling, 83(1), 55-66.

Karayigit, A.I., Oskay, R.G. and Çelik, Y., 2021, Mineralogy, petrography, and Rock-Eval pyrolysis of late Oligocene coal seams in the Malkara coal field from the Thrace Basin (NW Turkey). International Journal of Coal Geology, 244, p.103814.

Kaşar, S.,Bürkan, K., Siyako, M, Demir, O. 1983, Tekirdağ-Şarköy-Keşan-Enez Bölgesinin Jeolojisi ve Hidrokarbon Olanakları, TPAO Arama Grubu, Arşiv no:1771, Ankara.

Kesgin, Y., Varol, B. 2003, Gökçeada ve Bozcaada'nın Tersiyer jeolojisi (Çanakkale). Türkiye. Maden Tetkik ve Arama Dergis. 126, 49-67.

Keskin, C., 1966, Pınarhisar resif karmaşığı mikrofasiyes incelemesi, Rev. Fac. Scien. Univ. İst., Seri B, 31/3-4, s. 109-146.

Keskin, C., 1971, Pınarhisar alanının jeolojisi, Türkiye Jeoloji Kurumu Bülteni, 14/1, s. 31-84.

Ketin, İ., 1948, Uber die tektonisch-mechanischen folgerungen aus den grossen anatolischen Erdbeben des letzten Dezenniums. Geol. Rundsch. 36, 77–83.

Ketin, İ., 1969, Kuzey Anadolu Fayı hakkında. Bull. MTA 72, 1–24.

Kiaei, H., Sharghi, Y., Ilkhchi, A.K. and Naderi, M., 2015. 3D modeling of reservoir electrofacies using integration clustering and geostatistic method in central field of Persian Gulf. Journal of Petroleum Science and Engineering, 135, pp.152-160.

Kopp, K.O., Pavoni, N., ve Schindler, C., 1969, Geologie Thrakiens IV: Das Ergene-Becken. Beihzum Geol. Jahrb., Heft 76, 136 s., Hannover.

Koson, M., Grover, S. and Economics, E., 2014, Saving Energy, Lowering Bills, and Creating Jobs: An Economic Impact Analysis of Two Statewide Energy Efficiency Program Portfolios.

Krausert, R., and Z. Malal, 1957, Measured cross-section of the Koyunbaba Member: TPAO Exploration Group Archieve, unpublished technical report, no: 1433, 1 p.

Krige D.G., 1966, Two-dimensional weighted moving average trend surfaces for ore valuation, Journal S. African Institute Mining Metallurgy, special symposium vol. p 13, March 1966.

Krige, D. G., 1951, A statistical approach to some basic mine valuation problems on the Witwatersrand. Journal of the Chem., Metal and Mining Soc. of South Africa 52 (6): 119-139.

Labourdette, R., Casas, J. and Imbert, P., 2008, 3D sedimentary modelling of a Miocene Deltaic reservoir unit, Sincor Field, Venezuela: A new approach. Journal of Petroleum Geology, 31(2), pp.135-151.

Lavaud, B., Kabir N., and Chavent G., 1999, Pushing AVO inversion beyond linearized approximation: Journal of Seismic Exploration, 8(3), 279-302.

Lebküchner, R.F., 1974, Beitrag zur Kenntnis des Geologie des Oligozäns von MittelThrakien (Türkie). Bull. Mineral Res. Expl. Ins. Turkey, 83, 1-30.

Li, X., Zhang, J., Liu, L., Fan, Z., Zhang, G. and Li, C., 2016, Three-dimensional reservoir architecture modeling by geostatistical techniques in BD block, Jinhu depression, northern Jiangsu Basin, China. Arabian Journal of Geosciences, 9, pp.1-18.

Liu, L., Zhang, J., Wang, J., Li, C., Yu, J., Zhang, G., Fan, Z., Wei, G., Sun, Z., Xue, H. and Yu, T., 2015, Geostatistical modeling for fine reservoir description of Wei2 block of Weicheng oilfield, Dongpu depression, China. Arabian Journal of Geosciences, 8, pp.9101-9115.

Matheron, G., 1963. Traité de géostatistique appliquée. 2. le krigeage. Editions Technip.

Matheron, G., 1965, Les variables régionalisées et leur estimation, Masson, Paris.

McCormack, M.P., 1991, Neural networks in the petroleum industry. In SEG Technical Program Expanded Abstracts 1991 (pp. 728-731). Society of Exploration Geophysicists.

Morozov, Igor B., and Ma, J., 2009, Accurate Poststack Acoustic-impedance Inversion by Well-log Calibration: Geophysics, 74(5), R59-R67.

Moslow, et al., 2014, Fine grained turbidite reservoir facies of the Kesan Group tight gas exploitation in the Thrace basin of N.W. Turkey. In: CSPG Core Conference, Calgary, Ca.

Nazarpour, A., Shadizadeh, S.R. and Zargar, G., 2014, Geostatistical modeling of spatial distribution of porosity in the Asmari Reservoir of Mansuri oil field in Iran. Petroleum science and technology, 32(11), pp.1274-1282.

Nichols, G., 2009. Sedimentology and stratigraphy. John Wiley & Sons.

N.V. Turkse Shell, 1972, I no'lu Marmara petrol bölgesinde AR/NTS/832, 833, 835, 836, 997, 998 hak sıra no'lu arama ruhsatlarına ait terk raporu: TPAO Exploration Group Archieve, unpublished technical report, no: 769.

Okay A.I., Özcan E., Cavazza W., Okay N. & Less G., 2010, Basement types, Lower Eocene series, Upper Eocene olistostromes and the initiation of the southern Thrace Basin, NW Turkey. Turkish Journal of Earth Sciences 19, 1–25.

Okay AI, Satir M, Maluski H, Siyako M, Monie P, Metzger R, Akyüz A, 1996, Paleo- and Neo-tethyan events in northwestern Turkey: geologic and geochronologic constraints. In: Yin A, Harrison TM (eds) The tectonic evolution of Asia. Cambridge University Press, Cambridge, pp 420–441.

Okay, A. I., Siyako, M., Bürkan, K. A., 1990, Biga Yarımadası'nın Jeolojisi ve Tektonik Evrimi, Türkiye Petrol Jeologları Derneği Bülteni, 2/1, 83-121.

Olea, R.A. ed., 1991. Geostatistical glossary and multilingual dictionary (No. 3). Oxford University Press on Demand.

Othman, A., Metwaly, F., Fathy, M. and Salama, A., 2022, Use of PNN and Post Stack Inversion to Predict Reservoir Characterization in the Mediterranean Sea, Egypt, Sapphire Field.

Paréjas, E., 1939, Etude geologiqe des lignites de thrace. Maden Tetkik ve Arama Enstitüsü, yayınlanmamış teknik rapor, no. 981.

Pendrel, John, 2001, Seismic Inversion – The Best Tool for Reservoir Characterization: Canadian Society of Exploration Geophysicists, 26(1), 18-24.

Perinçek, D., 1987, Trakya Havzası renç fay zonunun sismik özellikleri. Türkiye 7th Petrol Kongresi, pp. 11–21.

Perinçek, D., 1991, Possible strand of the North Anatolian Fault in theThrace Basin, Turkey: an interpretation: American Association of Petroleum Geologists Bulletin, v. 75, p. 241-257.

Perinçek, D., Nurdan, A., Karatut, Ş. and Erensoy, E., 2015. Danişmen Formasyonu Stratigrafisi ve Birim İçindeki Linyit Düzeylerinin Havzadaki Dağılımı, Trakya Havzası, Türkiye. Türkiye Jeoloji Bülteni, 58(1), pp.19-62.

Pettijohn, F.J., Potter, P.E. & Siever, R., 1987, Sand and Sandstone. Springer-Verlag, New York.

Piessens, K., Barros, R., Dirix, K., Deckers, J., ten Veen, J., Debacker, T.N. and Jähne-Klingberg, F., 2020, May. Structural framework: a new way to organise and communicate geological information. In EGU General Assembly Conference Abstracts (p. 21081).

Pranter, M.J., Ellison, A.I., Cole, R.D. and Patterson, P.E., 2007, Analysis and modeling of intermediate-scale reservoir heterogeneity based on a fluvial point-bar outcrop analog, Williams Fork Formation, Piceance Basin, Colorado. AAPG bulletin, 91(7), pp.1025-1051.

Pranter, M.J., Vargas, M.F. and Davis, T.L., 2008, Characterization and 3D reservoir modelling of fluvial sandstones of the Williams Fork Formation, Rulison field, Piceance basin, Colorado, USA. Journal of Geophysics and Engineering, 5(2), pp.158-172.

Pyrcz, M. J. and Deutsch, C.V., 2014, Geostatistical Reservoir Modeling, 2nd Edition, Oxford University Press, 448 pp.

Renoux, P. and Bouteldja, M., 2010, TPAO, Ankara, pp. 1–52, Reservoir Facies Characterisation Yulaflı and Construction of the Reservoir Simulation Model.

Rutherford, S. R., and Williams, R. H., 1989, Amplitude versus-offset variations in gas sands: Geophysics, 54, 680-688.

Sacchi, Q., Borello, E.S., Weltje, G.J. and Dalman, R., 2016, Increasing the predictive power of geostatistical reservoir models by integration of geological constraints from stratigraphic forward modeling. Marine and Petroleum Geology, 69, pp.112-126.

Sakınç, M., Yaltırak, C., and Oktay, F.Y., 1999, Palaeogeographical evolution of the Thrace Neogene basin and the Tethys-Paratethys relations at northwestern Turkey (Thrace). Palaeo. Palaeo. Palaeo, 153, 17-40.

Sarı, R.., Türkecan, A., Dönmez, M., Küçükefe, Ş., Aydın, Ü. and Özmen, Ö., 2015, The geology of Gökçeada (Çanakkale). Bulletin of the Mineral Research and Exploration, 150(150), pp.1-18.

Sheriff, R. E., 2002, Encyclopedic dictionary of applied geophysics. IV. Edition. SEG, 429 p.

Shuey, R.T., 1985, A simplification of Zoeppritz Equations: Geophysics, 50, 609-814.

Siyako, M. and Huvaz, O., 2007, Eocene stratigraphic evolution of the Thrace Basin, Turkey. Sedimentary Geology, 198, 75-91.

Siyako, M., 2005, Trakya Ve Yakin Cevresinin Tersiyer Stratigrafisi. TPAO.

Siyako, M., 2006, Lignitic sandstones of the Trakya Basin. Bulletin of the Mineral Research and Exploration, 132, 63-72.

Siyako, M., 2006, Trakya havzası Tersiyer kaya birimleri. Trakya Bölgesi Litostratigrafi Birimleri'nde. Maden Tetkik ve Arama Genel Müdürlüğü, Stratigrafi Komitesi, Litostratigrafi Birimleri Serisi – 2, 43-83, Ankara.

Siyako, M., 2006a, Trakya Havzası'nın linyitli kumtaşları. Maden Tetkik Arama Dergisi 132, 63-73.

Siyako, M., 2006b, Trakya Bölgesi Litostratigrafi Birimleri (Tersiyer Bölümü). Stratigrafi Komitesi, Litostratigrafi Birimleri Serisi-2. Maden Tetkik ve Arama Genel Müdürlüğü yayını. 70 s.

Siyako, M., Bürkan, K.A. and Okay, A.İ., 1989, Biga ve Gelibolu yarımadalarının Tersiyer jeolojisi ve hidrokarbon olanakları. TPJD Bülteni, 1(3), pp.183-199.

Soleimani, M. and Jodeiri Shokri, B., 2015, 3D static reservoir modeling by geostatistical techniques used for reservoir characterization and data integration. Environmental Earth Sciences, 74, pp.1403-1414.

Soleimani, M., Jodeiri Shokri, B. and Rafiei, M., 2017. Integrated petrophysical modeling for a strongly heterogeneous and fractured reservoir, Sarvak Formation, SW Iran. Natural Resources Research, 26, pp.75-88.

Strebelle, S., Payrazyan, K. and Caers, J., 2003, Modeling of a deepwater turbidite reservoir conditional to seismic data using principal component analysis and multiple-point geostatistics. Spe Journal, 8(03), pp.227-235.

Sünnetçioğlu, M.A., 2008, A sequence stratigraphic approach to the depositional history analysis of the upper eocene sedimentary succession, northwest of the thrace basin, Turkey, METU, 2008, pp. 1–263.

Şen, Ş. and Yıllar, S., 2016, Nature, Genesis, and Significance of the Gaziköy and Kesan Formations (Thrace Basin, Turkey): Eocene Turbidites and Olistostromes Formed on an Active Tethyan Margin. The Journal of Geology, 124(4), pp.463-479.

Şengör, A.M.C., 1979, The North Anatolian Transform Fault. Its age offset and tectonic significance. J. Geol. Soc. London 136, 269–282.

Şengör, A.M.C., Görür, N., ¸ Şaroğlu, F., 1985, Strike-slip faulting and related basin formation in zones of tectonic escape: Turkey as a case study. Soc. Ecol. Paleontol. Mineral. Spec. Publ. 37, 227–264.

Tapırdamaz, C., Yaltırak, C., 1997, Trakya'nın Senozoyik volkaniklerinin paleomanyetik özellikleri ve tektonik konumu. Bull MTA 119, 27–42.

Ternek, Z., 1949, Geological study of the region of Keşan-Korudağ.

Timur, A., 1968, June. An investigation of permeability, porosity, and residual water saturation relationships. In SPWLA 9th annual logging symposium. OnePetro.

Tixier, M.P., 1949, Evaluation of Permeability from Resistivity Gradient on Electric Logs.

Tolosana-Delgado, R. and Mueller, U., 2021. Geostatistics for Compositional Data with R. Springer.

Turgut, S., Eseller, G., 2000, Sequence stratigraphy, tectonics and depositional History in Eastern Thrace Basin, NW Turkey, Marine and Petroleum Geology, 17, 61-100.

Turgut, S., Türkaslan, M. ve Perinçek, D., 1991., Evolution of the Thrace sedimentary basin and its hydrocarbon prospectivity. Spencer AM (ed) Generation, accumulation, and production of Europe's hydrocarbons. Special Publication of Eurapean Association of Petroleum Geoscientists, 1, 415-437.

Udden, J.A., 1914, Mechanical composition of clastic sediments. Geological Society of America Bulletin, 25, 655–744.

Umut M., Kurt Z., İmik M., Özcan I., Sarıkaya H., Saraç G., 1983, Tekirdağ, Silivri(İstanbul), Pınarhisar alanının jeolojisi, MTA Derleme Rapor no: 7349.

Uygur, E., et al., 2000, Doğu Trakya Projesi Değerlendirme Raporu. TPAO, Ankara, pp. 112–182.

Ünal, O. T., 1967, Trakya jeolojisi ve petrol imkanları: TPAO Exploration Group Archieve, unpublished technical report, no: 391, 80 p, Ankara.

Van Baaren, J., 1979, Quick-look permeability estimates using sidewall samples and porosity logs. Paper presented at the 6th annual European logging symposium transactions.

Varol B., Baykal M. and Ayyıldız T., 2009, Sedimentological-stratigraphical evaluation of Tertiary carbonates (Soğucak Formation) of Thrace Basin (Bozcaada-Kiyiköy). Bulletin of the Mineral Research and Exploration 139, 1–15.

Wentworth, C.K., 1922, A scale of grade and class terms for clastic sediments. Journal of Geology, 30, 377–394.

Wyllie, M.R.J. and Rose, W.D., 1950, Some Theoretical Considerations Related to Quantitative Evaluation of Physical Characteristics of Reservoir Rocks from Electrical Log Data. Transactions of the AIME, 189, 105-118.

Yaltırak, C., 1995, Gaziköy - Mürefte (Tekirdağ) arasının sedimanter ve tektonik özellikleri: The Association of Turkish Petroleum Geologists Bulletin, v. 6, p. 93-112.

Yamamoto, J.K., 2005, Correcting the smoothing effect of ordinary kriging estimates. Mathematical geology, 37, pp.69-94.

Yılmaz, Y., and A. Polat, 1998, Geology and evolution of the Thrace volcanism, Turkey: Acta Volcanologica, v. 10, p. 293-303.

Yılmaz, Y., Tüysüz, O., Yiğitbaş, E., Can Genç, S. and A.M.C. Şengör, 1997, Geology and tectonic evolution of the Pontides, in Robinson, A. G., ed., Regional and Petroleum Geology of the Black Sea and Surrounding Region: American Association of Petroleum Geologists Memoir 68, p. 183-226.,

Yilmaz, K., Umul, B., Davis, J. and Nilson, G., 2016, Tight gas development in the Mezardere Formation, Thrace Basin Turkey. Journal of Natural Gas Science and Engineering, 33, pp.551-561.

Zhao, S., Zhou, Y., Wang, M., Xin, X. and Chen, F., 2014, Thickness, porosity, and permeability prediction: comparative studies and application of the geostatistical modeling in an Oil field. Environmental Systems Research, 3, pp.1-24.

Zoeppritz, K., 1919, On reflection and propagation of seismic waves: Gottinger Nachrichten, 1, 66-8.

CURRICULUM VITAE

Surname, Name: Arpacı, Taner

EDUCATION

Degree	Institution	Year of Graduation
MS	Tulsa University, Geoscience	2013
BS	Ankara University, Geophysical Engineering,	2008
High School	Mamak Anadolu High School, Ankara	2002

WORK EXPERIENCE

Company	Position	Year
TPAO	QI Manager	2022-Present
TPAO	Reservoir Geophysicist	2013-2022

FOREIGN LANGUAGES

English

PUBLICATIONS

1. Arpacı, Taner, and Hüseyin Özdemir. “Step-out Well Positioning Using Hydrocarbon Indicators from Seismic Inversion: A Case Study.” First Break, vol. 38, no. 1, 2020, pp. 43–51., doi:10.3997/1365-2397.fb2020001.

2. Arpaci, T., and H. Ozdemir. “Step-out Well Position Optimisation Using Inverted Hydrocarbon Indicators.” 78th EAGE Conference and Exhibition 2016, 2016, doi:10.3997/2214-4609.201601557.

3. Arpaci, Taner, and Kumar Ramachandran. “Comparison of AVO, Prestack Impedance Inversion, and Poststack Impedance Inversion: Lithology and Pore Fluid Discrimination in the Scotian Basin, Nova Scotia, Canada.” SEG Technical Program Expanded Abstracts 2013, 2013, doi:10.1190/segam2013-0626.1. 2. Eryaman Y., Mert M. "Borik